2014

Cosmology

Sponsored by

. CNRS (Centre National de la Recherche Scientifique)
. FNRS (Fond National de la Recherche Scientifique)
. BSP (Belgian Science Policy)

49th Rencontres de Moriond

La Thuile, Aosta Valley, Italy – March 22-29, 2014

2014 Cosmology

© Published by ARISF, 2014

ISBN : 978-2-9546400-5-1

web

All rights reserved. This book, or parts thereof, may not be reproduced in any form or by any means, electronic or mechanical, including photocopying, recording or any information storage and retrieval system now known or to be invented, without written permission from the publisher.

Proceedings of the 49th RENCONTRES DE MORIOND

Cosmology

La Thuile, Aosta Valley Italy *March 22-29, 2014*

2014

Cosmology

edited by

Etienne Augé,
Jacques Dumarchez
and
Jean Trân Thanh Vân

The 49th Rencontres de Moriond

2014 Cosmology

was organized by :

Etienne Augé (IN2P3, Paris)
Jacques Dumarchez (LPNHE, Paris)

with the active collaboration of :

P. Astier (Paris)
F. Bernardeau (Saclay)
K. Ganga (Paris)
Y. Giraud-Héraud (Paris)
J.-M. Le Goff (Saclay)
Ch. Magneville (Saclay)
H. McCracken (Paris)
O. Perdereau (Orsay)
J. Silk (Oxford)
B. Wandelt (Paris)

2014 RENCONTRES DE MORIOND

The 49th Rencontres de Moriond were held in La Thuile, Valle d'Aosta, Italy.

The first meeting took place at Moriond in the French Alps in 1966. There, experimental as well as theoretical physicists not only shared their scientific preoccupations, but also the household chores. The participants in the first meeting were mainly french physicists interested in electromagnetic interactions. In subsequent years, a session on high energy strong interactions was added.

The main purpose of these meetings is to discuss recent developments in contemporary physics and also to promote effective collaboration between experimentalists and theorists in the field of elementary particle physics. By bringing together a relatively small number of participants, the meeting helps develop better human relations as well as more thorough and detailed discussion of the contributions.

Our wish to develop and to experiment with new channels of communication and dialogue, which was the driving force behind the original Moriond meetings, led us to organize a parallel meeting of biologists on Cell Differentiation (1980) and to create the Moriond Astrophysics Meeting (1981). In the same spirit, we started a new series on Condensed Matter physics in January 1994. Meetings between biologists, astrophysicists, condensed matter physicists and high energy physicists are organized to study how the progress in one field can lead to new developments in the others. We trust that these conferences and lively discussions will lead to new analytical methods and new mathematical languages.

The 49th Rencontres de Moriond in 2014 comprised three physics sessions:

- March 15 - 22: “Electroweak Interactions and Unified Theories”
- March 22 - 29: “QCD and High Energy Hadronic Interactions”
- March 22 - 29: “Cosmology”

We thank the organizers of the 49^{th} Rencontres de Moriond:

- A. Abada, E. Armengaud, J. Conrad, S. Davidson, P. Fayet, J.-M. Frère, P. Hernandez, L. Iconomidou-Fayard, P. Janot, M. Knecht, J. P. Lees, S. Loucatos, F. Montanet, L. Okun, J. Orloff, A. Pich, S. Pokorski, V. Tisserand, D. Wood for the "Electroweak Interactions and Unified Theories" session,
- E. Augé, E. Berger, S. Bethke, A. Capella, A. Czarnecki, D. Denegri, N. Glover, B. Klima, M. Krawczyk, L. McLerran, B. Pietrzyk, L. Schoeffel, Chung-I Tan, J. Trân Thanh Vân, U. Wiedemann for the "QCD and High Energy Hadronic Interactions" session,
- Pierre Astier, Francis Bernardeau, Jacques Dumarchez, Ken Ganga, Yannick Giraud-Héraud, Jean-Marc Le Goff, Christophe Magneville, Henry McCracken, Olivier Perdereau, Joe Silk, Ben Wandelt for the "Cosmology" session

and the conference secretariat and technical staff:

V. de Sá-Varanda and F. Amat, C. Bareille, I. Cossin, G. Dreneau, G. Perrin, S. Vydelingum.

We are also grateful to Francesco Cante, Ida Liseno, Ilir Isufi, Francesco Quinto and the Planibel Hotel staff who contributed through their hospitality and cooperation to the well-being of the participants, enabling them to work in a relaxed atmosphere.

The Rencontres were sponsored by the Centre National de la Recherche Scientifique, the Fonds de la Recherche Scientifique (FRS-FNRS), the Belgium Science Policy and the National Science Foundation. We would like to express our thanks for their encouraging support.

It is our sincere hope that a fruitful exchange and an efficient collaboration between the physicists and the astrophysicists will arise from these Rencontres as from previous ones.

E. Augé, J. Dumarchez and J. Trân Thanh Vân

Contents

Foreword

1. CMB

2. Clusters / SZ

3. Dark Energy

4. 21 cm

5. Dark Matter

6. Neutrinos and Cosmology

7. Theory

8. Future Programs in Cosmology

9. Posters

1.
CMB

The Planck nominal mission data

C. RENAULT on behalf of the Planck collaboration
LPSC, Université Grenoble-Alpes, CNRS/IN2P3, 53 rue des Martyrs, 38026 Grenoble cedex, France

The European Space Agency's Planck satellite, dedicated to studying the early universe and its subsequently evolution, was launched on 14 May 2009, and has been surveying the microwave and submillimetre sky continuously since August 2009. In March 2013, ESA and the Planck Collaboration publicly released the initial cosmology products based on the first 15.5 months of Planck operations [1]. Each of the two instrument consortia operated their respective high or low frequency instrument and processed all the data into usable scientific products. At the end of the mission the consortia delivered the final products to ESA, which archived and distributed them to the community via the Planck Legacy Archive (PLA). This proceedings briefly summarizes the products. The PLA can been accessed from the ESA or LAMBDA websites while all needed information are gathered in the Explanatory Supplement [2].

1 Instrument parameters and frequency maps

The Planck payload has two instruments on board: the high frequency one (HFI) and the low frequency one (LFI). LFI operates 22 radiometers cooled down at 20 K and measuring the sky at in 3 frequency bands centered at 30, 44 and 70 GHz. HFI detectors are 52 bolometers cooled down at 0.1 K and measuring the sky at in 6 frequency bands centered at 100, 143, 217, 353, 545 and 857 GHz. The RIMO, or Reduced Instrument Model is a FITS file containing selected instrument characteristics that are needed by users who work with the released data products. For instance it provides the focal plane geometry, beam description, band averaged spectral response, noise characteristics.

The timelines of both instruments are analyzed with a set of dedicated pipelines. The data analysis mainly consists of separating the instrumental contribution from the astrophysical signal, characterizing the beams and calibrating the maps. Fig. 1 presents the calibrated frequency maps in intensity. No data in polarization and no timeline were released in 2013.

2 The Planck catalogues

Many types of compact sources are expected in the Planck data: Galactic sources, radio galaxies, infrared galaxies, and clusters of galaxies. In Mars of 2013, the Planck Catalogue of Compact

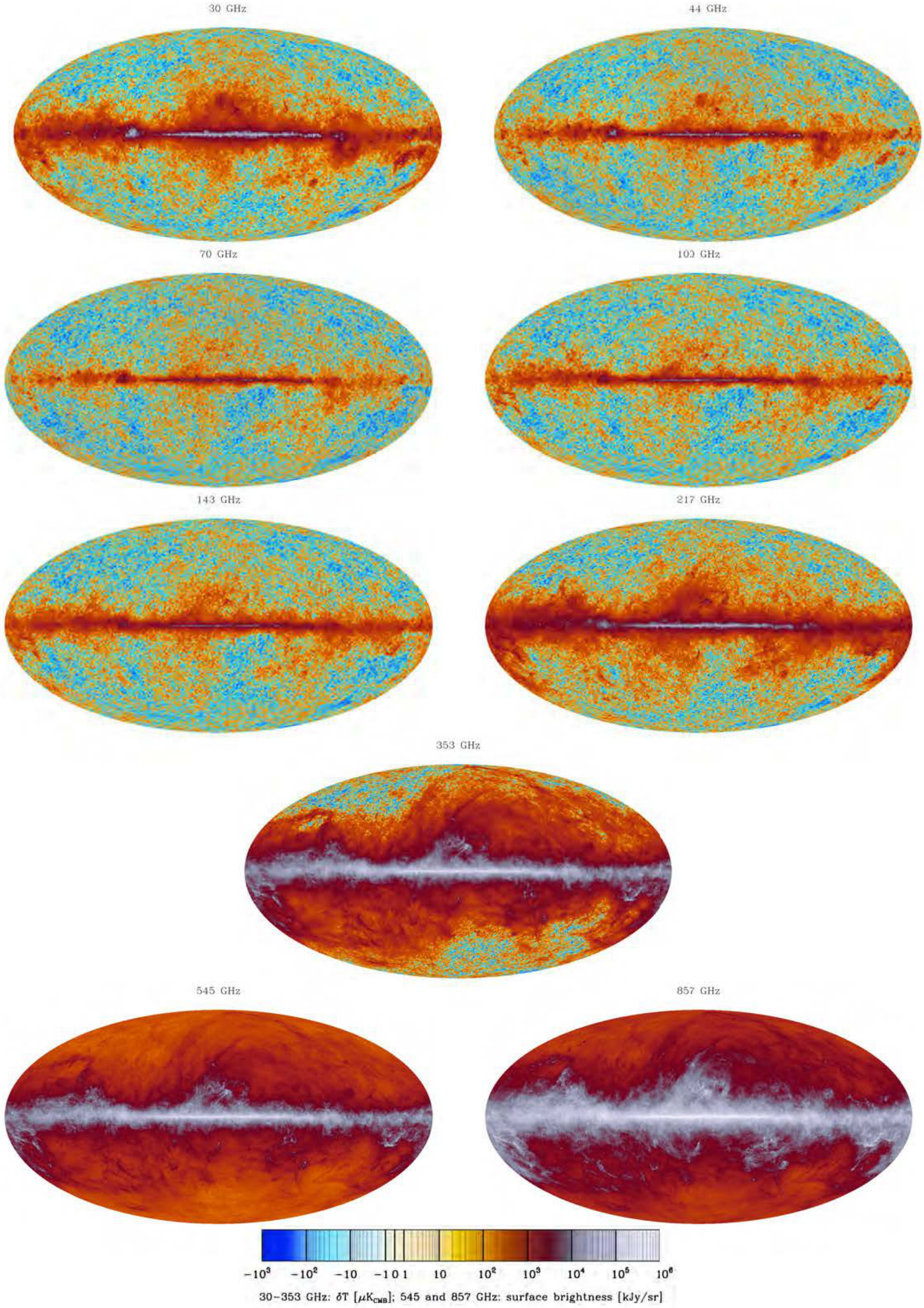

Figure 1 – The nine frequency maps in intensity from the Planck nominal mission data.

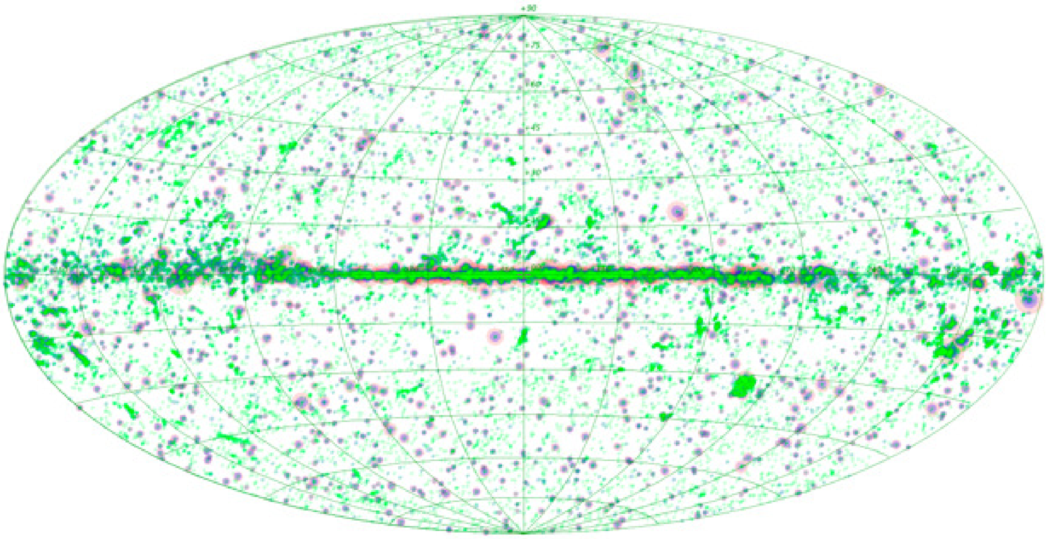

Figure 2 – Position and color of the compact sources of the Planck catalogue. The pink circles are proportional to the 30 GHz intensity, violet to the 143 GHz intensity and green to the 857 GHz intensity. So the radio sources appear in pink while the cold cores appear in green.

Sources (PCSC [3], Fig. 2), which included a catalogue of compact sources extracted independently from each map, and the Planck catalogue of sources detected via the Sunyaev-Zeldovich (SZ) effect have been published [4].

3 The Planck component maps

From the frequency maps, the collaboration has developed a set of dedicated pipelines optimized to extract the main components: zodiacal [5] and CO [6] emissions and of course the CMB [7]. Note that the cosmic infrared background (CIB) and the diffuse Sunyaev-Zeldovich (SZ) emissions have also been extracted for dedicated analyses but these maps are not released. The diffuse emission of the Galactic dust is described by the radiance, temperature, spectral index as well as the optical depth at 353 GHz maps [8]. Example of these products are shown in Fig. 3.

The map of CMB lensing potential is derived by minimum-variance using 143 and 217 GHz maps on about 70 % of the sky [9]. It is one of the main Planck advantages compared to the other CMB experiments as it provides information on the large-scale structures distribution over a large fraction of the sky a few billion years after the CMB emission from the CMB itself.

4 Cosmological products

While the non-gaussianity studies are based directly on the CMB map, most of other studies of the information embedded in the CMB are based on frequency maps.

To allow people to reproduce the Planck collaboration results, the masks for Galactic emission and point-sources with different thresholds and apodization schemes are provided as well as the effective beam description. These masks are optimized for each purpose, the foreground contamination and the sensitivity to the apodization depending on each study.

The power spectra are obtained from the frequency maps without any component separation [10]. Our Galaxy and detected point-sources are masked. The LFI map power spectra are based on 60% of the sky. For HFI, more than 40% of the sky are used to estimate auto- and cross-power spectra between SWB (Spiderweb bolometers) and between SWB and sub-set of detectors at 100, 143 and 217 GHz. The unbinned power spectra cover the multipole range [2-3508].

The likelihood code (and the associated data) is used to compute the likelihood of a model

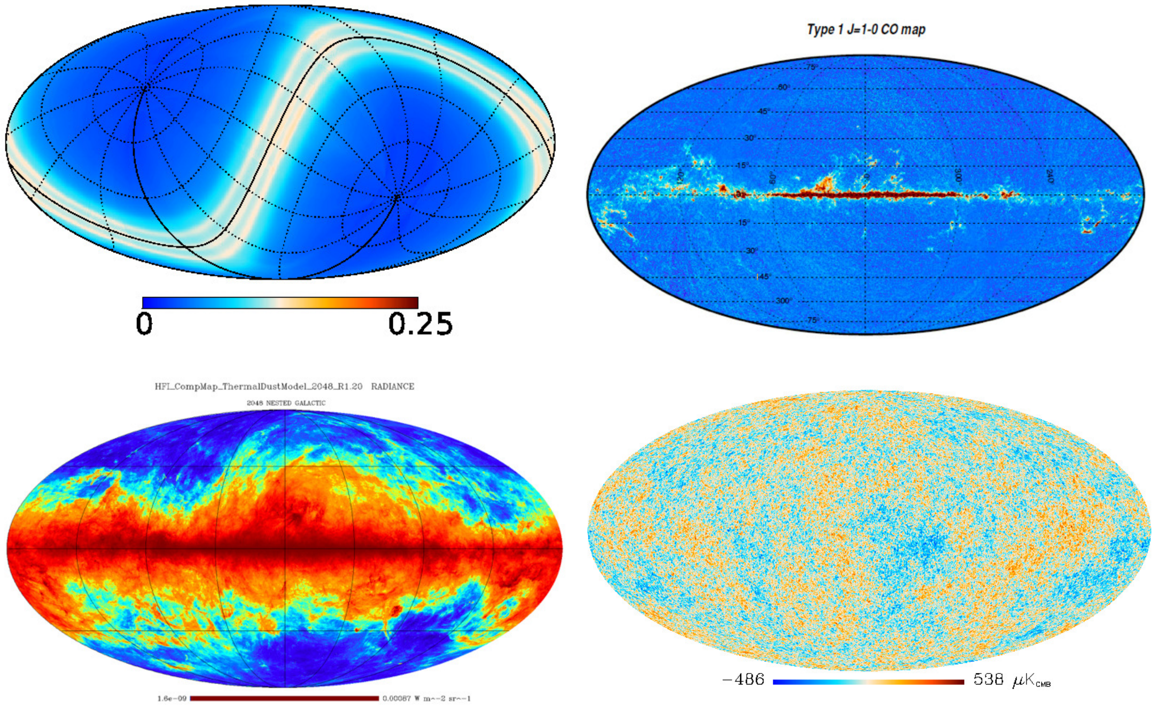

Figure 3 – From left to right, top to bottom: maps of the zodiacal emission at 545 GHz, the 1->0 CO line, radiance of the dust and the CMB.

that predicts the CMB and lensing power spectra, with some foreground and instrumental parameters. The Planck CMB power spectrum is estimated from the frequency maps and the 6-component LambdaCDM cosmological model. The CIB, unresolved point-sources, unresolved thermal and kinetic SZ emissions are taken into account via 11 nuisance parameters. Two methods are applied, optimized for the low and high multipoles. The multipole range [2-49] is constrained using the Commander method applied on data from 30 to 353 GHz over 91 % of the sky. The multipole range [50-2479] is constrained using the CAMspec method applied on data of about 58 % of the sky at 100 GHz and 37 % of the sky at 143 and 217 GHz. The CMB power spectrum and the likelihood are available from the PLA, in addition to a third likelihood in the multipole range [2-32] based on Planck temperature and WMAP polarization data.

A set of tables with the cosmological parameters arising from Planck data alone, plus a selection of other data sets are also distributed[11]. The number of references to this paper (1844 citations the 2014/05/26) shows that these values are widely used by the cosmology, neutrino physics, particle physics communities.

References

1. Planck collaboration, Astronomy & Astrophysics **accepted**, arXiv:1303.5062 (2013).
2. http://www.sciops.esa.int/wikiSI/planckpla, 2013.
3. Planck collaboration, Astronomy & Astrophysics **accepted**, arXiv:1303.5088 (2013).
4. Planck collaboration, Astronomy & Astrophysics **accepted**, arXiv:1303.5089 (2013).
5. Planck collaboration, Astronomy & Astrophysics **accepted**, arXiv:1303.5074 (2013).
6. Planck collaboration, Astronomy & Astrophysics **accepted**, arXiv:1303.5073 (2013).
7. Planck collaboration, Astronomy & Astrophysics **accepted**, arXiv:1303.5072 (2013).
8. Planck collaboration, Astronomy & Astrophysics **submitted**, arXiv:1312.1300 (2013).
9. Planck collaboration, Astronomy & Astrophysics **accepted**, arXiv:1303.5077 (2013).
10. Planck collaboration, Astronomy & Astrophysics **accepted**, arXiv:1303.5075 (2013).
11. Planck collaboration, Astronomy & Astrophysics **accepted**, arXiv:1303.5076 (2013).

PLANCK LENSING RESULTS: MEASUREMENT, COSMOLOGICAL IMPLICATIONS AND FORESEEN IMPROVEMENT

L. PEROTTO
Laboratoire de Physique Subatomique et de Cosmologie, Université Grenoble Alpes, CNRS/IN2P3, 53, rue des Martyrs, Grenoble, France

Planck provided the first nearly full-sky map of the gravitational potential integrated along the line of sight, in performing a Cosmic Microwave Background (CMB) lensing reconstruction in the CMB temperature map. This lensing map consists in a noisy yet invaluable tracer of the Dark Matter of the Universe back to the last scattering surface. It correlates with other matter probes such as external galaxy surveys, the Planck Cosmic Infrared Background estimate or the Planck CMB temperature via the Integrated Sachs-Wolfe effect, confirming a late stage of Dark Energy domination in the Universe history. Lensing results had several important impact on the Planck cosmological model, improving Planck sensitivity to late-evolution parameters, such as the neutrino mass, which would have been otherwise poorly constraint from Planck alone, or helping in breaking parameter degeneracies. In the next Planck 2014 data release, the lensing reconstruction will benefit from both two more surveys as well as four additional independent estimates using the polarisation data, with a forecast precision improvement of 35%. Moreover, Planck should provide a full-sky estimate of the lensing induced B-mode of polarization over a scale interval unreachable by ground experiments.

1 Introduction

The intervening matter slightly deflects the CMB photons on their path from the last scattering surface to us. Through this gravitational lensing effect, the CMB encodes all the information about Universe's Dark Matter distribution and structure formation, with a maximum sensitivity to linear growing structures at high redshift ($z \sim 2$) (See e. g. Lewis et al. [17] for a review).

Although described theoretically since the late 1980's (Blanchard et al. [2]), it remained undetected for near 30 years. Because of the physical scales involved in the lensing effect, which causes deflection angles at the arc minutes scale that are correlated over several degrees, its detection is experimentally demanding. The WMAP satellite reports the first detection by resorting to correlation to external galaxy surveys [34, 10, 11]. These pioneer results were limited due to WMAP angular resolution of the order of the tens arc minutes. The internal detection relying upon CMB data alone was reached by series of ground experiments, and in particular, the first reconstruction of the lensing potential using the non-Gaussianities that the lensing effect imprints in the CMB map was reported by the ACT [4] and the SPT [35] in the early 2010's.

The Planck satellite was measuring the lensing shortly after the beginning of its data integration using a local method on its first uncompleted survey. However, the choice were made to deliver a mature lensing map on nearly all the sky as part of the 2013 data release [26]. This map, which is one of the most striking achievement of the Planck collaboration, will last for decades as the reference within the domain. In addition to the experimental performance aspects, the lensing reconstruction opened a window to several new studies: probing the Dark matter distribution using the cross-correlation between the lensing map and other external Dark Matter tracers [26, 7]; probing the early star formation history via the correlation to the Cosmic Infrared

Background (CIB)[27]; probing the late Dark Energy domination stage via the measure of Integrated Sachs-Wolfe (ISW) effect[28]. Finally, as it confers to Planck a sensitivity to phenomena occurring well after the recombination epoch, the lensing reconstruction had several important implications on the cosmological model drawn up by Planck[25]. In particular, it helps in breaking degeneracies and in constraining late-evolution parameters, such as the neutrino mass[14].

By the end of 2014, the Planck collaboration will publish an update of its cosmological results, based on the final data release including the whole integration time and the polarization. In this context, the CMB lensing will still occupy a place of choice. As for the temperature, the polarization observables are perturbed by the lensing effect, and encode the gravitational potential information. This property can be exploited to further improve the lensing reconstruction precision, in addition to the statistical leverage improvement. Remarkably, the lensing induces a secondary B-mode of polarization, due to the E-mode leakage, which dominates over the primordial B-mode at sub-degree scales. Planck should provide a high-significance measure of the lensing-induced B-mode, including in the intermediate multipole range ($\ell < 500$) which is hardly reachable to ground experiments.

After some basics on the lensing effect, the reconstruction methodology for Planck will be reviewed. The second part is devoted to the main results, including the most important systematic tests that was performed to assess their robustness. The third part will give a quick overview of the cosmological impact. Finally, the Planck 2014 lensing results are forecast, including the foreseen improvement of the reconstruction and the lensing B-mode measurement.

2 Methodology

This section gives a brief review of the lensing effect and its reconstruction using quadratic estimators. Then the problematic of a real-world reconstruction in the Planck data will be addressed and the chosen methodological solutions presented.

2.1 Reconstructing the gravitational lensing effect

The gravitational lensing causes a remapping of the CMB temperature anisotropies, such that the *lensed* temperature $T(\vec{n})$ in the direction $\vec{n}$ is equal to the *unlensed* temperature $T\left(\vec{n} + \nabla\phi(\vec{n})\right)$ in a slightly deflected direction. $\phi(\vec{n})$ is the CMB lensing potential defined as the line-of-sight integral of the gravitational potential back to the last scattering surface with a broad kernel, such that linear growing structures at a redshift $z \sim 2$ are the most efficient deflectors. For a complete review, see e.g.[17].

The CMB lensing has some important signatures on the CMB observable, smoothing the angular power spectrum at high multipole range (e. g. 10% effect at $\ell = 2000$), and inducing some non-Gaussianities within the map. To first order of the lensing potential, it results in a correlation between the observed temperature and the gradient of the (unlensed) temperature. Building upon this property, *Quadratic Estimators* have been proposed to reconstruct the lensing potential[13, 18]. More precise estimators have also been proposed[9], however, at the Planck sensitivity, a QE is very close to the optimality. The power spectrum of the lensing potential estimated using the QE realises a measure of the 4-points information and provides an estimate of the lensing potential power spectrum after the subtraction of the Gaussian noise (unconnected part of the 4-point correlator), which is dominant at all scale for Planck.

2.2 Real-world reconstruction in Planck

Performing the lensing reconstruction in Planck data is a challenge, as any effects inducing anisotropies or non-Gaussianities at the map level can yield a spurious lensing signal.

First, the early steps of data processing from the time-lines to the maps have a critical impact[22], in particular the time constant deconvolution (affecting the beam shape) and the glitches removal (affecting the noise statistical properties). Right after the instrumental systematic effects, the astrophysical foregrounds emissions are the next major concern.

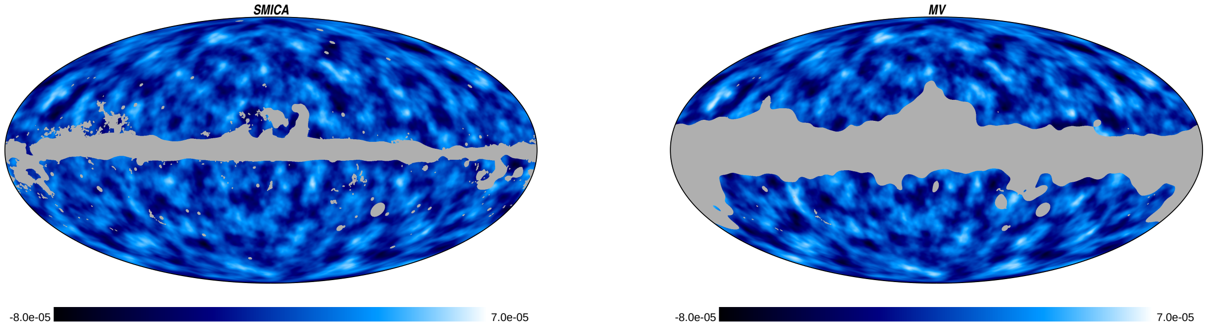

Figure 1 – Planck's Wiener-filtered gravitational potential map $\phi^{\rm WF}_{LM} \equiv C^{\phi}_{L}/N^{(0)}_{L}\,\hat{\phi}_{LM}$ using the SMICA foreground cleaned CMB map (left) and the minimum-variance combination of the 143 and 217 GHz maps (right). Whereas noise dominated at all scales, these maps encode the integrated Dark Matter distribution back to $z \sim 1100$ [26]

The Planck's frequency coverage capability allows to correct for the foreground emission, either in subtracting for a template obtained from the highest frequency maps or in using a more refined component separation algorithm [23]. However, the most contaminated regions of the sky must nevertheless be cut out. In Planck 2013 lensing analysis [26], meticulous attention has been paid in the mask making, accounting for every detected compact objects from the Planck catalogs [30, 31] and for the galactic diffuse emission using a thresholding on the 857 GHz map and on the carbon monoxides lines map [24].

Whereas resorting to a sky mask is mandatory, it yields a major systematic effect that must be accounted for. First of all, the masks, along with the other sources of statistical anisotropies, such as spacially inhomogeneous noise or elliptic beam, induce a spurious signal at the ϕ map level. This extra contribution, referred to as the *mean field* noise, can be estimated as an average over unlensed Monte-Carlo simulations, and then subtracted out from the ϕ estimate. Secondly, at the lensing power spectrum level, the mask impact is further mitigated by a pre-processing of the ϕ estimate that consists of an apodisation, which reduces the side lobes of the mask window function, and a whitening filter, which reduces the leakage due to these residual side-lobes [?]. Finally, the Planck lensing power spectrum estimator is given by

$$\widehat{C}^{\phi}_{L} = \frac{1}{N_{\rm dof}} \sum_{M} |\tilde{\phi}_{LM}|^{2} - N^{(0)}_{L} - N^{(mc)}_{L} - N^{(ps)}_{L} \tag{1}$$

where $N_{\rm dof}$ is the effective number of independent multipoles, $\tilde{\phi}_{LM}$ is the pre-processed version of the mean-field subtracted ϕ estimate, $N^{(0)}_{L}$ the Gaussian noise term, $N^{(mc)}_{L}$ is a residual sub-dominant bias estimated using a lensed Monte-Carlo, and which mostly accounts for the higher order $N^{(1)}_{L}$ correction term [15], and $N^{(ps)}_{L}$ is the small unresolved point sources shot-noise term.

3 Results

In the Planck 2013 lensing analysis [26], three lensing products were obtained and delivered, a map of the gravitational potential, its corresponding angular power spectrum and likelihood function. These results have nourished or led to several other Planck publications. In this section, a concise presentation of the lensing related results is given, along with the most stringent robustness tests that have been performed [26].

3.1 The lensing map

The Planck Collab. [26] exploited the large Planck frequency coverage, primarily as a way to assess the robustness of their estimate against foreground residuals. Several lensing potential reconstructions were performed, first from individual frequency map at 100, 143 and 217 GHz,

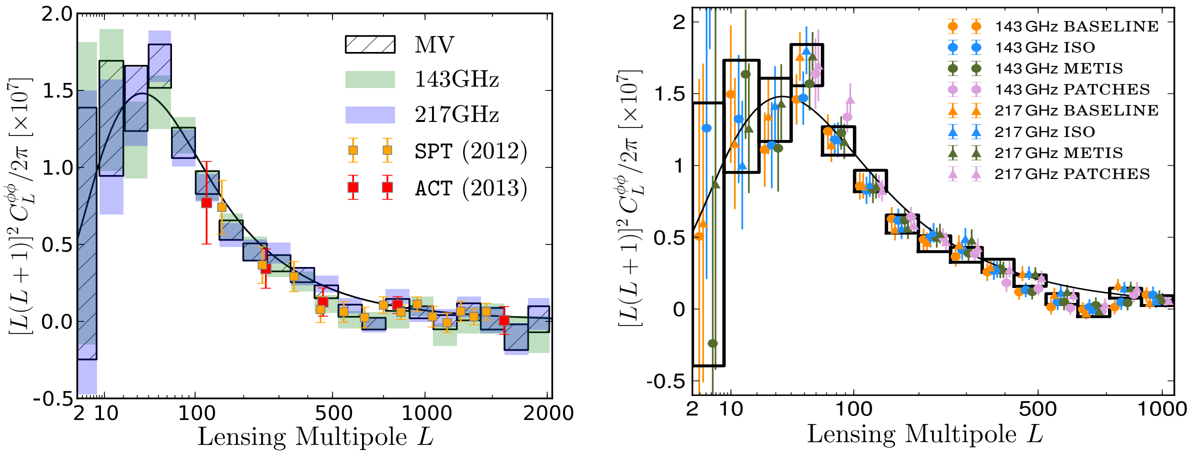

Figure 2 – Planck's lensing potential power spectrum for the minimum variance (MV) combination of 143 and 217 GHz (empty black boxes). Left panel shows a comparison to the reconstructions from the ACT [5] and the SPT [35] as well as the Planck's estimates for the 143 and 217 GHz maps. Right panel shows the C_L^{ϕ} estimates for the 143 and 217 GHz maps using the four analysis pipelines, based on different methodologies of sky cut treatment, that were developed by the Planck Collab. [26] to ensure robustness.

then from a combination of the two last frequency maps and finally from the CMB maps using component separation methods [23], which aim at removing the Galactic emissions to produce CMB maps on the largest possible sky coverage. The estimate from each data set were consistent with each other, indicating a negligible impact of the foreground residuals.

The foreground cleaned CMB maps from the component separation allowed a lensing reconstruction over around 85% of the sky, shown in Fig. 1, compatible within 1σ to the estimates from less aggressive mask. Whereas component separation optimally combined all Planck data to correct for any non-CMB emission, a higher signal-to-noise CMB map can be obtained using a minimum variance (MV) combination of the 143 and 217 GHz maps, after a foreground correction using the 857 GHz map as a dust emission template. The right panel of Fig. 1 shows the highest signal-to-noise reconstruction from the MV combination using a $\sim 30\%$ sky cut. This latter lensing map had been delivered as part of the Planck data release. This map is noise dominated on all scales. However, it is highly correlated with several other large scale structure probes at various redshifts. First, using external data, the Planck Collab. [26] reported significant correlation between the lensing map and the NVSS radio galaxies and quasars survey [3] at $z_{\rm mean} = 1.1$ (20σ), the SDSS Luminous Red Galaxies survey [12] at $z_{\rm mean} = 0.55$ (10σ) and the WISE satellite IR galaxy catalog [36] at $z_{\rm mean} = 0.1$ (7σ). Secondly, The Planck Collab. [27] reported the first (42σ) detection of a correlation between the lensing map and the CIB measured from the 545 GHz Planck map. This result helps in probing the origin of the CIB, which originates from the emission of unresolved star-forming dusty galaxies at high-redshift, and thereby helps in constraining the star formation history. Finally, the first detection of the ISW effect, i.e. the imprint of the large-scale evolving gravitational potential in the temperature map, from the CMB alone was reported by the Planck Collab. [28]. The cross-correlation between the temperature and the lensing potential maps was demonstrated a complementary and competitive approach w.r.t. the methods relying on external large scale structure data. The detection of the ISW effect signs the existence of a Dark Energy domination stage in the late Universe, and is a nuisance to the primordial CMB Non-Gaussianity searches [29].

3.2 The lensing power spectrum

The main Planck lensing result [26] is the angular power spectrum of the gravitational potential $C_L\phi$ that was obtained from the MV based ϕ estimate, using the method outlined in 2.2. The Planck C_L^{ϕ} corresponds to a 25σ detection of the lensing that is consistent with the measure from the ACT[5] and the SPT[35] in the multipole range from $\ell = 100$ to 2000, and in addition, covers the high-signal $\ell < 100$ domain, inaccessible to ground experiments (see Fig. 2).The robustness of this measurement against systematic effects and analysis choices was extensively tested[26]. The mask impact was primarily tested in developing four largely independent reconstruction methods that deal differently with the mask: *BASELINE*, which implements an approximation of the minimum variance estimator, allocates a null inverse variance to masked pixels, *ISO*[1] resorts to an inpainting of the small cut and a large apodization of the galactic mask, *METIS*[20] uses an inpainting technique based on the sparcity concept to restore masked signal and *PATCHES*[32], which uses a flat-sky QE on many sky patches, simply avoids the galactic cut and restore the point-sources cut by inpainting. Fig. 2 shows the reconstruction from two individual frequency maps using each pipelines. They all provide almost equivalent and fully consistent results, assessing to robustness against mask treatment, whereas the inter-frequency consistency further indicates the immunity to foreground residuals.

Although the C_L^{ϕ} estimate passed a wealth of consistency tests, more variance was found at low multipole ($\ell < 40$), where the *mean-field* bias (see Sect. 2.2) is large, and at high multipole ($\ell > 400$), where the $N_L^{(0)}$ is orders of magnitude above the signal. Only the conservative 40 to 400 multipole range is kept in the C_L^{ϕ} likelihood function, which retains 90% of the information.

4 Cosmology implication

The reconstruction of the CMB lensing, which encodes the matter distribution back to the last-scattering, improves the parameter constraints from Planck, thanks to a post-recombination leverage.

4.1 Degeneracy breaking using the CMB alone

First of all, the lensing offers a nice opportunity to assess the Planck data consistency: the 6-parameters Λ CDM best-fit model of the Planck's temperature power spectrum is in good agreement to the measured C_L^{ϕ}. Remarkably, this Cosmology which is calibrated from a measurement at $z = 1100$ provides a good description of the universe at $z \leq 5$. Then, the lensing measurement was combined to the temperature measurement to improve the precision to which the cosmological parameters can be constraint using CMB alone[25]. Within the 6-parameters cosmology, the lensing helps in breaking the degeneracy between the amplitude of the primordial power spectrum A_s and the optical depth to the recombination τ, providing an alternative to using WMAP τ measure. Both physical effects impact the C_ℓ^T amplitude, whereas the C_ℓ^{ϕ} amplitude does not depend on τ. The lensing implications are yet stronger when exploring extensions to the base Planck's model. It helps in breaking the *geometrical degeneracy* in a non-flat Universe, imposing a flat-geometry at the percent level and improving by a factor two the constraints on the cosmological constant density Ω_Λ w.r.t. the C_ℓ^T alone case, as it can be seen on the left panel of Fig. 3.

4.2 Constraint on neutrino mass

The domain to which the CMB lensing is expected to bring the largest constraining power is the neutrino physics sector, and in particular, the absolute scale of total neutrino mass $M_\nu = \sum_\nu m_\nu$[14, 16]. The C_ℓ^T measurements alone provides only weak constraints on neutrino mass below the threshold to which neutrino are still relativistic at the recombination (~ 1.3 eV). However, when non-relativistic (NR), the neutrinos contribute to the expansion rate but not to the clustering on scales smaller than the horizon size at the NR transition. When fixing the well-measured physical densities of CDM and Baryon, it translates into a power suppression of the C_ℓ^{ϕ} at small scales. This step-like signature is shown in Fig. 3 for $M_\nu \leq 1$ eV, along with the Planck C_ℓ^{ϕ} band powers. Within the free M_ν extension to the 6-parameters Λ CDM, the Planck C_ℓ^T measurement alone (albeit combined to the WMAP low multipole polarization

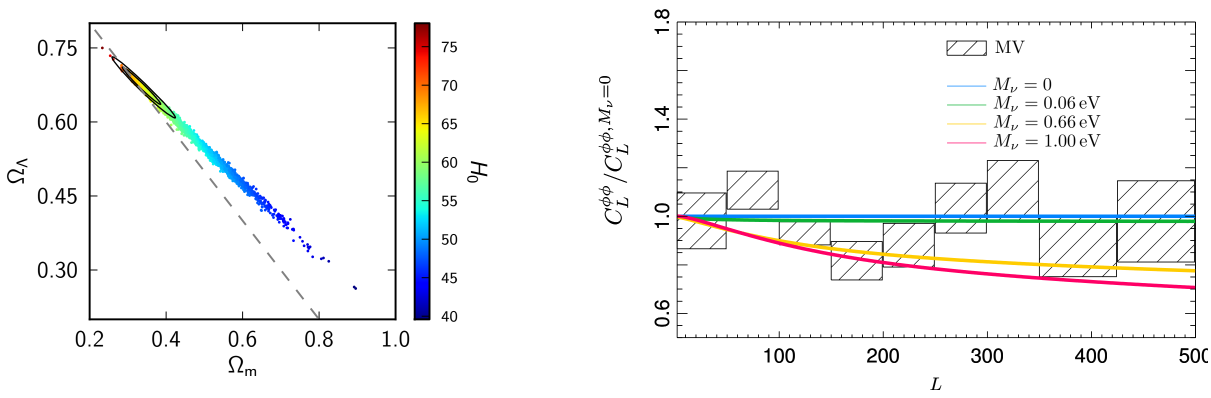

Figure 3 – Examples of the lensing reconstruction cosmological implications. *Left*: MCMC samples in the plan Λ density Ω_Λ vs Matter density Ω_m within the base ΛCDM6 cosmological model using Planck's C_ℓ^T information only (and low-ℓ WMAP polarization) along with the confidence intervals (black ellipses) when the Planck's C_L^ϕ estimate is included. Samples are color-coded by the H_0 values (Fig. from the Planck Collab. [25]). *Right*: C_L^ϕ calculated for various values of the total (active) neutrino mass M_ν ranging from 0 to 1 eV divided by the C_L^ϕ in the massless neutrino case. Planck's C_L^ϕ measure divided by the $M_\nu = 0$ model is plotted to give a hint of the sensitivity to M_ν.

data and the high multipole temperature data from grounds experiment), yield to an upper limit $M_\nu < 0.66$ eV $(95\% C.L.)$ [25]. Surprisingly, when including the Planck C_ℓ^ϕ measurement, this upper limit is *weakened* to $M_\nu < 0.85$ eV $(95\% C.L.)$. This result come from the fact that the C_ℓ^T measure disfavors large M_ν. Due to the low power measured in the $20 < \ell < 40$, any effect resulting in an increase of the C_ℓ^T at high mutipole would strengthen the tension between low and high mutipole range, and is consequently disfavored. A larger M_ν induces more C_ℓ^ϕ suppression, which in turn yields to less C_ℓ^T smoothing in the damping tail (high-multipole), providing less leverage to mitigate the C_ℓ^T tension. The lensing measure which does not suffer for any internal tension effect, leads to weakened but more robust M_ν constraints.

5 Forecast measurement using the polarization

In this section, we will forecast the lensing related measurements that will be within Planck's reach from its full-mission data, including polarisation observations, which will come out by the end of 2014.

5.1 Improving the deflection measurement

The lensing affects the CMB polarisation observables in the same way as for the temperature, hence several additional quadratic estimators (QE) between the temperature and the E and B modes of polarisation can be built [18], and then combined to improve the precision to which the lensing power spectrum C_L^ϕ can be measured. The variance of each QE being largely dominated by the Gaussian noise ($N_L^{(0)}$) term, the sensitivity improvement can be directly inferred from the $N_L^{(0)}$ estimates, which account for the CMB cosmic variance, angular resolution and instrumental noise. Within the Planck's best-fitting base model, we compute the Gaussian noise of each data combination (TT, TE, EE, TB, EB) using the public code FUTURCMB[a] [19]. The experimental characteristics are inferred from those reported by the Planck Collab. [21] by accounting for the two additional surveys and by resorting to the usual $\Delta P = \sqrt{2}\Delta T$ relation to obtain the noise level ΔP of the polarisation observations. As it can be seen in Fig. 4, at the Planck's polarisation sensitivity, the pure temperature QE provides the most sensitive lensing potential measure, whereas the largest polarisation-related improvement comes from correlations between the temperature and the E-mode of polarization. First, dealing with temperature only, we found

---

[a] available at the address `http://lpsc.in2p3.fr/perotto/`

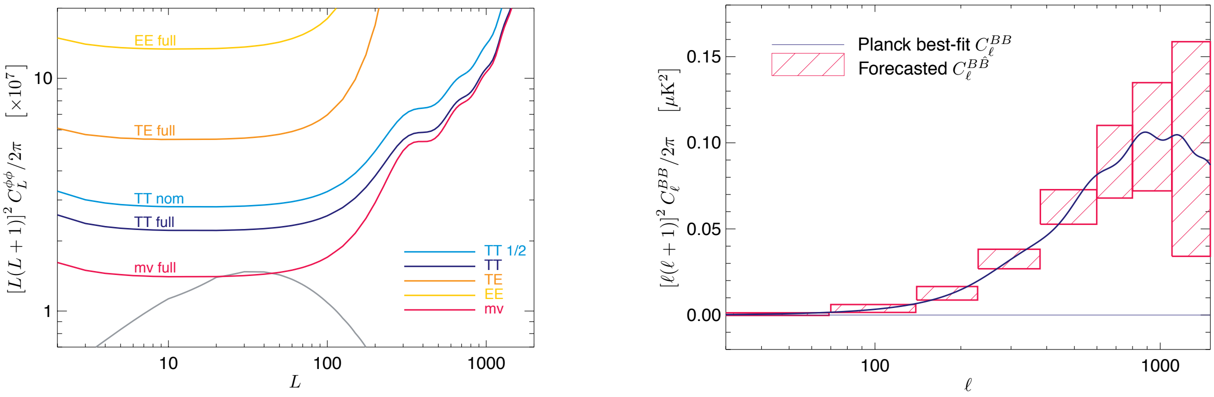

Figure 4 – Planck 2014 lensing results forecast. *Left*: The Gaussian noise of the Planck 2013 lensing estimate using temperature data from the nominal mission (TT nom.) is compared to the Gaussian noises from the full-mission (TT full.) and from the two best combinations including polarisation (TE and EE). The Gaussian noise associated to the minimum variance (MV) combination of all the estimate is also plotted. *Right*: Planck's lensing induced B-mode band powers forecast. Error bars are estimated from Eq. 2 using realistic Planck 2013 noise simulation interpolated to the full mission.

that going from the nominal mission (2 surveys) to the full-mission (4 surveys) yields a 20% decrease of the Gaussian noise, as part of it is due to the CMB temperature cosmic variance itself. Secondly, within measurements based on the full-mission, we evaluate that the Gaussian noise is further decreased by 35%, when including the polarisation. Eventually, as part of the uncertainties on the measured C_L^ϕ are due to the cosmic variance of the lenses, one can expect a 35% improvement in the next Planck's release w.r.t. Planck's 2013 results. This sensitivity improvement will come along with more robustness, steming from the comparison between individual lensing estimates and may allow less conservatism in the data cut choice, which will further improve C_L^ϕ measure constraining power.

5.2 B-mode measure

Aside from the lensing potential reconstruction, Planck will measure the lensing induced B mode of the polarization. Extending to the complete sky the works of the SPT [8] and Polarbear [33] collaboration, the favored method consists in cross-correlating the Planck's polarisation map to a pre-estimated template of the secondary B-mode contribution $\hat{B}$ which is obtained from the E-mode and lensing ϕ maps. In addition to the primordial to secondary B-mode disentanglement capability, this method leads to C_ℓ^B errors which are reduced by a factor three w.r.t. a direct auto-correlation method, and which are well-approximated by

$$\Delta \hat{C}_\ell^{B\hat{B}} = \frac{f_{\rm sky}^{-1}}{2\ell+1}\left((C_\ell^{B\hat{B}})^2 + C_\ell^{BB} C_\ell^{\hat{B}\hat{B}}\right) \qquad (2)$$

As seen in Fig. 4, Planck will provide a $C_\ell^{B\hat{B}}$ measure up to $\ell = 1000$, including a good measure of the scale below $\ell = 500$, hardly reachable by ground experiments.

6 Conclusion

Planck measured the first nearly full-sky map of the integrated mass distribution (thanks to its observational performances and high systematic control in the data-processing). This map is highly correlated to other mass tracers: first detections of the CIB-lensing (46σ) and ISW from CMB alone (2.5σ) were reported. Planck obtained a (26σ) measurement of the lensing potential power spectrum at high multipole (cleanest in the multipole range is $40 < L < 400$).

The CMB lensing reconstruction had several important cosmological implications (e.g. A_s-τ degeneracy breaking, probing the post-recombination history with CMB alone). It makes

Planck an autonomous cosmological probe as it provides an additional leverage to constrain late-evolution cosmological parameters, such as the neutrino masses. It improves the robustness of the neutrino masses constraint, which would be otherwise artificially tightened due to the tension between low and high multipoles in the temperature power spectrum.

The CMB lensing will go on occupying a prominent place among the next Planck cosmological results that will be published by the end of 2014. First, from the two more surveys and the inclusion of the polarization, a 35% decrease of the lensing potential power spectrum uncertainties is expected. Improvement will also come from further investigation of possible systematics, which will come along to a reduction of the level of conservatism of some choices (multipole cuts, apodisation, ...). Then, a high-significance measure of the lensing B-mode power spectrum using the potential estimate and the E-mode of polarization map is within Planck's reach. It will provide a complementary observable encoding the entire Universe Dark Matter distribution and a possible route of performing a *delensing* to retrieve pure primordial B-mode from inflation.

References

1. Benoit-Lévy, A., Déchelette, et al. A&A **555**, A37 (2013)
2. Blanchard, A. & Schneider, J., 1987, A&A, 184, 1
3. Condon, J. J., Cotton, W. D., et al., AJ **115**, 1693 (1998)
4. Das, S., Sherwin, B. D., et al., Phys. Rev. Lett. **107**, 021301 (2011), arXiv:1103.2124
5. Das, S., Louis, T., et al., JCAP **4**, 14 (2014), arXiv:1301.1037
6. Feng, C., Keating, B., et al., Phys. Rev. D **85**, 043513 (2012), arXiv:1111.2371
7. Hand, N., Leauthaud, A., et al., arXiv:1311.6200
8. Hanson, D., Hoover, S., et al., Phys. Rev. Lett. **111**, 141301 (2013), arXiv:1307.5830
9. Hirata, C. M. & Seljak, U., Phys. Rev. D **67**, 043001 (2003), astro-ph/0209489
10. Hirata, C. M., Padmanabhan, N.,et al., Phys. Rev. D **70**, 103501 (2004), astro-ph/0406004
11. Hirata, C. M., Ho, S., et al., Phys. Rev. D **78**, 043520 (2008), arXiv:0801.0644
12. Ho, S., Cuesta, A., et al., AJ **761**, 14 (2012), arXiv:1201.2137
13. Hu, W., Phys. Rev. D **64**, 083005 (2001), astro-ph/0105117
14. Kaplinghat, M., Knox, L., et al., Phys. Rev. Lett. **91**, 241301 (2003), astro-ph/0303344
15. Kesden, M. H., Cooray, A., et al., Phys. Rev. D **67**, 123507 (2003), astro-ph/0302536
16. Lesgourgues, J., Perotto, L., et al., Phys. Rev. D **73**, 045021 (2006), astro-ph/0511735
17. Lewis, A. & Challinor, A., Phys. Rep. **429**, 1 (2006), astro-ph/0601594
18. Okamoto, T. & Hu, W., Phys. Rev. D **67**, 083002 (2003), astro-ph/0301031
19. Perotto, L., Lesgourgues, J., et al., JCAP **610**, 13 (2006), astro-ph/0606227
20. Perotto, L., Bobin, J., et al., å **519**, 14 (2010), arXiv:0903.1308
21. Planck Collab., Planck 2013 results. I, A&A , accepted (2013), arXiv:1303.5062
22. Planck Collab., Planck 2013 results. VI, A&A , accepted (2013), arXiv:1303.5067
23. Planck Collab., Planck 2013 results. XII, A&A , accepted (2013), arXiv:1303.5072
24. Planck Collab., Planck 2013 results. XIII, A&A , accepted (2013), arXiv:1303.5073
25. Planck Collab., Planck 2013 results. XVI, A&A , accepted (2013), arXiv:1303.5076
26. Planck Collab., Planck 2013 results. XVII, A&A , accepted (2013), arXiv:1303.5077
27. Planck Collab., Planck 2013 results. XVIII, A&A , accepted (2013), arXiv:1303.5078
28. Planck Collab., Planck 2013 results. XIX, A&A , accepted (2013), arXiv:1303.5079
29. Planck Collab., Planck 2013 results. XXIV, A&A , accepted (2013), arXiv:1303.5084
30. Planck Collab., Planck 2013 results. XXVIII, A&A , accepted (2013), arXiv:1303.5088
31. Planck Collab., Planck 2013 results. XXIX A&A , accepted (2013), arXiv:1303.5089
32. Plaszczynski, S., Lavabre, A., et al.,A&A **544**, A27 (2012), arXiv:1201.5779
33. POLARBEAR Collab., (2013), arXiv:1312.6646
34. Smith, K. M., Zahn, O., et al.,Phys. Rev. D **76**, 043510 (2007), arXiv:0705.3980
35. van Engelen, A., Keisler, R., et al. A&A **756**, 142 (2012), arXiv:1202.0546
36. Wright, E. L., Eisenhardt, P. R., et al., AJ **140**, 1868 (2010), arXiv:1008.0031

Test of cosmic isotropy in the Planck era

Yabebal T. Fantaye
Departement of Mathematics, University of Tor Vergata Roma2, Rome, Italy Email: fantaye@mat.uniroma2.it

Part of the talk is presented on behalf of the Planck Collaboration.

The two fundamental assumptions in cosmology are that the Universe is statistically homogeneous and isotropic when averaged on large scales. Given the big implication of these assumptions, there has been a lot of statistical tests carried out to verify their validity. Since the first high-precision Cosmic Microwave Background (CMB) data release by the WMAP satellite, many anomalies that challenges the isotropy assumption, including dipolar power asymmetry on large angular scales, have been reported. In this talk I will present a brief summary of the test of cosmic isotropy we carried out in the latest WMAP and Planck temperature data.

1 Introduction

The European Space Agency (ESA) Planck satellite mission has recently produced the most accurate picture of the Universe by measuring the CMB with unprecedented precision. The scientific findings of this mission is presented in a series of science papers, which are mostly consistent with that of WMAP, the previous CMB satellite experiment by NASA. These papers[a] present a simple but challenging picture of the Universe. Despite being consistent with the standard picture, the Universe seen by Planck has some anomalies whose interpretation might require a new physics.

Amongst the Planck confirmed CMB anomalies the hemispherical power asymmetry [1,2] is one of the major one. This anomaly implies that the distribution of power in one side of the universe is different from that of the opposite one, leading to a breakdown of cosmic isotropy. In general, it is assumed that on large scales, scales that are not processed by non-linear gravity, the Universe is homogeneous and isotropic. The former implies that if we are able to zoom out and look at larger patches of the Universe, the statistical property of these patches should be the same; while the latter means if we set ourselves at one point, like on earth, and see all around us the statistical property of the universe in one direction should be similar to another one, hence rotation invariant.

The significance of the hemispherical power asymmetry, however, has often been called into question, in particular, due to the alleged *a-posteriori* nature of the statistics used; the significance of the anomaly is calculated using a statistical method that is designed to detect the observed feature. The challenge to this criticism was first given by [3] who showed that the 5-year WMAP data show a similar trend up to $\ell = 600$. Moreover, using an alternative approach which modelled the power asymmetry in terms of a dipolar modulation field, as suggested by [4], [5] found a 3.3σ detection using data smoothed to an angular resolution of 4.5° FWHM, with an axis in excellent agreement with previous results.

In this talk I will present a brief summary of the test of cosmic isotropy we carried out in the latest WMAP and Planck temperature data.

---

[a] http://sci.esa.int/planck/51551-simple-but-challenging-the-universe-according-to-planck/.

2 Power asymmetry analysis methods

There are in general two methods employed to test power asymmetry in the CMB map. The first one is to compute local-power on a disc at different sky directions and compare their consistency with isotropic power distribution. The effect of mask, noise and other complications are incorporated in such a method by using a set of simulations which are processed in a similar way to the data. The excess mismatch between the distribution of local-power in the data and simulations serve as a measure of significance of the power asymmetry. The second one is to assume a dipolar or higher order power asymmetry model and do a likelihood analysis. The two common analyses in this category are the pure dipole modulation by [5] and the generalised dipole modulation model as implemented in Bipolar spherical harmonics (BiPoSHs) technique [6].

In our analyses of the WMAP and Planck data in [7,9], we quantified the degree of anisotropy by measuring the distribution of local-power, which is measured as the variance or power spectrum of the local patches, in the CMB maps. The variance of a map is related to its power spectrum as

$$\sigma^2 = \frac{1}{4\pi}\sum_{\ell=0}^{\ell_{max}}(2\ell+1)C_\ell, \tag{1}$$

and hence using both of these quantities offers a possibility to study any deviation from isotropy in both real and harmonic space. Moreover, using power spectrum allows us easily study the scale dependence of a possible power variation in the CMB maps, while using variance we avoid mask induced complications in harmonic decomposition.

To incorporate a scale dependence study to the variance based method, we decomposed the map in to needlet components.

$$\beta_j(n) = \sum_{\ell=B^{j-1}}^{B^{j+1}} b^2\left(\frac{\ell}{B^j}\right)T_\ell(n), \tag{2}$$

where $T_\ell(n)$ denotes the component at multipole ℓ of the CMB map $T(n)$, e.g.

$$T(n) = \sum_\ell T_\ell(n),$$

$n \in S^2$ denotes the pointing direction, B is a fixed parameter (usually taken to be between 1 and 2) and $b(.)$ is a smooth function such that $\sum_j b^2(\frac{\ell}{B^j}) = 1$ for all ℓ.

The advantage of using needlets is that the needlet filter has a very good localisation property both in pixel and harmonic space, and the needlet component maps are minimally affected by masked regions, especially at high-frequency. In particular, of course the multipole components $T_\ell(n)$ cannot be reconstructed on masked data; nevertheless their linear combination (2) can be shown to be very robust to the presence of gaps, and more so on small scales/high frequencies.

In what follows we will refer the local-power method with variance measure as *local-variance* and local-power with power spectra measures as *local-C_ℓ*. A summary of the procedures we followed in both of these methods are as follows:

1. create a binary patch mask which are centred on low resolution `HEALPix` [10] pixels. For both local-C_ℓ and local-variance methods we have considered 3072 ($N_{\rm nside} = 16$) highly overlapping disc patches covering the entire sky. The radius of the discs varies from 1 to 90 degrees. The final local-C_ℓ results, however, are quoted from analysis performed using 12 non-overlapping patches, the base `HEALPix` $N_{\rm nside} = 1$ pixels. We have shown that there is no significant difference between the results obtained using overlapping or non-overlapping patches.

2. looping over patch numbers, create an analysis patch mask by multiplying the binary disc mask with that of a foreground confidence and point source masks. In the case of local-C_ℓ analysis, we have apodised the foreground confidence and point source masks to reduce correlations between modes.

3. apply the analysis patch mask to the CMB + noise maps which are either the WMAP and Planck data or realistic simulations.

4. for each patch compute C_ℓs using the `MASTER` technique[11] in bins of 16 multipoles; or variance of the unmasked pixels. For the local-C_ℓ case, the `MASTER` $16 - \ell$ blocks are further binned into $100 - \ell$ blocks to reduce bin to bin correlations as well as to compare our results with previous similar analyses.

5. for each patch estimate the mean and variance of local- C_ℓ or local-variance using N_{sim} realistic simulations. The mean is used to subtract the local mean-field from both data and simulations, while the variance is used to weight the corresponding patch.

6. estimate dipole amplitude and dipole directions of the local-power map using the `HEALPix` routine `remove_dipole` by applying an inverse variance weighting.

3 Results and Discussion

In this section I will present the summary of results presented in [7,9], and some updates which are not included in these published papers. In particular, I will describe the result we obtained using the local-variance analysis on needlet decomposed maps.

As outlined in the previous section, our test statistics is based on dipole amplitudes and dipole directions of the data and simulation local-power maps. For local-C_ℓs, which are estimated in 100-ℓ blocks, we obtained $\ell_{\rm max}/100$ $N_{\rm nside} = 1$ local-C_ℓ maps. For WMAP and Planck $\ell_{\rm max} = 600$ and $\ell_{\rm max} = 1500$ is used, which are corresponding to 6 and 15 dipole amplitude and directions, respectively. On the other hand, for the local-variance analysis we used 20 disc sizes with radius ranging from 1-90 degrees, and obtained 20 dipole amplitudes and directions. The later case is estimated for both the original real-space maps and the corresponding needlet decomposed maps.

In all cases we have used p-values to quantify the significance of the observed power asymmetry. The p-values are computed by comparing the anisotropic signal measured by our test-statistics, magnitude of dipole amplitudes or clustering of dipole directions, with those obtained from realistic simulations. For the WMAP case, we generated 1000 CMB-plus-noise Monte Carlo (MC) simulations based on the WMAP9 best-fit ΛCDM power spectrum [12]. Noise realisations are drawn as uncorrelated Gaussian realisations with a spatially varying RMS distribution given by the number of observations per pixel. For Planck we adopt the 1000 "Full Focal Plane" (FFP6) end-to-end simulations produced by the Planck collaboration based on the instrument performance and noise properties. These simulations also incorporate lensing and component separation effects. The simulations are treated identically to the data in all steps discussed below.

Using dipole modulated simulations, we found that clustering of dipole directions is more sensitive to measuring a small power asymmetry signal, small dipole modulation amplitudes, than comparing the magnitude of dipole amplitudes in data and simulations. The dipole directions clustering, however, can only be obtained when there are at least a few number of independent dipole direction estimates, which is only the case for local-C_ℓ analysis. For the local-variance method, however, the dipole directions for different disc sizes are correlated, and hence we can not use the alignment of dipole directions as a measure of significance. We compute p-values, therefore, based on excess of the data dipole amplitude from those of the simulations.

3.1 local-C_ℓ analysis

In [7] we performed a local-C_ℓ analysis on WMAP 9-year data using 12 patches. We found that the power asymmetry is statistically significant at the 3.2σ confidence level for $\ell = 2$–600, where the data is signal dominated. The preferred asymmetry direction is $(l, b) = (227, -27)$, consistent with previous claims. Individual asymmetry axes estimated from six independent multipole ranges are all consistent with this direction.

In the same paper, we did also MCMC analysis on the 12 independent patches to determine the local best-fit values of the six ΛCDM cosmological parameters: the Hubble constant today (H_0); fractional densities of baryons (Ω_b), cold dark matter (Ω_m) and cosmic curvature (Ω_k); the reionization optical depth (τ); the amplitude (A_s) and spectral index (n_s) of the initial scalar fluctuations. Since most of the information used to constrain these parameters comes from the CMB power spectrum, the observed power asymmetry may have been caused by asymmetry in one or more of these cosmological parameters. After doing local-MCMC analysis, we obtained a map of local best-fit values for each six parameters. Since we used all multipole blocks of the `MASTER` power spectra for a given patch to estimate the parameters, we obtain only a single dipole amplitude and direction per parameter per map. As a result of this we can not use the dipole directions to measure significance of parameter asymmetry. The significance of parameter asymmetry is, therefore, measured by comparing the data and simulation local-best-fit map dipole amplitudes. We found that none of the cosmological parameters show a significant asymmetry. This is probably because of the large error bars in the parameters. It is, however, interesting to note that the dipole direction for the parameters A_s, n_s and Ω_b are in alignment with the power asymmetry direction, implying these parameters are the most sensitive to the power asymmetry observed.

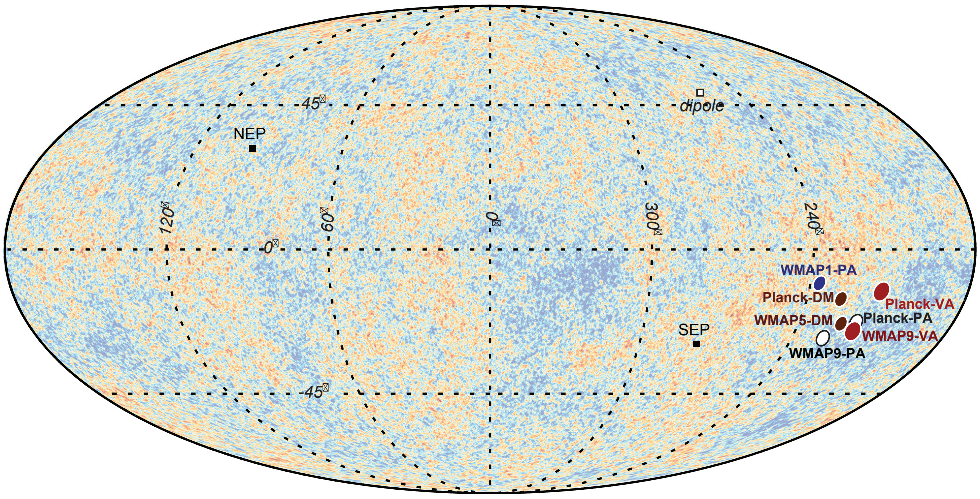

Figure 1 – Asymmetry directions found in different hemispherical power asymmetry analysis. The local variance of the WMAP 9-year and Planck 2013 data [denoted by WMAP9-VA and Planck-VA], as well as the directions found previously from the latest likelihood analyses of the dipole modulation model [denoted by WMAP5-DM and Planck-DM], and the local-power spectrum analyses [denoted by WMAP1-PA, WMAP9-PA and Planck-PA] for the WMAP and Planck data. The background map is the CMB sky observed by Planck (SMICA). VA, DM and PA stand for variance asymmetry, dipole modulation and power asymmetry, respectively. This figure is taken from Akrami et. al. 2013[9].

The local-C_ℓ analysis of the Planck collaboration [8] confirms a similar power asymmetry observed in the WMAP data, reassuring the power asymmetry is not due to systematic effects. This agreement across a wide range of scales as well as two different data sets clearly removes the statistical *a-posterior* interpretation of the effect, and poses a new challenge for a detail investigation of the effect. In the Planck paper it was shown that the power asymmetry extends up to $\ell \sim 600$ with a significance of at least 3σ. Beyond this scale, however, the doppler boosting, which is due to the motion of our solar system barycenter with respect to the CMB, becomes dominant. Boosting is a significant contamination for power asymmetry study, and it has to be taken into account when looking for power asymmetry at small scales, large multipoles.

3.2 local-variance analysis

In [9] we performed a local-variance analysis in both WMAP 9-year and Planck 1-year data. Left panel of Figure. (2) shows the results for Planck, which compares the dipole amplitudes of the data local-variance map (green stars) with that of the 1000 FFP6 simulations (grey stars) - none

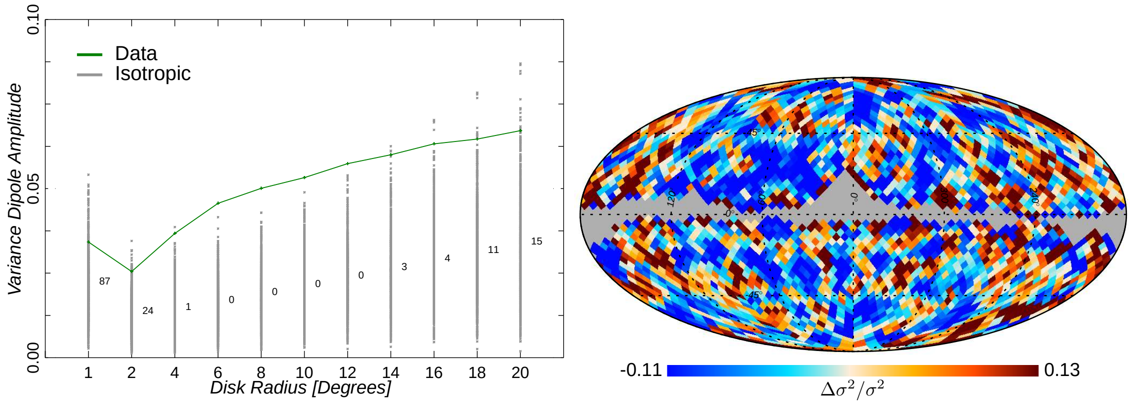

Figure 2 – Left panel: local-variance dipole amplitude as a function of disc radius for Planck `SMICA` data (in green) versus the 1000 isotropic FFP6 simulations (in grey). The labels above each scale indicate the number of simulations with amplitudes larger than the ones estimated from the data, and are located at the means of the amplitude values from the simulations. Right panel: mean-field subtracted, local-variance map computed with 6° discs for Planck data. This figure is taken from Akrami et. al. 2013[9].

of the 1000 isotropic simulations have local-variance dipole amplitudes larger than the data over the range $6^\circ \leq r_{\rm disc} \leq 12^\circ$. This implies that the variance in the Planck data exhibits a dipolar-like spatial variations that are statistically significant (at least) at the $\sim 3-3.5\sigma$ level or a p-value of less than 0.001. We showed that the distribution of the simulation dipole amplitudes are well fit by a Gaussian distribution for all discs sizes. The right panel of Figure. (2) visually illustrates mean-field subtracted local-variance map for the 6° radius disc. The dipole direction obtained from this map is $(l, b) = (212^\circ, -13^\circ)$.

Similar analysis using the WMAP 9-year data yields a statistical significance of $\sim 2.9\sigma$, and a direction fully consistent with those derived from Planck and other previous analyses. Our check shows that the difference in mask and input power spectra used to simulate the WMAP simulations seems to drive the difference in significance between Planck and WMAP, and a further investigation of this issue is necessary once the slight tension between WMAP and Planck data is resolved.

We have checked that the local-variance based results do not significantly change when we account for the doppler boosting effect either by including boosting in the simulations or by deboosting the data, similar to what we did for the Planck 143GHz channel map with the local-C_ℓ analysis. This is mostly because the local-variance method is mostly dominated by large scale modes where the effect of doppler boosting is small. As we will show below, however, this method actually is able to detect the boosting signal with $> 3\sigma$ significance when considering a high-pass filtered map.

The preferred directions obtained using local-variance and local-C_ℓ methods from our papers as well as a number of similar results obtained in previous papers are summarised in Figure 1.

3.3 Local-variance analysis on needlet components

To study the scale dependence of power asymmetry using the local-variance method, we decomposed the Planck SMICA data and FFP6 simulations into needlet components using (2), and performed the above analysis on each of the decomposed maps. The needlet parameters we used are such that a given map is decomposed into nine needlet component maps each having a compact support over a multipole range defined by $\ell = [B^{j-1}, B^{j+1}]$ where $j = 2, 3, ..10$ and $B = 2$.

As shown in Figure. (3), all but the $j = 9$ needlet component have dipole amplitudes consistent with the FFP6 simulations - hence no significant power asymmetry. The $j = 9$ needlet map, which has a support to multipole ranges $\ell = [256, 1024]$, shows a significant anisotropy with p-value of 0.003, and with a dipole direction close to the CMB dipole. This means what we have detected in this component is not the power asymmetry we talked about in the previous paragraphs, but

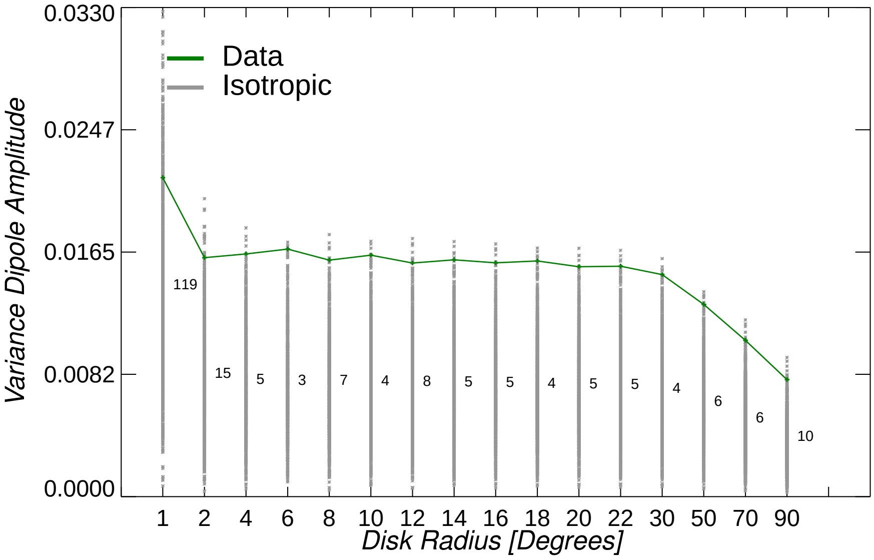

Figure 3 – Dipole amplitudes of the local-variance map for the $j = 9$, $256 \leq \ell \leq 1024$, needlet component as a function of disc radius. The Planck (`SMICA`) data (in green) versus the 1000 isotropic FFP6 simulations (in grey). The labels above each scale indicate the number of simulations with amplitudes larger than the ones estimated from the data.

the well-know doppler boosting effect caused by our motion with respect to the CMB frame. This effect has been detected for the first time by Planck using a completely different algorithm [13], and is used to measure our solar system barycenter velocity independent of the CMB dipole component. In addition, as shown in Figure. (4), the dipole direction of the $j = 10$ component has a dipole direction right on the CMB dipole. The Planck data local-variance dipole amplitude for this particular needlet component, however, is compatible with the FFP6 simulations. The reason for this may be due to the fact that the majority of the multipoles covered by the $j = 10$ component are sensitive to the boosting signal but with a small signal to noise values, while all of multipoles in the $j = 9$ component are signal dominated but with less sensitivity to the boosting signal, or possibly contaminated by a non-vanishing power asymmetry signal.

Some interesting features to note from Figure. (3) & (4) are: the dipole directions for the needlet component $j = 2 - 8$ are close to the power asymmetry direction; the dispersion of dipole amplitudes for isotropic simulations are large for small radius discs and becomes small for large discs. This is opposite to what we saw when using the full map. Of course, this is understandable since most of the needlet maps are not affected by the cosmic variance of the large scale modes.

The implication of Doppler boosting detection by our method implies that at least our method is sensitive to dipolar power asymmetry with amplitudes up to 0.1%. It is also a strong validation to our entire pipeline. Moreover, clustering of the lower multipole dipole directions, needlet components $j = 2 - 8$, to the power asymmetry dipole direction may hint existence of asymmetry at intermediate multipoles. Of course, a lot of verification work has to be done in this regard.

4 Summary

In this talk I have discussed the unique nature of the CMB in testing the statistical property of the Universe. Thanks to the high precision experiments like Planck, the test of cosmological principles, the assumption of statistical isotropy and homogeneity, is now becoming a major field in the CMB and large scale data analysis.

The current CMB data hints a lopsided Universe, more large scale structures in one side of the Universe than the other. The significance of this anomaly, however, is low, $< 4\sigma$, so one can not rule out yet the effect being just a statistical fluke. Moreover, although the persistence of the

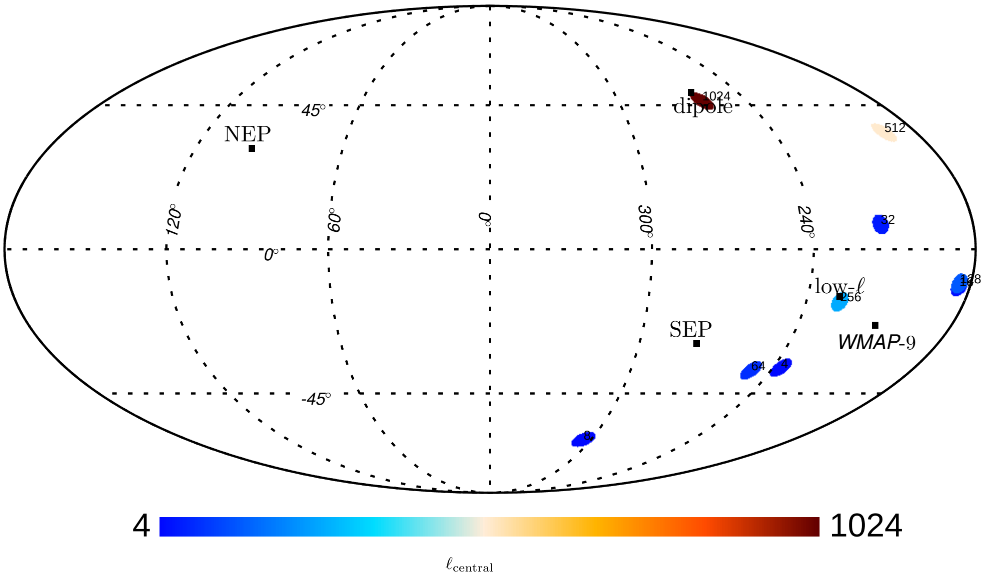

Figure 4 – Dipole directions of the local-variance maps of the nine needlet components, $j = 2, 3, \ldots, 10$ with a disc radius of $90\circ$. The labels in this plot indicates the central multipole of a given needlet map.

anomaly in both WMAP and Planck data seems to suggest the cause is unlikely to be foreground or systematic effects, we can not yet fully exclude the possibility of a local Universe phenomena. For this and other cases more work needs to be done to confirm the signal we are observing is truly cosmological. If that is proven, then this observation will represent another major discovery about the nature of our Universe and might lead to a new insight about the inner workings of inflation, which is responsible for laying out the initial conditions of the Universe from a mere quantum fluctuations.

In this endeavour there are different models in the literature trying to explain what is observed in the data, but to date there is no any single theoretical model that explains all the observations, power asymmetry both at large and intermediate scales.

While theorists are working out a viable model, there are going to be results from different experiments. For example, the full Planck temperature and polarisation data will be released in near future and it will be interesting to see what the outcomes will be. The planned CMB experiment PRISM [14] promises to deliver a high-precision CMB polarisation maps. Since the statistical nature of polarisation maps as well as its systematics and foregrounds are not necessarily similar to that of the temperature maps, PRISIM will be crucial in testing the isotropy hypothesis. On the other hand, EUCLID [15], a space-based survey mission from ESA, will map the large scale structure with an unprecedented precision. Such observations will be able to test the isotropic assumption in the large scale structure, hence providing an independent verification. The future possibilities of the study and characterisation of the statistical nature of our Universe is therefore bright. These studies will ultimately contribute to our understanding of the processes that shaped the Universe from its birth to where it is now and where it is going.

Acknowledgments

This conference proceeding is a summary of the work I did in collaboration with M. Axelsson, Y. Akrami, A. Shafieloo, H. K. Eriksen, F. K. Hansen, A. J. Banday and K. M. Górski. This work is supported by ERC Grant 277742 Pascal. I acknowledge the use of resources from the Norwegian national super-computing facilities, NOTUR. Maps and results have been derived using the `HEALPix` (http://healpix.jpl.nasa.gov) software package developed by [10].

References

1. H. K. Eriksen, F. K. Hansen, A. J. Banday, K. M. Gorski, and P. B. Lilje. Asymmetries in the Cosmic Microwave Background Anisotropy Field. *ApJ*, 605:14–20, April 2004.
2. F. K. Hansen, A. J. Banday, and K. M. Górski. Testing the cosmological principle of isotropy: local power-spectrum estimates of the WMAP data. *MNRAS*, 354:641–665, November 2004.
3. F. K. Hansen, A. J. Banday, K. M. Gorski, H. K. Eriksen, and P. B. Lilje. Power Asymmetry in Cosmic Microwave Background Fluctuations from Full Sky to Sub-degree Scales: Is the Universe Isotropic? *ApJ*, 704:1448–1458, 2009.
4. C. Gordon, W. Hu, D. Huterer, and T. Crawford. Spontaneous isotropy breaking: A mechanism for CMB multipole alignments. *Phys. Rev. D.*, 72(10):103002, November 2005.
5. J. Hoftuft, H. K. Eriksen, A. J. Banday, K. M. Gorski, F. K. Hansen, and P. B. Lilje. Increasing evidence for hemispherical power asymmetry in the five-year WMAP data. *ApJ*, 699:985–989, 2009.
6. A. Hajian and T. Souradeep. Testing global isotropy of three-year Wilkinson Microwave Anisotropy Probe (WMAP) data: Temperature analysis. *Phys. Rev. D.*, 74(12):123521, December 2006.
7. M. Axelsson, Y. Fantaye, F. K. Hansen, A. J. Banday, H. K. Eriksen, and K. M. Gorski. Directional dependence of ΛCDM cosmological parameters. *ArXiv e-prints*, March 2013.
8. Planck Collaboration, P. A. R. Ade, N. Aghanim, C. Armitage-Caplan, M. Arnaud, M. Ashdown, F. Atrio-Barandela, J. Aumont, C. Baccigalupi, A. J. Banday, and et al. Planck 2013 results. XXIII. Isotropy and Statistics of the CMB. *ArXiv e-prints*, March 2013.
9. Y. Akrami, Y. Fantaye, A. Shafieloo, H. K. Eriksen, F. K. Hansen, A. J. Banday, and K. M. Górski. Power asymmetry in WMAP and Planck temperature sky maps as measured by a local variance estimator. *ArXiv e-prints*, February 2014.
10. K. M. Górski, E. Hivon, A. J. Banday, B. D. Wandelt, F. K. Hansen, M. Reinecke, and M. Bartelmann. HEALPix: A Framework for High-Resolution Discretization and Fast Analysis of Data Distributed on the Sphere. *ApJ*, 699:759–771, April 2005.
11. E. Hivon, K. M. Górski, C. B. Netterfield, B. P. Crill, S. Prunet, and F. Hansen. MASTER of the Cosmic Microwave Background Anisotropy Power Spectrum: A Fast Method for Statistical Analysis of Large and Complex Cosmic Microwave Background Data Sets. *ApJ*, 567:2–17, March 2002.
12. G. Hinshaw et al. Nine-Year Wilkinson Microwave Anisotropy Probe (WMAP) Observations: Cosmological Parameter Results. *arXiv:1212.5226*, 2012.
13. Planck Collaboration, N. Aghanim, C. Armitage-Caplan, M. Arnaud, Ashdown, and et al. Planck 2013 results. XXVII. Doppler boosting of the CMB: Eppur si muove. *ArXiv e-prints*, March 2013.
14. PRISM Collaboration, P. Andre, C. Baccigalupi, D. Barbosa, and et. al. PRISM (Polarized Radiation Imaging and Spectroscopy Mission): A White Paper on the Ultimate Polarimetric Spectro-Imaging of the Microwave and Far-Infrared Sky. *ArXiv e-prints*, June 2013.
15. R. Laureijs, J. Amiaux, S. Arduini, J. . Augueères, J. Brinchmann, R. Cole, M. Cropper, C. Dabin, L. Duvet, A. Ealet, and et al. Euclid Definition Study Report. *ArXiv e-prints*, October 2011.

The CMB vs LSS: is there a tension?

Adam Moss
Centre for Astronomy & Particle Theory, University of Nottingham, University Park, Nottingham, NG7 2RD, U.K.

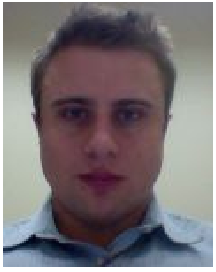

There is a tension between measurements of the amplitude of the power spectrum of density perturbations inferred using the Cosmic Microwave Background (CMB) and those directly measured by Large-Scale Structure (LSS) on smaller scales. I show that this tension exists, and is robust, for a range of LSS indicators including clusters, lensing and redshift space distortions and using CMB data from either Planck or WMAP+SPT/ACT. One obvious way to reconcile this is the inclusion of a massive neutrino, which could be either active or sterile. In both cases there is a significant detection of modification to the neutrino sector from the standard model, in excess of the 3.5σ level. I discuss the implications of this result, and also discuss if there are any other alternative explanations.

1 Introduction

A standard cosmological model has become established over the past few decades, known as the ΛCDM model. This appears to provide an excellent fit to a wide range of data, and the race is on to accumulate any evidence for extensions to this model. Our approach will be to compare measurements of the Cosmic Microwave Background (CMB) to those of Large-Scale Structure (LSS). The data we will use are:

- *Planck* **+ WP**: We use measurements of the temperature anisotropy power spectrum made by the *Planck*[1] satellite and polarisation and temperature-polarisation cross-corrrelation spectra from WMAP 9 year data[2].
- **WMAP + highL**: As an alternative to the *Planck* temperature measurements, we will use those made by WMAP[2] over the multipole range $\ell \approx 2-800$, complemented with higher resolution measurements made by ACT and SPT (see[3] and references within).
- **Baryonic Acoustic Oscillations (BAOs)**: We use observations of Baryonic Acoustic Oscillations (BAOs)[4,5,6,7], which constrains the ratio of the sound horizon at the drag epoch to the volume-averaged distance.
- **SZ cluster counts**: *Planck* has detected clusters via the Sunyaev-Zeldovich effect. Using a sample of 189 clusters, cosmological constraints were deduced in the $\sigma_8 - \Omega_{\rm m}$ plane[8].

We will implement this using two priors: $\sigma_8(\Omega_{\rm m}/0.27)^{0.3} = 0.78 \pm 0.01$, corresponding to fixed hydrostatic bias $(1-b = 0.8)$, and $\sigma_8(\Omega_{\rm m}/0.27)^{0.3} = 0.764 \pm 0.025$, corresponding to marginalised bias $(1-b = [0.7, 1.0])$.

- **Lensing**: We will use two types of weak lensing measurements, denoted simply as "lensing". The first is the coherent distortion of galaxy shapes, called cosmic shear, measured by the Canada France Hawaii Telescope Lensing Survey (CFHTLenS). In this analysis we have used the 3D blue galaxy sample[9]. In addition we use measurements of the lensing of the CMB. This has been detected over a wide range of scales and we use reconstructions from *Planck*[11] and SPT[10].

- **Redshift space distortions (RSDs)**: The relative amplitude between the monopole and the quadrupole of the anisotropic galaxy power spectrum in redshift space constrains the growth rate of structure. We DR11 measurements of the growth and Alcock-Paczynski (AP) parameters from the BOSS survey[12].

2 The Problem

In the left panel of Fig. 1 we show the results of constraining a 5 parameter model with parameters $\mathbf{p} = \{\Omega_{\rm b}h^2, \Omega_{\rm c}h^2, \Theta_{\rm MC}, A_{\rm S}, n_{\rm S}\}$ using LSS data only, where the physical densities of cold dark matter and baryons measured relative to the critical density are $\Omega_{\rm c}h^2$ and $\Omega_{\rm b}h^2$ respectively; the angular diameter of the acoustic scale, $\theta_{\rm MC}$; the amplitude, $A_{\rm S}$, and spectral index, $n_{\rm S}$, of primordial density perturbations. Initially we use the individual LSS measurements: SZ cluster counts, lensing and RSD in conjunction with *Planck* priors $\Theta_{\rm MC} = 1.04131 \pm 0.00063$ and $n_{\rm S} = 0.9603 \pm 0.0073$[1], and then combining the three to create a joint LSS constraint that yields $\sigma_8 = 0.7946 \pm 0.0094$ and $\Omega_{\rm m} = 0.2610 \pm 0.0093$. Visually it is clear that the three LSS datasets are in agreement with each other. This is compared with (using the standard 6 parameter model) $\sigma_8 = 0.825 \pm 0.012$ and $\Omega_{\rm m} = 0.309 \pm 0.011$ for *Planck*+WP+BAO and $\sigma_8 = 0.827 \pm 0.017$ and $\Omega_{\rm m} = 0.299 \pm 0.012$ for WMAP+highL+BAO. It is clear that there is a discrepancy between the joint LSS constraint and that from CMB+BAO, stronger for *Planck*+WP, but still significant for WMAP+highL.

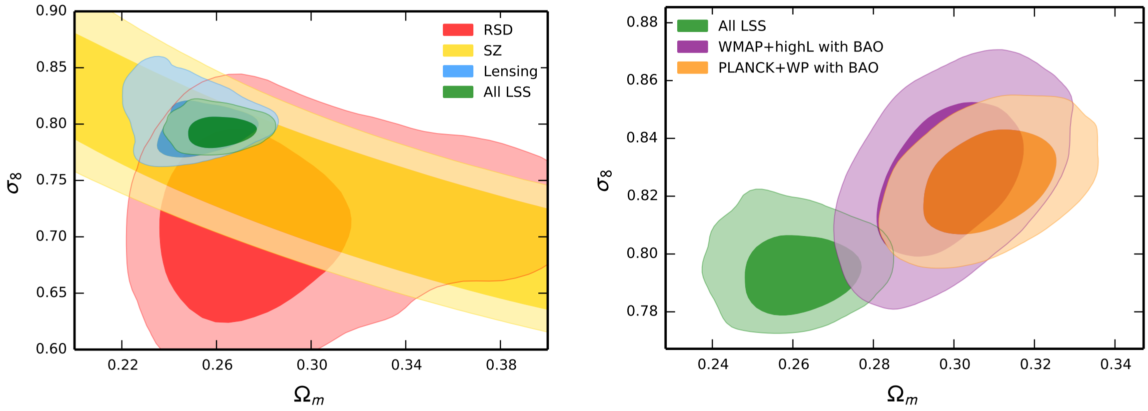

Figure 1 – The tension between CMB and LSS measurements. On the left we present constraints on the $\sigma_8 - \Omega_{\rm m}$ plane for LSS data only along with priors on $\Theta_{\rm MC}$ and $n_{\rm S}$. The red contours are for the RSD, gold for SZ clusters with $1-b$ in the range [0.7,1.0] and blue for lensing. The green contour is that which comes from combining the 3 different LSS probes into a joint LSS constraint. This contour is also presented on the right along with contours for *Planck*+WP+BAO (orange) and WMAP+highL+BAO (purple). It is clear that there is a discrepancy with the CMB and the joint LSS constraints on this parameter combination.

3 Inclusion of neutrinos

The inclusion of a neutrino component in the cosmological model can reduce the amount of power on small scales for a given large-scale normalisation, A_S. This is true both in the case of active neutrinos that correspond to the mass eigenstates of the standard 3 flavours and also for a sterile neutrino, which evades the strong bound on the number of neutrino species from particle physics experiments by not being involved in weak interactions.

3.1 Active neutrinos

The inclusion of active neutrinos is modelled by the addition of a single parameter, $\sum m_\nu$, assuming that this is distributed equally amongst the 3 species of massive neutrino. This approximates a degenerate hierarchy with $m_1 = m_2 = m_3 = \sum m_\nu/3$. We present the equivalent of the right-hand two plots in Fig.1 in the left-hand panels of Fig. 2 when $\sum m_\nu$ is allowed to vary. There is a significant reduction in the tension between the combined LSS constraint (green contours) and the CMB observations. However, there is still some residual tension in the case of *Planck*+WP+BAO (orange contours). For the combination of *Planck*+WP+RSD+lensing+SZ with $1 - b = [0.7, 1.0]$ we find that $\sum m_\nu = (0.357 \pm 0.099)\,\mathrm{eV}$.

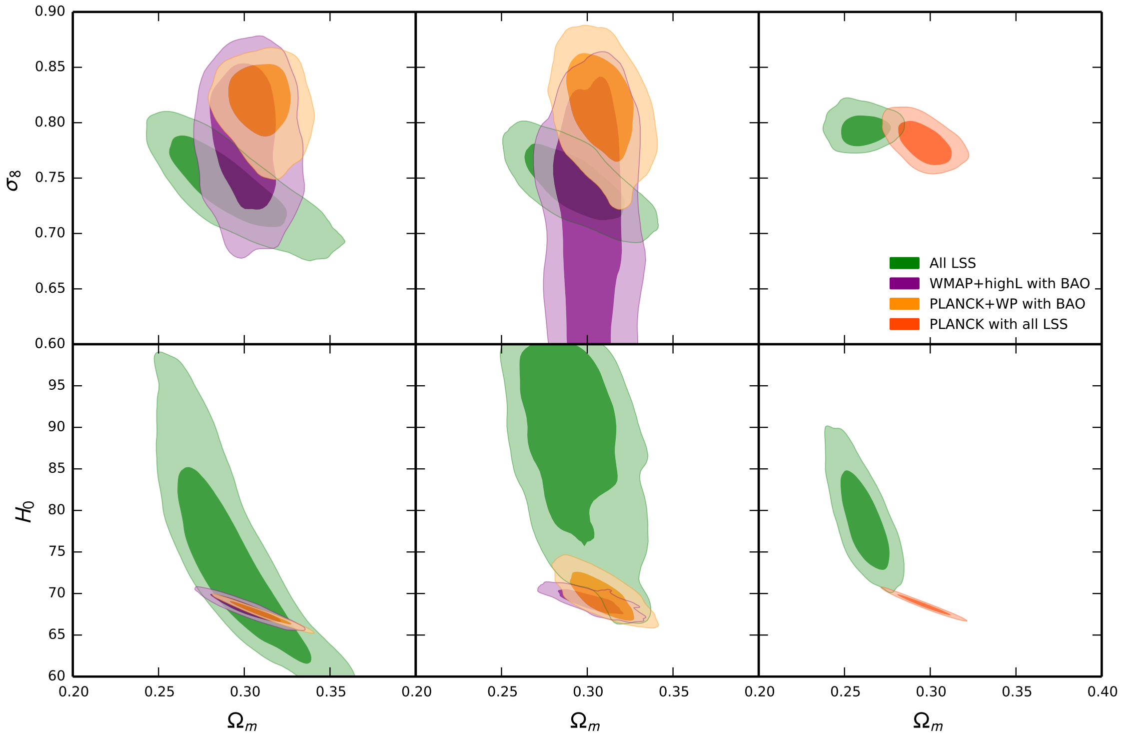

Figure 2 – Same as the right panel in Fig.1 but with the inclusion of (i) $\sum m_\nu$ in (left panel) (ii) $m_{\mathrm{sterile}}^{\mathrm{eff}}$ and ΔN_{eff} (middle panel). The right panel shows LSS (green) and *Planck* with RSD, lensing and SZ but *without* WP (dark orange), where the optical depth to reionization τ is allowed to vary.

3.2 Sterile neutrinos

The standard approach to modelling sterile neutrinos is to introduce two new parameters into the fitting process. The first is an effective mass of the neutrino, $m_{\mathrm{sterile}}^{\mathrm{eff}}$, and the other is the change in effective number of degrees of freedom, ΔN_{eff}, such that $N_{\mathrm{eff}} = 3.046 + \Delta N_{\mathrm{eff}}$. As with the case of active neutrinos there is clearly is some evidence that inclusion of sterile neutrinos can ameliorate the CMB-LSS discrepancy, but some residual tension remains. For the combination of *Planck*+WP+RSD+lensing+SZ with $1 - b = [0.7, 1.0]$ we find $m_{\mathrm{sterile}}^{\mathrm{eff}} = 0.67 \pm 0.18\,\mathrm{eV}$.

4 Discussion and conclusions

There is a prima facie case that the CMB and LSS measurements are in tension, the result of which could point to a significant detection of modification to the neutrino sector. However, the fit to LSS is significantly improved at the expense of slightly poorer fit the the CMB, particularly in the case of *Planck*. One must also bear in mind that the measurement of the E-mode polarisation on large-scales by WMAP is crucial in all the previous analyses. The CMB temperature anisotropies constrain the parameter combination $A_{\rm S}e^{-2\tau}$, where τ is the optical depth to reionization, so this requires a measurement of polarisation on large scales to infer τ and hence allow $A_{\rm S}$ to be deduced independently. In particular a reduction of σ_8 from ≈ 0.83 as suggested by CMB measurements to ≈ 0.78, which is closer to the value preferred by the LSS measurements, would require τ to be reduced from ≈ 0.09 to ≈ 0.05. We have also tested this possibility by removing WP from the likelihood. However, as shown in Fig. 2, the improved fit to the LSS data also leads to residual tension with *Planck* data.

Acknowledgments

This research was supported by STFC. I thank Richard Battye and Thomas Charnock for their collaboration on this topic, and the organisers for providing an excellent conference.

References

1. Planck Collaboration, ArXiv e-prints (2013), arXiv:1303.5076
2. G. Hinshaw et al., Astrophysical Journal Supp., **208**, 19 (2013), arXiv:1212.5226
3. J. Dunkley et al., ArXiv e-prints (2013), arXiv:1301.0776
4. F. Beutler et al., MNRAS, **416**, 3017 (2011), arXiv:1106.3366
5. C. Blake et al., MNRAS, **425**, 405 (2012), arXiv:1204.3674
6. N. Padmanabhan et al., MNRAS, **427**, 2132 (2012), arXiv:1202.0090
7. L. Anderson et al., MNRAS, **427**, 3435 (2012), arXiv:1203.6594
8. Planck Collaboration, ArXiv e-prints (2013), arXiv:1303.5080
9. C. Heymans et al., MNRAS, **427**, 146 (2012), arXiv:1210.0032
10. A. van Engelen et al., Astrophysical Journal, **756**, 142 (2012), arXiv:1202.0546
11. Planck Collaboration, ArXiv e-prints (2013), arXiv:1303.5077
12. F. Beutler et al., ArXiv e-prints (2013), arXiv:1312.4611

Searching for oscillations in the primordial power spectrum

P. Daniel Meerburg
Department of Astrophysical Sciences, Princeton University, Princeton, NJ 08540 USA.

David N. Spergel
Department of Astrophysical Sciences, Princeton University, Princeton, NJ 08540 USA.

Benjamin D. Wandelt
CNRS-UPMC Univ. Paris 06, UMR7095, Institut d'Astrophysique de Paris, 98bis Bd. Arago, F-75014, Paris, France

Departments of Physics and Astronomy, University of Illinois at Urbana-Champaign, Urbana, IL 61801, USA

A small deviation from scale invariance in the form of oscillations in the primordial correlation spectra has been predicted by various cosmological models. In this paper we review a recently developed method to search for these features in the data in a more effective way. By Taylor expanding the small features around the 'background' cosmology, we have shown we are able to improve the search for these features compared to previous analysese. In this short paper we will extend that work by combining this method with a multi nested sampler. We recover our previous findings and are able to do so in 192 CPU hours. We will also briefly discuss the possibility of a long wavelength feature in the data to alleviate some tension between the data and the ΛCDM + r concordance cosmology.

1 Introduction

The Planck data provided unprecedented detail of the small fluctuations in the cosmic microwave background (CMB) [1]. We know now that these fluctuations are adiabatic, Gaussian and almost scale invariant. This constrains models and model parameters of the early Universe, but despite the quality of the data they remain inconclusive of the details. In particular, small deviations from scale invariance are still permitted, and so are small levels of non-Gaussianity. In recent years models have been proposed which predict oscillatory features on top of an almost scale invariant spectrum [2,3,4,5]. The amplitude and frequency of these oscillations is usually associated with fundamental parameters of the model, be that the axion decay constant in axion-monodromy inflation, or the energy scale at which particles are injected into the free vacuum during inflation in more exotic models.

This proceedings is set up as follows. In Section 2 we will briefly review a recently proposed method to effectively search for small, vastly oscillating signatures in the CMB power spectrum [6,7]. The method is build upon the observation that these features have a small amplitude. Hence, it is possible to significantly speed up the calculation of the time consuming transfer functions through a Taylor expansion. We show that our method recovers oscillations in Planck-like simulated data at a few times 10^{-2} level. Applying our analysis to Planck and WMAP confirms that this method recovers previously obtained results and improves on existing constraints set by the Planck team [1]. We have recently combined our method with the nested sampler MULTINEST

[8,9], which allows us to recover the posterior distribution of the frequency parameter in the Planck data over a large range of frequencies in about 192 CPU hours. We will compare the results of MULTINEST with our previous work in Section 3. In Section 4 we will briefly comment on oscillations in light of the BICEP2 results [10] and will conclude in Section 5.

2 Background and Methodology

In this section we will review our developed method in [6] to search for resonant features applied to the recently released Planck CMB data [7]. We consider two distinct theoretically motivated models:

$$_1\Delta^2_{\mathcal{R}}(k) = A_1 \left(\frac{k}{k_*}\right)^m (1 + A_2 \cos[\omega_1 \log k/k_* + \phi_1])\,, \tag{1}$$

$$_2\Delta^2_{\mathcal{R}}(k) = B_1 \left(\frac{k}{k_*}\right)^m (1 + B_2 k^n \cos[\omega_2 k + \phi_2])\,. \tag{2}$$

We refer to the first model as the "log-spaced oscillations model" and the second model as the "linear oscillations model". For example, axion-monodromy inflation produces features that can be described by the logarithmic oscillations model with $A_1 = H^2/(8\pi^2\epsilon)$, $m = n_s - 1$, $A_2 = \delta n_s$, $\omega_1 = -(\phi_*)^{-1}$ and $\phi_1 = \phi_*$. Model that include the effects from a possible boundary on effective field theory (BEFT) predict features that can be described by the linear oscillations model with $B_1 = H^2/(8\pi^2\epsilon)$, $m = n_s - 1$, $B_2 = \beta/a_0 M$, $n = 1$, $\omega_2 = 2/a_0 H$ and $\phi_2 = \pi/2$. Both initial state modifications and multiverse models [5] can produce logarithmic oscillations, while sharp features generate a power spectrum with linear oscillations (although the amplitude is typically damped as a function of scale). Constraints on oscillations in the WMAP CMB data have been attempted in e.g. Refs. [11,12,13,14,15,16,17].

The method we develop relies on the observation that the features has a small amplitude and therefore we can write the final spectrum as

$$C_\ell \;\; = \;\; C^u_\ell + C^p_\ell, \tag{3}$$

where C^u_ℓ is the "unperturbed part" (i.e. without modulations) and C^p_ℓ is the perturbed part (i.e. with oscillations). The unperturbed part is computed in the usual way, while we can expand the perturbed part around the best-fit parameter values $\bar{\Theta}$ (containing all the plain vanilla ΛCDM parameters $\Omega_b h^2$, $\Omega_{cdm} h^2$, τ, A_s, n_s and H_0), i.e.,

$$C^p_\ell(\omega, \phi, A, \Theta) \;\; = \;\; \bar{C}^{p(\alpha)}_\ell + \bar{C}^{p(\beta)}_\ell + \sum (\Theta_i - \bar{\Theta}_i)(\bar{C}^{p(\alpha)}_{\ell,\Theta_i} + \bar{C}^{p(\beta)}_{\ell,\Theta_i}) + \mathcal{O}((\alpha+\beta)\Theta_i^2). \tag{4}$$

The superscript α and β refer the the phase of the primordial signal in Eq. 1 and Eq. 2, which can easily be rewritten as renormalized amplitudes of a sum of cosine and sine functions. The advantage of writing the spectrum in this form is clear: for rapidly oscillations functions, one needs to set high resolution both in k and in ℓ, hence computing the spectra is time consuming, taking of the order of several minutes on a single CPU for the highest oscillations. Through this expansion one can precompute the $\bar{C}$, $\bar{C}_{\ell,\Theta_i}$ and higher order derivatives, and store them for a large number of frequencies (writing it in the form above, the phase and amplitude can be altered by wighted sums). As a result, one can now perform a simple Metropolis-Hasting Markov Chain Monte Carlo (MH MCMC) using a modified version of COSMOMC [18] for a given frequency and obtain results relatively fast, while allowing all parameters to vary continuously. Higher accuracy is obtained by expanding to higher order in the Θ parameters.

We investigated the validity of this expansion in [6] by generating mock Planck data, and applying this method to recover the inserted signal. An example of such a search and its results in shown in Fig. 1a.

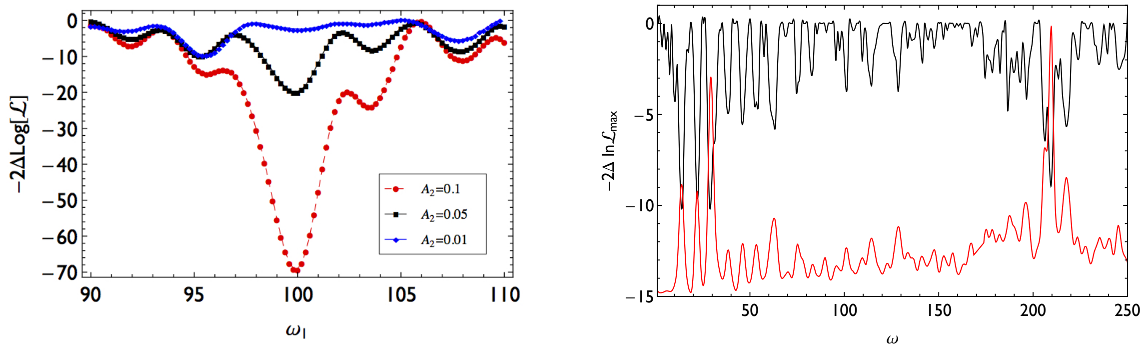

(a) Improvement of fit versus ω_1 for several input amplitude's. $A_2 = 0.1$ and 0.05 are recovered, while $A_2 = 0.01$ is not. The 'oscillations' are a consequence of the noise (which is the same for all 3 simulations). It is clear that features in the noise can amplify and de-amplify some of the signal.

(b) Results for the best-fit (black) and marginalized frequency distribution (red). Compare to top of Fig. 19 in Planck inflation paper.

Figure 1

We then applied this to the WMAP9 data [6] and Planck data [7]. Fig. 1b shows the resulting best-fit contour and the marginalized contour for the frequency parameter ω_1 for log spaced oscillations. There are several tentative hints of a significantly improved fit. The results shown are for the Planck data, which contain many more possible features at low frequency than WMAP9 (not shown). We investigated the highest peaks in more detail, by checking the improvement as a function of multiple ℓ which strongly suggested that the low frequency features are a consequence of an anomaly in the Planck 217 GHz channel around $\ell \sim 1800$. For linear oscillations the improvements are smaller, but we found no specific multipole that caused them. We did however ran several thousand simulations with a null signal, and applied a simple grid based search to estimate how much the noise can contribute to any given signal. This analysis showed that the distribution of $\Delta\chi^2$, is not a 3 parameter $\Delta\chi^2$ distribution, but instead a distribution that peaks around $\Delta\chi^2 \sim 10$, and $\Delta\chi^2 \sim 27$ is the 3 sigma limit (see Fig. 2). Hence, for highly oscillating features, it is very hard to say if one is simply fitting the noise, or an actual residual coming from the primordial power spectrum.

3 Multinest

In our analyst we used a MH MCMC for each frequency because a MH sampling is not fit to search a high irregular likelihood. The frequency parameter causes this irregularity and in order to obtain convergence, one needs to fix the frequency. As a result, the time needed to reconstruct the best-fit contours depends on the resolution in frequency space. In our work we considered about 1000 steps. Although these can run a in parallel, this is far from optimal and requires a substantial amount of CPU hours. The nested sampler MULTINEST [8,9] is a much better sampler in case of irregular posteriors. We recently modified our code to work with multinest. We still precompute the perturbed C_ℓ^u for many frequencies, but we added a spline routine that allows one to continuously sample through frequency space. The results of the search for log-spaced oscillations is shown in Fig. 1b. For reference, one should compare this to Fig. 19 in [1]. The advantages of our method compared to the result shown in that figure are twofold. First, we can vary all cosmological parameters (as opposed to just 3 in that particular work), which leads to slightly bigger improvements. Second, we can run up to high frequencies with only limited computational time increase. The total time to reproduce the posterior as shown in Fig. 1b is 192 CPU hours (16 hours x 12 cores). We plan to make the code publicly available.

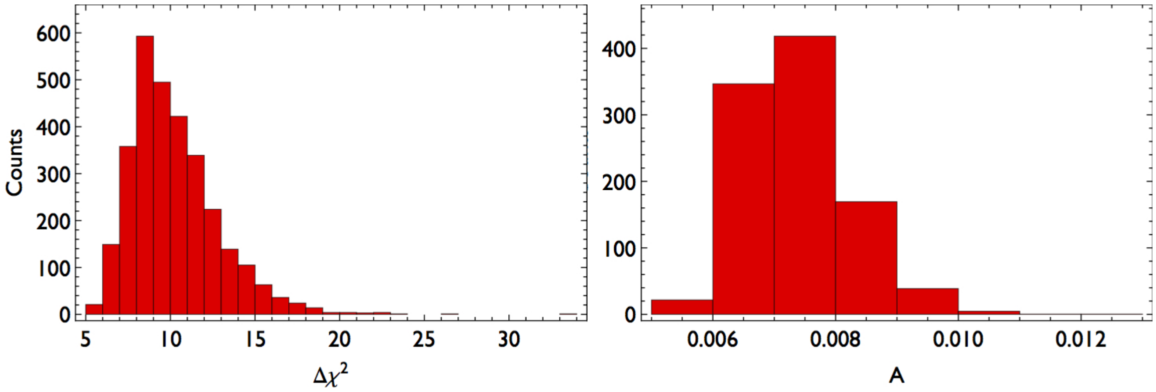

Figure 2: $\Delta\chi^2$ distribution for 5000 null simulations (right) and distribution of associated best-fit amplitudes (projected). The noise can account for improvement up to $\Delta\chi^2 \sim 30$.

4 BICEP

The BICEP detection of B-mode polarization, if primordial, increases tension between the TT data (Planck) and the ΛCDM + r concordance model. At the same time, $r \simeq 0.2$ violates the *Lyth* bound [19,20], and indicates the field responsible for inflation, underwent super Planckian displacement. Although a violation of the bound is a not an actual physical bound that can never be violated, it does pose a concern from a model building perspective, which usually relies on integrating out UV physics and working in an effective framework. When the *Lyth* bound is violated, it requires a UV complete theory to fully understand the mechanism of inflation. One working example is axion-monodromy inflation, in which a shift symmetry naturally produces a super Planckian displacements This models also produces features and we investigated if such a feature can lead to an improved fit. Such a feature should be a very long wavelength feature, complementary to the highly oscillating features investigated above. At these long wavelengths, one expects large degenerecies since an oscillation effectively causes a particular rescaling of the amplitude and scale dependence of the power spectrum. Hence, it is necessary to vary all parameters non-perturbatively. In order to avoid getting stuck in a local minimum of the posterior when running through frequency space, we considered a very narrow prior on the frequency, with $10^{-2} \leq \omega \leq 2$ for the log spaced oscillation template of Eq. 1. We also included oscillations in the BB power spectrum for completeness. Our analysis included Planck, BICEP2, ACT, SPT and WMAP polarization data. Quite interestingly, we find an improved fit with $\Delta\chi^2 \sim 11$, which has significant modification for $\ell < 100$, and no modulations on small scales; the long wavelength oscillation is compensated by a large tilt $n_s \sim 1$ to render the spectrum equivalent to scale dependent spectrum with a tilt $n_s = 0.96$ on small scales. We will explore the potential of such a feature in a forthcoming paper [21].

5 Conclusions

We reviewed a newly developed technique to look for highly oscillatory features in the CMB power spectrum. This method allows one to vary all cosmological parameters, which has typically been limited by the slow computation of the transfer functions. Applying the method to mock data recovers the mock signal. When applied to the Planck CMB data, we found several tentative hints, which we further investigated. We showed that cosmic variance + noise can account for these findings, as over a sample of 5000 Universes one expects a $\Delta\chi^2 \sim 10$ within the prior volume investigated. For log spaced oscillations the improvement appears to be entirely due a feature in the 217GHz map at $\ell \sim 1800$. We have recently implemented our code in the MULTINEST sampler, which allowed us to recover previous results in only 192 CPU hours. We briefly discussed the possibility of a large feature to release some of the tension between the data and the ΛCDM $+r$ concordance cosmology. We find that there exists a very clear feature that can improve the fit significantly. We will discuss these findings in a shortly forthcoming paper [21].

Acknowledgments

P.D.M would like to thank the organizers of the Moriond conference for organizing an excellent conference. P.D.M. was supported by the John Templeton Foundation grant number 37426.

References

1. Planck Collaboration, P. A. R. Ade, N. Aghanim, C. Armitage-Caplan, M. Arnaud, M. Ashdown, F. Atrio-Barandela, J. Aumont, C. Baccigalupi, A. J. Banday, and et al. Planck 2013 results. XXII. Constraints on inflation. *ArXiv e-prints*, March 2013.
2. B. Greene, K. Schalm, J. P. van der Schaar, and G. Shiu. Extracting New Physics from the CMB. In P. Chen, E. Bloom, G. Madejski, and V. Patrosian, editors, *22nd Texas Symposium on Relativistic Astrophysics*, pages 1–8, 2005.
3. R. Flauger, L. McAllister, E. Pajer, A. Westphal, and G. Xu. Oscillations in the CMB from axion monodromy inflation. *J. Cosm. Astropart. Phys.*, 6:9, June 2010.
4. A. Achúcarro, J.-O. Gong, S. Hardeman, G. A. Palma, and S. P. Patil. Features of heavy physics in the CMB power spectrum. *J. Cosm. Astropart. Phys.*, 1:30, January 2011.
5. G. D'Amico, R. Gobbetti, M. Kleban, and M. Schillo. Unwinding inflation. *J. Cosm. Astropart. Phys.*, 3:4, March 2013.
6. P. D. Meerburg, D. N. Spergel, and B. D. Wandelt. Searching for oscillations in the primordial power spectrum. II. Constraints from Planck data. Phys. Rev. *D*, 89(6):063537, March 2014.
7. P. D. Meerburg, D. N. Spergel, and B. D. Wandelt. Searching for oscillations in the primordial power spectrum. I. Perturbative approach. Phys. Rev. *D*, 89(6):063536, March 2014.
8. F. Feroz, M. P. Hobson, and M. Bridges. MULTINEST: an efficient and robust Bayesian inference tool for cosmology and particle physics. *Mon. Not. R. Astron. Soc.*, 398:1601–1614, October 2009.
9. F. Feroz, M. P. Hobson, E. Cameron, and A. N. Pettitt. Importance Nested Sampling and the MultiNest Algorithm. *ArXiv e-prints*, June 2013.
10. BICEP2 Collaboration. BICEP2 I: Detection Of B-mode Polarization at Degree Angular Scales. *ArXiv e-prints*, March 2014.
11. J. Martin and C. Ringeval. Superimposed oscillations in the WMAP data? Phys. Rev. *D*, 69(8):083515, April 2004.
12. C. Dvorkin and W. Hu. Complete WMAP constraints on band-limited inflationary features. Phys. Rev. *D*, 84(6):063515, September 2011.
13. J. Hamann, L. Covi, A. Melchiorri, and A. Slosar. New constraints on oscillations in the primordial spectrum of inflationary perturbations. Phys. Rev. *D*, 76(2):023503, July 2007.
14. C. Pahud, M. Kamionkowski, and A. R. Liddle. Oscillations in the inflaton potential? Phys. Rev. *D*, 79(8):083503, April 2009.
15. P. D. Meerburg, R. A. M. J. Wijers, and J. P. van der Schaar. WMAP7 constraints on oscillations in the primordial power spectrum. *Mon. Not. R. Astron. Soc.*, 421:369–380, March 2012.

16. H. Peiris, R. Easther, and R. Flauger. Constraining Monodromy Inflation. *ArXiv e-prints*, March 2013.
17. M. Aich, D. K. Hazra, L. Sriramkumar, and T. Souradeep. Oscillations in the inflaton potential: Complete numerical treatment and comparison with the recent and forthcoming CMB datasets. Phys. Rev. *D*, 87(8):083526, April 2013.
18. A. Lewis and S. Bridle. Cosmological parameters from CMB and other data: A Monte Carlo approach. Phys. Rev. *D*, 66(10):103511, November 2002.
19. D. H. D. H. Lyth and A. A. Riotto. Particle physics models of inflation and the cosmological density perturbation. *Phys. Rep.*, 314:1–146, June 1999.
20. R. Easther, W. H. Kinney, and B. A. Powell. The Lyth Bound and the end of inflation. *J. Cosm. Astropart. Phys.*, 8:4, August 2006.
21. P. D. Meerburg, F. Flauger, E. Pajer, and D. N. Spergel. Alleviating the tension at low ℓ through Axion Monodromy. *in preperation*, 2014.

The Cold Spot in the Cosmic Microwave Background: the Shadow of a Supervoid

István Szapudi[1], András Kovács[2,3], Benjamin R. Granett[4], Zsolt Frei[2,3], Joseph Silk[5], J. García-Bellido [6], Will Burgett[1], Shaun Cole[7], Peter W. Draper[7], Daniel J. Farrow[7], Nicholas Kaiser[1], Eugene A. Magnier[1], Nigel Metcalfe[7], Jeffrey S. Morgan[1], Paul Price[8], John Tonry[1], Richard Wainscoat[1]
[1] Institute for Astronomy, University of Hawaii 2680 Woodlawn Drive, Honolulu, HI, 96822, USA
[2] *Institute of Physics, Eötvös Loránd University, 1117 Pázmány Péter sétány 1/A Budapest, Hungary*
[3] *MTA-ELTE EIRSA "Lendület" Astrophysics Research Group, 1117 Pázmány Péter sétány 1/A Budapest, Hungary*
[4]*INAF OA Brera, Via E. Bianchi 46, Merate, Italy*
[5]*Department of Physics and Astronomy, The Johns Hopkins University, Baltimore MD 21218, USA*
[6] *Instituto de Física Teórica IFT-UAM/CSIC, Universidad Autónoma de Madrid, Cantoblanco 28049 Madrid, Spain*
[7]*Department of Physics, Durham University, South Road, Durham DH1 3LE, UK*
[8]*Department of Astrophysical Sciences, Princeton University, Princeton, NJ 08544*

Standard inflationary hot big bang cosmology predicts small fluctuations in the Cosmic Microwave Background (CMB) with isotropic Gaussian statistics. All measurements support the standard theory, except for a few anomalies discovered in the Wilkinson Microwave Anisotropy Probe maps and confirmed recently by the Planck satellite. The Cold Spot is one of the most significant of such anomalies, and the leading explanation of it posits a large void that imprints this extremely cold area via the linear Integrated Sachs-Wolfe (ISW) effect due to the decay of gravitational potentials over cosmic time, or via the Rees-Sciama (RS) effect due to late-time non-linear evolution. Despite several observational campaigns targeting the Cold Spot region, to date no suitably large void was found at higher redshifts $z > 0.3$. Here we report the detection of an $R = (192 \pm 15)\mathrm{h}^{-1}$Mpc size supervoid of depth $\delta = -0.13 \pm 0.03$, and centred at redshift $z = 0.22$. This supervoid, possibly the largest ever found, is large enough to significantly affect the CMB via the non-linear RS effect, as shown in our Lemaitre-Tolman-Bondi framework. This discovery presents the first plausible explanation for any of the physical CMB anomalies, and raises the possibility that local large-scale structure could be responsible for other anomalies as well.

1 Introduction

The Cosmic Microwave Background (CMB) Cold Spot (CS) is an exceptionally cold area centered on on $(l, b) \simeq (209^\circ, -57^\circ)$ and was first detected in the Wilkinson Anisotropy Probe [1] at $\simeq 3\sigma$ significance using wavelet filtering [2,3]. The CS is perhaps the most significant among the anomalies recently confirmed by Planck [4]. Given that these potential departures from Gaussianity and/or isotropy have relatively low significance, any of them could represent somewhat rare statistical fluctuations. Nevertheless, they are significant enough to warrant further studies, and indeed they have already spawned a score of interesting ideas. Some of these appeal to hitherto undiscovered physics, e.g., textures [5,6], while others [7,8,9,10] posit that the CS, and possibly other anomalies, are caused by the Integrated Sachs-Wolfe effect (ISW) [11,12] of the decaying gravitational potentials, which in turn is caused by Dark Energy. The latter explanation would require of a large, $\gtrsim 200\mathrm{h}^{-1}$Mpc supervoid centered on the CS [7,8], readily detectable in large scale structure surveys.

In the past, there have been several attempts to search for voids in large scale structure data in the direction of the CS. Rudnick et al.[13] detected a low density region approximately aligned with the CS, although the detection significance has been disputed[14]. Bremer et al.[15] conducted a redshift survey in the area, and found no evidence for a void in the redshift range of $0.35 < z < 1$, while Granett et al.[16] conducted an imaging survey with photometric redshifts, and excluded the presence of a large underdensity of $\delta \simeq -0.3$ between redshifts of $0.5 < z < 0.9$. Both of these surveys ran out of volume at low redshifts due to their small area, although the data[16]are consistent with the presence of a void at $z < 0.3$ with low significance and no void was found at $0.3 < z < 0.5$, even if the existence of one could not be excluded at high significance. The contribution to the ISW effect due to structures at low redshift was investigated as well[18]. Using a photometric redshift catalogue constructed from 2MASS[21] and SuperCOSMOS[22] surveys with a median redshift of $z = 0.08$, an under-density in the galaxy distribution was found in the CS direction. This under density can account for a CMB decrement of $\Delta T \simeq -7\mu$K in the Λ-Cold Dark Matter (ΛCDM) model, i.e. falling short of fully explaining the CS anomaly. Note that although no void has been found that could fully explain the CS anomaly, there is strong, $\gtrsim 4.4\sigma$, statistical evidence that superstructures imprint on the CMB as cold and hot spots[23,4,24].

The principal scientific question, whether a void causes the CS, can be approached on three levels: i) is there a low density region (supervoid) in the CS region ii) if there is, how rare is that superstructure iii) is that structure large and deep enough to significantly contribute to the CS in the framework of the (linear) ISW effect in ΛCDM (or alternative) theories? In particular, if the first question is answered affirmatively, and the resulting void is rare enough that chance alignment with the CS is unlikely, the connection can be established regardless the answer of the third question. Present work is focused on the observational question i) as it can be answered with our data set at high significance. As we show later, we detect a low density region centered on the CS. We also engage question iii) with simultaneous modeling of the underdensity in the galaxy field and the CS pattern observed in CMB maps. On the other hand, we will address ii) at an approximate fashion.

2 Methods

Next we describe some of our methods and procedures, while Szapudi etal.[19] and Finelli etal.[20] can be consulted for further details.

To probe the low redshift region unconstrained by previous studies, a large area survey is needed reaching up to $z \simeq 0.3$. The redshift distribution of the recently produced WISE-2MASS catalog[25] has a median redshift of $z \simeq 0.14$, and covers 21,200 square degrees after masking dusty regions. The catalog contains sources to flux limits of $W1_{WISE} \leq 15.2$ mag and $J_{2MASS} \leq 16.5$ mag. These conservative limits result in a dataset deeper than 2MASS and more uniform than WISE[26].

Galaxies are biased tracers of the underlying dark matter distribution, we thus measured and modeled the angular power spectrum of WISE-2MASS galaxies, and found a bias $b_g = 1.41 \pm 0.07$. We look for underdensity at the CS in this projected density field, and scan the full observable sky in order to identify the largest underdensities at $z < 0.3$.

We then set out to create a detailed map of the CS region in three dimensions. Therefore, WISE-2MASS galaxies have been matched with Pan-STARRS1[27] (PS1) objects within a $50^\circ \times 50^\circ$ area centred on the CS, except for a Dec ≥ -28.0 cut to conform to the PS1 boundary. We used PV1.2 reprocessing of PS1 in an area of 1,300 square degrees. For PS1, we required a proper measurement of Kron and PSF magnitudes in $g_{\rm P1}$, $r_{\rm P1}$ and $i_{\rm P1}$ bands that were used to construct photometric redshifts (photo-z's) with a Support Vector Machine algorithm. The training and control sets were created matching WISE-2MASS, PS1, and the Galaxy and Mass Assembly[28] (GAMA) redshift survey. Our three dimensional catalog of WISE-2MASS-PS1

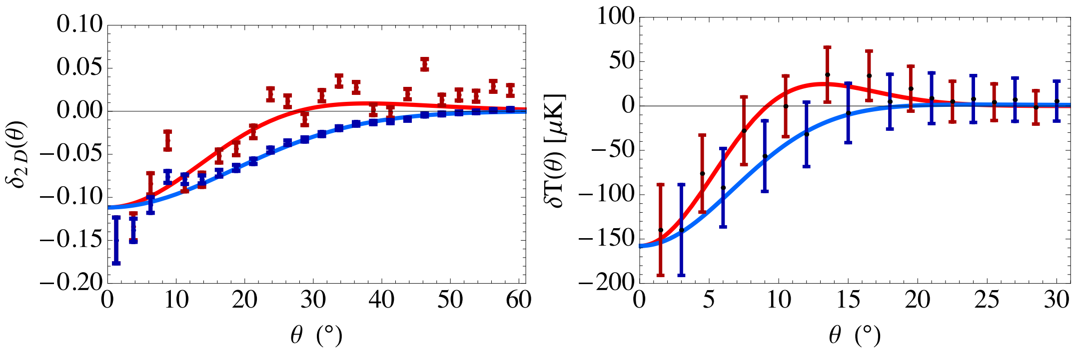

Figure 1 – The density profile from WISE-2MASS catalogue compared with the theoretical model for the underdensity (3) (left panel). The temperature profile from Planck SMICA map (right panel) compared with the predicted signal (4). The red (blue) lines are the theoretical profiles for rings (disks) and in dark red (blue) are the measurements.

galaxies contains photo-z's with an estimated error of $\sigma_z \approx 0.034$. Redshift distribution of our data set is shown in the upper left panel of Fig. 3.

For our measurements, we take the centre and the size of the CS from the literature as measured in the CMB temperature maps. In particular we use the latest Planck results [4] for the centre $(l, b) \simeq (209°, -57°)$ in Galactic coordinates, and $R = 5°$ [2,3] and $R = 15°$ [9,14] radii for the size. The $R \leq 5°$ region is the most anomalous part of the CS region, while an outer hot ring at $R \approx 15°$ makes the whole structure more significant [14].

3 Measurements with WISE-2MASS

The projected radial profile centred on the CS is shown in the left panel of Fig. 1. Measurement errors are due to Poisson fluctuations calculated from the expected number of galaxies in a ring or a disk. We detect a low density region with overwhelming significance. In particular, at our pre-determined radii, 5° and 15°, we find signal-to-noise ratios $S/N \sim 12$ for rings. The size of the underdense region is surprisingly large: it is detected to $\sim 20°$ with high ($\gtrsim 5\sigma$) significance. At larger radii, the radial profile is consistent with a supervoid surrounded by a gentle compensation (overdensity) that converges to the average galaxy density at $\sim 50°$ [17]. The supervoid might also contain a deeper inner void, with its own compensation at around $\simeq 8°$.

The underdensity in WISE-2MASS is modeled within a ΛLTB framework [29], assuming a spatial curvature profile $k(r) = k_0 \, r^2 \exp(-r^2/r_0^2)$. A linear metric perturbation in ΛCDM is defined as

$$\Phi(\tilde{r}) = \Phi_0 \, \tau^2 \, e^{-\frac{\tilde{r}^2}{\tilde{r}_0^2}} \, , \tag{1}$$

with an LTB radius r defined as $\tilde{r} = \sqrt{3/4\pi} \, H_0 r$ using the co-moving FRW radius and τ conformal time. A 3D density profile for the void corresponds to this scalar potential, given as

$$\delta(\tilde{r}) = -\delta_0 \left(1 - \frac{2\tilde{r}^2}{3\tilde{r}_0^2}\right) \, e^{-\frac{\tilde{r}^2}{\tilde{r}_0^2}} \, , \tag{2}$$

and characterized by two parameters, co-moving width $\tilde{r}_0$ and depth δ_0. Then the 3D density profile (2) is projected onto the transverse plane using the WISE-2MASS window function $\phi(y)$, with the center of the supervoid at co-moving distance y_0, and $\tilde{r}^2(y, \theta) = y^2 + y_0^2 - 2yy_0 \cos\theta$,

$$\delta_{2D}(\theta) = \int_0^\infty \delta\left(\tilde{r}(y, \theta)\right) \, y^2 \phi(y) dy \, . \tag{3}$$

The linear ISW and the non-linear RS effects are derived from the metric perturbation (1).

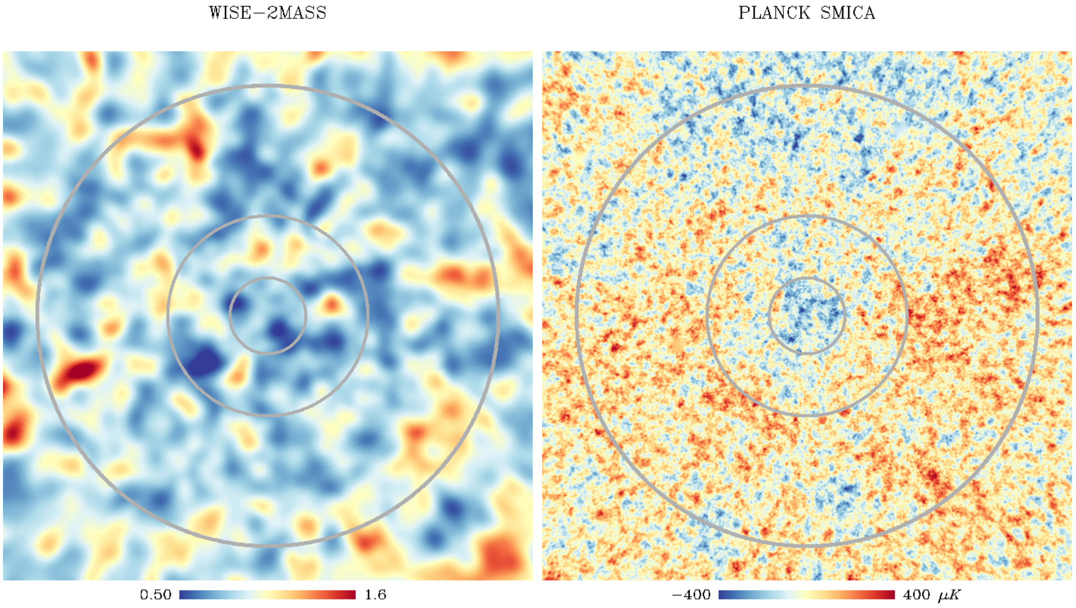

Figure 2 – The WISE-2MASS (left) and Planck SMICA (right) maps in the direction of the Cold Spot. Circles correspond to 5°, 14° and 29° radii.

Note that effect on the CMB is dominated by the non-linear Rees-Sciama effect for a large compensated void with a profile of Eq. 2, as given by

$$\delta T(\theta) = -A\left(1 - \frac{28}{13}\frac{\theta^2}{\tilde{\theta}_0^2}\right) e^{-2\frac{\theta^2}{\tilde{\theta}_0^2}}, \tag{4}$$

where $\tilde{\theta}_0 = \sqrt{3/4\pi}\,\theta_0$, assuming small angle approximation, $\tan\theta \simeq \theta$. The ISW effect is proportional to the time derivative of the potential, thus usually smoother then the density field. The RS effect, however, depends on higher derivatives, thus the size of the CMB pattern is more compact then the size of the void. The actual coupling is described by a $\sqrt{3/4\pi} \simeq 0.48$ scaling factor between the scales of the underdensity and the corresponding pattern on the CMB. The magnitude of the CMB temperature depression depends on the parameters of the void,

$$A = 51.0\,\mu\mathrm{K}\left(\frac{r_0}{155.3\,h^{-1}\mathrm{Mpc}}\right)^3\left(\frac{\delta_0}{0.2}\right)^2, \tag{5}$$

and $\theta_0 = (180°/\pi)(r_0/d_A(z_0))$, with $d_A(z)$ the angular diameter distance in a flat ΛCDM model ($\Omega_\mathrm{M} = 0.3, h = 0.7$), and z_0 the redshift of the center of the void, at co-moving distance $y_0 = y(z_0)$.

A large LTB void can explain a CMB cold spot of about half the size, or the same decrement can be explained by a shallower void than is allowed by ΛCDM cosmology. Note that the LTB model is only used as a general relativistic model for the void dynamics and its effect on the CMB, while the background cosmology is assumed to be standard ΛCDM.

For detailed measurements, a χ^2 statistic is constructed. We perform a simultaneous fit for the projected LTB void in the WISE-2MASS map, and the corresponding temperature depression effect in the CMB data. We carry out a 3-parameter fit δ_0, r_0, and z_0, which are fitted by the following statistic:

$$\chi^2_\mathrm{tot}(\delta_0, r_0, z_0) = \chi^2_\mathrm{LSS} + \chi^2_\mathrm{CMB}, \tag{6}$$

$$\chi^2_\mathrm{LSS} = \sum_i \frac{\left(\delta_{2D}(\theta_i) - \delta_i^\mathrm{LSS}\right)^2}{\sigma_i^2}, \tag{7}$$

$$\chi^2_{\rm CMB} \;=\; \sum_{ij}\Big(\delta T(\theta_i) - \delta T_i^{\rm CMB}\Big) C^{-1}_{ij}\Big(\delta T(\theta_j) - \delta T_j^{\rm CMB}\Big)\,. \tag{8}$$

The first term corresponds to the χ^2 of the projected LTB void profile (3) in the WISE-2MASS density field, using uncorrelated Poisson errors, σ_i. The second term is the χ^2 of the CMB profile compared with the LTB prediction (4) of the void observed in WISE-2MASS. Note that Poisson fluctuations are uncorrelated, while the covariance matrix of rings in the CMB indicates correlations, and it was determined from 10,000 Gaussian CMB realizations. The best fit LTB void parameters we have found are $\delta_0 = 0.25 \pm 0.10$ (1σ), $r_0 = (195 \pm 35)\mathrm{h}^{-1}$Mpc (1σ), and $z_0 = 0.16 \pm 0.04$ (1σ).

The LTB model parameter δ_0 is the 3D dark matter density, giving a 12% projected underdensity at the center of the void, i.e. $\delta_{\rm 2D}(\theta = 0) = -0.12$. The angular sizes $\theta_0 = 28.8^\circ \pm 5.2^\circ$, and $\tilde{\theta}_0 = 14.1^\circ \pm 2.5^\circ$ are derived parameters, which correspond to angular scales of the profile on the galaxy map and the CMB, respectively. Note that the radius of the LTB profile $\tilde{\theta}_0 = 14.1^\circ \pm 2.5^\circ$ on the CMB matches the outer hot ring around the cold spot discussed in [30]. For later comparison, we calculate the averaged underdensity within the best fit radius $r_0 = 195\,h^{-1}$Mpc. The 3D top-hat-averaged density from the LTB profile, see Eq. (2), is $\bar{\delta} = 3/r_0^3 \int_0^{r_0} r^2 dr \delta(r) = -\delta_0/e$. This finally gives the average void depth $\bar{\delta} = -0.10 \pm 0.03$.

4 Measurements with WISE-2MASS-Pan-STARRS1

Photometric redshifts in the WISE-2MASS-PS1 galaxy catalog provide a three-dimensional view of the superstructure. We count galaxies as a function of redshift in disks centred on the CS using the two pre-determined angular radii, $R = 5^\circ$, and 15°. The galaxy density calculated from the average redshift distribution is shown in the upper panel of Fig. 3. Note that the larger disk is not fully contained in our photo-z catalog due to the limited PS1 footprint. In photo-z bins of width of $\Delta z = 0.035$, we found $S/N \sim 5$ and $S/N \sim 6$ for the deepest under-density bins, respectively. The measurement errors are still due to Poisson fluctuations in the redshift bins. To extend our analysis to higher redshifts, we add a previous measurement [16] in a photo-z bin centred at $z = 0.4$.

For a rudimentary understanding of our counts, we build toy models from top-hat voids in the z direction convolved with the photo-z errors. This model has three parameters, redshift ($z_{\rm void}$), radius ($R_{\rm void}$), and depth (δ_g). We carry out the χ^2-based maximum likelihood parameter estimation for $R = 15^\circ$, using our first 10 bins combined with the extra bin measured by [16] for $n = 11$ data points. We find $\chi^2_0 = 92.4$ for the null hypothesis of no void. The marginalized results for the parameters of our toy model are $z_{\rm void} = 0.22 \pm 0.01$ (2σ), $R_{\rm void} = (192 \pm 15)\mathrm{h}^{-1}$Mpc (2σ), and $\delta_g = -0.18 \pm 0.01$ (2σ) finding $\chi^2_{min} = 5.97$. For $k = 3$ parameters, there is $\nu = n - k = 8$ degrees of freedom, i.e. the toy model is a surprisingly good fit and clearly preferred over the null hypothesis. We take the galaxy bias into account finding an average depth of $\delta = \delta_g/b_g \simeq -0.13 \pm 0.03$ (2σ).

While the toy model quantifies the properties of the void, careful inspection of the Figures reveals a complex structure. There appears to be a compensation in front of the supervoid at around $z \simeq 0.05 - 0.08$, and the significantly deeper counts at the smaller radii show that the void is deeper at the centre. An approximate tomographic imaging of the CS region is presented in Fig. 4. in three slices of $z < 0.09$, $0.11 < z < 0.14$, $0.17 < z < 0.22$ and smoothed at 2° scales. The Planck [4] SMICA CMB temperature map is over-plot with contours. While we characterized the profile in radial bins, the geometry of the supervoid is more complex. It is noteworthy that deepest part of the void is close to the centre of the CS in the middle slice. Given the enormous size, the rich structure is expected: the supervoid contains voids, their compensations, filaments, and appears to have its own compensation.

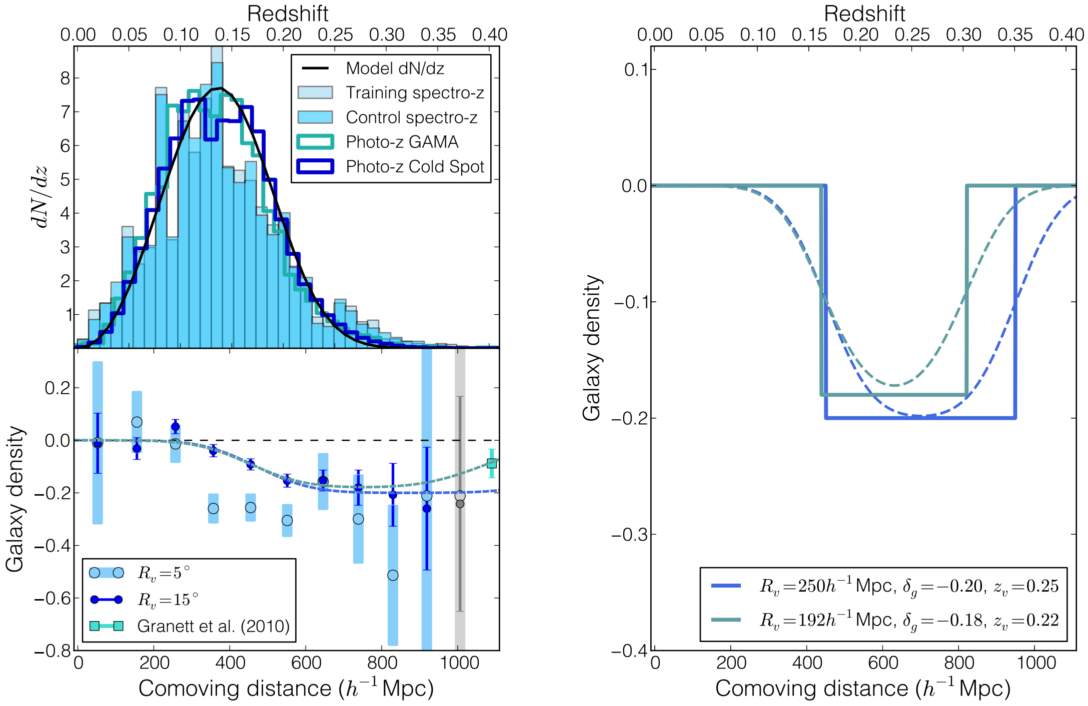

Figure 3 – Left: Redshift Space Distribution in the Cold Spot Region. The upper panel illustrates the normalized redshift distribution of our subsamples used in the photo-z pipeline; training and control sets selected in GAMA, photo-z distributions estimated for the WISE-2MASS-PS1-GAMA control sample, and photo-z's of interest in the WISE-2MASS-PS1 matched area. The median redshift of all samples is $z \simeq 0.14$. The lower left panel shows galaxy densities measured at the two fiducial radii in the CS region. The blue dashed lines show our best fit top hat toy model that folds in the photometric redshift errors. The green dashed lines illustrate that without the earlier measurement (the rightmost point [16]) we could not distinguish a much larger void. Right: Top-hat void models. The plot shows the best fit, and a slightly larger 3-parameter top hat toy model for a supervoid. The latter could not be excluded by PS1 data alone. Dashed curves represent the smearing of the profile by photo-z errors. The model redshift distribution of our observations was multiplied by this smeared profile, and the resulting profile was convolved with the photo-z error.

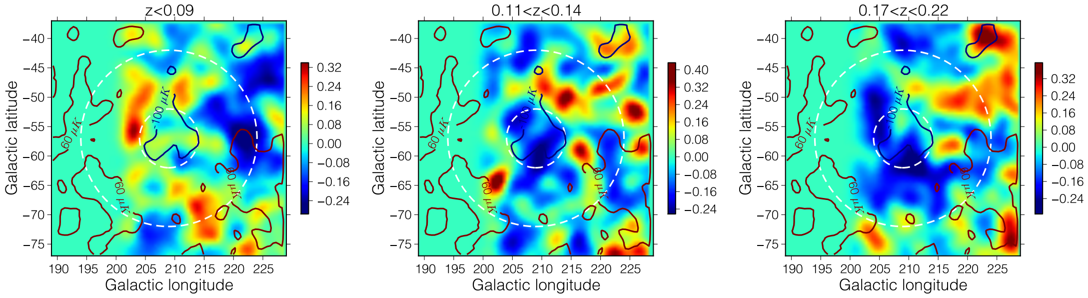

Figure 4 – Tomographic view of the CS region. Below $z < 0.09$ appears to show the front compensation (higher density area) of the large void, although there is an under dense structure to the right. The slice at $0.11 < z < 0.14$ cuts into front of the supervoid, and the ring round represents a slice of the compensation. Finally the slice $0.17 < z < 0.22$ cuts into the front half of the supervoid with compensation around it. The structure on the upper right reaching into the supervoid might be real, or a shadow of the same structure in the middle figure due to the photometric redshift errors. Note that the left side of the images reflects the mask of the PS1 data set.

5 Discussion & Conclusions

We have found evidence for a supervoid at redshift $z = 0.22 \pm 0.01$ with radius $R = (192 \pm 15)\,h^{-1}\mathrm{Mpc}$ and depth of $\delta = -0.13 \pm 0.03$. These parameters are in excellent agreement with the findings of our WISE-2MASS projected density analysis, with the redshift slightly closer, but only by 1.5σ. Note that the orthogonal nature of the two measurements suggest spherical symmetry for the void.

We conclude that a non-linear LTB model based on the projected profile in the WISE-2MASS catalog matches well the profile observed on the CMB. We also estimated the linear ISW effect due to such an underdensity from a simple approximation[13]. We found that it could significantly affect the CMB, of order -20 μK, falling short of a full explanation of the CS anomaly. The above findings address questions i) and iii) in the introduction.

The tomographic maps produced by photometric redshifts from PS1, while not extending to large enough radii at the moment, have an intriguing match with the Cold Spot region as observed on the CMB. The observed morphological similarity to a compensated surrounding over dense shell, which plausibly would have fragmented into galaxy clusters visible in the projected slices as several "hot spots" surrounding the CS, is noteworthy. Based on our toy model, and assuming a simple Gaussian model in ΛCDM cosmology, we now attempt to answer question ii), i.e the rarity of the supervoid. We estimate that the supervoid we detected corresponds to a rare, at least $\gtrsim 3.5\sigma$, density fluctuation; thus chance alignment with another rare structure, the CS, is negligible. As a further test, we smoothed the projected WISE-2MASS map with a 25° Gaussian finding only one underdensity as significant as the one we discovered in the CS region. This second void, to be followed up in future research, is clearly visible in shallow 2MASS maps[31,18] as a large underdensity, and in the corresponding reconstructed ISW map[32] as a cold imprint. Therefore we conclude that it is likely to be closer thus smaller in physical size, and not large enough to leave colder imprints on the CMB.

Any tension with ΛCDM, e.g. in the possible rarity of the observed supervoid, could be addressed in models of modified gravity, ordinarily screened in clusters, but resulting in an enhanced growth rate of voids as well as an additional contribution to the ISW signal.

Acknowledgments

The authors thank Fabio Finelli and Francesco Paci who had crucial roles in developing the LTB explanation for the Cold Spot[20]. We acknowledge the support of NASA grants NNX12AF83G and NNX10AD53G. AK and ZF acknowledge support from OTKA through grant no. 101666. In addition, AK acknowledges support from the Campus Hungary fellowship program. We make use of HEALPix[34] software in our project. The Pan-STARRS1 Surveys (PS1) have been made possible through contributions by the Institute for Astronomy, the University of Hawaii, the Pan-STARRS Project Office, the Max-Planck Society and its participating institutes, the Max Planck Institute for Astronomy, Heidelberg and the Max Planck Institute for Extraterrestrial Physics, Garching, The Johns Hopkins University, Durham University, the University of Edinburgh, the Queen's University Belfast, the Harvard-Smithsonian Center for Astrophysics, the Las Cumbres Observatory Global Telescope Network Incorporated, the National Central University of Taiwan, the Space Telescope Science Institute, and the National Aeronautics and Space Administration under Grant No. NNX08AR22G issued through the Planetary Science Division of the NASA Science Mission Directorate, the National Science Foundation Grant No. AST-1238877, and the University of Maryland, and Eotvos Lorand University (ELTE).

References

[1] C. L. Bennett, D. Larson, and J. L et al. Weiland. *ArXiv e-prints*, December 2012.

[2] P. Vielva et al. *ApJ*, 609:22–34, July 2004.

[3] M. Cruz et al. *MNRAS*, 356:29–40, January 2005.

[4] Planck 2013 results. XXIII. *ArXiv e-prints*, March 2013.

[5] M. Cruz et al. *MNRAS*, 390:913–919, November 2008.

[6] P. Vielva. *Advances in Astronomy*, 2010, 2010.

[7] K. T. Inoue and J. Silk. *ApJ*, 648:23–30, September 2006.

[8] K. T. Inoue and J. Silk. *ApJ*, 664:650–659, August 2007.

[9] K. T. Inoue, N. Sakai, and K. Tomita. *ApJ*, 724:12–25, November 2010.

[10] K. T. Inoue. *MNRAS*, 421:2731–2736, April 2012.

[11] R. K. Sachs and A. M. Wolfe. *ApJL*, 147:73, January 1967.

[12] M. J. Rees and D. W. Sciama. *Nature*, 217:511–516, February 1968.

[13] L. Rudnick, S. Brown, and L. R. Williams. *ApJ*, 671:40–44, December 2007.

[14] K. M. Smith and D. Huterer. *MNRAS*, 403:2–8, March 2010.

[15] M. N. Bremer et al. *MNRAS*, 404:L69–L73, May 2010.

[16] B. R. Granett, I. Szapudi, and M. C. Neyrinck. *ApJ*, 714:825–833, May 2010.

[17] P. Pápai, and I. Szapudi. *ApJ*, 725:2078–2086, 2010

[18] C. L. Francis and J. A. Peacock. *MNRAS*, 406:14–21, July 2010.

[19] Szapudi, I. and Kovács, A., Granett, B. R., et al. arXiv:1405.1566, 2014.

[20] Finelli, F., Garcia-Bellido, J., Kovacs, A., Paci, F., and Szapudi, I. arXiv:1405.1555, 2014.

[21] M. F. Skrutskie, R. M. Cutri, R. Stiening, and et al. *AJ*, 131:1163–1183, February 2006.

[22] N. C. Hambly and et al. *MNRAS*, 326:1279–1294, October 2001.

[23] B. R. Granett, M. C. Neyrinck, and I. Szapudi. *ApJ*, 683:L99–L102, August 2008.

[24] Y.-C. Cai et al. *ArXiv e-prints*, January 2013.

[25] A. Kovács and I. Szapudi. *ArXiv e-prints*, December 2014.

[26] E. L. Wright et al. *AJ*, 140:1868–1881, December 2010.

[27] N. Kaiser. In *SPIE Conference Series*, 2004.

[28] S. P. Driver, D. T. Hill, and et al. *MNRAS*, 413:971–995, May 2011.

[29] J. Garcia-Bellido and T. Haugbølle. *JCAP*, 4:3, April 2008.

[30] R. Zhang and D. Huterer. *Astroparticle Physics*, 33:69–74, March 2010.

[31] A. Rassat, J.-L. Starck, and F.-X. Dupé. *A&A*, 557:A32, September 2013.

[32] A. Rassat and J.-L. Starck. *A&A*, 557:L1, September 2013.

[33] The Dark Energy Survey Collaboration. *ArXiv Astrophysics e-prints*, October 2005.

[34] K. M. Gorski, E. Hivon, and et al. *ApJ*, 622:759–771, April 2005.

EBEX, THE E AND B EXPERIMENT

JOY DIDIER[1], ASAD M. ABOOBAKER[2], PETER ADE[3], FRANÇOIS AUBIN[2], CARLO BACCIGALUPI[5], KEVIN BANDURA[4], CHAOYUN BAO[2], JULIAN BORRILL[7], BIKRAMJIT CHANDRA[2], DANIEL CHAPMAN[1], MATT DOBBS[4], JULIEN GRAIN [14], WILL GRAINGER[3], SHAUL HANANY[2], KYLE HELSON[11], SETH HILLBRAND[1], GENE HILTON[18], HANNES HUBMAYR[18], KENT IRWIN[18], BRADLEY JOHNSON[1], ANDREW JAFFE[8], TERRY JONES[2], TED KISNER[7], JEFF KLEIN[2], ANDREI KOROTKOV[11], ADRIAN LEE[6], LORNE LEVINSON[12], MICHELE LIMON[1], KEVIN MACDERMID[4], AMBER MILLER[1], MICHAEL MILLIGAN[2], ENZO PASCALE[3], GIUSEPPE PUGLISI[5], KATE RAACH[2], BRITT REICHBORN-KJENNERUD[1], CARL REINTSEMA[18], ILAN SAGIV[12], GRAEME SMECHER[4], RADEK STOMPOR[15], MATTHIEU TRISTRAM[17], GREG TUCKER[11], BEN WESTBROOK[6], KYLE ZILIC[2]

[1]*Columbia University, New York, NY 10027,*
[2]*University of Minnesota School of Physics and Astronomy, Minneapolis, MN 55455,*
[3]*Cardiff University, Cardiff, CF24 3AA, United Kingdom,*
[4]*McGill University, Montréal, Quebec, H3A 2T8, Canada,*
[5]*Scuola Internazionale Superiore di Studi Avanzati, Trieste 34014, Italy,*
[6]*University of California, Berkeley, Berkeley, CA 94720,*
[7]*National Energy Research Supercomputing Center, Lawrence Berkeley National Laboratory,*
[8]*Imperial College, London, United Kingdom,*
[9]*University of California, San Diego,*
[10]*Oxford University, Oxford, OX1 3RH, England, United Kingdom,*
[11]*Brown University, Providence, RI 02912,*
[12]*Weizmann Institute of Science, Rehovot 76100, Israel,*
[13]*California Institute of Technology, Pasadena, CA 91125,*
[14]*Institut d'Astrophysique Spatiale, Universite Paris-Sud, Orsay, 91405, France,*
[15]*Laboratoire Astroparticule et Cosmologie (APC), Université Paris Diderot, 75205, France,*
[16]*University of California, Berkeley, Space Sciences Lab, Berkeley, CA 94720,*
[17]*Laboratoire de l'Accelerateur Lineaire, Universite Paris-Sud, Orsay, 91405, France,*
[18]*National Institute of Standards and Technology, MD 2089*

The E and B experiment (EBEX) is a balloon-borne telescope designed to measure the polarization of the cosmic microwave background radiation as well as that from Galactic dust. The instrument is equipped with a 1.5 meter aperture Gregorian-Dragone telescope, providing an 8' beam at three frequency bands centered on 150, 250 and 410 GHz. Polarimetry is achieved by rotating an achromatic half-wave plate on a superconducting magnetic bearing. In January 2013, EBEX completed 11 days of observations in a flight over Antarctica covering 6000 square degrees of the sky. This marks the first time that arrays with about 1000 transition-edge sensor bolometers have made science observations on a balloon-borne platform. These proceedings describe the EBEX instrument, the science flight and the status of the data analysis.

1 Introduction

Measurements of the temperature anisotropy in the Cosmic Microwave Background (CMB) have provided us with a tremendous amount of information about the origin, composition and dynamics of the universe, and played a major role in establishing the standard ΛCDM cosmological model. The inflationary paradigm is the leading model that accounts for the flatness of the universe, the uniformity of the CMB, the absence of magnetic monopoles, and the nearly scale-invariant spectrum of primordial fluctuations [1]. In this paradigm, quantum fluctuations stretched by the expanding universe to astronomical scales imprint a unique primordial B-mode polarization signal in the CMB at degree angular scales. Experiments that measure the polarization of the CMB can thus provide the strongest evidence yet supporting or ruling out the theories of inflation. B-modes can also be created on arcminute scales through the gravitational lensing of CMB photons by intervening large-scale structure along the line of sight. In recent years, experimentalists have made increasingly sensitive measurements of CMB polarization. In the past year, a measurement of inflationary B-modes was announced by the BICEP2 collaboration [2] and the SPTPol and POLARBEAR experiments have reported preliminary evidence of lensing B-modes [3,4].

2 The Instrument

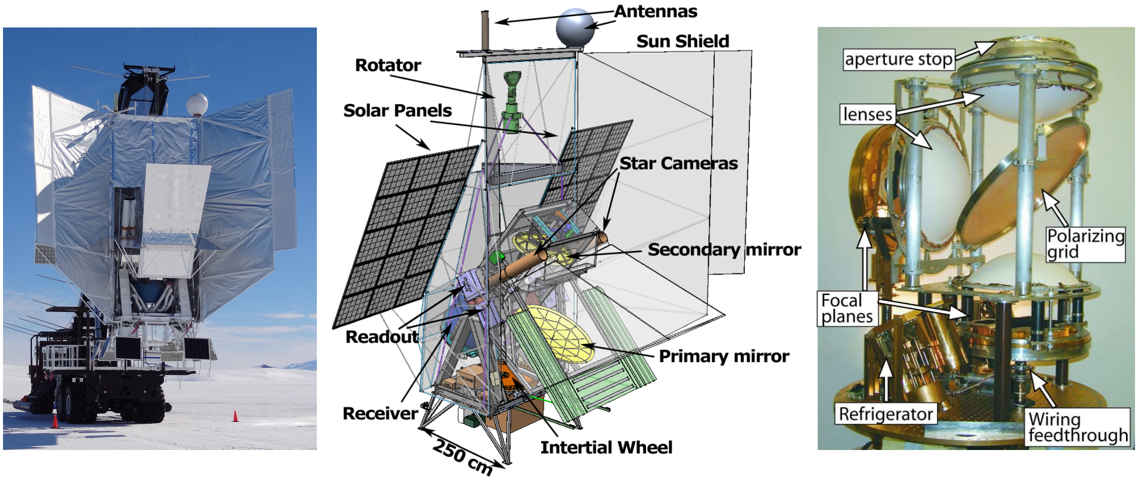

Figure 1 – **Left Panel**: EBEX on the launch pad in Antarctica prior to its long duration flight. **Middle Panel**: A 3D rendering with major gondola elements and overview of optical system. Telescope attitude can be adjusted in both azimuth and elevation. **Right Panel**: The EBEX optics box. As the light enters through the top, the polarization of the light gets rotated by the HWP (not shown), which is placed at the aperture stop. The light is then either reflected by the wire-grid polarizer into the vertical focal plane or transmitted to the horizontal focal plane.

EBEX is a balloon-borne telescope designed to measure the polarization of the CMB. The 2,700 kg (6,000 lb) instrument collects data while suspended from a 10^6 cubic meter stratospheric balloon at an altitude of ~35 km that circumnavigates Antarctica. The telescope is a compact, off-axis Gregorian Mizuguchi-Dragone system chosen to minimize polarization systematics. The 1.5 meter primary mirror combined with conical feedhorns produces an 8 arcminute beam. The telescope has a 6 degree field of view and observes the sky at three frequency bands centered on 150, 250 and 410 GHz. Observing the CMB from the stratosphere enables EBEX to collect data at relatively high frequencies, and be sensitive to only one significant foreground – galactic dust. The payload consists of a gondola with a telescope, detectors, pointing sensors and telemetry. Fig. 1 shows a picture of the telescope before it was launched and a view of the polarizing optics and the focal plane hardware. EBEX has two focal planes. They each consist of 7 silicon wafers with more than 100 transition edge sensor bolometers that are micro-fabricated on each wafer. The wafers are maintained at a temperature of 260 mK. The bolometers are read out using a digital frequency multiplexed system (DfMUX), in which 16 detectors are read out using only two wires. The current through each set of bolometers is measured by a superconducting quantum interference device (SQUID). The polarization of the incoming radiation is modulated by a continuously rotating achromatic half-wave plate (AHWP) located at the 4 K Lyot stop. To minimize power dissipation, the AHWP rotates on a superconducting magnetic bearing. The polarization is then analyzed by a fixed wire grid polarizer. The AHWP rotates at $f_o = 1.23$ Hz and the scanning of the telescope across the sky puts sky polarization signals at side bands of $4f_o = 4.92$ Hz.

3 Overview of The Antarctic Science Flight

On December 28th 2012 EBEX launched from the NASA long duration balloon facility near McMurdo station, Antarctica.

Shortly after reaching the float altitude, EBEX had 945 detectors in transition and collecting data. During flight we observed the CMB and calibrated the instrument through observations of RCW38 and the galaxy. This marks the first time that cosmological observations were conducted in a space-like environment with a kilo-pixel array of transition edge sensor bolometers, and the first time that a 16x DfMUX system was used.

Liquid Helium hold time was 12 days, matching pre-flight predictions, and matching the expected data collection time of 11 days. The sub-K cryogenic system was based on a ^{4}He-based adsorption refrigerator that cooled the cold optics cavity to 1 K, and a ^{3}He-based adsorption refrigerator that maintained the focal plane near 0.26 K. Both refrigerators worked well and, according to specification, required cycling once every 2.5 days. The AHWP levitated continuously on the superconducting magnetic bearing [5] during the entire flight, achieving about 645,000 rotations at 1.23 Hz with an estimated power dissipation of 15 mW at the 4K stage.

The attitude control system (ACS) of the telescope provided sensor information to reconstruct the pointing and actuated the motors to orient the gondola. To mitigate a malfunction with the azimuth motor controller we changed our planned observation pattern, covering a large strip in declination for a total of 6000 square degrees observed. The coverage map is shown in Fig. 2. All other critical ACS subsystems worked well. In particular we acquired continuous attitude information from both star cameras and the gyroscopes, enabling us to reconstruct the pointing with an accuracy that matches pre-flight prediction (see Fig. 2).

On January 23rd, 2013 the payload was terminated. The data and the payload were successfully recovered and shipped to home institutions.

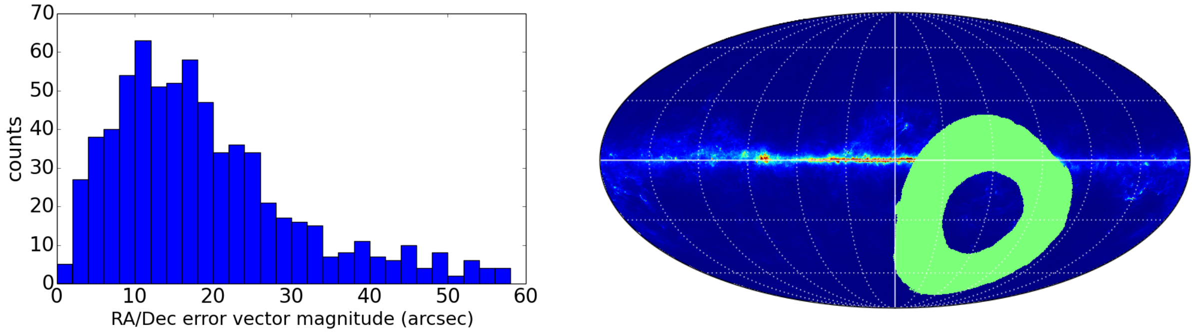

Figure 2 – **Left Panel**: Histogram of the reconstructed pointing error for the entire flight. The mean is 19 arcseconds, a factor of 3 better than required to extract information on the inflationary B-mode signal with negligible pointing systematic error. We expect the final error to be less than 11 arcseconds. **Right Panel**: EBEX coverage map, in galactic coordinates.

4 Current Status

Data from the science flight is currently being analyzed, and preliminary data products are presented in these proceedings. The attitude of the telescope is reconstructed with an Unscented

Kalman filter, using star camera solutions and gyroscope rates. The histogram of the reconstructed attitude is plotted in Fig. 2. As with other experiments using a continuously rotating HWP[6], the raw time streams are dominated by a rotation synchronous signal (HWPSS). The HWPSS is modeled and removed using the measured angle of the HWP. Fig. 3 shows a power spectrum of a section of in-flight data from one of the detectors before and after subtraction of the HWPSS, showing no residuals from the HWPSS in the signal bandwidth. The HWPSS-subtracted time streams are used to calibrate the instrument against Planck, using RCW38 and galaxy crossings. The time streams are then demodulated using the measured HWP angle to produce Q and U Stokes parameters. A preliminary map of galaxy temperature and polarized intensity is shown in Fig. 3 (right panel). The EBEX data analysis is well underway and we anticipate release of cosmological results within ~ 1 year.

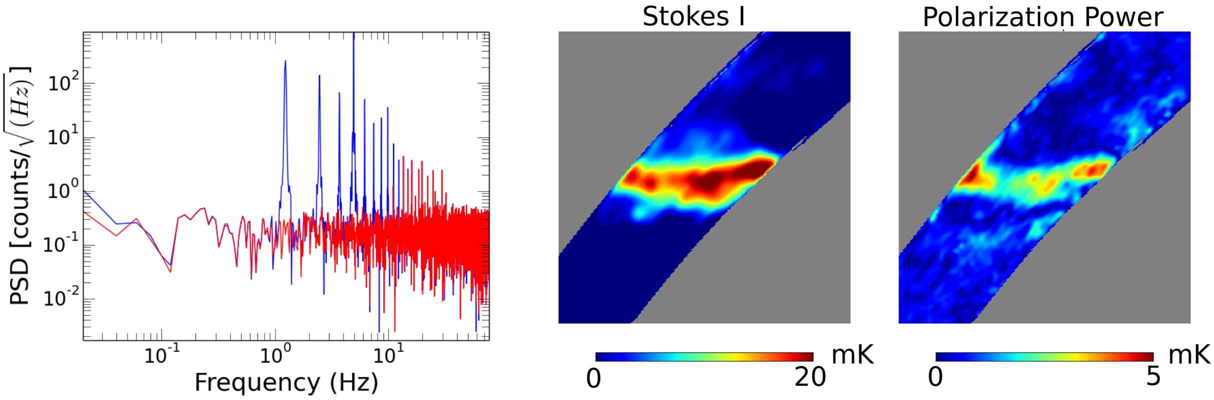

Figure 3 – **Left Panel:** Power Spectrum of a 250 GHz detector before (blue) and after (red) HWPSS subtraction. The HWPSS was removed only up to the 10th harmonic because sky signals are expected at frequencies below 7 Hz. The black peaks correspond to the higher harmonics not removed. **Right Panel**: Preliminary Stokes I and polarization power maps of the galactic plane using 91 250 GHz detectors over a 17 minute section of the flight.

Acknowledgments

EBEX is a NASA supported mission through grant numbers NNX08AG40G and NNX07AP36H. We thank Columbia Scientific Balloon Facility for their enthusiastic support of EBEX. We also acknowledge support from NSF, CNRS, Minnesota Super Computing Institute, Minnesota and Rhode Island Space Grant Consortia, the Science and Technology Facilities Council in the UK, Sigma Xi, and funding from collaborating institutions. This research used resources of the National Energy Research Scientific Computing Center, which is supported by the office of Science of the U.S. Department of Energy under contract No. DE-AC02-05CH11231. The McGill authors acknowledge funding from the Canadian Space Agency, Natural Sciences and Engineering Research Council, Canadian Institute for Advanced Research, Canadian Foundation for Innovation and Canada Research Chairs program.

References

1. Planck Collaboration, *ArXiv e-prints* **1303.5076**, 2013
2. BICEP2 Collaboration, *ArXiv e-prints* **1403.3985**, 2014
3. POLARBEAR Collaboration, *ArXiv e-prints* **1403.2369**, 2014
4. SPTPol Collaboration, *ArXiv e-prints* **1307.5830**, 2013
5. J. Klein and S. Hanany, *SPIE - Astronomical Instrumentation* **8150**, 2011
6. B. Johnson, J. Collins *et al.*, *ArXiv e-prints* **0611394**, 2006

The POLARBEAR experiment: results from the first observational campaign and prospects

G. Fabbian[1] for the POLARBEAR Collaboration: P.A.R. Ade, Y. Akiba, A.E. Anthony, K. Arnold, M. Atlas, D. Barron, D. Boettger, J. Borrill, S. Chapman, Y. Chinone, M. Dobbs, T. Elleflot, J. Errard, G. Fabbian, C. Feng, D. Flanigan, A. Gilbert, W. Grainger, N.W. Halverson, M. Hasegawa, K. Hattori, M. Hazumi, W.L. Holzapfel, Y. Hori, J. Howard, P. Hyland, Y. Inoue, G.C. Jaehnig, A.H. Jaffe, B. Keating, Z. Kermish, R. Keskitalo, T. Kisner, M. Le Jeune, A.T. Lee, E.M. Leitch, E. Linder, M. Lungu, F. Matsuda, T. Matsumura, X. Meng, N.J. Miller, H. Morii, S. Moyerman, M.J. Myers, M. Navaroli, H. Nishino, H. Paar, J. Peloton, D. Poletti, E. Quealy, G. Rebeiz, C.L. Reichardt, P.L. Richards, C. Ross, I. Schanning, D.E. Schenck, B.D. Sherwin, A. Shimizu, C. Shimmin, M. Shimon, P. Siritanasak, G. Smecher, H. Spieler, N. Stebor, B. Steinbach, R. Stompor, A. Suzuki, S. Takakura, T. Tomaru, B. Wilson, A. Yadav, O. Zahn

[1]*International School for Advanced Studies (SISSA), Trieste 34014, Italy*

The POLARBEAR experiment is one of the few ongoing ground-based Cosmic Microwave Background (CMB) polarization experiment. The experiment is located in the Atacama desert in northern Chile and is designed to target both large and small scales anisotropies thanks to the combination of high angular resolution and large sky-fraction accessible from its mid-latitude site. We review the results of the analysis activity conducted on the data collected during the first observational campaign. These include the first measurement of B-modes of polarization on sub-degree angular scales together with the first reconstruction of the projected matter distribution between us and the epoch of recombination (lensing potential) using CMB polarization data alone. The measurement of the lensing potential was validated through cross-correlation of the matter distribution measured by the Herschel satellite. Finally, we discuss the upcoming experimental upgrades of the experiment.

1 Introduction

Observations of the CMB temperature and polarization anisotropies are one of the most promising and precise tool for probing the physics of the early Universe. Both are in fact a direct consequence of the presence of primordial density fluctuations in the primordial plasma which serve as initial condition for the formation of large scale structures (LSS) in the universe. According to the current cosmological model, these perturbations are generated through quantum processes during an early phase of exponential expansion of the universe known as inflation. Measurements of CMB polarization can provide exquisite constrains on inflation through the so called B-modes of polarization. Polarization patterns on the sky can in fact be decomposed in even parity (E-modes) and odd parity patterns (B-modes). While E-modes are sourced to any kind of perturbations, including the density ones that generate temperature anisotropies, B-modes can only be produced by vector or tensor perturbations in the universe metric. The latter in particular imprint a characteristic B-mode polarization on the degree scale, whose detection has been recently announced by the BICEP2 collaboration. If this result is confirmed, a new window into physics at grand unified energy scales, when the electroweak and strong forces are expected to unify, would be opened.

The CMB radiation that we observe today, however, has been however modified by the presence of the growing LSS between us and the moment of CMB photon emission. These distort the primordial CMB temperature and polarization fluctuations through gravitational lensing, converting E-mode patterns into B-mode polarization and adding a significant amount of power to the B-mode angular power spectrum on sub-degree scale. Though lensing effect on the CMB was first observed in temperature by ACT, SPT and Planck, polarization measurements allow a more precise characterization as the lensing B-modes are not contaminated by confusion with the primordial CMB fluctuations. This would largely improve our ability to constrain the parameters affecting the structure formation rate (e.g. the neutrino mass or the dark energy equation of state) and also help separating the contamination of lensing generated signal to the inflationary B-modes.

2 The POLARBEAR experiment

The POLARBEAR experiment consist of a two-mirror reflective telescope the Huan Tran Telescope (HTT) coupled to a cryogenic receiver. The HTT reflectors are in an off-axis Gregorian configuration satisfying the Mizuguchi-Dragone condition to provide low cross-polarization and astigmatism over the diffraction-limited field of view. The instrument is installed at the James Ax Observatory in the Atacama Desert in Northern Chile at an altitude of 5200 m above sea level.

2.1 The instrument

The cryogenic receiver coupled to the HTT houses a cold half-wave plate (HWP), reimaging optics, aperture stop, and a focal plane of 637 dual-polarization pixels (1274 detectors) with a 2.4° diameter field of view. The pixels measure the incident optical power at $150GHz$ through a lenslet-coupled transition-edge sensor (TES) bolometric technology multiplexed in frequency domain. Accurate description of the experimental setup are reviewed in POLARBEAR collaboration (2014).[3]

2.2 Scan strategy

POLARBEAR operations began in January 2012. After a first period of initial calibration of the instrument, regular scientific observations of the CMB have been carried out since May 2012. The dataset used to derive the results reported here was collected between that time and June 2013. It consists of 3,300 hours of CMB observations and 500 hours of calibration data. During the first-season, the observations were focused on three patches, named RA4.5, RA12, RA23 following their right ascension coordinate location, which were chosen to simultaneously optimize the expected low dust emission, availability from the Chilean site and overlap with external data sets, like HERSCHEL and QUIET, for cross-correlation purposes. The locations of all the patches are shown in fig. 1.

Each patch is observed continuously for up to eight hours while that patch moves in elevation between $30° < el < 80°$. Observation of one patch is broken into 15 minutes scans at constant elevation, during which the telescope scans back and forth in azimuth 3° at a speed of $0.75°/s$ on the sky. The telescope then moves in azimuth and elevation to where the patch will be in 7.5 minutes, and the constant elevation scan (CES) pattern is repeated. The HWP position is kept stationary during each observation and stepped daily. This, together with the scanning strategy just outlined helps maximizing the attack angles with which each patch is observed (i.e. the so called cross-linking). This is particularly important to minimize instrumental systematics contamination (see sect. 6).

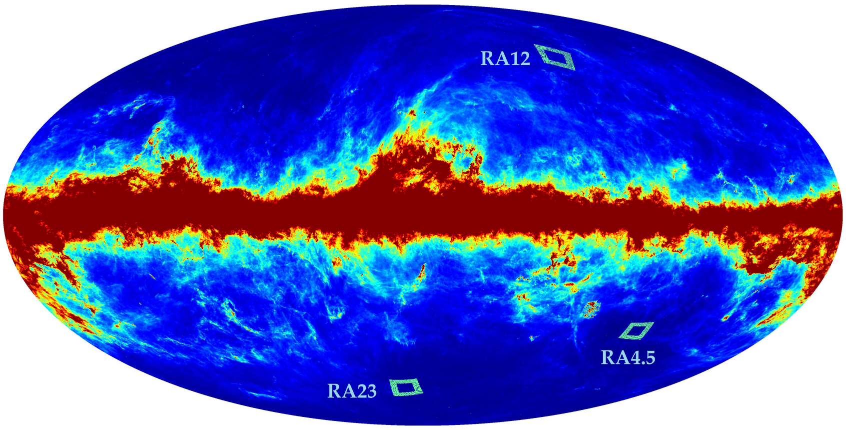

Figure 1 – The three POLARBEAR patches overlaid on the full-sky 857 GHz intensity map of the PLANCK satellite. Patches were chosen for low dust emission, overlap with other observations, and to allow nearly continuous CMB observations from the James Ax Observatory.

3 Instrument characterization

The instrument properties are measured and modeled through a combination of astrophysical and ground-based techniques. We briefly summarize the result of these processes while the impact of the uncertainties in these models are discussed in sect. 6.

3.1 Pointing

The actual pointing of the telescope on the sky is reconstructed observing bright, extended and point-like millimeter sources selected from known source catalogs to span a wide range in azimuth and elevation. The reconstructed pointing model recovers the source positions for the sources that were used to create it with an accuracy of $25''$ RMS. The model parametrizes known error sources between the telescope's encoder reading and the true boresight pointing like, e.g. encoder offsets. Each detector pointing is determined in terms of offsets relative to the boresight using raster scans across bright planet sources like Saturn and Jupiter. These offsets were measured throughout the observational season and were found to be stable with fluctuations of less than $6''$. The offsets show arcsecond-level differential pointing between the two detectors in a pixel, which contaminates the CMB signal at a negligible level.

3.2 Beam

The beam of the telescope is measured by computing the angular power spectrum of maps of Jupiter observed through raster scans. The beam can be approximated as azimuthally symmetric in intensity because of the rotation of the instrument beams as projected on the CMB patch due to changes in patch attack angle over the course of the day from our mid-latitude site. The uncertainties in the beam measurement related to error in the reconstructed pointing are measured in each of the three patches fitting for an additional blurring of the beam when observing point sources in each patch. These uncertainties are propagated to the power spectrum level and degrade our sensitivity to small-scale anisotropies.

3.3 Polarization response

Each of the detectors' response to polarized signal, including its polarization angle, polarization efficiency, and leakage due to relative-gain miscalibration, is modeled together with non-idealities in the HWP. The parameters of the model are constrained through observation of the Taurus A (TauA) supernova remnant, which has been observed among the others by WMAP and by the IRAM telescope at $90GHz$. We refer the reader elsewhere for a detailed description of the polarization angle calibration procedure.[3] Since the instrument model uncertainties are not expected to bias significantly the EB cross power spectrum, we can also use the measured C_ℓ^{EB} to calibrate our global polarization angle uncertainty. Assuming the cosmological C_ℓ^{EB} signal negligible, we can estimate the systematic error on our calibration and rotate our recovered polarization map so that the EB power spectrum is zero.[5]

3.4 Absolute and relative calibration

The Time-Ordered Data (TOD) acquired by the detectors are measurements of the electrical current in the detector, therefore they have to be converted into CMB temperature units measuring the detector responsivity, i.e. their gain. Both astrophysical and ground-based calibrators are used for this purpose. A chopped thermal source illuminating the focal plane through a light-pipe penetrating the secondary mirror is used as the primary relative calibrator. This source is modulated by a chopper rotating at six different frequencies. This allows to estimate simultaneously the gain and frequency response of each bolometer. The polarized response of individual detectors to the thermal source is characterized by referencing to measurements of TauA taken at different HWP rotation angles. The CMB C_ℓ^{TT} power spectrum based on WMAP9 cosmology is used to determine a single scale factor that provides an absolute gain calibration for the instrument.

4 Data reduction and mapmaking

The TOD corresponding to the fraction of the timestream, where the instrument was not functioning properly or glitches are clearly visible, are removed. Criteria for the data cuts are the too high or too low value of gain, gain drift in time during observations, high value of Precipitable Water Vapor (PWV) in the atmosphere or presence of clear glitches due to errors in the bolometer or pointing data acquisition system. Within each CES scan, only the data taken at constant scanning velocity are considered. TODs are downsampled and low-pass filtered to avoid aliasing effect. Individual bolometer timestreams are calibrated then pixel-pair bolometers are summed and differenced to derive polarization-free and temperature-free timestreams from each pixel respectively. The latter in particular are used for the extraction of Q and U stokes parameters. This technique allows reducing intensity to polarization leakage from atmosphere and CMB temperature in our polarization maps. TODs are noise weighted and filtered to reduce $1/f$ noise and scan synchronous signals like, e.g. sidelobes contamination. TODs of each CES are then binned into maps. More details on the data reduction and mapmaking step are provided elsewhere in these proceedings.[43]

5 Results

The goal of the POLARBEAR experiments is the measurement of B-modes of polarization. Evidence for the presence of this signal can be obtained using direct and indirect techniques which exploit information included in 2, 3 or 4-point correlation of CMB and tracers of LSS. We summarize the results obtained for all these techniques.

5.1 *Lensing reconstruction*

The gravitational lensing of LSS on CMB modifies the statistical properties of the primordial signal. Lensing in fact acts as a convolution in harmonic domain and correlates different Fourier modes which are otherwise independent. This off-diagonal non-Gaussian feature can be exploited to reconstruct the underlying lensing deflection field **d** from the observed CMB using quadratic combination its observables in the harmonic domains, i.e. temperature, E and B-modes. The POLARBEAR experiment presented the first direct evidence for gravitational lensing of the CMB using polarization data alone. The channel chosen for the reconstruction are the the so called EE and EB channel[7]. The power spectrum of these estimators

$$\langle d_\alpha(\mathbf{L}) d^*_\beta(\mathbf{L}')\rangle = (2\pi)^2\delta(\mathbf{L}-\mathbf{L}')(C_L^{dd} + N^{(0)}_{\alpha\beta}(L) + \text{higher-order terms}) \qquad \alpha,\beta \in \{EE, EB\} \quad (1)$$

proves information on the 4-point function on the CMB. This is affected by the presence of the so-called lensing Gaussian bias term $N^{(0)}_{\alpha\beta}$, which is the disconnected part in the 4-point correlation, and by higher order biases that depend on the lensing field itself. Though higher order terms are found to be negligible, the $N^{(0)}_{\alpha\beta}$ has to be subtracted as often it is larger than the deflection field power spectrum especially if $\alpha = \beta$. We chose to use the reconstruction channel ⟨EEEB⟩ and ⟨EBEB⟩ because they display the lower Gaussian bias. The Gaussian bias was estimated with Monte Carlo simulations together with the correlation between the two reconstruction channels. The final significance of our measurement has been measured as $\mathcal{A}/\Delta\mathcal{A}$ where $\mathcal{A}$ is the lensing amplitude parameter, which measures the amplitude of the reconstructed lensing potential with respect to a fiducial model, and $\Delta\mathcal{A}$ its uncertainty. The rejection of the hypothesis of no lensing on CMB polarization has a significance of 4.2σ combining statistical and systematic errors in quadrature.[1] We note however that since the lensing reconstruction exploits peculiar off-diagonal correlation, it is less sensitive to systematics than standard CMB analysis. Given the use of B-mode Fourier modes, the ⟨EEEB⟩ channel provides an evidence of lensing generated B-modes at 3.2σ level. If we include the presence of lensing in our data set, the measured lensing amplitude is consistent at 2σ level with ΛCDM predictions (see fig. 2).

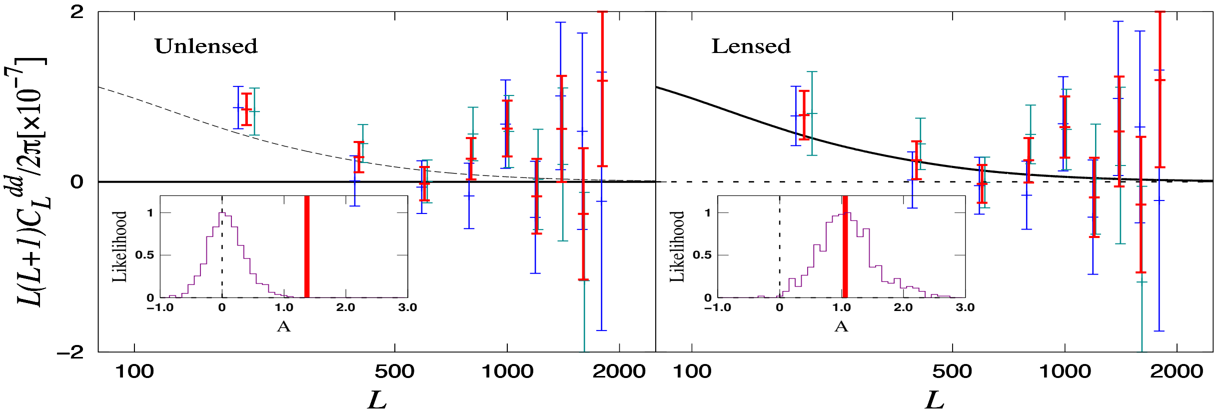

Figure 2 – Polarization lensing power spectra co-added from the three patches and two estimators (red). The lensing signal predicted by the ΛCDM model is shown in black curve while the reconstructed lensing potential from ⟨EEEB⟩ and ⟨EBEB⟩ is is shown in blue and green respectively. Left: A 4.2σ rejection of the null hypothesis of no lensing. Right: The same data, assuming the existence of gravitational lensing to calculate error bars, including sample variance and including the covariance between the two reconstruction channels. The histograms of the expected amplitudes of $\mathcal{A}$ from 500 unlensed and lensed simulations are shown in the inset boxes.

5.2 *POLARBEAR - Herschel cross-correlation*

The flux of the cosmic infrared background (CIB) has a redshift distribution remarkably similar to that of the structures that lensed the CMB. Both signals originate from a broad range of redshifts centered around $z \approx 2$. For this reason we expect the cross the correlation between the lensing convergence $\kappa \equiv -\nabla \cdot \mathbf{d}/2$ and the CIB sources distribution to be non zero. We used the observations of the Herschel H-ATLAS survey at $500\mu m$ as an estimate of the CIB emission in the RA12 and RA23 regions and the convergence extracted by POLARBEAR maps in the same field. We computed the cross-power spectrum for all the reconstruction channels. The correlation with the EB reconstruction channel provides evidence at 2.3σ level of the presence of lensing generated B-modes while the combination of all the channels in all the patches provides a 4σ measurement of polarized lensing (see fig. 3). No evidence of contamination by unresolved point sources was found.[2] These result agree with the findings of SPTpol collaboration [6].

5.3 Measuring the B-modes power spectrum

We estimate angular power spectra using a pseudo-spectrum technique, based on the MASTER algorithm[8], which corrects the effect of the cut-sky effect and filtering in the time-domain on the power spectrum level. The naive power spectrum of the maps are in fact biased by the filtering and partial sky coverage, which can be corrected for with Monte Carlo simulations and analytical calculations of the mode mixing. Error bars are calculated from the noise in the maps and validated with time-domain correlated noise simulations. Six power spectra $\tilde{C}_\ell(TT, EE, BB, TE, TB, EB)$ are formed by taking cross spectra of the apodized and Fourier transformed single-day temperature and polarization maps[a] $\tilde{\mathbf{m}}^X_{ik}$, where $X \in \{T, E, B\}$, from different days i, j.

$$\tilde{C}^{XY}_\ell = \frac{1}{\sum_{i,j\neq i,k\in \mathrm{bin}_\ell} w^X_i w^Y_j} \sum_{i,j\neq i,k\in \mathrm{bin}_\ell} w^X_i \tilde{\mathbf{m}}^X_{ik} w^Y_j \tilde{\mathbf{m}}^{Y*}_{jk} \qquad (2)$$

This estimator is free of noise bias. The weights w^X_i for the maps used in the cross-spectrum evaluation are the sum of the pixel inverse noise covariance estimate over all the map pixels, i.e. either the TT element for temperature or the minimum eigenvalue of the Q and U block for polarization. The results of the B-mode power spectrum is shown in fig. 3. Concurrently, we have been developing an alternate data processing pipeline that was used to cross-check the results obtained with the pipeline just presented. It applies the same filters as the primary pipeline, but corrects for them while estimating the sky signals as part of the map-making procedure.[9] The recovered maps provide unbiased renditions of the sky signal, with the filtered modes effectively marginalized over. The final spectra are calculated on the curved sky as weighted averages of the cross-spectra of 8 maps made of disjoint subsets of all the daily maps with E to B leakage corrected

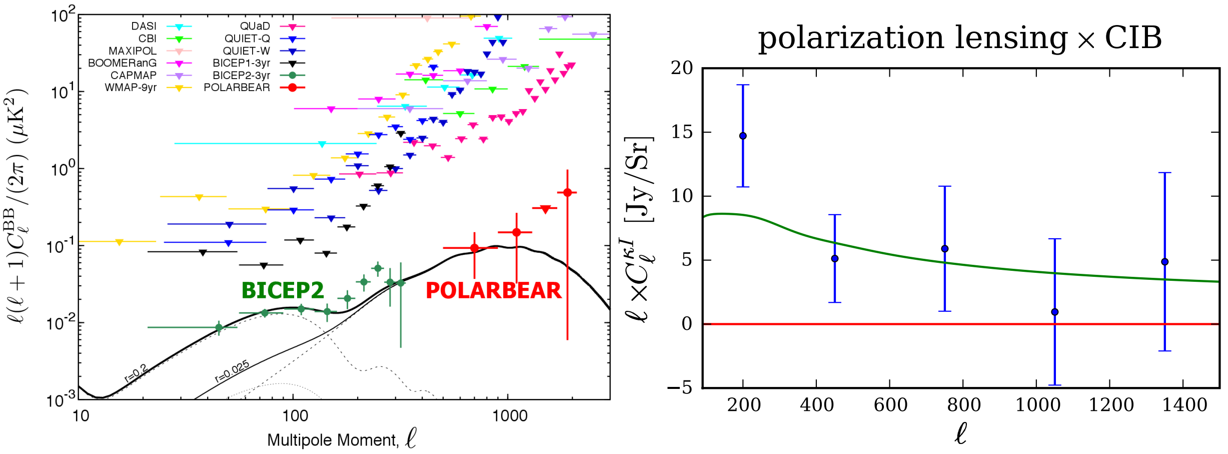

Figure 3 – Left: B-modes power spectrum as measured by POLARBEAR. Data points and upper limits derived by previous and current experiment are overplotted. Right: minimum variance combination of all polarization lensing measurements cross-correlated with the Herschel maps overlaid to the fiducial theory curve for the lensing CIB cross-spectrum is also shown.

---

[a] Since the size of the patches of POLARBEAR are small the computation are performed in the flat-sky limit.

analytically following Grain et al. (2009).[10] Monte Carlo simulations are employed to estimate the final uncertainties of the computed spectra. The results of this alternate pipeline are consistent with the results of the primary pipeline. These analysis are the first direct measurement of the B-modes of polarization on sub-degree scale. Assuming the measured signal is generated only from gravitational lensing, this measurement is sensitive to all the LSS present in the universe, unlike the results based on cross correlation techniques. These in fact establish the existence of B-modes from gravitational lensing relying on tracers that exist over a limited range of redshift.[6] However, being a direct measurement, it is also sensitive to all the processes that could have generated B-modes in the early universe like, e.g. vector perturbation or the presence of primordial magnetic fields.

6 Systematics error check

POLARBEAR adopted a blind-analysis framework to minimize observer bias. According to this strategy, no one in the team viewed any of the science data products based on B-modes until the choice of calibration, filtering, data selection, data validation were finalized and showed that all systematic uncertainties related to that particular choice were small. This framework forced us to develop quantitative tools, like null-tests and simulations, that convincingly argued for analysis choices and constraints without showing the final data products to avoid that people within the team would be more convinced by an argument or method because of the result that was produced. Other power spectra and maps were used as subsidiary information and they were unblinded in stages during the analysis procedure.[3]

6.1 Null-tests

In a null-test, the data set is split into two parts and those are then used to form a null-signal estimate in map or power spectrum space. We chose 9 different criteria to test for atmospheric and sidelobes contamination, telescope induced vibrations or glitches, fabrication defects, optical distortion, long term variation of calibration and beams. To probe the systematic contamination affecting a particular power spectrum or null test data split, we calculated the sum of χ^2 for EB and BB separately and of both these spectra for a specific test. We created test statistics based on these quantities to search for different manifestations of systematic effects like extreme values of χ_{null} test or χ^2_{null} test and found no significant contamination.

For the lensing reconstruction and POLARBEAR-Heschel cross-correlation analysis we developed specific null tests. We tested the presence of curl-mode of the deflection field and found it consistent with zero as well as the correlation of the reconstructed lensing field between two different patches. We also cross-correlated the Herschel maps with non-overlapping POLARBEAR maps or with curl-mode of the deflection field and found it consistent with zero.

6.2 Simulation pipeline

The impact of instrumental systematic uncertainties on our CMB result were estimated using accurate simulations of the effects on the timestream level. The timestreams including systematics were then propagated through the science pipeline up to the power spectrum level. We used signal-only simulations with B-mode power set to zero to highlight the leakage of other component of the CMB signal generated by each specific effect and the combination of all of those. Uncertainties due to differential beam properties relied on simulations focusing on CMB-gradient maps. As a result of this framework, any non-zero C_ℓ^{EB} or C_ℓ^{BB} power is spurious, and a measurement of the instrumental systematic effect. Given the statistical uncertainties reported here, we chose not to investigate effects distorting C_ℓ^{BB} itself. The method outlined above was used to investigate five systematic instrumental effects: error in instrument polarization angle, error in relative pixel polarization angles, error in instrument boresight pointing model, differential pointing between and relative gain calibration error between the two bolometers in a pixel. All effects are displayed in 4 and were found to produce leakages well below the statistical uncertainty.

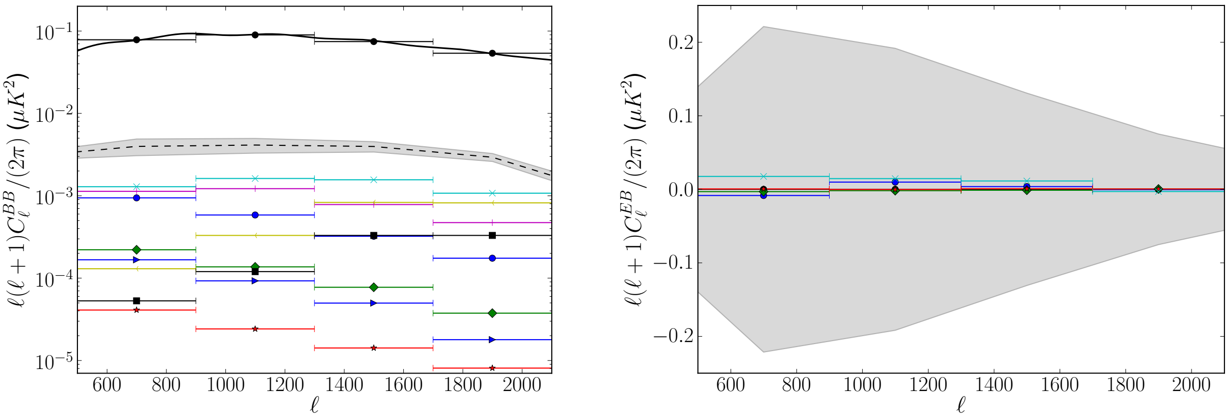

Figure 4 – Possible bias from instrumental systematics errors in the B-modes (left) and EB power spectra (right). Both individual sources of uncertainty (solid color) and the cumulative bias coming from their combination (black dashed) are displayed after the combination of all CMB patches. The grey-shaded region show the 1σ bounds on the cumulative bias limit. The effects included in this analysis were the boresight and differential pointing uncertainty (light blue, cross mark), the residual uncertainty in instrument polarization angle after self-calibration (purple, plus mark), the differential beamsize and ellipticity (yellow arrow and black square mark respectively), the electrical crosstalk (blue, arrow mark), the drift of the gains between two consecutive thermal source calibrator measurements (red star mark), and the HWP-independent and HWP-dependent terms of the relative gain model (green diamond and blue circle mark respectively).

7 Future instrumental upgrades

The current technology of POLARBEAR focal plane will be soon upgraded with 1,897 lenslet-coupled pixels, each of which is dual-polarization and dual-frequency (90 and 150GHz), with a total of 7,588 transition edge sensor (TES) bolometric detectors cooled at 100mK (POLARBEAR-2). The final stage of the experiment (Simons Array) will deploy three 3.5-meter telescopes identical to the HTT and 22,764 detectors distributed between 95, 150, and 220 GHz and based on the same technology of the POLARBEAR-2 phase. Simons Array will be able to constrain the sum of the neutrino masses $\sum m_\nu$ with a 1σ error bar of 53meV when combined with Planck satellite data. This precision can be increased to 19meV including Baryon Acoustic Oscillation measurements to break degeneracies between $\sum m_\nu$ and the matter density $\Omega_m h^2$. If $\sum m_\nu <$ 100meV, the neutrino mass hierarchy will be known. On the inflationary side, Simons array will be able to measure a tensor-to-scalar ration $r \simeq 0.002$ at 60% CL.

References

1. The POLARBEAR Collaboration: Ade, P. A. R., Akiba, Y., et al. 2013, accepted in Physical Review Letters, arXiv:1312.6646
2. The POLARBEAR Collaboration: Ade, P. A. R., Akiba, Y., Anthony, A. E., et al. 2014, Physical Review Letters, 112, 131302
3. The POLARBEAR Collaboration, Ade, P. A. R., Akiba, Y., et al. 2014, arXiv:1403.2369
4. Peloton, J. 2014, Proceedings of the 49th Rencontres de Moriond
5. Keating, B. G., Shimon, M., & Yadav, A. P. S. 2013, *Astrophysical Journal Lett., 762, L23*
6. *Hanson, D., Hoover, S., Crites, A., et al. 2013, Physical Review Letters, 111, 141301*
7. *Hu, W., & Okamoto, T. 2002,* Astrophysical Journal, 574, 566
8. Hivon, E., Górski, K. M., Netterfield, C. B., et al. 2002, *Astrophysical Journal, 567, 2*
9. *Stompor, R., Balbi, A., Borrill, J. D., et al. 2002,* Phys. Rev. *D, 65, 022003*
10. *Grain, J., Tristram, M., & Stompor, R. 2009,* Phys. Rev. *D, 79, 123515*

2.
Clusters / SZ

Cosmological contraints from *Planck* Sunyaev-Zeldovich cluster counts

A. Bonaldi, on behalf of the Planck Collaboration
Jodrell Bank Centre for Astrophysics, Alan Turing Building, School of Physics and Astronomy, The University of Manchester, Oxford Road, Manchester, M13 9PL, U.K.

I review the results presented in Planck Collaboratio 2014 XX [1] on the cosmological constraints from number counts as a function of redshift for a sub-sample of 189 galaxy clusters from the *Planck* SZ (PSZ) catalogue. The PSZ is selected through the signature of the Sunyaev–Zeldovich (SZ) effect, and the sub-sample has a signal-to-noise threshold of seven. I briefly describe the selection function, the relation between mass M and SZ signal Y and the likelihood. I then present the constraints on the power spectrum amplitude σ_8 and matter density parameter Ω_m in a flat ΛCDM model. The value of σ_8 is degenerate with the mass bias; if the latter is fixed to a value of 20% (the central value from numerical simulations) we find $\sigma_8(\Omega_\mathrm{m}/0.27)^{0.3} = 0.78 \pm 0.01$. We find that the larger values of σ_8 and Ω_m preferred by *Planck*'s measurements of the primary CMB anisotropies can be accommodated by a mass bias of about 40%. Alternatively, consistency with the primary CMB constraints can be achieved by the inclusion of processes that suppress power on small scales relative to the ΛCDM model, such as a component of massive neutrinos.

1 Introduction

Within the standard picture of structure formation, galaxies aggregate into clusters of galaxies at late times, forming bound structures at locations where the initial fluctuations create the deepest potential wells. The study of these galaxy clusters has played a significant role in the development of cosmology over many years. More recently, as samples of clusters have increased in size and variety, number counts inferred from tightly-selected surveys have been used to obtain detailed constraints on the cosmological parameters.

The Sunyaev–Zeldovich (SZ) effect is the inverse Compton scattering of cosmic microwave background (CMB) photons by the hot gas along the line of sight, and this is most significant when the line of sight passes through a galaxy cluster. It leads to a decrease in the overall brightness temperature in the Rayleigh–Jeans portion of the spectrum and an increase in the Wien tail, with a null around 217 GHz. The amplitude of the SZ effect is given by the integrated pressure of the gas within the cluster along the line of sight. Relating the observational properties of the clusters to their total mass is the key to exploit clusters for cosmology, since mass is the quantity most readily predicted using theoretical models. Evidence both from observation and from numerical simulations suggests that the SZ effect is an excellent mass proxy.

The *Planck* satellite has mapped the full sky in nine frequency bands covering 30–857 GHz with high sensitivity and angular resolution from 31 armin to 5 arcmin. A catalogue of SZ clusters (*Planck* SZ Catalogue, PSZ) has been presented in [2]. The *Planck* cluster sample is complementary to those from observations using the South Pole Telescope (SPT) and the Atacama Cosmology Telescope (ACT). The resolution of *Planck* is lower, but the sky coverage is much greater. This means that *Planck* typically finds larger, more massive, and lower-redshift clusters than those found by SPT and ACT.

In this article I review the cosmological results from the PSZ calalogue[1], which exploit a sub-sample having a signal-to-noise (S/N) of seven. This sub-sample has been selected to be pure, in the sense that all the objects have been confirmed as clusters via additional observations, either from the literature or undertaken by the Planck Collaboration. This is the largest SZ-selected sample of clusters used to date for this purpose. It is the systematic uncertainties from our imperfect knowledge of cluster properties that dominate the overall uncertainty on cosmological constraints.

2 Cluster number counts

The number of clusters predicted to be observed by a survey in a given redshift interval $[z_i, z_{i+1}]$ can be written

$$n_i = \int_{z_i}^{z_{i+1}} dz \frac{dN}{dz}, \tag{1}$$

with

$$\frac{dN}{dz} = \int d\Omega \int dM_{500}\, \hat{\chi}(z, M_{500}, l, b)\, \frac{dN}{dz\, dM_{500}\, d\Omega}\,, \tag{2}$$

where $d\Omega$ is the solid angle element and M_{500} is the mass within the radius where the mean enclosed density is 500 times the critical density.

2.1 Mass function

The quantity $\frac{dN}{dz\, dM_{500}}$ in Eq. 2 is the mass function, and it is predicted with numerical simulations. Our main results use the mass function from[3], while the mass function from[4] is used as a cross-check. The mass function has the form:

$$\frac{dN}{dM_{500}}(M_{500}, z) = f(\sigma)\, \frac{\rho_{\rm m}(z=0)}{M_{500}}\, \frac{d\ln\sigma^{-1}}{dM_{500}}\,, \tag{3}$$

where

$$f(\sigma) = A\left[1 + \left(\frac{\sigma}{b}\right)^{-a}\right] \exp\left(-\frac{c}{\sigma^2}\right)\,, \tag{4}$$

and $\rho_{\rm m}(z=0)$ is the mean matter density at $z = 0$. The coefficients A, a, b and c are tabulated in[3] for different overdensities, $\Delta_{\rm mean}$, with respect to the mean cosmic density, and depend on z. The quantity σ is the standard deviation, computed in linear perturbation theory, of the density perturbations in a sphere of radius R, which is related to the mass by $M = 4\pi\rho_{\rm m}(z=0)R^3/3$.

2.2 Scaling relations

The quantity $\hat{\chi}(z, M_{500}, l, b)$ in Eq. 2 is the survey completeness for a given mass M_{500} and redshift z, at a given location (l, b) on the sky. In order to determine it, one needs to relate the observable properties of the clusters (in our case the size θ_{500} and the SZ flux Y_{500}) to their mass and redshift. This is done through scaling relations.

We use a Y_{500}–M_{500} relation of the form

$$E^{-\beta}(z)\left[\frac{D_{\rm A}^2(z)\, \bar{Y}_{500}}{10^{-4}\,{\rm Mpc}^2}\right] = Y_*\left[\frac{h}{0.7}\right]^{-2+\alpha}\left[\frac{(1-b)\, M_{500}}{6\times 10^{14}\,{\rm M}_\odot}\right]^{\alpha}\,, \tag{5}$$

where $D_{\rm A}(z)$ is the angular-diameter distance to redshift z and $E^2(z) = \Omega_{\rm m}(1+z)^3 + \Omega_\Lambda$. Equation 5 has an estimated intrinsic scatter $\sigma_{\log Y}$.

Cosmological constraints are sensitive to the normalization Y_*, slope α and scatter $\sigma_{\log Y}$ of the assumed Y_{500}–M_{500} relation. We thus paid considerable attention to deriving them, by performing an observational calibration of the relation on one-third of the cosmological sample. We find $Y_* = -0.19 \pm 0.02$, $\alpha = 1.79 \pm 0.08$, $\beta = 0.66 \pm 0.50$ and $\sigma_{\log Y} = 0.01$.

The calibration uses M_{500}^{YX}, the mass derived from the relation between mass and Y_X (where Y_X is the X-ray analogue of the SZ signal), as a mass proxy. The mean bias between M_{500}^{YX} and the true mass, $(1-b)$, is assumed to account for all possible observational biases (departure from hydrostatic equilibrium HE, absolute instrument calibration, temperature inhomogeneities, residual selection bias, etc). This is the main systematic uncertainty in our analysis. In practice, the plausible range for this mean bias $(1-b)$ was estimated by comparing the observed relation with predictions from several sets of numerical simulations. A value $(1-b) = 0.8$ could be considered as a best guess given available simulations, with no clear dependence on mass or redshift. As a baseline we take $(1-b)$ to vary within the range $[0.7, 1.0]$ with a flat prior. We also consider, when analysing systematic uncertainties on the derived cosmological parameters, a case where the bias is fixed to the value $(1-b) = 0.8$.

In addition to Eq. 5 we need a relation between θ_{500} (the aperture used to extract Y_{500}), and M_{500}. Since $M_{500} = 500 \times 4\pi\rho_{\rm crit}R_{500}^3/3$ and $\theta_{500} = R_{500}/D_{\rm A}$, this can be expressed as

$$\bar{\theta}_{500} = \theta_* \left[\frac{h}{0.7}\right]^{-2/3} \left[\frac{(1-b)\,M_{500}}{3\times10^{14}{\rm M}_\odot}\right]^{1/3} E^{-2/3}(z) \left[\frac{D_{\rm A}(z)}{500\,{\rm Mpc}}\right]^{-1}, \tag{6}$$

where $\theta_* = 6.997\,$arcmin.

2.3 Limiting mass

One can use Eqs. 5 and 6 to compute the limiting mass at a point on the sky from the noise level, σ_Y. The noise estimate $\sigma_{Y_{500}}(\theta_{500}, l, b)$ is a by-product of the detection algorithm. The left panel of Figure 1 shows $\sigma_{Y_{500}}(\theta_{500}, l, b)$ for $\theta_{500} = 6\,$arcmin in a Mollweide projection with the Galactic mask used in the analysis applied. As expected, the noise at high Galactic latitude is lower than in the areas contaminated by diffuse Galactic emission. The ecliptic pole regions have the lowest noise level, reflecting the longer *Planck* integration time in these high-redundancy areas.

As the noise is not homogeneous on the sky, we show in the right panel of Fig. 1 the limiting mass, defined at 50% completeness, as a function of redshift for three different zones, deep, medium, and shallow, covering respectively, 3.5%, 47.8%, and 48.7% of the unmasked sky. For each line a S/N cut of 7 has been adopted.

2.4 The Planck cosmological sample

The reference cosmological sample is constructed from the PSZ Catalogue [2] and made public with the first release of *Planck* cosmological products. It is based on the SZ detections performed with the matched multi-filter (MMF) method, which relies on the use of a filter of adjustable width θ_{500} chosen to maximize the S/N of the detection. In order to ensure a high purity and to maximize the number of redshifts, the cosmological sample was constructed by selecting the SZ detections above a S/N threshold of 7 outside Galactic and point source masks covering 35% of the sky. This sample contains 189 candidates. All but one are confirmed bona fide clusters with measured redshifts (of which 184 are spectroscopic) and the remaining cluster is a high-reliability candidate.

3 The likelihood

To obtain cosmological constraints with the PSZ sample, we construct a likelihood function based on Poisson statistics:

$$\ln L = \ln \mathcal{P}(N_i|n_i) = \sum_{i=1}^{N_{\rm b}} [N_i \ln(n_i) - n_i - \ln(N_i!)]\,, \tag{7}$$

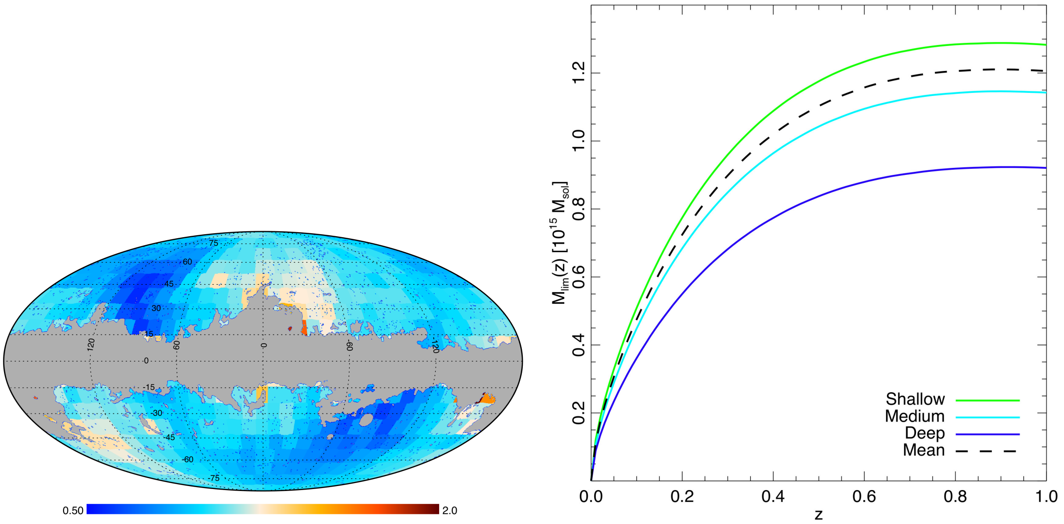

Figure 1 – *Left:* Noise map $\sigma_{Y_{500}}(\theta_{500})$ for $\theta_{500} = 6$ arcmin. The PSZ is limited by instrumental noise at high ($|b| > 20\,\mathrm{deg}$) Galactic latitude (deeper at ecliptic poles) and foreground noise at low Galactic latitude. The scale of the map ranges from 0.5 to 2 times the mean noise of the map, which is $\langle \sigma_{Y_{500}}(6\ \mathrm{arcmin}) \rangle = 2.2 \times 10^{-4}\mathrm{arcmin}^2$. *Right:* Limiting mass as a function of z for the selection function and noise level computed for three zones (deep, blue; medium, cyan; shallow, green), and on average for the unmasked sky (dashed black).

where $\mathcal{P}(N_i|n_i)$ is the probability of finding N_i clusters in each of N_b bins given an expected number of n_i in each bin in redshift. As a baseline, we assume bins in redshift of $\Delta z = 0.1$ and we checked that our results are robust when changing the bin size between 0.05 and 0.2. The modelled expected number n_i depends on the cosmological parameters and on the scaling relations and the selection function of the observed sample.

In order to impose constraints on cosmological parameters, we modified `CosmoMC`[5] to include the likelihood described above. We mainly study constraints on the spatially-flat ΛCDM model, varying Ω_m, σ_8, Ω_b, H_0, and n_s, but also adding in the total neutrino mass, $\sum m_\nu$, in Sect. 4.2. In each of the runs, the nuisance parameters (Y_*, α, $\sigma_{\log Y}$) follow Gaussian priors, with the characteristics detailed in Sec. 2.2, and are marginalized over. The bias $(1-b)$ follows a flat prior in the range [0.7,1]. The redshift evolution of the scaling, β, is fixed to its reference value.

When probing the six parameters of the ΛCDM model, we combine the *Planck* clusters with the Big Bang nucleosynthesis (BBN) constraints[6] $\Omega_\mathrm{b}h^2 = 0.022 \pm 0.002$. We also use either the H_0 determination from *HST*[7], $H_0 = (73.8 \pm 2.4)\ \mathrm{kms^{-1}Mpc^{-1}}$, or baryon acoustic oscillation (BAO) data, for which we used the combined likelihood of[8] and[15].

4 Cosmological Constraints

4.1 Constraints from clusters alone

Cluster counts in redshift for our *Planck* cosmological sample are not sensitive to all parameters of the ΛCDM model. We focus first on $(\Omega_\mathrm{m}, \sigma_8)$, assuming that n_s follows a Gaussian prior centred on the best-fit *Planck* CMB value $n_\mathrm{s} = 0.9603 \pm 0.0073$. We combine our SZ counts likelihood with the BAO and BBN likelihoods discussed earlier and we also incorporate the uncertainties on scaling parameters (Sect.2.2). Allowing the bias to range uniformly over the interval $[0.7, 1.0]$, we find the expected degeneracy between the two parameters, $\sigma_8(\Omega_\mathrm{m}/0.27)^{0.3} = 0.764 \pm 0.025$, with central values and uncertainties of $\Omega_\mathrm{m} = 0.29 \pm 0.02$ and $\sigma_8 = 0.75 \pm 0.03$ (Fig. 2, red contours). The cluster counts as a function of redshift for the best-fit model are plotted in Fig. 3. When fixing the bias to $(1-b) = 0.8$, the constraint on Ω_m remains unchanged while the constraint on σ_8 becomes stronger: $\sigma_8(\Omega_\mathrm{m}/0.27)^{0.3} = 0.78 \pm 0.01$ and $\sigma_8 = 0.77 \pm 0.02$).

To investigate how robust our results are when changing our priors, we repeat the analysis substituting the *HST* constraints on H_0 for the BAO results. Figure 2 (black contours) shows that the main effect is to change the best-fit value of H_0, leaving the $(\Omega_\mathrm{m}, \sigma_8)$ degeneracy almost unchanged.

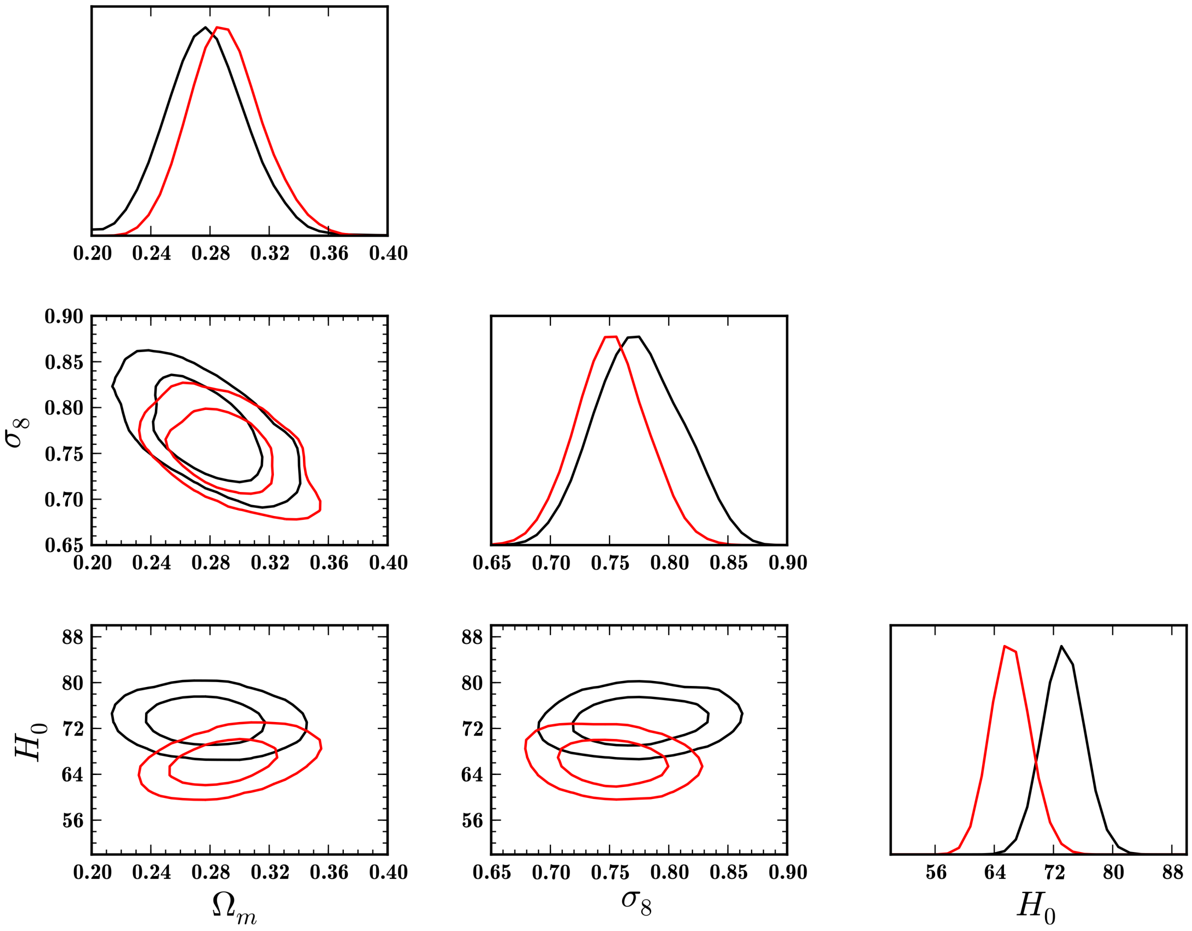

Figure 2 – *Planck* SZ constraints (+BAO+BBN) on ΛCDM cosmological parameters in red. The black lines show the constraints upon substituting *HST* constraints on H_0 for the BAO constrainsts. Contours are 68 and 95% confidence levels.

The left panel of Fig. 3 show some current constraints [10,11,12,13,14] on the combination $\sigma_8(\Omega_\mathrm{m}/0.27)^{0.3}$, which is the main degeneracy line in cluster constraints. For our own analysis we show our baseline result for SZ+BAO+BBN with a prior on $(1-b)$ distributed uniformly in $[0.7, 1]$. The figure demonstrates good agreement amongst all cluster observations, whether in optical, X-rays, or SZ.

4.2 Comparison with Planck primary CMB constraints

We now compare the PSZ cluster constraints to those from the analysis of the primary CMB temperature anisotropies given in [15], where σ_8 is derived from the standard six ΛCDM parameters. The *Planck* primary CMB constraints in the $(\Omega_\mathrm{m}, \sigma_8)$ plane differ significantly from our own, in particular through favouring a higher value of σ_8 (see Fig. 4). There is therefore some tension between the results from the *Planck* CMB analysis and the current cluster analysis. This is also illustrated in the left panel of Fig. 3 in terms of $\sigma_8(\Omega_\mathrm{m}/0.27)^{0.3}$, and in the right panel of Fig. 3 in terms of predicted cluster counts. For $(1-b) = 0.8$, the best-fit model from the primary CMB leads to a factor of 2 larger number of predicted clusters than is actually observed.

It is possible that the tension results from a combination of some residual systematics with a substantial statistical fluctuation. As we have noted, the modelling of the cluster gas physics

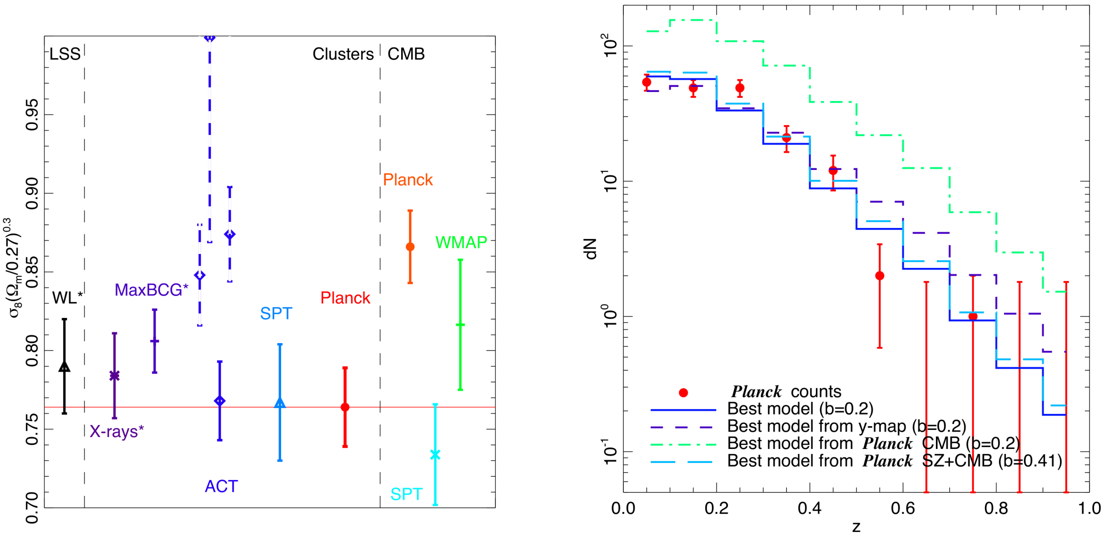

Figure 3 – *Left:* Comparison of constraints (68% confidence interval) on $\sigma_8(\Omega_\mathrm{m}/0.27)^{0.3}$ from different experiments of large–scale structure (LSS), clusters, and CMB. The solid line ACT point assumes the same universal pressure profile as this work. Probes marked with an asterisk have an original power of Ω_m different from 0.3. *Right:* Distribution in redshift for the *Planck* cosmological cluster sample. The observed number counts (red), are compared to our best-fit model prediction (blue). The dashed and dot-dashed histograms are the best-fit models from the *Planck* SZ power spectrum and *Planck* CMB power spectrum fits, respectively. The cyan long dashed histogram is the best fit CMB+SZ when the bias is free (see Section 4.2).

is the most important uncertainty in our analysis, in particular through its influence on the mass bias $(1-b)$. While we have argued for a preferred value of $(1-b) \simeq 0.8$ and we suggest a plausible range of $(1-b)$ from 0.7 to 1, a significantly lower value would substantially alleviate the tension between CMB and SZ constraints.

We have undertaken a joint analysis using the CMB likelihood presented in[9] and the cluster likelihood presented in[1], sampling $(1-b)$ in the range $[0.1, 1.5]$. This results in a 'measurement' of $(1-b) = 0.59 \pm 0.05$, which is enough to reconcile our observed SZ cluster counts with *Planck*'s best fit primary CMB parameters.

Such a large bias is difficult to reconcile with numerical simulations. Systematic discrepancies in the relevant scaling relations have, however, been identified and studied in stacking analyses of X-ray, SZ, and lensing data e.g. [16,17,18,19,20,21,22] suggesting that the issue is not yet fully settled from an observational point of view. The uncertainty reflects the inherent biases of the different mass estimates. Systematic effects arising from instrument calibration constitute a further source of uncertainty.

A different mass function may also help reduce the tension. Mass functions are calibrated against numerical simulations that may still suffer from volume effects for the largest haloes, as shown in the difference between the[3] and[4] mass functions. Also, the inclusion of baryons in the simulation has been found to lower the mass function, thus increasing the estimate of σ_8 from clusters[23].

Alternatively, the discrepancy may reflect a need to extend the minimal ΛCDM model in which the σ_8 constraints are derived from the primary CMB analysis. Any extension would need to modify the power spectrum on the scales probed by clusters, while leaving the scales probed by primary CMB observations unaffected. The inclusion of neutrino masses, quantified by their sum over all families, $\sum m_\nu$, can achieve this. Recently, the presence of massive neutrinos has been advocated by several works e.g.[24,25,26].

There is an upper limit of $\sum m_\nu < 0.93\,\mathrm{eV}$ from the *Planck* primary CMB data alone. If we combine the *Planck* CMB (*Planck*+WP) likelihood and the cluster count data using a fixed value $(1-b) = 0.8$, then we find a $2.8\,\sigma$ preference for the inclusion of neutrino masses with

$\sum m_\nu = (0.53 \pm 0.19)\,\mathrm{eV}$, as shown in Fig. 4. If, on the other hand, we adopt a more conservative point of view and allow $(1-b)$ to vary between 0.7 and 1.0, this preference drops to $1.9\,\sigma$ with $\sum m_\nu = (0.40 \pm 0.21)\,\mathrm{eV}$. Adding BAO data to the compilation lowers the value of the required mass but increases the significance, yielding $\sum m_\nu = (0.20 \pm 0.09)\,\mathrm{eV}$, due to a breaking of the degeneracy between H_0 and $\sum m_\nu$.

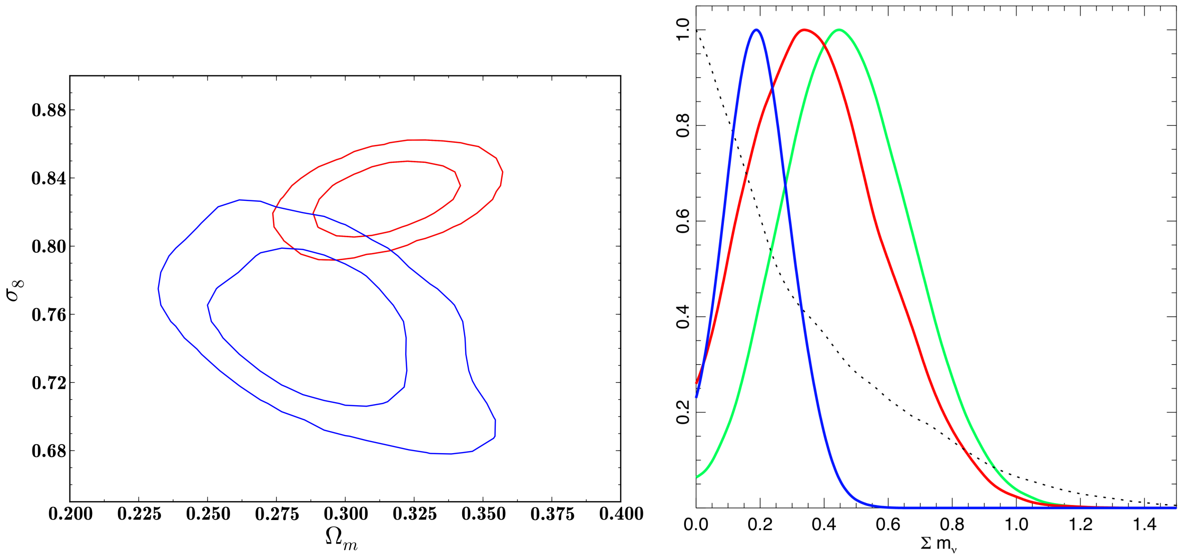

Figure 4 – *Left:* 2D Ω_m–σ_8 likelihood contours for the analysis with *Planck* CMB only (red); *Planck* SZ + BAO + BBN (blue) with $(1-b)$ in $[0.7, 1]$. *Right:* Marginalized posterior distribution for $\sum m_\nu$ from: *Planck* CMB data alone (black dotted line); *Planck* CMB + SZ with $1-b$ in $[0.7, 1]$ (red); *Planck* CMB + SZ + BAO with $1-b$ in $[0.7, 1]$ (blue); and *Planck* CMB + SZ with $1-b = 0.8$ (green).

5 Summary

We have used a sample of nearly 200 clusters from the PSZ, along with the corresponding selection function, to place strong constraints in the $(\Omega_\mathrm{m}, \sigma_8)$ plane. The relation between the mass and the integrated SZ signal plays a major role in the computation of the expected number counts. Uncertainties in cosmological constraints from clusters are no longer dominated by small number statistics, but by the gas physics and sample selection biases. Considering several ingredients of the gas physics of clusters, numerical simulations suggest a mass bias between the true mass and the estimated mass of $(1-b) = 0.8^{+0.2}_{-0.1}$. Adopting the central value we found constraints on Ω_m and σ_8 that are in good agreement with previous measurements using clusters of galaxies.

Comparing our results with *Planck* primary CMB constraints within the ΛCDM cosmology reveals some tension. This can be alleviated by permitting a large mass bias $(1-b \simeq 0.60)$, which is however significantly larger than expected. Alternatively, the tension may indicate a need for an extension of the base ΛCDM model that modifies its power spectrum shape. For example the inclusion of non-zero neutrino masses helps in reconciling the primary CMB and cluster constraints, a fit to *Planck* CMB + SZ + BAO yielding $\sum m_\nu = (0.20 \pm 0.09)\,\mathrm{eV}$.

6 References

1. Planck Collaboration XX. 2014, A&A, in press, [arXiv:astro-ph/1303.5080]
2. Planck Collaboration XXIX. 2014, A&A, in press, [arXiv:astro-ph/1303.5089]
3. Tinker, J., Kravtsov, A. V., Klypin, A., et al. 2008, ApJ, 688, 709
4. Watson, W. A., Iliev, I. T., D'Aloisio, A., et al. 2013, MNRAS, 433, 1230

5. Lewis, A. & Bridle, S. 2002, Phys. Rev., D66, 103511
6. Steigman, G. 2008, ArXiv e-prints, arxiv:0807.3004
7. Riess, A. G., Macri, L., Casertano, S., et al. 2011, ApJ, 730, 119
8. Hinshaw, G., Larson, D., Komatsu, E., et al. 2013, ApJS, 208, 19
9. Planck Collaboration XV. 2014, A&A, in press, [arXiv:astro-ph/1303.5075]
10. Kilbinger, M., Fu, L., Heymans, C., et al. 2013, MNRAS, 430, 2200
11. Vikhlinin, A., Kravtsov, A. V., Burenin, R. A., et al. 2009b, ApJ, 692, 1060
12. Rozo, E., Wechsler, R. H., Rykoff, E. S., et al. 2010, ApJ, 708, 645
13. Hasselfield, M., Hilton, M., Marriage, T. A., et al. 2013, J. Cosmology Astropart. Phys., 7, 8
14. Reichardt, C. L., Stalder, B., Bleem, L. E., et al. 2013, ApJ, 763, 127
15. Planck Collaboration XVI. 2014, A&A, in press, [arXiv:astro-ph/1303.5076]
16. Planck Collaboration XII. 2011, A&A, 536, A12
17. Biesiadzinski, T., McMahon, J., Miller, C. J., Nord, B., & Shaw, L. 2012, ApJ, 757, 1
18. Draper, P., Dodelson, S., Hao, J., & Rozo, E. 2012, Phys. Rev. D, 85, 023005
19. Rozo, E., Vikhlinin, A., & More, S. 2012a, ApJ, 760, 67
20. Sehgal, N., Addison, G., Battaglia, N., et al. 2013, ApJ, 767, 38
21. von der Linden A., et al., 2014, arXiv, arXiv:1402.2670
22. Israel H., Reiprich T. H., Erben T., Massey R. J., Sarazin C. L., Schneider P., Vikhlinin A., 2014, A&A, 564, A129
23. Cusworth S. J., Kay S. T., Battye R. A., Thomas P. A., 2014, MNRAS, 439, 2485
24. Hou, Z., Reichardt, C. L., Story, K. T., et al. 2014, ApJ, 782, 74
25. Battye R. A., Moss A., 2014, PhRvL, 112, 051303
26. Beutler F., et al., 2014, arXiv, arXiv:1403.4599

GALAXY CLUSTER COSMOLOGY WITH THE ATACAMA COSMOLOGY TELESCOPE

MATTHEW HASSELFIELD for the ACT COLLABORATION
Department of Astrophysical Sciences, 4 Ivy Lane, Peyton Hall,
Princeton University, Princeton NJ 08544, USA

We report on the galaxy cluster catalog and resulting cosmological parameter constraints derived from Atacama Cosmology Telescope (ACT) observations at 148 GHz from 2007–2013. We demonstrate agreement with *Planck* cluster results, provided the ACT clusters are analyzed under the same same assumptions that relate the SZE signal to the mass. As an alternative mass calibration, we introduce independent dynamical mass measurements of a subsample of our clusters. The dynamical mass calibration leads to higher values of σ_8 and Ω_m than those preferred by the *Planck* cluster analysis.

1 Introduction

Galaxy clusters are the most massive gravitationally collapsed systems in the universe, and provide important tests of models of structure formation along with independent measurements of key cosmological parameters. Millimeter wavelength survey instruments such as the Atacama Cosmology Telescope (ACT), South Pole Telescope (SPT), and *Planck* satellite exploit the Sunyaev-Zeldovich effect (SZE) to detect and characterize clusters. The SZE signal from clusters is expected to be related to halo mass with low intrinsic scatter, making cosmological parameter constraints possible with even modestly sized samples. For instruments with arcminute resolution, such as ACT and SPT, the SZE provides cluster samples with a cutoff mass that is nearly constant as a function of redshift.

A major limiting factor in the use of SZE selected cluster samples for cosmological parameter constraints is uncertainty in the "Y–M scaling relation" that is used to convert the SZE signal to a halo mass. Recent *Planck* Collaboration [1] results have shown tension between CMB-based and cluster-based constraints on σ_8 and Ω_m, with the cluster measurements preferring lower values for these parameters than are indicated by the CMB. The difference could be explained by a systematic overestimate of cluster masses.

The mass calibration used by *Planck* ultimately derives from X-ray measurements of relaxed clusters that permit the relation of predicted SZ signal to total cluster mass, under the assumption of hydrostatic equilibrium (HSE). The masses M_{500c}^{HSE} determined under these assumptions can be related to the halo masses M_{500c}^{halo} by a bias factor $b^{\mathrm{HSE}} \approx 0.2$, where

$$M_{500c}^{\mathrm{halo}} = (1 - b^{\mathrm{HSE}}) M_{500c}^{\mathrm{HSE}}. \tag{1}$$

In order to reconcile the observed cluster signal with CMB constraints, a bias factor of $b^{\mathrm{HSE}} \approx 0.45$ is required. Such a large bias is difficult to explain.

In this work we present cosmological parameter constraints from the ACT cluster catalogs. We begin by describing the observations and the cluster sample. We then turn to the

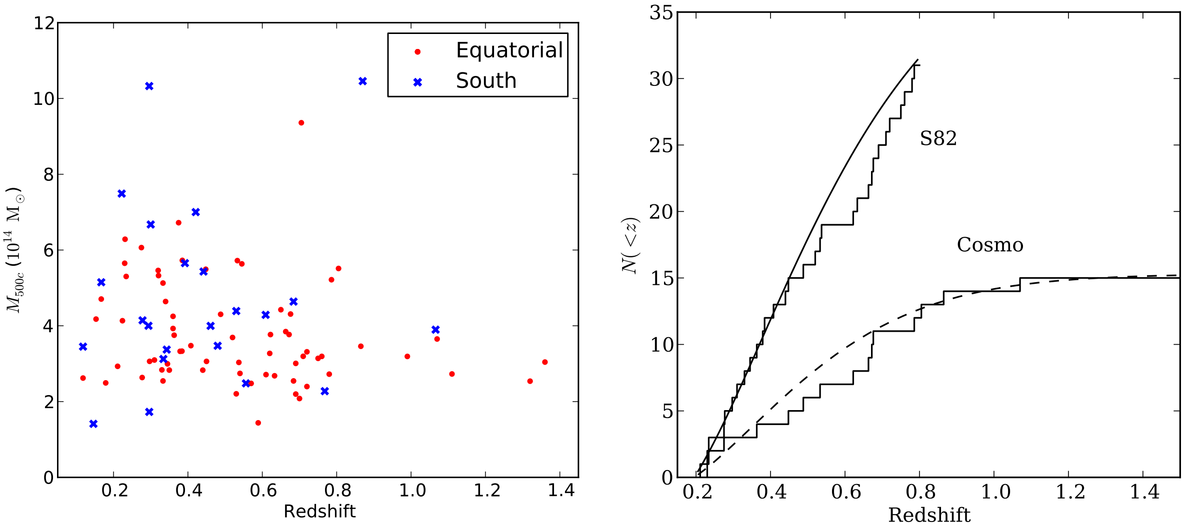

Figure 1 – *Left:* Mass and redshift for the Equatorial and Southern cluster samples. In this case masses are estimated assuming the A10 pressure profile and a mass bias of $b^{\rm HSE} = 0$. *Right:* Cumulative distributions of cluster redshifts for two subsamples of the Equatorial cluster sample. The "Cosmo" subsample corresponds to all Equatorial clusters with $S/N > 5.1$ and $z > 0.2$. The "S82" sample is all Equatorial clusters with $S/N > 4$ and $0.2 < z < 0.8$. Smooth curves are model fits. The model assumes a fiducial ΛCDM cosmology with only σ_8 as a free fit parameter; these fits show basic consistency between our sample and ΛCDM.

cosmological constraining power of the sample, demonstrating agreement with *Planck* cluster measurements. We then present our main cosmological results, which use an alternative mass calibration derived from velocity dispersion measurements to achieve parameter constraints that are somewhat more independent of the hydrostatic mass paradigm. The techniques and results discussed here are presented in greater detail by Hasselfield *et al.*[2]

2 Observations

ACT is a ground-based telescope with a 6 m primary mirror that observed at 148, 218, and 277 GHz from 2007–2010. The $1.4'$ resolution of the instrument is well matched to the typical angular scale of massive clusters at $z > 0.2$. The main ACT survey consists of the Southern and Equatorial regions, each of which covers roughly 500 deg^2. Cluster catalogs were obtained from the 148 GHz maps through the application of a suite of matched spatial filters covering a broad range of cluster angular scales. While the original analysis of the Southern sample [3] used β-profiles for the cluster signal templates, the present work makes use of the "Universal Pressure Profile" measured by Arnaud *et al* [4] (hereafter A10) for establishing the Equatorial cluster candidate list, and for cosmological analysis of the combined South and Equatorial sample.

Only cluster candidates that have been optically confirmed are included in the final cluster catalogs. The Equatorial region includes significant overlap with SDSS Stripe-82, and the deep optical data on this region facilitate confirmation of low to intermediate redshift candidates, as described by Menanteau *et al.*[5] These are combined with targeted optical and IR follow-up of strong SZ candidates to yield a catalog of 68 clusters, most with spectroscopic redshifts. Due to the significant existing optical data in this region, 49 of these clusters were previously known. However, the low scatter and redshift-independent nature of the SZE signal means that this sample is likely to trace the massive, high redshift component of the cluster distribution.

In the Southern region, targeted follow-up of high significance clusters yields a sample of 23 clusters, of which 10 are new discoveries. The median redshift of the combined sample is 0.45. Mass estimates (assuming $b^{\rm HSE} = 0$) and redshifts of the ACT cluster sample are shown in Figure 1.

The interpretation of the signal, and its relation to halo mass, is achieved within the "Profile

Based Amplitude Analysis" technique.[2] This approach makes use of a cluster's measured redshift and a spatial template for the cluster pressure profile (at a given mass) to model the signal observed in a smoothed (spatially filtered) 148 GHz map of the cluster. The cluster pressure profile and baseline Y–M are those from A10, though with additional degrees of freedom added to permit independent calibration of the Y–M scaling relation.

For the purposes of comparing the observed sample to cluster number densities predicted for a given cosmological model, one must have some understanding of the "selection function" of the survey, defined here as the fraction of clusters of a given mass and redshift that would be detected given the survey noise level, point spread function, and candidate identification and confirmation procedures. We thus restrict our sample, in both the Southern and Equatorial regions, to a subsample for which the "selection function" is well understood and easily stated. As a result we use the subsample of Equatorial (Southern) clusters that have $z > 0.2$ (0.3) and $S/N > 5.1$ (5.7). The cumulative redshift distribution of two (overlapping) cluster subsamples is shown in the right hand panel of Figure 1.

In addition to the SZE survey and optical confirmation campaigns, Sifon *et al*[6] have obtained dynamical mass measurements for the most significant clusters in the Southern sample. For each cluster, redshifts of $N \approx 60$ member galaxies were used to compute the one-dimensional velocity dispersion. Under the assumption that the galaxy velocity dispersion traces the dark matter velocity dispersion, the scaling relation from the N-body simulations of Evrard *et al*[7] is then used to obtain the cluster mass.

The dynamical mass measurements provide an independent calibration of the cluster mass, and allow us to relax priors on certain parameters in the Y–M scaling relation and permit them to be constrained instead by the simultaneous measurements of SZE signal and mass on the Southern clusters. The full cosmological analysis is described in the next section. However, we note, before proceeding, that the dynamical masses so obtained are clearly larger than expectations based on the A10 scaling and are more compatible with $b^{\rm HSE} \approx 0.5$.

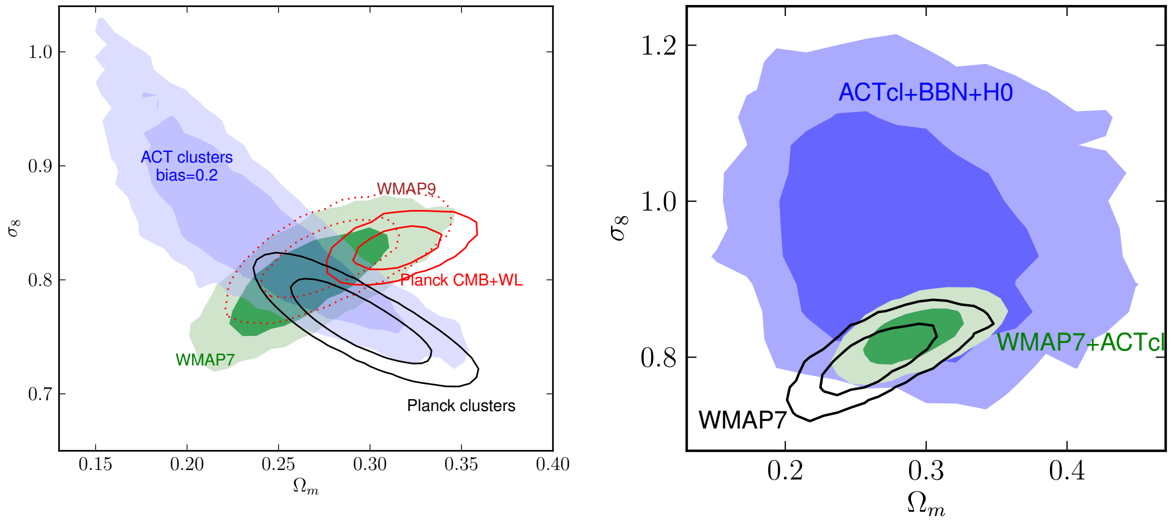

Figure 2 – *Left:* Parameter constraints on σ_8 and $\Omega_{\rm m}$ from the ACT equatorial cluster sample, with scaling relation assumptions similar to those made by *Planck*[1]. Also shown are the WMAP7, WMAP9, and *Planck* CMB+WL constraints. *Right:* Constraints due to ACT clusters, compared with WMAP7 results from CMB. In this case the scaling relation parameters vary freely, constrained by dynamical mass measurements of the Southern sample clusters. Non-CMB based priors are placed on $\Omega_{\rm b}$ and the Hubble constant for the cluster constraints.

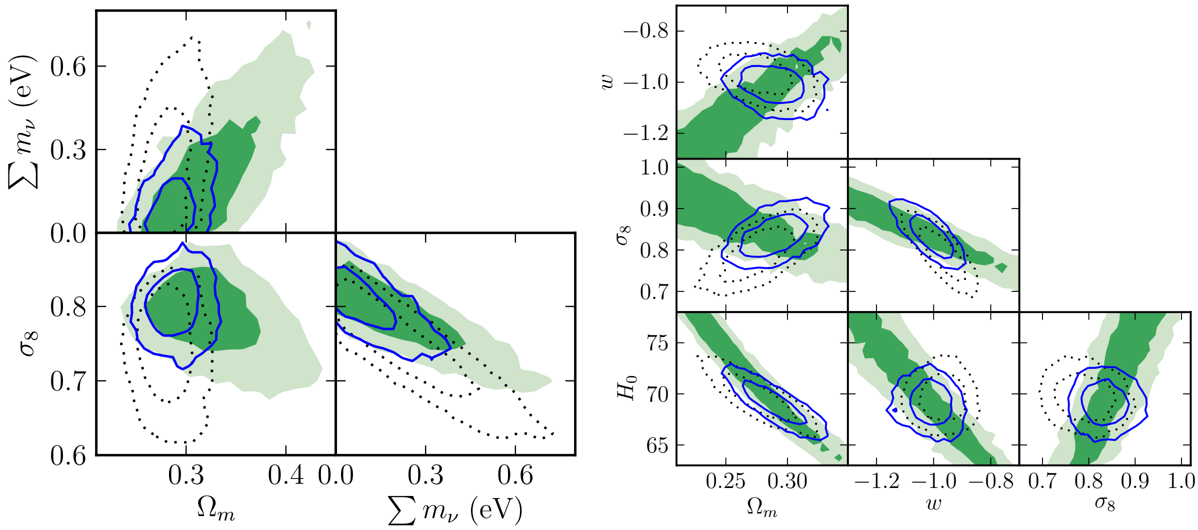

Figure 3 – *Left:* Parameter constraints in an to ΛCDM that includes a non-zero neutrino mass. Constraints from WMAP7+ACTcl (green contours) agree with constraints from WMAP7+H0+BAO (dotted line). Combining WMAP7+H0+BAO+ACTcl yields the blue contours, with $\sum m_\nu < 0.29$ eV at 95% CL. *Right:* Parameter constraints in wCDM. We compare the case of WMAP7+ACTcl (green contours) to WMAP7+Supernovae (dotted line). The cluster measurement provides useful constraints on σ_8 in this model. The combination WMAP7+ACTcl+Supernovae is also shown (blue contours).

3 Cosmological analysis

Cluster number counts are highly sensitive to the matter power spectrum at present times, and are thus most useful as an independent probe of σ_8. In certain extensions to the ΛCDM model, the probe of local structure provided by cluster measurements breaks parameter degeneracies in CMB constraints and sharpens limits on parameters such as the Dark Energy equation of state parameter, w, and the sum of the neutrino species masses, $\sum m_\nu$.

We perform a likelihood analysis of our cluster sample, along with other data sets, in order to recover the posterior likelihood distribution for cosmological parameters. The contribution to the likelihood function from clusters is able to incorporate the redshift and mass (if known) of clusters, as well as the SZE signal from the clusters. Parameters describing the Y–M scaling relation may be either fixed or set free to vary within a broad range. The complete details may be found in Hasselfield *et al.*[2]

In the left hand panel of Figure 2 we show parameter constraints within ΛCDM from the ACT equatorial cluster sample, comparing to recent CMB constraints [8,9,10] and the *Planck* cluster results.[1] The ACT and *Planck* cluster posterior distributions, in this case, do not include priors derived from CMB observations. In addition, the ACT analysis does not include any uncertainty on the Y–M scaling relation parameters. Rather, the scaling relation is based on the A10 Y–M relation with $b^{\mathrm{HSE}} = 0.2$, which is the mean relation assumed by the *Planck* cluster analysis. The *Planck* and ACT results are in nice agreement, particularly in the direction orthogonal to the natural CMB degeneracy.

Next, we introduce the Southern cluster sample, including the dynamical mass measurements, into the parameter likelihood analysis. Instead of fixing the scaling relation parameters, we permit the three key parameters (slope, normalization, and intrinsic scatter) to vary freely with non-informative priors. The posterior distribution for σ_8 and Ω_{m} within ΛCDM is shown in the right hand panel of Figure 2. While the region of parameter space favored by this analysis is broad compared to CMB constraints, we note the preference for the higher values of σ_8 and Ω_{m}, more consistent with the upper end of the WMAP7 constraints, and thus more consistent with *Planck* CMB than with *Planck* clusters. This is not surprising given the small values of the dynamical masses as compared with the A10 calibration of the Y–M relation.

We also study the impact of the dynamical mass calibration on two single-parameter extensions to ΛCDM, in combination with WMAP and other probes.[11,12] Marginalized two-dimensional posterior distributions for these cases are shown in Figure 3. For the case of non-zero neutrino mass, the measurement of σ_8 provides an important complement to CMB and BAO measurements. The resulting upper limit is $\sum m_\nu < 0.29\,\mathrm{eV}$, at 95% confidence, when combined with WMAP7 and BAO.[13] We note that this is comparable to the constraint from *Planck* CMB and BAO, with $\sum m_\nu < 0.25\,\mathrm{eV}$ (95% CL).

For the case of wCDM, the degeneracies broken by the cluster data are more slight, and only marginal improvements in constraints are seen when ACT clusters are added to, for example, WMAP7+Supernovae.

4 Conclusions

Millimeter wavelength observatories such as ACT are producing catalogs of high redshift, massive galaxy clusters. Such catalogs have the potential to constraint important parameters relating to the matter power spectrum and the growth of structure, provided that the cluster mass can be determined in an unbiased way. The ACT cluster results are in nice agreement with *Planck* cluster cosmological results when the same assumptions are made about the relationship between mass and SZE signal. However, when instead the ACT sample is calibrated using dynamical mass measurements, we find that the cluster masses are significantly smaller than those implied by the X-ray based Y–M relation, leading to parameter constraints more compatible with *Planck* CMB measurements than *Planck* cluster measurements.

References

1. *Planck* Collaboration XX, ArXiv e-prints, 1303.5080 (2013).
2. M. Hasselfield *et al*, J. Cosmology Astropart. Phys. **7**, 8 (2013).
3. T.A. Marriage *et al* ApJ **737**, 61 (2011).
4. M. Arnaud *et al*, A&A **517**, A92 (2010).
5. F. Menanteau *et al*, ApJ **765**, 67 (2013).
6. C. Sífon *et al*, ApJ **772**, 25 (2013).
7. A.E. Evrard *et al*, ApJ **672**, 122 (2008).
8. E. Komatsu *et al*, ApJS **192**, 18 (2011).
9. G. Hinshaw *et al*, ApJS **208**, 19 (2013).
10. *Planck* Collaboration XVI, ArXiv e-prints, 1303.5076 (2013).
11. M. Hicken *et al*, ApJ **700**, 1097 (2009).
12. A.G. Riess *et al*, ApJ **699**, 539 (2009).
13. W.J. Percival *et al*, MNRAS **401**, 2148 (2010).

ARCMINUTE MICROKELVIN IMAGER FOLLOWUP OF THE PLANCK 2013 SUNYAEV-ZEL'DOVICH CATALOGUE

Y. C. PERROTT
Astrophysics Group, Cavendish Laboratory, University of Cambridge,
J J Thomson Avenue, Cambridge CB3 0HE, U.K.

We present observations and analysis of a sample of 118 galaxy clusters from the 2013 *Planck* catalogue of Sunyaev-Zel'dovich (SZ) sources with the Arcminute Microkelvin Imager (AMI), a ground-based radio interferometer. The higher-resolution AMI observations provide validation of the cluster detections and a consistency check on the fitted 'size' (θ_s) and 'flux' (Y_{tot}) parameters in the Generalised Navarro, Frenk and White (GNFW) model. We detect 93 of the clusters. We find that Y_{tot} values as measured by AMI are biased downwards with respect to the *Planck* constraints, especially for high *Planck*-SNR clusters. We perform simulations to show that this can be explained by deviation from the 'universal' pressure profile shape used to model the clusters. We show that AMI data can constrain the α and β parameters describing the shape of the profile in the GNFW model provided careful attention is paid to the degeneracies between parameters, but one requires information on a wider range of angular scales than are present in AMI data alone to correctly constrain all parameters simultaneously.

1 The Arcminute Microkelvin Imager telescope

The Arcminute Microkelvin Imager[1] (AMI) is a dual-array interferometer designed for SZ studies and situated near Cambridge, UK. AMI consists of two arrays: the Small Array (SA), optimised for viewing arcminute-scale features, having an angular resolution of ≈ 3 arcmin and sensitivity to structures up to ≈ 10 arcmin in scale; and the Large Array (LA), with angular resolution of ≈ 30 arcsec, which is insensitive to the arcminute-scale emission due to clusters and is used to characterise and subtract confusing radio sources. Both arrays operate at a central frequency of ≈ 15 GHz with a bandwidth of ≈ 4.5 GHz, divided into six channels.

2 Selection of the cluster sample

The *Planck* 2013 SZ union catalogue consists of 1227 clusters down to a signal-to-noise limit of 4.5. An initial selection cut of $20^\circ \leq \delta < 87^\circ$ was applied to satisfy AMI's 'easy' observing limits, and clusters with known redshifts of $z \leq 0.100$ were excluded since these have large angular sizes and will be largely resolved out by AMI. Clusters were also excluded when there were bright radio sources near the phase centre, based on LA observations. In addition, clusters were manually inspected at various stages of the follow-up and analysis process, and some were rejected at later stages due to extra source environment problems. After these cuts we obtain the final sub-sample with *Plank* SNR ≥ 5, which we will refer to as the SZ sample, consisting of 118 clusters. Results for the remaining clusters with $4.5 \leq$ SNR < 5 will be released at a later date.

3 Analysing the SZ signal

3.1 Cluster model

For consistency with the *Planck* catalogue, we assume the electron pressure profile $P_{\rm e}(r)$ of each cluster follows a generalised Navarro-Frenk-White [2, 3] (GNFW) model, which is given by (assuming spherical geometry)

$$P_{\rm e}(r) = P_0 \left(\frac{r}{r_{\rm s}}\right)^{-\gamma} \left[1 + \left(\frac{r}{r_{\rm s}}\right)^{\alpha}\right]^{(\gamma-\beta)/\alpha}, \tag{1}$$

where P_0 is a normalisation coefficient, r is the physical radius, $r_{\rm s}$ is a characteristic scale radius, and the parameters (γ, α, β) describe the slopes of the pressure profile at radii $r \ll r_{\rm s}$, $r \approx r_{\rm s}$, and $r \gg r_{\rm s}$ respectively. As in the *Planck* analysis, we fix the slope parameters to their 'universal' values [4], $\gamma = 0.3081, \alpha = 1.0510, \beta = 5.4905$.

With (γ, α, β) fixed, a cluster's appearance on the sky may be described using four (observational) parameters only: $(x_0, y_0, \theta_{\rm s}, Y_{\rm tot})$, where x_0 and y_0 are the positional coordinates for the cluster, $\theta_{\rm s} = r_{\rm s}/D_{\rm A}$ is the characteristic angular scale of the cluster on the sky ($D_{\rm A}$ is the angular diameter distance to the cluster), and $Y_{\rm tot}$ is the SZ surface brightness integrated over the cluster's extent on the sky.

3.2 Analysis of AMI data

The model attempting to describe the AMI data is produced by a combination of the cluster model described above, the radio source environment as measured by the LA and a generalised Gaussian noise component comprising instrumental noise, confusion noise from radio sources below the detection threshold, and contamination from primordial CMB anisotropies. The flux density and spectral index of sources which are detected at $\geq 4\sigma$ ($< 4\sigma$) on the SA map are modelled simultaneously with the cluster (subtracted directly).

Model parameter estimation is performed in a fully Bayesian manner using the AMI in-house software package McADAM, in *uv*-space [5], using the nested sampler MultiNEST [6,7] to obtain the posterior distribution for all parameters and to calculate the Bayesian evidence, $\mathcal{Z}$. To assess the detection significance of a cluster, we perform two parameter estimation runs – one with the full cluster + radio source environment model, and one with only the radio source environment model (the 'null' run); the evidence ratio between these two runs is a measure of the detection significance for the cluster. We take $\Delta \ln(\mathcal{Z}) = 0$ as the boundary between detections and non-detections [8]. We also define an additional boundary $\Delta \ln(\mathcal{Z}) = 3$ between 'moderate' and 'clear' detections, and at $\Delta \ln(\mathcal{Z}) = -3$ to indicate cases where the cluster model is strongly rejected by the data.

3.3 Results

In the SZ sample, 74 are clear detections, 19 are moderate detections, 21 are non-detections and 4 are clear non-detections. For each cluster, maps, parameter posterior distributions and source environment information are available at http://www.mrao.cam.ac.uk/facilities/surveys/ami-planck/. The AMI detections include 66 previously known clusters, re-confirmations of 15 new clusters already confirmed by other follow-up campaigns, and confirmation of 12 new clusters not previously confirmed.

$Y_{\rm tot}$-θ_s comparison

A major conclusion of a previous AMI-Planck comparison of 11 clusters [9] was that the clusters were found overall to be smaller in angular size and fainter (lower $Y_{\rm tot}$) by AMI than by *Planck*. Fig. 1 illustrates the overall trend for the larger sample by showing AMI and PwS mean values

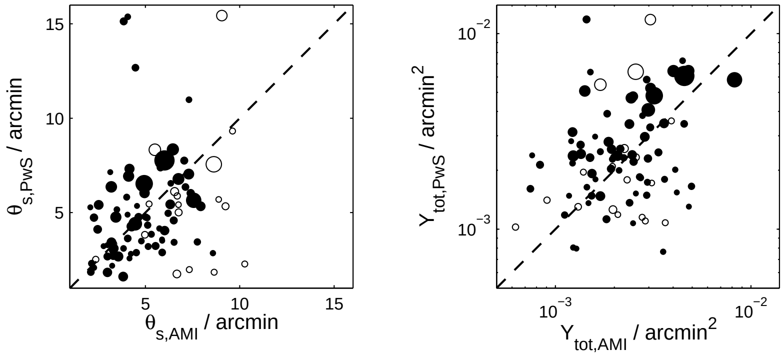

Figure 1 – Comparison between PwS and AMI mean $Y_{\rm tot}$ and θ_s values. The size of the points plotted increases with increasing *Planck* SNR; clear detections are plotted as filled circles, and moderate detections as empty circles. The one-to-one relationship is plotted as a black dashed line.

for θ_s and $Y_{\rm tot}$ for the entire sample of clear and moderate detections. Aside from some outliers, the θ_s values do not seem to be biased, but only correlate weakly. However, the $Y_{\rm tot}$ values for the high-SNR clusters as measured by AMI are still lower overall than the *Planck* values; for lower SNR clusters, the bias may be obscured by the noise. The comparison between AMI values and the values produced by the MMF algorithms is very similar.

4 Profile investigation

One potential reason for the discrepancy is the 'universal' profile shape assumed for all clusters. Since AMI is an interferometer, it resolves out large angular scales and can therefore never measure $Y_{\rm tot}$ (the integral of the Comptonisation parameter over all angular scales) directly; AMI 'constraints' on $Y_{\rm tot}$ are actually projections from the angular scales it does measure, assuming a particular profile.

To investigate how much of an effect this might have, we generated a set of simulations with realistic thermal, CMB and source confusion noise levels. For each representative (θ_s, $Y_{\rm tot}$), we generated simulations with α and γ set to the 31 individual fitted values from the REXCESS sample [4], and with β drawn from a uniform distribution between 4.5 and 6.5. We then ran our usual analysis pipeline on these simulations, with (γ, α, β) fixed to their 'universal' values. Some example two-dimensional constraints on θ_s and $Y_{\rm tot}$ are shown for the largest angular size cluster in Fig. 2; because the 'universal' profile is not a good fit to the data, the posteriors are biased downward by the prior, in agreement with the results from the real sample.

We next reanalysed the simulations, allowing the shape parameters to vary. Due to the lack of information on $Y_{\rm tot}$ in the data, there are very strong degeneracies between θ_s and α and β. These strong degeneracies lead to spurious constraints in α and β in the one-dimensional marginalised posterior distributions. These biases can be decreased by using a Gaussian prior based on the REXCESS sample on α, namely $\mathcal{N}(1.0510, 0.47)$ truncated at 0.3, and a tighter uniform prior on β, $\mathcal{U}[4.5, 6.5]$ (with γ fixed to the 'universal' value). For clusters of angular size $\theta_s \approx 3\,$arcmin ($\approx 5\,$arcmin), this results in correct recovery of θ_s, $Y_{\rm tot}$ and β (α). For larger angular-size clusters (see Fig. 2), α and β are constrained correctly but the input values of θ_s and $Y_{\rm tot}$ are *not* recovered, because there is not enough information available in the angular scales measured by the SA to constrain all of these parameters simultaneously.

5 Analysis of real data

We reanalysed the clear detections in the sample allowing α and β to vary (see Fig. 3). The preferred values for β are on the whole centred around the 'universal' value predicted by simulations, and do not show a trend towards the lower value derived from the *Planck* stacked profile[10]. The preferred values for α are also on the whole centred around the 'universal' value.

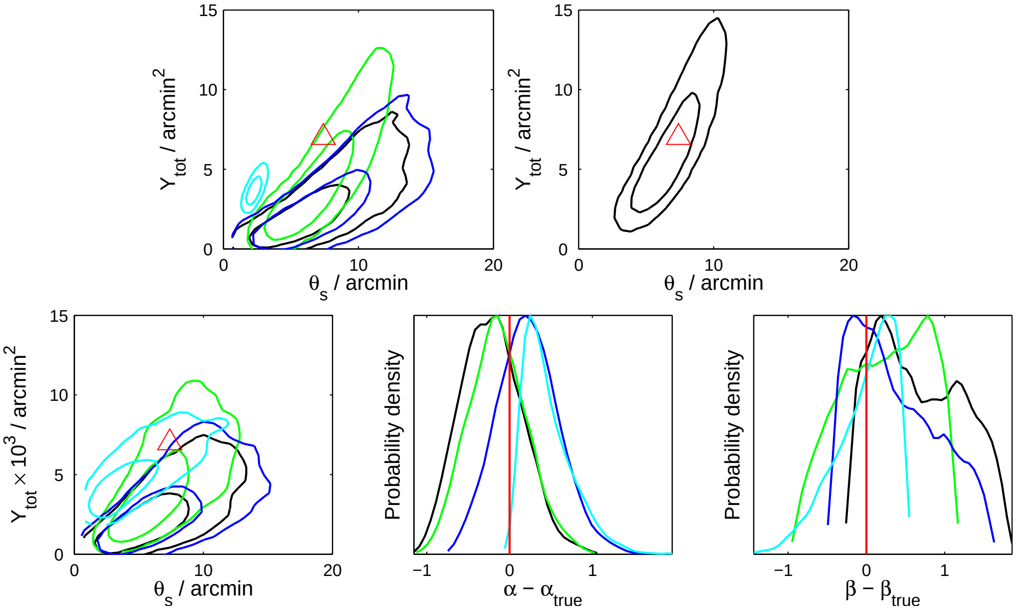

Figure 2 – Example posterior distributions for simulated clusters (see text for details), with (top left and bottom) differing GNFW shape parameter values (γ, α, β) based on the REXCESS sample, and (top right) simulated with the 'universal' values. In the top row, the model used for recovering the parameters has the shape parameter values fixed to the 'universal' values. In the bottom row, the model used for recovering the parameters has γ fixed to the 'universal' value but allows α and β to vary. The input parameter values are marked with red lines and triangles, and the two-dimensional contours are at the 68% and 95% confidence boundaries.

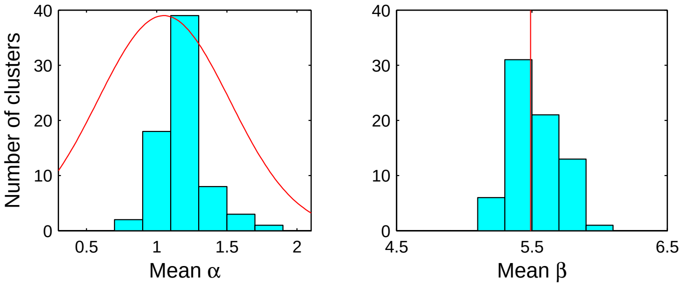

Figure 3 – The distribution of mean values of α and β obtained from AMI data. For comparison, the REXCESS-based prior on α is plotted in red, and the 'universal' value of β predicted from numerical simulations is indicated with a red line.

References

1. AMI Consortium: J.T.L. Zwart *et al.*, MNRAS **391**, 1545 (2008).
2. J.F. Navarro *et al.*, ApJ **490**, 493 (1997).
3. D. Nagai *et al.*, ApJ **668**, 1 (2007).
4. M. Arnaud *et al.*, A&A **517**, A92 (2010).
5. F. Feroz *et al.*, MNRAS **398**, 2049 (2009).
6. F. Feroz and M.P. Hobson, MNRAS **384**, 449 (2008).
7. F. Feroz *et al.*, MNRAS **398**, 1601 (2009).
8. H. Jeffreys, *Theory of Probability, 3rd edn.* (Oxford, England, 1961).
9. Planck Collaboration, AMI Collaboration, *et al.*, A&A **550**, A128 (2013)
10. Planck Collaboration, *et al.*, A&A **550**, A131 (2013)

High resolution SZ observations at the IRAM 30-m telescope with NIKA

R. Adam[1], A. Adane[2] P. Ade[3], P. André[4], A. Beelen[5], B. Belier[6], A. Benoît[7], A. Bideaud[3], N. Billot[8], N. Boudou[7], O. Bourrion[1], M. Calvo[7], A. Catalano[1], G. Coiffard[2], B. Comis[1], A. D'Addabbo[7,14], F.-X. Désert[9], S. Doyle[3], J. Goupy[7], C. Kramer[8], S. Leclercq[2], J. F. Macías-Pérez[1], J. Martino[5], P. Mauskopf[3,13], F. Mayet[1], A. Monfardini[7], F. Pajot[5], E. Pascale[3], L. Perotto[1], E. Pointecouteau[10,11], N. Ponthieu[9], V. Revéret[4], L. Rodriguez[4], F. Ruppin[1], G. Savini[12], K. Schuster[2], A. Sievers[8], C. Tucker[3], R. Zylka[2]

[1]*LPSC, Université Grenoble-Alpes, CNRS/IN2P3, 53, rue des Martyrs, Grenoble, France*
[2]*Institut de RadioAstronomie Millimétrique (IRAM), Grenoble, France*
[3]*Astronomy Instrumentation Group, University of Cardiff, UK*
[4]*AIM, CEA/IRFU, CNRS/INSU, Uni. Paris Diderot, CEA-Saclay, 91191 Gif-Sur-Yvette, France*
[5]*Institut d'Astrophysique Spatiale (IAS), CNRS and Université Paris Sud, Orsay, France*
[6]*Institut d'Electronique Fondamentale (IEF), Université Paris Sud, Orsay, France*
[7]*Institut Néel, CNRS and Université de Grenoble, France*
[8]*Institut de RadioAstronomie Millimétrique (IRAM), Granada, Spain*
[9]*IPAG, CNRS and Université de Grenoble, France*
[10]*Université de Toulouse, UPS-OMP, IRAP, Toulouse, France*
[11]*CNRS, IRAP, 9 Av. colonel Roche, BP 44346, F-31028 Toulouse cedex 4, France*
[12]*UCL, Department of Physics and Astronomy, Gower Street, London WC1E 6BT, UK*
[13]*School of Earth and Space Exploration and Dep. of Physics, Arizona State Uni., Tempe, AZ 85287*
[14]*Dipartimento di Fisica, Sapienza Università di Roma, Piazzale Aldo Moro 5, I-00185 Roma, Italy*

High resolution observations of the thermal Sunyaev-Zel'dovich (tSZ) effect are necessary to allow the use of clusters of galaxies as a probe for large scale structures at high redshifts. With its high resolution and dual-band capability at millimeter wavelengths, the NIKA camera can play a significant role in this context. NIKA is based on newly developed Kinetic Inductance Detectors (KIDs) and operates at the IRAM 30m telescope, Pico Veleta, Spain. In this paper, we give the status of the NIKA camera, focussing on the KID technology. We then present observations of three galaxy clusters: RX J1347.5-1145 as a demonstrator of the NIKA capabilities and the recent observations of CL J1226.9+3332 ($z = 0.89$) and MACS J0717.5+3745 ($z = 0.55$). We also discuss prospects for the final NIKA2 camera, which will have a 6.5 arcminute field of view with about 5000 detectors in two bands at 150 and 260 GHz.

1 Introduction

The observations of clusters of galaxies, from radio to gamma-ray, have proved to be a powerful probe of large scale structure formation. Clusters are mainly composed of dark matter ($\sim 85\%$ of their total mass) that drives the gravitational processes. Their baryonic component, mostly made of hot ionized gas, *i.e.* the intra cluster medium (ICM), is subdominant but responsible for more complex physics that can limit their use for cosmology. Consequently, a detailed characterization of the complex gravitational and non-gravitational processes acting in galaxy clusters is mandatory not only for a deep understanding of their physics, but also in order to properly use them as robust cosmological probes. One way of detecting and studying them is to use the thermal Sunyaev-Zel'dovich (tSZ) effect [18,19]. When traveling trough the ICM, Cosmic Microwave Background (CMB) photons can Compton inverse interact on the energetic electrons of the hot gas. This leads to a characteristic spectral distortion of the CMB where clusters appear as a decrement in the CMB intensity for frequencies below 217 GHz, and as an increment above (see [3] for a review on the tSZ effect). Recent tSZ observations have been performed by the South Pole Telescope [7], the Atacama Cosmology Telescope [10] and the Planck satellite [15,16] leading to large tSZ selected cluster samples. Nevertheless, the relatively poor resolution of these observations (larger than 1 arcminute) does not allow to probe their inner structure, especially for intermediate and high redshift clusters. In this context, the New IRAM KID Arrays (NIKA) will play a significant role in the study of such systems. NIKA is a high angular resolution imaging camera based on recently developed Kinetic Inductance Detectors (KIDs). This camera is the prototype of the future larger camera NIKA2. In this proceeding, we present the status of NIKA, show recent tSZ results, and discuss perspectives for NIKA2.

2 NIKA: a KID based camera at the IRAM 30-m telescope

In order to push the study of galaxy clusters to higher redshifts, tSZ observations require instruments with high sensitivity, high angular resolution and large mapping speed. Since traditional detectors are already photon noise limited, in particular for ground-based observations, such goals require the development of large arrays of detectors. Cryogenics constraints impose to read as many detectors as possible with a single wire to limit the number of dissipative elements. Kinetic Inductance Detectors (KIDs) offer a promising alternative to other detectors since they are intrinsically frequency multiplexed. KIDs are high quality superconducting resonator. They are made of a capacitor C and an inductance $L = L_g + L_k$ that is the sum of a geometric and a kinetic part. Absorbed photons of high enough energy can break Cooper pairs in the material (aluminum). The induced variation in the density of the charge carriers changes the kinetic part of the inductance that, in turn, leads to a variation of the resonance frequency of the resonator, $f_0 = \frac{1}{2\pi\sqrt{LC}}$. This frequency shift can be used to monitor the incoming optical power as both quantities are directly proportional [5].

The New IRAM KID Arrays (NIKA) is a KID based instrument that operates at the IRAM 30m telescope, Pico Veleta, Spain. It uses Hilbert dual-polarization design LEKID pixels (Lumped Element KID [9,17]) read with the dedicated NIKEL electronics [4]. Two arrays of 132 and 224 detectors simultaneously image astrophysical sources with beam FWHM of 18 and 12 arcsecond at 150 and 260 GHz respectively. The NIKA sensitivities have improved continuously with development and are now reaching state-of-the-art performance at both frequencies (see [11,12,5,6] for more details). NIKA is the prototype of the final camera NIKA2, which will cover a 6.5 arcminute instantaneous field of view with 1000 detectors at 150 GHz and 4000 at 260 GHz. This future camera will also have polarization capabilities at 260 GHz.

3 Sunyaev-Zel'dovich observations with NIKA

3.1 A dedicated tSZ analysis

In order to recover the diffuse tSZ emission, we make use of the dual-band capability of NIKA to separate the atmospheric component and the tSZ one. To do so, we take advantage of their different dependance with the observing frequency ν: the atmospheric noise is roughly proportional to ν^2 while the tSZ signal follows the characteristic spectrum given by

$$\frac{\delta I_{\mathrm{tSZ}}}{I_0} = -y \, \frac{x^4 e^x}{(e^x-1)^2}\left(4 - x\,\coth\left(\frac{x}{2}\right)\right), \tag{1}$$

where $x = \frac{h\nu}{k_B T_{\mathrm{CMB}}}$ is the dimensionless frequency, $y = \frac{\sigma_{\mathrm{T}}}{m_{\mathrm{e}}c^2}\int P_{\mathrm{e}} dl$ is the Compton parameter (that gives the amplitude of the tSZ effect integrating the electronic pressure P_e along the line-of-sigh), T_{CMB} is the CMB temperature. For more details concerning the tSZ mapmaking process, see [1].

3.2 RX J1347.5-1145

The cluster RX J1347.5-1145 was observed in November 2012 as a demonstrator of the tSZ capability of a KID based instrument. The left panel of Fig. 1 shows the map at 140 GHz. In the South-East, a sub-cluster is merging with the main cluster (see for example [14,2] and references therein). This heats the ICM and increases the tSZ signal at about 20 arcsecond on the SE of the X-ray peak. X-ray contours from XMM photon count are displayed on the map and highlight the merger. As X-ray emission is proportional to the density squared and depends weakly on the temperature, we can see the expected tSZ extension on the NIKA map. In order to model the structure of the cluster, we fit a generalized NFW pressure profile model [13] centered on the X-ray peak, excluding the southern shocked area and subtract it from the whole map. The best fit model and the residual are given respectively on the middle and right panel of Fig. 1. Details on the observation and analysis can be found in [1].

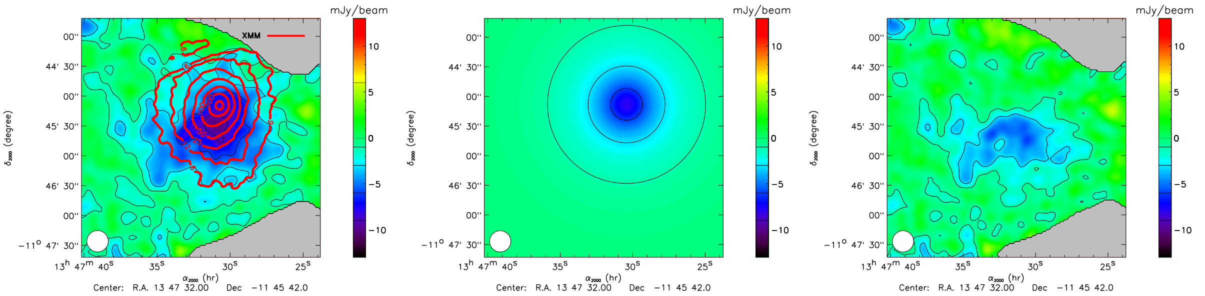

Figure 1 – Left: 140 GHz flux density map of the intermediate redshift cluster ($z = 0.45$) RX J1347.5-1145. A $\sim$ 4 mJy radio source is located within 3 arcseconds of the X-ray center, and has been remove in these maps. XMM X-ray photon counts contours are over-plotted in red. Middle: best fit model map of the northern part of the cluster. Right: residual map highlighting the overpressure caused by the merger on the south-east of RX J1347.5-1145. The maps have been smoothed with an 11 arcsecond gaussian filter.

3.3 Observations of February 2014

The two clusters CL J1226.9+3332 and MACS J0717.5+3745, at $z = 0.89$ and $z = 0.55$ respectively, have been observed during the first NIKA open pool in February 2014. In both cases, we detect the clusters with signal to noise of about 15 at 150 GHz. The two maps present diffuse emission and will be used to study the ICM and the dynamical state of the clusters in a forthcoming paper. Here, we only show their signal to noise maps in Fig. 2.

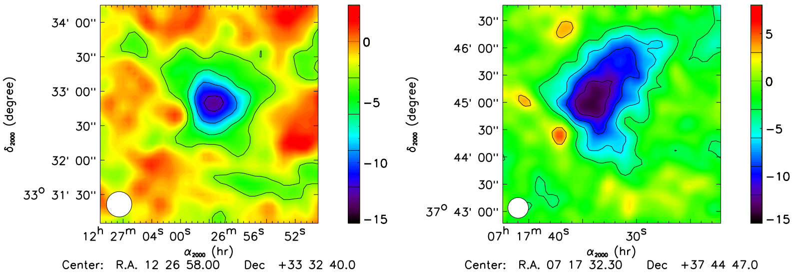

Figure 2 – 150 GHz signal to noise map of CL J1226.9+3332 (left) and MACS J0717.5+3745 (right). The clusters are clearly detected with a peak tSZ decrement reaching a SNR of about 15. The contours are 3, -3, -6, -9 and -12 σ. The maps presents diffuse emission up to more than 1 arcminute radius. The effective beam is shown on the bottom left part of the maps and accounts for the 13 arcsecond gaussian smoothing and the 18 arcsecond native NIKA beam, *i.e.* a total of 22 arcsecond. Note the presence of a foreground galaxy detected on the south-east of MACS J0717.5+3745.

4 Conclusions and perspectives

The use of galaxy clusters as a cosmological probe will require high resolution tSZ observations. The NIKA camera has proved to be an instrument capable of such study with the observation of RX J1347.5-1145 at $z = 0.45$. Using a gNFW pressure profile model of the cluster, we have further characterized the cluster ICM and highlighted the merging of a sub-cluster on its south-east part. We also report observations of the clusters MACS J0717.5+3745 and CL J1226.9+3332 that are respectively a dynamically complex system and a high redshift cluster (z=0.89). The NIKA2 camera is being built and will replace NIKA in 2015. It will push tSZ studies a step further. It will enable the characterization of the tSZ morphology of clusters at both large and small angular scales. NIKA2 will be used to calibrate the tSZ flux as a mass proxy and its evolution with redshift precisely. It will also help to characterize the dynamical state of clusters of galaxies.

Acknowledgments

We would like to thank the IRAM staff for their support during the observations. This work has been partially funded by the Foundation Nanoscience Grenoble, the ANR under the contracts "MKIDS" and "NIKA". This work has been partially supported by the LabEx FOCUS ANR-11-LABX-0013. This work has benefited from the support of the European Research Council Advanced Grant ORISTARS under the European Union's Seventh Framework Programme (Grant Agreement no. 291294). The NIKA dilution cryostat has been designed and built at the Institut Néel. In particular, we acknowledge the crucial contribution of the Cryogenics Group, and in particular Gregory Garde, Henri Rodenas, Jean Paul Leggeri, Philippe Camus. R. A. would like to thank the ENIGMASS French LabEx for funding this work. B. C. acknowledges support from the CNES post-doctoral fellowship program. E. P. acknowledges the support of grant ANR-11-BS56-015. We would like to thank Céline Combet for useful comments.

References

1. R. Adam, B. Comis, J.-F. Macías-Pérez, *et al.* (2013) arXiv:1310.6237
2. S. W. Allen, R. W. Schmidt, & A. C. Fabian, (2002), MNRAS, 335, 256
3. M. Birkinshaw (1999), Phys. Rep., 310, 97
4. O. Bourrion, A. Bideaud, A. Benoit, *et al.* (2011), JINST, 6, P06012
5. M. Calvo, M. Roesch, F.X. Désert, *et al.* (2012), A&A
6. A. Catalano, M. Calvo, N. Ponthieu, *et al.* (2014) arXiv:1402.0260
7. J. E. Carlstrom, P. A. R. Ade, K. A. Aird, *et al.* (2011), PASP, 123, 568
8. P. K. Day, H. G. LeDuc, B. A. Mazin, A. Vayonakis, & J. Zmuidzinas (2003), Nature, 425, 817
9. S. Doyle, P. Mauskopf, & L. Naylon, (2008), J. Low Temp. Phys., 151, 530
10. A. Kosowsky (2003), New A Rev., 47, 939
11. A. Monfardini, L. J. Swenson, A. Bideaud, *et al.* (2010), A&A, 521, A29
12. A. Monfardini, A. Benoit, A. Bideaud, *et al.* (2011), ApJS, 194, 24
13. D. Nagai, A. Vikhlinin, & A. V. Kravtsov (2007), ApJ, 655, 98
14. T. J. Plagge, D. P. Marrone, Z. Abdulla, *et al.* (2013), ApJ, 770, 112
15. Planck Collaboration I (2013) arXiv:1303.5062
16. Planck Collaboration XXIX (2013) arXiv:1303.5089
17. M. Roesch, A. Benoit, A. Bideaud, *et al.* (2012), arXiv:1212.4585
18. R. A. Sunyaev, & Y. B. Zel'dovich (1972), Astrophys. Space Phys. Res., 4, 173
19. R. A. Sunyaev, & Y. B. Zel'dovich (1980), ARA&A, 18, 537

An improved dark matter map from weak and strong lensing in A1689

J.M. Diego
Instituto de Física de Cantabria (CSIC-UC),
39005 Santander, Spain

We present an improved solution for the dark matter distribution on the galaxy cluster Abell 1689 based on a free-form algorithm and a combination of weak and strong lensing data. Our new model is accurate enough to reproduce the multiple systems lensed by this cluster but it also allows us to identify 10 new system candidates bringing the total system candidates for this cluster to 50. We study the variability of the possible solutions and identify a region where the reconstructed dark matter is insensitive to the assumptions made in the reconstruction.

1 Introduction

The galaxy cluster A1689 is probably the best studied gravitational lens. Hubble Space Telescope imaging of the galaxy cluster Abell 1689 has revealed an exceptional number of strongly lensed multiply-imaged galaxies, including high-redshift candidates. Previous studies have used this data to obtain the most detailed dark matter reconstructions of any galaxy cluster to date, based on parametric methods and resolving substructures ∼25 kpc across. A fuller exploration of non-parametric cluster lensing is increasingly motivated by new dedicated deep Hubble imaging surveys, with the aim of examining dark matter structures in the least biased way. Multiple sets of lensed images are now typically identified in deep, high resolution images of any cosmologically distant cluster imaged with Hubble, allowing systematic exploration of the cluster dark matter and discovery of the most distant galaxies [2,4,5,6,7,23,24,25,22]. In practice, secure identification of multiple images need the guidance of a reasonably accurate lens model as even the counter images of large arcs are typically hard to find given the complexities in the central mass distribution of clusters, so that images for a given source are far from symmetrically located.

To date, the galaxy cluster A1689 remains the best studied cosmic lens with hundreds of magnified images in the central region visible in deep Hubble images [2]. Over a hundred of these arcs have been matched to their corresponding background galaxies by several authors and their redshifts estimated [2,15,16,5], including several of the brightest highest redshift galaxies known, extending to $z \simeq 7.6$ [12,13,14,1].

Several studies have used these arcs to reconstruct the mass distribution using the strong lensing data alone [2,9,15,17,5] and in combination with weak lensing (or WL hereafter) measurements [3,16,20] including the use of background red galaxies whose surface density is depleted by lens

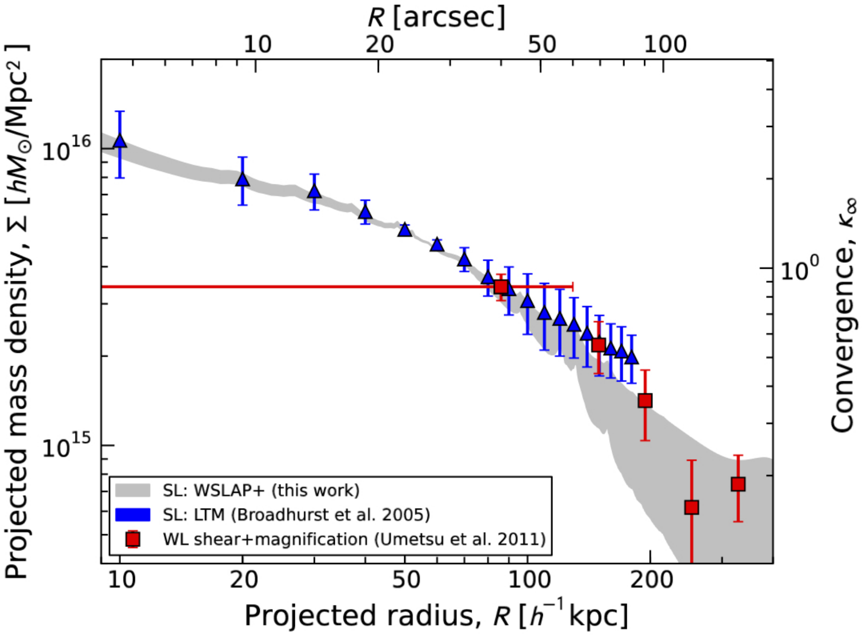

Figure 1 – Comparison of the profiles from our solution (grey region from table 1) with previous results from the literature. **The profile is centered in the type-cD galaxy**.

magnification and independent observationally from weak lensing shear.

In this talk we revisit this cluster to obtain a truly joint solution combining in a single inversion (i.e. not *a posteriori*) the SL and WL data. By doing this, our 2-dimensional model of the mass distribution has to account simultaneously for the multiple lensed systems observed in A1689 and for the **reduced** shear measurements that extend well beyond the Einstein radius. A detailed description of the results of this work can be found in [11]

2 results

We use the improved method, WSLAP+, to combine the weak and strong lensing data and perform the mass reconstruction. The reader can find the details of the method in our previous papers [8,9,10,19]. The unknowns of the lensing problem are in general the surface mass density and the positions of the background sources. As shown in [10], the weak and strong lensing problem can be expressed as a system of linear equations that can be represented in a compact form,

$$\Theta = \Gamma X, \tag{1}$$

where the measured strong and weak lensing observables are contained in the array Θ of dimension $N_\Theta = 2N_{SL} + 2N_{WL}$, the unknown surface mass density and source positions are in the array X of dimension $N_X = N_c + N_g + 2N_s$ and the matrix Γ is known (for a given grid configuration and fiducial galaxy deflection field, see below) and has dimension $N_\Theta \times N_X$. N_{SL} is the number of strong lensing observables (each one contributing with two constraints, x, and y) N_{WL} is the number of weak lensing observables (each one contributing with two constraints, γ_1, and γ_2), N_c is the number of grid points (or cells) that we use to divide the field of view. N_g is the number of deflection fields (from cluster members) that we consider. N_s is the number of background sources (each contributes with two unknowns, β_x, and β_y, see [19] for details). The solution is found after minimizing a quadratic function that estimates the solution of the system of equations 1. For this minimization we use a quadratic algorithm which is optimized for solutions with the constraint that the solution, X, must be positive. This is particularly important since by imposing this constraint we avoid the unphysical situation where the masses associated to the galaxies are negative (that

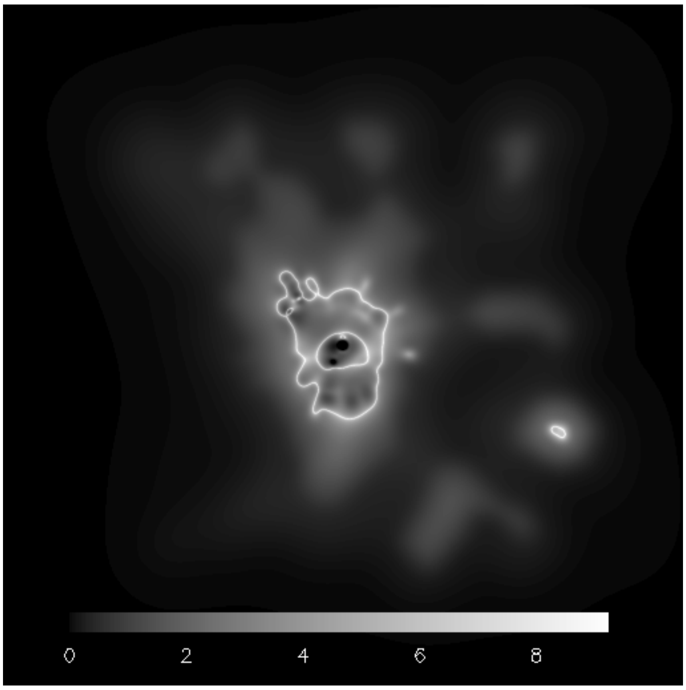

Figure 2 – Magnification map in the entire field of view of 10x10 arcmin^2 for the SL+WL case. The colors are in log-scale to increase contrast. The two small black regions in the centre correspond to magnifications less than 1 (that have been set to 0 in the log-scale for contrast purposes). The drop in the outer region (buffer zone) is a systematic effect due to the larger cell size in the grid. The features close to the phase transition region between the two grid resolutions are not always to be trusted.

could otherwise provide a reasonable solution, from the formal mathematical point of view, to the system of linear equations 1). Imposing the constrain $X > 0$ also helps in regularizing the solution as it avoids large negative and positive contiguous fluctuations.

Earlier work has shown how the addition of the small deflection fields from member galaxies can help improve the mass determination when enough constraints are available In our previous paper [19] we quantified via simulations how the addition of deflections from all the main member galaxies helps improve the mass reconstruction with respect to our previous standard non-parametric method. Strongly lensed galaxies are often locally affected by member galaxies, however, these perturbations cannot be recovered in grid based reconstructions because the lensing information is too sparse to resolve member galaxies. For our study we select the 73 brightest elliptical galaxies in the cluster central region and associate to them a mass according to their luminosity. We assume the fiducial deflection field comprising these member galaxies just scales by a fixed luminosity–mass ratio.

As a data set, we use 26 strongly lensed galaxies and the WL data from [20]. The set of 26 strongly lensed galaxies is a subset of a larger sample but where some of the systems are dubious. The subset of 26 systems is a reliable subset with many of the systems having spectroscopic redshift. We have explored the changes in the derived solution when the set of strongly lensed systems that are feed to the algorithm is changed. We find that the choice of systems has a relatively small impact in the final solution. Details can be found in [11]. The solution is shown in figure 1 where we show the density profiles of the surface mass density in terms of critical density. The critical density, $\Sigma_{crit} = 4.746 \times 10^{15} M_{\odot} h/Mpc^2$, is computed for $z_{mean} = 1.07$. By solving the system of linear equations with different inital conditions we are able to find a range of solutions that we use to determine the mean value and dispersion. Our solution is compared with previously published results of A1689 based on different lensing techniques. In the SL regime, our solution overlaps well with the SL modeling results of [2]. Our results are also in good agreement with the model-independent mass profile of [21] derived from combined WL shear-and-magnification measurements based on the Subaru data. When compared with previous work, we find a good agreement between our solution and other solutions, in terms of the profile and the location and shape of the radial critical curve. Although the tangential critical curve we obtain extends further to the south than previous SL solutions. Figure 2 shows the magnification map from the combined SL and WL data. Some pf the filamentary features in the magnification could be related to real structures in the cluster. After performing an analysis of the significance of the mass structures beyond the critical curves, we find that some of them have a relatively high signal-to-noise ratio suggesting that they may be real. Some of these structures have no obvious counterpart in the galaxy distribution as detailed in [11] that makes them interesting candidates for future studies. We have performed extensive tests to explore the variability of our solutions when some of the assumptions made in the reconstruction are changed. We find that for most of the cases, the solutions remain stable and we identify a circular region inside the tangential critical curve where the solutions are practiaccly insensitive to changes in the assumptions made in the reconstruction. These analysis and their results are detailed in [11]. Additional material, including stamps for all systems used in our analysis as well as the predictions made by our model can be found at our website[a]

Acknowledgments

J.M.D acknowledges support of the consolider project CAD2010-00064 and AYA2012-39475-C02-01 funded by the Ministerio de Economia y Competitividad. JMD also acknowledges the hospitality of the Department of Physics and Astronomy at UPenn during part of this research.

References

1. L.D. Bradley, *et al*, ApJ **678**, 647 (2008)
2. T. Broadhurst, *et al*, ApJ **621**, 53 (2005)
3. T. Broadhurst, M. Takada, K. Umetsu, X. Kong, N. Arimoto, M. Chiba, T. Futamase, ApJ **619**, L143 (2005)
4. D. Clowe *et al*, ApJ **648**, L109 (2006).
5. D. Coe, N. Benitez, T. Broadhurst, L. Moustakas, ApJ **723**, 1678 (2010).
6. D. Coe *et al*, ApJ **757**, 22 (2012).
7. D. Coe *et al*, ApJ **762**, 32 (2013).
8. J.M. Diego, P. Protopapas, H.B. Sandvik, M. Tegmark, MNRAS **360**, 477 (2005)
9. J.M. Diego, P. Protopapas, H.B. Sandvik, M. Tegmark, N. Benitez, T. Broadhurst, MNRAS **362**, 1247 (2005)
10. J.M. Diego, P. Protopapas, H.B. Sandvik, M. Tegmark, MNRAS **375**, 958 (2007)
11. J.M. Diego, T. Broadhurst, N. Benitez, *et al* MNRAS submitted, arXiv:1402.4170, (2014)
12. B. Frye, *et al*, ApJ **568**, 558 (2002).
13. B. Frye *et al*, ApJ **665**, 921 (2007).
14. B. Frye *et al*, ApJ **754**, 17 (2012).
15. A. Halkola, S. Seitz, M. Pannella, MNRAS **372**, 1425 (2006).
16. M. Limousin *et al*, ApJ **668**, 643 (2007).
17. E. Jullo, J.P. Kneib, MNRAS **395**, 1319 (2009).
18. E. Jullo *et al*, Science **329**, 924 (2010).
19. I. Sendra, J.M. Diego, T. Broadhurst, R. Lazkoz, MNRAS **437**, 2642 (2014).
20. K. Umetsu, T. Broadhurst, ApJ **684**, 177 (2008).
21. K. Umetsu, T. Broadhurst, A. Zitrin, E. Medezinski, L.Y. Hsu, ApJ **729**, 127 (2011).
22. X. Zheng *et al*, Nature **489**, 406 (2012).
23. A. Zitrin, T. Broadhurst, Y. Rephaeli, S. Sadeh, ApJ **707**, L102 (2009).
24. A. Zitrin *et al*, MNRAS **408**, 1916 (2010).
25. A. Zitrin, T. Broadhurst, R. Barkana, Y. Rephaeli, N. Benitez, MNRAS **410**, 1939 (2011).

---

[a] http://max.ifca.unican.es/diego/FigsA1689/

CONSTRAINING GALAXY-CLUSTER MASSES WITH JOINT X-RAY AND SZ ANALYSIS OF MULTI-WAVEBAND OBSERVATIONS

M.Olamaie
Astrophysics Group,Cavendish Laboratory, JJ Thomson Avenue
Cambridge CB3 0HE, England

A bayesian framework for the analysis of X-ray and SZ observations of galaxy clusters is presented. The approach of the analysis pipeline is illustrated by using it to analyse a simulated cluster (a JKCS041 like cluster) at $z = 1.8$ as it would be observed by *Chandra* and AMI. The results of the joint analysis show that the model and analysis technique can robustly return the simulated cluster input quantities and constrain the cluster physical parameters.

1 Introduction

Obtaining an unbiased estimate of physical properties of galaxy clusters such as their total and baryonic mass along with their redshifts is key to using clusters to constrain cosmological parameters. This may be achieved by studying clusters in different wave bands as their multi-component nature offers observable signals across the electromagnetic spectrum.

The motivation for our work is to augment the high resolution X-ray and SZ observations of clusters with an analysis pipeline that comprises a cluster model consistent with both numerical simulations and real observations of clusters and a Bayesian statistical method.

2 X-ray and SZ observables

The fundamental sources of X-ray emission in clusters of galaxies include both continuum and line emission processes. The emissivities of these processes are proportional to the square of the electron density.

The observed X-ray surface brightness, $S_{\rm X}$, in a given direction towards a cluster of redshift z is proportional to the line integral of the total emissivity,$\epsilon_{\rm X}$, through the cluster,

$$S_{\rm X} = \frac{1}{4\pi(1+z)^4}\int_{-\infty}^{+\infty} \epsilon_{\rm X}\,{\rm d}l. \tag{1}$$

In general, the photon flux density incident at the telescope is related to the observed photon count rate through an integral equation involving the instrumental response (Davis 2001).

$$C(X_l, Y_m, i) = T_s \int_E dER(E,i) S_{\rm X}(X_l, Y_m, E), \tag{2}$$

where $C(X_l, Y_m, i)$ is the observed photon counts within a pixel (X_l, Y_m) and instrument energy channel i (PI column in the event file), T_s is exposure time for the source and $R(E, i)$ is the instrumental response function. $R(E, i)$ is a continuous function of energy E and a discrete function of channel number i.

Both the X-ray source counts and the background data follow Poisson statistics so that the X-ray likelihood function, $\mathcal{L}_{\rm X}$, is given by

$$\ln(\mathcal{L}_{\rm X}) \;=\; \sum_i \Big\{ C^s_{\rm obs}(i)\ln(C_{\rm pred}(i)) - C_{\rm pred}(i) - \ln\left[(C^s_{\rm obs}(i))!\right] +$$

$$C^b_{\mathrm{obs}}(i)\ln(C^b_{\mathrm{pred}}(i)) - C^b_{\mathrm{pred}}(i) - \ln\left[(C^b_{\mathrm{obs}}(i))!\right]\Big\}, \tag{3}$$

where i runs over all the energy channels at each pixel (X_l, Y_m), $C_{\mathrm{pred}}(i)$ is the total predicted count rates (including source and background components)from the model, $C^b_{\mathrm{pred}}(i)$ is the background predicted rates from a model for the expected background, $C^s_{\mathrm{obs}}(i)$ is the observed source counts detected in energy channel i and $C^b_{\mathrm{obs}}(i)$ is observed background counts.

The observed SZ surface brightness, δI_ν in the direction of electron reservoir is proportional to the dimensionless parameter y, known as Comptonisation parameter,

$$\delta I_\nu \propto y \propto \int_{-\infty}^{+\infty} P_{\mathrm{e}}(r)\mathrm{d}l, \tag{4}$$

where $P_{\mathrm{e}}(r)$ is the ICM pressure. An interferometer like AMI operating at a frequency ν measures samples from the complex visibility plane $\tilde{I}_\nu(\mathbf{u})$. These are given by a weighted Fourier transform of the SZ surface brightness $I_\nu(\mathbf{x})$, namely

$$\tilde{I}_\nu(\mathbf{u}) = \int A_\nu(\mathbf{x}) I_\nu(\mathbf{x}) \exp(2\pi i \mathbf{u}\cdot\mathbf{x})\mathrm{d}\mathbf{x}, \tag{5}$$

where $\mathbf{x}$ is the position relative to the phase centre, $A_\nu(\mathbf{x})$ is the (power) primary beam of the antennas at observing frequency ν (normalised to unity at its peak) and $\mathbf{u}$ is the baseline vector in units of wavelength. We assume a Gaussian distribution for the generalised noise. This component then defines the likelihood function for the data

$$\mathcal{L}_{\mathrm{SZ}} = \frac{1}{Z_N}\exp\left(-\frac{1}{2}\chi^2\right), \tag{6}$$

where χ^2 is the standard statistic quantifying the misfit between the observed data $\boldsymbol{D}$ and the predicted data $\boldsymbol{D}^p$:

$$\chi^2 = \sum_{\nu,\nu'}(\boldsymbol{D}_\nu - \boldsymbol{D}^p_\nu)^T(\boldsymbol{C}_{\nu,\nu'})^{-1}(\boldsymbol{D}_{\nu'} - \boldsymbol{D}^p_{\nu'}), \tag{7}$$

where ν and ν' are channel frequencies. $\boldsymbol{C}$ is the generalised noise covariance matrix and Z_N is a normalisation factor. The joint likelihood of X-ray and SZ data is then given by

$$\mathcal{L} = \mathcal{L}_{\mathrm{X}} \times \mathcal{L}_{\mathrm{SZ}}. \tag{8}$$

3 Modelling X-ray and SZ signals

We use the model described in Olamaie et al. (2012) and (2013) to determine a map of S_{X} and y parameter.

The model assumes that the dark matter density follows a NFW profile (Navarro et al. 1996, 1997) and the plasma pressure is described by the GNFW profile (Nagai et al. 2007),

$$\rho_{\mathrm{DM}}(r) = \frac{\rho_{\mathrm{s}}}{\left(\frac{r}{R_{\mathrm{s}}}\right)\left(1+\frac{r}{R_{\mathrm{s}}}\right)^2}, \tag{9}$$

$$P_{\mathrm{e}}(r) = \frac{P_{\mathrm{ei}}}{\left(\frac{r}{r_{\mathrm{p}}}\right)^c\left(1+\left(\frac{r}{r_{\mathrm{p}}}\right)^a\right)^{(b-c)/a}}, \tag{10}$$

To calculate the halo concentration parameter, c_{200} we use the relation derived by Neto et al. (2007) from N-body simulations, namely

$$c_{200} = \frac{5.26}{1+z}\left(\frac{M_{\mathrm{tot}}(r_{200})}{10^{14}h^{-1}\mathrm{M}_\odot}\right)^{-0.1}. \tag{11}$$

The cluster model parameters ρ_{s}, R_{s} and P_{ei} are derived under the following assumptions: spherical symmetry; hydrostatic equilibrium; and that the local gas fraction is much less than unity (equations (3) to (11) in (Olamaie et al. 2012).

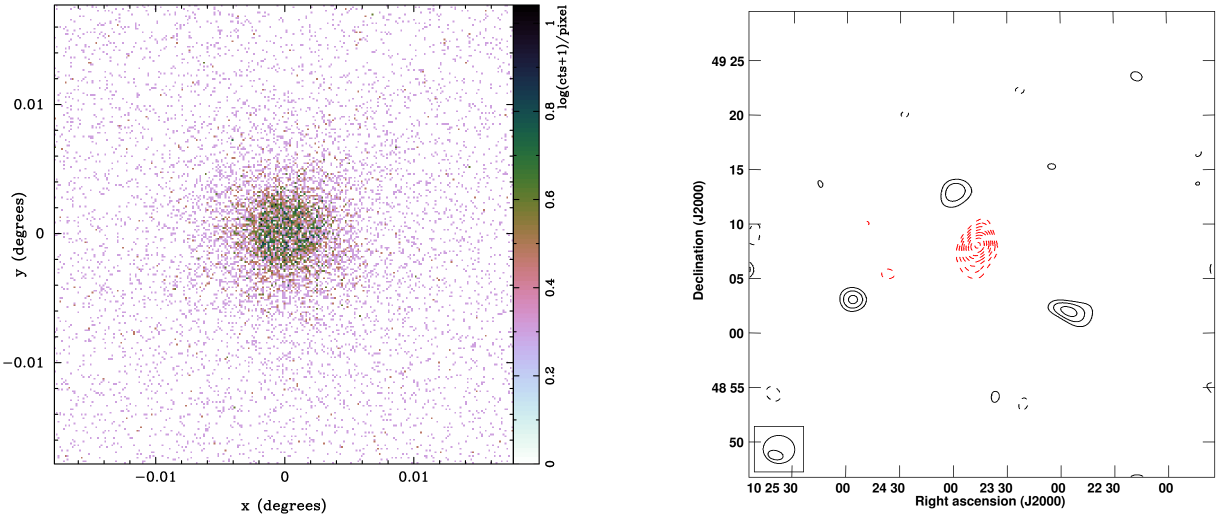

Figure 1 – *left*: Simulated *Chandra* map (on a logarithmic colour scale) and *right*: AMI SZ map of the cluster at $z = 1.8$

Our sampling parameter space comprises of $\mathbf{\Theta}_\mathrm{c} \equiv (x_0, y_0, M_\mathrm{T}(r_{200}), f_\mathrm{g}(r_{200}), z, c_{500}, a, b, c)$, where x_0 and y_0 are cluster projected position on the sky. We further assume that the priors on sampling parameters are separable (Feroz et al. 2009) such that

$$\begin{aligned}\pi(\mathbf{\Theta}_\mathrm{c}) &= \pi(x_0)\,\pi(y_0)\,\pi(M_\mathrm{T}(r_{200}))\pi(f_\mathrm{g}(r_{200}))\pi(z)\,\times \\ &\quad \pi(c_{500})\pi(a)\,\pi(b)\,\pi(c). \end{aligned} \tag{12}$$

4 Bayesian joint analysis of X-ray and SZ clusters

Our Bayesian inference tool, for the analysis of X-ray observations of galaxy clusters is called Bayes-X. The Bayes-X software which is implemented in Fortran 90 is available at http://www.mrao.cam.ac.uk/facilities/software/bayesx/ and its full description is given in Olamaie et al. (2013).

Bayes-X uses nested sampler MultiNest (Feroz & Hobson 2008; Feroz et al. 2009) to explore the parameter space. It also uses MEKAL model (Mewe et al. 1995) to calculate the emission rate and considers the photoelectric absorption of X-rays en-route to us. It allows for both stochastic instrument response via a photon redistribution matrix and the effective area of the telescope and allows for modelling of the background. It calculates the likelihood assuming a Poissonian distribution for both the photon and background counts. It then determines profiles of the ICM properties and the cluster mass.

Our SZ analysis pipeline, McAdam, (see e.g. Feroz et al. 2009 and AMI Consortium: Olamaie et al. 2012) also uses MultiNest to explore the parameter space and calculates the likelihood using equation 6.

We perform a joint X-ray and SZ analysis using simulated data in order to investigate the capability of the data, our model and the analysis to return the simulated cluster quantities and clearly reveal structure of degeneracies in the cluster parameter space. We generate an X-ray and SZ simulated cluster data as it would be observed by both *Chandra* and AMI. The simulated cluster is at $z = 1.8$ and has the same properties as JKCS041 cluster. Fig. 1 shows the X-ray and SZ maps of the cluster. Fig. 2 shows 1-D marginalised posterior distributions of both sampling and derived parameters of simulated cluster data. The green solid lines on the 1-D posterior distributions of the parameters show the input values used to generate the simulated cluster and magneta dashed lines show the mean of the distributions.

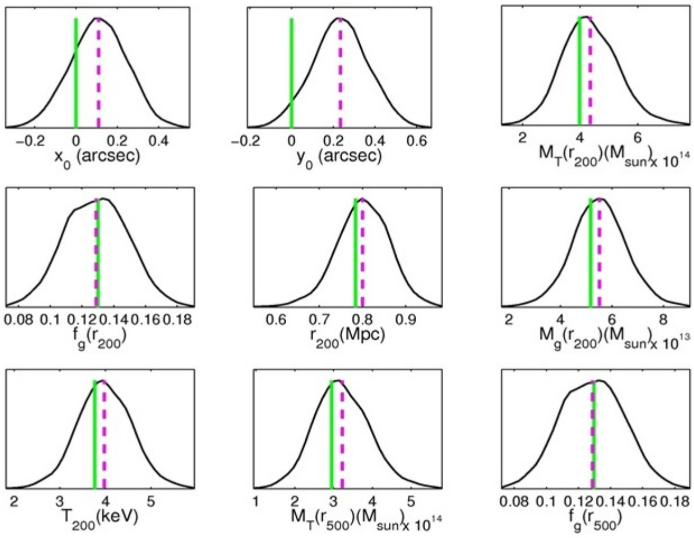

Figure 2 – 1-D marginalised posterior distributions of sampling and derived parameters of joint X-ray and SZ analysis of the simulated cluster at redshift $z = 1.8$. The vertical green solid lines show the input values used to generate the simulated cluster and the dashed magenta lines are the mean values of the distributions.

5 conclusion

We have demonstrated that our analysis pipeline faithfully recovers the input values of the model parameters used in the simulations and can constrain clusters positions on the sky and clusters physical parameters including $M_{\rm g}$, $T_{\rm g}$ and $M_{\rm T}$.

We find that we can still constrain $f_{\rm g}$ as well as other cluster parameters even when we assume a wide uniform prior on $f_{\rm g}(r_{200})$.

We find that the results of the analyses do not depend on the choice of prior probability distributions on the sampling parameters.

We therefore conclude that our analysis pipeline is robust and can be used in future multi-wavelength analysis of clusters of galaxies.

Acknowledgments

The author acknowledges a Research Fellowship from Sidney Sussex College, Cambridge, UK.

References

AMI Consortium: Olamaie et al. 2012. MNRAS, 421,1136
Davis J.E.,2001,APJ,548,1010
Feroz F., Hobson M.P.,2008, MNRAS,384,449
Feroz F.,et al. , 2009, MNRAS,398,1601
Feroz F., et al., 2009, MNRAS,398,2049
Mewe R., et al., 1995,Legacy6,16
Nagai D., et al., 2007, ApJ,668,1
Navarro J.F., et al., 1996, ApJ,462,563
Navarro J.F., et al., 1997, ApJ,490,493
Neto A.F., et al., 2007,MNRAS, 381,1450
Olamaie M., et al., 2012, MNRAS, 423,1534
Olamaie M., et al., 2013, MNRAS, 430, 1344

3.
Dark Energy

An overview of the completed Canada-France-Hawaii Telescope Lensing Survey (CFHTLenS)

H. Hildebrandt on behalf of the CFHTLenS collaboration
Argelander-Institut für Astronomie, Universität Bonn, Auf dem Hügel 71, 53121 Bonn, Germany

The Canada-France-Hawaii Telescope Legacy Survey (CFHTLS) represents the most powerful weak lensing survey carried out to date. The CFHTLenS (Canada-France-Hawaii Telescope Lensing Survey) team was formed in 2008 to analyse the data from the CFHTLS focussing on a rigorous treatment of systematic effects in shape measurements and photometric redshifts. Here we review the technical challenges that we faced in analysing these data and their solutions which set the current standard for weak lensing analyses. We also present some science highlights that were made possible by this effort including cosmic shear tomography, tests for modified gravity models, and the mapping of dark matter structures over unprecedentedly large scales. An outlook is given on current and future surveys that are analysed with the tools prepared for CFHTLenS. **CFHTLenS represents the first and only weak lensing data set that has been made publicly available so far.** We encourage other surveys to follow this example.

1 Introduction

The first observations of cosmic shear [1, 2, 3] opened up a new window to study cosmology. Measuring the build up of the large scale distribution of dark matter structures over cosmic time with cosmic shear tomography represents a very powerful cosmological tool that ideally complements the high-redshift observations of the cosmic microwave background (CMB) with observations at low-redshift. Large volumes have to be surveyed to yield cosmologically meaningful results, and the three-dimensional distribution of structures has to be resolved for the tightest cosmological constraints. These requirements naturally lead to the design of deep multi-band imaging surveys over large areas of the sky with the data being taken under the best possible seeing conditions. The multi-band data are important for estimating photometric redshifts of millions of background galaxies that are used for the lensing measurement whereas the high-resolution is crucial for measuring accurate ellipticities for the same objects.

The Canada-France-Hawaii Telescope Legacy Survey (CFHTLS) is the most ambitious project with such a focus that has been completed so far. Here we describe the work of the CFHTLenS (Canada-France-Hawaii Telescope Lensing Survey) team that was formed to analyse the data from the CFHTLS focussing on a rigorous treatment of the main sources of systematic errors in such an analysis. In Sect. 2 we describe the CHFTLS data set and in Sect. 3 we illustrate some of the technical challenges that we were faced with analysing those data. Section 4 presents a few highlights from the scientific papers that were made possible by the unprecedented quality of the CFHTLenS data products. In Sect. 5 we give an outlook and report on some projects that are currently carried out with the tools developed for CFHTLenS.

2 The CFHTLS

CFHTLenS is based on the Wide part of the CFHTLS, an imaging survey carried out with the MegaCam instrument mounted at the CFHT. It consists of 171 pointings of this 1 square degree camera, which are arranged in four different contiguous patches to allow observations all year. All patches are located at high-galactic latitude and three of them are close to the equator whereas one is at higher declination. All pointings have been observed in the *ugriz*-bands to a 5σ depth of 25.2, 25.6, 24.9, 24.6, and 23.5, respectively. The best seeing time is reserved for the *i*-band data so that the data from this band with a median seeing of $0\farcs7$ are ideally suited for weak lensing shape measurements.

3 Data analysis

3.1 The CFHTLenS team

The CFHTLenS team was formed to re-analyse the CFHTLS data with the goal of understanding all systematic effects that affect cosmic shear science to a level that is better than the statistical precision of this data set. To reach this goal we apply and further develop the most advanced shape measurement and photometric redshift (photo-z) algorithms. The team originally consisted of members from different European countries and Canada which had been working together on the STEP shape measurement challenge [4] and other projects.

3.2 Data reduction

All MegaCam data are pre-reduced at the Canadian Astronomical Data Centre (CADC). We are using these pre-reduced individual exposures as the basis for our data reduction. Subsequent reduction steps are carried out with the THELI wide-field imaging reduction pipeline [5, 6]. These include astrometric and photometric calibration, stacking, masking, and creation of weight and flag images. Details can be found in [7]. While the deep stacks are used for the extraction of multi-colour photometry we measure galaxy shapes from individual exposures to avoid a number of systematic effects that are created by the stacking procedure.

3.3 Photometry and photo-z

The point spread function (PSF) is typically different in the different bands of a pointing. In order to extract accurate colours for all objects this has to be accounted for. We convolve the five images (i.e. the *ugriz* stacks) of one pointing so that the PSF in all bands is Gaussian and has the same size. This is done with the shapelet-based code described in [8].

The photometry is then extracted from these Gaussianised stacks with SExtractor [9] in dual-image mode. The unconvolved *i*-band image is used for detection. This procedure yields unbiased colours with close to optimal signal to noise ratio (S/N).

Photometric redshifts are then estimated with the BPZ photo-z code [10] and the results are compared to different spectroscopic redshift catalogues that are overlapping with the CFHTLS footprint. Details of the multi-colour photometry and photo-z methods can be found in [11].

3.4 Shape measurement

A particular focus within CFHTLenS is given to shape measurements [12] since this area had been identified as being affected by different systematic effects. In particular redshift dependent systematics [a] are harmful for cosmic shear tomography, one of the main science drivers for CFHTLenS. While we started with a number of different shape measurement techniques we quickly concentrated on the Bayesian *lens*fit algorithm [13, 14] that showed the most promise to meet our requirements.

*Lens*Fit is a Bayesian forward fitting shape measurement code that employs a suite of analytical galaxy light profiles convolved with the measured PSF to fit the data. The resulting multidimensional likelihoods are then multiplied with empirical prior distributions for galaxy size, ellipticity, and bulge to disk ratio to yield a posterior probability distribution. Marginalising over all uninteresting parameters then yields an unbiased estimate of the ellipticity of each galaxy. Furthermore, a weight is calculated that parametrises the error of the ellipticity measurement and can readily be used in shear measurements to properly weigh background sources.

As mentioned above *lens*fit is run on the individual, astrometrically-calibrated exposures. Results from different exposures of one field (typically 7 per field) are combined in a statistically optimal way. Working on individual exposures instead of stacks has the advantage that different PSFs are not mixed. Besides that, it also avoids the correlation of noise that is an inevitable result of sub-pixel stacking.

3.5 Tests for shape systematic

An important aspect of the work of the CFHTLenS team is the development of cosmology-independent systematic tests to check the robustness of the shear catalogue.

The most important tool to identify residual effects from an imperfect PSF correction is the star-galaxy cross-correlation function [15]. Here, the shapes of the corrected galaxies are cross-correlated with the shapes of the uncorrected stars that were used to measure the PSF. Naively one could assume that a signal significantly different from zero would indicate the presence of residual systematics. However, not only shot noise contributes here, and the significance has to be estimated taking into account a signal that can be created by cosmic shear itself [see 15, for details]. This means that the amplitude of the star-galaxy cross-correlation function has to be compared to results from detailed simulations with - by construction - perfect PSF correction. We find that the amplitude of the star-galaxy cross-correlation function for all fields is considerably higher than the one found in the simulations. However, this undesired signal is dominated by a few fields that seem to have larger systematic errors than others. Rejecting $\sim 25\%$ of the fields with the strongest star-galaxy cross-correlation leads to a star-galaxy cross-correlation function amplitude consistent with simulations.

We also run *lens*fit on detailed image simulations that are carefully matched to the data in terms of the distributions in ellipticity, S/N, size, and bulge to disk ratio [12]. This is done to test the output ellipticities e_1 and e_2 against the known input ellipticities as functions of S/N and size (both of which can be relatively easily be measured from the data itself). This reveals some residual multiplicative biases that we correct for on a object-by-object basis in the data. Note that this kind of bias is expected in noisy measurements and can not be completely avoided.

The image simulations do not reveal any additive bias. However, averaging the e_2 ellipticity component for all CFHTLenS data reveals some residual bias that is significantly different from zero. We characterise this bias as a function of size and S/N and subtract it from the measured e_2 [15].

The combination of rejecting fields with bad PSF (identified by their anomalously high star-galaxy cross-correlation) and the correction of all residual biases with image simulations and directly from the data yields a state of the art shear catalogue that is free from systematic errors to the level required by the size of the CFHTLS.

---

[a] Those can originate from flux/size dependent systematics and the correlation between redshift and flux/size.

4 Science highlights

4.1 Cosmic shear

One of the main science drivers of CFHTLenS is cosmic shear tomography. Measuring the statistical properties of the large scale structure of the dark matter density field over cosmic time has become one of the most promising cosmological tools. This cosmological probe is studied in great detail in a number of CFHTLenS publications [16, 17, 18, 19, 20].

A pure 2D cosmic shear analysis is presented in [16] where the individual redshifts of the sources are not taken into account and the colour information are purely used to constrain the redshift distribution. In this paper we explore different ways of measuring the signal from small, non-linear scales out to large radii ($\gtrsim 2^\circ$). It is shown how such measurements yield tight constraints on the total cosmic matter density, Ω_m, the amplitude of the fluctuations of the matter power spectrum, σ_8, and the curvature, Ω_K. These constraints are complementary to constraints from the CMB and improve on what has been found in the seven-year data set of the WMAP satellite [21]. An extension of this 2D cosmic shear measurement to third-order statistics can be found in [20]. It is shown that these higher-order statistics add some statistical power to the cosmic shear result at the expense of more complicated systematic errors.

For tomographic cosmic shear we split up the source sample into different redshift bins. A basic tomography study with two broad redshift bins and concentrating on the systematic robustness of the photo-z is presented in [17]. A much more detailed cosmic shear tomography measurement is presented in [18]. There we split up the source sample into six narrower redshift bins and measure all 21 possible shear cross- and auto-correlation functions. In this study we also correct for the major astrophysical systematic associated with cosmic shear measurements: intrinsic alignments of galaxy ellipticities, which are especially important at low redshift. The inclusion of redshift information yields tighter constraints on the cosmological parameters discussed above and allows for testing the dark energy equation of state, w. Assuming flatness and combining our results with different external data sets we constrain this crucially important cosmological parameter to $w = -1.02 \pm 0.09$.

Instead of binning galaxies in discrete photo-z bins one can also use the redshift information for each galaxy individually. This is known as 3D cosmic shear and an application to CFHTLenS is presented in [19]. Taking into account the full redshift probability distribution of each object that is provided by the photo-z code we can suppress non-linear scales much more rigorously. This is advantageous because it means that we can compare our measurements to theory in a regime where cosmic structure formation is better understood than on the small scales where baryonic effects and non-linear evolution play a great role. Hence, the uncertainty of the models is considerably reduced. It is clear that precision suffers if the small scales with high S/N are neglected. However, this is not a problem of 3D cosmic shear itself (it could easily be used on smaller scales) but rather stresses the importance of better modelling these small-scale effects for future dark energy mission which will have considerably greater statistical power.

4.2 Modified gravity

One of the most interesting aspects of cosmic shear tomography is that it is sensitive to both measurable effects of dark energy, the influence dark energy has on the geometry of the Universe as well as on the growth of the large scale structure. It is the combination of these two different aspects that has the potential to reveal deviations from general relativity and test alternative theories of gravity. This becomes even more powerful when cosmic shear is combined with a tracer of non-relativistic physics. In [22] we use redshift-space distortions (RSD) from the WiggleZ dark energy survey [23] and 6dFGS [24] for that purpose. Combining these RSD measurements with the 2-bin cosmic shear tomography results from [17] we obtain constraints on several parametrisations of modified gravity models. All our constraints are compatible with general relativity excluding large parts of the parameter space for possible deviations. This study illustrates the power of this combination to potentially falsify one of the pillars of our physical world model, and such measurements are the basis for very large projects that are starting just now (e.g. 2dFLens).

4.3 Dark matter maps

The large contiguous patches of CFHTLenS and the high-quality data resulting in high number densities of lensing sources represent ideal conditions for mapping the dark matter distribution directly. This creation of mass maps and their scientific exploitation is described in [25]. The value of these maps goes beyond the mere visualisation of dark matter structures. Maps are especially useful to study higher-order statistics and the relationship between luminous and dark matter [see also 25]. The CFHTLenS dark matter maps are the largest created so far and reveal giant voids on scales of several degrees that were undetectable with previous surveys. Furthermore, the maps offer the exciting opportunity to cross-correlate the dark matter structures to signals extracted from very different experiments [for an example see 26].

5 Summary and outlook

The work of the CFHTLenS team represents the next crucial step in controlling systematic effects in state of the art weak gravitational lensing surveys. The analysis tools developed in the course of the project go a long way beyond what has been used in the past and form the basis for current and upcoming Stage III and IV weak lensing projects that are 1-2 orders of magnitude larger than CFHTLS and require much tighter control of systematic errors.

In certain areas (dark energy equation of state, modified gravity parameters, dark matter mapping) the data analyses from CFHTLenS yield competitive or even unprecedented results showing the full potential of weak lensing as a cosmological tool. The scientific relevance of CFHTLenS goes beyond pure cosmological results, and the data have been used by the CFHTLenS team for studies of galaxy evolution [27, 28, 29] as well as galaxy group and cluster science [30, 31, 32].

The CFHTLenS data are publicly available at `http://www.cfhtlens.org` as well as at `http://www.cadc-ccda.hia-iha.nrc-cnrc.gc.ca/community/CFHTLens/query.html`

We provide calibrated images, photometry and shear catalogues, masks, random catalogues matching the geometry of the data, cosmological data vectors for several of the measurements discussed here, covariance matrices, and redshift distributions. The data have been downloaded by a large number of different researchers (as evidenced by the number of unique IP addresses), and a growing number of external papers using CFHTLenS data are coming out. **It should be noted that CFHTLenS is the only weak lensing data set that has been released publicly so far.** We strongly encourage the community to follow our example and support the credibility of weak lensing as a cosmological tool in general and our understanding and treatment of systematic effects in particular through open access of weak lensing data.

The suite of tools developed within CFHTLenS is currently being applied to a number of similar surveys. CFHTLenS members are strongly involved in the European Kilo Degree Survey [KiDS 33] as well as in a re-analysis of the data from the Red Sequence Cluster Survey 2 data (this project is dubbed RCSLens[b]). Combined with similar data analysis on smaller projects like CS82 (CFHT Stripe 82 Survey), NGVS [34, The Next Generation Virgo Survey], and CODEX (weak lensing calibration to Constrain Dark Energy with X-ray clusters) this will yield a state of the art lensing data set of $\sim 3000\text{deg}^2$ in the near future rivalling a project like the Dark Energy Survey in area and surpassing it in image quality. We feel committed to make also these data publicly available once the main science analyses by the teams are done.

References

[1] D. J. Bacon, A. R. Refregier, and R. S. Ellis. Detection of weak gravitational lensing by large-scale structure. *MNRAS*, 318:625–640, October 2000.

[2] L. Van Waerbeke, Y. Mellier, T. Erben, J. C. Cuillandre, F. Bernardeau, R. Maoli, E. Bertin, H. J. McCracken, O. Le Fèvre, B. Fort, M. Dantel-Fort, B. Jain, and P. Schneider. Detection

---

[b] `http://www.rcslens.org`

of correlated galaxy ellipticities from CFHT data: first evidence for gravitational lensing by large-scale structures. *A&A*, 358:30–44, June 2000.

[3] D. M. Wittman, J. A. Tyson, D. Kirkman, I. Dell'Antonio, and G. Bernstein. Detection of weak gravitational lensing distortions of distant galaxies by cosmic dark matter at large scales. *Nature*, 405:143–148, May 2000.

[4] C. Heymans, L. Van Waerbeke, D. Bacon, J. Berge, G. Bernstein, E. Bertin, S. Bridle, M. L. Brown, D. Clowe, H. Dahle, T. Erben, M. Gray, M. Hetterscheidt, H. Hoekstra, P. Hudelot, M. Jarvis, K. Kuijken, V. Margoniner, R. Massey, Y. Mellier, R. Nakajima, A. Refregier, J. Rhodes, T. Schrabback, and D. Wittman. The Shear Testing Programme - I. Weak lensing analysis of simulated ground-based observations. *MNRAS*, 368:1323–1339, May 2006.

[5] M. Schirmer, T. Erben, P. Schneider, G. Pietrzynski, W. Gieren, S. Carpano, A. Micol, and F. Pierfederici. GaBoDS: The Garching-Bonn Deep Survey. I. Anatomy of galaxy clusters in the background of NGC 300. *A&A*, 407:869–888, September 2003.

[6] T. Erben, M. Schirmer, J. P. Dietrich, O. Cordes, L. Haberzettl, M. Hetterscheidt, H. Hildebrandt, O. Schmithuesen, P. Schneider, P. Simon, E. Deul, R. N. Hook, N. Kaiser, M. Radovich, C. Benoist, M. Nonino, L. F. Olsen, I. Prandoni, R. Wichmann, S. Zaggia, D. Bomans, R. J. Dettmar, and J. M. Miralles. GaBoDS: The Garching-Bonn Deep Survey. IV. Methods for the image reduction of multi-chip cameras demonstrated on data from the ESO Wide-Field Imager. *Astronomische Nachrichten*, 326:432–464, July 2005.

[7] T. Erben, H. Hildebrandt, L. Miller, L. van Waerbeke, C. Heymans, H. Hoekstra, T. D. Kitching, Y. Mellier, J. Benjamin, C. Blake, C. Bonnett, O. Cordes, J. Coupon, L. Fu, R. Gavazzi, B. Gillis, E. Grocutt, S. D. J. Gwyn, K. Holhjem, M. J. Hudson, M. Kilbinger, K. Kuijken, M. Milkeraitis, B. T. P. Rowe, T. Schrabback, E. Semboloni, P. Simon, M. Smit, O. Toader, S. Vafaei, E. van Uitert, and M. Velander. CFHTLenS: the Canada-France-Hawaii Telescope Lensing Survey - imaging data and catalogue products. *MNRAS*, 433:2545–2563, August 2013.

[8] K. Kuijken. GaaP: PSF- and aperture-matched photometry using shapelets. *A&A*, 482:1053–1067, May 2008.

[9] E. Bertin and S. Arnouts. SExtractor: Software for source extraction. *A&AS*, 117:393–404, June 1996.

[10] N. Benítez. Bayesian Photometric Redshift Estimation. *ApJ*, 536:571–583, June 2000.

[11] H. Hildebrandt, T. Erben, K. Kuijken, L. van Waerbeke, C. Heymans, J. Coupon, J. Benjamin, C. Bonnett, L. Fu, H. Hoekstra, T. D. Kitching, Y. Mellier, L. Miller, M. Velander, M. J. Hudson, B. T. P. Rowe, T. Schrabback, E. Semboloni, and N. Benítez. CFHTLenS: improving the quality of photometric redshifts with precision photometry. *MNRAS*, 421:2355–2367, April 2012.

[12] L. Miller, C. Heymans, T. D. Kitching, L. van Waerbeke, T. Erben, H. Hildebrandt, H. Hoekstra, Y. Mellier, B. T. P. Rowe, J. Coupon, J. P. Dietrich, L. Fu, J. Harnois-Déraps, M. J. Hudson, M. Kilbinger, K. Kuijken, T. Schrabback, E. Semboloni, S. Vafaei, and M. Velander. Bayesian galaxy shape measurement for weak lensing surveys - III. Application to the Canada-France-Hawaii Telescope Lensing Survey. *MNRAS*, 429:2858–2880, March 2013.

[13] L. Miller, T. D. Kitching, C. Heymans, A. F. Heavens, and L. van Waerbeke. Bayesian galaxy shape measurement for weak lensing surveys - I. Methodology and a fast-fitting algorithm. *MNRAS*, 382:315–324, November 2007.

[14] T. D. Kitching, L. Miller, C. E. Heymans, L. van Waerbeke, and A. F. Heavens. Bayesian galaxy shape measurement for weak lensing surveys - II. Application to simulations. *MNRAS*, 390:149–167, October 2008.

[15] C. Heymans, L. Van Waerbeke, L. Miller, T. Erben, H. Hildebrandt, H. Hoekstra, T. D. Kitching, Y. Mellier, P. Simon, C. Bonnett, J. Coupon, L. Fu, J. Harnois Déraps, M. J. Hudson, M. Kilbinger, K. Kuijken, B. Rowe, T. Schrabback, E. Semboloni, E. van Uitert, S. Vafaei, and M. Velander. CFHTLenS: the Canada-France-Hawaii Telescope Lensing Survey. *MNRAS*, 427:146–166, November 2012.

[16] M. Kilbinger, L. Fu, C. Heymans, F. Simpson, J. Benjamin, T. Erben, J. Harnois-Déraps, H. Hoekstra, H. Hildebrandt, T. D. Kitching, Y. Mellier, L. Miller, L. Van Waerbeke, K. Benabed, C. Bonnett, J. Coupon, M. J. Hudson, K. Kuijken, B. Rowe, T. Schrabback, E. Semboloni, S. Vafaei, and M. Velander. CFHTLenS: combined probe cosmological model comparison using 2D weak gravitational lensing. *MNRAS*, 430:2200–2220, April 2013.

[17] J. Benjamin, L. Van Waerbeke, C. Heymans, M. Kilbinger, T. Erben, H. Hildebrandt, H. Hoekstra, T. D. Kitching, Y. Mellier, L. Miller, B. Rowe, T. Schrabback, F. Simpson, J. Coupon, L. Fu, J. Harnois-Déraps, M. J. Hudson, K. Kuijken, E. Semboloni, S. Vafaei, and M. Velander. CFHTLenS tomographic weak lensing: quantifying accurate redshift distributions. *MNRAS*, 431:1547–1564, May 2013.

[18] C. Heymans, E. Grocutt, A. Heavens, M. Kilbinger, T. D. Kitching, F. Simpson, J. Benjamin, T. Erben, H. Hildebrandt, H. Hoekstra, Y. Mellier, L. Miller, L. Van Waerbeke, M. L. Brown, J. Coupon, L. Fu, J. Harnois-Déraps, M. J. Hudson, K. Kuijken, B. Rowe, T. Schrabback, E. Semboloni, S. Vafaei, and M. Velander. CFHTLenS tomographic weak lensing cosmological parameter constraints: Mitigating the impact of intrinsic galaxy alignments. *MNRAS*, 432:2433–2453, July 2013.

[19] T. D. Kitching, A. F. Heavens, J. Alsing, T. Erben, C. Heymans, H. Hildebrandt, H. Hoekstra, A. Jaffe, A. Kiessling, Y. Mellier, L. Miller, L. van Waerbeke, J. Benjamin, J. Coupon, L. Fu, M. J. Hudson, M. Kilbinger, K. Kuijken, B. T. P. Rowe, T. Schrabback, E. Semboloni, and M. Velander. 3D Cosmic Shear: Cosmology from CFHTLenS. *ArXiv e-prints*, January 2014.

[20] L. Fu, M. Kilbinger, T. Erben, C. Heymans, H. Hildebrandt, H. Hoekstra, T. D. Kitching, Y. Mellier, L. Miller, E. Semboloni, P. Simon, L. Van Waerbeke, J. Coupon, J. Harnois-Déraps, M. J. Hudson, K. Kuijken, B. Rowe, T. Schrabback, S. Vafaei, and M. Velander. CFHTLenS: Cosmological constraints from a combination of cosmic shear two-point and three-point correlations. *ArXiv e-prints*, April 2014.

[21] E. Komatsu, K. M. Smith, J. Dunkley, C. L. Bennett, B. Gold, G. Hinshaw, N. Jarosik, D. Larson, M. R. Nolta, L. Page, D. N. Spergel, M. Halpern, R. S. Hill, A. Kogut, M. Limon, S. S. Meyer, N. Odegard, G. S. Tucker, J. L. Weiland, E. Wollack, and E. L. Wright. Seven-year Wilkinson Microwave Anisotropy Probe (WMAP) Observations: Cosmological Interpretation. *ApJS*, 192:18, February 2011.

[22] F. Simpson, C. Heymans, D. Parkinson, C. Blake, M. Kilbinger, J. Benjamin, T. Erben, H. Hildebrandt, H. Hoekstra, T. D. Kitching, Y. Mellier, L. Miller, L. Van Waerbeke, J. Coupon, L. Fu, J. Harnois-Déraps, M. J. Hudson, K. Kuijken, B. Rowe, T. Schrabback, E. Semboloni, S. Vafaei, and M. Velander. CFHTLenS: testing the laws of gravity with tomographic weak lensing and redshift-space distortions. *MNRAS*, 429:2249–2263, March 2013.

[23] M. J. Drinkwater, R. J. Jurek, C. Blake, D. Woods, K. A. Pimbblet, K. Glazebrook, R. Sharp, M. B. Pracy, S. Brough, M. Colless, W. J. Couch, S. M. Croom, T. M. Davis, D. Forbes, K. Forster, D. G. Gilbank, M. Gladders, B. Jelliffe, N. Jones, I.-H. Li, B. Madore, D. C. Martin, G. B. Poole, T. Small, E. Wisnioski, T. Wyder, and H. K. C. Yee. The WiggleZ Dark Energy Survey: survey design and first data release. *MNRAS*, 401:1429–1452, January 2010.

[24] D. H. Jones, M. A. Read, W. Saunders, M. Colless, T. Jarrett, Q. A. Parker, A. P. Fairall, T. Mauch, E. M. Sadler, F. G. Watson, D. Burton, L. A. Campbell, P. Cass, S. M. Croom,

J. Dawe, K. Fiegert, L. Frankcombe, M. Hartley, J. Huchra, D. James, E. Kirby, O. Lahav, J. Lucey, G. A. Mamon, L. Moore, B. A. Peterson, S. Prior, D. Proust, K. Russell, V. Safouris, K.-I. Wakamatsu, E. Westra, and M. Williams. The 6dF Galaxy Survey: final redshift release (DR3) and southern large-scale structures. *MNRAS*, 399:683–698, October 2009.

[25] L. Van Waerbeke, J. Benjamin, T. Erben, C. Heymans, H. Hildebrandt, H. Hoekstra, T. D. Kitching, Y. Mellier, L. Miller, J. Coupon, J. Harnois-Déraps, L. Fu, M. Hudson, M. Kilbinger, K. Kuijken, B. Rowe, T. Schrabback, E. Semboloni, S. Vafaei, E. van Uitert, and M. Velander. CFHTLenS: mapping the large-scale structure with gravitational lensing. *MNRAS*, 433:3373–3388, August 2013.

[26] L. Van Waerbeke, G. Hinshaw, and N. Murray. Detection of warm and diffuse baryons in large scale structure from the cross correlation of gravitational lensing and the thermal Sunyaev-Zeldovich effect. *Phys. Rev. D*, 89(2):023508, January 2014.

[27] P. Simon, T. Erben, P. Schneider, C. Heymans, H. Hildebrandt, H. Hoekstra, T. D. Kitching, Y. Mellier, L. Miller, L. Van Waerbeke, C. Bonnett, J. Coupon, L. Fu, M. J. Hudson, K. Kuijken, B. T. P. Rowe, T. Schrabback, E. Semboloni, and M. Velander. CFHTLenS: higher order galaxy-mass correlations probed by galaxy-galaxy-galaxy lensing. *MNRAS*, 430:2476–2498, April 2013.

[28] M. J. Hudson, B. R. Gillis, J. Coupon, H. Hildebrandt, T. Erben, C. Heymans, H. Hoekstra, T. D. Kitching, Y. Mellier, L. Miller, L. Van Waerbeke, C. Bonnett, L. Fu, K. Kuijken, B. Rowe, T. Schrabback, E. Semboloni, E. van Uitert, and M. Velander. CFHTLenS: Co-evolution of galaxies and their dark matter haloes. *ArXiv e-prints*, October 2013.

[29] M. Velander, E. van Uitert, H. Hoekstra, J. Coupon, T. Erben, C. Heymans, H. Hildebrandt, T. D. Kitching, Y. Mellier, L. Miller, L. Van Waerbeke, C. Bonnett, L. Fu, S. Giodini, M. J. Hudson, K. Kuijken, B. Rowe, T. Schrabback, and E. Semboloni. CFHTLenS: the relation between galaxy dark matter haloes and baryons from weak gravitational lensing. *MNRAS*, 437:2111–2136, January 2014.

[30] M. Milkeraitis, L. van Waerbeke, C. Heymans, H. Hildebrandt, J. P. Dietrich, and T. Erben. 3D-Matched-Filter galaxy cluster finder - I. Selection functions and CFHTLS Deep clusters. *MNRAS*, 406:673–688, July 2010.

[31] B. R. Gillis, M. J. Hudson, T. Erben, C. Heymans, H. Hildebrandt, H. Hoekstra, T. D. Kitching, Y. Mellier, L. Miller, L. van Waerbeke, C. Bonnett, J. Coupon, L. Fu, S. Hilbert, B. T. P. Rowe, T. Schrabback, E. Semboloni, E. van Uitert, and M. Velander. CFHTLenS: the environmental dependence of galaxy halo masses from weak lensing. *MNRAS*, 431:1439–1452, May 2013.

[32] J. Ford, H. Hildebrandt, L. Van Waerbeke, T. Erben, C. Laigle, M. Milkeraitis, and C. B. Morrison. Cluster magnification and the mass-richness relation in CFHTLenS. *MNRAS*, 439:3755–3764, April 2014.

[33] J. T. A. de Jong, G. A. Verdoes Kleijn, K. H. Kuijken, and E. A. Valentijn. The Kilo-Degree Survey. *Experimental Astronomy*, 35:25–44, January 2013.

[34] L. Ferrarese, P. Côté, J.-C. Cuillandre, S. D. J. Gwyn, E. W. Peng, L. A. MacArthur, P.-A. Duc, A. Boselli, S. Mei, T. Erben, A. W. McConnachie, P. R. Durrell, J. C. Mihos, A. Jordán, A. Lançon, T. H. Puzia, E. Emsellem, M. L. Balogh, J. P. Blakeslee, L. van Waerbeke, R. Gavazzi, B. Vollmer, J. J. Kavelaars, D. Woods, N. M. Ball, S. Boissier, S. Courteau, E. Ferriere, G. Gavazzi, H. Hildebrandt, P. Hudelot, M. Huertas-Company, C. Liu, D. McLaughlin, Y. Mellier, M. Milkeraitis, D. Schade, C. Balkowski, F. Bournaud, R. G. Carlberg, S. C. Chapman, H. Hoekstra, C. Peng, M. Sawicki, L. Simard, J. E. Taylor, R. B. Tully, W. van Driel, C. D. Wilson, T. Burdullis, B. Mahoney, and N. Manset. The Next Generation Virgo Cluster Survey (NGVS). I. Introduction to the Survey. *ApJS*, 200:4, May 2012.

LENSING DISPERSION OF SNIa AND SMALL SCALES OF THE PRIMORDIAL POWER SPECTRUM

IDO BEN-DAYAN
Deutsches Elektronen-Synchrotron DESY, Theory Group, D-22603 Hamburg, Germany

Probing the primordial power spectrum at small scales is crucial for discerning inflationary models, especially if BICEP2 results are confirmed. We demonstrate this necessity by briefly reviewing single small field models that give a detectable gravitational waves signal, thus being degenerate with large field models on CMB scales. A distinct prediction of these small field models is an enhancement of the power spectrum at small scales, lifting up the degeneracy. We propose a way to detect this enhancement, and more generally, different features in the power spectrum at small scales $1 \lesssim k \lesssim 10^2 - 10^3\,\mathrm{Mpc}^{-1}$ by considering the existing data of lensing dispersion in Type Ia supernovae. We show that for various deviations from the simplest $n_s \simeq 0.96$ the lensing dispersion cuts considerably into the allowed parameter space by PLANCK and constrains the spectrum to smaller scales beyond the reach of other current data sets.

1 Introduction

State of the art CMB and Ly_α measurements probe only about 8 e-folds, ($H_0 \lesssim k \lesssim 1\,\mathrm{Mpc}^{-1}$) out of the expected 60 e-folds of observable inflation [1], rendering a huge degeneracy between inflationary models. Even a confirmation of the BICEP2 measurement will not break all the degeneracy. For example, small field models with a non-monotonic ϵ reproduce a spectrum similar to that of a monomial $V \sim \phi^n$ for a limited range of wave numbers [2]. Even within the class of large field models there is a degeneracy that can only be lifted by probing enough e-folds of the power spectrum. The answer lies in probing smaller scales of the power spectrum. In [3] we proposed using the lensing dispersion of type Ia supernovae as a novel cosmological probe and specifically as a constraint on the primordial power spectrum at small scales. See also [4].The lensing dispersion, σ_μ is sensitive to $0.01 \lesssim k \lesssim 10^2 - 10^3\,\mathrm{Mpc}^{-1}$, thus giving access to $2-3$ more decades ($4-7$ e-folds) of the spectrum, even using only *current data*.

In the next section, we review the non-monotonic ϵ idea. In section 3 we present how the lensing dispersion probes the primordial power spectrum on small scales. Section 4 describes the results for various parameterizations of the spectra, complementing [3], and some discussion.

2 Small field models and large r

Consider canonically normalized, single field models $V(\phi) = \Lambda^4 \sum_{n=0} a_n \phi^n$, assuming CMB scales are at $\phi \simeq 0$. Generically a_0 sets the scale of inflation, a_1 sets the tensor to scalar ratio $r = 16\epsilon$, a_2 sets n_s etc. A small field model $\Delta\phi < 1$ requires parametric tuning of a few parameters for a successful model of inflation, i.e. $\epsilon, |\eta| \ll 1$, to get 60 e-folds and $n_s \simeq 0.96$. This generically means $a_1 \ll 1$ and hence $r \ll 0.01$ in odds with the BICEP2 result [a]. A large

---

[a] In [5], I erroneously claimed a non-monotonic ϵ evades the Lyth bound from 1996 [6], contributing to confusion in the literature. This was promptly corrected in [2]. The strict '96 bound cannot be evaded, only the BL bound

field generically means functional tuning, for example $a_{n\neq 2} = 0$, for all n, which gives a free massive inflaton. Such models give $r \sim 0.1$, in accord with the BICEP2 findings. One would like a UV theory that explains the functional tuning we use. Moreover, taken at face value, the $r = 0.2$ BICEP2 result is in tension with PLANCK, unless the cosmological model is further extended to include primordial Helium, additional light degrees of freedom or a scale dependent spectral index $n_s(k)$, in a way that suppresses the power on intermediate scales. Regardless, hints of "running" $\alpha(k_0) \equiv dn_s/d\ln k$ have been around since WMAP1[8].

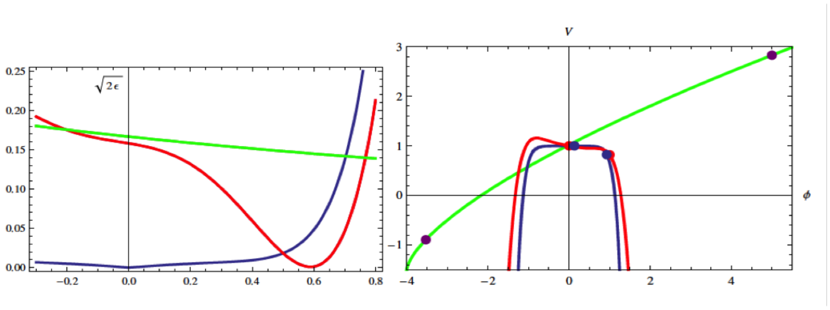

Figure 1 – $\sqrt{2\epsilon(\phi)}$ (left panel) and $V(\phi)$ (right panel) for typical hilltop (blue), monomial $V \sim \phi^{2/3}$ with a constant shift for clarity (green) , and the non-monotonic ϵ models (red).

Several years prior to PLANCK and BICEP2, in[2] we demonstrated the key idea, that non-monotonic $\epsilon = \frac{1}{2}\left(\frac{V'}{V}\right)^2$ allows small field models to have $r \sim 0.1$, avoiding the need of functional tuning, which is especially interesting in light of BICEP2. If at CMB scales, ϵ is rather large, then from $r = 16\epsilon$ we get detectable signal, $r \sim 0.1$. However, away from the CMB scales, ϵ decreases, giving many e-folds of inflation, $N = \int d\phi/\sqrt{2\epsilon}$. In Figure 1, reproduced from[2], we demonstrate the behaviour of $\sqrt{2\epsilon} = |V'/V|$ and the potential V as a function of the inflation. The main limitation is the scale dependence of the power spectrum, $P \sim V/\epsilon$, since by now about 8 e-folds have been measured with limited amount of scale dependence parameterized by $\alpha(k_0) \equiv dn_s/d\ln k, \beta(k_0) \equiv d^2n_s/d\ln k^2$.

Because of the non-monotonic ϵ, a distinct *prediction* of the models, which was made prior to PLANCK and BICEP2 results, is the enhancement of the power spectrum at small scales. In[2] the spectrum was calculated numerically by solving the Mukhanov-Sasaki equation, and in [9] it was argued that a spectrum with a bend at some k_i is a good approximation of the model, which we will use in section 4. Knowing the power spectrum at smaller scales is interesting by itself for a better understanding of inflation. Specifically, it can break the degeneracy between the above models and the monomial ones, because the former will have enhanced power at small scales[b]. We therefore suggest the lensing dispersion of SNe as a probe of the small scale power spectrum and a novel cosmological probe in general.

3 Lensing Dispersion of SNIa

Using the light-cone averaging approach up to second order in the Poisson (longitudinal) gauge [12], a simple expression for the lensing dispersion in[3] was derived:

$$\sigma_\mu^2 \simeq \left(\frac{5}{\ln 10}\right)^2 \frac{\pi}{\Delta\eta^2} \int_{\eta_s^{(0)}}^{\eta_o} \frac{d\eta_1 dk}{k} P_\Psi(k,\eta_1) k^3 (\eta_1 - \eta_s^{(0)})^2 (\eta_o - \eta_1)^2, \tag{1}$$

$$\simeq \left(\frac{5}{\ln 10}\right)^2 \frac{\pi}{\Delta\tilde{\eta}^2} \left(\frac{k_{eq}}{H_0}\right)^3 \int d\tilde{\eta}_1 dp P_\Psi(p,\tilde{\eta}_1) p^2 (\tilde{\eta}_1 - \tilde{\eta}_s^{(0)})^2 (\tilde{\eta}_o - \tilde{\eta}_1)^2. \tag{2}$$

---

[7], which assumes a monotonic ϵ.

[b] Measuring the spectrum for enough e-folds we will be able to discriminate even between the simplest models via spectral distortions[10], and perhaps even get a hint of a stringy origin[11].

where η_o is the observer conformal time, $\eta_s^{(0)}$ is the conformal time of the source with unperturbed geometry, $\Delta\eta(z) = \eta_o(z) - \eta_s^{(0)}(z) = \int_0^z \frac{dy}{H_0\sqrt{\Omega_{m0}(1+y)^3+\Omega_{\Lambda 0}}}$, and P_Ψ is the linear (LPS, P_L) or non-linear dimensionless power spectrum (NLPS, P_{NL}) of the *gravitational potential.* In the second line we switched to dimensionless variables, $\tilde{\eta} = H_0\eta$ and $p = k/k_{eq}$ [c]. Equation (2) demonstrates the relevant physical scales H_0 and k_{eq}, the sensitivity to scales smaller than the equality scale $p > 1$, and the expected enhancement pattern $(k_{eq}/H_0)^3$ in the linear regime and potentially additional $(k_{NL}/k_{eq})^3$ at a redshift dependent non-linearity scale, k_{NL}. So we have a direct probe of the integrated late-time power spectrum and of the cosmological parameters.

At redshift $z \sim 1$ the dispersion, σ_μ, grows approximately linearly with redshift, so the best constraints will be obtained from the maximal available redshift of current data, $z = 1$. We do not have a definite detection, but a conservative 2-sigma upper bound $\sigma_\mu(z = 1) \leq 0.12$ [13]. It is conservative because all analyses [12,13,14,15] point to a lower value of the dispersion, at most $\sigma_\mu(z) \simeq 0.093z$, [14]. Moreover, the most up-to-date JLA analysis uses the actual [13] value $\sigma_\mu = 0.055z$ and still sees a decrease as a function of redshift in the left over 'coherent' or 'intrinsic' dispersion, suggesting that even the *total dispersion* at $z \simeq 1$ is only $\sigma_\mu^{tot} \lesssim 0.12$, [15]. Additionally, partial sky coverage and higher redshift SN, which have already been used for cosmological parameter inference, will increase the dispersion, making our analysis even more conservative.

The main limitation of (2) is the validity of the spectrum [12], because for $k \gg H_0$ standard cosmological perturbation theory breaks down, and one has to resort to numerical simulations to get an approximate fitting formula for the power spectrum. We use the HaloFit model [16] with $k_{UV} = 320h\,\mathrm{Mpc}^{-1}$. For the standard case $P_k = A_s(k/k_0)^{n_s(k_0)-1}$, $\sigma_\mu(z = 1, k_{UV} = 320h\,\mathrm{Mpc}^{-1}) \simeq 0.08$. Within a certain range, varying H_0, Ω_{m0}, k_{UV} can account at most for 15% difference[3]. Hence the bound cannot be saturated by varying the background parameters and/or integrating up to arbitrarily small scales. Hence, it can be used for probing small scales of the power spectrum. After fixing all the background parameters, including $A_s, n_s(k_0 = 0.05\,\mathrm{Mpc}^{-1})$ to the most likelihood value of [1], we achieve accuracy of about 20%.

4 Results

We analyze four different, more general parameterizations of the spectrum and the corresponding panel in Figure 2:

$$P_k = A_s\left(\frac{k}{k_0}\right)^{n_s(k_0)-1+\frac{\alpha(k_0)}{2}\ln\frac{k}{k_0}+\frac{\beta(k_0)}{6}\ln^2\frac{k}{k_0}}, \qquad \text{top left panel} \tag{3}$$

$$P_k = A_s\left(\frac{k}{k_0}\right)^{n_s(k_0)-1} + B\left(\frac{\pi e}{3}\right)^{3/2}\left(\frac{k}{k_i}\right)^3 e^{-\pi/2(k/k_i)^2}, \qquad \text{top right panel} \tag{4}$$

$$P_k = A_s\left(\frac{k}{k_0}\right)^{n_s(k_0)-1}\left[1 + \frac{B}{A_s}\Theta(k-k_i)\right], \qquad \text{bottom left panel} \tag{5}$$

$$P_k = A_s\left(\frac{k}{k_0}\right)^{n_s(k_0)-1}\left[\Theta(k_i-k) + \left(\frac{k}{k_i}\right)^{n_s^*-1}\Theta(k-k_i)\right]. \qquad \text{bottom right panel} \tag{6}$$

where Θ is the Heaviside function, $\alpha(k_0) \equiv dn_s/d\ln k, \beta(k_0) \equiv d^2n_s/d\ln k^2$ are the "running" and "running of running" of the spectral index, (4) is a typical parameterization of one episode of particle production [17], (5) describes a step in the power spectrum, for instance due to several episodes of inflation [18], and (6) describes an enhancement which is not necessarily captured just by running. The models discussed in section 2 fit the latter parameterization.

---

[c] The choice of the equality scale $p = k/k_{eq}$ is because we know the general behaviour of P_L, or more precisely, its transfer function $T(k)$ which is constant for $p < 1$ and scales like $p^{-2}\ln p$ for $p \gg 1$

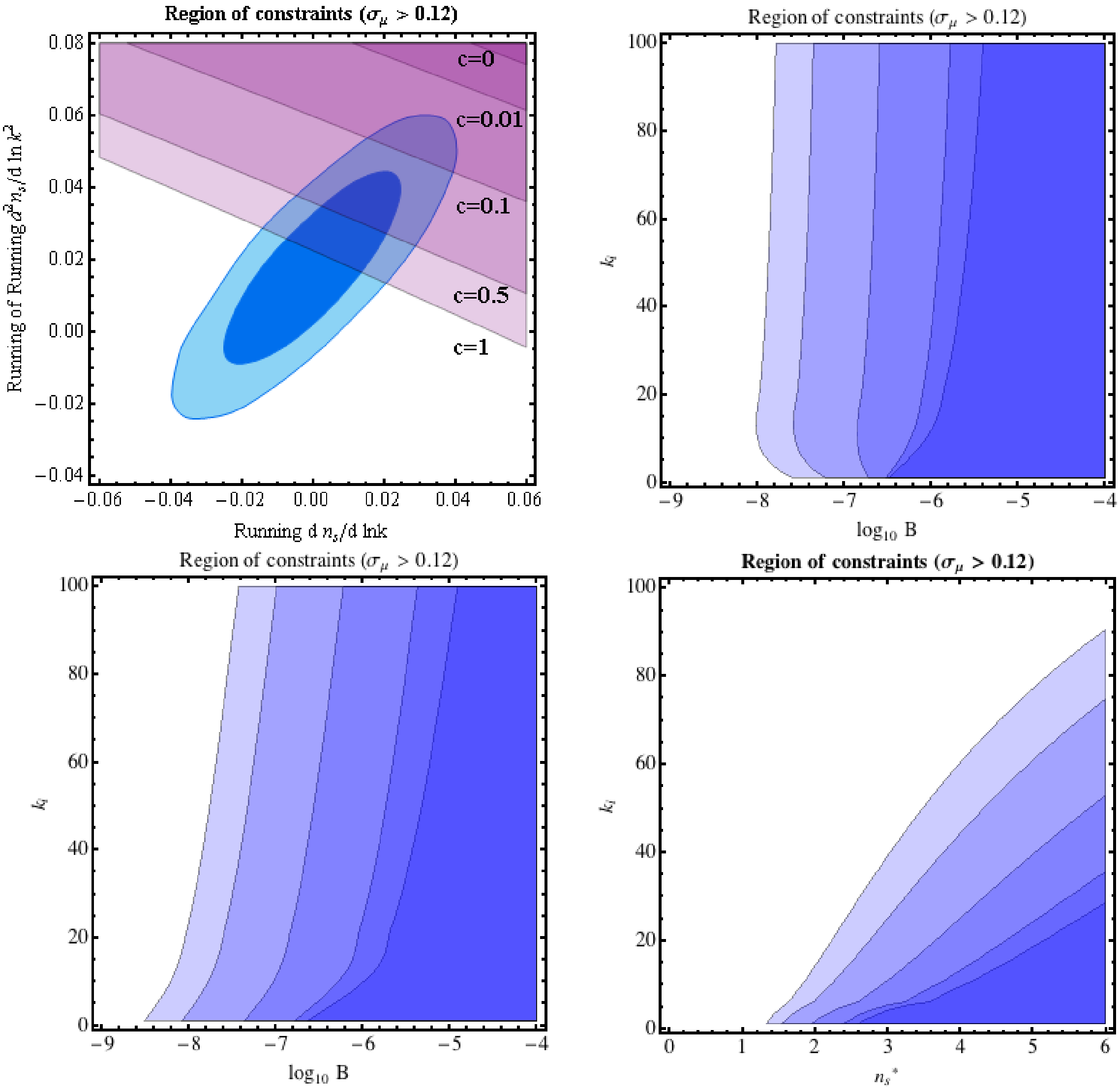

Figure 2 – Exclusion plots for the different parameterizations. Shaded regions correspond to $\sigma_\mu(z = 1) > 0.12$ with $c = 0, 0.01, 0.1, 0.5, 1$ respectively from dark to light and are disfavoured. The different parameterizations are: top left eq. (3), top right eq. (4), bottom left eq. (5), bottom right eq. (6). In the top left panel the ellipses correspond to 68% and 95% likelihood contours from PLANCK.

For the above parameterizations, the HaloFit formula is not reliable anymore due to its sensitivity to initial conditions. It is nevertheless obvious that the non-linear evolution causes clustering and enhances the power spectrum. We therefore define a ratio, $F(k,z) \equiv \frac{P_{NL}(k,z)}{P_L(k,z)}$, where P_{NL} is the non-linear power spectrum, $P_L = (3/5)^2 P_k T^2(k) g^2(z)$ is the linear spectrum, $g(z)$ is the growth factor and $T(k)$ is the transfer function with baryons [12], in the standard scenario $n_s \simeq 0.96$. We take the enhancement into account by substituting in (1):

$$P_\Psi \to P_L(k,z)(1 - c + cF(k,z)) \,, \tag{7}$$

and evaluate σ_μ with $c = 0, 0.01, 0.1, 0.5, 1$. $c = 0$ corresponds to computing the dispersion with the linear power spectrum only, while $c = 1$ corresponds to exactly following the HaloFit enhancement pattern. Except $c = 1$ all values of c are underestimates[d]. The results are presented

---

[d] In [3], we also considered a step function of the sort $P_\Psi \to P_L(k,z)(1 + b\,\Theta(k - k_{NL}))$, for $b = 0, 3, 10, 50$ with corresponding $k_{NL} = 1, 1, 2, 15\,\mathrm{Mpc}^{-1}$ always underestimating the ratio F. The results are very similar to that of (7).

in Figure 2. In all panels, coloured regions give $\sigma_\mu(z=1) \geq 0.12$ for $c = 0, 0.01, 0.1, 0.5, 1$ from dark to light and are disfavoured. From Fig. 2, it is obvious that the lensing dispersion or its absence is an extremely powerful cosmological probe. Even if a scale dependent spectral index induces clustering which is *an order of magnitude smaller* than the standard constant n_s scenario, some of the parameter space allowed by PLANCK is ruled out. Moreover, the analysis probes the spectrum up to $k \sim 320h\,\mathrm{Mpc}^{-1}$, more than two orders of magnitude beyond PLANCK's lever arm (~ 5 e-folds more). Calling $c = 0.1$ 'realistic' and $c = 1$ 'optimistic', the spectrum never goes above $(6, 3.7) \times 10^{-7}$ up to $k \leq 320h\,\mathrm{Mpc}^{-1}$ respectively for features up to $k_i \leq 100\,\mathrm{Mpc}^{-1}$. The only exception is (6) which gives $P_k(320h\,\mathrm{Mpc}^{-1}) = 2.3 \times 10^{-6}$ in the realistic case for $k_i \leq 50\,\mathrm{Mpc}^{-1}$. This is due to a slow enhancement and on smaller scales so it is quickly erased via Silk damping. Combining SN lensing in analyses (present and forthcoming missions), will undoubtedly allow a much better determination of the cosmological parameters.

Acknowledgments

We thank Tigran Kalaydzhyan for collaborating in the early stage of the work. This work is supported by the German Science Foundation (DFG) within the Collaborative Research Center (CRC) 676 "Particles, Strings, and the Early Universe".

References

1. P. A. R. Ade *et al.* [Planck Collaboration], [arXiv:1303.5082 [astro-ph.CO]]. G. -B. Zhao *et al.*, Mon. Not. Roy. Astron. Soc. **436**, 2038 (2013) P. A. R. Ade *et al.* [BICEP2 Collaboration], Phys. Rev. Lett. **112**, 241101 (2014)
2. I. Ben-Dayan and R. Brustein, JCAP **1009**, 007 (2010)
3. I. Ben-Dayan and T. Kalaydzhyan, [arXiv:1309.4771 [astro-ph.CO]].
4. T. Hamana and T. Futamase, Astrophys. J. **534**, 29 (2000) E. M. Minty, A. F. Heavens and M. R. S. Hawkins, Mon. Not. Roy. Astron. Soc. **330**, 378 (2002) S. Dodelson and A. Vallinotto, Phys. Rev. D **74**, 063515 (2006) V. Marra, M. Quartin and L. Amendola, Phys. Rev. D **88**, 063004 (2013) M. Quartin, V. Marra and L. Amendola, Phys. Rev. D **89**, 023009 (2014) C. Fedeli and L. Moscardini, [arXiv:1401.0011 [astro-ph.CO]]. T. Castro and M. Quartin, MNRAS Letters 2014 443 (1): L6-L10
5. I. Ben-Dayan, [arXiv:0910.5515 [astro-ph.CO]].
6. D. H. Lyth, Phys. Rev. Lett. **78**, 1861 (1997)
7. L. Boubekeur and D. .H. Lyth, JCAP **0507**, 010 (2005)
8. H. V. Peiris *et al.* [WMAP Collaboration], Astrophys. J. Suppl. **148**, 213 (2003)
9. J. Chluba, A. L. Erickcek and I. Ben-Dayan, Astrophys. J. **758**, 76 (2012)
10. J. Chluba and D. Jeong, [arXiv:1306.5751 [astro-ph.CO]].
11. I. Ben-Dayan, S. Jing, A. Westphal and C. Wieck, JCAP **1403**, 054 (2014)
12. M. Gasperini, G. Marozzi, F. Nugier and G. Veneziano, JCAP **1107**, 008 (2011) I. Ben-Dayan, M. Gasperini, G. Marozzi, F. Nugier and G. Veneziano, JCAP **1204**, 036 (2012) , Phys. Rev. Lett. **110**, 021301 (2013), JCAP **1211**, 045 (2012) JCAP **1306**, 002 (2013).
13. J. Jonsson *et al.*, [arXiv:1002.1374 [astro-ph.CO]].
14. D. E. Holz and E. V. Linder, Astrophys. J. **631**, 678 (2005) T. Kronborg *et al.* [SNLS Collaboration], [arXiv:1002.1249 [astro-ph.CO]]. N. V. Karpenka, M. C. March, F. Feroz and M. P. Hobson, [arXiv:1207.3708 [astro-ph.CO]]. M. Smith *et al.* [SDSS Collaboration], Astrophys. J. **780**, 24 (2014)
15. M. Betoule *et al.* [SDSS Collaboration], [arXiv:1401.4064 [astro-ph.CO]].
16. K. T. Inoue and R. Takahashi, Mon. Not. Roy. Astron. Soc. **426**, 2978 (2012)
17. N. Barnaby and Z. Huang, Phys. Rev. D **80**, 126018 (2009)
18. J. A. Adams, G. G. Ross and S. Sarkar, Nucl. Phys. B **503**, 405 (1997)

The Impact of Magnification and Size Bias on Weak Lensing Power Spectrum and Peak Statistics

JIA LIU
Department of Astronomy and Astrophysics, Columbia University, New York, NY 10027, USA

At present, several weak lensing surveys are underway or will come online soon, all aiming to push our understanding of dark energy. The weak lensing power spectrum is a powerful tool to probe cosmological parameters. Additionally, lensing peak counts contain cosmological information beyond the power spectrum. Both of these statistics can be affected by the preferential selection of source galaxies in patches of the sky with high magnification, as well as by the dilution in the source galaxy surface density in such regions. We found that if this magnification bias is ignored, cosmological parameters can be biased by a few standard deviation for a Large Synoptic Survey Telescope-sized survey.

1 Introduction

Dark energy (DE) is one of the biggest mysteries in science, contributing to 70% of the energy density in the universe yet being the least understood form of energy. It was not until the 1990s, through type Ia supernovae observations that we confirmed the accelerating expansion of the universe. In the 2006 report of the Dark Energy Task Force[1], weak lensing (WL) has been identified as one of the four key DE probes, with the other three being baryon acoustic oscillations, galaxy cluster counts, and type Ia supernova. Weak gravitational lensing happens when a light ray from a background galaxy passes through the potential well of a foreground halo or any other inhomogeneity in the foreground structure. Each light ray follows a slightly different path, resulting in a galaxy image that is tangentially stretched ("sheared") around the foreground halo. Therefore, by measuring the distortion of background galaxy shapes, the matter density at different redshifts can be mapped to infer the nature of DE.

Because of the statistical nature of WL surveys, it is important to have an unbiased sample of source galaxies, fairly sampling the foreground density fluctuations across the sky. We investigate possible sources of bias in flux-limited surveys, arising from a preferential selection of source galaxies in patches of the sky with high magnification, as well as by the dilution in the source galaxy surface density in such regions (known as magnification bias; hereafter MB).

2 Magnification Bias

Gravitational lensing causes a bias by modulating the apparent surface density of galaxies on the sky, through two competing effects. First, lensing can magnify (or demagnify) individual source galaxies in the background, increasing (or decreasing) their total flux. In a flux-limited WL surveys, some otherwise excluded faint galaxies can therefore make it into (or drop out of) the sample because of this (de)magnification. Second, a similar (de)magnification applies to the patch of the sky around the galaxy, geometrically diluting (or enhancing) the apparent surface density of galaxies in this region. These two effects counteract each other, and the net bias depends on the slope of the intrinsic (unlensed) galaxy luminosity function at the survey flux limit. In addition to these effects, lensing can increase (or decrease)

	Magnitude limit	$s(z=0.5)$	$s(z=1.0)$	ref
LSST	I $\leq$ 24.8	0.19	0.38	[3]
Euclid	R+I+Z $\leq$ 24.5	0.20	0.43	[4]
COSMOS	I $\leq$ 25	0.19	0.35	[5]
CFHTLS	I $\leq$ 24.7	0.19	0.39	[6]
DES	I $\leq$ 24.3	0.21	0.46	[7]
DUNE	R+I+Z $\leq$ 24.5	0.20	0.43	[8]
KiDS	R $\leq$ 25.2 (*)	0.24	0.69	[9]
HSC	I $\leq$ 26.2 (*)	0.18	0.32	[10]

Table 1: Magnitude limits and corresponding s (number count slope) at $z = 0.5$ and 1.0 for current and future WL surveys. For surveys in which only the point source magnitude limit was available (marked by a "*"), we reduced $m_{\rm lim}$ by 1 magnitude to represent an extended source magnitude cut. In the broad multi-band (R+I+Z), we calculated s for the central I band.

the apparent angular size of spatially resolved individual galaxies. Including the effect of lensing on both the flux and on the geometrical surface density, we have the relation[2]

$$n(\boldsymbol{\theta}) = n_g(\boldsymbol{\theta})\left[1 + (5s-2)\kappa(\boldsymbol{\theta})\right], \tag{1}$$

where $n(\boldsymbol{\theta})$ is the observed (lensed) galaxy number density at position $\boldsymbol{\theta}$, as viewed by the observer, $n_g(\boldsymbol{\theta})$ is the intrinsic (unlensed) galaxy number density, s is the slope of the cumulative number counts evaluated at $m_{\rm lim}$, and $\kappa(\boldsymbol{\theta})$ is the convergence. If we assume a survey with a sharp magnitude cut-off at $m_{\rm lim}$:

$$s = \left.\frac{\partial \log_{10} n_g}{\partial m}\right|_{m_{\rm lim}} . \tag{2}$$

Table 1 lists the magnitude limits and the corresponding values of s for several current and future WL surveys.

3 Simulations

This work uses in total 35 different N-body simulations, covering 7 different cosmological models (1 fiducial cosmology plus 6 variations), each with 5 independent realizations of the same input primordial power spectrum. The 6 non-fiducial models have values of $\Omega_m = \{0.23, 0.29\}$ (while $\Omega_\Lambda = \{0.77, 0.71\}$ to keep a spatially flat universe), $w = \{-1.2, -0.8\}$ and $\sigma_8 = \{0.75, 0.85\}$.

We then perform ray-tracing to construct convergence maps. We also add galaxy ellipticity noise to our maps, due to variations in the intrinsic shapes of galaxies, and their random orientations on the sky. For simplicity, we use only convergence maps for source galaxies at the single redshift $z = 1$, as the z–dependence of MB has shown to be weak. And finally, MB is applied as:

$$\kappa_G = \frac{\int d^2\theta W_G\left[\left(1+(5s-2)\,\kappa\right)\kappa + \kappa_{noise}\right]}{\int d^2\theta W_G\left[1+(5s-2)\,\kappa\right]}. \tag{3}$$

where κ_G is the smoothed κ value and W_G is the Gaussian kernel with a smoothing scale $\theta_G = 1$ arcmin.

4 Results and Conclusions

Since we run simulations with different cosmological parameters, we can construct a cosmological model with a simple linear interpolation, and find the best fits for the mock MB maps. The impact of MB on the power spectrum and peak counts is illustrated in Fig. 1.

The biases are shown in two dimensions in Fig. 2, where the Monte Carlo error ellipses, enclosing 68% of the best-fits, are explicitly shown for the fiducial unbiased maps and biased maps ($s = 0.2, 0.8$).

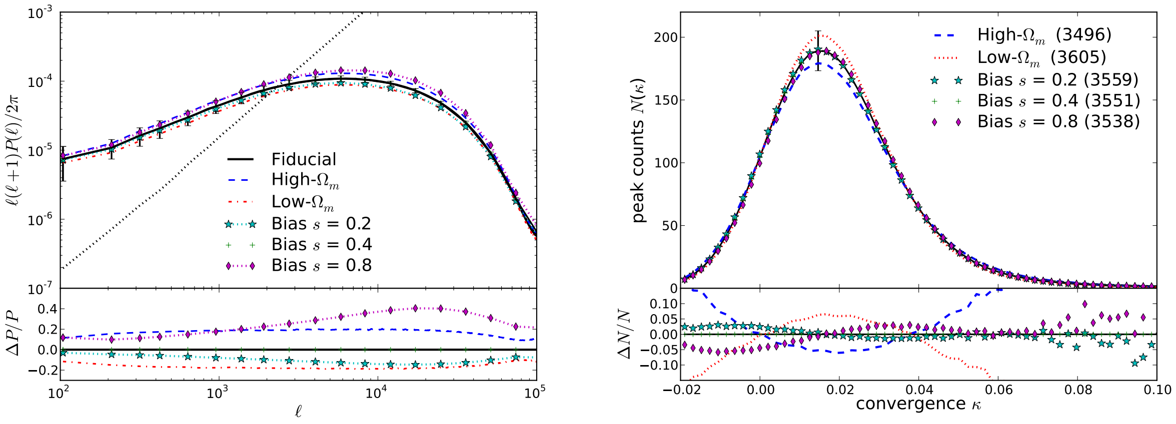

Figure 1 – Changes in the convergence power spectrum (left panel) and peak counts (right panel) caused by magnification bias, as well as by varying Ω_m. Three levels of bias on the fiducial model are shown. Error bars are for a 12 deg^2 sky; we expect them to decrease by a factor of $\sim$ 40 after scaling the results to LSST's 20,000 deg^2 survey. The black dotted line (left panel) is the galaxy noise for $n_{gal} = 30$ arcmin^2.

The value $s = 0.2$ is close to that expected in LSST and $s = 0.8$ is close to the value expected in the presence of an additional size bias induced by a sharp cut on galaxy sizes.

In conclusion, WL observations in a survey as large as LSST will need to take MB into account, by including it in the modeling when fitting the observations. Combining information from both the power spectrum and the peak counts will be useful, as these two observables are impacted by MB in different ways, and their combination can help mitigate the biases. The value of s (or other parameters describing higher-order lensing corrections) could be potentially additional parameters in a fitting procedure, simultaneously with the cosmological parameters. We expect that MB has a smaller impact on the current surveys, mainly due to their smaller sky coverage (e.g. COSMOS: $\approx$2 deg^2, CFHTLenS: 150 deg^2). After scaling σ by their sky coverage, we found the deviations to be of order $\sim 0.01\sigma$ for COSMOS, and $\sim 0.1\sigma$ for CFHTLenS.

Acknowledgments

This summary is based on Liu et al. (2014) [11]. I thank my co-authors for their permission to present our joint work This research utilized resources at the New York Center for Computational Sciences, a cooperative effort between Brookhaven National Laboratory and Stony Brook University, supported in part by the State of New York. This work is supported in part by the U.S. Department of Energy under Contract No. DE-AC02-98CH10886 and by the NSF under grant AST-1210877. The simulations were created on the IBM Blue Gene/L and /P New York Blue computer and the maps were created analyzed on the LSST/Astro Linux cluster at BNL.

References

1. A. Albrecht, G. Bernstein, R. Cahn, W. L. Freedman, J. Hewitt, W. Hu, J. Huth, M. Kamionkowski, E. W. Kolb, L. Knox, J. C. Mather, S. Staggs, and N. B. Suntzeff. Report of the Dark Energy Task Force. *ArXiv Astrophysics e-prints*, September 2006.
2. L. Hui, E. Gaztañaga, and M. Loverde. Anisotropic magnification distortion of the 3D galaxy correlation. I. Real space. Phys. Rev. *D*, 76(10):103502, November 2007.
3. LSST Science Collaboration, P. A. Abell, J. Allison, S. F. Anderson, J. R. Andrew, J. R. P. Angel, L. Armus, D. Arnett, S. J. Asztalos, T. S. Axelrod, and et al. LSST Science Book, Version 2.0. *ArXiv e-prints*, December 2009.

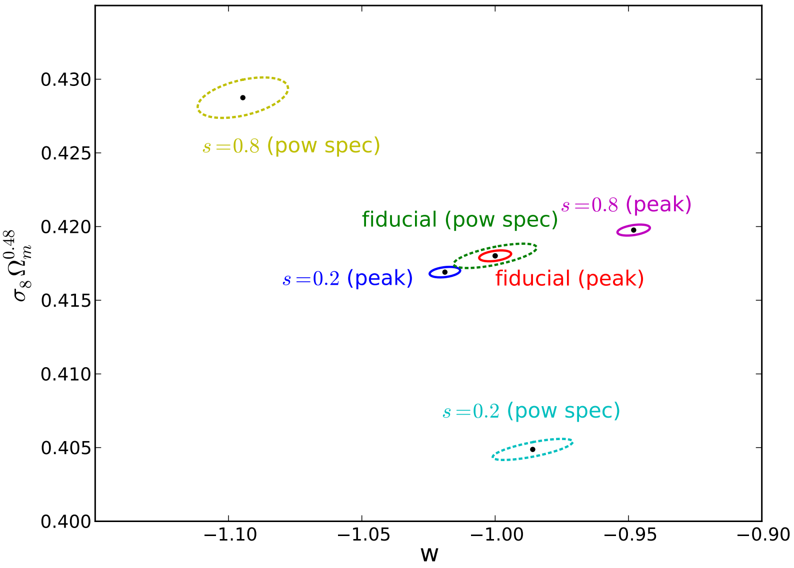

Figure 2 – Error ellipses for the fiducial (unbiased) maps and in the case of magnification bias with $s = 0.2$ and 0.8, for both the power spectrum (using $100 < \ell < 20,000$) and the peak counts (with 200 convergence bins and smoothing scale $1/\sqrt{2}$ arcmin). Error ellipses contain 68% of the best-fits, and have been scaled to LSST's sky coverage of 20,000 deg^2.

4. R. Laureijs. Euclid Assessment Study Report for the ESA Cosmic Visions. *ArXiv e-prints*, December 2009.
5. N. Scoville, R. G. Abraham, H. Aussel, J. E. Barnes, A. Benson, A. W. Blain, D. Calzetti, A. Comastri, P. Capak, C. Carilli, J. E. Carlstrom, C. M. Carollo, J. Colbert, E. Daddi, R. S. Ellis, M. Elvis, S. P. Ewald, M. Fall, A. Franceschini, M. Giavalisco, W. Green, R. E. Griffiths, L. Guzzo, G. Hasinger, C. Impey, J.-P. Kneib, J. Koda, A. Koekemoer, O. Lefevre, S. Lilly, C. T. Liu, H. J. McCracken, R. Massey, Y. Mellier, S. Miyazaki, B. Mobasher, J. Mould, C. Norman, A. Refregier, A. Renzini, J. Rhodes, M. Rich, D. B. Sanders, D. Schiminovich, E. Schinnerer, M. Scodeggio, K. Sheth, P. L. Shopbell, Y. Taniguchi, N. D. Tyson, C. M. Urry, L. Van Waerbeke, P. Vettolani, S. D. M. White, and L. Yan. COSMOS: Hubble Space Telescope Observations. *ApJS*, 172:38–45, September 2007.
6. C. Heymans, L. Van Waerbeke, L. Miller, T. Erben, H. Hildebrandt, H. Hoekstra, T. D. Kitching, Y. Mellier, P. Simon, C. Bonnett, J. Coupon, L. Fu, J. Harnois Déraps, M. J. Hudson, M. Kilbinger, K. Kuijken, B. Rowe, T. Schrabback, E. Semboloni, E. van Uitert, S. Vafaei, and M. Velander. CFHTLenS: the Canada-France-Hawaii Telescope Lensing Survey. *MNRAS*, 427:146–166, November 2012.
7. The Dark Energy Survey Collaboration. The Dark Energy Survey. *ArXiv Astrophysics e-prints*, October 2005.
8. A. Refregier. The Dark UNiverse Explorer (DUNE): proposal to ESA's cosmic vision. *Experimental Astronomy*, 23:17–37, March 2009.
9. J. T. A. de Jong, G. A. Verdoes Kleijn, K. H. Kuijken, and E. A. Valentijn. The Kilo-Degree Survey. *Experimental Astronomy*, 35:25–44, January 2013.
10. M. Takada. Subaru Hyper Suprime-Cam Project. In N. Kawai and S. Nagataki, editors, *American Institute of Physics Conference Series*, volume 1279 of *American Institute of Physics Conference Series*, pages 120–127, October 2010.
11. Jia Liu, Zoltán Haiman, Lam Hui, Jan M. Kratochvil, and Morgan May. Impact of magnification and size bias on the weak lensing power spectrum and peak statistics. *Phys. Rev. D*, 89:023515, Jan 2014.

BOSS UPDATE ON GALAXY CLUSTERING

M. MANERA
for the SDSS-III Galaxy Clustering Working Group
[1] *University College London, Gower Street, London WC1E 6BT, UK*
[2] *Institute of Cosmology and Gravitation, Portsmouth University, Dennis Sciama Building, PO1 3FX, Portsmouth, UK*

The Baryon Oscillation Spectroscopic Survey Data Release 11 (BOSS, DR11) has measured with unprecedented accuracy the scale of the Baryon Acoustic Oscillation peak (BAO) from galaxy clustering at $z \simeq 0.32$ and $z \simeq 0.57$, thus providing the best estimate to date of the cosmic distance scale at these redshifts, with errors that are respectively less than 2% and 1%. The error analysis of the data has been made possible by the use of a large number of mock galaxy catalogues, created using the PTHalos methodology. These mocks were crucial for providing the covariance matrices and understanding the systematics of the observations.

1 The CMASS and LOWZ DR11 galaxy samples

BOSS [1] is a spectroscopic survey that uses imaging data from SDSS-III [2] to map the positions of 1.35 million galaxies over a quarter of the sky. It targets two distinct galaxy samples: the LOWZ sample, a low redshift sample $0.2 \lesssim z \lesssim 0.45$ with galaxies selected following an algorithm close to that designed for Luminous Red Galaxies (LRG) in SDSSS-I/II, and the CMASS sample, a high redshift sample $0.4 \lesssim z \lesssim 0.7$ that targets galaxies with roughly a constant stellar mass.

The BOSS LOWZ and CMASS Data Release 11 (DR11) galaxy samples cover respectively an area of $7,998$ and $8,976$ square degrees, which is splitted into a Northern Galacic Cap ($5,793$ and $6,769$ square degrees respectively) and a Southern Galactic Cap ($2,205$ and $2,207$ square degrees). The volume of these samples more than doubles what was available in the DR9.

For the clustering analysis the BOSS galaxy working group have used $690,286$ galaxies for CMASS and $313,780$ for LOWZ; these include those targeted galaxies that have good spectroscopic redshifts and pass the redshift cuts, as well as the SDSS-II spectroscopic known galaxies that also pass the sample cuts.[3,4]

2 Measuring the Cosmic Distance and the BAO peak scale

The two-point correlation function measured from the CMASS sample using the Landy-Szalay estimator, is shown in the top panel of Figure 2. The BAO peak feature is clearly seen, and is detected with a significance of over 7 sigma. The position of the peak, commonly used as a "standard ruler", is given by the distance the sound waves travel before the coupling between baryons and radiation breaks down, r_d, which is 148.28 Mpc in our fiducial flat ΛCDM cosmology with $\Omega_m = 0.274$, $h = 0.7$, and $\Omega_b h^2 = 0.0224$.

We have measured the cosmic distance $D_V(z) \equiv \left[cz(1+z)^2 D_A(z)^2 H^{-1}(z)\right]^{1/3}$ by fitting the averaged correlation function ξ as a function of the distance in redshift space s:

$$\xi^{\rm fit}(s) = B^2 \xi^{\rm mod}(\alpha s) + \frac{a_1}{s^2} + \frac{a_2}{s} + a_3 \tag{1}$$

where $\xi^{\rm mod}$ is the model, $H(z)$ the Hubble distance at redshift z and D_A the angular distance. B is a multiplicative constant allowing for an unknown large scale bias and a_1, a_2, a_3 the coefficients of a polynomial that helps marginalize over the broadband signal. The parameter α rescales the correlation function and gives a measure of the cosmic distance, $D_V(z) r_{d,\rm fid} = \alpha D_V^{\rm fid}(z) r_d$, We find $D_V = (1264 \pm 25{\rm Mpc})(r_d/r_{d,fid})$ for the LOWZ sample and $D_V = (2056 \pm 20{\rm Mpc})(r_d/r_{d,fid})$ for the CMASS sample. These measurements have taken advantage of the reconstruction technique [5] that extrapolates the galaxy positions back in time to recover a more linear acoustic fetature, and incorporate as well the information from the power spectrum. The CMASS measurement, at 1.0 per cent accuracy, includes also anisotropic information, and is the most precise distance constraint ever obtained from a galaxy survey.[3] Complementary cosmological measurements have been made for $H(z)$, D_A and D_V using Redshift Space Distortions.[6,7,8,9]

3 Mock Galaxy Catalogues

Mock galaxy catalogues are essential to obtaining statistical errors and covariance matrices, calibrating the pipelines, testing the systematics, and linking theoretical predictions to the observed measurements. Mock galaxy catalogues (600 for CMASS and 1000 for LOWZ) have been created using the PTHalos methodology, with the basic steps summarised as follows[10]:

- Given a set of cosmological parameters, and an initial linear power spectrum, create a dark matter particle field based 2nd-Order Lagrangian Perturbation Theory (2LPT). This step is very fast (orders of magnitude faster than an N-Body run) and consequently allows for the creation of a large number of mock catalogues.

- Identify halos using a Friends-of-Friends (FoF) halo-finder with an appropriately chosen linking length ℓ, which is derived by comparing the spherical collapse of structures in 2LPT versus full (spherical) Eulerian dynamics. We argue that for LOWZ and CMASS ℓ should be respectively 0.39 and 0.38 times the comoving interparticle distance.[10,11] After the dark matter halos are identified we use Halo Abundance Matching technique to reassign the masses of the halos such as to recover the theoretical (or the N-Body) mass function of our chosen cosmological parameters.

- Populate halos with galaxies using a Halo Occupation Distribution (HOD) algorithm calibrated to fit the observational data. For CMASS we have used the DR9 correlation function with $30 < r < 80$ Mpc/h and for LOWZ the DR10 power spectrum with $0.02 < k < 0.15$ h/Mpc. and allowed a redshift dependence for the HOD.

- Apply the survey angular mask and (if necessary) the galaxy redshift distribution. The mock catalogues also take into account the completeness of the survey as a function of the position of the sky. The mock include galaxy close-pair corrections, which happen when two targeted galaxies are very close together in angular separation: one of these might not be observed due to the fact that two spectroscopic fibers in the focal plane cannot be placed closer than the equivalent of 62 arc seconds.

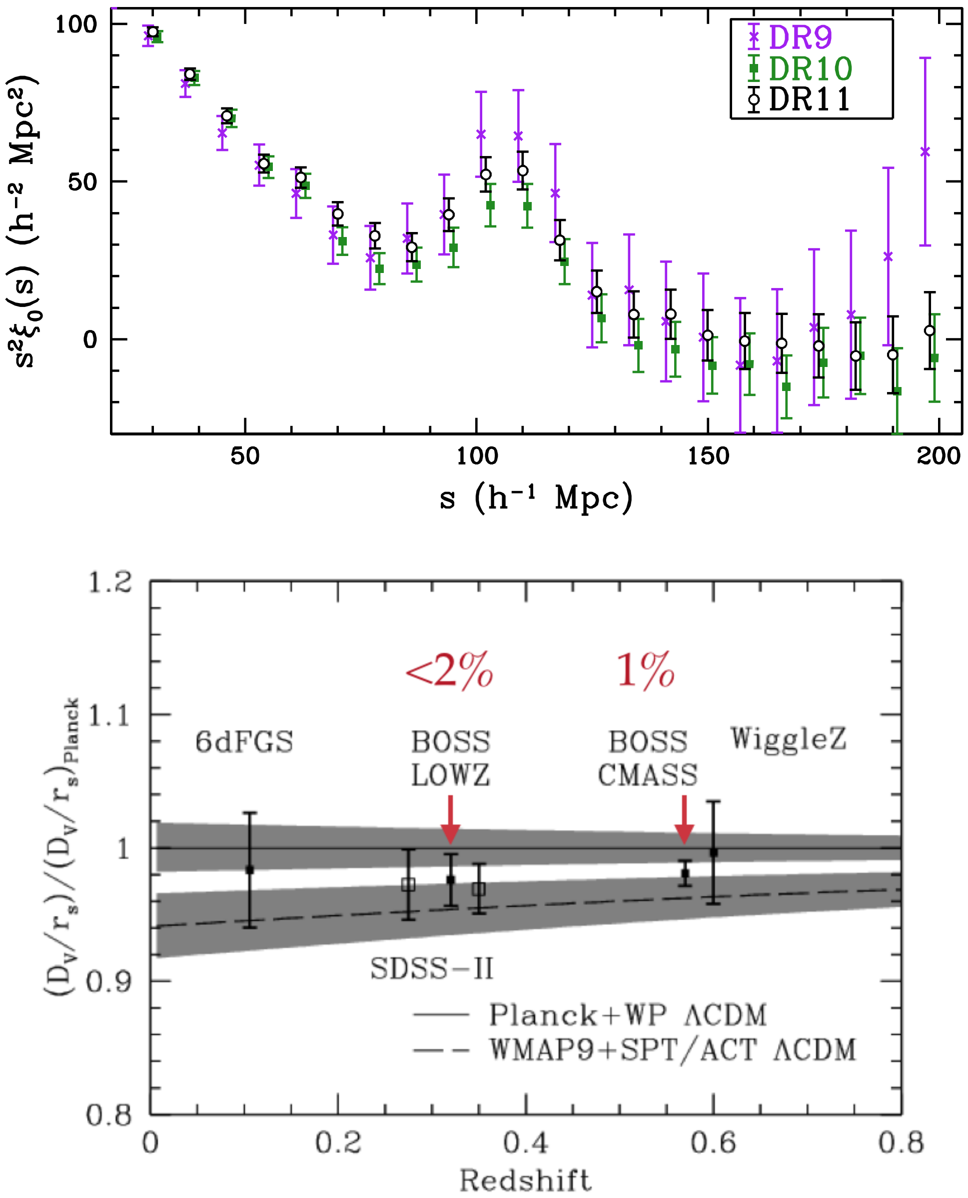

Figure 1 – Top: Two point correlation function of the CMASS DR9, DR10 and DR11 galaxy samples. The position of the BAO peak is clearly seen and can be accurately measured. The covariance matrix for these measurements have been obtained from the PTHalos mocks galaxy catalogues. Bottom: The cosmic distance scale derived from the BAO measurement for the LOWZ DR11 ($z \simeq 0.32$) and CMASS DR11 ($z \simeq 0.57$) galaxy samples. Results are compared with other measurements from 6dF, SDSS-II and WiggleZ. The volume observed partially overlaps between measurements at the same redshift, thus they are not statistically independent. The bands give the 1-sigma range of values allowed by Planck + WMAP Polarization and by WMAP + SPT/ACT data. Top and bottom panels correspond to figures 10 and 22 in Anderson et al. 2014[3], where an extended explanation can be found.

The PTHalos mock galaxy catalogues have been crucial for the error analysis of the BOSS galaxy clustering data, including a) estimating the systematic and statistical errors of α, and (thus, through D_V) of the cosmological parameters;[3,14] b) determining the optimal number of bins for the anallysis;[13] c) obtaining the correlation between the power spectrum and the correlation function estimator of α and thus allowing for a combined measurement;[3,14] d) understanding the improvement of the errors from the reconstruction technique; and e) determining the best way to correct for the systematic effects of observations.[12] The most important of the latter is the correlation between the number of galaxies in a region of the sky and the number of stars in that region. This local signal leaks into our measurement of the galaxy clustering correlation. It changes the correlation function by more than one sigma at the BAO scale[8], and it needs to be corrected. This is especially relevant for studies involving the full shape of the correlation function, as the position of the BAO peak is more robust to changes in the broad shape of $\xi(s)$.

Finally, an accurate estimation of the cosmic distance measurement error, requires correcting for the error in the inverse covariance matrix caused by the finite number of mocks available. A correction is required for the inversion of the covariance matrix, and for the derived parameter error. Furthermore the parameter error corrections depend on the way in which the parameter error is determined, and are different if this is calculated from the distribution of recovered values from the mocks, or the likelihood surface.[13] For the cosmoic distance measurement of the LOWZ and CMASS galaxy samples, we achieve an accuracy of less than 2% and 1% respectively, the latter being the most precise distance constraint ever obtained from a galaxy survey.[3]

Acknowledgments

MM acknowledges support from European Research Council, through grant "MDEPUGS". SDSS-III is managed by the Astrophysical Research Consortium for the Participating Institutions of the SDSS-III Collaboration including the University of Arizona, the Brazilian Participation Group, Brookhaven National Laboratory, University of Cambridge, Carnegie Mellon University, University of Florida, the French Participation Group, the German Participation Group, Harvard University, the Instituto de Astrofisica de Canarias, the Michigan State/Notre Dame/JINA Participation Group, Johns Hopkins University, Lawrence Berkeley National Laboratory, Max Planck Institute for Astrophysics, Max Planck Institute for Extraterrestrial Physics, New Mexico State University, New York University, Ohio State University, Pennsylvania State University, University of Portsmouth, Princeton University, the Spanish Participation Group, University of Tokyo, University of Utah, Vanderbilt University, University of Virginia, University of Washington, and Yale University.

References

1. Dawson K. S., et al., 2013, AJ, 145, 10
2. Eisenstein D.J., et al., 2011, AJ 142, 72
3. Anderson L., et al., 2014, MNRAS 441, Issue1, p24-62, BOSS collaboration paper
4. Tojeiro, R., et al., 2012, MNRAS, 424, 136
5. Padmanabhan N., Xu X., Eisenstein D.J., et al., 2012, MNRAS, 427, Issue 3, pp. 2132-2145.
6. Beutler F., et. al. 2013, eprint arXiv:1312.4611
7. Samushia L., et al, MNRAS, 439, Issue 4, p.3504-3519
8. Chuang C., et. al., MNRAS, 433, Issue 4, p.3559-3571
9. Sanchez A., et al., MNRAS, 440, Issue 3, p.2692-2713
10. Manera M., et al., 2013, MNRAS 428, Issue 2, p.1036-1054
11. Manera M., et al., 2014, eprint arXiv:1401.4171
12. Ross A., et al., 2012, MNRAS, 424, Issue 1, pp. 564-590.
13. Percival W.J, 2014, MNRAS, 439, Issue 3, p.2531-2541
14. Vargas-Magana M., et al., eprint arXiv:1312.4996

BOSS UPDATE ON QUASARS

T. DELUBAC
On behalf of the BOSS collaboration
[1]*CEA, Centre de Saclay, IRFU, F-91191 Gif-sur-Yvette, France*
[2]*Laboratoire d'astrophysique, Ecole Polytechnique Fédérale de Lausanne (EPFL), Observatoire de Sauverny, CH-1290 Versoix, Switzerland*

We report detection of the Baryon Acoustic Oscillations (BAO) peak in the auto-correlation function of the Lyman-α forest as well as in the cross-correlation of the Lyman-α forest with quasars. The studies use 137,562 quasars spectra from the Baryon Oscillations Spectroscopic Survey (BOSS) from the SDSS-III eleventh data release (DR11). We obtain a 3% constraint on $H(z = 2.34)$ from the auto-correlation function alone.

1 Introduction

The position of the Baryon Acoustic Oscillations (BAO) peak in the matter correlation function can be used as a tool to constrain cosmological models. If observed transverse to the line of sight, it appears at an angular separation given by $\Delta\theta = r_d/[(1+z)D_A(z)]$ where z is the redshift of the measurement, r_d is the sound horizon at the drag epoch and D_A is the angular distance. If observed along the line of sight, the BAO peak appears at a redshift separation of $\Delta z = r_d/D_H(z)$ where $D_H = c/H$ is the Hubble distance.

The BAO peak has been observed for the first time in the correlation function of galaxy redshift surveys [1,2]. Using a sample of nearly one million galaxies, the Baryon Oscillations Spectroscopic Survey (BOSS) of SDSS-III has obtained detections of the BAO peak at redshifts 0.32 and 0.57 with significances greater than 7σ [3].

To probe higher redshifts, it is possible to use the Lyman-α forest of quasar. The Lyman-α forest corresponds to a succession of absorption lines in quasar spectra caused by the neutral hydrogen (HI) of the intergalactic medium (IGM) and can be used to trace mass. An example of a quasar spectrum obtained by BOSS is shown in figure 1. The first detection of the BAO peak in the auto-correlation function of the Lyman-α forest was obtained by the BOSS collaboration using a sample of nearly 49,000 quasar spectra [4,5].

In the following we report new measurements [6,7] of the BAO peak using the eleventh data release (DR11) of the SDSS-III. Section 2 details the quasar sample used while sections 3 and 4 present BAO detections respectively in the Lyman-α forest auto-correlation function and in the Lyman-α forest - quasar cross-correlation.

2 The BOSS quasar sample

DR11 contains 158,401 visually inspected quasars with $2.1 \leq z_q \leq 3.5$ covering 8377 deg^2 on the sky. The footprint is visible in figure 1. The visual inspection [8] allows to verify the automated classification, redshift estimation and to flag atypical spectra. After a few quality cuts, our

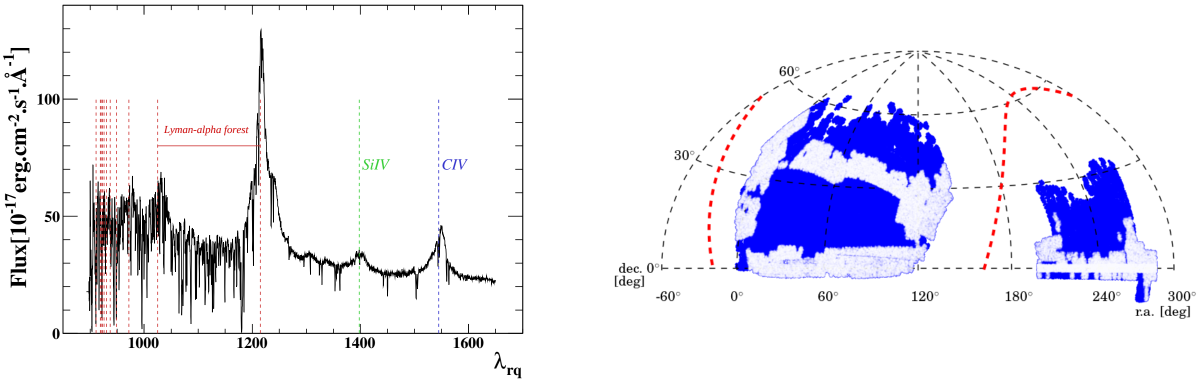

Figure 1 – *Left panel:* Example of a quasar spectrum from BOSS transposed in the rest-frame of the quasar. The strong Lyman-α emission of the quasar is visible at 1215Å together with other emission lines such as SiIV and CIV. The vertical red dashed lines indicate the Lyman series in the quasar rest frame with the rightmost line being the Lyman-α. The succession of absorptions by the HI of the IGM is visible on the lefthand side of the Lyman-α emission of the quasar. The Lyman-α forest is define as the region between the Lyman-α and the Lyman-β lines. *Right panel:* Footprint of the 158,401 quasars of DR11 (blue) compared to the footprint of quasars used for the first BAO detections (white). The red dashed line corresponds to the galactic plane.

sample is reduced to 137,562 quasars. In our analysis, we only consider pixels of the Lyman-α forest in the rest-frame wavelength interval $1040 < \lambda_{rf} < 1200$ Å. We do not include pixels closer to the quasar Lyman-α and Lyman-β emission lines to avoid contamination from the large pixel variance on the slope of the two lines due to an important quasar to quasar diversity of emission amplitude. The mean redshift of the pixel pairs is 2.34. This corresponds to the redshift at which we measure the auto-correlation function.

3 Measurement of the Lyman-α auto-correlation function

We compute the full two dimensional correlation function as well as its covariance matrix in comobile coordinates using a flat ΛCDM fiducial model with $(\Omega_M = 0.27, h = 0.7)$. Figure 2 shows the resulting correlation function parallel to the line of sight. The BAO peak is clearly visible with an overall significance of detection of 5σ.

3.1 Fitting procedure

The fit of the correlation function is performed using a model composed of a cosmological term and a "broadband" term. The cosmological term consists of the linear-theory matter power spectrum obtained from CAMB [9] on top of which we have added nonlinear effects plus the Lyman-α forest bias and redshift-space distortion parameters. The broadband term is a smooth component that makes the fit insensitive to non-BAO cosmology, astrophysical effects (e.g. damped Lyman-α, UV fluctuations, etc.) and to distortions introduced by the analysis.

3.2 Mock spectra

To test our fitting procedure, we analysed 100 sets of mock spectra [10,11]. Each mock realisation is composed of the same number of quasar as DR11 with the same angular positions on the sky and redshifts. Those mock data sets allow us to look for potential systematics in the recovering of the BAO peak position and to verify that confidence intervals are correctly estimated. This exercise did not revealed any significant systematic in the fitting procedure.

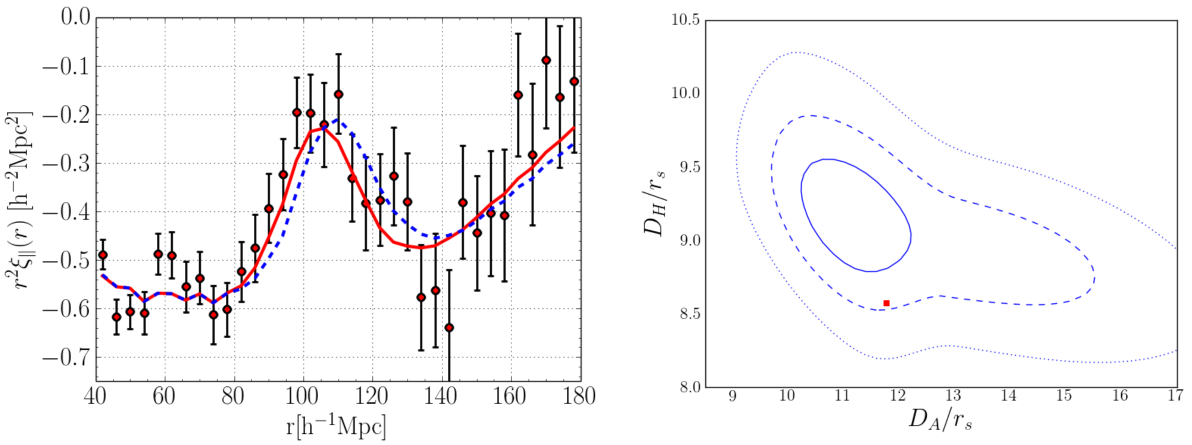

Figure 2 – *Left panel:* The line of sight Lyman-α auto-correlation function. The BAO peak is clearly visible at about 105 h^{-1}Mpc. The blue dashed line corresponds to the fiducial model while the red line corresponds to the best fit model.
Right panel: 1, 2 and 3σ constraints on D_H/r_d and D_A/r_d obtained from the position of the BAO peak in the correlation function ($r_s = r_d$). The red square corresponds to Planck best fit value for a flat ΛCDM model [12].

3.3 Cosmological constraints

The constraints on $D_H(2.34)/r_d$ and $D_A(2.34)/r_d$ obtained from the fit of the data are shown in figure 2. Those can be expressed as constraints over $H(z = 2.34)$ and $D_A(z = 2.34)$ as follow:

$$\begin{aligned} H(z = 2.34) &= (222 \pm 7\,\mathrm{km\,s^{-1}\,Mpc^{-1}}) \times \frac{147.4\,\mathrm{Mpc}}{r_d} \\ D_A(z = 2.34) &= (1662 \pm 96\,\mathrm{Mpc}) \times \frac{r_d}{147.4\,\mathrm{Mpc}}, \end{aligned} \tag{1}$$

where the value of r_d is taken from Planck [12]. The constraints are more stringent on H than on D_A. This is due to the strength of the redshift-space distortions in the Lyman-α forest that enhance the BAO peak along the line of sight but not in the transverse direction. Note that those constraints are independent of the fiducial cosmology.

4 Measurement of the quasar-Lyman-α cross-correlation function

Together with the Lyman-α forest auto-correlation function, we computed the cross-correlation of the Lyman-α forest with the quasars, i.e. the correlation between the position of the quasars and the Lyman-α forest pixels. The resulting constraints on the position of the BAO peak in the cross-correlation are shown in figure 3. While the constraint on H is slightly weaker than the one of the Lyman-α auto-correlation function, the constraint on D_A is tighter. This is because of the high bias together with the low redshift-space distortions of the quasars. It is worth mentioning that while the auto-correlation and cross-correlation functions use the same data, they are limited by entirely different kinds of noise. The auto-correlation function is limited by aliasing and instrumental noises while the cross-correlation function is limited by shot noise. Therefore the constraints coming from the two measurements can in principle be directly combined [6].

Acknowledgements

Funding for SDSS-III has been provided by the Alfred P. Sloan Foundation, the Participating Institutions, the National Science Foundation, and the U.S. Department of Energy Office of Science. The SDSS-III web site is http://www.sdss3.org/.

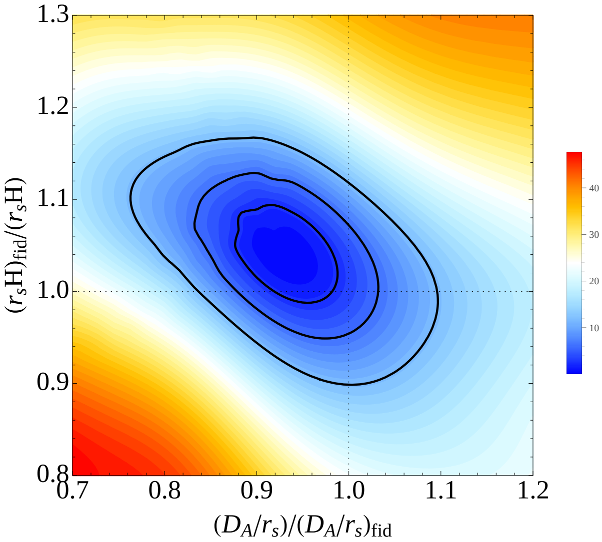

Figure 3 – same figure with draft option (left), normal (center) and rotated (right)

SDSS-III is managed by the Astrophysical Research Consortium for the Participating Institutions of the SDSS-III Collaboration including the University of Arizona, the Brazilian Participation Group, Brookhaven National Laboratory, Carnegie Mellon University, University of Florida, the French Participation Group, the German Participation Group, Harvard University, the Instituto de Astrofisica de Canarias, the Michigan State/Notre Dame/JINA Participation Group, Johns Hopkins University, Lawrence Berkeley National Laboratory, Max Planck Institute for Astrophysics, Max Planck Institute for Extraterrestrial Physics, New Mexico State University, New York University, Ohio State University, Pennsylvania State University, University of Portsmouth, Princeton University, the Spanish Participation Group, University of Tokyo, University of Utah, Vanderbilt University, University of Virginia, University of Washington, and Yale University.

The French Participation Group of SDSS-III was supported by the Agence Nationale de la Recherche under contracts ANR-08-BLAN-0222 and ANR-12- BS05-0015-01.

Timothée Delubac acknowledge support from the ERC advanced grant LIDA.

References

1. Eisenstein D. J., Zehavi, I., Hogg, D.W. et al. 2005, ApJ, 633, 560
2. Cole, S. et al. 2005, MNRAS, 362, 505
3. Anderson, L., Aubourg, É., Bailey, S., et al. 2014, MNRAS, 441, 24
4. Busca, N.G. et al. 2013, A&A, 552, 96
5. Slosar, A, V. Irsic, D. Kirkby, et al. 2013, J. Cosmology Astropart. Phys., 04, 026
6. Delubac, T., Bautista, J. E., Busca, N. G., et al. 2014, arXiv:1404.1801
7. Font-Ribera, A., D. Kirkby, N. Busca et al. 2013, arXiv:1311.1767, submitted to J. Cosmology Astropart. Phys.
8. Pâris, I., P. Petitjean, E. Aubourg et al. 2013, arXiv:1311.4870
9. Lewis, A., A. Challinor & A. Lasenby 2000, ApJ, 538, 473
10. Font-Ribera, A., P. McDonald & J. Miralda Escudé 2012, J. Cosmology Astropart. Phys., 01, 001
11. Bautista, J. et al. 2014, in preparation
12. Ade, P. A. R., N. Aghanim, C. Armitage-Caplan, et al. 2013, arXiv:1303.5076

Robust measurements of the clustering of photometric quasars through blind mitigation of systematics

Boris Leistedt and Hiranya V. Peiris [a]
Department of Physics and Astronomy, University College London, London WC1E 6BT, U.K.

1 Motivation

Quasars are bright, highly biased tracers of the large scale structure (LSS) of the universe, and are useful for testing cosmological models in large volumes and over extended redshift ranges. In particular, photometric quasar surveys can be used to tightly constrain primordial non-Gaussianity (PNG) of local type, parametrised by the parameter $f_{\rm NL}$, which is predicted to enhance the bias of LSS tracers on large scales [*e.g.,* 1, 2, 3]. However, this requires accurate auto- and cross-correlation power spectrum measurements, which are complicated by the presence of significant systematics in the data. These systematics can be intrinsic (*e.g.,* dust extinction), observational (*e.g.,* seeing, airmass), or instrumental (*e.g.,* instrument calibration), and affect the properties of the raw images in complex ways, propagating into the final quasar catalogues, and creating spurious spatial correlations. Previous studies of the clustering of quasars from the Sloan Digital Sky Survey (SDSS) exhibited power excesses on large and small scales [*e.g.,* 4], which were even more significant in the DR6 photometric quasar catalogue [5]. Although cuts to the data were not sufficient to remove this excess power, thus pointing to PNG [6, 7, 8, 9, 10], recent work has demonstrated that the excess power was due to systematics [11, 12, 13] and could be eliminated using mode projection [14].

2 Data samples

We consider the XDQSOz catalogue of photometric quasars [15], which contains quasar candidates selected from the set of point sources of the SDSS DR8 imaging data, covering $\sim 10^4$ deg^2 of the southern and northern Galactic sky. We consider all objects with $\mathrm{P}_{\mathrm{QSO}} > 0.8$, and exclude regions of the sky with $\textsc{Psfwidth}_i > 2.0$, $\textsc{Score} > 0.6$, and $E(B-V) > 0.08$, to remove more dusty regions in the South Galactic Cap. XDQSOz also includes photometric redshift estimates $\hat{z}_p$, defined as the highest peak in the posterior distribution of the individual photo-z estimates. We separate this catalogue into four samples by selecting objects with photometric redshifts $\hat{z}_p$ in top-hat windows ranging $[0.5, 1.35]$, $[1.35, 1.7]$, $[1.7, 2.2]$ and $[2.2, 3.5]$, which have comparable numbers of objects, and thus similar shot noise.

---

[a] boris.leistedt.11, h.peiris@ucl.ac.uk

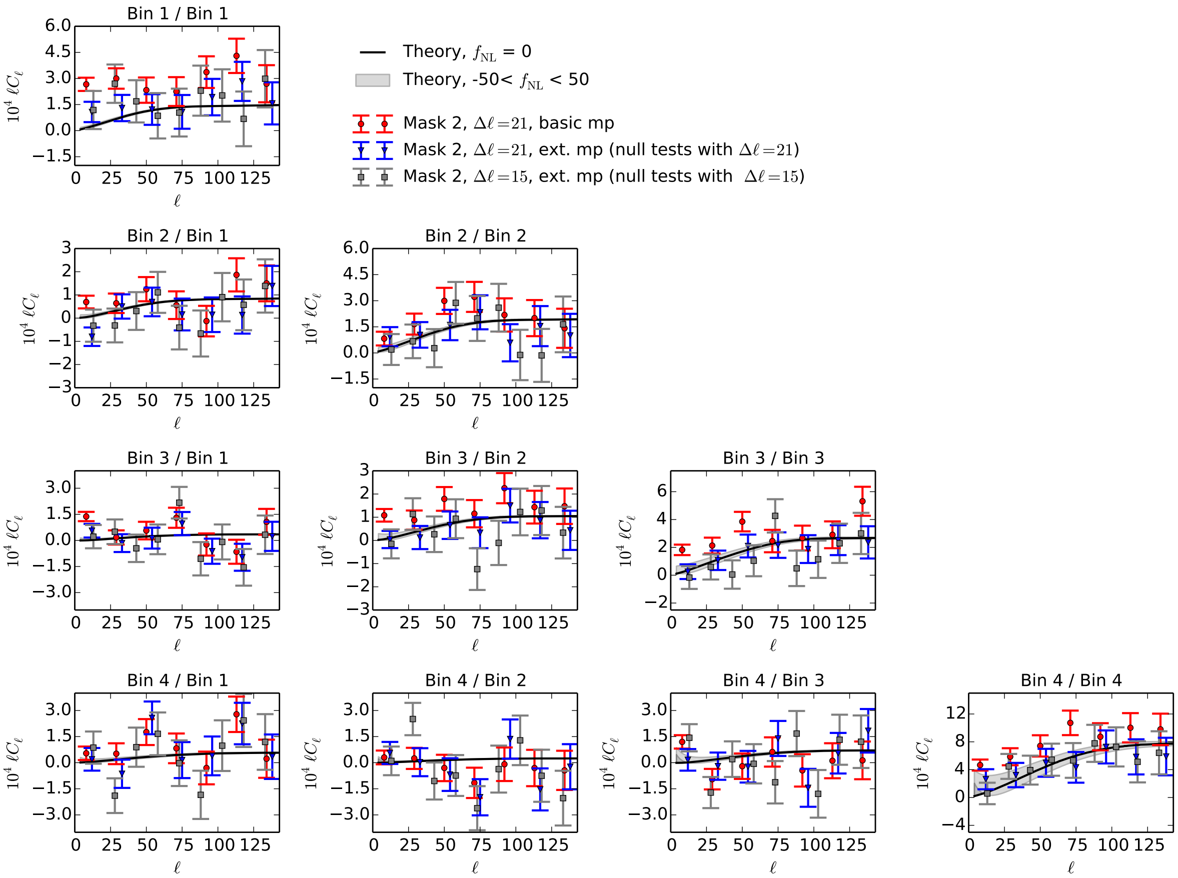

Figure 1 – Angular power spectra of the four XDQSOz quasar samples. The effects of systematics are mitigated using either simple mode projection (linear contamination model of ~ 200 templates), or the novel extended mode projection approach (quadratic model with $\sim 20,000$ templates, decorrelated on the sky and cross-correlated with the data). See text and Ref. [17] for more details.

3 Power spectrum measurements

We use a Quadratic Maximum Likelihood estimator (QML) to simultaneously estimate the angular power spectra of these four quasar samples. The resolution of the data and the settings of the estimator are fixed to obtain accurate power spectra for $\ell \in [2, 140]$ (smaller scales are dominated by shot noise).

Following the approach of Ref. [14], we create a set of 220 templates of potential systematics, using external data (*e.g.,* maps of extinction by dust and stellar density), and numerous calibration and observing condition quantities. Figure 1 shows the power spectra resulting from the QML estimator when projecting out the modes of this base set of templates ('basic mp'). The black lines denote the theoretical power spectra corresponding to a *Planck* ΛCDM cosmology [16], $f_{\rm NL} = 0$, and fiducial linear quasar bias $b(z) = 1+[(1+z)/2.5]^5$. The shaded band indicates the zone spanned by the theory curves when varying $-50 < f_{\rm NL} < 50$.

Projecting out these templates in the estimator is equivalent to marginalizing their linear effect on the quasar maps, therefore removing their influence on the measured power spectra to first order. However, the latter still suffer from excess power on large scales when compared to the theoretical prediction. This points to significant non-linear effects of the systematics, which cannot be addressed by marginalizing over the base templates.

4 Extended mode projection

To enable a more complicated treatment of systematics and cleaner power spectrum measurements, we exploit a novel technique of extended mode projection. This involves having a more complete set of systematics templates but only projecting out the ones which are significantly correlated with the data. For this purpose, we complement the base set of systematics with pairs of products of them, yielding a set of $\sim 20,000$ templates. We then decorrelate them on the sky, by applying a principal component analysis and discarding the modes with eigenvalues consistent with noise or numerical precision, leading to $\sim 3,700$ uncorrelated templates (replacing the $\sim 20,000$ input templates). We then cross-correlate each template with the four data samples in order to obtain cross-angular power spectra which can be used as null tests. We only marginalize (through mode projection) over the modes which fail the null tests, *i.e.,* which cross-power spectra are not consistent with zero, as measured by the reduced χ^2 using a simple gaussian likelihood. Figure 1 shows the results of this approach with two multipole resolutions $\Delta\ell = 15$ and $\Delta\ell = 21$. In both cases, the excess power due to systematics is eliminated, and the measurements are in good agreement with the theoretical predictions, while not showing further evidence for contamination by systematics (i.e., their effects lie within the statistical errors).

5 Conclusions

The effects of systematics on angular power spectrum measurements can be robustly marginalized through mode projection [14]. However, quasar surveys are subject to strong non-linear systematics which require a more complicated treatment, for example involving non-linear contamination models with large numbers of templates. Extended mode projection can deal with this setting by decorrelating the templates and only projecting out the ones which are significantly correlated with the data. This approach is entirely based on mapping potential systematics and performing null tests with the data, and is therefore a robust way to handle systematics in a blind fashion. More details on extended mode projection and the power spectra of the XDQSOz data can be found in Ref. [17].

Figure 1 also demonstrates that the measured power spectra reach a sufficient precision and robustness to constrain PNG, which effect is significant on large scales. The constraints on PNG from the XDQSOz power spectra are presented in Ref. [18].

References

[1] N. Dalal, O. Doré, D. Huterer, and A. Shirokov. Imprints of primordial non-Gaussianities on large-scale structure: Scale-dependent bias and abundance of virialized objects. *Phys. Rev. D.*, 77(12):123514, June 2008.

[2] S. Matarrese and L. Verde. The Effect of Primordial Non-Gaussianity on Halo Bias. *Astrophys. J. Lett.*, 677:L77–L80, April 2008.

[3] M. LoVerde, A. Miller, S. Shandera, and L. Verde. Effects of scale-dependent non-Gaussianity on cosmological structures. *Astrophys. J. Lett.*, 4:14, April 2008.

[4] A. D. Myers, R. J. Brunner, G. T. Richards, R. C. Nichol, D. P. Schneider, and N. A. Bahcall. Clustering Analyses of 300,000 Photometrically Classified Quasars. II. The Excess on Very Small Scales. *Astrophys. J.*, 658:99–106, March 2007.

[5] G. T. Richards, A. D. Myers, A. G. Gray, R. N. Riegel, R. C. Nichol, R. J. Brunner, A. S. Szalay, D. P. Schneider, and S. F. Anderson. Efficient Photometric Selection of Quasars from the Sloan Digital Sky Survey: II. ˜1,000,000 Quasars from Data Release Six. *Astrophys. J. Supp.*, 180(1):67, 2009.

[6] J.-Q. Xia, M. Viel, C. Baccigalupi, and S. Matarrese. The high redshift Integrated Sachs-Wolfe effect. *Journal of Cosmology and Astroparticle Physics*, 9:3, September 2009.

[7] J.-Q. Xia, C. Baccigalupi, S. Matarrese, L. Verde, and M. Viel. Constraints on primordial non-Gaussianity from large scale structure probes. *Journal of Cosmology and Astroparticle Physics*, 8:33, August 2011.

[8] Tommaso Giannantonio, Robert Crittenden, Robert Nichol, and Ashley J. Ross. The significance of the integrated sachswolfe effect revisited. *Mon. Not. Roy. Astron. Soc.*, 426(3):2581–2599, 2012.

[9] D. Karagiannis, T. Shanks, and N. P. Ross. Search for primordial non-Gaussianity in the quasars of SDSS-III BOSS DR9. *ArXiv e-prints*, October 2013.

[10] T. Giannantonio, A. J. Ross, W. J. Percival, R. Crittenden, D. Bacher, M. Kilbinger, R. Nichol, and J. Weller. Improved Primordial Non-Gaussianity Constraints from Measurements of Galaxy Clustering and the Integrated Sachs-Wolfe Effect. *ArXiv e-prints*, March 2013.

[11] A. R. Pullen and C. M. Hirata. Systematic effects in large-scale angular power spectra of photometric quasars and implications for constraining primordial nongaussianity. *ArXiv e-prints*, December 2012.

[12] N. Agarwal, S. Ho, A. D. Myers, H.-J. Seo, A. J. Ross, N. Bahcall, J. Brinkmann, D. J. Eisenstein, D. Muna, N. Palanque-Delabrouille, I. Pâris, P. Petitjean, D. P. Schneider, A. Streblyanska, B. A. Weaver, and C. Yèche. Characterizing unknown systematics in large scale structure surveys. *ArXiv e-prints*, September 2013.

[13] S. Ho, N. Agarwal, A. D. Myers, R. Lyons, A. Disbrow, H.-J. Seo, A. Ross, C. Hirata, N. Padmanabhan, R. O'Connell, E. Huff, D. Schlegel, A. Slosar, D. Weinberg, M. Strauss, N. P. Ross, D. P. Schneider, N. Bahcall, J. Brinkmann, N. Palanque-Delabrouille, and C. Yèche. Sloan Digital Sky Survey III Photometric Quasar Clustering: Probing the Initial Conditions of the Universe using the Largest Volume. *ArXiv e-prints*, November 2013.

[14] B. Leistedt, H. V. Peiris, D. J. Mortlock, A. Benoit-Lévy, and A. Pontzen. Estimating the large-scale angular power spectrum in the presence of systematics: a case study of Sloan Digital Sky Survey quasars. *Mon. Not. Roy. Astron. Soc.*, 435:1857–1873, November 2013.

[15] J. Bovy, A. D. Myers, J. F. Hennawi, D. W. Hogg, R. G. McMahon, D. Schiminovich, E. S. Sheldon, J. Brinkmann, D. P. Schneider, and B. A. Weaver. Photometric Redshifts and Quasar Probabilities from a Single, Data-driven Generative Model. *Astrophys. J.*, 749:41, April 2012.

[16] Planck Collaboration. Planck 2013 results. XVI. Cosmological parameters. *ArXiv e-prints*, March 2013.

[17] B. Leistedt and H. V. Peiris. Exploiting the full potential of photometric quasar surveys: Optimal power spectra through blind mitigation of systematics. *ArXiv e-prints*, 2014.

[18] B. Leistedt, H. V. Peiris, and N. Roth. Constraints on primordial non-Gaussianity from 800,000 photometric quasars. *ArXiv e-prints*, 2014.

The shape of the universe and cosmological parameters estimation

A. BLANCHARD[1] & Y. ZOLNIEROWSKI[2]
[1] *Université de Toulouse, UPS-OMP, IRAP*
CNRS, UMR 5277
31400 Toulouse, France
[2] *LAPP, Université de Savoie, CNRS/IN2P3*
9 Chemin de Bellevue, BP 110, 74941 Annecy-le-Vieux, France

Current tight observational constraints on cosmological parameters describing the universe depend on the nature of the initial fluctuations, regardless of the model and the theory of gravity, which is generally assumed to be general relativity (GR). Of particular interest, its spatial curvature is well constrained in standard model but these constraints do not result from purely geometrical measurements and depend on its energy contents as well as on theory of gravity one uses. Newtonian approach allows to derive dynamical evolution of the expansion, but the connection to spatial curvature is specified by general relativity. We examine the constraints that can be placed on the these quantities from commonly used cosmological probes if GR is not assumed. This approach can lead to a new vision on the subject of cosmological parameters estimation, allowing to test GR in cosmology at the background level.

1 Introduction

In modern cosmology the inflation paradigm is certainly one of the most prolific idea allowing the possible investigation of fundamental physics at energy scale potentially close to the Planck scale, which is likely to remain unreachable by direct means. The possible detection of B-modes as recently claimed offers the very specific confirmation of this paradigm. Another prediction of inflation was the (nearly) flatness of the universe, at least on the scale of the observable universe. Modern constraints as those established by appropriate combination of relevant cosmological observations, including the statistical properties of the CMB fluctuations, provide a convincing evidence for a flat geometry of our 3D space as first established by Lineweaver and Barbosa[3]. The recent measurements by Planck, combined with high-l CMB data and BAO have allowed a very tight constraint on Ω_k[6]:

$$\Omega_k = -0.0005 \pm 0.0065 \tag{1}$$

This limit however does not result from an actual **geometrical test** on our 3D space and is intimaly related to the assumptions of the model (LCDM within GR). This limit cannot therefore been regarded as a limit on the actual curvature of space. It is well known that luminosity (or angular-diameter) distance measurements do not allow to determine the curvature scale[8]. Constraints within the framework of GR depend on assumptions on the dark energy components[2]. Allowing large flexibility on dark energy behavior Okouma et al. [5] found a more relax constraint:

$$-0.12 \leq \Omega_k \leq 0.01 (2\sigma) \tag{2}$$

ten times wider than the above range from Planck.The actual curvature of space can in principle be obtained in a totally model independent way within a metric theory of space time, from the measurement of the proper distance[1] or the look back time, but in practice using present-day data, such an approach leads to a rather wide range of allowed values[4].

2 From Newtonian Cosmology to General Relativity (GR)

The metric description of space-time is provide by the RW metric:

$$ds^2 = -c^2 dt^2 + a(t)^2 [r^2 (d\theta^2 + \sin^2\theta d\phi^2) + \frac{dr^2}{1 - kr^2}] \tag{3}$$

k being -1, 0, +1 according to the sign of curvature. Angular distance can be expressed through the general matting relation:

$$r = S_k \left(\int_{t_S}^{t_0} \frac{c dt}{a(t)} \right) \tag{4}$$

It is interesting to remember that one can derive the dynamical equation driving the scale factor $a(t)$ of the universe from purely Newtonian arguments, assuming that $\rho + 3P$ is the source of gravity :

$$\dot{a}^2 + K = \frac{8\pi G}{3} \sum \rho a^2. \tag{5}$$

where K in an *arbitrary* constant. This constant is set in GR and gives:

$$K = c^2 \tag{6}$$

so that GR *predicts* the value of the curvature in connection to its energy contents:

$$\Omega_k = \frac{-kc^2}{H^2 a^2} = 1 - \sum \Omega_{contents} \tag{7}$$

Clearly verifying this equality is testing GR at the background level. Accordingly, we defined two Ω_k. The first one being directly connected to the true spatial curvature:

$$\Omega_{kgeo} = -\frac{k}{(a_0 H_0)^2} \tag{8}$$

and the second one being connected to the energy contents, i.e. source of gravity :

$$\Omega_{kdyn} = 1. - \sum \Omega_{contents} \tag{9}$$

Going back to classical tests, SNIa Hubble diagram, Cosmic microwave background fluctuations, BAO, we can fit data using a new degree of freedom with Ω_{kgeo} and Ω_{kdyn}.

However, it has been realized that the actual contents of the universe and their various equations of state cannot be determined from observations on a one by one basis, the total energy momentum being the only relevant quantity[2]. In practice, in the following, we first assume a classical matter content $w = 0$ and a dark energy component $w = -1$ and then examine the consequence of allowing a constant w with values in the $-3, 1$ interval. We used the usual combination of classical tests (SNIa, CMB, BAO), using reduced parameters as in Wang & Wang[7] and we examine constraints that can be set on our two Ω_k parameters. Results are presented Figure 1.

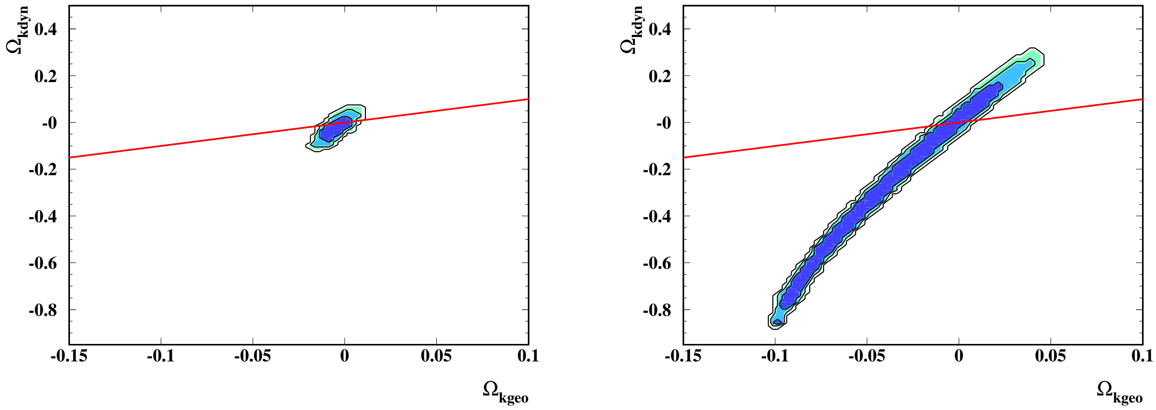

Figure 1 – Left : 1, 2 and 3 σ contours in the plane $\Omega_{kgeo} - \Omega_{kdyn}$ for models with a dark energy component $w = -1$. Right : 1, 2 and 3 σ contours in the plane for models with constant equation of state parameters w for the dark energy component and marginalized for $-3 < w < 3$.

3 Conclusions

We have established a new type of constraints on the curvature of space without assuming general relativity, allowing to separate clearly the curvature from the dynamics. This provides in principle a new test of general relativity at cosmological scale at the background level. With this approach we found :

$$\Omega_{kgeo} = -0.0095 \pm 0.0045 \tag{10}$$

$$\Omega_{kdyn} = -0.044 \pm 0.033 \tag{11}$$

for $w = -1$ and

$$\Omega_{kgeo} = -0.05 \pm 0.03 \tag{12}$$

$$\Omega_{kdyn} = -0.33 \pm 0.22 \tag{13}$$

when marginalized on w. Not surprisingly, there is a significant degeneracy between curvature and energy contents but general relativity is doing well with $w = -1$. Limits on Ω_{kdyn} is similar to those obtained in different approaches[5]. Our limits on Ω_{kgeo} is similar to the ones based on Planck, but clearly depends on our assumptions on dark energy : constant equation of state w and the speed of sound equal to unity. Investigation of more general dark energy models will be presented in a forthcoming work.

References

1. Clarkson, C., Cortês, M., & Bassett, B., *JCAP*, **8**, 11 (2007)
2. Kunz, M., *Phys. Rev.* D **80**, 123001 (2009).
3. Lineweaver, C. H., & Barbosa, D., *ApJ.* , **496**, 624 (1998)
4. Mortsell, E., & Jonsson, J. 2011, arXiv:1102.4485
5. Okouma, P. M., Fantaye, Y., & Bassett, B. A., *Phys. Lett.* B **719**, 1 (2013).
6. Planck Collaboration, Ade, P. A. R., Aghanim, N., et al. 2013, arXiv:1303.5076
7. Wang, Y. & Wang, S., *Phys. Rev.* D **88**, 043522 (2013).
8. Weinberg, S., *ApJ. Lett.*, **161**, L233 (1970)

H-ATLAS HIGH-Z SOURCES: AN OPTIMAL SAMPLE FOR CROSS-CORRELATION ANALYSES

J. GONZÁLEZ-NUEVO
Inst. de Fisica de Cantabria (CSIC-UC), Avda. los Castros s/n, 39005 Santander, Spain
SISSA, Via Bonomea 265, I-34136 Trieste, Italy

A. LAPI
Dipartimento di Fisica, Università di Roma 'Tor Vergata', Via Ricerca Scientifica 1, 00133 Roma, Italy
SISSA, Via Bonomea 265, I-34136 Trieste, Italy

F. BIANCHINI
SISSA, Via Bonomea 265, I-34136 Trieste, Italy

We report a highly significant ($> 10\sigma$) spatial correlation between galaxies with $S_{350\mu\mathrm{m}} \geq 30\,\mathrm{mJy}$ detected in the equatorial fields of the *Herschel* Astrophysical Terahertz Large Area Survey (H-ATLAS) with estimated redshifts $\gtrsim 1.5$, and SDSS or GAMA galaxies at $0.2 \leq z \leq 0.6$. The significance of the cross-correlation is much higher than those reported so far for samples with non-overlapping redshift distributions selected in other wavebands.

1 Introduction

Light rays coming from a distant source are deflected by the foreground gravitational field. This, on the one hand, stretches the area of a given sky region, thus decreasing the surface density of sources and, on the other hand, magnifies the background sources, increasing their chances of being included in a flux-limited sample. The net effect, termed "magnification bias", is extensively described in the literature (see, e.g., Schneider et al.[1]). It implies that an excess/decrease of background sources from a flux-limited sample will be found in the vicinity of matter overdensities. Thus, gravitational lensing constitutes a direct probe of the cosmic gravitational field.

The most dramatic manifestations of lensing, called "strong lensing", which includes multiple images, arcs or "Einstein rings", are rare however. These manifestations show up on angular scales of arcseconds and provide information on high density structures such as galaxies or galaxy clusters. The lower density structures, which include most of the mass in the Universe, nevertheless, can still produce observable effects via "weak lensing". An unambiguous manifestation of weak lensing is the cross-correlation between two source samples with non-overlapping redshift distributions.

Since gravitational magnification decreases the effective detection limit, the amplitude of the magnification bias increases with increasing steepness of the number counts of background sources, and is then particularly large at sub-mm wavelengths, where the counts are extremely steep. As demonstrated by Negrello et al.[2] this property can be used to effectively identify strongly lensed galaxies in the sub-mm band, opening a new era of gravitational lensing studies. At the same time, for a survey covering a sufficiently large area the counteracting effect on the

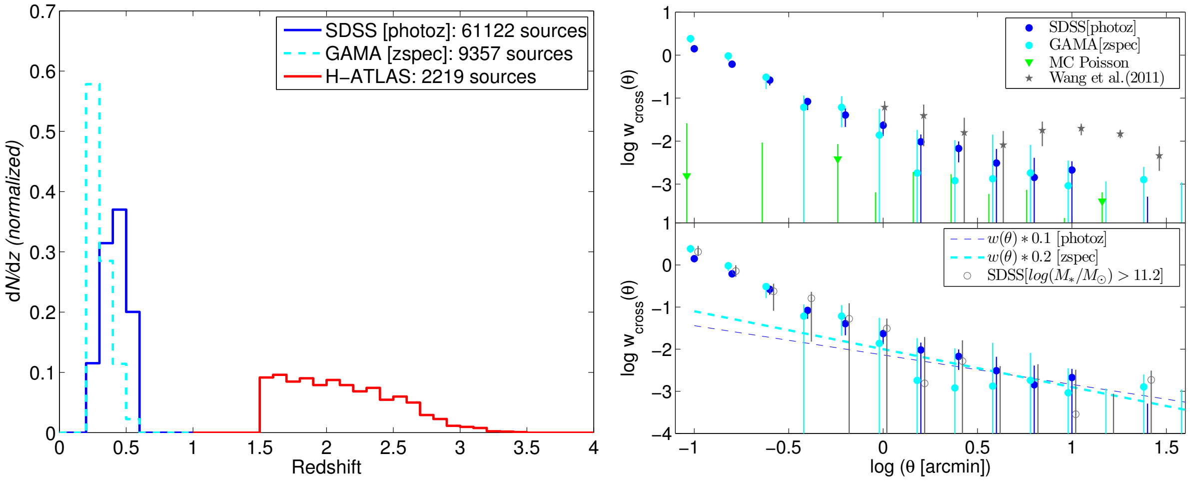

Figure 1 – *Left panel*: Redshift distributions of the background H-ATLAS sample (red histogram), the SDSS photometric sample (in blue), and the GAMA spectroscopic one (in cyan) for one of the tiles. *Top right panel*: Cross-correlation between the H-ATLAS sample and the photometric and spectroscopic foreground samples (blue and cyan circles, respectively). Measurements from Wang et al.[4] are also plotted for comparison (grey stars). The green upper limits are the result of ∼ 2000 realistic Monte Carlo simulations, not accounting for the effect of lensing. Such simulations were made to check our procedure and to further illustrate the significance of the detected cross-correlation signal. *Bottom right panel*: comparison of the measured cross-correlations with the auto-correlation functions of the photometric and spectroscopic foreground samples, scaled down by a factor of ∼ 10 (blue dashed line) and ∼ 20 (cyan dashed lines), respectively. The cross-correlation between the H-ATLAS sample and the photometric foreground sample, limited to $\log(M_\star/\mathrm{M}_\odot) > 11.2$, is also shown.

solid angle is small. A substantial fraction of galaxies detected by deep large area *Herschel* surveys at 250, 350 and 500 μm with the Spectral and Photometric Imaging Receiver (SPIRE) reside at $z \gtrsim 1.5$[3] and therefore constitute an excellent background sample for the Sloan Digital Sky Survey (SDSS) galaxies, which are located at $z \lesssim 0.8$ (with a median redshift of $z \sim 0.1$).

2 Sample selection

We have selected our background sample from the catalogue of sources detected in the three H-ATLAS equatorial fields, covering altogether $\simeq 161\,\mathrm{deg}^2$. The H-ATLAS is the largest area extragalactic survey carried out by the *Herschel* space observatory, covering $\sim 550\,\mathrm{deg}^2$ with PACS and SPIRE instruments between 100 and 500 μm.

To extract high-redshift ($z \geq 1.5$) candidate galaxies we have adopted, similar to Lapi et al.[3], the following criteria: (i) 250 μm flux density $S_{250} \geq 35\,\mathrm{mJy}$; (ii) no Sloan Digital Sky Survey (SDSS) counterpart with reliability $R > 0.8$, as determined by Smith et al.[5]; and (iii) $\geq 3\sigma$ detection at 350 μm.

Our background sample comprises all sources with photometric redshift $z \geq 1.5$, 26,630 sources in total. The photometric redshifts were estimated in the same way as in Lapi et al.[3] and Gonzalez-Nuevo et al.[6]. The estimated redshift distribution of selected sources in one of the "tiles" (one of the four partially overlapping regions that compose each of the three regions) is shown in Fig. 1. Similar redshift distributions are found with the other tiles. The accuracy of our photometric redshift estimates is enough to avoid any overlap with foreground sources, for which we require $z \leq 0.6$.

The main foreground sample is extracted from the Ninth Data Release (DR9) of the SDSS and comprises all galaxies in the H-ATLAS fields with $r < 22$ and *photometric* redshifts in the range $0.2 \leq z \leq 0.6$ (hereafter the *photoz* sample). We have arbitrarily set a lower limit of $M_\star > 10^{10.4}\mathrm{M}_\odot$ and we have also imposed an upper limit to the r-band luminosity, $L_r < 10^{11.6}\mathrm{L}_\odot$, in order to remove sources with anomalously bright r-band luminosities. The sample comprises $\sim 5 \times 10^4$ galaxies per tile, i.e. 686,333 galaxies in total. The redshift distribution for one of the tiles is shown by the blue histogram in Fig. 1. The median value is $z_{\rm phot,med} = 0.42$.

Accurate redshift measurements of the foreground sources are important to carry out realistic simulations of the effect of the gravitational lensing, which is related to the relative angular diameter distances between the observer, the lens and the source. On account of that, we have also defined a spectroscopic sample (hereafter the *zspec* sample) drawn from the GAMA II spectroscopic survey.[7] The GAMA II equatorial survey regions are 12° × 5° in size, and were surveyed down to a limit of $r < 19.8$ mag. For our *zspec* sample we select all GAMA II galaxies (from TilingCatv40) with reliable redshift measurements and $0.2 < z < 0.6$. This sample is smaller than the *photoz* one. It comprises $\simeq 9000$ galaxies per tile, i.e. 101,514 galaxies in total. Their median redshift, $z_{\rm spec,med} = 0.28$ is significantly lower than for the *photoz* sample, as shown by the cyan histogram in Fig. 1. Note that the magnification is far less sensitive to errors in the photometric redshifts of background sources, $\sigma_z \simeq 0.115(1+z)$, since they have a small effect on the ratios of observer–source/lens–source angular diameter distance ratios.

3 Cross-correlation functions

The cross-correlation function of two population of sources is the fractional excess probability, relative to a random distribution, of finding a source of population 1 and a source of population 2, respectively, within infinitesimal solid angles separated by an angle θ. We have computed the cross-correlation between our background and foreground samples using a modified version of the Landy & Szalay estimator

$$w_{\rm cross}(\theta) = \frac{\rm D_1D_2 - D_1R_2 - D_2R_1 + R_1R_2}{\rm R_1R_2} \tag{1}$$

where $\rm D_1D_2$, $\rm D_1R_2$, $\rm D_2R_1$ and $\rm R_1R_2$ are the normalized data1-data2, data1-random2, data2-random1 and random1-random2 pair counts for a given separation θ.

We have divided each tile in 16 equal-area mini-tiles (a total of 192) and we have estimated the median values and the associated uncertainties using the "median statistics" of Gott et al.[8]. Use of this procedure attempts to minimize the sample variance effect.

The measured angular cross-correlations between the foreground and background samples are shown in Fig. 1. The small angular scale limit is dictated by the H-ATLAS positional error (relatively to which the SDSS error is negligibly small) whose rms value at 250 μm is ~ 2.4 arcsec for $5\,\sigma$ sources. [9] To be conservative, we have limited our computations to angular scales $\gtrsim 6$ arcsec. Our results are in broad agreement with those of Wang et al.[4], although we do not confirm the strong signal reported by them on scales of tens of arcmin. The significance of the signal from the *photoz* sample is very high. This is in fact the best detection of lensing-induced cross-correlation reported so far.

The limited number of foreground galaxies slightly diminishes the significance of the signal derived from the *zspec* sample. However, the similarity between the signal from both foreground samples makes us confident that potential systematic uncertainties in the photometric redshift estimation are not an issue.

We have verified that below $20-30$ arcmin the measured cross-correlation is almost independent of the mini-tile size used. At larger angular scales the observed signal, using 16 or 4 mini-tiles per tile, are biased low. However, we decided to continue dividing the tiles in 16 smaller areas due to the lower uncertainties at angular scales below ~ 3 arcmin.

The bottom panel of Fig. 1 compares the measured cross-correlations with the auto-correlation functions of the photometric and spectroscopic foreground samples, scaled down by factors of ~ 10 and ~ 20, respectively. These factors correspond to the probability of lensing with moderate amplifications, $\mu < 2$, for the different median redshifts of the samples.[10] This comparison suggests that, above a few arcmin, the cross-correlation functions reflect the clustering properties of the foreground samples.

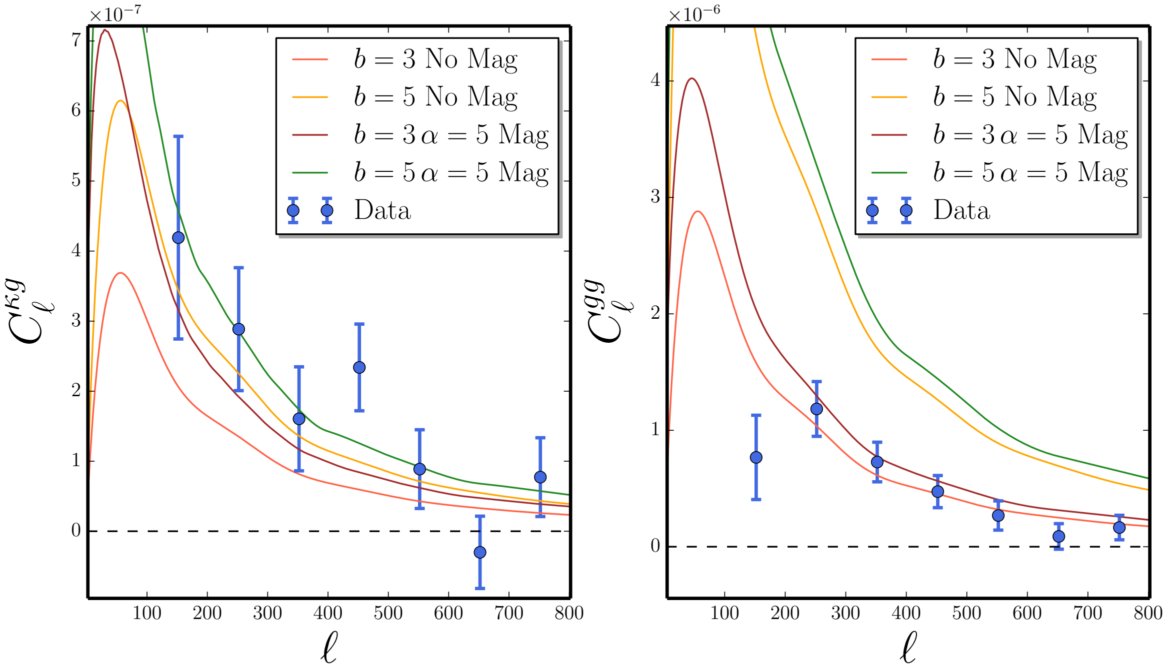

Figure 2 – Cross-correlation function between the high-z H-ATLAS sources and the lensing map of the cosmic microwave background (*left panel*) and the galaxy auto-correlation function (*right panel*). Different theoretical estimations of the expected bias is shown as a comparison.

Finally, we have checked that most of the cross-correlation signal for the *photoz* sample is produced by the most massive SDSS sources, $\log(M_\star/\mathrm{M}_\odot) > 11.2$ or $\log(M_h/\mathrm{M}_\odot) \gtrsim 13.2$ (Fig. 1, grey circles). However, the lower number of such objects translates into a larger uncertainty in the measured signal.

4 Assessment of the potential cross-contamination

As described in Sect. 2, we removed from the background sample those sources that have an SDSS counterpart with reliability R> 0.8, even if this requirement introduces a bias against H-ATLAS strongly lensed sources. However, for the rest of the background sources, so far we have assumed that errors on photometric redshifts do not cause any overlap between background and foreground samples.

The typical colour value used to separate between elliptical and spiral galaxies increases with redshift, but remains approximately constant around $g - r \sim 1.5$ in the redshift range $0.2 < z < 0.6$, for typical elliptical SEDs. We have checked that, for the background sources with $0.1 < \mathrm{R} < 0.8$, $\sim 91.4\%$ of the closest foreground sources have colours compatible with elliptical galaxies, $g - r > 1.5$, and therefore are expected to have sub-mm emission hardly detectable by *Herschel*. For the remaining $\sim 8.6\%$, following Gonzalez-Nuevo et al.[6], we have verified that the ratio between the r-band flux density and those at 350 and 500 μm are much higher than expected for spiral galaxies, or even for the median local starburst SED [11], both put at $z = 0.6$ (only $\sim 0.8\%$ and $\sim 8.3\%$ of the remaining sources shows compatible ratios). In other words, if those background sources were at $z < 0.6$, they would be brighter in the optical band and, as a consequence, with a reliability higher than R> 0.8. Therefore, from this photometric analysis, we estimated that the SDSS/GAMA sources that we could have incorrectly considered as H-ATLAS sources at $z > 1.5$ is lower than 0.7% (the median local starburst SED case).

The H-ATLAS parent sample selection procedure produces a redshift gaussian-like distribution peaked around $z \sim 2$ with a lower tail that extends until $z \sim 0.5$ (see Figure 4 of Lapi et al.[3]). By selecting only those sources with $z > 1.5$ we are minimizing the potential cross-contamination and maintaining the bulk of the sample at the same time. However, we can relax this minimum redshift in order to verify that, if an overlap exists, its cross-contamination effect in the measured cross-correlation signal is negligible. The measured signal remains almost the same independently of the lower redshift limit used, hence confirming the non-overlap assumption.

Finally, we have assessed the potential cross-contamination produced by a non-negligible fraction of mismatched background versus foreground sources. For this particular test, the background sources are randomly distributed and a fraction of them are randomly selected and moved to the position of randomly selected foreground ones. The results show that a $\sim 10\%$ contamination by overlapping background/foreground sources is ruled out, because it would yield a far stronger cross-correlation signal on scales ≥ 1 arcmin than measured for our samples, yet falling short of accounting for the observed signal on smaller scales.

5 Summary and future

We have reported a highly significant correlation between the spatial distribution of H-ATLAS galaxies with estimated redshift $\gtrsim 1.5$ and that of SDSS/GAMA galaxies at $0.2 \leq z \leq 0.6$. The cross-correlation is explained by weak gravitational lensing. The much higher significance compared to those reported so far is a result of the extreme steepness of the sub-mm source counts.

Future work will try to extract quantitative astrophysical information about the foreground dark matter halos by comparing the measured cross-correlation signal with dedicated simulations, considering the distribution of sub-halos and their densities, as well as observational constraints like angular resolution and sensitivity.

Let us conclude with drama by ‘spoilering’ some news from a related work in progress. We are exploiting the data of the full Herschel-ATLAS survey (about 550 deg^2) for yet another cross correlation analysis, this time involving the lensing map of the cosmic microwave background, as recently measured to an unprecedented sensitivity by the Planck satellite.[12]

How can a cross correlation of this kind happen? CMB photons, toward the travel from the last scattering surface toward us, are slightly deflected via gravitational lensing by the large-scale dark matter field, mainly in the (quasi-)linear regime; on the other hand, H-ATLAS galaxies constitute signposts of nonlinear, virialized dark matter structures. In the standard, hierarchical paradigm for structure formation, nonlinear objects are preferentially formed on the peaks of the underlying linear density field, thus a cross-correlation between the H-ATLAS galaxies and the CMB lensing is expected; even more, such a cross-correlation should contain information on the bias of nonlinear structures in the Universe.

Now take a seat and a profound breath. It is a pleasure to announce that for the first time we (preliminarily) detect such a cross-correlation signal at a robust significance (OK, we cannot tell you the number for obvious reasons, but it is not 2-sigma...), and we measure from the cross-correlation spectrum a value $b \sim 3 - 5$ of the bias for the H-ATLAS galaxies (see Fig. 2)!

This is somewhat higher than what can be estimated from the galaxy autocorrelation function (actually marginally consistent within the large uncertainties), and we are trying to understand the origin of this slight discrepancy. One possibility is constituted by the magnification bias effect mentioned at the beginning of this proceeding, that in principle acts differentially on the auto and cross correlation spectra, and if neglected would imply different bias determinations; in the present context it may be particularly relevant since H-ATLAS galaxies have steep slopes ($\alpha \gtrsim 5$) of their number counts. Preliminary tests (see Fig. 2) show that the effect may help in solving the issue.

Our results on the cross correlation between Herschel-ATLAS and Planck CMB lensing will be extensively presented and discussed in a forthcoming paper (Bianchini et al. in preparation), so stay tuned on the SISSA team.

Acknowledgments

The work has been supported in part by the Spanish Ministerio de Ciencia e Innovacion, AYA2012-39475-C02-01, and Consolider-Ingenio 2010, CSD2010-00064, projects and by ASI/INAF Agreement I/072/09/0 for the *Planck* LFI activity of Phase E2. JGN acknowledges financial support from the Spanish CSIC for a JAE-DOC fellowship, co-funded by the European Social Fund.

References

1. Schneider, P. *et al* in Gravitational Lenses, XIV, 560 pp. 112. (Springer-Verlag, 1992).
2. Negrello, M. *et al*, *Science* **330**, 800 (2010).
3. Lapi, A. *et al.*, *ApJ* **742**, 24 (2011).
4. Wang, L. *et al.*, *MNRAS* **414**, 596 (2011).
5. Smith, D. J. B. *et al.*, *MNRAS* **416**, 857 (2011).
6. González-Nuevo, J., *et al.*, *ApJ* **749**, 65 (2012).
7. Driver, S. P., *et al.*, *MNRAS* **413**, 971 (2011).
8. Gott, III, J. R., *et al.*, *ApJ* **549**, 1 (2001).
9. Rigby, E. E, *et al.*, *MNRAS* **415**, 2336 (2011).
10. Lapi, A. *et al.*, *ApJ* **755**, 46 (2012).
11. Smith, D. J. B. *et al.*, *MNRAS* **427**, 703 (2012).
12. Planck Collaboration XVIII, arXiv:1303.5077.

4.
21 cm

Measuring the 21 cm Global Brightness Temperature Spectrum During the Dark Ages with the SCI-HI Experiment

Jeffrey B. Peterson[1], Tabitha C. Voytek[1], Aravind Natarajan[1,2], José Miguel Jáuregui García[3], Omar López-Cruz[3]
[1]*McWilliams Center for Cosmology, Carnegie Mellon University, Department of Physics, 5000 Forbes Ave., Pittsburgh PA 15213, USA*
[2]*Department of Physics and Astronomy & Pittsburgh Particle physics, Astrophysics and Cosmology Center, University of Pittsburgh, 100 Allen Hall, 3941 O'Hara Street, Pittsburgh, PA 15260*
[3]*Instituto Nacional de Astrofísica, Optica y Electrónica (INAOE), Coordinación de Astrofísica, Luis Enrique Erro No. 1 Sta. Ma. Tonantzintla, Puebla, 72840 Mexico*

We present an update on the SCI-HI experiment, which is designed to measure the all-sky (global) 21 cm brightness temperature during the end of the Dark Ages. Results from preliminary observations in June 2013 are discussed, along with system improvements and planned future work.

1 Introduction

Very few observations constrain models of the Dark Ages, during which the simple initial conditions seen with the Cosmic Microwave Background (CMB) evolved into the complex structures we see today. A key process during the Dark Ages is the formation of the first (Pop III.1) stars in dark matter minihalos of mass $\approx 10^6 - 10^8 M_\odot$ at redshift $z \approx$ 20-30. [1] [2] These first, short-lived stars provided the Universe with the heavy elements necessary for subsequent generations of stars and planets.

Besides providing heavy elements, the first stars impacted the intergalactic medium (IGM), transforming it from neutral hydrogen into the ionized state we see today. We can learn about star formation by examining the all-sky (global) 21 cm brightness temperature (T_b). This is possible because the evolution of the IGM prior to reionization is characterized by decrement followed by increment in T_b, described in the following process. Lyman-α photons, produced by the first stars, couple the spin (T_s) and kinetic (T_k) temperature of the IGM through the Wouthuysen-Field mechanism. [3] [4] Because $T_\mathrm{k} \propto (1+z)^2$ is well below the CMB temperature (T_γ) at $z \approx$ 20-30 this coupling causes a decrement in $T_\mathrm{b} \propto 1 - T_\gamma/T_\mathrm{k}$. Later the IGM is heated by x-rays or γ-rays and T_s rises above T_γ, ending the T_b trough. Observations of the T_b trough can be made by measurement of the 21 cm global spectrum. [5] [6] The predicted depth (≈0-300 mK), width (≈0-50 MHz), and center frequency (≈60-100 MHz) are all dependent on the model of first star formation.

Several experiments seek to measure the T_b trough in the 21 cm global spectrum. These include the Large Aperture Experiment to Detect the Dark Ages (LEDA), [7] an expanded EDGES, [8] the LOFAR Cosmic Dawn Search (LOCOS), [9] [10] "Sonda Cosmológica de las Islas para la Detección de Hidrógeno Neutro" (SCI-HI), [11] and the proposed Dark Ages Radio Explorer (DARE). [12] In the following sections, we will focus on the SCI-HI global spectrum experiment. We will discuss the recent results from the first experiment deployment, [11] the experiment structure, and describe recent system improvements.

Figure 1 – HIbiscus Antenna on-site on Isla Guadalupe, Mexico.

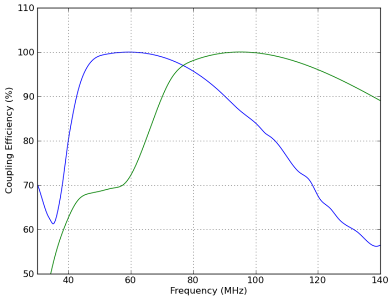

Figure 2 – Antenna coupling efficiencies ($\eta(\nu)$) for two scaled HIbiscus antennas, calculated using the measured antenna and amplifier impedances.

2 Experimental Setup

In order to probe the 21 cm global spectrum, we designed a single antenna experiment. Because the HI global spectrum structure is distributed over a wide frequency range, it was necessary to develop a specialized antenna. Several antenna designs were considered, modelled and tested in the lab and field; log periodic, fat inverted vee, horn, sleeve dipole, and four square antennas. Our best results were obtained by modifying a four-square design into the HIbiscus antenna (see Fig. 1). Working with a finite element simulation software and scale model testing, the HIbiscus antenna was tuned to provide an optimal combination of bandwidth, impedence and beam shape. This design has a smooth 55° beam (FWHM) at its center frequency and a coupling efficiency ($\eta(\nu)$) above 90% for nearly an octave of bandwidth.

The SCI-HI experiment is intended to collect data from 40-130 MHz, larger than the bandwidth of a single HIbiscus antenna. To solve this problem, we built scaled copies of the HIbiscus design with center frequencies at 70 MHz and 100 MHz, allowing data collection over the entire band. The antennas have $\eta(\nu)$ above 90% for 55-90 MHz and 70-140 MHz respectively, as is shown in Fig. 2.

Besides allowing data collection over a wider band, the use of overlapping antennas allows a cross-check of data. Signals from the sky will appear in datasets from both antennas in the overlap region (70-90 MHz). A single sampling system is used alternately with either of the scaled antennas. This limits the rate of data collection but provides consistency between the two datasets. Additional details of the sampling system can be found in Voytek et al. [11]

3 Deployment Sites

In the frequency range of 40-130 MHz, major interfering flux contributions include broadcast emissions from television stations and FM radio stations which transmit in our band. Even at the U.S. National Radio Quiet Zone in Green Bank, West Virginia, the FM signal exceeds the sky signal by 10 dB over the entire FM band of 88-108 MHz (see Fig. 3). The equivalent T_b averages about 20,000 Kelvin. To achieve an RFI level below the 21 cm signal requires deployment to a significantly isolated radio-quiet location. We achieve this isolation by travelling to lightly inhabited islands located far from the mainland. Our islands of choice are located in the eastern Pacific Ocean, off the coast of Mexico (see Fig. 4).

We have already deployed twice to Isla Guadalupe, the northern-most of our potential sites. Isla Guadalupe (Latitude 28° 58′ 24″ N, Longitude 118° 18′ 4″ W), is 260 km off the Baja California peninsula in the Pacific Ocean. It is a Mexican biosphere reserve and has a population of less than 100; ecology-resoration teams, Mexican Marines, and members of a fishing cooperative. We spent two weeks on Isla Guadalupe (June 1-15, 2013) observing with SCI-HI on the western side of the island. Even at this remote site, we still detect some RFI from the mainland; although residual FM is only about 0.1 dB ($\leq$70 K) above the Galactic foreground level (see Fig. 3).

Additional distance from the Mexican coast can provide further attenuation of RFI. Isla Socorro

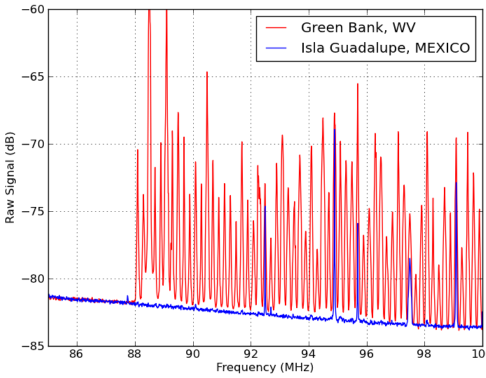

Figure 3 – Comparison of RFI in the FM frequency band between Green Bank, WV and Isla Guadalupe, Mexico. Except for a few stations the noise on Guadalupe is about 0.1 dB above foregrounds, while Green Bank is ∼10 dB above foregrounds.

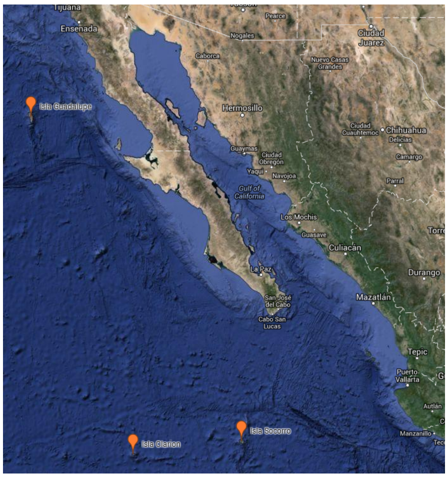

Figure 4 – Map of eastern Pacific Ocean, including Isla Guadalupe, Isla Socorro and Isla Clarión.

(Latitude 18° 48′ 0″ N, Longitude 110° 90′ 0″ W), is ∼600 km off the Pacific coast of Mexico. This island is also a biosphere reserve and has similarly minimal infrastructure to Isla Guadalupe. Operation of SCI-HI at this location should provide an RFI environment sufficiently quiet in our frequency band.

Isla Socorro may still not be quiet enough due to insufficient mainland distance or RFI from the island's Mexican naval contingent. If this proves to be the case, Isla Clarión (Latitude 18° 22′ 0″ N, Longitude 114° 44′ 0″ W) is ∼700 km off the coast, has a much smaller naval contingent, and can be utilized as well.

4 Current Results

Data is processed through a series of steps. First, the data is cleaned to excise RFI contaminated data. Second, amplifier noise is removed and the data is corrected using the coupling efficiency ($\eta(\nu)$). Third, brightness response is calibrated using the Galactic Global Sky Model (GSM) [13] and the simulated antenna beam pattern. This calibration is done using the diurnal variation of the data (see Fig. 5), and is analagous to an on-source/off-source calibration of a single dish radio telescope.

Data processing is done independently for each day of data. After calibration, fitting the daily mean spectrum to a log-polynomial shape with three terms yields residuals that are dominated by systematic uncertainty. Residual mean and variance, weighted for exposure, are shown in Fig. 6, along with the foreground signal prior to fit. Predictions from three cosmological models with mean brightness temperature removed, obtained using the SIMFAST code, [14] [15] are also shown.

To check that data processing does not cause significant attenuation to the 21 cm signal, a simulation calibration technique [16] was used. This technique adds a simulated signal of appropriate shape (and varying magnitude) to the data prior to processing and compares residuals before/after addition of the simulated signal. Results from this check showed that ≈75% of the added signal remains in the residuals. For more detail on data processing, see Voytek etal. [11]

5 Discussion and Future Work

The first results from the SCI-HI experiment yield residuals of ≈5-10 Kelvin with 4.4 hours of integration. Given that the foregrounds have brightness temperatures >1000 Kelvin, this means that residuals are <1% of foreground signal. Residual levels are lower than early predictions based on possible spatial structure in the spectral index of the foregrounds. [17] This is a promising sign for the future of 21 cm global experiments.

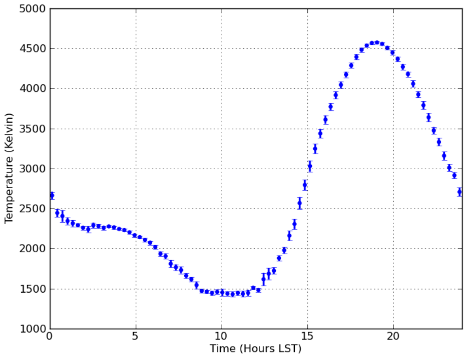

Figure 5 – Diurnal variation of a single 2 MHz wide bin centered at 70 MHz. Calibrated mean with RMS error bars from day-to-day variation are shown for 9 days of observation binned in ∼ 18 minute intervals. Larger error bars correspond to LSTs where the quantity of useable data is smaller.

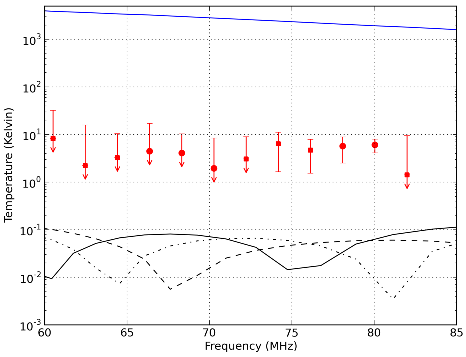

Figure 6 – Log magnitude comparison of foregrounds (blue), residuals from 4.4 hours of integration (red) and predictions from three different reionization models (black). For the residuals, circles are positive values and squares are negative values and error bars show the daily variance.

Despite the promise of the first results from the SCI-HI experiment, a further decrease in residuals of 1-2 orders of magnitude is necessary to measure the 21 cm signal (300 mK peak-to-peak temperature amplitude). As calculated using the radiometer equation, thermal noise is ∼2 orders of magnitude below the current residual levels. This indicates that residuals are dominated by systematic errors and residual foregrounds. Improvements to the apparatus are underway, and should help decrease systematic errors.

Systematic errors can be described in two major categories. First, the experiment faraday cage does not contain self-generated RFI to sufficient levels. In particular, self-generated RFI contributes substantially to the residuals above 90 MHz and can also be found minimally at lower frequencies. This self-generated RFI varies with time and introduces frequency dependent structures. Improvements are therefore in progress to the sampling system and its shielding. Repeated deployment to quiet sites is necessary to test the system because the low level of the self-generated RFI makes it undetectable in lab tests, where the noise is dominated by strong broadcast signals.

Second, much of the residuals are related to calibration error associated with the lack of full 24 hour days of data. During this preliminary data collection, the system power source was 12 V lead-acid batteries, which yielded time variable voltages and caused frequent gaps in data collection. Improvements to the sampling system and replacement of our power generation system with a stable power source will facilitate the collection of complete days of data, thereby reducing the calibration errors.

Deployment of the SCI-HI experiment is planned for Isla Socorro and Isla Clarión, taking advantage of the additional distance from the mainland. These islands are expected to provide an RFI environment where the FM band signals are below the thermal noise level, allowing a substantial increase in the frequency range studied. With two full weeks of data and complementary datasets from multiple HIbiscus antennas, our goal is to achieve residuals below the 100 mK level from 40-130 MHz.

Acknowledgements

Travel to Isla Guadalupe would not have been possible without support from local agencies in Mexico, including Grupo de Ecología y Conservación de Islas A.C. (GECI), Secretaría de Marina (SEMAR), Secretaría de Gobernación (SEGOB), Comisión Nacional de Areas Naturales Protegidas (CONANP), Reserva de la Biosfera de la Isla Guadalupe, Sociedad Cooperativa de Producción Pesquera de Participación Estatal Abuloneros y Langosteros, S.C.L., and Dr. Raúl Michel.

A.N., J.B.P., and T.C.V. acknowledge funding from NSF grant AST-1009615. A.N. thanks the McWilliams Center for Cosmology for partial financial support. J.M.G.C. and O.L.-C. thank INAOE for financial support. J.M.G.C. acknowleges a CONACyT Beca Mixta that allowed him to spend a year at the McWilliams Center for Cosmology

References

1. K. Omukai and F. Palla. Formation of the First Stars by Accretion. *ApJ*, 589:677–687, June 2003.
2. V. Bromm. Formation of the First Stars. *ArXiv e-prints*, May 2013.
3. S. A. Wouthuysen. On the excitation mechanism of the 21-cm (radio-frequency) interstellar hydrogen emission line. *AJ*, 57:31–32, 1952.
4. G. B. Field. Excitation of the Hydrogen 21-CM Line. *Proceedings of the IRE*, 46:240–250, January 1958.
5. P. A. Shaver, R. A. Windhorst, P. Madau, and A. G. de Bruyn. Can the reionization epoch be detected as a global signature in the cosmic background? *Astronomy and Astrophysics*, 345:380–390, May 1999.
6. J. R. Pritchard and A. Loeb. 21 cm cosmology in the 21st century. *Reports on Progress in Physics*, 75(8):086901, August 2012.
7. Large-Aperture Experiment to detect the Dark Ages (LEDA). LEDA, $http://www.cfa.harvard.edu/LEDA/science.html$. July 2013.
8. J. D. Bowman, A. E. E. Rogers, and J. N. Hewitt. Toward Empirical Constraints on the Global Redshifted 21 cm Brightness Temperature During the Epoch of Reionization. *ApJ*, 676:1–9, March 2008.
9. M. P. van Haarlem, M. W. Wise, etal.
   LOFAR: The LOw-Frequency ARray. *Astronomy and Astrophysics*, 556:A2, August 2013.
10. H. K. Vedantham, L. V. E. Koopmans, A. G. de Bruyn, S. J. Wijnholds, B. Ciardi, and M. A. Brentjens. Chromatic effects in the 21 cm global signal from the cosmic dawn. *ArXiv e-prints*, June 2013.
11. T. C. Voytek, A. Natarajan, J. M. Jauregui-Garcia, J. B. Peterson, and O. Lopez-Cruz. Probing the Dark Ages at Z˜20: The SCI-HI 21 cm All-Sky Spectrum Experiment. *ArXiv e-prints*, October 2013.
12. J. O. Burns, J. Lazio, S. Bale, J. Bowman, R. Bradley, C. Carilli, S. Furlanetto, G. Harker, A. Loeb, and J. Pritchard. Probing the first stars and black holes in the early Universe with the Dark Ages Radio Explorer (DARE). *Advances in Space Research*, 49:433–450, February 2012.
13. A. de Oliveira-Costa, M. Tegmark, B. M. Gaensler, J. Jonas, T. L. Landecker, and P. Reich. A model of diffuse Galactic radio emission from 10 MHz to 100 GHz. *Mon. Not. R. Astron. Soc.*, 388:247–260, July 2008.
14. M. G. Santos, L. Ferramacho, M. B. Silva, A. Amblard, and A. Cooray. Fast large volume simulations of the 21-cm signal from the reionization and pre-reionization epochs. *Mon. Not. R. Astron. Soc.*, 406:2421–2432, August 2010.
15. A. Mesinger, S. Furlanetto, and R. Cen. 21CMFAST: a fast, seminumerical simulation of the high-redshift 21-cm signal. *Mon. Not. R. Astron. Soc.*, 411:955–972, February 2011.
16. G. Paciga, J. G. Albert, K. Bandura, T.-C. Chang, Y. Gupta, C. Hirata, J. Odegova, U.-L. Pen, J. B. Peterson, J. Roy, J. R. Shaw, K. Sigurdson, and T. Voytek. A simulation-calibrated limit on the H I power spectrum from the GMRT Epoch of Reionization experiment. *Mon. Not. R. Astron. Soc.*, 433:639–647, July 2013.
17. A. Liu, J. R. Pritchard, M. Tegmark, and A. Loeb. Global 21 cm signal experiments: A designer's guide. *Phys. Rev. D*, 87(4):043002, February 2013.

New light on 21 cm intensity fluctuations from the dark ages

Yacine Ali-Haïmoud
School of Natural Sciences, Institute for Advanced Study, Princeton, NJ 08540, USA

Fluctuations of the 21 cm brightness temperature before the formation of the first stars hold the promise of becoming a high-precision cosmological probe. This proceeding summarizes recent work by Ali-Haïmoud, Meerburg and Yuan[1] where the effect of the baryon-cold dark matter relative velocity[2] (RV) on 21 cm brightness temperature fluctuations from redshifts $z \geq 30$ is computed. On small scales (comoving wavenumbers $k \sim 50 - 1000$ Mpc^{-1}, multipoles $\ell \sim 10^6 - 2 \times 10^7$), the signal is typically suppressed by several tens of percent due to the RV, except for extremely small scales ($k \gtrsim 10^3$ Mpc^{-1}, $\ell \gtrsim 2 \times 10^7$) for which the fluctuations are boosted by resonant excitation of acoustic waves. On large scales ($k \lesssim 0.1$ Mpc^{-1}, $\ell \lesssim 2000$), 21 cm fluctuations are enhanced due to the nonlinear dependence of the brightness temperature on the underlying gas density and temperature, whose small-scale power is modulated on large scales by the RV field. This large-scale enhancement is proportional to the matter power spectrum at very small scales ($k \gtrsim 50$ Mpc^{-1}), which can therefore in principle be probed indirectly in the large-scale fluctuations of the 21 cm signal.

1 Introduction: high-redshift 21 cm cosmology

A new scale frontier – In the last two decades, cosmology has become a high-precision field, owing to increasingly sensitive cosmic microwave background (CMB) and large-scale structure (LSS) experiments. Most cosmological parameters of the Λ-cold dark matter (CDM) standard model are now known to a precision of a few percent[3], and the measured primordial power spectrum is consistent with near scale invariance as expected from an early inflationary epoch.

Yet, neither CMB anisotropies nor LSS measurements can be used to probe very small scales, $k \gtrsim 1$ Mpc^{-1}, which remain an open frontier. On the one hand, CMB anisotropies are exponentially damped by photon diffusion for $k \gtrsim 0.15$ Mpc^{-1}. On the other hand, galaxies and the underlying CDM do strongly cluster on these small scales at low redshifts, but their fluctuations are non-linear and cannot be accurately modelled theoretically.

Loeb and Zaldarriaga[4] pointed out that the 21 cm spin-flip transition of neutral hydrogen could be used to obtain a three-dimensional map of the universe during the dark ages preceding the formation of the first stars, at $z \gtrsim 30$. In principle, scales as small as the baryonic Jeans scale $k_J \sim 300$ Mpc^{-1} could be reached, and the properties of fluctuations could be predicted to high accuracy since the growth of density perturbations is still very well described by perturbation theory at these high redshifts. Measuring the power spectrum at such small scales would give an unprecedented lever-arm to measure the tilt and running of the primordial power spectrum, an eventual suppression by a warm dark matter or massive neutrinos, and would provide a large number of modes needed to detect very small levels of primordial non-gaussianity[5].

While the promises of 21 cm cosmology are great, so are the challenges that need to be overcome before this signal is measured. First, the 21 cm line redshifted from $z \geq 30$ falls at frequencies $\nu \leq 50$ MHz, for which the opacity of the Earth's ionosphere becomes significant. Secondly, galactic synchrotron emission raises steeply at low frequencies and is many orders of magnitude brighter than the signal itself. Finally, the scale $k_J \sim 300$ Mpc^{-1} corresponds to angular scales of ~ 0.1 arcsec, extremely challenging to access for observations in the 10-meter wavelength regime in which redshifted 21 cm radiation falls today.

Basic physics – The current state of the art calculation of the 21 cm signal from the dark ages (save for the RV effect) is given by Lewis and Challinor[6]. Here we briefly review the basics.

The ground state of neutral hydrogen is split into two hyperfine states, the singlet ground state (total angular momentum 0) and the triplet excited state (total angular momentum quantum number 1). Their energy differs by $E_{10} = 68$ mK. The ratio of abundances of hydrogen in the excited state to that in the singlet state $\frac{n_1}{n_0} \equiv 3\ \mathrm{e}^{-E_{10}/T_s}$ defines the **spin temperature** T_s. Its value is determined by the competition between (i) photon absorption and emission, which tend to set $T_s \rightarrow T_{\rm cmb} = (1+z) \times 2.73$ K, and (ii) collisions with other neutral hydrogen atoms (and to less extent, with free electrons and protons), which tend to set $T_s \rightarrow T_{\rm gas}$, the kinetic temperature of the gas[a]. As a result $T_s = f(n_{\rm H}, T_{\rm gas}, T_{\rm cmb})$ is a non-linear function of the local gas density and temperature, intermediate between $T_{\rm gas}$ and $T_{\rm cmb}$.

As resonant photons interact with the hyperfine transition, they are redshifted in the local gas rest frame, due to cosmological expansion (with Hubble expansion rate $H(z)$) and peculiar velocity gradients along the direction of propagation, $\partial_{||} v_{||}$. The Sobolev **optical depth** τ in the line is then $\tau \propto n_{\rm H}(H + \partial_{||} v_{||})^{-1}$. At all times $\tau \ll 1$ and the contrast between the brightness temperature of the radiation field after its interaction with the line and $T_{\rm cmb}$ is approximately

$$T_b = \tau\,(T_s - T_{\rm cmb})\,. \tag{1}$$

T_b itself is usually referred to as the **brightness temperature** for short. During the dark ages, and in the absence of any non-standard heating source such as dark matter annihilations, $T_{\rm gas} < T_s < T_{\rm cmb}$, so $T_b < 0$ and the 21 cm line appears in absorption against the CMB.

The basic idea of 21 cm cosmology is to measure $T_b(\hat{n}, z)$ and its statistical properties as a function of redshift, and use them to infer the properties of the underlying matter fluctuations.

2 The relative velocity (RV) effect

Until kinetic decoupling at redshift $z \approx 1020$, baryons are tightly coupled to CMB photons and undergo acoustic oscillations, their overdensity remaining at the level of a few times 10^{-5}. Meanwhile, CDM perturbations grow under their own gravity, reaching overdensities of $\sim 10^{-3}$ at $k \sim 0.1$ Mpc^{-1} and at $z \approx 1000$. Once the universe has significantly recombined baryons decouple from photons and start behaving as a cold fluid on all scales larger than their post-recombination Jeans scale, $k_{\rm J} \sim 300$ Mpc^{-1}. However, baryons and CDM start at $z \approx 1020$ with very different "initial" conditions. In particular, their peculiar velocity fields are very different (though of comparable characteristic magnitude), so that there exists a non-vanishing **relative** velocity $v_{\rm bc}$ between them. This RV has a rms fluctuation of approximately 30 km/s at $z \approx 1020$, and fluctuates mostly on large scales $k \sim 0.01 - 0.5$ Mpc^{-1}. In particular, it is nearly homogeneous across patches of a few Mpc in size.

Whereas the RV field can readily be obtained from linear cosmological perturbation codes such as CAMB[7], Tseliakhovich and Hirata[2] pointed out that it has a fundamentally non-linear and non-perturbative[b] effect on the growth of small-scale fluctuations. Let us consider a patch of a few comoving Mpc across, with a locally uniform RV, and place ourselves in the local baryon rest frame. In this frame, the CDM fluctuation is advected across a characteristic comoving distance $l_{v_{\rm bc}} \approx v_{\rm bc}(aH)^{-1}$ over a Hubble time, where a is the scale factor. If this distance is

---

[a] We only consider times before the formation of luminous objects, and neglect the effect of Lyman-α scattering.

[b] The RV effect is fundamentally non-linear as it arises from the quadratic advection term in the fluid equations. For instance, in the local CDM rest-frame the continuity equation for the baryons is $\dot{\delta}_b + \vec{v}_{\rm bc} \cdot \vec{\nabla}\delta_b + \vec{\nabla} \cdot (\delta\vec{v}_b) = 0$, where $\delta\vec{v}_b$ is the perturbation of the baryon velocity with respect to the locally homogeneous flow with velocity $\vec{v}_{\rm bc}$. The effect of the advection term is non-perturbative for $v_{\rm bc} k \gtrsim aH$, as it is comparable to the term $\dot{\delta}_b$.

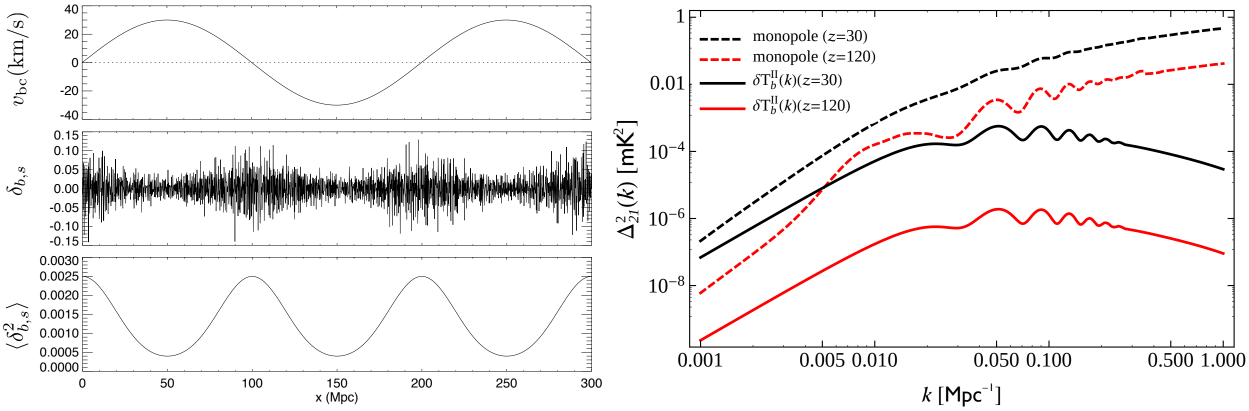

Figure 1 – *Left*: Visual illustration of the RV effect. The top panel shows a long-wavelength fluctuation of the RV. The middle panel shows the resulting small-scale baryon density fluctuations, and the bottom panel the local variance of the baryon fluctuation. Where the RV is small, the fluctuations have their standard amplitude, and where it is large, the local small-scale power spectrum is suppressed. The fractional suppression is exaggerated by a factor of ~ 2 for the sake of visual clarity. *Right*: Additional large-scale 21 cm fluctuations computed in this work, compared to the standard monopole term. We have computed the large-scale enhancement assuming a primordial power spectrum with tilt $n_s = 0.96$ and no running, but the results could be significantly different if one changed the small-scale power at $k \gtrsim 50$ Mpc^{-1}.

larger than the wavelength of a given perturbation, the net gravitational pull of the CDM on the baryons will average out, and similarly for that of the baryons on the CDM. This is the case for very small scale perturbations with wavenumber $k \gtrsim l_{v_{\rm bc}}^{-1} \approx 40$ Mpc^{-1}. Perturbations on these small scales therefore grow at a slower pace than they would if baryons and CDM remained in phase. Because the RV is supersonic by a factor of a few, the scale of suppression is a few times larger than the baryonic Jeans scale and the RV does have a noticeable effect on the growth of small-scale perturbations. Since the scale of suppression is much smaller than the coherence scale of the RV field, one can compute the small-scale power spectrum $P(\vec{k}, \vec{v}_{\rm bc})$ as a function of the local value of the RV. We illustrate the RV effect in the left panel of Fig. 1.

3 Impact on 21cm intensity fluctuations

Small scales – To obtain the local small-scale brightness temperature power spectrum one can simply expand Eq. (1) to linear order in the baryon density, velocity and temperature perturbations, which remain small for $z \geq 30$. The effect of the RV is to suppress these perturbations and consequently those of T_b. The level of suppression depends on the local value of the RV, but the sky-averaged small-scale power spectrum is suppressed by several tens of percent at $k \sim 50 - 1000$ Mpc^{-1}.

On extremely small scales ($k \gtrsim 10^3$ Mpc^{-1}), we find an *enhancement* of all perturbation, an effect which was not previously realized. This is due to the near resonant pumping of baryon acoustic waves by the periodic CDM gravitational force (as seen from the baryons). Indeed, the relative velocity initially decreases faster than the sound speed, and for $z \lesssim 200$ we find that the characteristic RV along a given axis is very close to the sound speed.

Large scales – The most non-intuitive and most important result of this work is that the RV leads to an *enhancement* of large-scale 21 cm fluctuations. This can be understood as follows.

First, let us notice that the baryon overdensity (or any other perturbation) is a scale-dependent quantity. While $\delta_b \ll 1$ is always true during the dark ages, there is also a *hierarchy* between the large-scale fluctuations $\delta_{b,l}$, with $k_l \sim 0.01 - 0.5$ Mpc^{-1}, and the small-scale fluctuations $\delta_{b,s}$, with $k_s \sim 50 - 1000$ Mpc^{-1}: at all times after recombination, $\delta_{b,l} \ll \delta_{b,s}$. In fact, around $z \sim 100$, $\delta_{b,l} \sim \delta_{b,s}^2 \sim$ few times 10^{-3}. Therefore, whenever expanding a quantity to linear order in $\delta_{b,l}$, one should consistently expand to *quadratic order* in $\delta_{b,s}$.

Second, let us remark that the 21 cm brightness temperature is a *fully non-linear function* of the underlying baryonic perturbations. This can be illustrated simply in the following limit. Consider redshifts $z \lesssim 50$ when collisions become inefficient at coupling T_s to $T_{\rm gas}$. In this case, the small difference $T_s - T_{\rm cmb}$ is proportional to the rate of collisions, which is itself proportional to the local density. Therefore $T_b \propto \tau \times n_{\rm H} \propto n_{\rm H}^2 \propto (1 + 2\delta_b + \delta_b^2)$ in that limit. According to the previous remark, one should therefore expand T_b linearly in $\delta_{b,l}$ and to quadratic order in $\delta_{b,s}$. Note that the gas temperature (on which T_b depends as well) is also a non-linear function of the overdensity: in the limit of adiabatic cooling (valid at $z \ll 200$), $T_{\rm gas} \propto n_{\rm H}^{2/3}$.

Finally, without RVs, $\delta_{b,s}^2$ would not fluctuate on large scales, and the quadratic terms in the expansion of δT_b would only amount to adding a (small) offset to the mean brightness temperature. However, RVs modulate the small-scale power spectrum on large scales by several tens of percent, therefore $\delta_{b,s}^2$ fluctuates by order itself on large scales (see left panel Fig. 1). Since $\delta_{b,s}^2 \sim \delta_l$, these additional fluctuations are actually comparable to those obtained from the linear terms, and must be accounted for when computing 21 cm fluctuations.

We show the resulting power spectrum of the additional large-scale 21 cm fluctuations in the right panel of Fig. 1, where we compare it to the standard "monopole" term[6]. We see that the new term represents an enhancement of several percent at $k \lesssim 0.1$ Mpc^{-1}. This enhancement depends on the amount of power in small-scale ($k \gtrsim 50$ Mpc^{-1}) matter fluctuations. This implies our most important result, namely that the large-scale 21 cm fluctuations carry information about these very small scales, which would be very difficult to measure directly.

4 Conclusions

We have recomputed the power spectrum of 21 cm fluctuations from the dark ages, consistently accounting for the relative velocity of baryons and CDM. We showed that the RV leads to a suppression of small-scale 21 cm fluctuations, and more importantly, to an enhancement on large scales, $k \lesssim 0.1$ Mpc^{-1}. This enhancement depends on the currently poorly constrained amount of power in small-scale ($k \gtrsim 50$ Mpc^{-1}) matter fluctuations. In principle one could therefore access information about these very small scales with future 21 cm experiments, even with a limited angular resolution. We shall quantify this assertion in future work, where we will explore the detectability of several modifications to the small-scale matter power spectrum, such as a running of the primordial power spectrum or a cutoff due to a warm or hot dark matter component. We shall also study the effect of dark matter annihilations, which may have an enhanced effect on the 21 cm signal when relative velocities are accounted for.

Acknowledgments

I thank the organizers of the 2014 rencontres de Moriond for a very enjoyable and stimulating conference. This proceeding is based on work in collaboration with Daan Meerburg and Sihan Yuan. I acknowledge financial support from the Frank and Peggy Taplin fellowship at the IAS.

References

1. Y. Ali-Haïmoud, P. D. Meerburg, and S. Yuan. *PRD*, 89:083506, 2014.
2. D. Tseliakhovich and C. Hirata. *PRD*, 82:083520, 2010.
3. Planck Collaboration. *arXiv:1303.5076*, 2013.
4. A. Loeb and M. Zaldarriaga. *PRL*, 92:211301, 2004.
5. A. Pillepich, C. Porciani, and S. Matarrese. *ApJ*, 662:1–14, 2007.
6. A. Lewis and A. Challinor. *PRD*, 76:083005, 2007.
7. A. Lewis, A. Challinor, and A. Lasenby. *ApJ*, 538(2):473, 2000.

BINGO - A novel method to detect BAOs using a total-power radio telescope

Clive Dickinson[a]
Jodrell Bank Centre for Astrophysics, School of Physics & Astronomy, Alan Turing Building,
The University of Manchester, Oxford Road, Manchester, M13 9PL, U.K.

BINGO is a novel single-dish total-power telescope that will map the redshifted HI sky in a $\sim 15^\circ$ strip, at frequencies of 960–1260 MHz ($z = 0.12$–0.48). BINGO will have the sensitivity to accurately measure the HI power spectrum and to detect Baryon Acoustic Oscillations (BAOs) for the first time at radio wavelengths. This will provide complementary cosmological information to existing surveys and will measure the acoustic scale to $\approx 2\,\%$ precision. We provide an update on BINGO including an improved two-mirror optical configuration, final site selection and foreground removal simulations.

1 Introduction - HI intensity mapping and BINGO concept

We are now firmly in the "era of precision cosmology", with a range of cosmological probes available that allow accurate measurements of cosmological parameters. However, with such precise measurements it is critical that we are not limited by systematic errors. One of the most important tools is the Baryon Acoustic Oscillations (BAOs) that provide a precise standard ruler (set by the sound horizon at the time of recombination) that we can use at much later times ($z < 3$) to measure the expansion history of the Universe. Large optical galaxy surveys have now measured the BAO feature to $\approx 1\,\%$ precision [1]. The Square Kilometre Array (SKA), to be built in the next 10–15 years, will allow a similar analysis to be made. In the mean time, a more efficient and cheap method is available: HI intensity mapping [3]. The idea is to make a deep HI spectral survey at relatively low angular resolution ($\sim 1^\circ$) to map the *fluctuations* in HI brightness from many galaxies within the beam.

BINGO[b] is a novel and cost-effective way to map the large-scale redshifted hydrogen using the intensity mapping technique. BINGO will map the HI line over the redshift range $z = 0.12$–0.48 (observing frequencies 960–1260 MHz), with a mean redshift $z \approx 0.3$. This will allow a measurement of the acoustic scale to a few %, thus providing an independent measurement of BAOs at radio wavelengths and constraints on cosmological parameters, such as the equation-of-state of dark energy. The guiding principle with BINGO is *simplicity*. We are using a single-dish total power design, with no moving parts. The dish(es) will be wire mesh and static, utilising the Earth's rotation to map a $\sim 15^\circ$ strip of the sky using a focal plane horn array. We will use a standard correlation receiver

---

[a] On behalf of the BINGO collaboration.

[b] The Baryon acoustic oscillations In Neutral Gas Observations (BINGO) experiment is a collaboration between the University of Manchester and University College London in the UK, ETH in Zurich, Switzerland, University of Sao Paolo and INPE in Brazil, University of Montevideo in Uruguay and KACST in Saudi Arabia

to reduce $1/f$ noise in the receivers, using the South Celestial Pole (SCP) as a reference to provide almost perfect matching of the sky and reference inputs. The detectors will use room-temperature Low Noise Amplifiers (LNAs) that should allow us to achieve a total system temperature $T_{\rm sys} = 50\,{\rm K}$. Much of the receiver will be in digital hardware, which is reasonably cost effective at these frequencies. The total cost is expected to be less than US$4M and if funded (we are currently awaiting decisions on a number of funding proposals), we expect to be operational within 18 months.

2 BINGO update: Two-mirror design and site selection

2.1 Two-mirror design

The original BINGO concept was to use a single 40 m dish at the bottom of a large ($\approx 90\,$m) cliff edge [2]. The horn array would be supported at the top of the cliff on a boom. This was believed to the most economical option while still meeting the requirements for beam performance and focal plane area to support ~50 horns. However, we found it difficult to find an appropriate cliff, away from cites and facing roughly N-S (§ 2.2). We considered using a large tower to house the horn array, but this would be very expensive. This opened up the idea of using a two-mirror design, since the cost of a second mirror would be of order the same as a tower.

The most obvious choice is the crossed-Dragone (or Compact Range Antenna) configuration which has been extensively used by ultra-sensitive, wide field-of-view (FOV) CMB experiments [4]. This design offers a very large FOV, with a flat focal plane that does not require refracting optics. The horn dimensions are also reduced to 1.7 m diameter and 4.7 m length, which is an important consideration given that the fabrication of 50 large metal horns is likely to be the greatest challenge and cost. Furthermore, the new optics offer exceptional beam performance, both in terms of sidelobe response and polarization purity; see Table 1. In particular, the cross-polar response is exceptionally low even for horns at the edge of the array, which will mitigate polarized synchrotron radiation from leaking into the cosmological intensity signal. Fig. 1 shows the new BINGO optics, highlighting the very compact nature of this optical configuration. Perhaps more importantly, it gives us many more options in terms of site selection (we only require a ~ 40 m cliff and a slope; § 2.2). With some optimization, it may also allow us to cover a larger sky area and/or increase the number of horns to increase the overall sensitivity.

Table 1: Representative performance figures for the optical performance of the two-mirror design as a function of offset from the optical axis.

Position	0 m	6 m	7 m
Sky position	$0°$	$-5.2°$	$6.3°$
Optical gain	51.68 dB	51.45 dB	51.22 dB
Peak cross-pol	<-60 dB	-43 dB	-41 dB
Beam ellipticity	0.7 %	4 %	10 %

2.2 Site selection

The original concept of a ~ 90 m cliff was challenging. With the new optical design (§ 2.1), we can afford to consider a number of sites. Due to the opportunities of funding in South America via Brazil/Uruguay, and the requirement to observe near the Celestial Equator (dec. $\approx -5°$ is about ideal in terms of sky area and observing low-foreground regions) with reference horns pointing towards the SCP, Uruguay was our country of choice. We have recently surveyed several mines and valleys for Radio Frequency Interference (RFI), which have showed that the frequency band just above the GSM mobile phone band (above 960 MHz) is indeed very clean. In the end, we found an unused mine in the North of Uruguay, near the town of Minas Corales. The mine is called "Castrillon" and is shown in Fig. 2. It features a large hole with a ~ 45° slope to the South, a ~ 40 m slope to the North, and a flat area above the slope allowing the SCP to be observed. It is therefore well suited

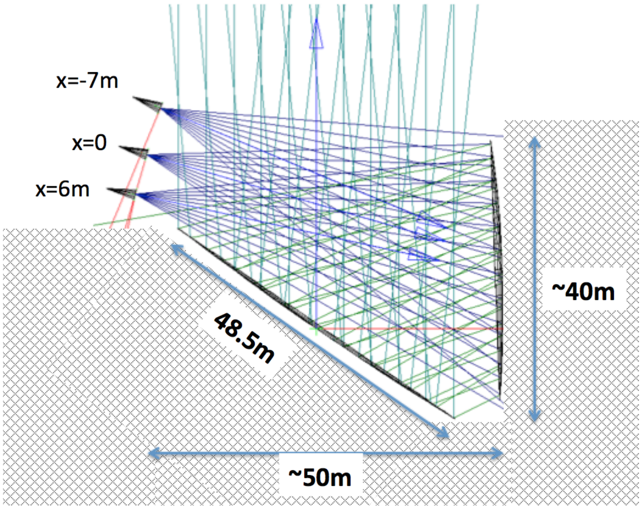

Figure 1 – Two-mirror crossed-Dragone design for BINGO. This design uses two $\approx$ 40 m dishes in a very compact configuration, which offers better optical performance than a single dish as well as reducing the size of the horns. It also makes more sites available (§ 2.2).

to the new BINGO configuration.[c]

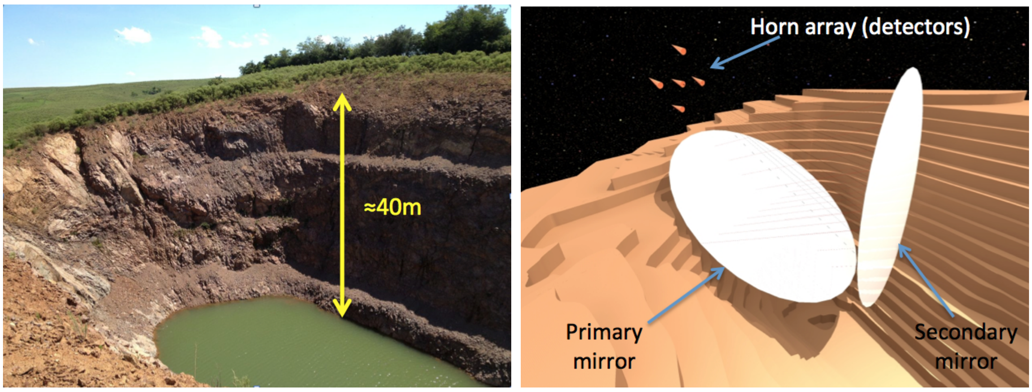

Figure 2 – *Left*: Photo of the Castrillon mine, which will be the site for the BINGO telescope. *Right*: 3-D model of the Castrillon site showing approximately how the two-mirror design will fit inside.

3 Sensitivity and foreground removal

If BINGO is deployed with at least 50 horns, with an average system temperature $T_{\rm sys} \approx 50\,$K, it will be able to map a large ($\approx$ 3000 sq. deg.) region of the sky with a temperature sensitivity of $\approx 0.1\,$mK per 1 MHz channel. This will allow a detection of BAOs at $>5\sigma$. Note that the new optical design allows a larger FOV ($\sim 15^\circ$) than originally discussed [2], and potentially more horns, which would reduce the uncertainties, particularly on large angular scales. Fig. 3 (*left*) shows the predicted sensitivity to the BAOs for a full 1-year observation (this would likely take $\sim$ 2 years in practice) for 70 horns and 15° FOV. This provides a measurement of the acoustic scale to about 2 %, which is about the level of the current state-of-the-art large optical surveys.

One of the most important considerations for HI intensity mapping experiments is foreground removal. The Galactic synchrotron radiation and emission from extragalactic sources is expected to be several orders of magnitude ($\sim 70\,$mK rms at 1 GHz) above the cosmological signal ($\sim 0.1\,$mK rms). Although this presents a major challenge, we know that the foreground spectrum will be exceptionally smooth - to first order it is a power-law with some curvature. If the data can be

---

[c] The site is not quite ideal in that it is not exactly N-S. Also, the water at the bottom of the mine needs pumping out but we believe this is a surmountable task!

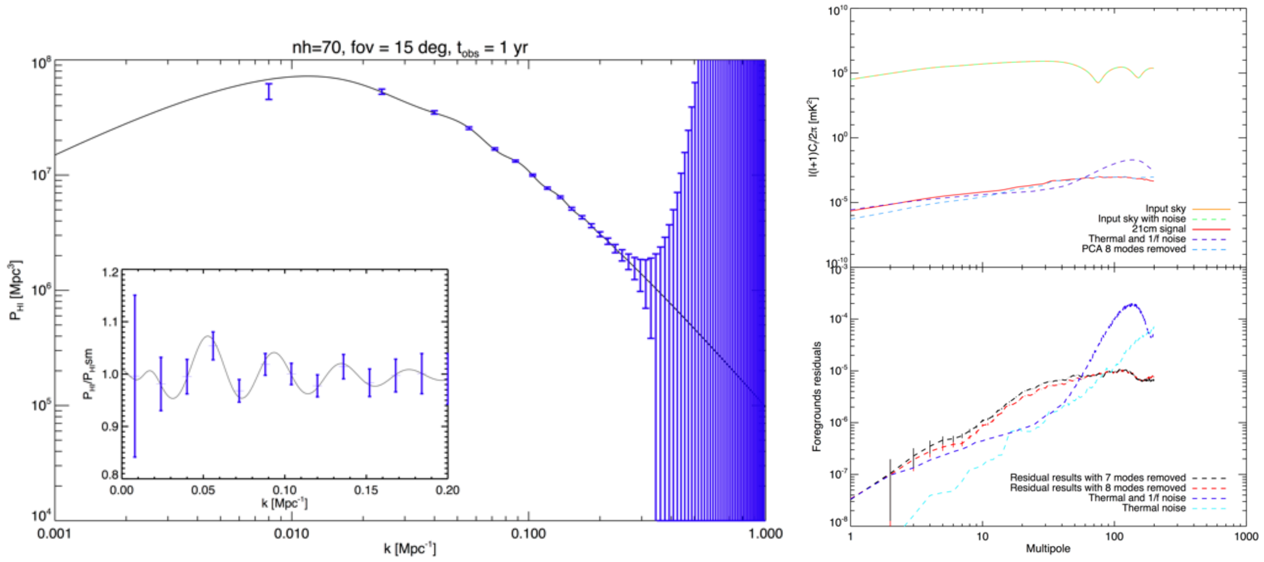

Figure 3 – *Left*: Projected power spectrum sensitivity for a full 1-year of BINGO observations, with 70 horns and 15° FOV, providing a high S/N detection of BAOs. The panel insert highlights the BAO features after dividing out the smoothed spectrum. *Right*: Application of PCA to remove foregrounds for simulated BINGO at 982 MHz (*top panel*). The bulk of the foreground power has been removed close to the thermal noise level (*bottom panel*).

calibrated sufficiently accurately, this will allow the foregrounds to be removed from the data since the cosmological HI signal is uncorrelated between frequency channels.

A number of foreground removal techniques are available. A simple blind method is Principal Component Analysis (PCA), which decomposes the covariance matrix of the data into eigenmodes, of which only a small number contain the foreground (smooth) component. Fig. 3 (*right*) shows an example power spectrum before and after applying PCA on simulated BINGO data, including thermal and $1/f$ noise. Virtually all of the foreground power can be removed to close to the thermal noise level by subtracting 8 modes; the foreground residuals are below the thermal noise level for ℓ>100. More detailed simulations of $1/f$ noise and systematics will be needed to quantify the level of residual foreground contamination.

4 Conclusion and outlook

BINGO is a novel and cost-effective way to map redshifted HI at z = 0.12–0.48 with the aim of detecting BAOs at radio wavelengths. As well as providing independent cosmological data, it will have different systematics compared to optical BAO surveys. We are ready to start construction when funding has been secured[d]. The deep spectroscopic survey will have a wide range of scientific applications from cosmology to our Galaxy. With an upgrade to the digital backend, we may also be able to detect a number of Fast Radio Bursts (FRBs) of which only ≈ 10 have currently been detected so far and whose origin is unknown.

Acknowledgments

CD acknowledges support from an ERC Starting Grant (no. 307209). We thank the Orosur mining company (Uruguay) for providing accurate drawings of the Castrillon mine.

References

1. Anderson, L., Aubourg, É., Bailey, S., et al. 2014, MNRAS, 441, 24
2. Battye, R. A., Browne, I. W. A., Dickinson, C., et al. 2013, MNRAS, 434, 1239
3. Peterson, J. B., Bandura, K., & Pen, U. L. 2006, arXiv:astro-ph/0606104
4. Tran, H., Johnson, B., Dragovan, M., et al. 2010, Proc. SPIE, 7731, id. 77311R

---

[d] We are currently awaiting the outcome of funding proposals.

5.
Dark Matter

Indirect Dark Matter searches at very high energies with the H.E.S.S. telescope

A. Viana for the H.E.S.S. collaboration
Max-Planck-Institut für Kernphysik, P.O. Box 103980, D 69029 Heidelberg, Germany

H.E.S.S. is an array of four identical imaging atmospheric Cherenkov telescopes, designed to detect very-high energy (VHE, E $\geq$ 100 GeV) gamma rays. Such high energy gamma rays can be used to search for annihilations of Dark Matter particles in dense environments. Dwarf galaxies, galaxy clusters and the Galactic Center are compelling candidates to harbour a sizeable very-high energy gamma-ray signal. Several observation campaigns were launched by H.E.S.S. towards these objects. A review of the published observations is presented. In the absence of clear signals, constraints on the Dark Matter particle annihilation cross-section have been derived in different particle physics scenarios. Some possible enhancements of the gamma-ray flux are studied, *i.e.*, the Sommerfeld effect, the internal bremsstrahlung and the substructures in the Dark Matter halo.

1 Introduction

The Standard Model of Cosmology assumes that in the early Universe dark matter particles, in the form of *weakly interacting massive particles* (WIMPs), were produced in collisions between particles of the thermal plasma during the radiation-dominated era. Production and annihilation of DM particle pairs into Standard Model (SM) particles were the main reactions taking place and controlling the initial thermal equilibrium. After freeze out, DM pair annihilation becomes greatly suppressed. However, even if nowadays its impact on the dark matter relic density must be negligible, dark matter still annihilates and may be observable in dense environments, such as dwarf galaxies satellites of the Milky-Way, galaxy clusters and the Galactic Center (GC). Dark matter may therefore be detected indirectly: dark matter pair-annihilates somewhere, creating as sub-product of annihilation SM particles, which might then be detected. Among the sub-products used as probes for indirect DM searches the predominant are neutrinos, positron and electrons, and γ-rays. Here we focus on the search for secondary γ-rays from annihilations of DM particles. The main advantages of this powerful indirect detection technique are: (*i*) γ-rays do not suffer deviation of their trajectories from propagation effects, (*ii*) the γ-ray signal should be proportional to the square of the DM density, and (*iii*) characteristic features such as bumps, steps or cut-offs may be present in the energy spectrum, given by the fact that no more energy than DM particle mass per particle can be released in the annihilation of two non-relativistic DM particles. On the other hand γ-rays are also abundantly produced by astrophysical sources in electromagnetic and hadronic processes, thus the unambiguous identification of a DM emission above such astrophysical background is difficult. Imaging atmospheric Cherenkov telescopes (IACTs), such as H.E.S.S., are particularly well suited for deep searches of targeted objects because of their large effective areas ($\sim 10^5$m^2 above 100 GeV). Up to date no clear detection of a γ-ray signal coming from a DM annihilation has been confirmed. In the absence of a significant signal, constraints on DM models, from astrophysics and particle physics, can be derived.

2 The H.E.S.S. instrument

The H.E.S.S. (High Energy Stereoscopic System) experiment is an array of four identical imaging atmospheric Cherenkov telescopes, observing VHE gamma rays. H.E.S.S. is located in the Khomas Highland of Namibia (23°16′18″ South, 16°30′00″ East) at an altitude of 1800 m above sea level. Each telescope has an optical reflector consisting of 382 round facets of 60 cm diameter each, yielding a total mirror area of 107 m^2. The Cherenkov light, emitted by charged particles in the electromagnetic showers initiated by primary gamma rays, is focused on cameras equipped with 960 photomultiplier tubes, each one subtending a field-of-view of 0.16°. The large field-of-view (∼5°) permits survey coverage in a single pointing. The direction and the energy of the primary gamma rays are reconstructed by a stereoscopic technique.

3 H.E.S.S. observations

Among the potential targets for the detection of a DM annihilation signal the H.E.S.S. telescope has observed the dwarf galaxies Sagittarius (distance ∼ 24 kpc [1]) , Sculptor (distance ∼ 79 kpc [3]), Carina (distance ∼ 101 kpc [3]), and the overdensity Canis Major (distance ∼ 8 kpc [2]), for a total of 11 h, 11.8 h, 14.8 h and 9.6 h (live time) of high quality data, respectively. The Fornax galaxy cluster (distance ∼ 19 Mpc, [4]) was observed for a total of 11.3 hrs live time. Since no significant gamma-ray excess was found above the estimated backgrounds at the nominal positions of these objects , 95% confidence level upper limits on the total observed numbers of gamma rays were derived ($N^{95\%\,\mathrm{C.L.}}_{\gamma,\,\mathrm{tot}}$). In case of the Galactic Center, the γ-rays from a DM annihilation were searched for in a circular source region of radius of 1.0° centered at the GC. Contamination of the DM signal by local astrophysical γ-ray sources was excluded by restricting the analysis to Galactic latitudes $|\mathrm{b}| > 0.3°$, effectively cutting the source region into two segments above and below the Galactic plane. The analysis was carried out using 112 h (live time) of GC observations with the H.E.S.S.. Again no significant gamma-ray excess was found above the estimated background, and a 95% confidence level upper limits on the total observed numbers of gamma rays were derived [5,6].

4 Exclusion limits on dark matter annihilation

The energy-differential γ-ray flux from dark matter annihilations is given by the following equation:

$$\frac{\mathrm{d}\Phi_\gamma(\Delta\Omega,\mathrm{E}_\gamma)}{\mathrm{dE}_\gamma} = \frac{1}{8\pi}\,\frac{\langle\sigma v\rangle}{m_{\mathrm{DM}}^2}\,\frac{\mathrm{dN}_\gamma}{\mathrm{dE}_\gamma} \times \overline{J}(\Delta\Omega)\Delta\Omega\,, \tag{1}$$

where $\langle\sigma v\rangle$ is the velocity-weighted annihilation cross-section, m_{DM} the mass of the DM particle and $\mathrm{dN}_\gamma/\mathrm{dE}_\gamma$ the photon spectrum per annihilation from all final states weighted by their corresponding branching ratios. The factor

$$\overline{J}(\Delta\Omega) = \frac{1}{\Delta\Omega}\int_{\Delta\Omega}\mathrm{d}\Omega\int_{\mathrm{l.o.s.}}\mathrm{dl}\times\rho^2[\mathrm{r(l)}] \tag{2}$$

reflects the dark matter density distribution inside of the observed target. The annihilation luminosity scales with the squared dark matter density ρ^2. This luminosity is integrated along the line of sight (l.o.s.) and within an angular region $\Delta\Omega$, whose optimal value depends on the dark matter profile of the target and the angular resolution of the instrument. Thus in order to calculate the exclusion limits on the DM annihilation cross section, one needs to model the density distribution of DM in the observed target that will be used in the calculation of $\overline{J}$. Two classes of spherical DM halo profiles are assumed: cored profiles, such as the isothermal [1,2,3,5] or the Burkert [4] profiles, and cuspy profiles, such as the *Navarro, Frenk, and White* (NFW) [1,2,3,4,5] or the Einasto [5] profiles. The 95% C.L. upper limit on the velocity-weighted annihilation cross section as function of the DM particle mass for a given halo profile is given by

$$\langle\sigma v\rangle^{95\%\,\mathrm{C.L.}}_{\mathrm{min}} = \frac{8\pi}{\overline{J}(\Delta\Omega)\Delta\Omega} \times \frac{m_{\mathrm{DM}}^2\,N^{95\%\,\mathrm{C.L.}}_{\gamma,\,\mathrm{tot}}}{T_{\mathrm{obs}}\int_0^{m_{\mathrm{DM}}} A_{\mathrm{eff}}(E_\gamma)\,\frac{\mathrm{dN}_\gamma}{\mathrm{dE}_\gamma}(E_\gamma)\,\mathrm{dE}_\gamma}\,, \tag{3}$$

where $A_{\rm eff}(E_\gamma)$ and $T_{\rm obs}$ are the effective area of the detector as function of the gamma ray energy and the observation live time, respectively.

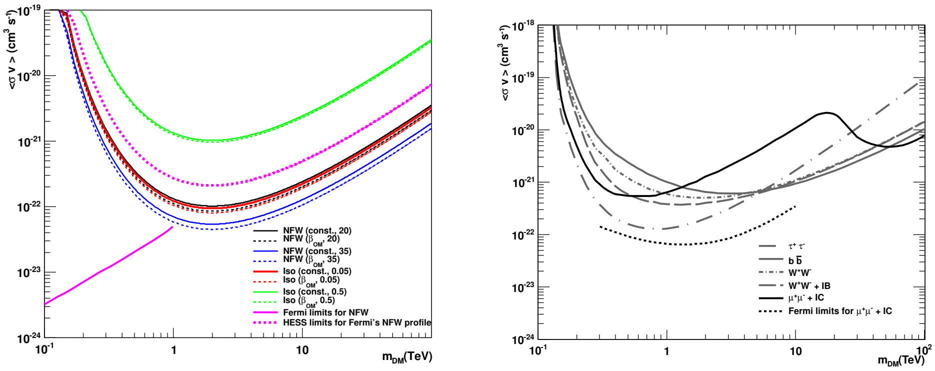

Figure 1 – *Left:* Upper limit at 95% C.L. of $\langle\sigma v\rangle$ as function of the DM particle mass for several NFW halo profiles and the pseudo-isothermal (cored) DM halo profiles for Sculptor. The *Fermi-LAT* limits for a NFW profile are also plotted as well as the H.E.S.S. limits for this NFW profile (pink dashed line). *Right:* Upper limit at 95% C.L. of $\langle\sigma v\rangle$ as function of the DM particle mass for a NFW profile of Fornax and DM particles annihilating into $b\bar{b}$ (gray solid line) , W^+W^- (gray dash-dotted line), $\tau^+\tau^-$ (gray long-dash-dotted line) pairs. See [3,4] and references therein for more details.

The exclusion limits for the Sculptor dSph are plotted in Figure 1 (*left*) for a DM particle annihilating into $b\bar{b}$ pairs and several DM halo profiles parametrizations. The *Fermi-LAT* exclusion limit for Sculptor is also plotted for a NFW profile and a DM particle annihilating into $b\bar{b}$ [3]. The exclusion limits for the Fornax galaxy cluster are plotted in Figure 1 (*right*) for DM particles annihilating into $b\bar{b}$, W^+W^- and $\tau^+\tau^-$ pairs and a NFW profile. The *Fermi-LAT* exclusion limit for Fornax is added extending up to 1 TeV [4]. The exclusion curves for the Galactic Center halo are plotted in Figure 3 for a DM particle annihilating into quark-antiquark pairs (*left*) and a DM particle annihilating directly into two photons, producing a spectral line (*right*) [5,6]. Two DM halo profiles are assumed, a NFW and an Einasto profile.

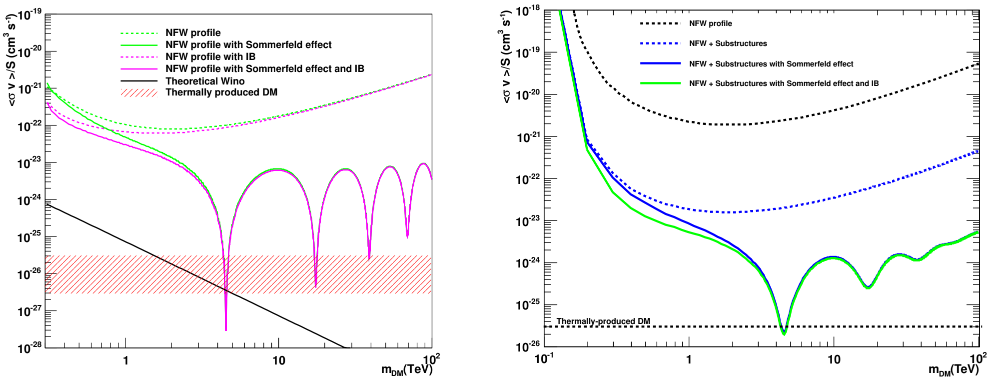

Figure 2 – *Left:* Upper limit at 95% C.L. on $\langle\sigma v\rangle/S$ as function of the DM particle mass enhanced by the Sommerfeld effect and the internal Bremsstrahlung for a NFW profile of Sculptor. *Right:* Upper limit at 95% C.L. on $\langle\sigma v\rangle/S$ as function of the DM particle mass enhanced by the Sommerfeld effect, the internal Bremsstrahlung and halo substructures for a NFW profile of Fornax. See [3,4] and references therein for more details.

5 Enhancement effects of the gamma-ray flux

Three cases that can modify their exclusion limits were considered for the dwarf galaxies and the Fornax galaxy cluster: two particle physics effects, namely the *Sommerfeld enhancement* and the

Internal Bremsstrahlung (IB) from the DM annihilation, and an astrophysical effect due to the mass distribution of *dark-matter substructures* [3,4]. The joint enhancement due to the Sommerfeld effect added to the IB and the substructures contribution is plotted in Figure 2 for Sculptor (*right*) and for Fornax (*left*). Some specific wino masses can be excluded at the level of $\langle\sigma v\rangle_0 \sim 10^{-26}$ cm^{3}s^{-1}. The effect of the IB is only significant in the exclusion limits for the low mass DM particle regime. The enhancement of the gamma-ray flux due to substructures, and thus the improvement of the exclusion limits, is particularly important for galaxy clusters, but its effect is negligible for dwarf galaxies.

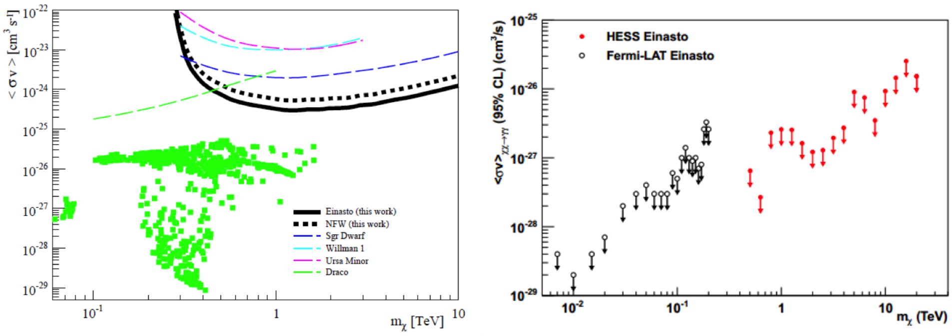

Figure 3 – Upper limit at 95% C.L. of $\langle\sigma v\rangle$ as function of the DM particle mass for the Einasto and NFW density profiles of the Galactic halo for a DM particle annihilating into quark-antiquark pairs (*left*) and a DM particle annihilating directly into two photons, producing a spectral line (*right*). *Fermi-LAT* results as well as other limits derived from the observation of dwarf galaxies are showed for comparison. See [5,6] and references therein for more details.

6 Conclusions

The H.E.S.S. collaboration has observed several candidates to harbour a sizeable very-high energy gamma-ray signal from DM particles self-annihilation, such as Sagittarius, Canis Major, Scultor and Carina dwarf galaxies, the Fornax galaxy cluster and the Galactic Center halo. No significant gamma-ray excess was found at the position of these objects. Constraints have been obtained for the velocity weighted annihilation cross section $\langle\sigma v\rangle$ as a function of the DM particle mass for several particle models and DM density distribution profiles of each target. H.E.S.S. limits are among the best derived by IACTs in the TeV mass range, and well-complementary to MeV-GeV limits derived by *Fermi-LAT* . Recently H.E.S.S. has achieved more than 90 hours of observation on the Sagittarius dwarf galaxy [7] and the stacking of all the dwarf galaxies observation is promised to significatively improve the actual limits. Moreover, the phase 2 of the H.E.S.S. telescope has already started to take data. It consists of a new large 28 m diameter telescope located at the center of the existing array. The analysis energy threshold is lowered down to ∼50 GeV, allowing to explore a lower DM mass range.

References

1. F. Aharonian, et al., (H.E.S.S. Coll.), Astropart. Phys. 29 (2008) 55 [Erratum-ibid. 33 (2010) 174].
2. F. Aharonian, et al., (H.E.S.S. Coll.), Astrophys. J., 691 (2009) 175.
3. A. Abramowskiet al., (H.E.S.S. Coll.), Astropart. Phys. 34 (2011) 608.
4. A. Abramowskiet al., (H.E.S.S. Coll.), Astrophys. J., 750 (2012) 123.
5. A. Abramowskiet al., (H.E.S.S. Coll.), Phys. Rev. Lett., 106 (2011) 161301.
6. A. Abramowskiet al., (H.E.S.S. Coll.), Phys. Rev. Lett., 110 (2013) 041301.
7. Lamana, G. et al. (2013). (H.E.S.S. Collaboration). arXiv:1307.4918

Indirect search of Dark Matter with the MAGIC telescopes

P. Colin[1], J. Aleksić[2], J. Rico[2] and S. Lombardi[3] for the MAGIC collaboration
[1] *Max-Plank-Institut für Physik, D-80805 München, Germany*
[2] *IFAE, Campus UAB, E-08193 Bellaterra, Spain*
[3] *INAF Notional Institute for Astrophysics, I-00736 Roma, Italy*

Determining the nature of dark matter (DM) is one of the most exciting and difficult tasks of modern science. In most of the suggested hypothesis, the DM particles should annihilate or decay into standard matter that would produce high energy gamma-ray signal. The MAGIC telescopes search for such DM signatures in the 50 GeV–50 TeV energy range. Suitable targets are the Galactic Centre, local DM clumps, satellite dwarf spheroidal galaxies and galaxy clusters. We concentrated our effort on one of the most promising candidates, the dwarf spheroidal galaxy Segue 1, which has a mass-to-light ratio estimated to the order of 1000. The 160 hours of observation, carried out between 2011 and 2013, were analyzed with a likelihood approach optimized for signals with characteristic spectral features of different DM theoretical scenarios. Our results represent the most stringent constraints to the annihilation cross-section and decay lifetime obtained from satellite galaxy observations, for masses above few hundred GeV.

1 Introduction

Observational evidence at all scales and cosmological predictions indicate that Dark Matter (DM) must represent almost 85% of the Universe matter content, and about 25% of its total energy budget[1]. Discovering its essence is one of the most exiting tasks of modern sciences. Nevertheless, despite strong efforts, no experiment has been able to detect it (directly or indirectly) beyond its gravitational effects. The current searches are mainly focused on weakly interacting massive particles (WIMPs), produced thermally in the early Universe, stable on cosmological scales. WIMPs are expected to annihilate or decay into Standard Model (SM) particles, such as gamma-rays, that could be detected by the existing experiments.

The characteristic of the gamma-ray flux from DM, that is to be measured on Earth, is determined by two independent factors: one coming from the particle physics (properties of the DM particles) and the other one from the astrophysics (spatial distribution of DM). The particle physics term fixes the shape of the expected spectrum for all possible sources. The astrophysical factor determines the flux intensity for a specific source, depending on its DM density profile and distance.

The best astrophysical objects to search for DM gamma-ray signal are the structures that are supposed to harbour a peak of DM density in comparison to the surrounding. The object with the highest astrophysical factor is the Centre of the Galaxy. However, this region is strongly contaminated with standard astrophysical gamma-ray sources and may not be the best candidate for the detection of DM signal. The Galactic halo and the substructures of the halo are more suited for such searches because they are outside of the gamma-ray bright Galactic plane. Another interesting class of object is the ones dynamically dominated by DM, such as dwarf spheroidal galaxies (dSphs) and galaxy clusters.

2 The MAGIC telescopes

2.1 An evolving instrument

MAGIC is a very high energy gamma-ray observatory located on the Canary Island of La Palma, using 17 m Cherenkov telescopes with an energy threshold of about 50 GeV. Since its deployment, the instrument is regularly improved with major hardware upgrades. The first telescope (MAGIC-I) started operation in 2004 in stand-alone mode. In 2008, the electronic readout was exchanged with a 4 times faster system (2 GSample/s). In 2009, a second telescope (MAGIC-II) with an improved camera (double number of pixels and larger trigger area) entered in operation. In 2012, the camera of MAGIC-I was upgraded with a clone of the MAGIC-II camera. Ever since, the observations are carried out in stereoscopic mode with a symmetrical system. The current MAGIC performance[2] above 250 GeV is: an integral sensitivity in 50 h of 0.7% of the Crab Nebula flux, an angular resolution of 0.07°, and an energy resolution of ∼15%.

2.2 The DM search programme

MAGIC efforts in DM searches were first performed in single mode (with MAGIC-I), directed towards the Galactic Centre [3], considered as the best DM candidate. However, the difficulty to isolate DM signal in this very crowded region incited us to investigate also in other directions.

Very promising targets with high DM density in relative proximity to the Earth (less than 100 kpc) are the dSph satellite galaxies of the Milky Way. These galaxies are believed to be the smallest (size ∼1 kpc), faintest (luminosities 10^2-10^8 $L_\odot$) astronomical objects whose dynamics are dominated by DM (mass-to-light ratios up to 10^3 $M_\odot/L_\odot$), and without expected astrophysical gamma-ray sources. MAGIC observed, for few tens of hours in single mode, the dSph Draco[4], and the ultra-faint dSphs Willman 1[5] and Segue 1[6]. The latest observation provided the most stringent constraints to DM models. When MAGIC became a stereoscopic system, it was opted to invest in a long-term observational campaign of the best DM candidate available to MAGIC. The resulting sample is to be used as a test area for the ever-evolving DM theories. The chosen source was the ultra-faint dSph Segue 1. Next section summarizes the results obtained with this deep observation that represents the longest exposure of any dSph galaxy by any Cherenkov telescope experiments so far [7].

Clusters of galaxies are the biggest known gravitationally bound systems with total masses around 10^{14}- 10^{15} $M_\odot$. These systems must host enormous amounts of DM (∼80% of the mass), which should concentrate at their centre and present many substructures that could significantly boost the flux from DM annihilation. MAGIC observed the nearby Perseus Cluster in both single and stereoscopic modes. DM constraints were derived from the MAGIC-I observation[8], whereas the stereo observation resulted in the detection of two radiogalaxies[9]. Interpretations in terms of DM physics become more difficult because of the presence of these astrophysical sources.

According to cosmological simulations, the Galactic DM halo must be clumpy. Local DM subhalos are good targets for the DM detection as they should appear where no paricular astrophysical source is expected. Steady *Fermi*-LAT sources with no counterpart observed at any other wavelengths are promising DM subhalo candidates. We observed unassociated *Fermi* objects, which have the highest chance to be detected with MAGIC, and look for common spectral features. Unfortunately, these observations have not been successful so far, and no signal was found in the MAGIC range[10,11].

3 Deep observation of Segue 1

3.1 Segue 1

Located at a distance of 23 kpc, the dSph Segue 1 lies in the Northern hemisphere, outside of the Galactic plane in a region well suited for MAGIC observation at low zenith angles. This galaxy has a mass-to-light ratio estimated to $\sim 3400\,\mathrm{M}_\odot/\mathrm{L}_\odot$, making it the most DM dominated object known so far[12]. In addition, almost no gamma-ray background of conventional origin is expected from this source at very high energy.

Observations of Segue 1 were performed by MAGIC between January 2011 and February 2013, under the dark night conditions, for zenith angle range between 13° and 37°, ensuring a low energy threshold. During this period, the telescopes underwent a series of significant changes and MAGIC performance varied during the total period of Segue 1 observations. Therefore, data from each of the different telescope states are analyzed separately. After the selection and data reduction procedures of the MAGIC standard analysis chain, the total effective observation time amounted to 157.9 h of good-quality data.

3.2 Full likelihood analysis

The typical annihilation (decay) gamma-ray spectrum is predicted to be continuous and featureless, with photons mainly produced from the pion decay and the final state radiation of charged particles. However, some distinctive spectral features could be present, like monochromatic line or pronounced peak towards the kinematic limit from emission of virtual internal bremsstrahlung (VIB) photons[13]. The full likelihood method is optimized for recognition of characteristic signatures such as DM signal may leave in the gamma-ray spectrum [14].

The basic concept of full likelihood method is to compare the measured and expected energy spectrum. Thus, it requires a gamma-ray signal model (here based on the DM model studied) and a background model (here based on off-source measurements). It takes maximal advantage of the spectral information, and achieves significantly better sensitivity than the standard analysis chains. Moreover, with a simple multiplication of the likelihood, it allows straightforward combination of results from different periods, instruments, or even different sources.

3.3 MAGIC results

The stereo MAGIC observations of Segue 1 were analyzed using the full likelihood approach [7]. No significant gamma-ray excess was found above the background, thus the 95% c.l. upper and lower limits were calculated instead, for different models of DM annihilation and decay. The considered scenarios include: annihilation and decay into the final state SM particles, direct annihilation and decay into photon(s) and 3-body annihilation with VIB contribution. To make the study as model-independent as possible, the branching ratio is assumed to be 100% for all of the channels. The DM particle mass takes values from the 100 GeV–10 TeV range (200 GeV–20 TeV for the decay scenarios). Furthermore, no additional boosts to the signal, either from the presence of substructures or from quantum effects were taken into the account.

Figure 1 shows the resulting upper limits on the annihilation cross section and the lower limits on the decay lifetime. These are the strongest bounds from dSph observations by Cherenkov telescopes. The limits for leptonic channels are more stringent than the strongest *Fermi*-LAT ones from the joint analysis of 25 dSphs [15], for DM masses above 300 GeV and 500 GeV, for annihilation into $\mu^+\mu^-$ and $\tau^+\tau^-$, respectively. In addition, the constraints from this work are at least an order of magnitude stronger than the previous most sensitive MAGIC results[6].

Searches for monochromatic lines were done as well assuming direct annihilation into two photons, and one photon and one Z boson. Although these processes are highly loop suppressed, potential detection of such a feature would provide a firm proof of the DM existence, and reaveal information regarding its nature. The bounds derived from this work are at least one order of magnitude less constraining than the results from HESS[16] and *Fermi*-LAT[17] line searches from the Galactic central region. This, however, is expected, given the different targets considered in these analysis. In comparison with results derived from dSphs observations, MAGIC results are highly competitive.

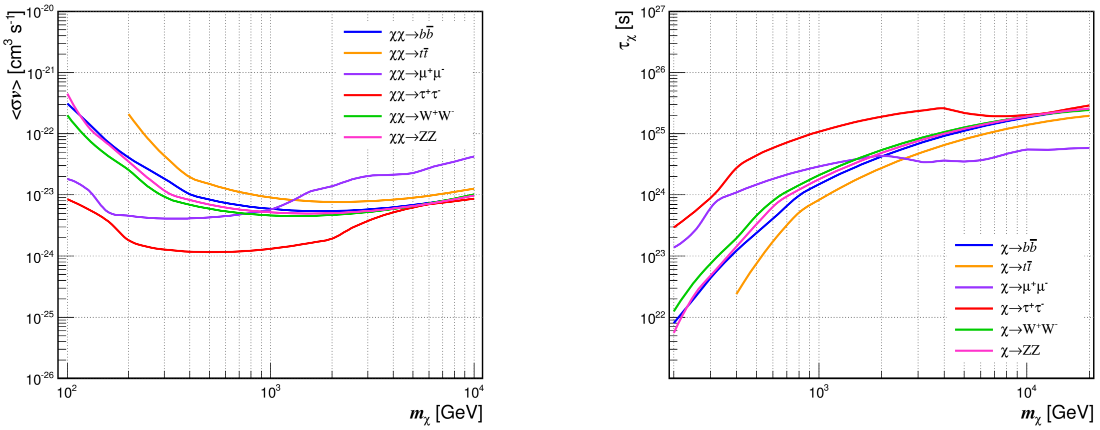

Figure 1 – Upper limits on the annihilation cross-section (left) and lower limit on the decay lifetime (right), for secondary gamma-rays from several final states, obtained from deep observation of Segue 1 with MAGIC[7]

Acknowledgments

We would like to thank the Instituto de Astrofísica de Canarias for the excellent working conditions at the Observatorio del Roque de los Muchachos in La Palma. The support of the German BMBF and MPG, the Italian INFN, the Swiss National Fund SNF, and the Spanish MICINN is gratefully acknowledged. This work was also supported by the CPAN CSD2007-00042 and MultiDark CSD2009-00064 projects of the Spanish Consolider-Ingenio 2010 programme, by grant 127740 of the Academy of Finland, by the DFG Cluster of Excellence "Origin and Structure of the Universe", by the Croatian Science Foundation (HrZZ) Project 09/176, by the DFG Collaborative Research Centers SFB823/C4 and SFB876/C3, and by the Polish MNiSzW grant 745/N-HESS-MAGIC/2010/0.

References

1. G. Bertone, D. Hooper& J. Silk, Physics Report **405**, 279 (2005).
2. J. Sitarek *et al.* (MAGIC collaboration),Proc. of 33nd ICRC , Rio (2013) - arXiv:1308.0141
3. MAGIC collaboration, J. Albert *et al.*, ApJ **638**, L101 (2006).
4. MAGIC collaboration, J. Albert *et al.*, ApJ **679**, 428 (2008).
5. MAGIC collaboration, E. Aliu *et al.*, ApJ **697**, 1299 (2009).
6. MAGIC collaboration, J. Aleksić *et al.*, JCAP **06**, 035 (2011).
7. MAGIC collaboration, J. Aleksić *et al.*, JCAP **02**, 008 (2014).
8. MAGIC collaboration, J. Aleksić *et al.*, ApJ **710**, 634 (2010).
9. P. Colin *et al.* (MAGIC collaboration), AIP Conf. Proc. **1505**, 578 (2012).
10. D. Nieto *et al.* (MAGIC collaboration), Proc. of 32nd ICRC , Beijing (2011).
11. J. Aleksić *et al.* (MAGIC collaboration), Proc. of 33nd ICRC , Rio (2013).
12. J. Simon *et al.*, ApJ **733**, 46 (2011).
13. T. Bringmann *et al.*, JCAP **07**, 054 (2012).
14. J. Aleksić, J. Rico & M. Martinez, JCAP **10**, 032 (2012).
15. *Fermi*-LAT collaboration, M. Ackermann *et al.*, Phys. Rev. D **89**, 042001 (2014).
16. H.E.S.S. collaboration, M. Abramowski *et al.*, Phys. Rev. Lett. **L110**, 041301 (2013).
17. *Fermi*-LAT collaboration, M. Ackermann *et al.*, Phys. Rev. D **86**, 022002 (2012).

Detecting WIMP Dark Matter Signatures by Cross-Correlating Gamma-Ray Anisotropies and Cosmic Shear

Stefano Camera
CENTRA, Instituto Superior Técnico, Universidade de Lisboa, Avenida Rovisco Pais 1, 1049-001 Lisboa, Portugal

Both the gravitational lensing effect of cosmic shear and cosmological γ-ray emission are strongly related to the presence of dark matter (DM) in the Universe. Indeed DM structures are responsible for bending the light due to gravitational lensing, and those same objects can emit gamma rays, either because they host astrophysical sources, or directly by WIMP (Weakly Interacting Massive Particle) DM annihilations or decays. Such γ rays should therefore exhibit strong correlation with the cosmic shear signal, thus potentially providing novel information on the composition of the extragalactic γ-ray background (EGB). If the WIMP DM contribution to the EGB is significant enough, its strong correlation with cosmic shear makes such signal in principle detectable by combining forthcoming experiments.

1 State of the Art and Motivations

Despite the huge abundance of dark matter (DM) in the Universe, very little is known about its nature.[1] For this reason, a tremendous experimental effort aiming at delivering the first, much awaited non-gravitational detection of DM has been put by the cosmologists' and particle physicists' communities over the last decade or so. One of the theoretically more promising techniques that have been pursued is the search for WIMP DM signatures in the extragalactic γ-ray background.[2] The underlying hypothesis is that the DM structures in the Universe can themselves emit light at various wavelengths, including the γ-ray range. On the one hand, γ-rays are produced by astrophysical sources hosted inside DM haloes—e.g. star-forming galaxies (SFGs) or active galactic nuclei (AGNs)—, whilst on the other hand DM itself may be a source of γ-rays, through its self annihilation or decay (depending on the properties of the DM particle).

2 Auto-Correlation of Gamma-Ray Anisotropies

The most recent measurement of the EGB was performed by the Fermi Large Area Telescope (LAT), covering a range between 200 MeV and 100 GeV.[3] The emission is obtained by subtracting from the whole Fermi-LAT data the contribution of resolved sources (both point-like and extended) and the Galactic foreground (due to cosmic-ray interaction with the interstellar

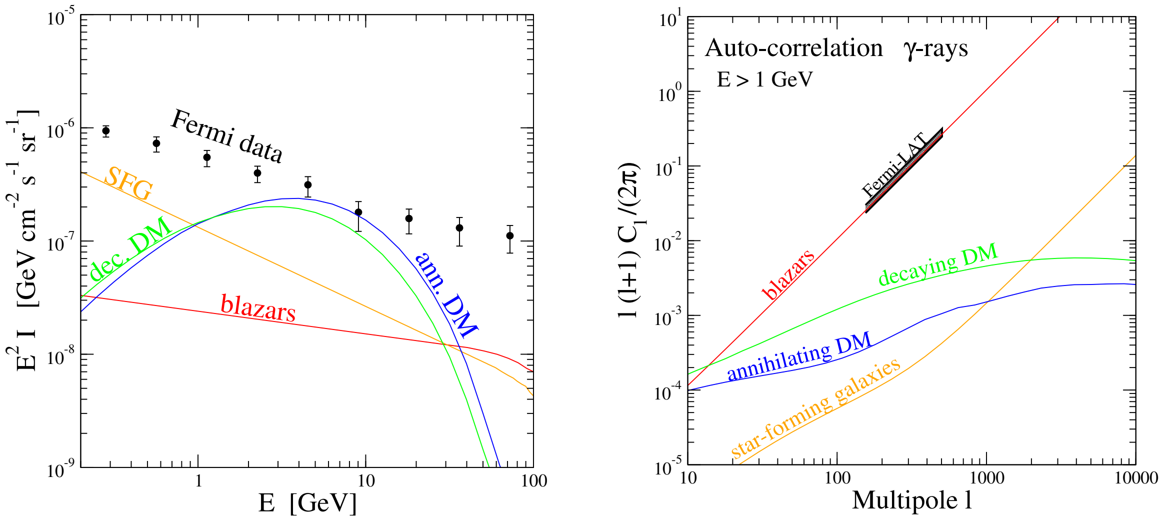

Figure 1 – *Left*: EGB emission as a function of observed energy for the four extragalactic components described in the text and current Fermi-LAT data.[3] *Right:* γ-ray angular PS at $E > 1$ GeV for the same models of the left panel alongside the observed angular PS, summarised by the black band.[4]

medium). Unresolved astrophysical sources like blazars and radio galaxies still contribute to the EGB, but the exact amount of their contribution is unknown. Similarly, γ-rays produced by DM annihilation or decay in principle also contribute to EGB. The situation is summarised in Fig. 1: the left panel shows the EGB emission as a function of the observed energy for SFGs, blazars and a viable WIMP with mass $m_\chi = 100(200)$ GeV for annihilating(decaying) DM and final state $b\bar{b}$, together with current Fermi-LAT data; the right panel illustrates the γ-ray angular PS at $E > 1$ GeV for the same models of the left panel, alongside the observed angular power spectrum (PS; black band).[4]

The fact that the EGB energy spectrum (Fig. 1a) is compatible with a power law, without any evident spectral feature, suggests that DM cannot play a leading rôle in the whole energy range.[3] In the angular anisotropies of the EGB emission (Fig. 1b), DM is even more subdominant. Indeed, a detection of a significant auto-correlation angular PS has been recently reported for multipoles $\ell > 100$—the range of interest for our analysis, since the contamination of the Galactic foreground can be there neglected—but the features of such a signal suggest an interpretation in terms of blazars.[4,5]

3 Cross-Correlation of Gamma-Ray Anisotropies and Cosmic Shear

Weak gravitational lensing refers to the small distortions of images of distant galaxies, produced by the distribution of matter located between galaxies and the observer.[6,7] Weak lensing studies aim at reproducing the statistical properties of the density field acting as a lens, as well as investigating the geometrical properties of the Universe. A distorted image can be described by the so-called distortion matrix, normally parameterised in terms of the convergence κ (controlling modifications in the size of the image) and the shear γ (accounting for shape distortions). The auto-correlation between the gravitational shear in two different directions can provides information on the clustering of the large scale structures, responsible for the lensing effect. Future surveys, like the Dark Energy Survey (DES) and Euclid, due to their large coverage and improved sensitivities, will reconstruct two-dimensional shear maps, from which one can extract the auto-correlation cosmic shear PS.[8,9,10]

Besides, as we have seen, the same DM structures that act as lenses can themselves emit γ-rays. Those γ-rays emitted by DM should therefore exhibit some degree of correlation with the gravitational lensing signal. In the context of the current endeavour aiming at detecting the first non-gravitational detection of DM, Camera et al. (2013) proved, for the first time, how

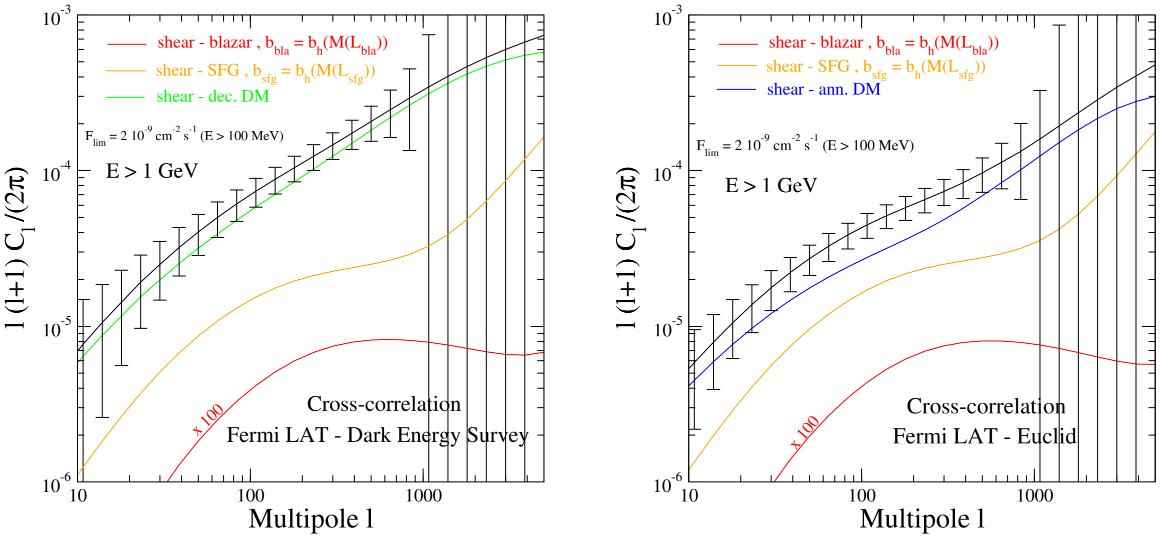

Figure 2 – *Left*: cross-correlation between cosmic shear and γ-ray emission, for SFGs, blazars and decaying DM, with a γ-ray threshold as expected for Fermi-LAT after 5 yr of exposure and DES as the reference lensing survey. Error bars are estimated for the total signal (in black). *Right*: same as in the left panel but for annihilating DM and with Euclid as reference lensing survey.

distinctive signatures of DM can be detected in the cross-correlation between the cosmic shear and the so-called (EGB).[11] The core of their results can be understood by looking at Fig. 2. The strength of this method—which can provide novel information on the composition of the EGB—lays in the fact that the shear signal is stronger for larger halo masses and most of the γ-ray emission from annihilating/decaying DM is produced in large mass haloes as well. Thus, their cross-correlation is more significant than for the case of astrophysical sources (which are associated with galaxy-mass haloes). For more details see Camera et al. (2013) and references therein.[11]

Since then, Shirasaki et al. (2014) measured the 2-point cross-correlation function of Fermi-LAT data gathered until January 2014 with the cosmic shear signal detected by the Canada-France-Hawaii Telescope Lensing Survey (CFTHLenS).[12,13] The measurement was consistent with no signal and the null detection was used to derive constraints on the DM annihilation cross section. The upper limits excluded values smaller than the thermal cross section, 3×10^{-26} cm^3/s—an additional proof of the potential of such a technique for indirect detection of DM.

3.1 Tomography of the Cross-Correlation of Gamma-Ray Anisotropies and Cosmic Shear

An even more effective technique is being pursued in Camera et al. (2014).[14] It involves a tomographic approach to the study of the cross-correlation between cosmic shear and γ-ray emission. Tomography takes advantage of the different behaviours of the abundances of astrophysical sources and DM as a function of redshift or γ-ray energy. Then, by computing the cross-correlation PS in different redshift and energy bins, and studying how the PS changes as a function of z or E_γ, this significantly boosts the capability of the cross-correlation PS to determine the composition of the EGB and to distinguish DM from astrophysical components.

This is particularly useful because, on the one hand, the redshift dependence of γ-rays generated by astrophysical objects is peculiarly different from what expected for DM-sourced γ-rays, and, on the other hand, the energy spectrum of DM-produced γ-rays peaks at an energy proportional to the WIMP mass, whereas unresolved astrophysical sources contribute to the EGB with well defined power laws. Preliminary results have been obtained by performing a Fisher matrix analysis for the cross-correlation of gamma-ray anisotropies and cosmic shear to forecast the capabilities of a weak lensing survey like DES and a gamma-ray experiment as Fermi-LAT in constraining the WIMP DM mass, m_χ, and its annihilation cross-section, $\langle\sigma_a v\rangle$,

Table 1: Forecast 1σ marginal errors on decaying DM model parameters for the fiducial values $\{m_\chi,\, \Gamma_d,\, \mathcal{A}_B,\, \mathcal{A}_{\rm SFG},\, \mathcal{A}_{\rm AGN}\} = \{200\,{\rm GeV},\, 0.33\times10^{-26}\,{\rm s}^{-1},\, 1,\, 1,\, 1\}$.

Binning	m_χ [GeV]	Γ_d [$10^{-26}\,{\rm s}^{-1}$]	$\mathcal{A}_B$ [$-$]	$\mathcal{A}_{\rm SFG}$ [$-$]	$\mathcal{A}_{\rm MAGN}$ [$-$]
—	5.7×10^4	25	1.5×10^7	1.4×10^4	2.0×10^3
E_γ	40	1.1×10^{-2}	1.1×10^5	6.1×10^2	13
z	1.1×10^3	4.7×10^{-2}	9.1×10^4	3.2×10^2	21
E_γ-z	13	3.5×10^{-3}	1.6×10^4	1.7×10^4	3.8

or its decay rate, Γ_d (for annihilating or decaying DM, respectively).[14] Besides SFGs and blazars, misaligned AGNs too have been considered as astrophysical gamma-ray emitters, for they are too significantly contribute to the EGB. To account for the underlying ignorance on the relative abundances, the amplitudes of the one-halo power spectra of astrophysical sources are included as nuisance parameters. The cosmic shear signal is divided into 3 redshift bins of width $\Delta z = 0.4$ from 0.3 to 1.5, whilst gamma-ray measurements into 6 energy bins between 1 and 300 GeV. As an example, the forecast marginal errors on decaying DM model parameters are summarised in Table 1, with different slicing strategies to better illustrate impact and rôle of tomography.

4 Conclusions

The cross-correlation of γ-ray anisotropies and cosmological observables related to the clustering of DM structures—such as the weak lensing effect of cosmic shear—clearly appears as a promising method to detect peculiar signatures of the particle nature of DM. Furthermore, if successful, such an approach could provide direct evidence that what is measured by weak-lensing surveys is indeed due to DM and is not for instance to a manifestation of alternative theories of gravity.

Acknowledgments

SC is funded by FCT-Portugal under Post-Doctoral Grant No. SFRH/BPD/80274/2011. SC warmly thanks Mattia Fornasa, Nicolao Fornengo and Marco Regis for allowing him to show results from a common project.

References

1. Planck Collaboration, *eprint* , arXiv:1303.5076 (2013).
2. N. Fornengo, L. Pieri and S. Scopel, *Phys. Rev.* D **70**, 103529 (2004).
3. A.A. Abdo *et al.*, *Phys. Rev. Lett.* **104**, 101101 (2010).
4. M. Ackermann *et al.*, *Phys. Rev.* D **85**, 083007 (2012).
5. J.P. Harding and K.N. Abazajian, *J. Cosmol. Astroparticle Phys.* **1211**, 026 (2012).
6. M. Bartelmann and P. Schneider, *Phys. Rept.* **340**, 291 (2001).
7. M. Bartelmann, *Class. Quant. Grav.* **27**, 233001 (2010).
8. T. Abbott *et al.*, *eprint* , arXiv:astro-ph/0510346 (2005).
9. R. Laureijs *et al.*, *ESA-SRE* **12**, (2011).
10. L. Amendola *et al.*, *Living Rel. Rev.* **16**, 6 (2013).
11. S. Camera, M. Fornasa, N. Fornengo and M. Regis, *Astrophys. J. Lett.* **771**, L5 (2013).
12. M. Shirasaki, S. Horiuchi, and N. Yoshida, *eprint* , arXiv:1404.5503 (2014).
13. C. Heymans *et al.*, *Mon. Not. Roy. Astron. Soc.* **427**, 146 (2012).
14. S. Camera, M. Fornasa, N. Fornengo and M. Regis, *in prep.* (2014).

Overview of ANTARES results on Dark Matter Searches

J.D. Zornoza[a]
IFIC (Univ. of Valencia - CSIC, c/Catedrátcico José Beltrán, 2, 46980, Paterna, Valencia, Spain

The search for dark matter is one of the most important goals of neutrino telescopes. The ANTARES detector, installed in the Mediterranean Sea, is taking data since 2007. Neutrino telescopes have interesting advantages for this kind of searches, as it will be discussed. In this talk we will review the status and results of the analyses performed in ANTARES for several sources: the Sun, Galactic Centre and the Earth.

1 Introduction

There is compelling evidence that a large part of the matter content of the Universe is made of some something beyond the Standard Model of particle physics. Among these experimental proofs we can mention the observations from Planck, the results on the Big Bang Nucleosynthesis, the rotation curves of galaxies and the studies of highly red-shifted Ia supernovae. The conclusion from these experimental results is that about about 85% of the matter of the Universe is non-baryonic. In the most studied scenarios, it is assumed that the properties of this matter are the following: weak interaction with matter, no interaction with photons, non-zero mass and stability. The list of possible candidates for explaining this component is large, but one of the most appealing frameworks is SuperSymmetry, in particular in the models which offer neutralino as a dark matter candidate. The stability of neutralino would be preserved by the R-parity conservation.

The search for dark matter is one of the main goals of neutrino telescopes like ANTARES. The potentially interesting sources include the Sun, the Galactic Centre, the Earth, dwarf galaxies and galaxy clusters. Each source has advantages and disavantages. The same applies to the different detection techniques (direct, indirect, accelerators), as it will explained.

If dark matter is made of weakly interacting particles (WIMPs), like neutralinos, they can scatter in astrophysical objects like the Sun or the Earth and become gravitationally trapped. Their self annihilation would produce, directly or (more commonly) indirectly high energy neutrinos. Dark matter forming part of the halo of the Galaxy can also annhilite and produce a signal, in particular in the direction of the Galactic Centre.

---

[a] on behalf of the ANTARES Collaboration

2 The ANTARES detector

The ANTARES collaboration finished the installation of a neutrino detector [1] in the Mediterranean Sea in 2008. By 2007, five of the final twelve lines were already taking data. The detector is deployed at a depth of 2500 m and about 40 km of the French coast, near Toulon. It consists of 885 photomultipliers installed along twelve vertical lines anchored to the sea bed. The operation principle is based on the detection of the Cherenkov light induced by the relativistic muons produced after the charged-current interaction of high energy muon neutrinos close/inside the detector.

In the analyses presented in this paper, about 1300 days of data are used, corresponding to the period from 2007 to 2012. As mentioned before, only five lines were installed during 2007.

There are two sources of background. On the one hand, the so-called atmospheric muons, which are produced by the interaction of cosmic rays in the atmosphere. This is a huge background that can be partially reduced by installing the detector at a large depth, as it is the case for ANTARES. Even at a depth of 2000-2500 m, the atmospheric muon background is quite important, so only upgoing events are selected for the analysis, so that the Earth acts as a shield stopping atmospheric muons. An additional cut in the quality of the events is also needed in order to reject down-going atmospheric muons which are badly reconstructed as upgoing. The second kind of background are the atmospheric neutrinos produced also by cosmic rays. This is an irreducible background, but expected to be distributed diffusely in the sky, while the signal would be concentrated around the source.

3 Analysis method and results

Different methods have been used for reconstructing the muon track. For low masses (below ~250 GeV), an algorithm called BBFit has been used [4], which offers a better response for low energies. In particular, it is used for the events reconstructed with only one line. For these events, the azimuth information is not available, but the information on the zenith angle helps to distinguish between signal and background. For higher masses, a likelihood algorithm is used [5].

The analyses presented in this paper have been done using a binned method. The strategy consists in finding the optimum selection in terms of neutrino flux sensitivity. The selection variables are the opening cone angle (i.e. the maximum angular distance to the source) and a cut in a parameter which describes the quality of the track reconstruction. All these cuts are chosen following a blind procedure.

3.1 The Sun

For the Sun, the signal is simulated with WIMPSim [3], which takes into account the main ingredients of the neutrino production and propagation. Since the compostion of the neutralino is not known, we consider several channels (pessimistic and optimistic) assuming a branching ratio of one. The real situation should be between these extreme cases. One of the advantages of the searches for dark matter in the Sun, compared with other indirect searches, is that a potential signal would be free of astrophysical background. Neutrinos from nuclear reactions in the Sun are of much lower energies. The background from cosmic rays interacting in the Sun corona is very low. Concerning the atmospheric background, it can be accurately estimated from scrambled data.

After unblinding the data, no excess of data over expected background is found, so limits on the neutrino flux limit and on the WIMP-nucleon cross section can be set (see [2] for a previous search with 2007-2008 data). The results from the search can be seen in Figure 1 (top), where the limits of the WIMP-proton scattering cross section are shown. It is important to note that neutrino telescopes offer the best limits for spin-dependent cross section (since the Sun is made basically of protons), better than those from direct searches (other indirect searches set limits on $< \sigma v >$).

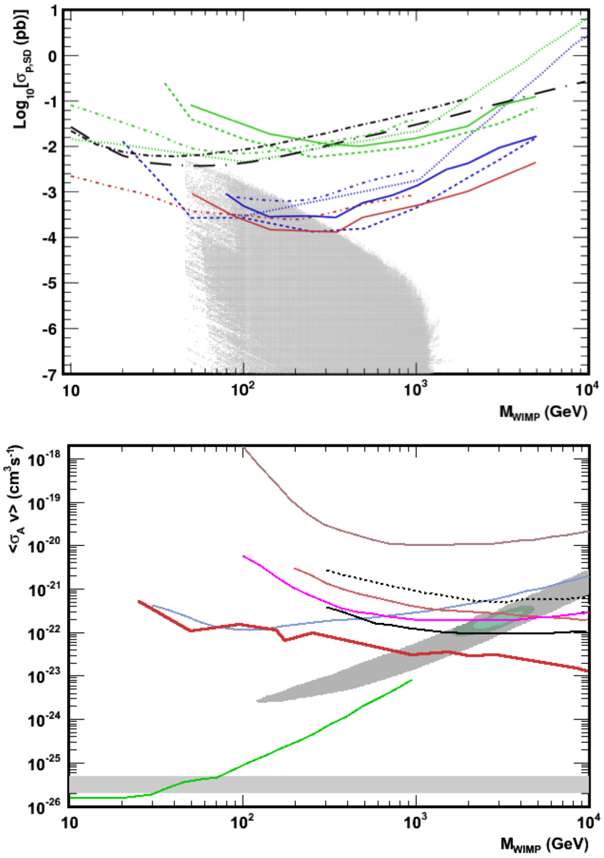

Figure 1 – Top: Spin-dependent cross-section limits for the search on the Sun: ANTARES 2007-2012 (thick solid lines): $\tau^+\tau^-$ (red), W^+W^- (blue), $b\bar{b}$ (green), IceCube-79 (dashed lines), SuperKamiokande (colored dash-dotted lines), SIMPLE (black short dash-dotted line), COUPP (black long dash-dotted line) and XENON-100 (black long dashed line). The results are compared with a scan in MSSM-7. (Preliminary). Bottom: Limits on $< \sigma v >$ for the Galactic Centre for the $\tau^+\tau^-$ channel (red solid line) with IC40 for the GC (brown solid line), IC59 for dwarf galaxies (dashed black line), IC79 for the Galactic Halo (magenta solid line), IC59 for the VIRGO cluster (black solid line), DeepCore+IC79 for the GC (blue solid line) and Fermi for dwarf galaxies (green solid line). The grey/green area represent leptophilic dark matter models which would explain the PAMELA (grey) and Fermi+PAMELA+HESS (green) excess in the Galactic Centre. (Preliminary).

3.2 The Galactic Centre

The Galactic Centre is also a very promising source for neutrino telescopes. The distance is much larger, but the total mass involved is also larger. Moreover, there is no absorption of neutrinos, contrary to what happens in the Sun, which is particularly relevant for high energy/masses, where the angular resolution improves. The signal is simulated using the simulation by Cirelli et al.[6]. The profile of the dark matter halo has been simulated with the package CLUMPY. The background, as in the case of the Sun, is evaluated by scrambling real data. After unblinding the data, no significant excess is found so limits are set in $< \sigma v >$, as shown in Figure 1 (bottom) for a NFW halo profile and the $\tau^+\tau^-$ channel. These limits exclude the leptophilic dark matter interpretation of the Fermi+PAMELA+HESS excess. It can also be seen that above ∼150 GeV the limits set by ANTARES are the best limits from neutrino telescopes, since the visibility of ANTARES of the Galactic Centre and its angular resolution are better than those of IceCube.

3.3 The Earth

Dark matter would also accumulate in the Earth after scattering, like in the case of the Sun. However, in this case we cannot assume that an equilibrium between caputre and annihilation has been reached. Moreover, since the scattering is mostly on the heavy elements in the Earth core, the limits are set on the spin-independent cross section of WIMP scattering. These limits are particularly interesting for WIMP masses close to the masses of scattering nuclei (iron and nickel). The signal is evaluated with WIMPSim and the background is calculated from the background in the zenith angle band between 160° and 170° degrees (>95% of the signal is found at zenith >170°). The sensitivity of ANTARES is shown in Figure 2.

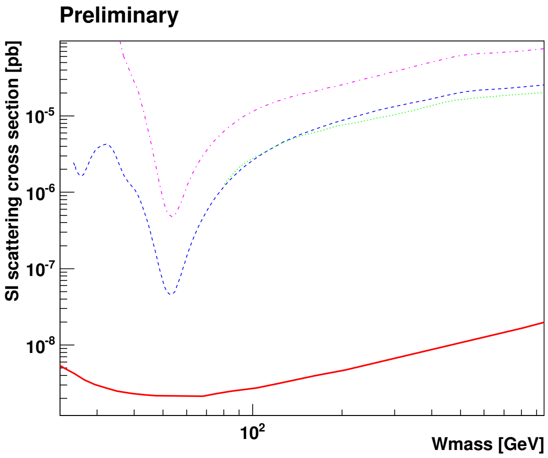

Figure 2 – Spin-independent cross section sensitivity (90% CL) for the Earth analysis, assuming $< \sigma v > \sim 3x10^{-26} cm^{-3} s^{-1}$ for three different channels: $\tau^+\tau^-$ (dash, blue), W^+W^- (dot, green) and $b\bar{b}$ (dash-dot, magenta). This sensitivity is also compared with the results of XENON-100 (solid, red). (Preliminary).

4 Conclusions

The search for dark matter is one of the main scientific goals of neutrino telescopes. ANTARES, installed in the Mediterranean Sea, has been taking data since 2007. Several sources have been studied. In this paper we have presented the results of the analysis for the Sun and the Galactic Centre (in terms of limits) and the Earth (in terms of sensitivity). Although no significant excess has been seen in the unblinded data, competitive limits have been set.

Acknowledgments

The authors acknowledge the financial support of the Spanish Ministerio de Ciencia e Innovación (MICINN), grants FPA2009-13983-C02-01, FPA2012-37528-C02-01, ACI2009-1020, Consolider MultiDark CSD2009-00064 and of the Generalitat Valenciana, Prometeo/2009/026.

References

1. M. Ageron et *al.*, Nucl. Inst.. and Meth. in Phys. Res. A **656** (2011) 11-38, arXiv:1104.1607 [astro-ph.IM]
2. S. Adrián-Martínez *et al.*, arXiv:1302.6516v1 [astro-ph.HE]
3. J. Edsjö, http://www.physto.se/edsjo/ wimpsim
4. J.A. Aguilar et *al.*, ANTARES collaboration Astropart. Phys. **34** (2011) 652-662, arXiv:1105.4116 [astro-ph.IM]
5. A. Heijboer, Ph.D. thesis, University of Amsterdam, 2004.
6. M. Cirelli *et al.*, arXiv:1012.4515 [hep-ph].

Searches for Dark Matter and High Energy Neutrinos with the IceCube Detector

Sofia Vallecorsa [a]
for the IceCube Collaboration [b]

The IceCube neutrino observatory at the South Pole offers many opportunities for astrophysics and low-energy neutrino physics: cosmic-ray air showers, atmospheric and astrophysical neutrinos, neutrinos from dark matter annihilation and a variety of searches for exotica, including supersymmetric particle produced in neutrino interactions or magnetic monopoles. Here we report on two different topics: searches for dark matter annihilating into heavy astrophysical objects and the observation of high energy astrophysical neutrinos. Although very different, these two subjects illustrate the capabilities of the cubic-kilometer IceCube array over a wide energy spectrum.

1 Introduction

The IceCube detector [1] is a cubic-kilometer Cherenkov array deployed in the ice at the geographic South Pole. Neutrino interactions in IceCube have two primary topologies: hadronic showers and muon tracks. Muon tracks are created primarily in ν_μ charged current interactions. With energies above 100 GeV, they have a typical range that is of the order of kilometers, larger than the dimensions of the detector. Showers are created by the secondary leptons produced in ν_e and ν_τ charged current interactions and in the neutral current interactions of neutrinos of all flavours. Using the timing information from individual PMTs allows for reconstruction of shower and track directions and deposited energies. The main systematic uncertainties arise from uncertainties in modelling of photon propagation in the natural ice and from uncertainties on the absolute energy scale. For showers, uncertainties on the reconstructed deposited energy are of the order of 15%, while the typical median angular resolution is 10°-15° (at about 100 TeV), whereas it is much better for tracks due to their extension (1° or better, depending on their energy and length). Although optimised for energies above 100 GeV, the IceCube detector achieves good performance also at lower energies thanks to the completion of the DeepCore subarray [2]. Newly developed veto methods against atmospheric muons significantly improve the sensitivities of analyses focused on low-energy events in the Southern Hemisphere: this can be achieved by using the DeepCore array as a fiducial volume and the surrounding IceCube detector as an active muon veto [3,4]. This procedure turns IceCube into an efficient 4π detector.

The report is split into two main sections: Sec. 2 describes the analyses leading to the observation of high energy neutrino events; Sec. 3 contains a review of most recent results on Dark Matter searches.

2 High Energy Neutrinos

Observation of high-energy neutrinos provides information on the origin and acceleration mechanism of high-energy cosmic rays. Neutrinos are produced through the decay of charged pions and

---

[a] Université de Genève, 24 quai E. Ansermet, Geneva, Switzerland

[b] http://icecube.wisc.edu

kaons, by the interaction of cosmic-ray protons and nuclei with gas and photons present in the surroundings of sources and in the interstellar space. They point back to their sources since they are neither affected by magnetic fields or absorbed by matter opaque to radiation. Large-volume Cherenkov detectors like IceCube detect these neutrinos through production of secondary leptons and hadronic showers when they interact with the detector material.

An initial analysis on 2010-2012 data resulted in the observation of two Extremely High Energy (EHE), around 1 PeV, neutrinos[5]. Atmospheric background was removed by setting a high threshold on the number of detected photo-electrons (deposited energy), with a higher value in the downward-going region (where most atmospheric muons come from). Topologies were consistent with either a neutral-current interaction or a charged-current interaction of ν_e or ν_τ . The atmospheric origin of the two events could be excluded with a 2.8σ significance.

After this first observation, a second analysis, based on the selection of high energy neutrino events with vertices well contained in the detector volume, was implemented: it improved the sensitivity for energies up to 10 TeV and it extended the energy coverage down to approximately 50 TeV. The data was collected from May 2010 using 79 strings and continuing with the completed detector (86 strings) from May 2011 to May 2013, for a total livetime of 988 days.

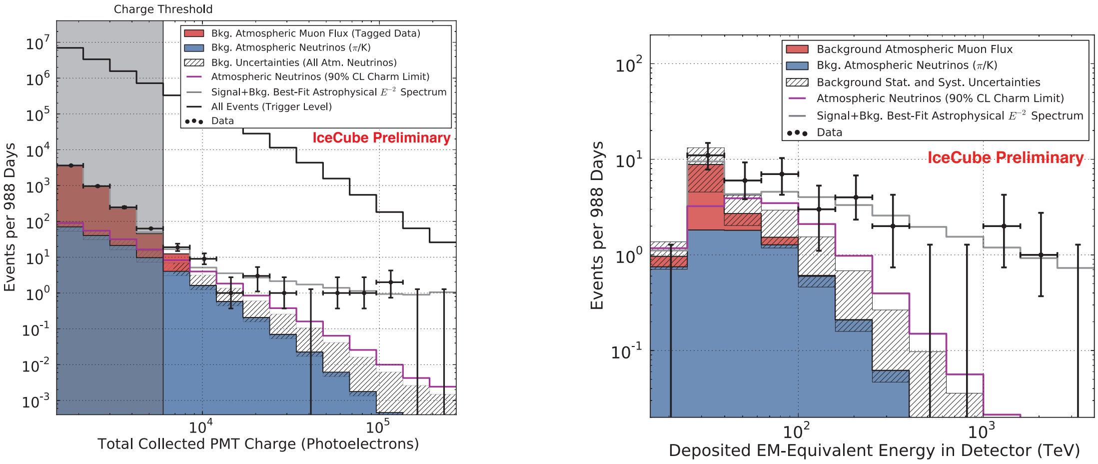

Figure 1 – (Left)Distribution of deposited summed PMT charge (Q_{tot}) for events in IceCube. The data events in the unshaded region, at $Q_{tot} > 6000$p.e., are the events reported in this work. Muons are estimated from simulation (red). The atmospheric neutrino flux (blue) is determined from previous measurements[8]. The best-fit astrophysical spectrum is represented by the grey line. The hatched region shows uncertainties on the atmospheric neutrino background including a potential component from charmed meson decays and uncertainties on the normalization of the conventional atmospheric neutrino spectrum. (Right) Deposited energies of observed events, compared to backgrounds and the best-fit astrophysical spectrum, as in figure on the left.

2.1 Backgrounds and event selection

Backgrounds for cosmic neutrino searches arise entirely from interactions of cosmic rays in the Earths atmosphere. These produce secondary muons that penetrate into underground neutrino detectors from above, as well as atmospheric neutrinos that reach the detector from all directions: the low interaction cross-section allows neutrinos to penetrate the Earth also from the opposite hemisphere.

Neutrino candidates were selected by finding events that originated within an internal fiducial volume, setting a threshold on the number of photoelectrons (p.e.) allowed at the IceCube boundary (only 3 out of the first 250 p.e.). In addition, events producing at least 6000 p.e. overall were selected to ensure a large light yield (high energy tracks). This event selection rejects 99.999% of the muon background above 6000 p.e., while retaining approximately 98% of all neutrino events interacting within the fiducial volume at energies above a few hundred TeV (Fig. 1). The remaining atmospheric muon background in the analysis came from tracks that produced too little light at the edge of the detector to be vetoed and, instead, emitted their first detected photons in the interior volume, mimicking a starting neutrino. Their rate was evaluated from data by tagging entering events using the outer layer of IceCube. In the signal region above 6000 p.e., 8.4 ± 4.2 veto-penetrating muon events were predicted in total. The energy and veto requirements also removed 70% of atmospheric neutrinos in the Southern Hemisphere, where atmospheric neutrinos are usually accompanied into the detector by muons produced in the same parent air shower[7] (suppression factor is estimated using the CORSIKA air-shower simulation). An atmospheric neutrino background of $6.6^{+5.9}_{-1.6}$ events was estimated in a 988 days livetime, with uncertainties coming from charmed meson decays (prompt neutrinos), chemical composition of cosmic rays, hadronic interaction models and the detector energy scale.

2.2 Results

In addition to the two EHE events, 35 new events were observed: this was a 5.7σ excess above expected backgrounds from atmospheric muons and neutrinos. The entire sample of 37 events included the highest energy neutrinos ever observed: nine events contained visible muon tracks, while the remaining 28 had shower-like topologies.

Following the procedure in [6], events with 60 TeV $< E <$ 3 PeV were fit in arrival angle and deposited energy to a combination of background muons, atmospheric neutrinos from π/K decay, atmospheric prompt neutrinos, and an isotropic 1:1:1 astrophysical E^{-2} test flux: the best-fit astrophysical flux in this energy range was found to be $E^2\phi(E) = 0.95 \pm 0.3 \cdot 10^{-8} \mathrm{GeV cm^{-2} s^{-1} sr^{-1}}$. This model describes the data well, with both the energy spectrum (Fig. 1) and arrival directions of the events (Fig. 2) consistent with expectations for an origin in a hard isotropic 1:1:1 neutrino flux. Moreover, the best-fit atmospheric-only alternative model would require a prompt neutrinos normalization 3.6 times higher than the current 90% CL upper limit from the northern hemisphere ν_μ spectrum measurement [8]. Even this extreme scenario was disfavored at 5.7σ with respect to a model allowing an astrophysical contribution.

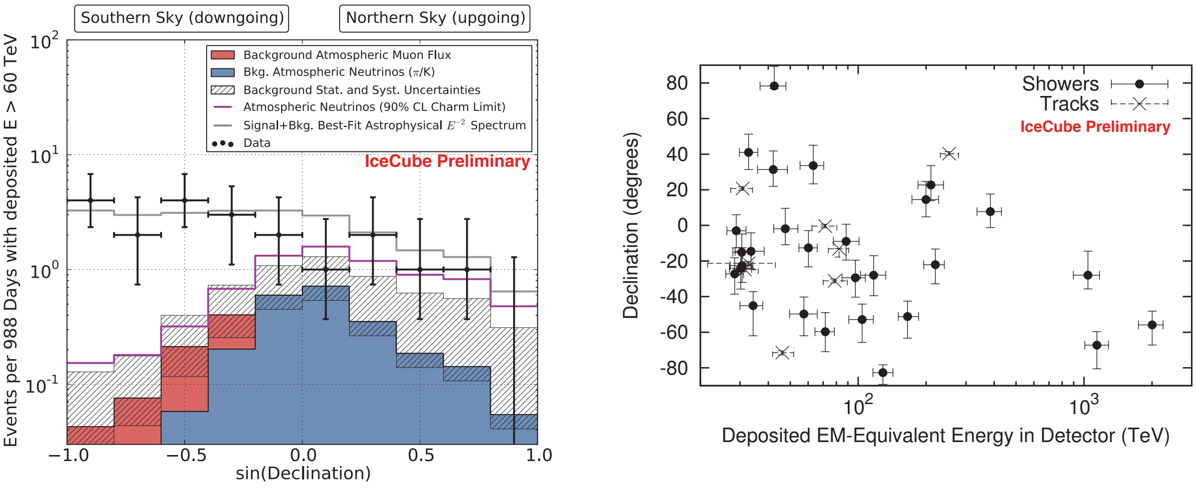

Figure 2 – (Left) Arrival angles of events with $E_{dep} > 60$ TeV, as used in the fit. The increasing opacity of the Earth to high energy neutrinos is visible at the right of the plot. Vetoing atmospheric neutrinos by muons from their parent air showers depresses the atmospheric neutrino background on the left. (Right) Arrival angles and deposited energies of the events.

As in [6], a maximum-likelihood clustering search was performed to identify the presence of neutrino sources in the data, together with a search for directional correlations with TeV gamma-ray sources. Results were consistent with expectations for equal fluxes of all three neutrino flavors and with isotropic arrival directions, suggesting either numerous or spatially extended sources.

3 Dark Matter searches

The existence of dark matter is well established by astrophysical and cosmological evidence[9]: galaxies are believed to be embedded in halos of dark matter. A variety of models exist to describe the dark matter density distribution, based on N-body simulations, observations of the motion of stars within galaxies or individual galaxies within clusters of galaxies. The Navarro-Frenk-White (NFW) model [13] is chosen as a benchmark by most IceCube analyses. The exact nature of dark matter is also unknown: many theories beyond the Standard Model[10] predict stable or extremely long-lived particles that are well-motivated dark matter candidates. Weakly Interacting Massive Particles (WIMPs) are one of the most promising and experimentally accessible classes of dark matter. In most models, WIMPs are their own antiparticles and can self-annihilate. In halos, they may be captured by gravitational wells (the Sun, for example), where their density increases over time, until the rate of self-annihilation equals the capture rate, and equilibrium is reached. The products of WIMPs annihilation depend on the details of the model, but in general, a flux of neutrinos (or gamma ray or charged cosmic rays) may be detected in large detectors such as IceCube. Signal from self-annihilating or decaying dark matter would appear as an excess of neutrinos coming from the direction of a variety of sources: the Sun[11], the Earth[4], the Galactic Halo and Galactic Center, as well as extragalactic sources such as Dwarf Spheroidal Galaxies and Galaxy Clusters [4]. Given the variety of models and the corresponding expected neutrino spectra, benchmark annihilation channels producing a soft or hard neutrino spectra are used to set limits: typically W^+W^- (or $\tau^+\tau^-$ below threshold) annihilation channel represents the hard spectrum benchmarks, with $b\bar{b}$ being the soft benchmark channel. In general neutrinos from dark matter annihilation have energies below or around 100 GeV, at the lower edge of IceCube energy reach. This is especially true for low mass dark matter candidates or sources (such as the Sun) that stop or absorb high energetic primary annihilation products before they can decay to neutrinos.

3.1 Solar WIMPs

Searches for dark matter from the Sun are sensitive to the WIMP-proton scattering cross section, which initiates the capture process. They complement direct searches on Earth as they scale with the averaged dark matter density along the solar circle, they are more sensitive to low WIMP velocities and they depend only weakly on the underlying WIMP velocity distribution [9]. Moreover, since the Sun is composed mostly of hydrogen, it is an ideal target to study WIMPs spin-dependent couplings to matter. The analysis presented here searched from neutrinos from WIMPs with masses down to 35 GeV, using data collected by the 79 string detector configuration from May 2010 to May 2011. For the first time, at such low energies, this search extended to the southern hemisphere, bringing the livetime to 318 days. The use of the DeepCore array, allowed a strong reduction of the energy threshold. The full dataset was split into three independent non-overlapping event selections; first into summer and winter seasons, when the Sun was above and below the horizon, respectively. The winter dataset was further split into a low energy sample (WL), with focus on starting neutrino-induced muon tracks inside DeepCore, and a higher energy sample (WH), aiming at selecting track-like events with no particular containment requirement. The summer selection was a dedicated low energy event sample (SL), for which the surrounding IceCube strings were used as an active muon veto in order to select starting neutrino-induced events within DeepCore. The choice of using three separate samples was due to the different characteristics of the overwhelming down-going muon background within each dataset. The event selection was carried out separately for each independent sample and the final search was conducted using a combined likelihood function. In order to avoid potential bias, a strict blindness criterion was imposed by scrambling the azimuthal position of the Sun in data. After unblinding the direction of the events in the final data samples, the observed distributions were compared to the expected background distributions from atmospheric muons and neutrinos. The observed number of events from the direction of the Sun were consistent with the background-only hypothesis. 90% CL upper limits on the ν flux were calculated and translated into limits on the annihilation rate in the Sun (Γ_A). Under the assumption of equilibrium between WIMP capture and annihilation in the Sun, limits on Γ_A could be converted into limits on the spin-dependent, σ_{SD} and spin-independent, σ_{SI}, WIMP-proton scattering cross-sections, using the method from [12]. They were compared to direct detection experiment results as shown in Fig.3. They represented the most stringent limits to date on the spin-dependent WIMP-proton cross- section for WIMP masses above 35 GeV.

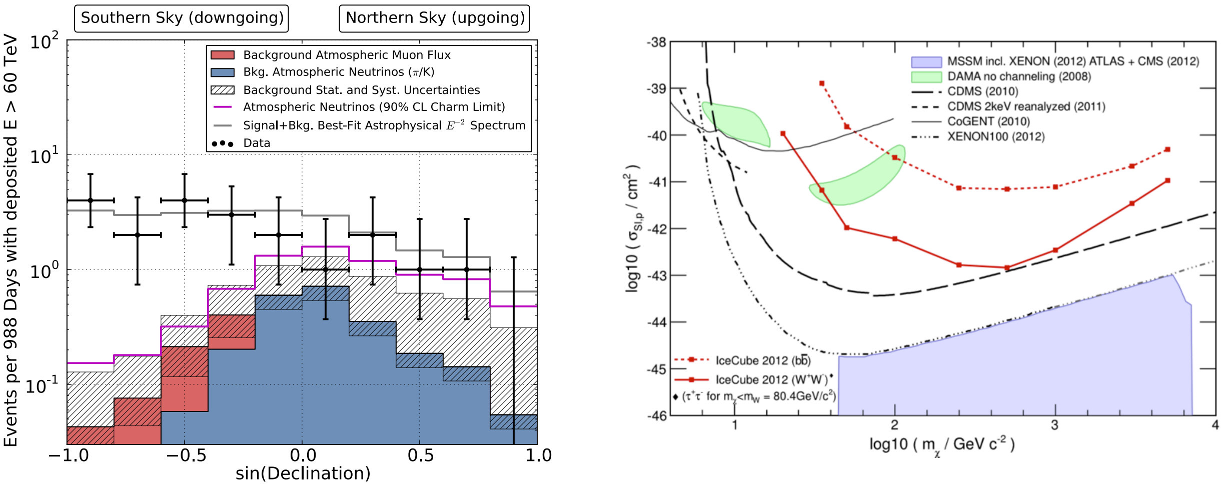

Figure 3 – (Left) IceCube limits on Spin Dependent interaction cross sections[11]. (Right) Icecube limits for Spin Independent interaction cross sections. IceCube results are compared to exclusion limits by several direct detection experiments (see references in[11]).

3.2 Galactic and Extra-Galactic sources

Searching for dark matter self-annihilation in the Milky Way probes the thermal average of the annihilation rate, which is proportional to the product of the annihilation cross section and the relative velocity of WIMPs, $\langle \sigma v \rangle$. This is complementary to indirect Solar and Earth WIMP searches, and to direct searches, which probe the WIMP- nucleon cross-section and results can be compared directly to limits from gamma ray or charged comic ray searches. Both the Galactic Center and Galactic Halo analyses use IceCube data in the 79-string configuration. Neutrinos from the direction of the Galactic Center, located in the southern hemisphere, are down-going events within IceCube. Searches for such neutrinos must overcome a background of down-going atmospheric muons penetrating the detector. Again, this background can be reduced by active veto techniques. In order to be sensitive to a wide range of possible WIMP masses, two independent analyses were performed. A DeepCore based event selection was optimized to search for low WIMP mass signals (30 GeV to 500 GeV). The second search used larger parts of IceCube as fiducial volume to improve the sensitivity to WIMP mass signals above 500GeV. As in the case of the Sun search, the right ascension in data was scrambled during the development of the analyses. Figure 4 compares the IceCube expected limits on $\langle \sigma v \rangle$, as a function of WIMP mass, with those obtained by the PAMELA and FERMI experiments[14]. The IceCube sensitivity increases for heavier WIMPs, due to the higher neutrino cross-section (in IceCube) and larger muon range.

The Galactic Halo analysis searched for large scale anisotropy in the distribution of incoming neutrinos. The additional flux from dark matter annihilation depends on the density of dark matter in the direction of sight and is expected to be larger in the direction of the galactic center and smaller in the direction of the anti-center. Given the large field of view of IceCube, such a large-scale anisotropy would leave a characteristic imprint on multipole expansion coefficients of the observed set of arrival directions in a high-purity muon neutrino event sample that can be obtained by selecting up-going muon events. This imprint could be interpreted in terms of the thermally averaged self-annihilation cross-section of dark-matter particles. The resulting exclusion limits on the velocity averaged annihilation cross-section $\langle\sigma v\rangle$ are shown in Fig. 4.

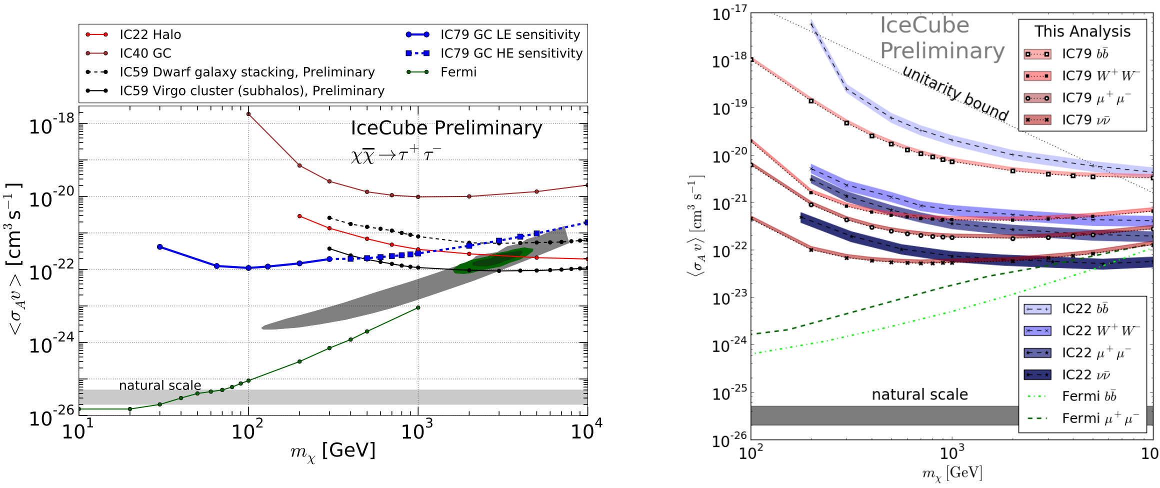

Figure 4 – (Left) 90%CL limit (w/o systematics) for WIMP annihilation in the GC into $\mu^+\mu^-$ (solid blue) compared to other analyses / experiments (see text). (Right) Upper limits on velocity-averaged WIMP self-annihilation cross-section compared to IceCube-22 results[17] and from the Fermi collaboration[18]

4 Conclusions

We have presented the first observation of neutrino events with energies up to the PeV scale. Detailed analyses of their characteristics have excluded their atmospheric origin with a 5.7σ significance, and found them to be compatible with isotropic arrival directions. Further observations with the present or upgraded IceCube detector will be required to answer many questions about the nature of the unknown sources of this astrophysical flux, in particular clustering searches and measurements of the neutrino energy spectrum and flavor distribution [15].

IceCube has also a very rich program of searches from dark matter from a variety of sources. In particular, limits on spin-dependent interaction cross section obtained by the solar analysis represent the most stringent limits available to date. Other searches are being updated to the full 86 strings detector configuration and are producing competitive results. The next low energy IceCube extension, PINGU[16], will reduce the neutrino energy threshold to a few GeV, and will play a major role in the low dark matter mass range.

1. R. Abbasi *et al.*, *Nucl. Instrum. Methods* A **601**, 294 (2009).
2. R. Abbasi *et al.*, *Astropart. Phys.* **35** 615 (2012).
3. M.G. Aartsen *et al.*, *Phys. Rev. Lett.* **110**, 151105 (2013).
4. M.G. Aartsen *et al.*, Presented at ICRC 2013, arXiv:1309.7007.
5. M.G. Aartsen *et al.*, *Phys. Rev. Lett.* **111**, 021103 (2013).
6. M.G. Aartsen *et al.*, *Science*, **342**, 1242856 (2013), arXiv:1311.5238.
7. S. Schonert *et al.*, *Phys. Rev.* D **79**, 043009 (2009), arXiv:0812.4308.
8. M.G. Aartsen *et al.*, *Phys. Rev.* D **89**, 062007 (2014), arXiv:1311.7048.
9. G. Bertone, D. Hooper and J. Silk, *Phys. Rept.* **405** 279 (2005).
10. J Ellis, *Phil.Trans.Roy.Soc.Lond.* **A370** 818-830 (2012).
11. M.G. Aartsen *et al.*, *Phys. Rev. Lett.* **110**, 131302 (2013).
12. G. Wikstrom and J. Edsjo, Presented at JCAP 07, 008 (2004).
13. J. F. Navarro, C. S. Frenk and S. D. M. White, *Astrophys. J.* **462** 563 (1996).
14. P. Meade *et al.*, *Nucl. Phys.* B **831** 178 (2010).
15. R. Laha *et al.*, *Phys. Rev.* D **88**, 043009 (2013), arXiv:1306.2309.
16. The IceCuce-PINGU collaboration, arXiv:1401.2046.
17. R. Abbasi *et al.*, *Phys. Rev.* D **84**, 022004 (2011).
18. M. Ackermann *et al.*, *Astrophys. J.* **761** 91 (2012).

First Dark Matter Search Results from the Large Underground Xenon (LUX) Experiment

C.H. Faham, for the LUX Collaboration
Lawrence Berkeley National Laboratory, 1 Cyclotron Rd., Berkeley CA 94720, USA

The Large Underground Xenon (LUX) dark matter experiment is operating 1.5 km underground at the Sanford Underground Research Facility in Lead, South Dakota, USA. In 2013, the experiment had a WIMP search exposure of 10,091 kg-days over a period of 85.3 live days. This first dark matter search placed the world's most stringent limits on WIMP-nucleon interaction cross-sections over a wide range of WIMP masses, and is in tension with signal hints of low-mass WIMPs from DAMA, CoGeNT and CDMS-II Si. LUX will commence a 300 day run in 2014 that will improve the sensitivity by a factor of 5. Low-energy calibrations obtained from a neutron double-scattering technique will further constrain and reduce systematics, particularly for low WIMP masses.

1 Introduction

The existence of non-baryonic cold dark matter is well established through a wealth of complementary observations such as Supernova Type Ia, the Cosmic Microwave Background, Big Bang Nucleosynthesis, Baryon Acoustic Oscillations and the kinematics of galaxies and galaxy clusters [1]. Despite the overwhelming cosmological evidence, the particle nature of dark matter remains unknown. One of the leading candidates for dark matter is the Weakly Interacting Massive Particle (WIMP), which is expected to interact with a terrestrial detector through low-energy (∼keV scale) nuclear recoils (NR). Direct-detection experiments aim to identify these faint and rare recoils by utilizing a large target mass, achieving a low energy threshold and reducing background radioactivity levels, mainly from electron recoils (ER) and neutrons. Furthermore, direct-detection experiments need to operate deep underground in order to significantly reduce the otherwise insurmountable cosmic-ray background rate.

2 The LUX Detector

The Large Underground Xenon (LUX) dark matter experiment has been operating 1.5 km (4300 mwe) underground at the Sanford Underground Research Facility (SURF) in Lead, South Dakota, USA since 2012 [2]. LUX is a two-phase xenon time-projection chamber (TPC) constructed from ultra-low radioactivity materials. The detector consists of 370 kg of liquid xenon, 250 kg of which comprises the 47 cm diameter by 48 cm high cylindrical active volume. The detector is immersed in a 7.6 m diameter by 6.1 m high water tank to reduce the background from ambient radioactivity.

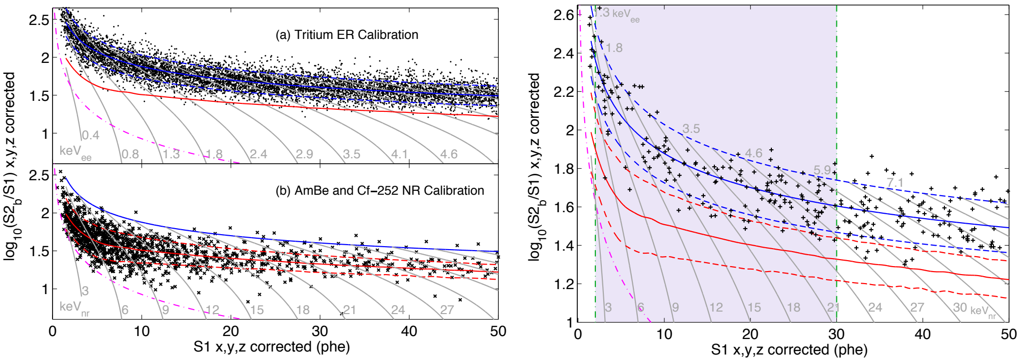

Figure 1 – *Left*: The LUX low-energy response to tritium ER (panel a) and AmBe and ^{252}Cf NR (panel b) calibrations inside the fiducial volume. The ER band mean (solid blue) and $\pm 1.28\sigma$ (dashed blue) of the parametrized tritium distribution are shown in panel b. The NR band mean (solid red) and $\pm 1.28\sigma$ (dashed red) obtained from simulations are shown in panel b. The approximate location of the 200 phe S2 cut is shown with a dot-dashed magenta line in both panels. *Right*: The fiducial volume events passing all cuts in the 2-30 phe S1 range (shaded purple) during the LUX 85.3 live-day WIMP search. The same parametrized ER and NR band distributions from the left panel are shown. A Profile Likelihood Ratio analysis shows that all events are consistent with the ER background-only hypothesis.

A particle interaction in the liquid xenon volume, through either an ER or an NR, produces primary scintillation photons (S1 signal) and ionization electrons, which are drifted with an electric field into the gas phase, where they produce secondary scintillation light (S2) via electroluminescence. A total of 122 Hamamatsu R8778 low-radioactivity photomultiplier tubes (PMTs) are used for the detection of both S1 and S2 signals. The PMTs are split into top and bottom arrays of 61 PMTs each. The LUX PMTs have an average photon detection efficiency[a] of about 30% at the xenon scintillation wavelength of 175 nm. The inner walls of the detector and the space between PMTs are lined with polytetrafluoroethylene (PTFE), which has been measured in LUX to be >95% reflective at 175 nm when immersed in liquid xenon. These detection factors, combined with the reflectivity of the grids' stainless steel wires and a finite photon absorption length in xenon, yield a measured 14% LUX photon detection efficiency for events at the center of the detector. This large photon detection efficiency gives LUX good sensitivity to WIMP masses above 6 GeV/c^2. For further details about the LUX experiment, refer to [3].

3 The First LUX Dark Matter Search and Limits on WIMP-Nucleon Interactions

A total of 85.3 live-days of background WIMP search data were acquired between the end of April and the beginning of August 2013. During this run, the background rate inside the fiducial volume in the energy range of interest (2-30 phe S1 signals) was measured to be 3.6 ± 0.3 mDRU (mDRU $= 10^{-3}$ counts/keV/kg/day), which is the lowest for any xenon TPC thus far. About half of the fiducial background rate are low-energy scatters from gamma rays (mostly originating from residual radioactivity in the PMTs). Other sources of background are residual ^{85}Kr in the xenon (rendered subdominant by using chromatographic separation [2]), ^{214}Pb naked β^- from the ^{222}Rn chain and x-rays from the cosmogenically produced ^{127}Xe ($t_{1/2}$ = 36.4 days), which decayed throughout the WIMP search run.

The detector was extensively calibrated with internal sources (for ER) and external sources (for NR). The internal sources, ^{83m}Kr and tritiated methane, were injected in gaseous form into the xenon circulation stream. These internal sources have the advantage of spreading evenly throughout the active volume, providing a homogeneous calibration. The mono-energetic 9.4 keV and 32.1 keV energy depositions of ^{83m}Kr were used to constantly monitor the electron drift

---

[a] The PMT photon detection efficiency, or DE, is the product of the often quoted quantum efficiency (QE) times the first dynode electron collection efficiency (CE).

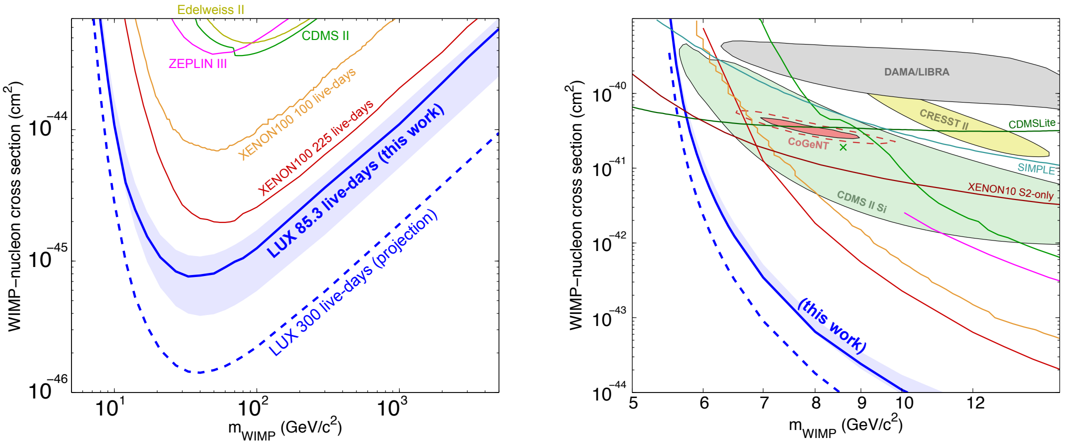

Figure 2 – *Left*: 90% CL spin-independent WIMP exclusion limits shown the LUX 85.3 live-day result (solid blue) and the 300-day projection (dashed blue). *Right*: Close-up view of exclusion plot in the low-mass regime showing the tension between the LUX result and previous hints of low-mass WIMP signals.

attenuation length, the light yield and the x,y,z detector response corrections. The novel tritiated methane β^- source (endpoint of ∼18 keV) provided the ER response of the detector at low energies, as shown in the left panel (a) in Fig. 1 in $\log_{10}(\mathrm{S2_b/S1})$ vs. S1 space (the "b" subscript denotes that only the bottom PMT signals were used in order to eliminate systematics from two deactivated top PMTs). The mean (blue solid) and $\pm1.28\sigma$ (blue dashed) contours used to characterize the ER band from this calibration are shown on top of the data. AmBe and ^{252}Cf external neutron sources were used to calibrate the NR response of the detector, shown in the left panel (b) in Fig. 1. The mean (red solid) and $\pm1.28\sigma$ (red dashed) NR band parametrization was derived from the NEST simulation model [4].

The WIMP search analysis cuts for this unblind analysis were kept minimal, with a focus on maintaining a high acceptance. Single-scatter interactions (one S1 and one S2) in the liquid xenon with areas between 2-30 phe for the x,y,z corrected S1 signal were selected, which approximately corresponds to 3-25 keV$_{\mathrm{nr}}$ or about 0.9-5.3 keV$_{\mathrm{ee}}$, where the subscripts represent the energy scales for NR and ER, respectively.[b] The upper bound of 30 phe was chosen to avoid contamination from the 5 keV x-ray from ^{127}Xe. The fiducial volume was defined as the inner 18 cm in radius and a drift time between 38-305 μs (roughly 7-47 cm above the bottom PMT array). The fiducial mass enclosed by the aforementioned bounds was calculated to be 118.3 ± 6.5 kg from the tritium calibration. An analysis threshold of 200 phe (∼8 extracted electrons) was used to exclude small S2 signals with poor x,y position reconstruction. The S2 finding efficiency at 200 phe is >99%. The overall WIMP detection efficiencies after all cuts were roughly 17% at 3 keV$_{nr}$, 50% at 4.3 keV$_{nr}$ and $> 95\%$ above 7.5 keV$_{nr}$.

A total of 160 events passed the selection criteria, which are shown inside the purple shaded region in the right panel of Fig. 1. A Profile Likelihood Ratio (PLR) analysis utilized the distribution of measured background and expected signal as a function of radius, depth, S1 and S2 parameter spaces in order to attempt to reject the null (background-only) hypothesis. For further details about the PLR limit, see [2] and [5]. The PLR result could not reject this null hypothesis with a p-value of 0.35, and 90% confidence spin-independent WIMP exclusion limits were placed as a function of WIMP-nucleon cross-section and WIMP mass as shown in Fig. 2. The WIMP exclusion limits set by LUX provide a significant improvement in sensitivity over existing limits. In particular, the LUX low-mass WIMP sensitivity shown in the right panel of Fig. 2 improves on the previous best limit set by XENON100 by more than a factor of 20 above

---

[b] For the same energy, a NR produces less signal than an ER due to the fact that the former has a large energy loss fraction in the form of heat, which produces no photons or electrons.

6 GeV/c^2. These low-mass limits do not support the near-threshold signal hints seen by DAMA [6], CoGeNT [7] and CDMS-II Si [8].

The WIMP exclusion limit in LUX was derived using a conservative xenon response to NR at low energies, which placed an unphysical cutoff in the signal yields for electrons and photons below 3 keV$_{\text{nr}}$, the lowest calibration point available at the time of the limit calculation. New measurements from a DD neutron generator show available signal below this imposed cutoff (measured down to 0.7 keV$_{\text{nr}}$ for the ionization channel) [9].

4 Conclusions and Outlook

During an 85.3 live-day commissioning run with a 118 kg of fiducial xenon mass, the LUX experiment has achieved the most sensitive spin-independent WIMP exclusion limits over a wide range of masses. Under the assumption of isospin invariance, this result excludes the low-mass WIMP region where hints of signal have been published. LUX will commence a 300 day run in 2014 that will further improve the WIMP sensitivity by a factor of 5. The increased sensitivity factor is greater than the ratio of exposures due to lower radioactivity backgrounds from the decay of the cosmogenically activated ^{127}Xe. The sensitivity interpretation at low masses will also benefit from using the novel low-energy calibration of electron and photon yields from the DD neutron source.

Acknowledgments

This work was partially supported by the U.S. Department of Energy (DOE) under award numbers DE-FG02-08ER41549, DE-FG02-91ER40688, DE-FG02-95ER40917, DE-FG02-91ER40674, DE-NA0000979, DE-FG02-11ER41738, DE-SC0006605, DE-AC02-05CH11231, DE-AC52-07NA27344, and DE-FG01-91ER40618; the U.S. National Science Foundation under award numbers PHYS-0750671, PHY-0801536, PHY-1004661, PHY-1102470, PHY-1003660, PHY-1312561, PHY-1347449; the Research Corporation grant RA0350; the Center for Ultra-low Background Experiments in the Dakotas (CUBED); and the South Dakota School of Mines and Technology (SDSMT). LIP-Coimbra acknowledges funding from Fundação para a Ciência e Tecnologia (FCT) through the project-grant CERN/FP/123610/2011. Imperial College and Brown University thank the UK Royal Society for travel funds under the International Exchange Scheme (IE120804). The UK groups acknowledge institutional support from Imperial College London, University College London and Edinburgh University, and from the Science & Technology Facilities Council for PhD studentship ST/K502042/1 (AB). The University of Edinburgh is a charitable body, registered in Scotland, with registration number SC005336. This research was conducted using computational resources and services at the Center for Computation and Visualization, Brown University.

We acknowledge the work of the following engineers who played important roles during the design, construction, commissioning, and operation phases of LUX: S. Dardin from Berkeley, B. Holbrook, R. Gerhard, and J. Thomson from UC Davis, and G. Mok, J. Bauer, and D. Carr from Livermore. We gratefully acknowledge the logistical and technical support and the access to laboratory infrastructure provided to us by the Sanford Underground Research Facility (SURF) and its personnel at Lead, South Dakota. SURF was developed by the South Dakota Science and Technology authority, with an important philanthropic donation from T. Denny Sanford, and is operated by Lawrence Berkeley National Laboratory for the Department of Energy, Office of High Energy Physics.

References

[1] J. Beringer *et al.* [Particle Data Group Collaboration], "Review of Particle Physics (RPP)," Dark Matter Review, Phys. Rev. D **86**, 010001 (2012).

[2] D. S. Akerib *et al.* [LUX Collaboration], "First results from the LUX dark matter experiment at the Sanford Underground Research Facility," Phys. Rev. Lett. **112**, 091303 (2014) arXiv:1310.8214.

[3] D. S. Akerib *et al.* [LUX Collaboration], "The Large Underground Xenon (LUX) Experiment," Nucl. Instrum. Meth. A **704**, 111 (2013) arXiv:1211.3788.

[4] M. Szydagis, A. Fyhrie, D. Thorngren and M. Tripathi, "Enhancement of NEST Capabilities for Simulating Low-Energy Recoils in Liquid Xenon," JINST **8**, C10003 (2013) arXiv:1307.6601.

[5] M. Szydagis *et al.* [LUX Collaboration], "A Detailed Look at the First Results from the Large Underground Xenon (LUX) Dark Matter Experiment," arXiv:1402.3731.

[6] R. Bernabei *et al.* [DAMA Collaboration], "First results from DAMA/LIBRA and the combined results with DAMA/NaI," Eur. Phys. J. C **56**, 333 (2008) arXiv:0804.2741.

[7] C. E. Aalseth *et al.* [CoGeNT Collaboration], "CoGeNT: A Search for Low-Mass Dark Matter using p-type Point Contact Germanium Detectors," Phys. Rev. D **88**, no. 1, 012002 (2013) arXiv:1208.5737.

[8] R. Agnese *et al.* [CDMS Collaboration], "Silicon Detector Dark Matter Results from the Final Exposure of CDMS II," Phys. Rev. Lett. **111**, 251301 (2013) arXiv:1304.4279.

[9] J. Verbus *et al.* [LUX Collaboration], Calibration of the LUX dark matter detector, UCLA Dark Matter, 26-28 February 2014, (https://hepconf.physics.ucla.edu/dm14/agenda.html).

SuperCDMS: Recent results on low-mass WIMPs

DAVID G. CERDEÑO
Departamento de Física Teórica & Instituto de Física Teórica IFT UAM/CSIC,
Universidad Autónoma de Madrid, 28049 Madrid, Spain

We present the first search for weakly interacting massive particles (WIMPs) using the background rejection capabilities of SuperCDMS [1]. A blind analysis of data from an exposure of 577 kg-days leads to an upper limit on the spin-independent WIMP-nucleon cross section of 1.2×10^{-42} cm^2 at 8 GeV. This result probes new parameter space for WIMP-nucleon scattering cross section for light WIMPs with masses < 6 GeV/c^2 and is in tension with WIMP interpretations of recent experiments.

The detection and identification of the dark matter in the Universe constitutes one of the greatest challenges in modern Physics. A generic weakly interacting massive particle (WIMP) is a well motivated candidate, as it can be produced in the right amount and searched for in direct and indirect detection experiments. Recent excesses of events reported by CDMS II (Si)[2], CoGeNT [3], CRESST-II [4], DAMA [5], and possible indirect evidence from gamma rays from the galactic centre [6], can be interpreted in terms of WIMPs with mass in the 6–30 GeV/c^2 range. Various theoretical constructions also provide WIMP candidates in this mass range [7,8,9,10,11].

The direct search for light WIMPs is extremely challenging, since they produce only low-energy nuclear recoils, forcing experiments to lower their analysis energy thresholds [12,13,14,15,16]. Following this approach, low-energy recoils in the range 1.6–10 keV$_{\rm nr}$ (nuclear-recoil equivalent energy) from the SuperCDMS experiment at the Soudan Underground Laboratory [17] have been analysed, exploiting the excellent background discrimination capabilities of the new detectors [1].

SuperCDMS at Soudan is an upgrade to the Cryogenic Dark Matter Search (CDMS II) [18] with new detector hardware, operating in the same location with the same low-radioactivity setup [19] since March 2012. The target consists of five towers, with three 0.6-kg cylindrical germanium crystals each. These detectors (iZIPs) are instrumented with interleaved ionization and phonon sensors on their flat faces. From the measured ionization and phonon energy, we derive the recoil energy and the "*ionization yield*," the ratio between ionization and recoil energy. This is a key quantity to discriminate nuclear recoils (expected from WIMP interactions) from electron recoils (expected from most backgrounds), since nuclear recoils exhibit a reduced ionization yield compared to electron recoils. Moreover, the iZIP sensor layout greatly improves the determination of a fiducial volume in the bulk, designed to reject events in the peripheral regions of the detectors (which present a reduced ionization yield and pollute the signal region) [20]. The fraction of the total phonon or ionization energy measured by the guard sensors is encoded in "*radial partition*" parameter through which radial fiducialization is defined. Similarly, a "*z partition*" parameter is constructed from the fraction measured by the sensors on each face and used to define the z fiducialization.

The data presented here was recorded between October 2012 and June 2013 using the seven detectors with the lowest trigger thresholds. The remaining detectors are used to reject events which deposit energy in more than one detector (incompatible with WIMP interactions). Periods of abnormal detector behavior and elevated noise are removed from the analysis. After accounting for these losses, the exposure is 577 kg-days. To prevent bias when defining the event-selection criteria, all single-detector hits with recoil energies between a time-dependent noise threshold and 10 $\mathrm{keV_{nr}}$, and with ionization energy consistent with nuclear recoils, were removed from study, i.e. blinded. A distinct open set of data, containing 97 kg-days of exposure, was constructed from periods following ^{252}Cf calibrations.

The relation between the total phonon energy and the mean ionization energy of nuclear recoils for each detector, as determined from ^{252}Cf calibration data, is consistent with Lindhard's model. The nuclear-recoil band is defined by accepting events within 3σ of the mean ionization energy. The nuclear-recoil equivalent energy is constructed from the total phonon energy by subtracting the contribution of Luke-Neganov phonons corresponding to the mean nuclear-recoil ionization response for the respective total phonon energy.

Hardware trigger thresholds for each detector were adjusted several times during the WIMP search. For each period of constant trigger threshold, the trigger efficiencies as functions of total phonon energy were measured using ^{133}Ba calibration data. Analysis thresholds are set to be 1σ below the energy at which the detector trigger efficiency is 50% in periods of time for which this quantity is above the noise threshold used in the data blinding, and equal to such threshold otherwise. The combined efficiency is an exposure-weighted sum of the measured efficiency for each detector and period, and is shown in the left-hand side of Figure 1.

Three levels of data-selection criteria have been used to identify triggered events as WIMP candidates. A first data-quality cut rejects poorly reconstructed and noise-induced events, removing also periods of abnormal noise and spurious triggers (for which the pulse shape is inconsistent with that expected for real events). The second level (preselection) singles out event configurations consistent with WIMPs, requiring single-scattered events that feature energies within the 3σ nuclear-recoil band and phonon partitions consistent with bulk nuclear recoils. A loose fiducial volume, constructed from the ionization partitions, further restricts events to be consistent with bulk nuclear recoils. Similarly, events near the detectors' sidewalls are rejected by requiring the guard electrodes on both faces to be within 2σ from the mean of the baseline noise. Events coincident with the muon veto are also rejected. The final level of event-selection (discrimination) uses a boosted decision tree (BDT) with four discriminators: the total phonon energy, ionization energy, phonon radial partition and phonon z partition. A BDT was trained for each detector using simulated background events and nuclear recoils from ^{252}Cf calibration weighted to mimic a WIMP energy spectrum, accounting for the selection criteria acceptance. The BDT discrimination thresholds for individual detectors were chosen simultaneously to minimize the expected 90% confidence level (C.L.) Poisson upper limit of the rate of passing events per WIMP exposure. The BDT was trained and optimized separately for 5, 7, 10, and 15 GeV/c^2 WIMPs. Events that pass any of the four WIMP-mass optimizations are accepted into the signal region as candidates. The left-hand side of Figure 1 shows the cumulative efficiency after applying each level of selection criteria and the analysis thresholds.

A background model was developed that includes Compton recoils from the gamma-ray background; 1.1–1.3 keV X-rays and Auger electrons from L-shell electron-capture (EC) decay of ^{65}Zn, ^{68}Ga, ^{68}Ge and ^{71}Ge; and decay products from ^{210}Pb contamination on the detectors and their copper housings. The right-hand side of Figure 1 shows the individual components of the background model as a function of the 10 GeV/c^2 BDT discrimination parameter after applying the preselection criteria. This background model was finalized prior to unblinding and predicted $6.1^{+1.1}_{-0.8}$ (stat.+syst.) events passing the BDT selection. Simulations of radiogenic and cosmogenic neutrons predict an additional 0.098 ± 0.015 (stat.) events. These estimates included only known systematic effects. Because the accuracy in background modeling required for a full likelihood analysis is difficult to achieve in a blind analysis of this type, the decision was made before unblinding to report an upper limit on the WIMP-nucleon cross section.

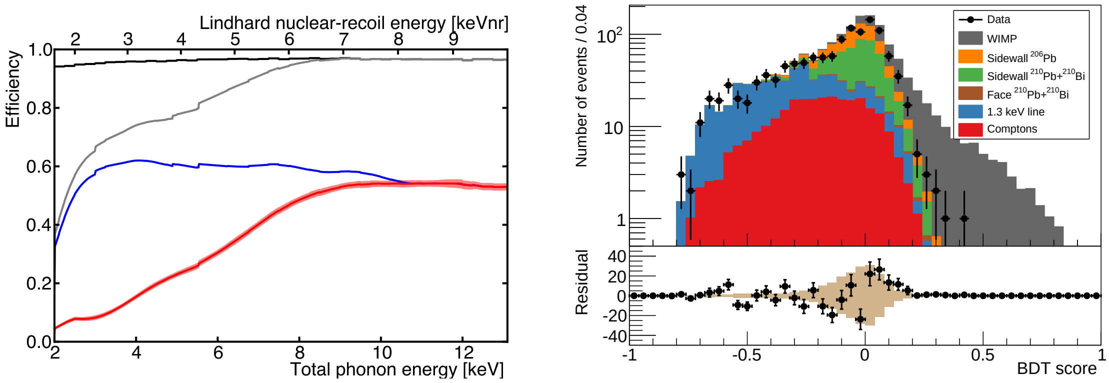

Figure 1 – Left) Cumulative efficiencies after sequential application of each stage of event selection. From top to bottom, these are data-quality criteria, trigger and analysis thresholds, preselection criteria, and BDT discrimination with 68% C.L. (stat. + syst.) uncertainty band. Right) Components of the background model passing the preselection criteria, summed over all detectors. For comparison, a 10 GeV/c^2 WIMP with cross section 6×10^{-42} cm^2 is shown on top of the total background. Events passing preselection criteria are overlaid showing the statistical errors. The bottom plot shows the difference between the data and the background expectation. Tan bars indicate the systematic uncertainty (68% C.L.) on the background estimate.

Upon unblinding, eleven candidates were observed, which are shown on the left-hand side of Figure 2. This is consistent with the background prediction for most detectors, except for the three high-energy events in detector T5Z3 (for which there is a probability of only 4×10^{-4} to observe this many background events). However, this detector has an ionization guard electrode shorted to ground and, although the background model was developed to account for this, the altered electric field may have affected the selection of background model templates, and thus the background estimate. Otherwise, the background model has been found to reproduce correctly most features of the true background, as evidenced in the right-hand side of Figure 1. The systematic uncertainty is dominated by the uncertainty of the expected ionization of sidewall events originating from ^{210}Pb and ^{210}Bi. P-value statistics comparing the data passing the preselection criteria with the blind background model prediction range from 8–26% for the BDTs trained to each of the four WIMP masses.

On the right-hand side of Figure 2 we show the 90% C.L. upper limit on the spin-independent WIMP-nucleon cross section, calculated using the optimum interval method without background subtraction for standard halo assumptions. Statistical and systematic uncertainties in the fiducial-volume efficiency, the nuclear-recoil energy scale, and the trigger efficiency were propagated into the limit by Monte Carlo and are represented by the narrow gray band around the limit. The limit is consistent with the expected sensitivity for masses below 10 GeV/c^2 as shown by the green band in Figure 2. The discrepancy above 10 GeV/c^2 is due to the three high-energy events in T5Z3, which are in tension with the background expectation. These results strongly disfavour a WIMP interpretation of the CoGeNT excess, which also uses a germanium target. Similar tension exists with WIMP interpretations of several other experiments, including CDMS II (Si), assuming spin-independent interactions and a standard halo model. New regions of WIMP-nucleon scattering for WIMP masses below 6 GeV/c^2 are excluded. This constitutes the first search for WIMPs exploiting the full background rejection capability of SuperCDMS.

Acknowledgments

D.G.C. is supported by MultiDark CSD2009-00064, the Spanish MICINN under Grant No. FPA2012-34694, the Spanish MINECO under Grant No. SEV-2012-0249, and the Community of Madrid under Grant No. HEPHACOS S2009/ESP-1473.

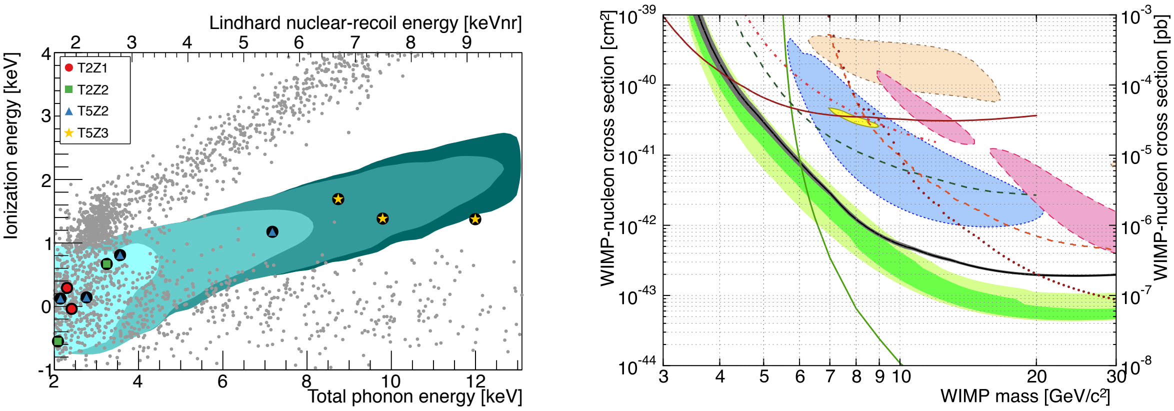

Figure 2 – Left) Veto-anticoincident single-scatter events within the ionization-partition fiducial volume that pass the data-quality selection criteria. Large encircled shapes are the 11 candidate events. Shaded regions (from light to dark) are the 95% confidence contours expected for 5, 7, 10 and 15 GeV/c^2 WIMPs. The band of events above the expected signal contours corresponds to bulk electron recoils, including the 1.3 keV activation line at a total phonon energy of ∼3 keV. High-radius events near the detector sidewalls form the wide band of events with near-zero ionization energy. For illustrative purposes, an approximate nuclear-recoil energy scale is provided. Right) The 90% confidence upper limit (solid black) based on all observed events is shown with 95% C.L. systematic uncertainty band (gray). The pre-unblinding expected sensitivity in the absence of a signal is shown as 68% (dark green) and 95% (light green) C.L. bands.

References

1. R. Agnese *et al.* [SuperCDMS Collaboration], Phys. Rev. Lett. **112** (2014) 241302.
2. R. Agnese *et al.* [CDMS Collaboration], Phys. Rev. Lett. **111** (2013) 251301.
3. C. E. Aalseth *et al.* [CoGeNT Collaboration], Phys. Rev. D **88** (2013) 1, 012002.
4. G. Angloher*et al.* [CRESST-II Collaboration], Eur. Phys. J. C **72** (2012) 1971.
5. R. Bernabei *et al.* [DAMA/ LIBRA Collaboration], Eur. Phys. J. C **67** (2010) 39.
6. D. Hooper and T. Linden, Phys. Rev. D **84** (2011) 123005.
7. D. B. Kaplan, Phys. Rev. Lett. **68** (1992) 741.
8. A. Falkowski, J. T. Ruderman and T. Volansky, JHEP **1105** (2011) 106.
9. C. Cheung, J. T. Ruderman, L. -T. Wang and I. Yavin, Phys. Rev. D **80** (2009) 035008.
10. J. Kozaczuk and S. Profumo, Phys. Rev. D **89** (2014) 095012.
11. D. G. Cerdeño, M. Peiró and S. Robles, JCAP **08** (2014) 005.
12. D. S. Akerib *et al.* [CDMS Collaboration], Phys. Rev. D **82** (2010) 122004.
13. Z. Ahmed *et al.* [CDMS Collaboration], Phys. Rev. Lett. **106** (2011) 131302.
14. E. Armengaud *et al.* [EDELWEISS Collaboration], Phys. Rev. D **86** (2012) 051701.
15. J. Angle *et al.* [XENON10 Collaboration], Phys. Rev. Lett. **107** (2011) 051301 [Erratum-ibid. **110** (2013) 249901].
16. D. S. Akerib *et al.* [LUX Collaboration], Phys. Rev. Lett. **112** (2014) 091303.
17. R. Agnese *et al.* [SuperCDMS Collaboration], Phys. Rev. Lett. **112** (2014) 041302.
18. Z. Ahmed *et al.* [CDMS Collaboration], Science **327** (2010) 1619.
19. D. S. Akerib *et al.* [CDMS Collaboration], Phys. Rev. D **72** (2005) 052009.
20. R. Agnese *et al.* [SuperCDMS Collaboration], Appl. Phys. Lett. **103** (2013) 164105.
21. J. D. Lewin and P. F. Smith, Astropart. Phys. **6** (1996) 87.

The EDELWEISS Experiment Status

Q. ARNAUD for the EDELWEISS collaboration
IPNL, Université de Lyon, Université Lyon 1, CNRS/IN2P3, 4 rue E. Fermi,
69622 Villeurbanne cedex, France

We report on the results of the EDELWEISS-II direct dark matter search experiment and on the status of the ongoing subsequent phase EDELWEISS-III. The experiment employs HPGe bolometers cooled to cryogenic temperatures of ~ 18 mK with the primary aim of detecting nuclear recoils induced by elastic scattering of WIMPs. Despite being initially tuned for 100 GeV WIMPs, a dedicated analysis set new limits for lower mass WIMPs down to 7GeV. Also, competitive limits on the coupling of axions were deduced, in particular on g_{Ae} from the solar Compton-bremsstrahlung-recombination flux. Since 2012, an upgrade of the setup has been undertaken to significantly improve the sensitivity. This upgrade includes new generation detectors (FID800), improved shieldings reducing background, as well as better energy resolutions through new cabling and a new cryogenic system. The scientific results of EDELWEISS-II are reviewed. We describe the EDELWEISS-III setup, its physics prospects and first feedback from commissioning runs.

1 Experimental Setup

EDELWEISS is a direct dark matter search experiment dedicated to a WIMP search in the GeV-TeV mass range using HPGe bolometers. Its primary goal is to detect nuclear recoils induced by WIMPs through their elastic scattering within the detectors. Due to the extremely low event rates expected of < 1/kg/year, the main limitations arise from the background radioactivity. The experimental setup is therefore located in the Underground Laboratory of Modane (LSM, France), using the mountain as a natural shielding of 4850 m.w.e that reduces the muon flux [1] down to about 5 μ/m^2/day. Remaining muons are tagged by a 100 m^2 plastic scintillator that surrounds the setup, ensuring a $> 98\%$ efficiency for the muon flux. Additionally, 50 cm of polyethylene are used to moderate neutrons and a 20 cm layer of both newly produced Pb and Roman Pb is used to shield the detectors from external β- and γ-rays. These shields enclose the dilution cryostat which cools the detectors to ~ 18 mK. In addition, a continuous control of the Rn level is performed near the cryostat. With such protection, most of the residual background radioactivity comes from the inside of the shields.

The experiment benefits from its simultaneous double measurement of heat and ionisation, the ratio of which depends on the nature of the recoil : electronic recoils lead to 3 times more $\mathrm{e}^-/\mathrm{h}^+$ pair creation than nuclear recoils. The temperature increase following an energy deposit is measured using Neutron Transmutation Dopped (NTD) germanium as a thermistor. Electronic recoils induced by β- and γ-rays can then be identified and rejected through their ionisation yield set to $Q = 1$ from ^{133}Ba γ calibration, leading in an average value of $Q = 0.3$ for nuclear recoils. This already powerful discrimination of the β/γ background is accompanied with an efficient surface rejection enabled by a specific pattern of electrodes [2]. These are alternatively biased in order to define an inner fiducial volume, electrodes involved in charge collection varying from bulk to surface interactions (see Fig.1). This bulk event selection is also required due to surface events being sometimes associated with poor charge collection leading to a low ionisation yield. The 400 g Interdigitised Detectors (ID) used during the second phase of the experiment (EDELWEISS-II) only had interleaved electrodes on the top and bottom surfaces, leading in a small fiducial volume of 40%. For EDELWEISS-III, detectors have now interleaved electrodes even on the latteral surfaces, so-called Fully Interdigitised Detectors (FID). This increased the fiducial volume to 75%, which in addition to the larger crystal masses of 800 g resulted in a consequently higher fiducial mass of 600 g compared to previous 160 g in EDELWEISS-II. The second phase has been completed, and ensuing results are summarized in the following section. The upgrade to EDELWEISS-III has been finished and is described in Sec. 3. The scientific goal of EDELWEISS-III is to reach a sensitivity of $\sigma_{\mathrm{SI}} = 10^{-9}$pb for the WIMP-nucleon spin-independent cross section by 2015/2016.

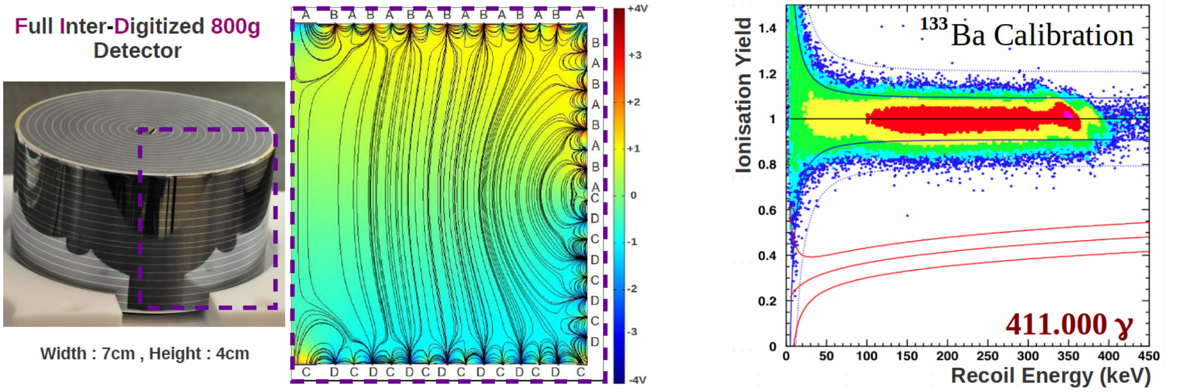

Figure 1 – Left: Picture and cross section of a FID800 detector. For bulk events, charge carriers are collected by the fiducial electrodes B and D whereas for surface or mixed events, at least one veto electrode (A,C) is involved in charge collection. Right: Ionisation Yield as a function of the recoil energy. Continuous and dashed blue lines are respectively the electronic recoil bands at 90%CL and 99.99%CL. Out of 400000 γ-events from a ^{133}Ba calibration, no single one stands above 20 keV in the NR band at 90%CL represented in continuous red lines.

2 EDELWEISS-II Results

The following results are based over more than one year of continuous data taking from April 2009 to May 2010. Ten 400-g ID detectors were operating at the time, among which two were also running between July and November 2008 and included in the whole data set.
A total effective exposure of 384 kg.days was achieved for a 90% acceptance nuclear recoil band in the NR energy range [20, 200] keV. Five candidates were observed in the WIMP search region while 3.0 were expected from background estimations at the time. This result was interpreted in terms of limits on the spin-independent WIMP-nucleon interaction cross-section: $\sigma_{\mathrm{SI}} < 4.4 \times 10^{-8}$pb (90%CL) for a WIMP mass of 85GeV[3]. New constraints were also set on inelastic scattering scenarios[3] that were originally proposed to explain the DM evidences claimed from DAMA/LIBRA in parameter regions yet excluded by the other experiments. As CDMS and EDELWEISS-II had similar results, both collaborations worked together on computing a combined limit. Gathering both data resulted in a total exposure of 614 kg.days and consequently improved the sensitivity to $\sigma_{\mathrm{SI}} < 3.3 \times 10^{-8}$pb (90% C.L.) for a WIMP mass of 90 GeV[4].

A dedicated analysis to low mass WIMPs in the range 7-30 GeV was also performed[5]. A restricted data set was used, selected on the basis of detector threesholds and backgrounds. Only four of the ten IDs were used, reducing the total exposure to 113 kg.days. The recoil energy higher cut was set to 20 keV, the standard analysis threshold, in order that the resulting limit is totally independent from the previous one. For a WIMP mass of 10 GeV, one event was observed in the WIMP search region where 2.9 events were expected, which lead to $\sigma_{\rm SI} < 1.0 \times 10^{-5}$pb (90% C.L.)[5]. This analysis extended the sensitivity of EDELWEISS-II down to WIMP masses below 20 GeV, which considerably constrained parameter space regions associated with the claim of signals reported by the CoGeNT, DAMA and CRESST experiments.

Axions should generate electronic recoils either by Primakoff effect or Axio-electric effect. Mostly thanks to the surface rejection enabled by the ID design, EDELWEISS-II had an extremely good electronic recoil background down to 5 keV. It was thus possible to put constraints on different couplings of axions depending on the mechanisms involved both in production and detection within four scenarios: 3 different solar axion scenarios and one in which axions do constitute all of the galactic dark matter halo. The detailed analysis related article is available[6]. Here we summarize that combining all obtained results we exclude the mass range 0.91 eV < mA < 80 keV for DFSZ (Dine-Fischler- Srednicki-Zhitnitskii) axions and 5.73 eV < mA < 40 keV for KSVZ (Kim-Shifman-Vainstein-Zakharov) axions. Up to recently[7], EDELWEISS-II produced the best model independent limit on $g_{\rm Ae}$ from the solar Compton-bremsstrahlung-recombination flux.

3 EDELWEISS-III Upgrade

EDELWEISS-II limitations are now identified and known to arise mainly from internal shielding (α,n) reactions in the cabling and missidentified γ-events. Also, looking for lower mass WIMPs has shown the extreme necessity to lower the thresholds and work therefore on the improvement of the baseline resolutions. Considering these aspects, huge efforts have been undertaken, leading to the following upgrades.

New PE pieces have been added both outside and inside the cryostat, including one at the 1K stage between the detectors and the cold electronic. Previous st.steel coaxial cabling has been replaced by new radiopure Kapton cabling. A neutron background suppression of a factor ~ 100 is expected from these upgrades. An improvement of the γ background is also performed by the use of more radiopure (NOSV) copper for the new thermal screens. Also, additional modules have been added to complete the muon veto system, increasing the coverage of the muon flux.

Previous pulse tubes that were close to the cryostat have been replaced by GM thermal machines at the outside of the shields, consequently reducing microphonics noise. All the resistances of the electronics have been removed, the active feedback being replaced by mechanical relays to avoid Johnson noise. From these upgrades, $\sim 30\%$ better baseline resolutions have been achieved both in heat and ionisation, going respectively from 1.2 keV to 1 keV, and from 900 eV to 650 eV (FWHM). Further improvement should arise from the ongoing R&D on HEMTs planned to replace current JFETs for the front-end readout.

New FID800 detectors have already proved their performances in commissioning runs. A high γ rejection is ensured with no single event leaking in the NR band in the nuclear recoil energy range $[20, 200]$ keV out of 4.10^5 γ-rays from a ^{133}Ba calibration[8] (Fig 1). The surface rejection was already good with IDs, with an evaluated rejection power of 6.10^{-5} above 20 keV recoil energy (90%CL). FIDs have shown an even better rejection power of 4.10^{-5} despite a lower analysis threshold of 15 keV (90%CL)[9]. With increased individual fiducial masses of 600 g and having now 36 FID detectors installed in the cryostat, a background-free exposure of 3000 kg.days should be reached by the end of 2014. The final goal is to obtain 12000 kg.days, exposure from which background should start to appear, reaching eventually 1.10^{-9}pb. The next phase of EDELWEISS is EURECA[10 11], a one ton scale experiment of multi-nuclei target. EURECA is supported by different European dark matter groups and a closer collaboration with SuperCDMS experiment is foreseen. EURECA will probe in its one ton phase a WIMP-nucleon SI interaction down to 10^{-11}pb.

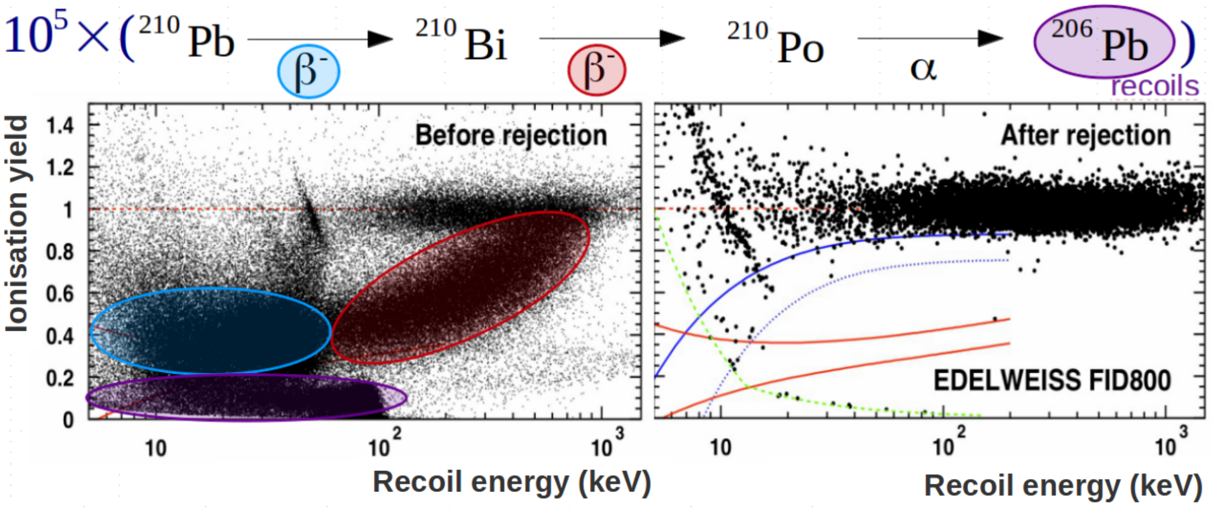

Figure 2 – Surface event rejection in two FID800 detectors submitted to a ^{210}Pb source. This resulted in the exposure of 10^5 of each product of the decay chain, the equivalent of what is expected in 10^5 kg.days of WIMP search. The ionisation yield of β-events ranges from 0.3 to 1 with the recoil energy due to the increased penetration length.^{210}Pb recoils ranging up to 100 keV have a really low Q value of 0.1 due to its only $\sim$ 50nm penetration length.

Acknowledgments

The help of the technical staff of the Laboratoire Souterrain de Modane and the participant laboratories is gratefully acknowledged. The EDELWEISS project is supported in part by the German ministry of science and education (BMBF Verbundforschung ATP Proj.-Nr. 05A11VK2), by the Helmholtz Alliance for Astroparticle Phyics (HAP) funded by the Initiative and Networking Fund of the Helmholtz Association, by the French Agence Nationale pour la Recherche, by Science and Technology Facilities Council (UK) and the Russian Foundation for Basic Research (grant No. 07-02-00355-a). This work has been partially supported by the LABEX Lyon Institute of Origins (ANR-10-LABX-0066) of the Université de Lyon funded through the program "Investissements dAvenir" (ANR-11-IDEX-0007) of the French government operated by the National Research Agency (ANR).

References

1. B. Schmidt et al., *Astropart. Phys.* 44, 28 (2013).
2. A. Broniatowski et al., *Phys. Lett.* B **681**, 305 (2009).
3. E. Armengaud et al., *Phys. Lett.* B **702**, 329 (2011).
4. Z. Ahmed et al., *Phys. Rev.* D **84**, 011102(R) (2011).
5. E. Armengaud et al., *Phys. Rev.* D **86**, 051701(R) (2012).
6. E. Armengaud et al., *JCAP* 11 (2013) 067.
7. E. Aprile et al., arXiv:1404.1455 [astro-ph.CO]
8. A. Juillard for the EDELWEISS Collaboration., *JLTP* 167, 1056 (2012).
9. J. Gascon and N. Bastidon for the EDELWEISS Collaboration., *JLTP* doi:10.1007/s10909-014-1096-6
10. H. Kraus et al., Nucl. Phys. B, (Proc. Suppl.) 173, 168 (2007).
11. G. Angloher et al. (EURECA conceptual design report), acc. for publ. in Physics of the Dark Universe.

STATUS OF XMASS

Y. KISIMOTO for XMASS collaboration
Kamioka Observatory, Institute for Cosmic Ray Research, the University of Tokyo,
Higashi-Mozumi, Kamioka, Hida, Gifu 506-1205, JAPAN,
Kavli Institute for Physics and Mathematics of the Universe (WPI), the University of Tokyo,
Kashiwa, Chiba 277-8582, JAPAN

The XMASS experiment is a multi-purpose detector for rare events, such as direct detection of dark matter, using single-phase liquid xenon. The current phase of the XMASS(XMASS-I) is focused on direct dark-matter detection with the largest target mass (835kg). In this paper, we report results of searches carried out with commissioning runs of the XMASS-I and current status of XMASS-I after hardware modification to reduce background followed by the commissioning runs.

1 The XMASS experiment

1.1 The XMASS project

The XMASS project was proposed to observe rare events such as elastic scattering of electron by *pp* solar neutrinos, neutrinoless double beta decay, and elastic scattering of nuclei by dark matter particles with a large liquid-Xe detector [1]. In the XMASS detector, scintillation lights from liquid xenon are observed by photo-multiplier tubes(PMTs) arranged around the liquid xenon volume. This simple configuration is very much suitable for observing the rare events because liquid xenon is an efficient scintillator and attenuation of scintillation light is quite small and also because liquid xenon has hight atomic number and high density and so it is worked as shield material against radiation from outside. We can, therefor, search for the rate events by extracting events in a low-background volume. Other important advantages of the liquid xenon scintillator are existence of no long-lived isotopes and capability to reduce contamination. Distillation [2] and active charcoal [3] can be used to remove krypton and radon, respectively.

1.2 XMASS-I

The first stage of the XMASS project concentrates on the search for the dark matter. One of the candidates for the dark matter is weakly interacting massive particles (WIMPs). The XMASS-I detector was constructed in 2010 with 835kg of liquid xenon (100kg of fiducial target mass) in the Kamioka underground site, and commissioning runs were conducted from 2010 to 2012. During the commissioning, we performed calibrations and tested its performance. The detailed results of these are presented in a reference [4].

2 Results of XMASS-I

During the commissioning period, we conducted several searches using the acquired data. These physics results are presented in this section.

2.1 *Search for light WIMPs*

Since deposited energy by WIMPs is small, the lower energy threshold of XMASS is advantageous for detecting them. Some of the commissioning runs were taken in a low threshold setting. The threshold was set to four hits of PMTs and it corresponds to 300 eV_{ee}. The data set we used is total 6.7 days with 835 kg liquid-xenon in this low-threshold data. A simple and robust cut is applied to reduce Čerenkov events that occur in quartz windows of the PMTs. To constrain light WIMPs, we compare each expected energy spectrum of a certain mass of WIMPs with the observed one as in Fig. 1. Upper limits of cross section for each WIMP's mass are set. (See a reference [5] for details.)

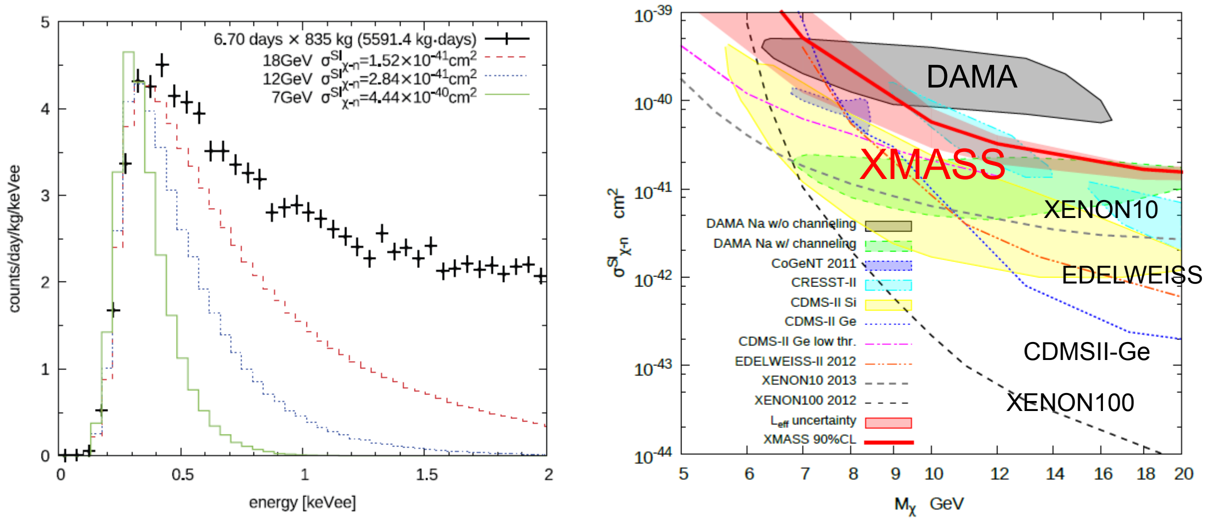

Figure 1 – Energy spectrum (left): The observed spectrum after the cut is shown by the black crosses. Solid green, dotted blue and dashed red lines are expectation for 7, 12 and 18 GeV WIMPs with cross section indicated in the figure, respectively. Upper limit of cross section for light WIMPs (right): The red line shows our limit and the red band shows the uncertainty comes from L_{eff}.

2.2 *Seasonal modulation analysis*

We also searched for WIMPs signal with the seasonal moderation analysis. We selected runs which were taken in the same run-condition from the commissioning runs with high statistics. The data we used here is 835 kg × 136.1 days-livetime from Dec. 2010 to May 2012. The analysis threshold was set to $E_{\text{th}} = 1.0\,\text{keV}_{ee}$. We do not observe any seasonal moderation components and so set limits of cross-section as shown in Fig. 2.

2.3 *Inelastic scattering ^{129}Xe by WIMPs*

WIMPs are expected to cause inelastic scattering off nuclei as well as elastic scattering. ^{129}Xe has an exited states at 39.58 keV. This state is low enough to be excited by spin-dependent coupling between WIMPs and nucleons [6]. The lifetime of the exited states is short (~ 1 ns), so we searched for a peak at 38.59 keV with high energy tail by the nuclear recoil. For sensitive search for the events, we applied various cuts to reduce the background as shown in the left panel of Fig. 3. These include the standard cut to remove noise and Čerenkov events in the quartz windows of PMTs, one based on reconstructed vertex positions, ones based on timing information and on a hit patterns to reject surface events between PMTs. Because we do not find peak structure in the final spectrum, we set an upper limit on the cross section of inelastic scattering as plotted in the right panel of Fig. 3.

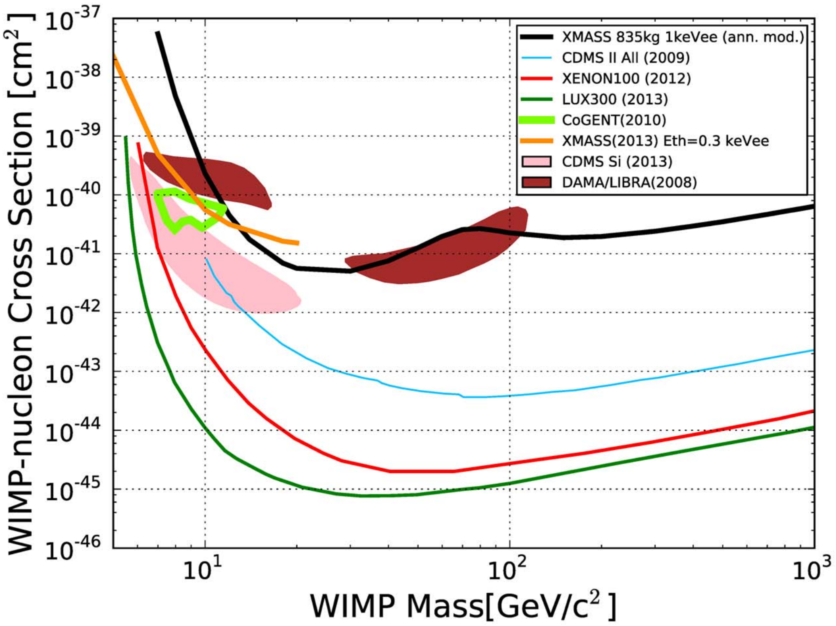

Figure 2 – Limit by seasonal modulation analysis in XMASS-I: The black line shows the upper limit as a function of WIMPs' mass.

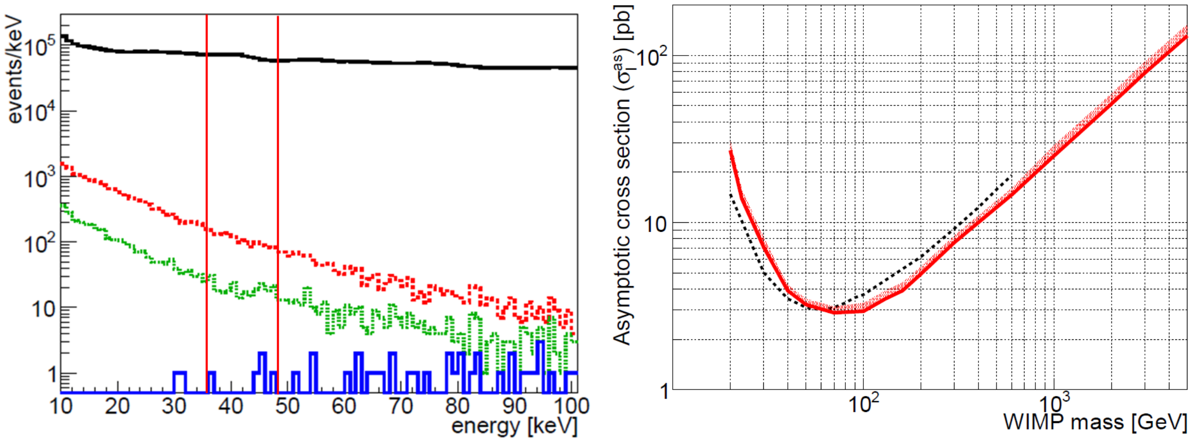

Figure 3 – The spectrum after each cut (left) and the exclusion plot (right): The spectra after the cuts are presented in the left. The black line is the spectrum after the standard cut. The dotted red and green are ones after the radius cut and after the timing cut, respectively. The blue solid is the final one after the cut by the hit pattern. In the right panel, the red line shows the upper limit on the asymptotic cross-section for inelastic scattering on ^{129}Xe using the same form factor used as DAMA(black dashed line). The hatched region represents the uncertainty in the analysis.

2.4 Search for solar axions

Axion is a hypothetical particle introduced by Pecci and Quinn to solve one long standing problem in the quantum chromodynamics, the strong CP problem. The search for axion, as well as axion-like particles (ALPs), can be performed by considering the Sun as a strong source of these hypothetical particles. As axions and ALPs are generated in the core of the Sun, their typical energy would be a few keV corresponding to the temperature of the Sun's core. They can couple to electrons and cause the axio-electric effect to deposit their total energy in the XMASS-I detector. To carry out search for them, we uses the data for light WIMPs search. The data spectrum and expected ones for various axion masses are shown in the left of Fig. 4. In the right of Fig. 4, the limit on the axion-electron-electron coupling constant, g_{aee}, is also drawn. The limit is calculated by requiring the expected spectrum of each axion mass is not exceed any observed data points.

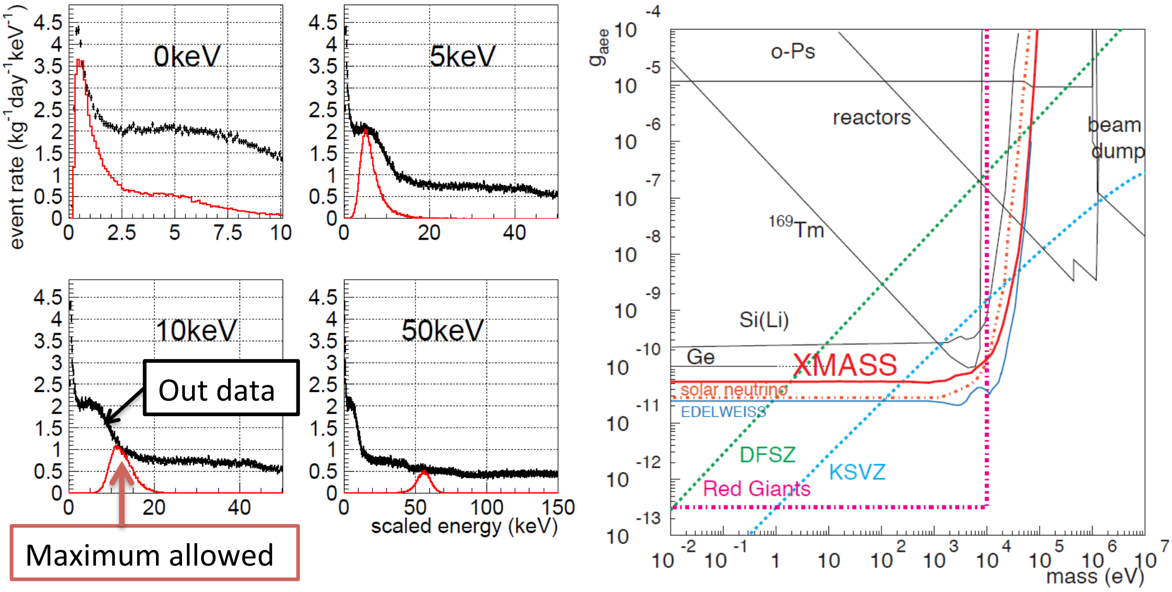

Figure 4 – Spectra of various axion masses(0, 5, 10, and 50 keV) together with the observed data (The left four) and upper limit on the axion-electron-electron coupling constant, g_{aee} (The right).

2.5 Search for bosonic super-WIMPs

There remains issues in the cold dark matter (CDM) models of the Universe: the galaxy structure of the Universe in the CDM model is too complicated comparing with the actual structure. Lighter dark-matter particles in keV to MeV range are motivated in the literatures [7] [8]. One of such hypothetical particle is discussed as "bosonic super-WIMPs" [7]. In particular, the vector super-WIMPs in this mass range are not experimentally constrained and are a good candidate for the dark matter in the Universe. When the bosonic super-WIMPs are absorbed in a target material, all of their energy including their rest mass is deposited. With this nature of the bosonic super-WIMPs, we can expect their energy spectrum to have a monochromatic peak at their rest mass.

The same data set and the same reduction method as the inelastic scattering from ^{129}Xe are used in this search. We optimized cut parameters in the reduction steps in order to obtain the best sensitivity for the various rest masses of the vector super-WIMPs. After applying the optimized reduction steps, both of Monte Carlo spectra and the observed one are compared. We found no signal of the super-WIMPs to set a stringent limit on the coupling constant (see Fig. 5). This is the first experimental constraint on the electron coupling of bosonic super-WIMPs.

3 Refurbishment of XMASS-I and the current status of XMASS-I

During the commissioning we conducted detailed studies on XMASS-I and found that the aluminum seal of the PMT windows was the major origin of observed events. Some other candidates for these events were also identified. To reduce the background, we carried out a plan to refurbish the detector: the PMTs were covered with copper rings as shown in the left two of Fig. 6.

After the refurbishment work was accomplished in November, 2013, DAQ was started and now is steadily continued. Thin copper plates were also used to cover gaps between the rings in order that scintillation lights emitted between the gaps could stop to go into XMASS-I's

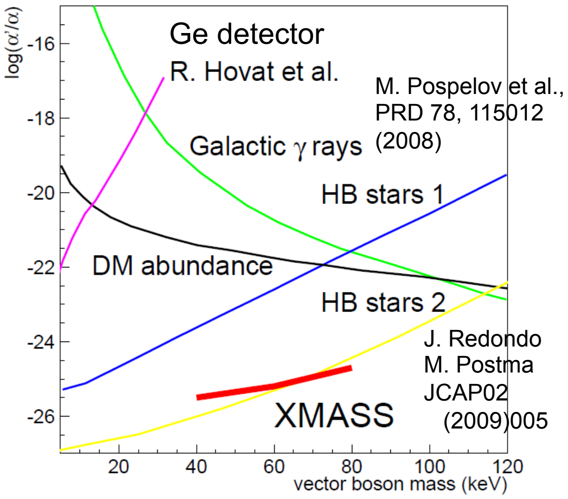

Figure 5 – Upper limit on fine structure constant of vector boson α' relative to one of the electromagnetic interaction(The red solid line). The black line is a prediction of dark matter in case of $\Omega_{\rm DM} = 0.2$. The yellow and the blue ones are the constraints by arguments by horizontal branch stars. The green is based on the diffuse gamma rays in the Universe. The purple line comes from a experimental limit by a germanium detector.

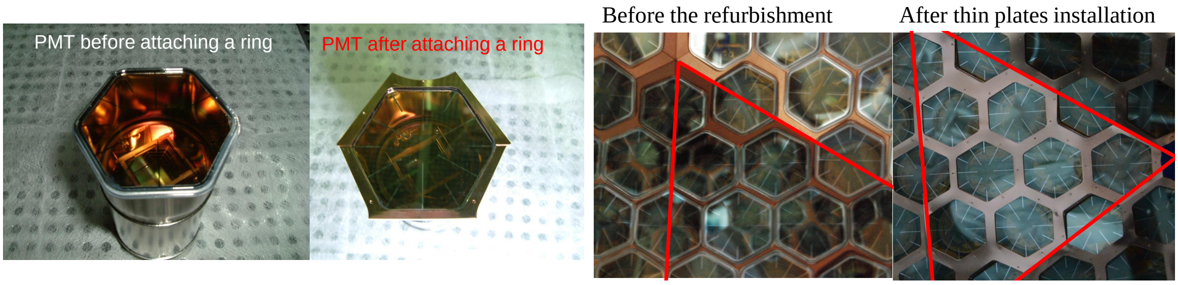

Figure 6 – The photographs of PMTs before installing a copper ring and after (The left two). The ones of before the refurbishment and after (The right two).

sensitive volume. (See the right two of Fig. 6) Now we are working on the detailed analysis of data. A result of a quick test is shown in Fig. 7.

We can see the effect of the refurbishment by checking the distribution of the ratio of the largest photo-electron(PE) charge to the total one in a event because the dark matter signals would be uniformly distributed and if the events happen near the center of the detector then the ratio would be small, on the other hand, background events from around the detector surface would deposit the energy near the detector surface and it means larger PE should be observed in one PMT. According to this quick test, we seem successively to reduce the background about one order of magnitude.

4 Summary

The goal of the XMASS project is to observe the various rare events with a large volume of liquid xenon. The current XMASS-I detector has the largest target mass (835 kg) and achieve the lowest energy threshold (300 eV_{ee}). We discussed herein the results of the XMASS-I from the commissioning runs. We also mentioned about the hardware modification of the XMASS-I to reduce the background and discussed about the current status of the XMASS after the refurbishment.

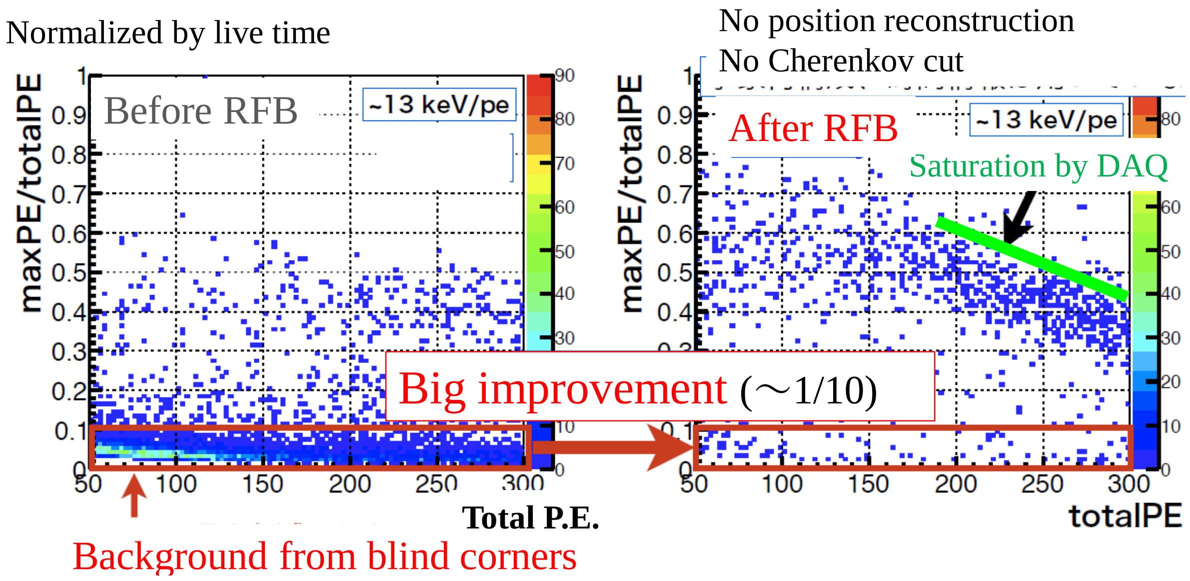

Figure 7 – Two dimensional scattering plots to compare before (left) and after (right) the refurbishment: The vertical axis is the ratio of the largest photo-electron(PE) charge to the total one in a event. The horizontal axis is the total PE.

References

1. Y. Suzuki, arXive:hep-ph/008296
2. K. Abe *et al.*, Astroparticle Physics 31 (2009) 290
3. K. Abe *et al.*, Nucl. Instr. Meth. 661 (2012) 50
4. K. Abe *et al.*, Nucl. Instr. Meth. 716 (2013) 78
5. K. Abe *et al.*, Phys. Lett. B 719 (2013) 78
6. H. Uchida *et al.*, in press in Prog. Theor. Exp. Phys., DOI: 10.1093/ptep/ptu064
7. M. Pospelov, A. Ritz and M. Voloshin, Phys. Rev. D 78 (2008) 115012
8. J. Redondo and M. Postma, JCAP 02 (2009) 005

NEWS: NUCLEAR EMULSION WIMP SEARCH

N. DI MARCO, N. D'AMBROSIO, F. PUPILLI
INFN-Laboratori Nazionali del Gran Sasso, I-67010 Assergi (LAquila), Italy

C. SIRIGNANO
Padova University and INFN, I-35131 Padova, Italy

A. ALEKSANDROV, G. DE LELLIS, A. DI CRESCENZO, V. TIOUKOV
University of Naples and INFN, I-80125 Napoli, Italy

T. NAKA, T. ASADA, T. KATSURAGAWA, M. YOSHIMOTO, K. HAKAMATA, M. ISHIKAWA, K. KUWABARA, A. UMEMOTO, S. FURUYA, S. MACHII and Y. TAWARA
Nagoya University, J-464-8602 Nagoya, Japan

In the field of direct Dark Matter (DM) search a different and promising approach is the directionality: the observation of the incoming apparent direction of WIMPs would in fact provide a new and unambigous signature. The standard approach in designing a direction sensitive experiment consists of using gaseous detectors, in which nuclear recoils are sufficiently long to allow the observation of the track of the recoiled nucleus; nevertheless the sensitivity of such experiments is strongly limited by the small detector mass achievable. The use of a solid target would allow to build a detector of large mass, the challenge being the sub-micrometric track length resulting in the WIMP-nucleus scattering. The only detector able to see such short trajectories is a nuclear emulsion based detector, thus combining the advantages of large mass and high tracking accuracy detectors. In this paper we will illustrate a novel detection technique based on new developments of the nuclear emulsion technology: films with nanometric silver grains, emulsion expansion and fully automated emulsion scanning systems operating at very high speed. Nuclear emulsions would act both as WIMP target and as tracking detector capable of measuring the direction of the nuclear recoil. This unique feature can provide an unprecedented sensitivity in WIMP directional searches.

1 Introduction

The evidence of the existence of DM comes from well-established astrophysical measurements[1]. The most convincing candidate for DM particle is the Weakly Interacting Massive Particle (WIMP) which interact with ordinary matter with cross sections typical or smaller than the weak processes.

Current direct search techniques are based on the detection of the nuclear recoil scattered-off by a WIMP. A WIMP with a mass in the GeV-TeV range has a mean momentum of few tens of MeV and the energy transferred to the scattered nucleus of the target is below 100 KeV. To observe a WIMP-induced signal a low-energy threshold, a low-background level and a large target mass are needed. The analysis of present DM experiments, using solid or liquid targets, is based on the detection of an excess of events over the expected background or on the detection of an annual modulation of the event rate. At present, direct DM search experiments have produced controversial results. As shown in figure 1, while DAMA/LIBRA and CoGeNT

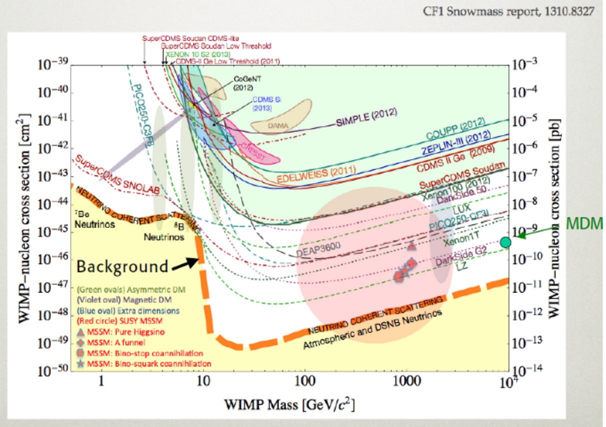

Figure 1 – Present experimental limits and allowed regions in the WIMP cross-section and mass plane.

suggest a signal of an annual modulation, other experiments like LUX and Xenon100 exclude a wide region of the parameter space.

The detection of the direction in the lab frame of the apparent WIMP flux, first proposed by Spergel [3] in 1988, would provide a strong DM signature: the motion of the Sun inside the galaxy causes in fact a peak in the nuclear recoils induced by WIMPs in the direction opposite to the motion of the Sun in the galaxy (i.e. toward the Cygnus costellation). The detection of the anisotropy of the recoiled nucleus direction with respect to the isotropically distributed background, would provide an unambiguous proof of the galactic origin of DM particles with only few tens of events. In directional detectors the challenge is the reconstruction of low energy tracks. Several projects of directional detectors are being developed on purpose, mainly based on the development of a large TPC [4]: in low pressure gaseous detectors the nuclear recoils are long enough (O(mm)) to be reconstructed as tri-dimensional tracks, but the target mass is rather small being limited by the low gas density. The sensitivity of such experiments is therefore quite poor and they cannot cover a significant area of the WIMP search parameter space. The use of a solid target would allow to explore lower cross section sectors in the phase space indicated by recent limits drawn by direct search experiments, the challenge being the shorter track length (O(100 nm)) resulting in the WIMP-nucleus scattering. The ground-breaking approach of the NEWS project, using very high resolution nuclear emulsions as solid target, would overcome this problem. In next section a description of the project and of the results of the R&D will be reported together with a projection of the expected sensitivity.

2 NEWS: a novel approach to directional Dark Matter detection

Nuclear emulsions are the most accurate position detector for elementary particles. The emulsions currently used in particle physics have grains with linear dimensions of 200 nm, too large to detect WIMP-induced nuclear recoils. In 2007 the Nagoya University group completed a R&D project for the production of films with a grain diameter of 40 ± 9 nm, almost an order of magnitude smaller than conventional ones, such as those used in the OPERA experiment[5]. These emulsions with nano-grains, called Nano Imaging Tracker (NIT)[6], allow to reconstruct tracks with path lengths equal or less than 200 nm if scanned by X-ray or optical microscopes, after the use of an appropriate film expansion technique developed at the Nagoya University[7]. A further R&D on the NIT technology has recently led to the production of emulsion films with grain size of the order of 18 ± 5 nm: the use of the Ultra Nano Imaging Tracker (U-NIT) technique would lower the tracking threshold to the level of 100 nm.

The NIT consists of AgBr crystals immersed in an organic gelatin: it contains, in addition to the nuclei of silver and bromine, also lighter nuclei such as carbon, oxygen and nitrogen. The

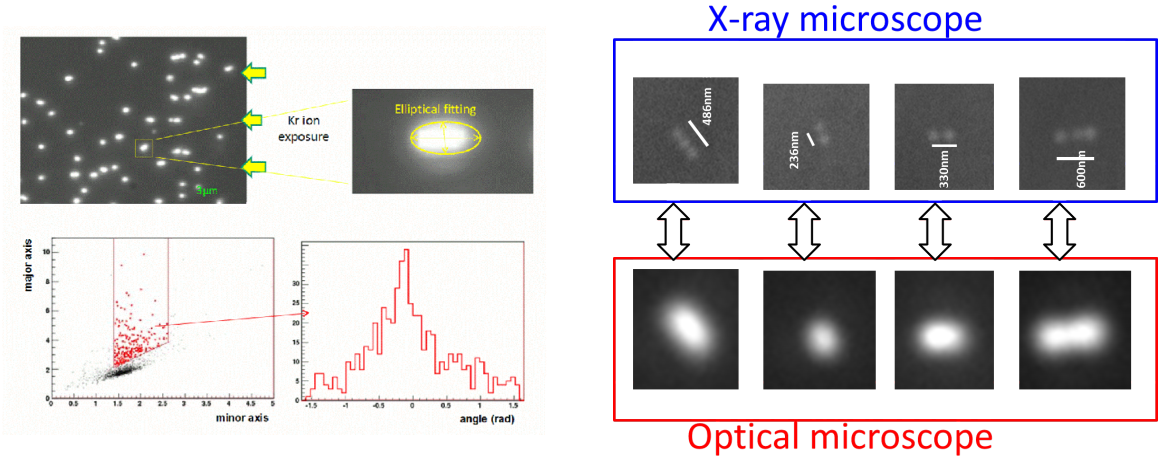

Figure 2 – Left: principle of the selection of sub-micrometric tracks with an optical microscope. Right: comparison between the reconstruction of tracks of 200-300 nm length with the optical microscope and with the X-ray microscope.

weight fractions are ∼ 80% for AgBr and ∼ 20% for CNO. The sensitivity of an experiment using NITs strongly depends on the minimum detectable track length: the path length of the recoiled track depends on the kinetic energy of the scattered nucleus, being the kinematics determined both by the mass of the incident WIMP and by that of the target nucleus. WIMP with a mass of around 100 GeV/c^2 prefers Ag and Br as target, producing a Br recoil with an average kinetic energy of 47 KeV. Although Ag and Br are the most effective targets for these WIMP masses, the detection capability is reduced since their ranges are shorter than lighter elements. Instead, for a WIMP with a mass around 10 GeV/c^2, the kinematics favors the lighter nuclei that, for a given kinetic energy, have a longer range. Therefore, if we consider only Ag and Br, the sensitivity is extremely low for WIMP masses around 10 GeV/c^2, while the contribution of the C, N and O ions becomes essential.

The read-out of such sub-micrometric recoil tracks is done in two steps: nuclear emulsion films will be at first scanned using optical microscopes[9,10] in order to preselect candidate signal tracks; then the X-ray microscope will be used to improve the signal to background ratio. Fig. 2 shows the principle of the track selection with the optical microscope (left plots): on the top part of the figure the images taken on samples of NIT exposed to a Kr ion beam are shown. The track length is about 300 nm. Given the resolution of the optical microscope, the sequence of several grains making a track of a few hundred nanometers appears as a single cluster. It is thus not possible to distinguish clusters made of several grains from single grains produced by thermal agitation. This problem is solved by analyzing the shape of the cluster: a cluster made by several grains tends to have an elliptical shape with the major axis coincident with the direction of the trajectory, while a cluster produced by a single grain tends to have a spherical shape. With this technique a clear separation between the two populations can be obtained, as reported in the bottom left plot of figure 2, where the signal clusters are shown in red[8]. The angular resolution on the direction is of the order of 35 degrees.

The second step of the read-out process requires the use of the X-ray microscopy: with this technique, a spatial resolution of ∼30 nm is achievable using Fresnel lenses called *zone plates* that form the image by focusing X-rays emitted from a synchrotron. On the right part of fig. 2 the comparison between the reconstruction of tracks with a path length between 200 and 300 nm made with an optical microscope and with a X-ray microscope is shown. The single grains are clearly visible with the X-ray microscope. The efficiency of the matching is evaluated to be ∼ 99% and the angular resolution is ∼ 16 degrees.

In Fig. 3 a projection of the sensitivity for an experiment with an exposure of 25, 100, 1000 kg × year of nuclear emulsions respectively, with a minimum detectable track length equal to

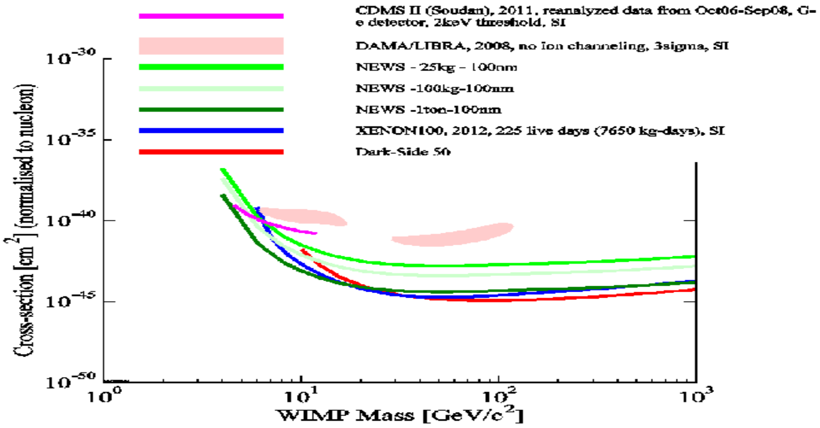

Figure 3 – Sensitivity projection at 90% C.L. for a NIT detector with an exposure of 25 kg × year, 100 kg × year, 1000 kg × year respectively, a threshold of 100 nm, in the zero background hypothesis and without including the directionality information.

100 nm and in the zero background hypothesis, is shown at 90% C.L.. Even not including the directionality discrimination of the signal and assuming to reach a negligible background level, such an experiment would cover the parameter space indicated by the DAMA/LIBRA results with a rather small (25 kg) detector mass. Increasing the detector mass up to 1 ton it would be able to explore signals possibly coming from current DM experiments, but using a powerful and complementary approach.

3 Conclusions

The evidence for the existence of dark matter comes from cosmological observations. A final confirmation of the existence of Dark Matter should come from direct or indirect detection of dark matter candidates. One of the commonly used approaches is the search for elastic WIMP scatterings on ordinary nuclei. The expected signal is difficult to be separated from background in particular from neutron interactions induced either by cosmic rays or by natural radioactivity. An unambiguous proof of dark matter could come from experiments able to measure the direction of the nuclear recoils induced by WIMP interactions with ordinary matter. The use of the nuclear emulsion technology combines the capability to detect sub-micrometric tracks with the possibility to build large mass detectors, thus achieving a very high sensitivity to WIMPs. The NEWS project would open a new window in the DM research field: an experiment based on the use of the novel NIT technology could lead to confirm or disprove, with a complementary and alternative approach, signals possibly coming from current non-directional DM experiments.

References

1. G. Bertone, D. Hooper and J. Silk, *Phys. Rept.* **405** 279 (2005).
2. P. Cushman *et al.*, Snowmass CF1 summary: WIMP dark matter direct detection, arXiv:1310.8327
3. D. N. Spergel, *Phys. Rev.* D **37** 1353 (1988).
4. F.Mayet, J.Billard, *J.Phys.Conf.Ser.* **469** 012013 (2013).
5. R. Acquafredda *et al.*, *JINST* **4** P04018 (2009).
6. M. Natsume *et al.*, *Nucl. Instr. Meth.* A **575** 439 (2007)
7. T. Naka *et al.*, *Nucl. Instr. Meth.* A **581** 761 (2007)
8. M. Kimura and T. Naka *Nucl. Instr. Meth.* A **680** 12 (2012)
9. M. De Serio *et al.*, *Nucl. Instrum. Meth.* A **554** 247 (2005)
10. N. Armenise *et al.*, *Nucl. Instrum. Meth.* A **551** 261 (2005)

MILLI-INTERACTING DARK MATTER AND THE DIRECT-SEARCH EXPERIMENTS

QUENTIN WALLEMACQ
IFPA, AGO Department, University of Liège, Sart Tilman,
4000 Liège, Belgium

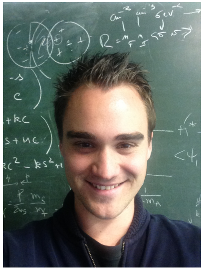

Hydrogen-like dark atoms interact with standard matter because of two mixings, a kinetic mixing between standard photons and dark massless photons and a mass mixing of σ mesons and dark scalars. After having thermalized in terrestrial matter, they reach underground detectors with thermal energies and form bound states with atoms in the active media, which causes the emission of photons that produce the observed signals. The model explains well the positive results from DAMA/LIBRA and CoGeNT without any contradiction with the null results from XENON100, LUX, CDMS-II/Ge and superCDMS.

Due to the clear contradictions between direct-search experiments when they are interpreted in terms of WIMPs [1,2], alternative scenarios have been proposed to reinterpret the data. Their common feature is a complex composition of the dark sector and more sophisticated interactions with standard matter, leading to a richer phenomenology, in particular in underground detectors.

The scenario presented here is part of this rising class of models. Hydrogen-like dark atoms, bound through a dark $U(1)$ gauge coupling carried by dark massless photons, interact with terrestrial matter because of two different mixings: a kinetic mixing between the standard and the dark photon and a mass mixing between the σ meson and a neutral dark scalar. In underground detectors, after dark atoms have thermalized in terrestrial matter through elastic collisions, dark nuclei get radiatively captured by atomic nuclei of the active medium, and the emitted photons produce the observed signals.

In the following, we present the regions in the parameter space of the model that reproduce the results of DAMA/LIBRA and CoGeNT at the 2σ level, in full consistency with the null results from XENON100, LUX, CDMS-II/Ge and superCDMS. Further details about the model can be found in Refs. [3] and [4].

The dark sector is composed of two kinds of fermions, F and G, with opposite dark electric charges $+e'$ and $-e'$ respectively, that bind to from hydrogen-like dark atoms. In that system, F plays the role of a dark nucleus and G of a dark electron, i.e. $m_F \gg m_G$, where m_F and m_G are the masses of F and G. The size of these dark atoms is determined by their Bohr radius $a_0' = 1/(m_G \alpha')$, where $\alpha' = \frac{e'^2}{4\pi}$. The massless dark photons associated with the dark $U(1)$

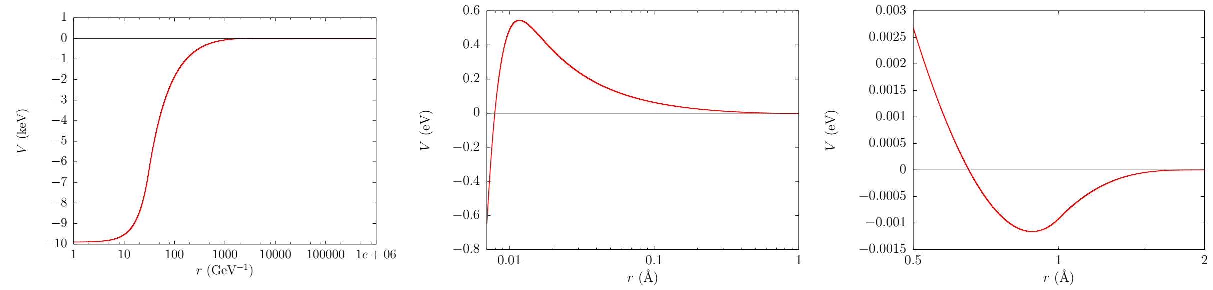

Figure 1 – Atom-dark atom potential for iodine and typical values of the parameters: $\eta = 10^{-7}$, $\epsilon = 10^{-5}$ and $m_S = 1$ MeV. Left: the whole potential. Center: a zoom on the Coulomb barrier. Right: a zoom on the atomic well.

gauge symmetry are kinetically mixed with the standard photons via the dimensionless mixing parameter ϵ. Thus, F and G have Coulomb interactions with the charged standard particles, in particular the proton and the electron, respectively with electric millicharges $+\epsilon e$ and $-\epsilon e$, where e is the charge of the proton. In addition, the dark nuclei F exchange dark neutral scalars S of mass m_S, to which they are coupled via a Yukawa coupling of strength g'. A mass mixing, characterized by a dimensionless mixing parameter η, of S with the σ meson of the standard model induces a scalar interaction between the dark nuclei and nucleons. For this attractive Yukawa-like interaction, F has a charge ηg, where g is the Yukawa coupling of the nucleon to σ.

The relevant model parameters for the direct searches are therefore m_F, m_S, η, ϵ and a_0'. However, a_0' is fixed to 1 Å, i.e. the typical size of standard atoms, in order to have sufficiently large elastic atom-dark-atom cross sections and hence facilitate the thermalization process between the surface of the Earth and detectors located 1 km underground.

The kinetic and mass mixings produce interactions between standard and dark particles. At the atomic level, and in the non-relativistic limit, this results in a potential of interaction V between standard and dark atoms. To determine it, an atom is modelled by a finite sphere of radius 1 Å with a uniform charge distribution representing the electronic distribution. For a standard atom of atomic number Z, the total charge is $-Ze$ while it is $-\epsilon e$ for a dark one. At the center of the electronic spheres stands the nucleus, which has a finite radius, a total charge $+Ze$ and a uniform charge distribution in the case of a standard atom, whereas it is point-like and of charge $+\epsilon e$ in the dark case.

The potential is represented in Figure 1 as a function of the distance r between the two nuclei, for iodine and typical values of the parameters: $\eta = 10^{-7}$, $\epsilon = 10^{-5}$, $m_S = 1$ MeV. In the left figure, corresponding to the whole potential, we mainly see the attractive well at short distance due to the σS-exchange between nuclei, of range m_S^{-1}. A zoom at larger distance shows the Coulomb barrier at the center, due to the electrostatic repulsion betwen the two positively charged nuclei. The very shallow well on the right is the result of an attraction between the electronic cloud of an atom and the nucleus of the other, but it has no effect in the model.

Hitting the Earth, dark atoms penetrate under the surface and undergo elastic collisions with terrestrial atoms, the elastic cross section being obtained from the interaction potential V through $\left(\frac{d\sigma}{d\Omega}\right)_{el} = \frac{\mu^2}{4\pi^2}\left|\int e^{-i\vec{q}.\vec{r}}V(\vec{r})\right|^2$, where μ is the reduced mass of the nucleus-F system and $\vec{q}$ is the transferred momentum. This makes them lose energy at a rate $\frac{dE}{dx}$ until they acquire thermal energies. We require that this thermalization process occurs before 1 km under the surface, which is the typical depth of underground detectors, so that the penetration length x must satisfy $x = \int_{E_{th}}^{E_0} \frac{dE}{|dE/dx|} \leq 1$ km, where the integral is performed from the incident energy E_0 to the thermal energy in the terrestrial crust $E_{th} = \frac{3}{2}T_{crust}$ with $T_{crust} \simeq 300$ K.

Afterwards, the dark atoms drift down towards the center of the Earth by gravity and arrive in detectors. The equilibrium between the incident flux at the surface of the Earth and the downfalling thermalized flux in the crust determines the number density of dark atoms in detectors, which is annualy modulated just as the incident flux.

In a detector, dark atoms collide with atoms of the active medium and have some probability to tunnel through the Coulomb barrier of Figure 1 and hence to be captured radiatively on a bound state in the well at short distance. The transition from the continuum with energy E to this bound state of energy E_p is of electric-dipole type and since the incident plane wave, to order v/c, is mainly an s-wave, the final state of the transition has to be a p-state. This capture is accompanied by the emission of a photon of energy $|E - E_p| \simeq |E_p|$. Then, a second electric dipole transition causes the de-excitation of the nucleus-F system to a lower s-state in the well, of energy E_s, together with the emission of a photon of energy $|E_p - E_s|$. Two photons are therefore released in the detector and to avoid the observation of double-hit events, we require that the energy of the first one is below the threshold of the experiment. In principle, several transitions in the well are possible, corresponding to as many lines and hence to an emitted spectrum, but for simplicity only the transition from the lowest p-state to the ground state, which is dominant, is considered. This monochromatic line has then to lie in the detection interval, i.e. $(2 - 6)$ keV and $(0.5 - 3)$ keV respectively for DAMA and CoGeNT.

We solve the radial Schrödinger equation with the potential V for a positive energy E, which gives the radial part $R(r)$ of the initial diffusion eigenstate. Similarly, by solving the nucleus-F bound state problem, we get the radial part $R_p(r)$ of the final bound eigenfunction and the eigenstate E_p. The capture cross section σ_{capt} is then obtained by computing the matrix element $D = \int_0^\infty r R_p(r) R(r) r^2 dr$ of the dipole operator between these two states:

$$\sigma_{capt} = \frac{32\pi^2 Z^2 \alpha}{3\sqrt{2}} \left(\frac{m_F}{m_F + m}\right)^2 \frac{1}{\sqrt{\mu}} \frac{(E - E_p)^3}{E^{3/2}} D^2, \tag{1}$$

where α is the fine structure constant and m is the mass of a nucleus of the detector.

The bound-state-formation rate per unit volume is given by $R = n_F n \langle \sigma_{capt} v \rangle$, where n_F and n are the number densities of dark and standard atoms. It is obtained by averaging $\sigma_{capt} v$, where v is the relative velocity, over the velocity distributions. These are taken to be of Maxwell-Boltzmann type both for the atoms and the dark atoms, depending on the operating temperature T of the detector. Obviously, R inherits the annual modulation of n_F. The temperature T in the detector is a key parameter of the model: it allows to explain why, in two experiments made of very similar nuclei but operating at different temperatures, such as DAMA (iodine: $(Z, A) = (53, 127)$, $T \simeq 300$ K) and XENON100/LUX (xenon: $(Z, A) = (54, 132)$, $T \simeq 173$ K), only the former observes a signal. Due to the lower incident energies in the colder detector, tunneling through the Coulomb barrier will be much less efficient and hence the capture rate will be suppressed with respect to the detector operating at room temperature. A direct consequence is that this model naturally predicts no event in cryogenic detectors (CDMS-II/Ge, CDMS-II/Si, superCDMS), where temperatures $T \simeq 1$ mK are much too low to allow any tunneling.

It should be noted that the emitted photons will produce electronic recoils instead of nuclear recoils as in the usual WIMP scenario. In a detector that does not make a difference between both types of recoils, as DAMA and CoGeNT, the reinterpretation of the results is straightforward. But in XENON100, LUX or CDMS, which can clearly discriminate between electronic and nuclear recoils, there is a major difference, since the bound-state-formatrion events will be interpreted as backgrounds. If such an experiment has negative results (XENON100, LUX, CDMS-II/Ge, superCDMS), even if the rate cannot be suppressed completely, our model still predicts no detection, as the remaining events will be considered as background and rejected. We just have to ensure that the predicted electronic background is still consistent with the observed one. However, some difficulties might appear if the three events of CDMS-II/Si are confirmed, since no nuclear recoil can be produced in the model as is.

We explored the 4-dimensional parameter space of the model in order to reproduce the integrated modulation amplitudes and energy intervals of DAMA/LIBRA and CoGeNT at the 2σ level. The regions projected in two dimensions are given in Figure 2 in light red and light

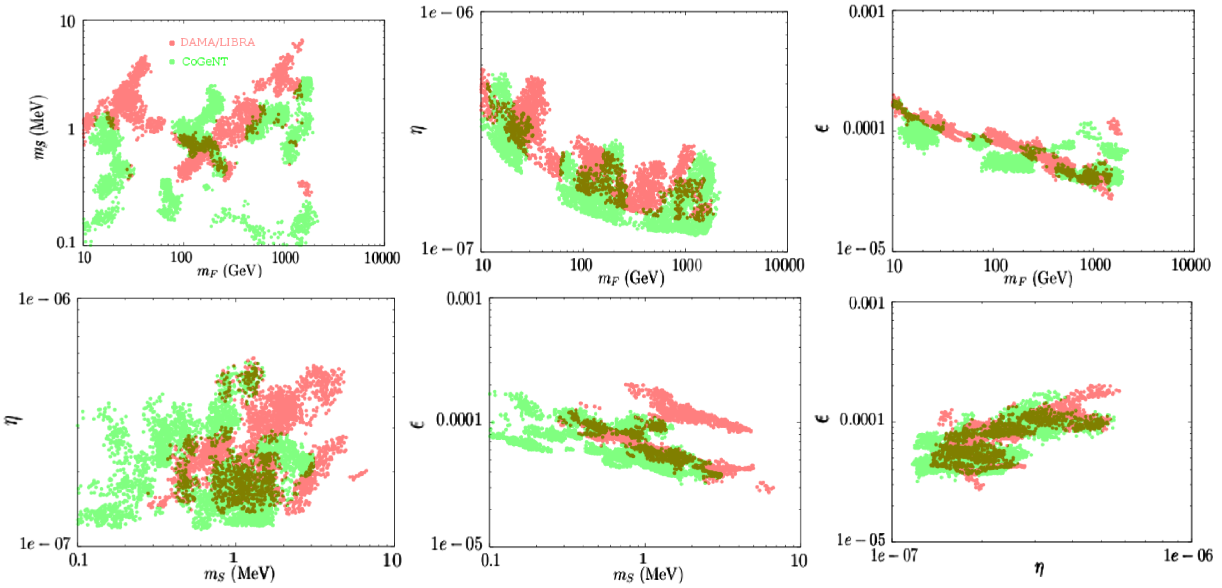

Figure 2 – Two-dimensional regions of the parameter space reproducing DAMA/LIBRA (light red) and CoGeNT (light green) at the 2σ level. Overlapping regions appear in olive green. Top left: (m_F, m_S) plane. Top center: (m_F, η) plane. Top right: (m_F, ϵ) plane. Bottom left: (m_S, η) plane. Bottom center: (m_S, ϵ) plane. Bottom right: (η, ϵ) plane.

green for DAMA/LIBRA and CoGeNT respectively, while the overlapping regions are in olive green. They show wide allowed intervals for all the parameters, with m_F going from 10 GeV to more than 1 TeV, m_S around 1 MeV, η between 10^{-7} and 10^{-6} and ϵ between 10^{-5} and 10^{-4}. We used the isotopes ^{127}I and ^{74}Ge respectively, as the detectors are made of NaI and Ge crystals. The choice of iodine instead of sodium for DAMA is to avoid the existence of bound states with light elements, i.e. the formation of heavy isotopes on Earth or during Big Bang Nucleosynthesis.

The positive results of DAMA/LIBRA and CoGeNT are consistent with the negative ones of XENON100 and LUX. By taking the models of Figure 2 and calculating the corresponding rates in liquid xenon at $T = 173$ K, we can select the ones that are consistent with the observed background. The strongest constraints on the expected and observed electron-recoil backgrounds come from LUX, but it does not really change the allowed intervals for the parameters. Finally, the predicted rates in CDMS-II/Ge and superCDMS, which are cryogenic, are consistent with zero and hence in agreement with the data.

We have briefly presented our milli-interacting dark matter model and shown the regions in its parameter space that reproduce the results of DAMA/LIBRA and CoGeNT at the 2σ level. The overlapping regions indicate wide allowed intervals for all the parameters that are in agreement with the negative results from XENON100, LUX, CDMS-II/Ge and superCDMS.

Acknowledgments

I thank the Belgian fund F.R.S-FNRS for supporting my participation to the Rencontres de Moriond 2014.

References

1. D.S. Akerib et al. *Phys. Rev. Lett.*, 112:091303, 2014.
2. R. Agnese et al. Search for Low-Mass WIMPs with SuperCDMS. 2014.
3. Quentin Wallemacq. Milli-interacting Dark Matter. *Phys. Rev.*, D88:063516, 2013.
4. Quentin Wallemacq. *Adv. High Energy Phys.*, 2014:525208, 2014.

The DEAP Search For Dark Matter

J.J. Walding
Department of Physics, Royal Holloway, University of London, Egham Hill,
Egham TW20 0EX, England

DEAP-3600 is a single-phase liquid argon dark matter detector currently under construction at SNOLAB in Canada with first physics data expected in the fall, 2014. DEAP has been designed to achieve extremely low background rates, including those from ^{39}Ar β decays, neutron scatters, and surface α contamination, with the goal of measuring the spin-independent WIMP-nucleon cross section down to 10^{-46} cm^2 for a 100 GeV WIMP - a factor of ten below current limits. An overview of the DEAP program is presented including new results from DEAP-1.

1 The DEAP Program

1.1 DEAP-3600 Overview

The DEAP collaboration was formed in 2005 and consists of more than 70 collaborators from nine institutions. DEAP-3600 is the latest experiment in the DEAP program. The goal of DEAP-3600 is to perform a weakly interacting massive particle (WIMP) dark matter search using argon with a sensitivity to the spin-independent WIMP-nucleon cross-section of 10^{-46} cm^2 for a WIMP mass of 100 GeV after three tonne-years of running. This will be approximately a factor of ten better than the current world's best limit set by the LUX experiment [1].

The detector consists of a central volume of 3,600 kg of liquid argon (1,000 kg fiducial mass) contained inside a transparent acrylic vessel. Scintillation light generated from interactions in the argon is reconstructed by 255 high quantum efficiency (32%) Hamamatsu R5912 photomultiplier tubes (PMTs) attached to the acrylic vessel via 50 cm long cylindrical light guides. These PMTs give the detector 75% photocathode coverage over 4π steradians. The acrylic vessel, light guides and polystyrene filler blocks are used as both thermal insulation and as shielding from (α,n) neutrons emitted by the PMT glass. A schematic of the detector can be seen in figure 1.

The dark matter detection principle for DEAP-3600 is conceptually very simple; interactions in argon can be characterised as either electronic-type or nuclear-type recoils. These recoils produce argon excimers which emit UV scintillation light when they decay back to their ground state. Tetraphenyl butadiene (TPB), coated onto the inside of the acrylic vessel, is used to shift the scintillation light into the visible spectrum, detectable by the PMTs.

1.2 Pulse Shape Discrimination

A WIMP dark matter particle scatter in DEAP will result in a nuclear recoil, it is therefore essential for DEAP-3600 to be able to distinguish nuclear recoils (signal) from electronic recoils (background). To distinguish nuclear from electronic recoils DEAP takes advantage of the large difference in the singlet and triplet argon excimer state lifetimes (7 ns and 1.6 μs respectively)

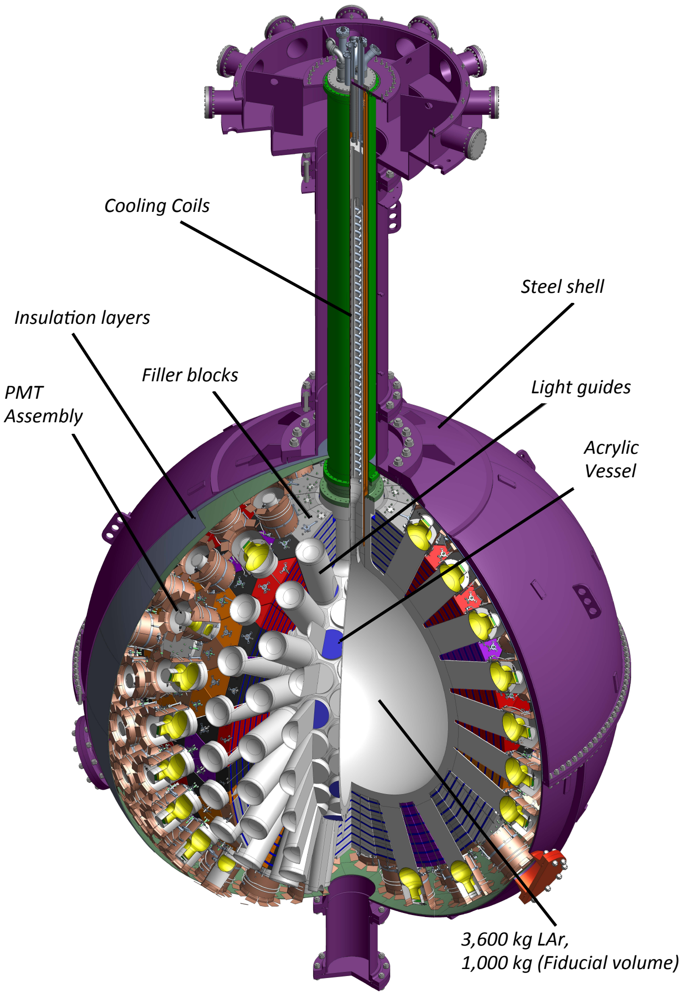

Figure 1 – Section of the DEAP-3600 detector. The 7 m × 7 m (Ø × H) veto water tank is not shown.

and the fact that electronic and nuclear recoils produce different ratios of the singlet and triplet states. Discrimination of the recoils is achieved by constructing a pulse shape discriminant (PSD) called F_{prompt} [2,3,4]. F_{prompt} is the the ratio of the number of photoelectrons (PE) registered in a prompt time window (the first 200 ns for DEAP-1) to the total number of photoelectrons in an event. Figure 2 shows the F_{prompt} distribution for a ^{22}Na gamma source and an AmBe neutron source deployed in DEAP-1 [4]. There is a clear separation between the nuclear recoils (AmBe neutrons) and the electronic recoils (^{22}Na gammas) for an F_{prompt} value of ∼0.65.

Figure 3 (left) shows the expected PSD leakage for light yields of four and eight PE/keVee. By doubling the light yield of DEAP-1 from four PE/keVee to eight PE/keVee decreases the PSD leakage by approximately 5×10^4 at 15 keVee. This strong dependence on light yield drove the decision to maximise the photocathode coverage in DEAP-3600 [6]. Figure 3 (right) shows the F_{prompt} distribution versus reconstructed number of photoelectrons in DEAP-1 for an AmBe calibration source. AmBe sources emit both neutrons and gammas, in particular a high rate of 60 keV gammas, intrinsic to ^{241}Am. A clear separation between the nuclear recoil band (F_{prompt} = 0.7) and the electronic recoil band (F_{prompt} = 0.3) can be seen. The green box represents the dark matter search region of interest for DEAP-1. The red box represents the proposed dark matter search region of interest for DEAP-3600. The lower reach in PE for DEAP-3600 comes from the increased discrimination power due to the higher light yield expected in DEAP-3600.

As well as studies of the PSD, DEAP-1 also studied radon and surface α backgrounds [5].

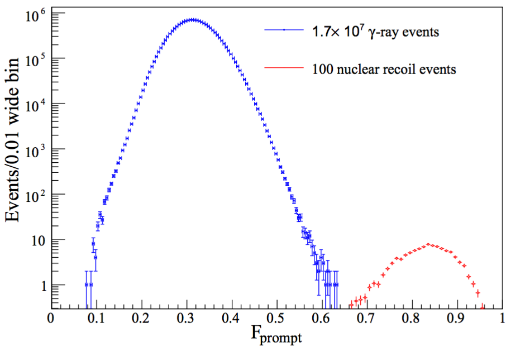

Figure 2 – The F_{prompt} distribution for a ^{22}Na gamma source and an AmBe neutron source deployed in the DEAP-1 detector. There is a clear separation in F_{prompt} between the neutrons from the AmBe source (nuclear recoils) and the gammas from the ^{22}Na source (electronic recoils).

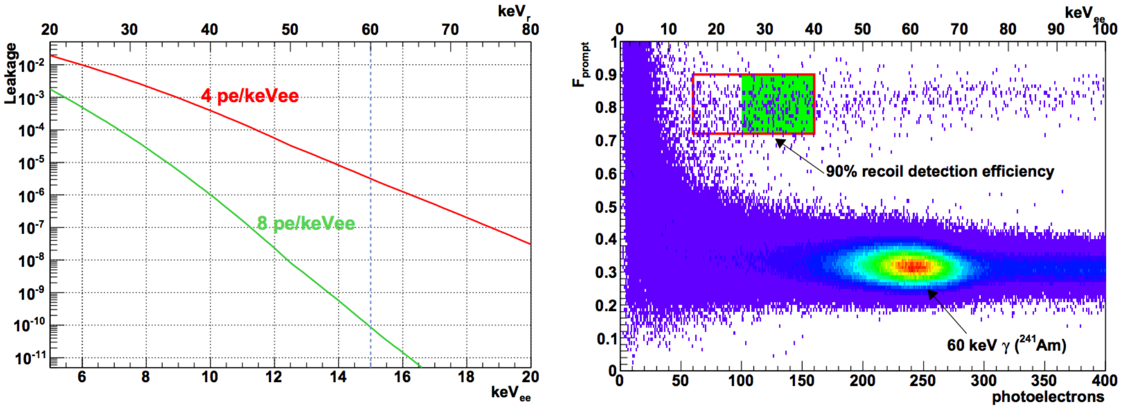

Figure 3 – (Left) The discrimination of β events versus energy for light yields of four and eight PE/keVee. Increasing the light yield decreases the PSD leakage by approximately 5×10^4 at 15 keVee. (Right) The F_{prompt} distribution as a function of the reconstructed number of PE for an AmBe source in DEAP-1. AmBe sources produce neutrons as well as a high rate of 60 keV gammas intrinsic to ^{241}Am. A clear band exists for an F_{prompt} value of ~0.3 associated with the ^{241}Am gammas. The nuclear recoils from the AmBe neutrons are visible as a band for an F_{prompt} value of ~0.7. The green box represents the WIMP search region of interest for DEAP-1. The red box represents the proposed WIMP search region of interest for DEAP-3600. The lower reach in PE for DEAP-3600 comes from the increased light yield expected in DEAP-3600.

Table 1 shows the expected background rates in DEAP-3600 determined by extrapolating measurements made by DEAP-1.

1.3 Calibration Systems

Three external calibration systems have been developed to monitor the detector response and stability during physics data runs. These are the optical fibre calibration system, the gamma calibration source system and the neutron calibration source system.

The optical fibre calibration system consists of twenty optical fibres attached to twenty light guides. The fibres are angled such that flashing the optical fibre system results in light reflecting off the front face of the PMT illuminating the entire detector. This system will be used to monitor the PMT gains and the timing offsets between PMTs.

The gamma calibration source system consists of a tagged ^{22}Na source. This is deployed in the external calibration tubes that surround DEAP-3600, allowing the source to populate various locations within the detector with gammas. This gamma spectrum is well understood and so will be used to map the detector response across a range of energies. Additionally, by placing the source next to the neck of the detector the reconstruction of neck events can be

Table 1: DEAP-3600 background targets. These target values were extrapolated from DEAP-1 data and correspond to one background event in DEAP-3600 every 5Gg-days.

Background Parameters	Target
Radon in Argon	< 1.4 nBq/kg
Surface α's	< 100 μBq/m^2
Neutrons (all sources, in fiducial volume)	< 2 pBq/kg
^{39}Ar (after PSD)	< 2 pBq/kg
Total Backgrounds	< 0.6 events (3 tonne-years)

studied. This is of importance as it is the only part of the detector without PMT coverage.

The neutron calibration system consists of a tagged 74 MBq AmBe (α, n) source, corresponding to a neutron rate of $\sim$ 5000 n/s. Neutrons are tagged by reconstructing the 4.4 MeV gamma emitted by the de-excitation of ^{12}C using NaI crystals surrounding the AmBe source.

Like the gamma source the neutron source is to be deployed in the external calibration tubes. This source will be used to study the detector response to nuclear recoils, allowing monitoring of the region of interest for the dark matter search.

All three calibration systems are in the final stages of construction with completion of the optical fibre calibration system expected in June 2014. Construction of the neutron and gamma calibration systems is expected to be completed by August 2014.

1.4 Outlook

The construction of the detector is almost complete. The detector will be sealed in June 2014 at which point commissioning will begin. Commissioning will take approximately five months and will include running the optical fibre calibration system and both the gamma and neutron calibration sources. During commissioning the detector will be filled with gaseous argon and cooled. The calibration systems will be used to monitor the detector response when under vacuum, filled with gaseous argon and filled with liquid argon. Upon completion of the detector commissioning first physics data will be taken, expected to be in the fall, 2014.

1. D. S. Akerib *et al*, *Phys. Rev. Lett.* **112**, 091303 (2014).
2. M. G. Boulay and A. Hime. *Astroparticle Physics* **25**,179182 (2006).
3. W. H. Lippincott *et al. Phys. Rev.* C **78**, 035801 (2008).
4. M. G. Boulay *et al. arXiv.org* 0904.2930 (2009).
5. P. A. Amaudruz *et al. arXiv.org* 1211.0909 (2014).
6. M. G. Boulay (For the DEAP Collaboration) *J. Phys.: Conf. Ser.* **375** 012027 (2012).

A CoGeNT analysis: Is there evidence for a dark matter signal?

Jonathan H. Davis
Institute for Particle Physics Phenomenology, Durham University, Durham, DH1 3LE, United Kingdom

We present an independent analysis of data from the CoGeNT experiment, for a dark recoil matter signal. We separate the bulk events (where a dark matter signal may be present) from the surface event background by fitting log-normals to the rise-time data. From this, we calculate the energy-dependent bulk fraction $\mathcal{R}(E)$ and parameterise this with cubic splines. By marginalising over all possible splines we find less than 1σ evidence for dark matter in CoGeNT data.

1 Introduction

CoGeNT is a direct detection experiment searching for evidence of dark matter particles recoiling off germanium nuclei. If the dark matter particle has a mass ~ 10 GeV then the distribution of recoil events in energy should exhibit a characteristic exponential rise below $\sim 1\,\mathrm{keV_{ee}}$. The CoGeNT collaboration [1,2] claim to have observed such a rise in their data which can not be accounted for by known backgrounds. This low-energy excess of events is consistent with an 8 GeV dark matter particle and an interaction cross section with nucleons $\sigma \approx 3 \cdot 10^{-41}$ cm^2.

However, such a scenario is not consistent with, for example, the results of CDEX [3], LUX [4], SuperCDMS [5] and XENON100 [6], which do not observe any events above the known backgrounds. Due to this, we have performed an independent analysis of CoGeNT data, focusing on the treatment of surface events, which mimic the low-energy rise characteristic of light dark matter.

In these proceedings we summarise our methodology and results. Further details, including discussions on rise-time cuts and backgrounds, can be found in Davis, McCabe & Boehm [7].

2 The CoGeNT experiment and data-set

The CoGeNT experiment[1,2] operates using a p-type point-contact germanium detector; an image of one of the modules used in CoGeNT is shown in the left panel of figure 1. An event constitutes a change in the measured voltage, and as can be seen in the right panel of figure 1, this sharp change occurs over a time of a few μs. The magnitude of the change is proportional to the recoil energy, while the duration is quantified as the rise-time of each event.

The majority of the volume of the CoGeNT modules is a p-type semiconductor with a charge collection efficiency ϵ of unity. Following the CoGeNT collaboration, we label this as the bulk of the detector. Towards the outer edge of the detector modules is the millimetre-thick transition layer, where $0 < \epsilon < 1$. Events occurring here are denoted as surface events (again following the CoGeNT collaboration). This is shown in the central panel of figure 1.

Backgrounds from e.g. low-energy gammas induce events preferentially towards the outside of the detector volume. However, dark matter particles are weakly-interacting, and so they are considerably more likely to scatter in the bulk than the surface, whose volume is much smaller. Due to this, the surface population will be dominated by background events. Additionally,

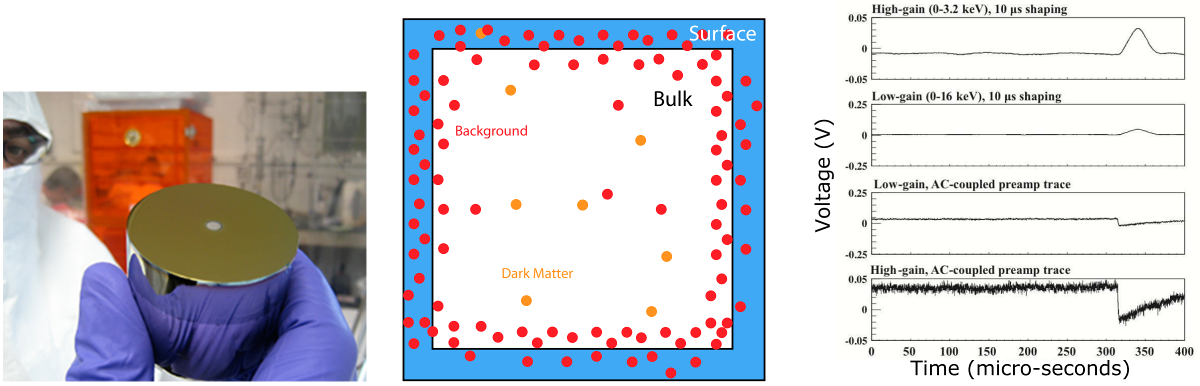

Figure 1 – From left to right: an image of one of the CoGeNT detector modules, a sketch of events in the bulk and surface of the CoGeNT detector, and an example event.

the partial charge collection means these surface events will be measured with typically lower energies, resulting in a spectrum which can mimic a dark matter recoil.

Similarly to the method employed by the CoGeNT collaboration, we separate the bulk and surface populations by fitting log-normal distributions (an alternative distribution for the bulk events is considered in Davis et al.[7]). We show such a fit for two different energy-bins in figure 2. As expected, the surface events occur generally at higher rise-times, but there is significant overlap with the bulk events at low energy. Additionally, the fraction of bulk events (or the ‘bulk fraction’) is clearly reduced at lower energies. This bulk fraction is defined as $\mathcal{R}$ = Number of bulk events / Total number of events for each energy-bin.

3 Analysing the 1136 live days data

Before comparing the energy-spectrum of events to a dark matter recoil signal, we need to remove the surface event population using the bulk fraction $\mathcal{R}$ from the previous section. We show values of $\mathcal{R}$ for different energy bins in the left-panel of figure 3.

In order to parameterise the energy-dependence of the bulk fraction, we fit a function $\mathcal{R}(E)$. Since no well-motivated function exists for this quantity we use a cubic spline, whose knots are allowed to vary to give the best possible fit. Three choices of spline are shown in figure 3.

To remove the surface events, we multiply the CoGeNT spectrum by $\mathcal{R}(E)$, leaving only bulk events. We show in the central panel of figure 3 the resulting bulk-only spectrum after using each of these splines, along with an estimate of the bulk background taken from Aalseth et al.[1]. For splines 1 and 3, there is an excess of events above the background estimate, leaving

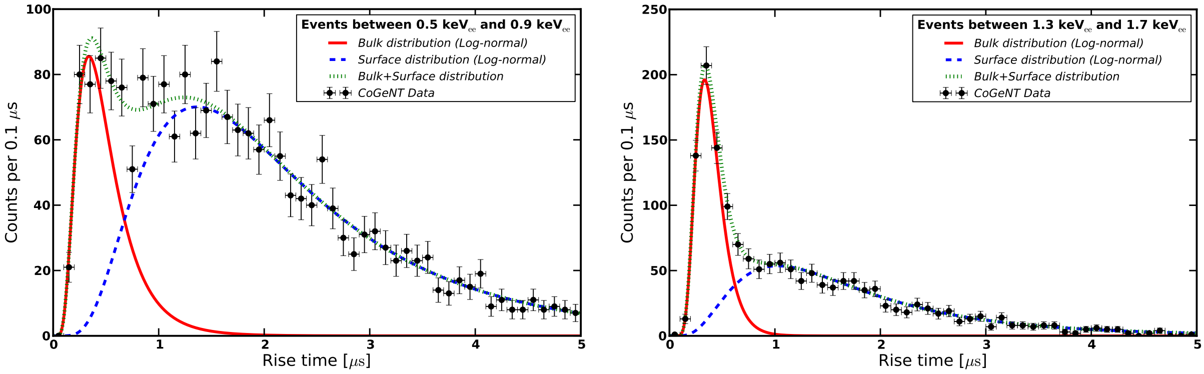

Figure 2 – Log-normal fits to the bulk and surface populations using rise-time data, for two different energy bins.

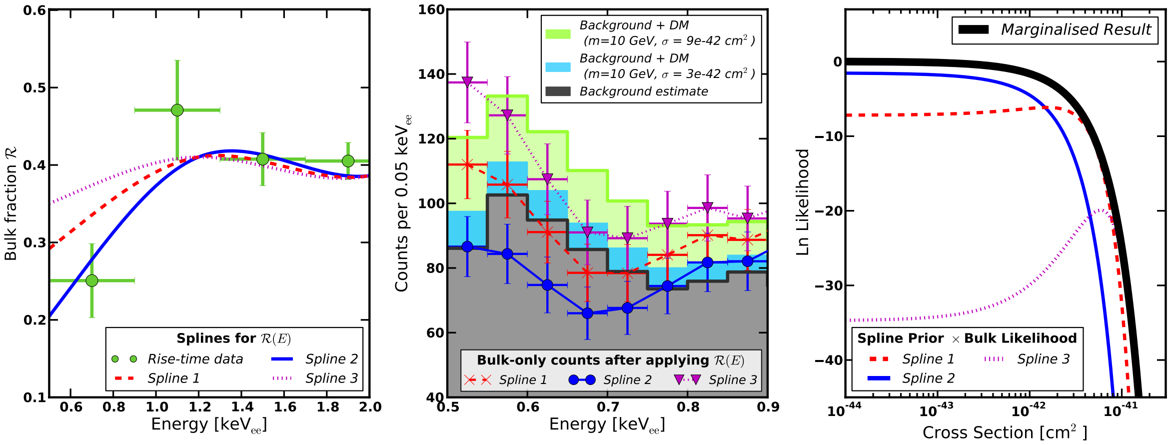

Figure 3 – Analysis of the 1136 live days data for a 10 GeV dark matter recoil signal. We show three different splines for the bulk fraction $\mathcal{R}(E)$, each of which gives a different fit to a dark matter signal. When marginalising over all splines, there is less than 1σ evidence for dark matter in the data.

room for a dark matter recoil signal. However for spline 2 there is no such excess. Hence, the consistency of CoGeNT data with dark matter recoils depends crucially on the choice of $\mathcal{R}(E)$.

This can be seen in the right-panel of figure 3, where we show the likelihood of a dark matter recoil fit (for a mass of 10 GeV) to the bulk-only data as a function of cross section σ, for each spline. This is multiplied also by a prior, which acts as a weighting factor proportional to the likelihood for the spline fit to values of $\mathcal{R}$ in the left-panel. For splines 1 and 3 the likelihood peaks at non-zero values of σ, indicating a best-fit cross section and a positive identification of a dark matter signal. However, spline 2 gives no preferred non-zero value of σ.

To account for this uncertainty in $\mathcal{R}(E)$, we marginalise over all splines. We calculate the marginalised posterior by summing the likelihoods (times the priors for each spline) in the right-panel of figure 3, along with those for splines not shown in this figure. The result is shown as the black solid line, which is essentially flat below $\sigma \sim 10^{-42}$ cm^2. Hence, marginalising over $\mathcal{R}(E)$ has washed-out any dark matter signal, leaving less than 1σ significance.

4 Analysing the 807 live days data

Our findings for the 1136 live days data are in contrast with the CoGeNT 'region of interest' for a light dark matter recoil signal [1]. In order to understand why we disagree, we analyse also the older 807 live days data, used by the collaboration to define this region.

Here we use the values of bulk fraction $\mathcal{R}$ determined directly by the CoGeNT collaboration[1]. The collaboration derived their 'region of interest' for light dark matter by using a one-parameter exponential for $\mathcal{R}(E)$, labelled as 'CoGeNT exponential' in the left-panel of figure 4.

Following the method employed by the CoGeNT collaboration [1], we multiply the CoGeNT spectrum by $\mathcal{R}(E)$ to obtain the bulk-only spectrum. When using the 'CoGeNT exponential' we see in the central panel that the data gives a clear excess of events above the background estimate, consistent with an 8 GeV dark matter recoil signal. This results in a peaked likelihood in the right-panel, indicating a strong preference for light dark matter recoils, and we reproduce exactly the 'region of interest' when using this function for $\mathcal{R}(E)$.

Up until this point, our analysis of the 807 live days data has mirrored that performed by the CoGeNT collaboration in Aalseth et al. [1]. However we consider now two cubic splines as alternative fits to the bulk fraction data, shown in the left panel of figure 4. Both of these fit better to the data than the exponential, and in the absence of any theoretically-motivated function there is no reason to ignore these splines for $\mathcal{R}(E)$. We show in the central panel the result of using these splines instead of the exponential function. In this case the low-energy excess

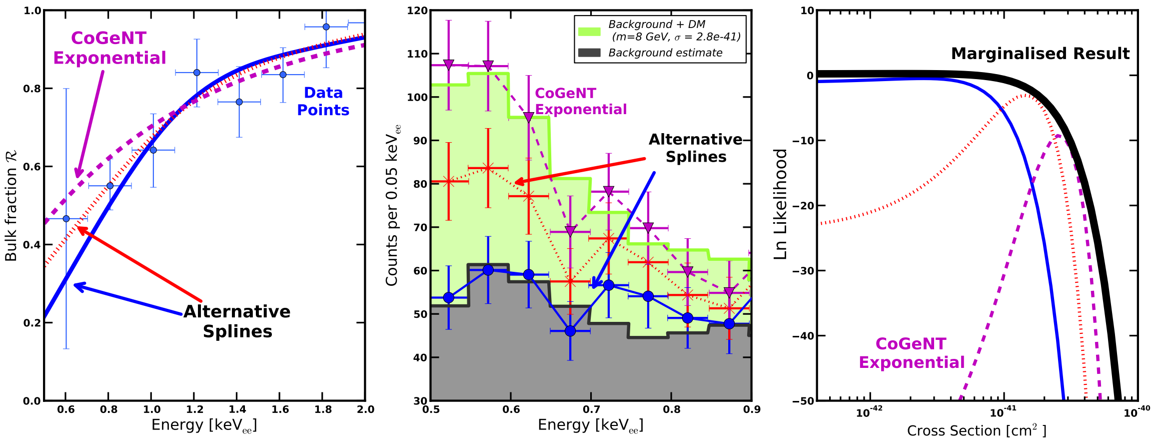

Figure 4 – Analysis of the 807 live days data for 8 GeV dark matter. We show the exponential function used by the CoGeNT collaboration for $\mathcal{R}(E)$, and two alternative cubic splines. Using the exponential, we obtain the same best-fit parameters as CoGeNT. However, the cubic splines are also viable choices for $\mathcal{R}(E)$, but give small or vanishing evidence for a signal. Marginalising over all splines, we find less than 1σ evidence for dark matter.

is either reduced or has vanished. Hence, the likelihoods for these splines in the right-panel show either a smaller preference for light dark matter, or no preference at all above background.

The exponential choice for $\mathcal{R}(E)$ biases the analysis towards a dark matter fit; when accounting for other possible functions using marginalisation the dark matter 'region of interest' vanishes, and we obtain less than 1σ significance as before.

5 Conclusions

We have performed an independent analysis of data from the CoGeNT experiment, for dark matter recoils. In section 2 we separated the surface and bulk populations using the rise-time data. To do so, we followed the collaboration and fit two separate log-normal distributions to this data in discrete energy bins. We used these fits in section 3 to calculate the bulk fraction $\mathcal{R}(E)$, and parameterised its energy-dependence using cubic splines. Marginalising over all splines, we showed that there is less than 1σ evidence for dark matter recoils in the 1136 live days data.

In section 4 we analysed the older 807 live days data, used by the CoGeNT collaboration to define their 'region of interest'. We used their calculated values of the bulk fraction, however we differed in our choice of function for its energy-dependence $\mathcal{R}(E)$: the collaboration employ a one-parameter exponential, while we used a variety of cubic spline fits. From this, we showed that the choice of exponential function biases the analysis towards a dark matter signal.

Acknowledgments

The author acknowledges the STFC for financial support. This work was performed in collaboration with Christopher McCabe and Céline Bœhm.

References

1. C. Aalseth et al. (CoGeNT Collaboration), *Phys. Rev.* D **88**, 012002 (2013).
2. C. Aalseth et al. (CoGeNT Collaboration), arXiv:1401.3295 (2014).
3. Q. Yue et al. (CDEX Collaboration), arXiv:1404.4946 (2014).
4. D. Akerib et al. (LUX Collaboration), *Phys. Rev. Lett.* **112**, 091303 (2014).
5. R. Agnese et al. (SuperCDMS Collaboration), arXiv:1402.7137 (2014).
6. E. Aprile et al. (XENON100 Collaboration), *Phys. Rev. Lett.* **109**, 181301 (2012).
7. Jonathan H. Davis, Christopher McCabe and Céline Bœhm, arXiv:1405.0495 (2014).

6.

Neutrinos & Cosmology

NEUTRINO MASSES

CARLO GIUNTI
INFN, Sezione di Torino, Via P. Giuria 1, I–10125 Torino, Italy

We review the status of three-neutrino mixing and the results of global analyses of short-baseline neutrino oscillation data in 3+1, 3+2 and 3+1+1 neutrino mixing schemes.

1 Introduction

Neutrino oscillations have been measured with high accuracy in solar, atmospheric and long-baseline neutrino oscillation experiments. Hence, we know without doubt that neutrinos are massive and mixed particles (see Ref. [1]). In this short review we discuss the status of the standard three-neutrino mixing paradigm (Section 2) and the indications in favor of the existence of additional sterile neutrinos given by anomalies found in some short-baseline neutrino oscillation experiments (Section 3).

2 Three-Neutrino Mixing

Solar neutrino experiments (Homestake, GALLEX/GNO, SAGE, Super-Kamiokande, SNO, Borexino) measured $\nu_e \to \nu_\mu, \nu_\tau$ oscillations generated by the solar squared-mass difference $\Delta m^2_{\text{SOL}} \simeq 7 \times 10^{-5}\,\text{eV}^2$ and a mixing angle $\sin^2\vartheta_{\text{SOL}} \simeq 0.3$. The KamLAND experiment confirmed these oscillations by observing the disappearance of reactor $\bar{\nu}_e$ with average energy $\langle E \rangle \simeq 4\,\text{MeV}$ at the average distance $\langle L \rangle \simeq 180\,\text{km}$.

Atmospheric neutrino experiments (Kamiokande, IMB, Super-Kamiokande, Soudan-2, MACRO, MINOS) measured ν_μ and $\bar{\nu}_\mu$ disappearance through oscillations generated by the atmospheric squared-mass difference $\Delta m^2_{\text{ATM}} \simeq 2.3 \times 10^{-3}\,\text{eV}^2$ and a mixing angle $\sin^2\vartheta_{\text{ATM}} \simeq 0.5$. The K2K and MINOS long-baseline experiments confirmed these oscillations by observing the disappearance of accelerator ν_μ with $\langle E \rangle \simeq 1.3\,\text{GeV}$ and $3\,\text{GeV}$ at distances $L \simeq 250\,\text{km}$ and $730\,\text{km}$, respectively.

The Super-Kamiokande atmospheric neutrino data indicate that the disappearance of $\overset{(-)}{\nu}_\mu$ is likely due to $\overset{(-)}{\nu}_\mu \to \overset{(-)}{\nu}_\tau$ transitions with a statistical significance of 3.8σ [2]. This oscillation channel is confirmed at 3.4σ by the observation of three $\nu_\mu \to \nu_\tau$ events in the OPERA long-baseline accelerator experiment [3] in which the detector was exposed to the CNGS (CERN–Gran Sasso) beam with $\langle E \rangle \simeq 13\,\text{GeV}$ at $L \simeq 730\,\text{km}$.

The two independent solar and atmospheric Δm^2's are nicely accommodated in the standard framework of three-neutrino mixing in which the left-handed components of the three active flavor neutrino fields ν_e, ν_μ, ν_τ are superpositions of three massive neutrino fields ν_1, ν_2, ν_3 with masses m_1, m_2, m_3: $\nu_{\alpha L} = \sum_{k=1}^{3} U_{\alpha k} \nu_{kL}$, for $\alpha = e, \mu, \tau$. The unitary mixing matrix can be written in the standard parameterization in terms of three mixing angles ϑ_{12}, ϑ_{23}, ϑ_{13} and a

parameter	s.t.	b.f.	1σ range	2σ range	3σ range	r.u.
$\Delta m^2_{\mathrm{S}}/10^{-5}\,\mathrm{eV}^2$		7.54	7.32 – 7.80	7.15 – 8.00	6.99 – 8.18	3%
$\sin^2\vartheta_{12}/10^{-1}$		3.08	2.91 – 3.25	2.75 – 3.42	2.59 – 3.59	5%
$\Delta m^2_{\mathrm{A}}/10^{-3}\,\mathrm{eV}^2$	NS	2.44	2.38 – 2.52	2.30 – 2.59	2.22 – 2.66	3%
	IS	2.40	2.33 – 2.47	2.25 – 2.54	2.17 – 2.61	3%
$\sin^2\vartheta_{23}/10^{-1}$	NS	4.25	3.98 – 4.54	3.76 – 5.06	3.57 – 6.41	11%
	IS	4.37	4.08 – 6.10	3.84 – 6.37	3.63 – 6.59	11%
$\sin^2\vartheta_{13}/10^{-2}$	NS	2.34	2.16 – 2.56	1.97 – 2.76	1.77 – 2.97	9%
	IS	2.39	2.18 – 2.60	1.98 – 2.80	1.78 – 3.00	9%

Table 1: Best fit (b.f.) values of the neutrino mixing parameters obtained in the global analysis of neutrino oscillation data presented in Ref. [11] in the framework of three-neutrino mixing with the two spectrum types (s.t.): normal spectrum (NS) and inverted spectrum (IS). The relative uncertainty (r.u.) has been obtained from the 3σ range divided by 6.

CP-violating phase[a] δ:

$$U = \begin{pmatrix} c_{12}c_{13} & s_{12}c_{13} & s_{13}e^{-i\delta} \\ -s_{12}c_{23} - c_{12}s_{23}s_{13}e^{i\delta} & c_{12}c_{23} - s_{12}s_{23}s_{13}e^{i\delta} & s_{23}c_{13} \\ s_{12}s_{23} - c_{12}c_{23}s_{13}e^{i\delta} & -c_{12}s_{23} - s_{12}c_{23}s_{13}e^{i\delta} & c_{23}c_{13} \end{pmatrix} , \tag{1}$$

where $c_{ab} \equiv \cos\vartheta_{ab}$ and $s_{ab} \equiv \sin\vartheta_{ab}$. It is convenient to choose the numbers of the massive neutrinos in order to have

$$\Delta m^2_{\mathrm{SOL}} = \Delta m^2_{21} \ll \Delta m^2_{\mathrm{ATM}} = \frac{1}{2}\left|\Delta m^2_{31} + \Delta m^2_{32}\right| , \tag{2}$$

with $\Delta m^2_{kj} = m^2_k - m^2_j$. Then, there are two possible hierarchies for the neutrino masses: the normal hierarchy (NH) with $m_1 < m_2 < m_3$ and the inverted hierarchy (IH) with $m_3 < m_1 < m_2$.

With the conventions in Eqs. (1) and (2), we have $\vartheta_{\mathrm{SOL}} = \vartheta_{12}$ and $\vartheta_{\mathrm{ATM}} = \vartheta_{23}$. Moreover, the mixing angle ϑ_{13} generates $\overset{(-)}{\nu}_e$ disappearance and $\overset{(-)}{\nu}_\mu \to \overset{(-)}{\nu}_e$ transitions driven by $\Delta m^2_{\mathrm{ATM}}$, which can be observed in long-baseline neutrino oscillation experiments.

In 2011 the T2K experiment reported the first indication of long-baseline $\nu_\mu \to \nu_e$ transitions [4], followed by the MINOS experiment [5]. Recently, the T2K Collaboration reported a convincing 7.5σ observation of $\nu_\mu \to \nu_e$ transitions through the measurement of 28 ν_e events with an expected background of 4.92 ± 0.55 events [6].

The most precise measurement of the value of ϑ_{13} comes from the measurement of $\bar{\nu}_e$ disappearance in the Daya Bay reactor experiment: $\sin^2 2\vartheta_{13} = 0.090^{+0.008}_{-0.009}$ [7]. This result has been confirmed by the data of the RENO [8] and Double Chooz [9] reactor experiments. Hence, we have a robust evidence of a non-zero value of ϑ_{13}. It is very important, because it opens promising perspectives for the observation of CP violation in the lepton sector and matter effects in long-baseline oscillation experiments, which could allow to distinguish the normal and inverted neutrino mass spectra. (see Ref. [10]).

The three-neutrino mixing parameters can be determined with good precision with a global fit of neutrino oscillation data. In Tab. 1 we report the results of the latest global fit presented in Ref. [11]. One can see that all the oscillation parameters are determined with precision between about 3% and 11%. The largest uncertainty is that of ϑ_{23}, which is known to be close to maximal ($\pi/4$), but it is not known if it is smaller or larger than $\pi/4$. For the Dirac CP-violating phase δ, there is an indication in favor of $\delta \approx 3\pi/2$, which would give maximal CP violation, but at 3σ all the values of δ are allowed, including the CP-conserving values $\delta = 0, \pi$.

---

[a] For simplicity, we do not consider the two Majorana CP-violating phases which contribute to neutrino mixing if massive neutrinos are Majorana particles, because they do not affect neutrino oscillations (see Ref. [1]).

3 Beyond Three-Neutrino Mixing: Sterile Neutrinos

The completeness of the three-neutrino mixing paradigm has been challenged by the following indications in favor of short-baseline neutrino oscillations, which require the existence of at least one additional squared-mass difference, Δm^2_{SBL}, which is much larger than Δm^2_{SOL} and Δm^2_{ATM}:

1. The reactor antineutrino anomaly [12], which is a deficit of the rate of $\bar{\nu}_e$ observed in several short-baseline reactor neutrino experiments in comparison with that expected from a new calculation of the reactor neutrino fluxes [13,14]. The statistical significance is about 2.8σ.

2. The Gallium neutrino anomaly [15–19], consisting in a short-baseline disappearance of ν_e measured in the Gallium radioactive source experiments GALLEX [20] and SAGE [21] with a statistical significance of about 2.9σ.

3. The LSND experiment, in which a signal of short-baseline $\bar{\nu}_\mu \to \bar{\nu}_e$ oscillations has been observed with a statistical significance of about 3.8σ [22].

In this review, we consider 3+1, 3+2, and 3+1+1 neutrino mixing schemes in which there are one or two additional massive neutrinos at the eV scale and the masses of the three standard massive neutrinos are much smaller (see Ref. [23–27]). Since from the LEP measurement of the invisible width of the Z boson we know that there are only three active neutrinos (see Ref. [1]), in the flavor basis the additional massive neutrinos correspond to sterile neutrinos, which do not have standard weak interactions.

The possible existence of sterile neutrinos is very interesting, because they are new particles which could give us precious information on the physics beyond the Standard Model. The existence of light sterile neutrinos is also very important for astrophysics (see Ref. [28]) and cosmology. (see Ref. [29]).

In the 3+1 scheme, the effective probability of $\overset{(-)}{\nu}_\alpha \to \overset{(-)}{\nu}_\beta$ transitions in short-baseline experiments has the two-neutrino-like form

$$P_{\overset{(-)}{\nu}_\alpha \to \overset{(-)}{\nu}_\beta} = \delta_{\alpha\beta} - 4|U_{\alpha4}|^2 \left(\delta_{\alpha\beta} - |U_{\beta4}|^2\right) \sin^2\left(\frac{\Delta m^2_{41} L}{4E}\right) , \tag{3}$$

where U is the mixing matrix, L is the source-detector distance, E is the neutrino energy and $\Delta m^2_{41} = m^2_4 - m^2_1 = \Delta m^2_{\text{SBL}} \sim 1\,\text{eV}^2$. The electron and muon neutrino and antineutrino appearance and disappearance in short-baseline experiments depend on $|U_{e4}|^2$ and $|U_{\mu4}|^2$, which determine the amplitude $\sin^2 2\vartheta_{e\mu} = 4|U_{e4}|^2|U_{\mu4}|^2$ of $\overset{(-)}{\nu}_\mu \to \overset{(-)}{\nu}_e$ transitions, the amplitude $\sin^2 2\vartheta_{ee} = 4|U_{e4}|^2 \left(1 - |U_{e4}|^2\right)$ of $\overset{(-)}{\nu}_e$ disappearance, and the amplitude $\sin^2 2\vartheta_{\mu\mu} = 4|U_{\mu4}|^2 \left(1 - |U_{\mu4}|^2\right)$ of $\overset{(-)}{\nu}_\mu$ disappearance.

Since the oscillation probabilities of neutrinos and antineutrinos are related by a complex conjugation of the elements of the mixing matrix (see Ref. [1]), the effective probabilities of short-baseline $\nu_\mu \to \nu_e$ and $\bar{\nu}_\mu \to \bar{\nu}_e$ transitions are equal. Hence, the 3+1 scheme cannot explain a possible CP-violating difference of $\nu_\mu \to \nu_e$ and $\bar{\nu}_\mu \to \bar{\nu}_e$ transitions in short-baseline experiments. In order to allow this possibility, one must consider a 3+2 scheme, in which, there are four additional effective mixing parameters in short-baseline experiments: $\Delta m^2_{51} \geq \Delta m^2_{41}$, $|U_{e5}|^2$, $|U_{\mu5}|^2$ and $\eta = \arg\left[U^*_{e4} U_{\mu4} U_{e5} U^*_{\mu5}\right]$ (see Ref. [23, 25–27]). Since this complex phase appears with different signs in the effective 3+2 probabilities of short-baseline $\nu_\mu \to \nu_e$ and $\bar{\nu}_\mu \to \bar{\nu}_e$ transitions, it can generate measurable CP violations.

A puzzling feature of the 3+2 scheme is that it needs the existence of two sterile neutrinos with masses at the eV scale. We think that it may be considered as more plausible that sterile neutrinos have a hierarchy of masses. Hence, it is interesting to consider also the 3+1+1 scheme [24], in which m_5 is much heavier than 1 eV and the oscillations due to Δm^2_{51} are averaged.

	3+1 LOW	3+1 HIG	3+1 noMB	3+1 noLSND	3+2 LOW	3+2 HIG	3+1+1 LOW	3+1+1 HIG
χ^2_{min}	291.7	261.8	236.1	278.4	284.4	256.4	289.8	259.0
NDF	256	250	218	252	252	246	253	247
GoF	6%	29%	19%	12%	8%	31%	6%	29%
$(\chi^2_{\text{min}})_{\text{APP}}$	99.3	77.0	50.9	91.8	87.7	69.8	94.8	75.5
$(\chi^2_{\text{min}})_{\text{DIS}}$	180.1	180.1	180.1	180.1	179.1	179.1	180.1	180.1
$\Delta\chi^2_{\text{PG}}$	12.7	4.8	5.1	6.4	17.7	7.5	14.9	3.4
NDF_{PG}	2	2	2	2	4	4	3	3
GoF_{PG}	0.2%	9%	8%	4%	0.1%	11%	0.2%	34%
$\Delta\chi^2_{\text{NO}}$	47.5	46.2	47.1	8.3	54.8	51.6	49.4	49.1
NDF_{NO}	3	3	3	3	7	7	6	6
$n\sigma_{\text{NO}}$	6.3σ	6.2σ	6.3σ	2.1σ	6.0σ	5.8σ	5.8σ	5.8σ

Table 2: Results of the fit of short-baseline data [27] taking into account all MiniBooNE data (LOW), only the MiniBooNE data above 475 MeV (HIG), without MiniBooNE data (noMB) and without LSND data (noLSND) in the 3+1, 3+2 and 3+1+1 schemes. The first three lines give the minimum χ^2 (χ^2_{min}), the number of degrees of freedom (NDF) and the goodness-of-fit (GoF). The following five lines give the quantities relevant for the appearance-disappearance (APP-DIS) parameter goodness-of-fit (PG) [48]. The last three lines give the difference between the χ^2 without short-baseline oscillations and χ^2_{min} ($\Delta\chi^2_{\text{NO}}$), the corresponding difference of number of degrees of freedom (NDF_{NO}) and the resulting number of σ's ($n\sigma_{\text{NO}}$) for which the absence of oscillations is disfavored.

Hence, in the analysis of short-baseline data in the 3+1+1 scheme there is one effective parameter less than in the 3+2 scheme (Δm^2_{51}), but CP violations generated by η are observable.

Global fits of short-baseline neutrino oscillation data have been presented recently in Ref. [26, 27]. These analyses take into account the final results of the MiniBooNE experiment, which was made in order to check the LSND signal with about one order of magnitude larger distance (L) and energy (E), but the same order of magnitude for the ratio L/E from which neutrino oscillations depend. Unfortunately, the results of the MiniBooNE experiment are ambiguous, because the LSND signal was not seen in neutrino mode [30] and the signal observed in 2010 [31] with the first half of the antineutrino data was not observed in the second half of the data [32]. Moreover, the MiniBooNE data in both neutrino and antineutrino modes show an excess in the low-energy bins which is widely considered to be anomalous because it is at odds with neutrino oscillations [33, 34][b].

In the following we summarize the results of the analysis of short-baseline data presented in Ref. [27] of the following three groups of experiments:

(A) The $\overset{(-)}{\nu}_{\mu} \to \overset{(-)}{\nu}_{e}$ appearance data of the LSND [22], MiniBooNE [32], BNL-E776 [37], KARMEN [38], NOMAD [39], ICARUS [40] and OPERA [41] experiments.

(B) The $\overset{(-)}{\nu}_{e}$ disappearance data described in Ref. [19], which take into account the reactor [12–14] and Gallium [15–18, 42] anomalies.

(C) The constraints on $\overset{(-)}{\nu}_{\mu}$ disappearance obtained from the data of the CDHSW experiment [43], from the analysis [44] of the data of atmospheric neutrino oscillation experiments, from the analysis [33] of the MINOS neutral-current data [45] and from the analysis of the SciBooNE-MiniBooNE neutrino [46] and antineutrino [47] data.

Table 2 summarizes the statistical results obtained in Ref. [27] from global fits of the data above in the 3+1, 3+2 and 3+1+1 schemes. In the LOW fits all the MiniBooNE data are

---

[b] The interesting possibility of reconciling the low–energy anomalous data with neutrino oscillations through energy reconstruction effects proposed in Ref. [35, 36] still needs a detailed study.

considered, including the anomalous low-energy bins, which are omitted in the HIG fits. There is also a 3+1-noMB fit without MiniBooNE data and a 3+1-noLSND fit without LSND data.

From Tab. 2, one can see that in all fits which include the LSND data the absence of short-baseline oscillations is disfavored by about 6σ, because the improvement of the χ^2 with short-baseline oscillations is much larger than the number of oscillation parameters.

In all the 3+1, 3+2 and 3+1+1 schemes the goodness-of-fit in the LOW analysis is significantly worse than that in the HIG analysis and the appearance-disappearance parameter goodness-of-fit is much worse. This result confirms the fact that the MiniBooNE low-energy anomaly is incompatible with neutrino oscillations, because it would require a small value of Δm^2_{41} and a large value of $\sin^2 2\vartheta_{e\mu}$ [33,34], which are excluded by the data of other experiments (see Ref. [27] for further details)[c]. Note that the appearance-disappearance tension in the 3+2-LOW fit is even worse than that in the 3+1-LOW fit, since the $\Delta\chi^2_{\mathrm{PG}}$ is so much larger that it cannot be compensated by the additional degrees of freedom (this behavior has been explained in Ref. [49]). Therefore, we think that it is very likely that the MiniBooNE low-energy anomaly has an explanation which is different from neutrino oscillations and the HIG fits are more reliable than the LOW fits.

The 3+2 mixing scheme, was considered to be interesting in 2010 when the MiniBooNE neutrino [30] and antineutrino [31] data showed a CP-violating tension. Unfortunately, this tension reduced considerably in the final MiniBooNE data [32] and from Tab. 2 one can see that there is little improvement of the 3+2-HIG fit with respect to the 3+1-HIG fit, in spite of the four additional parameters and the additional possibility of CP violation. Moreover, since the p-value obtained by restricting the 3+2 scheme to 3+1 disfavors the 3+1 scheme only at 1.2σ [27], we think that considering the larger complexity of the 3+2 scheme is not justified by the data[d].

The results of the 3+1+1-HIG fit presented in Tab. 2 show that the appearance-disappearance parameter goodness-of-fit is remarkably good, with a $\Delta\chi^2_{\mathrm{PG}}$ that is smaller than those in the 3+1-HIG and 3+2-HIG fits. However, the χ^2_{min} in the 3+1+1-HIG is only slightly smaller than that in the 3+1-HIG fit and the p-value obtained by restricting the 3+1+1 scheme to 3+1 disfavors the 3+1 scheme only at 0.8σ [27]. Therefore, there is no compelling reason to prefer the more complex 3+1+1 to the simpler 3+1 scheme.

Figure 1 shows the allowed regions in the $\sin^2 2\vartheta_{e\mu}$–Δm^2_{41}, $\sin^2 2\vartheta_{ee}$–Δm^2_{41} and $\sin^2 2\vartheta_{\mu\mu}$–$\Delta m^2_{41}$ planes obtained in the 3+1-HIG fit of Ref. [27]. These regions are relevant, respectively, for $\overset{(-)}{\nu}_{\mu} \to \overset{(-)}{\nu}_{e}$ appearance, $\overset{(-)}{\nu}_{e}$ disappearance and $\overset{(-)}{\nu}_{\mu}$ disappearance searches. The corresponding marginal allowed intervals of the oscillation parameters are given in Tab. 3. Figure 1 shows also the region allowed by $\overset{(-)}{\nu}_{\mu} \to \overset{(-)}{\nu}_{e}$ appearance data and the constraints from $\overset{(-)}{\nu}_{e}$ disappearance and $\overset{(-)}{\nu}_{\mu}$ disappearance data. One can see that the combined disappearance constraint in the $\sin^2 2\vartheta_{e\mu}$–Δm^2_{41} plane excludes a large part of the region allowed by $\overset{(-)}{\nu}_{\mu} \to \overset{(-)}{\nu}_{e}$ appearance data, leading to the well-known appearance-disappearance tension [25, 26, 33, 34, 49–52] quantified by the parameter goodness-of-fit in Tab. 2.

It is interesting to investigate what is the impact of the MiniBooNE experiment on the global analysis of short-baseline neutrino oscillation data. With this aim, the authors of Ref. [27] performed two additional 3+1 fits: a 3+1-noMB fit without MiniBooNE data and a 3+1-noLSND fit without LSND data. From Tab. 2 one can see that the results of the 3+1-noMB fit are similar to those of the 3+1-HIG fit and the exclusion of the case of no-oscillations remains at the level of 6σ. On the other hand, in the 3+1-noLSND fit, without LSND data, the exclusion of the case of no-oscillations drops dramatically to 2.1σ. In fact, in this case the main indication in favor of short-baseline oscillations is given by the reactor and Gallium anomalies which have a

---

[c] One could fit the three anomalous MiniBooNE low-energy bins in a 3+2 scheme [25] by considering the appearance data without the ICARUS [40] and OPERA [41] constraints, but the corresponding relatively large transition probabilities are excluded by the disappearance data.

[d] See however the somewhat different conclusions reached in Ref. [26].

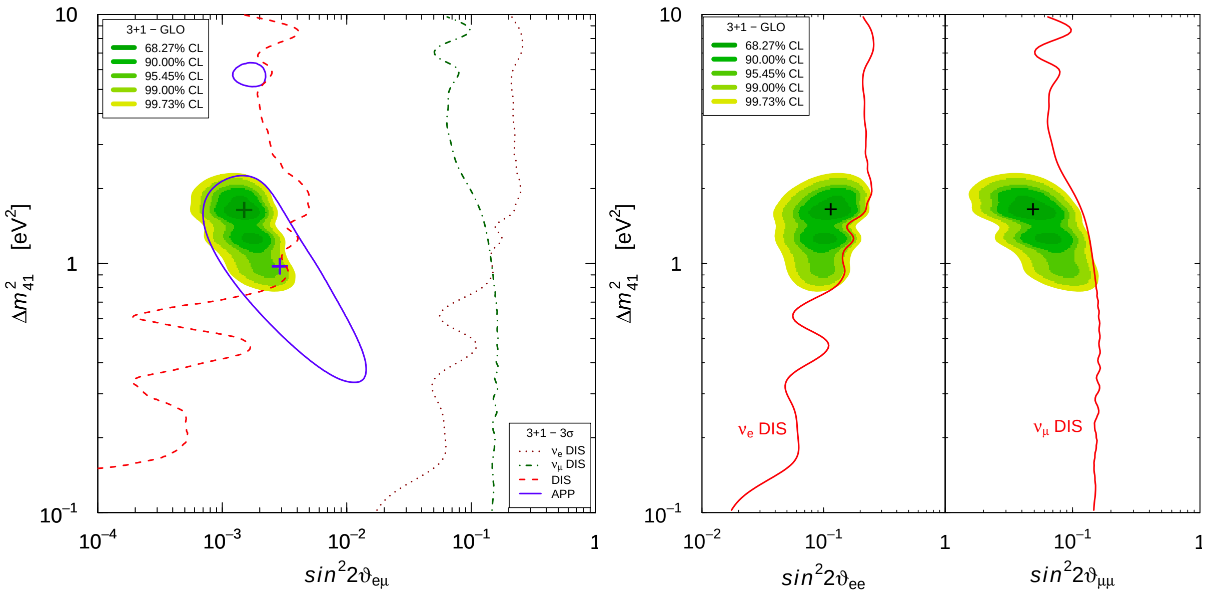

Figure 1 – Allowed regions in the $\sin^2 2\vartheta_{e\mu}$–Δm^2_{41}, $\sin^2 2\vartheta_{ee}$–Δm^2_{41} and $\sin^2 2\vartheta_{\mu\mu}$–$\Delta m^2_{41}$ planes obtained in the global (GLO) 3+1-HIG fit [27] of short-baseline neutrino oscillation data compared with the 3σ allowed regions obtained from $\overset{(-)}{\nu}_\mu \to \overset{(-)}{\nu}_e$ short-baseline appearance data (APP) and the 3σ constraints obtained from $\overset{(-)}{\nu}_e$ short-baseline disappearance data (ν_e DIS), $\overset{(-)}{\nu}_\mu$ short-baseline disappearance data (ν_μ DIS) and the combined short-baseline disappearance data (DIS). The best-fit points of the GLO and APP fits are indicated by crosses.

CL	Δm^2_{41}[eV^2]	$\sin^2 2\vartheta_{e\mu}$	$\sin^2 2\vartheta_{ee}$	$\sin^2 2\vartheta_{\mu\mu}$
68.27%	1.55 − 1.72	0.0012 − 0.0018	0.089 − 0.15	0.036 − 0.065
90.00%	1.19 − 1.91	0.001 − 0.0022	0.072 − 0.17	0.03 − 0.085
95.00%	1.15 − 1.97	0.00093 − 0.0023	0.066 − 0.18	0.028 − 0.095
95.45%	1.14 − 1.97	0.00091 − 0.0024	0.065 − 0.18	0.027 − 0.095
99.00%	0.87 − 2.09	0.00078 − 0.003	0.054 − 0.2	0.022 − 0.12
99.73%	0.82 − 2.19	0.00066 − 0.0034	0.047 − 0.22	0.019 − 0.14

Table 3: Marginal allowed intervals of the oscillation parameters obtained in the global 3+1-HIG fit of short-baseline neutrino oscillation data [27].

similar statistical significance (see Section 1). Therefore, it is clear that the LSND experiment is still crucial for the indication in favor of short-baseline $\bar{\nu}_\mu \to \bar{\nu}_e$ transitions and the MiniBooNE experiment has been rather inconclusive.

In conclusion, the results of the global fit of short-baseline neutrino oscillation data presented in Ref. [27] show that the data can be explained by 3+1 neutrino mixing and this simplest scheme beyond three-neutrino mixing cannot be rejected in favor of the more complex 3+2 and 3+1+1 schemes. The low-energy MiniBooNE anomaly cannot be explained by neutrino oscillations in any of these schemes. Moreover, the crucial indication in favor of short-baseline $\bar{\nu}_\mu \to \bar{\nu}_e$ appearance is still given by the old LSND data and the MiniBooNE experiment has been inconclusive. Hence new better experiments are needed in order to check this signal.

References

1. C. Giunti and C. W. Kim. *Fundamentals of Neutrino Physics and Astrophysics*. Oxford University Press, Oxford, UK, 2007. ISBN 978-0-19-850871-7.
2. K. Abe et al. A Measurement of the Appearance of Atmospheric Tau Neutrinos by Super-Kamiokande. *Phys.Rev.Lett.*, 110:181802, 2013.
3. N. Agafonova et al. Evidence for $\nu_\mu \to \nu_\tau$ appearance in the CNGS neutrino beam with

the OPERA experiment.

4. K. Abe et al. Indication of Electron Neutrino Appearance from an Accelerator-produced Off-axis Muon Neutrino Beam. *Phys. Rev. Lett.*, 107:041801, 2011.
5. P. Adamson et al. Improved search for muon-neutrino to electron-neutrino oscillations in MINOS. *Phys. Rev. Lett.*, 107:181802, 2011.
6. K. Abe et al. Observation of Electron Neutrino Appearance in a Muon Neutrino Beam. *Phys.Rev.Lett.*, 112:061802, 2014.
7. F.P. An et al. Spectral measurement of electron antineutrino oscillation amplitude and frequency at Daya Bay. *Phys.Rev.Lett.*, 112:061801, 2014.
8. Soo-Bong Kim et al. Observation of Reactor Electron Antineutrino Disappearance in the RENO Experiment. *Phys. Rev. Lett.*, 108:191802, 2012.
9. Y. Abe et al. First Measurement of θ_{13} from Delayed Neutron Capture on Hydrogen in the Double Chooz Experiment. *Phys.Lett.*, B723:66–70, 2013.
10. Mauro Mezzetto and Thomas Schwetz. ϑ_{13}: phenomenology, present status and prospect. *J. Phys.*, G37:103001, 2010.
11. F. Capozzi et al. Status of three-neutrino oscillation parameters, circa 2013.
12. G. Mention et al. The Reactor Antineutrino Anomaly. *Phys. Rev.*, D83:073006, 2011.
13. Th. A. Mueller et al. Improved Predictions of Reactor Antineutrino Spectra. *Phys. Rev.*, C83:054615, 2011.
14. Patrick Huber. On the determination of anti-neutrino spectra from nuclear reactors. *Phys. Rev.*, C84:024617, 2011.
15. J. N. Abdurashitov et al. Measurement of the response of a Ga solar neutrino experiment to neutrinos from an Ar-37 source. *Phys. Rev.*, C73:045805, 2006.
16. Marco Laveder. Unbound neutrino roadmaps. *Nucl. Phys. Proc. Suppl.*, 168:344–346, 2007. Workshop on Neutrino Oscillation Physics (NOW 2006), Otranto, Lecce, Italy, 9-16 Sep 2006.
17. Carlo Giunti and Marco Laveder. Short-Baseline Active-Sterile Neutrino Oscillations? *Mod. Phys. Lett.*, A22:2499–2509, 2007.
18. Carlo Giunti and Marco Laveder. Statistical Significance of the Gallium Anomaly. *Phys. Rev.*, C83:065504, 2011.
19. C. Giunti, M. Laveder, Y.F. Li, Q.Y. Liu, and H.W. Long. Update of Short-Baseline Electron Neutrino and Antineutrino Disappearance. *Phys. Rev.*, D86:113014, 2012.
20. F. Kaether, W. Hampel, G. Heusser, J. Kiko, and T. Kirsten. Reanalysis of the GALLEX solar neutrino flux and source experiments. *Phys. Lett.*, B685:47–54, 2010.
21. J. N. Abdurashitov et al. Measurement of the solar neutrino capture rate with Gallium metal, Part III. *Phys. Rev.*, C80:015807, 2009.
22. A. Aguilar et al. Evidence for neutrino oscillations from the observation of $\bar{\nu}_e$ appearance in a $\bar{\nu}_\mu$ beam. *Phys. Rev.*, D64:112007, 2001.
23. Michel Sorel, Janet Conrad, and Michael Shaevitz. A combined analysis of short-baseline neutrino experiments in the (3+1) and (3+2) sterile neutrino oscillation hypotheses. *Phys. Rev.*, D70:073004, 2004.
24. Ann E Nelson. Effects of CP Violation from Neutral Heavy Fermions on Neutrino Oscillations, and the LSND/MiniBooNE Anomalies. *Phys. Rev.*, D84:053001, 2011.
25. J.M. Conrad, C.M. Ignarra, G. Karagiorgi, M.H. Shaevitz, and J. Spitz. Sterile Neutrino Fits to Short Baseline Neutrino Oscillation Measurements. *Adv.High Energy Phys.*, 2013:163897, 2013.
26. Joachim Kopp, Pedro A. N. Machado, Michele Maltoni, and Thomas Schwetz. Sterile Neutrino Oscillations: The Global Picture. *JHEP*, 1305:050, 2013.
27. C. Giunti, M. Laveder, Y.F. Li, and H.W. Long. A Pragmatic View of Short-Baseline Neutrino Oscillations. *Phys.Rev.*, D88:073008, 2013.
28. Antonaldo Diaferio and Garry W. Angus. The Acceleration Scale, Modified Newtonian

Dynamics, and Sterile Neutrinos.

29. Maria Archidiacono, Elena Giusarma, Steen Hannestad, and Olga Mena. Cosmic dark radiation and neutrinos. *Adv.High Energy Phys.*, 2013:191047, 2013.
30. A. A. Aguilar-Arevalo et al. Unexplained Excess of Electron-Like Events From a 1-GeV Neutrino Beam. *Phys. Rev. Lett.*, 102:101802, 2009.
31. A. A. Aguilar-Arevalo et al. Observed Event Excess in the MiniBooNE Search for $\bar{\nu}_\mu \to \bar{\nu}_e$ Oscillations. *Phys. Rev. Lett.*, 105:181801, 2010.
32. A.A. Aguilar-Arevalo et al. Improved Search for $\bar{\nu}_\mu \to \bar{\nu}_e$ Oscillations in the MiniBooNE Experiment. *Phys.Rev.Lett.*, 110:161801, 2013.
33. Carlo Giunti and Marco Laveder. Status of 3+1 Neutrino Mixing. *Phys.Rev.*, D84:093006, 2011.
34. Carlo Giunti and Marco Laveder. Implications of 3+1 Short-Baseline Neutrino Oscillations. *Phys. Lett.*, B706:200–207, 2011.
35. M. Martini, M. Ericson, and G. Chanfray. Neutrino energy reconstruction problems and neutrino oscillations. *Phys. Rev.*, D85:093012, 2012.
36. M. Martini, M. Ericson, and G. Chanfray. Energy reconstruction effects in neutrino oscillation experiments and implications for the analysis. *Phys. Rev.*, D87:013009, 2013.
37. L. Borodovsky et al. Search for muon-neutrino oscillations $\nu_\mu \to \nu_e$ $(\bar{\nu}_\mu \to \bar{\mu}_e)$ in a wide band neutrino beam. *Phys. Rev. Lett.*, 68:274–277, 1992.
38. B. Armbruster et al. Upper limits for neutrino oscillations $\bar{\nu}_\mu \to \bar{\nu}_e$ from muon decay at rest. *Phys. Rev.*, D65:112001, 2002.
39. P. Astier et al. Search for $\nu_\mu \to \nu_e$ Oscillations in the NOMAD Experiment. *Phys. Lett.*, B570:19–31, 2003.
40. M. Antonello et al. Search for anomalies in the ν_e appearance from a ν_μ beam. *Eur.Phys.J.*, C73:2599, 2013.
41. N. Agafonova et al. Search for $\nu_\mu \to \nu_e$ oscillations with the OPERA experiment in the CNGS beam. *JHEP*, 1307:004, 2013.
42. Mario A. Acero, Carlo Giunti, and Marco Laveder. Limits on ν_e and $\bar{\nu}_e$ disappearance from Gallium and reactor experiments. *Phys. Rev.*, D78:073009, 2008.
43. F. Dydak et al. A search for ν_μ oscillations in the Δm^2 range $0.3 - 90\,\mathrm{eV}^2$. *Phys. Lett.*, B134:281, 1984.
44. Michele Maltoni and Thomas Schwetz. Sterile neutrino oscillations after first MiniBooNE results. *Phys. Rev.*, D76:093005, 2007.
45. P. Adamson et al. Active to sterile neutrino mixing limits from neutral-current interactions in MINOS. *Phys. Rev. Lett.*, 107:011802, 2011.
46. K. B. M. Mahn et al. Dual baseline search for muon neutrino disappearance at $0.5 < \Delta m^2 < 40\,\mathrm{eV}^2$. *Phys. Rev.*, D85:032007, 2012.
47. G. Cheng et al. Dual baseline search for muon antineutrino disappearance at $0.1\mathrm{eV}^2 < \Delta m^2 < 100\mathrm{eV}^2$. *Phys. Rev.*, D86:052009, 2012.
48. M. Maltoni and T. Schwetz. Testing the statistical compatibility of independent data sets. *Phys. Rev.*, D68:033020, 2003.
49. Maria Archidiacono, Nicolao Fornengo, Carlo Giunti, Steen Hannestad, and Alessandro Melchiorri. Sterile Neutrinos: Cosmology vs Short-BaseLine Experiments. *Phys.Rev.*, D87:125034, 2013.
50. Joachim Kopp, Michele Maltoni, and Thomas Schwetz. Are there sterile neutrinos at the eV scale? *Phys. Rev. Lett.*, 107:091801, 2011.
51. Carlo Giunti and Marco Laveder. 3+1 and 3+2 Sterile Neutrino Fits. *Phys.Rev.*, D84:073008, 2011.
52. Maria Archidiacono, Nicolao Fornengo, Carlo Giunti, and Alessandro Melchiorri. Testing 3+1 and 3+2 neutrino mass models with cosmology and short baseline experiments. *Phys. Rev.*, D86:065028, 2012.

RELIC NEUTRINOS, THERMAL AXIONS AND COSMOOGY IN EARLY 2014

E. GIUSARMA
Physics Department and INFN, Università di Roma “La Sapienza”, Ple Aldo Moro 2,
00185, Rome, Italy

We present up to date cosmological bounds on the sum of active neutrino masses as well as on extended cosmological scenarios with additional thermal relics, as thermal axions or sterile neutrino species. Our analyses consider all the current available cosmological data in the beginning of year 2014, including the very recent and most precise Baryon Acoustic Oscillation (BAO) measurements from the Baryon Oscillation Spectroscopic Survey and the recent B-mode polarization measurements made by the BICEP2 experiment.

1 Description

Standard cosmology includes hot thermal relics which refer to the three light, active neutrino flavours of the Standard Model of elementary particles. The largest effect of neutrino masses on the different cosmological observables arises from their free streamig nature: the non-relativistic neutrino overdensities will contribute to clustering only at scales larger than their free streaming scale, suppressing the growth of matter density fluctuations at small scales. CMB measurements from the Planck satellite, including the lensing likelihood, low-ℓ polarization measurements from WMAP 9-year data and Baryon Acoustic Oscillation (BAO) measurements from a number of surveys lead to the bound $\sum m_\nu < 0.26$ eV at 95% CL (see recent work of De Putter. [1]).

However, the former bounds are obtained assuming that neutrinos are the only hot thermal relic component in the universe. The existence of extra hot relic components, as sterile neutrino species and/or thermal axions will change the cosmological neutrino mass constraints. Massless, sterile neutrino-like particles, arise naturally in the context of models which contain a dark radiation sector that decouples from the Standard Model. A canonical example are asymmetric dark matter models, in which the extra radiation degrees of freedom are produced by the annihilations of the thermal dark matter component [2], see also Refs. [3,4] for extended weakly-interacting massive particle models. On the other hand, extra sterile massive, light neutrino species, whose existence is not forbidden by any fundamental symmetry in nature, may help in resolving the so-called neutrino oscillation anomalies [5,6], see also Refs. [7,8,9,10,11] for recent results on the preferred sterile neutrino masses and abundances considering both cosmological and neutrino oscillation constraints. Another candidate is the thermal axion [12], which constitutes the most elegant solution to the strong CP problem, i.e. why CP is a respected symmetry of Quantum Chromodynamics (QCD) despite the existence of a natural, four dimensional, Lorentz and gauge invariant operator which badly violates CP. Both extra, sterile neutrino species and axions have an associated free streaming scale, reducing the growth of matter fluctuations at small scales. These extra species will also contribute to the effective number of relativistic degrees of freedom $N_{\rm eff}$, being $N_{\rm eff} = 3.046$ the standard value, corresponding to the three active neutrino contribution. The existence of extra light species at the Big Bang Nucleosynthesis (BBN) epoch modifies the light element abundances, especially the primordial helium mass fraction.

2 Data and cosmological parameters

We have presented here the constraints on the masses of the different thermal relics in different scenarios using the available cosmological data in the beginning of this year 2014. We consider the data on CMB temperature anisotropies measured by the Planck satellite (including information on the lensing potential) [13,14,15] combined with 9-year polarization data from WMAP [16] and with additional temperature data from high-resolution CMB experiments, namely the Atacama Cosmology Telescope (ACT) [17] and the South Pole Telescope (SPT) [18].

Moreover galaxy clustering measurements are considered in the analyses via BAO signals. As a novelty, we add to the existing BAO data sets (SDSS Data Release 7 [19,20], WiggleZ survey [21], 6dF [22]) the most recent and most accurate BAO measurements to date, arising from the BOSS Data Release 11 (DR11) results [23].

We also exploit here the WiggleZ survey large scale structure measurements in their full matter power spectrum form [24], in order to quantify the benefits of using *shape* measurements of the matter power spectrum versus *geometrical* BAO information in extended cosmological scenarios,

Our cosmological data analyses will also address the effect of a gaussian prior on the Hubble constant $H_0 = 73.8 \pm 2.4$ km/s/Mpc, accordingly with the measurements from the Hubble Space Telescope [25].

We also consider the σ_8 measurements using the CFHTLens survey data [26] and The Planck Sunyaev-Zeldovich (SZ) selected clusters catalog [27] . These measurements are included in our analysis by post-processing the chains that were previously generated without accounting for these data.

Lastly we exploit the primordial deuterium values from Ref. [28] $(D/H)_p = (2.87 \pm 0.22) \times 10^{-5}$ as well as the most recent deuterium measurements $(D/H)_p = (2.53 \pm 0.04) \times 10^{-5}$ [29], to compare the cosmological constraints obtained with these two diferent primordial deuterium estimates, including also the measurements of the helium mass fraction $Y_p = 0.254 \pm 0.003$ [30].

The baseline scenario we analyse here is light active massive neutrino scheme with three degenerate massive neutrinos, described by the parameters:

$$\{\omega_b, \omega_c, \Theta_s, \tau, n_s, \log[10^{10} A_s], \sum m_\nu\} \ , \tag{1}$$

$\omega_b \equiv \Omega_b h^2$ and $\omega_c \equiv \Omega_c h^2$ being the physical baryon and cold dark matter energy densities, Θ_s the ratio between the sound horizon and the angular diameter distance at decoupling, τ is the reionization optical depth, n_s the scalar spectral index, A_s the amplitude of the primordial spectrum and $\sum m_\nu$ the sum of the masses of the three active neutrinos in eV. We then consider simultaneously the presence of two hot relics, both massive neutrinos and axions, enlarging the former scenario with one thermal axion of mass m_a. The other possibility is the existence of extra dark radiation species, that we have firstly addressed by introducing a number of massless sterile neutrino-like species, parameterized via $N_{\rm eff}$ (together with the baseline three massive neutrino total mass $\sum m_\nu$). We also constrain here simultaneously the $N_{\rm eff}$ massive sterile neutrino scenario and the sum of the three active neutrino masses $\sum m_\nu$.

3 Results

In the baseline scenario with three active neutrino degenerate species, without the inclusion of the constraints on σ_8 and Ω_m, the upper limits on the neutrino mass are mostly driven by the new BOSS DR11 BAO measurements, being the tightest limit $\sum m_\nu < 0.22$ eV at 95% CL from the combination of CMB data, BAO and HST measurements of the Hubble constant. The addition of the constraints on σ_8 and Ω_m from the CFHTLens survey displaces the bounds on the neutrino mass to higher values, the reason for that being the lower σ_8 preferred by CFHTLens weak lensing measurements. Due the poor constraining power of the weak lensing

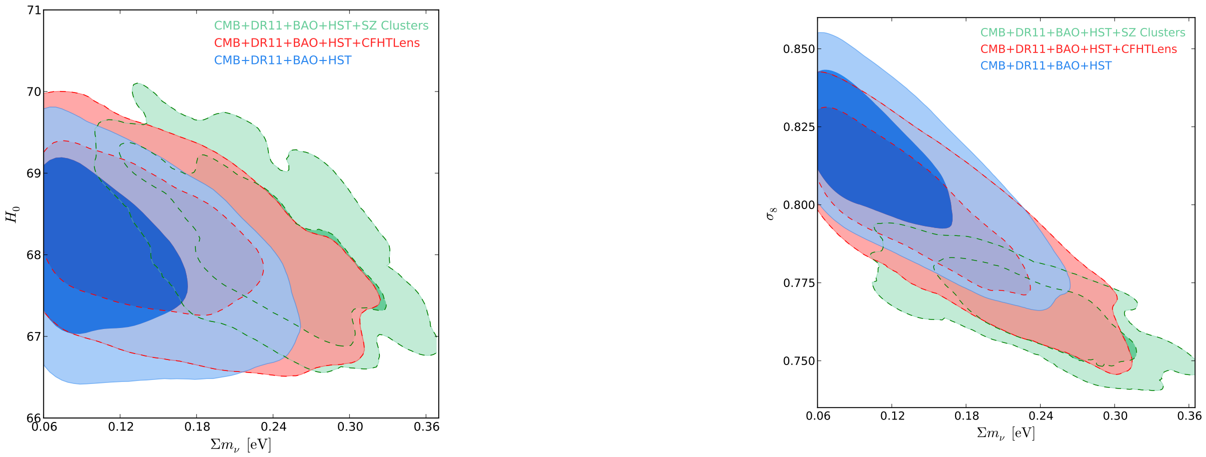

Figure 1 – Left panel: the blue contours show the 68% and 95% CL allowed regions from the combination of CMB data, BOSS DR11 BAO measurements, additional BAO measurements and a prior on the Hubble constant from HST in the ($\sum m_\nu$ (eV), H_0) plane. The red (green) contours depict the results when the $\sigma_8 - \Omega_m$ weak lensing (galaxy number counts) constraint is added in the analysis. Right panel: as in the left panel but in the ($\sum m_\nu$ (eV), σ_8) plane.

data the neutrino mass bounds are not significantly altered. On the other hand, when adding the constraint on σ_8 and Ω_m from the Planck-SZ cluster catalog on galaxy number counts, a non zero value for the sum of the three active neutrino masses of ~ 0.3 eV is favoured at 4σ.

Figure 1 illustrates our findings for three possible data combinations.

In a scenario including both massive neutrinos and a thermal axion, only when further information on the $\sigma_8 - \Omega_m$ relationship from the Planck SZ cluster number counts is considered in the MCMC analyses, there exists evidence for a neutrino mass of ~ 0.2 eV at the $\sim 3\sigma$ level exclusively for the case in which CMB data is combined with BOSS BAO DR11 measurements and full-shape power spectrum information from the WiggleZ galaxy survey ($\sum m_\nu = 0.20^{+0.13}_{-0.14}$ eV at 95% CL). However, there is no evidence for neutrino and axions masses simultaneously.

Figure 2, left panel, depicts the 68% and 95% CL allowed regions arising from the combination of CMB data, BOSS DR11 BAO measurements, additional BAO measurements and a prior on the Hubble constant from HST in the ($\sum m_\nu$ (eV), m_a(eV)) plane. Once the Planck SZ cluster number counts information on the $\sigma_8 - \Omega_m$ relationship is added, a non zero value of the axion mass is favoured by data at the $\sim 2.2\sigma$. The right panel of Fig. 2 shows the 68% and 95% CL contours in the ($\sum m_\nu$ (eV), m_a(eV)) plane resulting from the analysis of CMB data, BOSS DR11 BAO measurements, additional BAO measurements - except for the WiggleZ galaxy survey information which is removed and considered in its full-shape form - and the HST H_0 prior.

In the case in which we consider both massive neutrinos and $\Delta N_{\rm eff}$ dark radiation species, the neutrino mass bounds are less stringent than in standard three neutrino massive case due to the large degeneracy between $\sum m_\nu$ and $N_{\rm eff}$, finding $\sum m_\nu < 0.31$ eV and $N_{\rm eff} = 3.45^{+0.59}_{-0.54}$ at 95% CL from the combination of CMB data and BOSS DR11 BAO measurements.

Big Bang Nucleosynthesis constraints reduce both the mean value and the errors of $N_{\rm eff}$ significantly. After the addition of the most recent measurements of deuterium [29] and helium [30], and using the theoretically derived fitting functions of Ref. [28], we find $\sum m_\nu < 0.24$ eV and $N_{\rm eff} = 3.25^{+0.25}_{-0.24}$ at 95% CL from the analysis of CMB data, WiggleZ power spectrum measurements and the HST H_0 prior finding no evidence for $N_{\rm eff} > 3$. If previous estimates of the deuterium primordial aundances are used in the analysis [28], there exists a $4(2.5)\sigma$ preference for $N_{\rm eff} > 3$, with (without) HST data included in the numerical analyses ($\sum m_\nu < 0.31$ eV and $N_{\rm eff} = 3.52^{+0.27}_{-0.24}$ at 95% CL). If the additional sterile neutrino states are considered as massive species, a $\sim 3.5\sigma$ preference for $N_{\rm eff} > 3$ still appears when considering BBN measurements (with

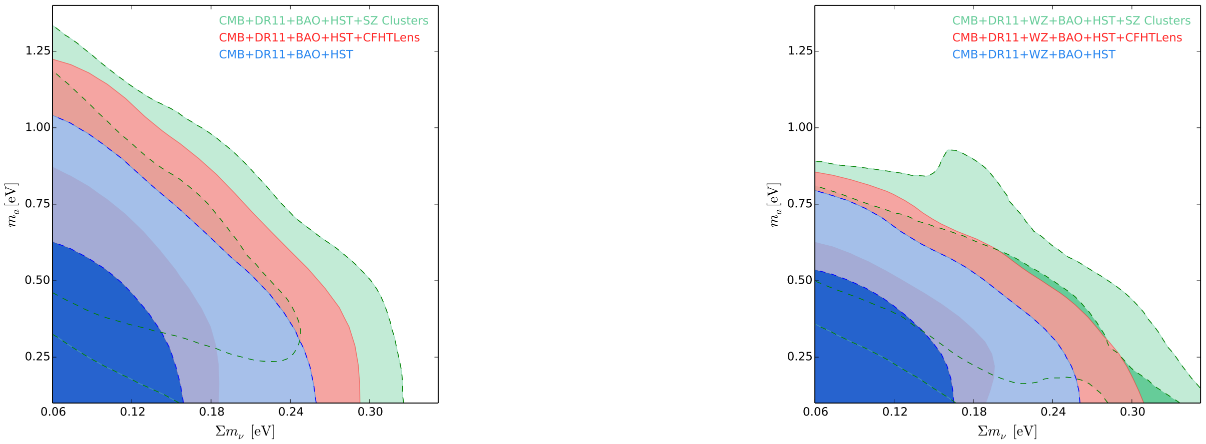

Figure 2 – Left panel: the blue contours show the 68% and 95% CL allowed regions from the combination of CMB data, BOSS DR11 BAO measurements, additional BAO measurements and a prior on the Hubble constant from HST (depicted by the blue contours) in the ($\sum m_\nu$ (eV), m_a (eV)) plane. The red (green) contours depict the results when the $\sigma_8 - \Omega_m$ weak lensing (galaxy number counts) constraint is added in the analysis. Right panel: as in the left panel but replacing the WiggleZ BAO geometrical information by the WiggleZ full-shape matter power spectrum measurements.

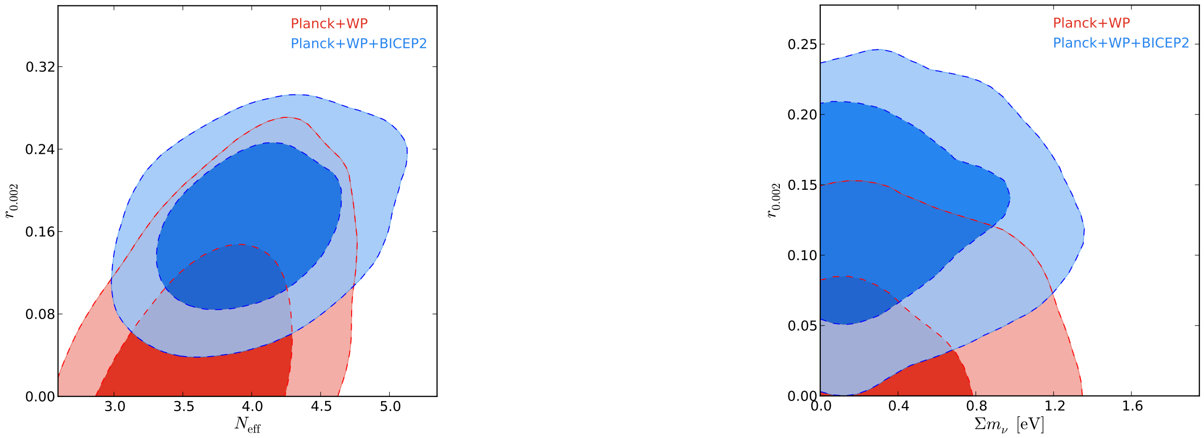

Figure 3 – Left panel: Constraints in the N_{eff} vs r plane from Planck+WP and Planck+WP+BICEP2 data. Notice how the inclusion of the BICEP2 constraint shifts the contours towards $N_{\rm eff} > 3$. Right panel: constraints on the Σm_ν vs r plane from Planck+WP and Planck+WP+BICEP2 data.

previous estimates of the deuterium abundances from Ref. [28]) and the HST prior on the Hubble constant. Accurate measurements as well as sharp theoretical predictions of the primordial deuterium and helium light element abundances are therefore crucial to constrain the value of $N_{\rm eff}$.

The BICEP2 experiment [31] claimed a detection at about 5.9σ for B-mode polarization on large angular scales, compatible with the presence of a tensor component with amplitude $r_{0.002} = 0.2^{+0.06}_{-0.05}$ at 68% c.l.. It is therefore interesting to evaluate the impact of this measurement for the effective number of relativistic species and neutrino masses. We have therefore performed an analysis including a tensor component (with zero running). The results are presented in Fig. 3. When the BICEP2 data are included, an extra background of relativistic particle is preferred with $N_{eff} = 4.00 \pm 0.41$ at 68% c.l.. CMB data alone is therefore suggesting a value for $N_{\rm eff} > 3$ at good significance. The tension between the Planck+WP limit of $r < 0.11$ at 95% c.l. and the recent BICEP2 result appears as less evident when extra relativistic particles are included. The BICEP2 result does not affect the current constraints on neutrino masses as we can see from the right side of figure Fig. 3.

References

1. R. de Putter, E. V. Linder and A. Mishra, arXiv:1401.7022 [astro-ph.CO].
2. M. Blennow, E. Fernandez-Martinez, O. Mena, J. Redondo and P. Serra, JCAP **1207**, 022 (2012) [arXiv:1203.5803 [hep-ph]].
3. R. Diamanti, E. Giusarma, O. Mena, M. Archidiacono and A. Melchiorri, Phys. Rev. D **87**, no. 6, 063509 (2013) [arXiv:1212.6007 [astro-ph.CO]].
4. U. Franca, R. A. Lineros, J. Palacio and S. Pastor, Phys. Rev. D **87**, 123521 (2013) [arXiv:1303.1776 [astro-ph.CO]].
5. K. N. Abazajian, M. A. Acero, S. K. Agarwalla, A. A. Aguilar-Arevalo, C. H. Albright, S. Antusch, C. A. Arguelles and A. B. Balantekin *et al.*, arXiv:1204.5379 [hep-ph].
6. J. Kopp, P. A. N. Machado, M. Maltoni and T. Schwetz, JHEP **1305**, 050 (2013) [arXiv:1303.3011 [hep-ph]].
7. A. Melchiorri, O. Mena, S. Palomares-Ruiz, S. Pascoli, A. Slosar and M. Sorel, JCAP **0901**, 036 (2009) [arXiv:0810.5133 [hep-ph]].
8. M. Archidiacono, N. Fornengo, C. Giunti and A. Melchiorri, Phys. Rev. D **86**, 065028 (2012) [arXiv:1207.6515 [astro-ph.CO]].
9. M. Archidiacono, N. Fornengo, C. Giunti, S. Hannestad and A. Melchiorri, arXiv:1302.6720 [astro-ph.CO].
10. A. Mirizzi, G. Mangano, N. Saviano, E. Borriello, C. Giunti, G. Miele and O. Pisanti, Phys. Lett. B **726**, 8 (2013) [arXiv:1303.5368 [astro-ph.CO]].
11. E. Di Valentino, A. Melchiorri and O. Mena, JCAP **1311**, 018 (2013) [arXiv:1304.5981].
12. R. D. Peccei and H. R. Quinn, Phys. Rev. Lett. **38**, 1440 (1977); R. D. Peccei and H. R. Quinn, Phys. Rev. D **16**, 1791 (1977).
13. P. A. R. Ade *et al.* [Planck Collaboration], arXiv:1303.5062 [astro-ph.CO].
14. P. A. R. Ade *et al.* [Planck Collaboration], arXiv:1303.5075 [astro-ph.CO].
15. P. A. R. Ade *et al.* [Planck Collaboration], arXiv:1303.5077 [astro-ph.CO].
16. C. L. Bennett, D. Larson, J. L. Weiland, N. Jarosik, G. Hinshaw, N. Odegard, K. M. Smith and R. S. Hill *et al.*, arXiv:1212.5225 [astro-ph.CO].
17. S. Das, T. Louis, M. R. Nolta, G. E. Addison, E. S. Battistelli, J R. Bond, E. Calabrese and D. C. M. J. Devlin *et al.*, arXiv:1301.1037 [astro-ph.CO].
18. C. L. Reichardt, L. Shaw, O. Zahn, K. A. Aird, B. A. Benson, L. E. Bleem, J. E. Carlstrom and C. L. Chang *et al.*, Astrophys. J. **755**, 70 (2012) [arXiv:1111.0932 [astro-ph.CO]].
19. W. J. Percival *et al.* [SDSS Collaboration], Mon. Not. Roy. Astron. Soc. **401**, 2148 (2010) [arXiv:0907.1660 [astro-ph.CO]].
20. N. Padmanabhan, X. Xu, D. J. Eisenstein, R. Scalzo, A. J. Cuesta, K. T. Mehta and E. Kazin, arXiv:1202.0090 [astro-ph.CO].
21. C. Blake, E. Kazin, F. Beutler, T. Davis, D. Parkinson, S. Brough, M. Colless and C. Contreras *et al.*, Mon. Not. Roy. Astron. Soc. **418**, 1707 (2011) [arXiv:1108.2635 [astro-ph.CO]].
22. F. Beutler, C. Blake, M. Colless, D. H. Jones, L. Staveley-Smith, L. Campbell, Q. Parker and W. Saunders *et al.*, Mon. Not. Roy. Astron. Soc. **416**, 3017 (2011) [arXiv:1106.3366 [astro-ph.CO]].
23. L. Anderson, E. Aubourg, S. Bailey, F. Beutler, V. Bhardwaj, M. Blanton, A. S. Bolton and J. Brinkmann *et al.*, arXiv:1312.4877 [astro-ph.CO].
24. D. Parkinson, S. Riemer-Sorensen, C. Blake, G. B. Poole, T. M. Davis, S. Brough, M. Colless and C. Contreras *et al.*, Phys. Rev. D **86**, 103518 (2012) [arXiv:1210.2130 [astro-ph.CO]].
25. A. G. Riess, L. Macri, S. Casertano, H. Lampeitl, H. C. Ferguson, A. V. Filippenko, S. W. Jha and W. Li *et al.*, Astrophys. J. **730**, 119 (2011) [Erratum-ibid. **732**, 129 (2011)] [arXiv:1103.2976 [astro-ph.CO]].
26. C. Heymans, E. Grocutt, A. Heavens, M. Kilbinger, T. D. Kitching, F. Simpson, J. Benjamin and T. Erben *et al.*, arXiv:1303.1808 [astro-ph.CO].

27. P. A. R. Ade *et al.* [Planck Collaboration], arXiv:1303.5080 [astro-ph.CO].
28. F. Iocco, G. Mangano, G. Miele, O. Pisanti and P. D. Serpico, Phys. Rept. **472**, 1 (2009) [arXiv:0809.0631 [astro-ph]].
29. R. Cooke, M. Pettini, R. A. Jorgenson, M. T. Murphy and C. C. Steidel, arXiv:1308.3240 [astro-ph.CO].
30. Y. I. Izotov, G. Stasinska and N. G. Guseva, arXiv:1308.2100 [astro-ph.CO].
31. P. A. R. Ade *et al.* [BICEP2 Collaboration], arXiv:1403.3985 [astro-ph.CO].

Robustness of Planck results to statistical methods: the case of neutrinos

MARTA SPINELLI
Laboratoire de l'Accélérateur Linéaire,
Bat.200, 91400 Orsay, France

With its wide frequency coverage Planck is a unique tool not only to test the standard cosmological model (LCDM) but to explore beyond it, looking, for example, for the absolute scale of neutrino masses. Cosmological parameters are traditionally determined using a Bayesian approach based on Markov chains (MCMC) but a Frequentist approach based on profiles-Likelihood is also possible.

The two methods are presented, with special focus on the latter, which gives results remarkably consistent with Bayesian approach for the LCDM model.

The interesting case of neutrinos is discussed. Here the presence of a physical boundary on the masses induces differences in the two approaches nevertheless giving results in perfect agreement.

1 Introduction

Since its detection in the sixties, the cosmic microwave background (CMB) has been considered a very powerful probe for cosmology and early-universe physics.

The search for *anisotropies* in the CMB temperature has reached with the ESA satellite Planck the ultimate precision. The combination of this experimental measurements and accurate theoretical predictions can be used to set tight constraints on cosmological parameters.

This is generally done using Bayesian statistic but, since a such high precision has been reached, it is worth to compare the Bayesian results with a different methodology. We present here the comparison with the frequentist Profile-likelihood technique. The two different statistical approaches to parameters estimation give consistent results and allow, for the case of neutrino, a deeper understanding of the outcomes.

2 Statistical methodologies

The Planck satellite consists in a 1.5m off-axis Gregorian telescope, equipped with two different instrument: the Low Frequency Instrument (LFI) and the High Frequency Instrument (HFI) that scan the sky in 9 frequency bands.

Going from raw data to cosmological parameters estimation requires a complex analysis pipeline that involves reconstruction of sky maps at each frequency. High resolution maps at 100, 143 and 217 GHz are used to constrain the CMB power spectrum $\mathcal{C}_\ell$ for $\ell \geq 50$.

A component separated CMB map is used to build a temperature low-ℓ likelihood, complemented by the WMAP low-ℓ polarization measurements[1] (WP).

In the final likelihood $\mathcal{L}_{Planck}(\mathcal{C}_l, \psi)$, the $\mathcal{C}_l$ depends on the cosmological parameters and some nuisances ψ that include foreground modeling and experimental parameters (they can be up to

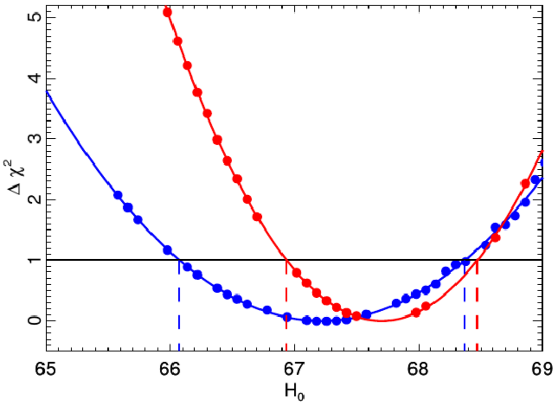

Figure 1 – Profile H_0 CMB data alone (in blue) and with the addition of the BAO information (in red)

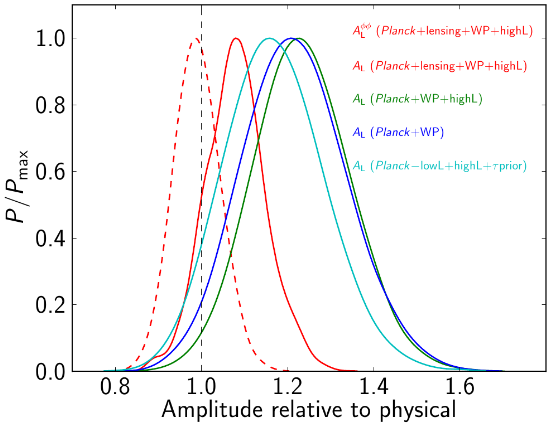

Figure 2 – Despite the consistency of the lensing measurement with the ΛCDM expectations ($A_L^{\phi\phi} = 1$), several data combinations show a preference for $A_L > 1$ from the *Planck* temperature power spectrum.

$\sim$ 50 parameters).
The goal is to search for the parameter values $\theta = (\mathbf{\Omega} \rightarrow \mathcal{C}_l, \psi)$ that fit the data best.

2.1 *Bayesian approach*

In the Bayesian approach, the value of the *true* parameters θ is obtained from the posterior probability (the likelihood is multiplied by some priors encoding the previous knowledge). Because of the high dimensionality of the problem the MCMC technique is used and then inference on each parameter is trivially done, once the chains are built, marginalizing on all the others parameters. Planck results are obtained using the classical softwares *CAMB* and *CosmoMC*[1].

2.2 *Frequentist approach*

In our frequentist analysis[3] there are no priors (true parameters do not have a distribution) and the global Maximum Likelihood Estimate (MLE, χ^2_{min}) is invariant with respect to the choice of the set of parameters. Moreover there are no *volume effects* that can arise from the marginalization process.
We use the CLASS[6] Boltzmann code and MINUIT[4], a high precision minimizer developed at CERN that calculates the multi-dimentional minimum of the $\chi^2 = -2\ln\mathcal{L}$ function and its Hessian matrix.
Since the Hessian is only a crude approximation and the problem is highly non linear, it cannot be used directly and an error estimation is performed by *profiling* each parameter. For a given value of the parameter θ of interest, we calculate:

$$\chi^2_p(\theta) = \chi^2(\theta, \hat{\hat{\nu}}(\theta)) \tag{1}$$

where $\hat{\hat{\nu}}(\theta)$ is given by the ν that minimises the χ^2 for fixed θ.
We repeat this procedure scanning several values of θ, obtaining a *profile* (see Fig.1 for an example on H_0).
The 68% CL interval is then easily obtained by fitting and cutting the curve at $\chi^2_{min} + 1$.

2.3 *Results and Comparison*

In table 1 we report the comparison between the official Bayesian Planck result[1] and the Profile-likelihood analysis[3]. Both the Planck result (adding also the very *highℓ* information from ACT

Table 1: Comparison between the official Planck results[1] and the Profile-likelihood analysis

	CMB		CMB+BAO	
Parameter	MCMC	Profile-likelihood	MCMC	Profile-likelihood
H_0	67.3 ± 1.2	67.2 ± 1.2	67.8 ± 0.8	67.7 ± 0.8
$100\omega_b$	2.207 ± 0.027	2.208 ± 0.027	2.214 ± 0.024	2.215 ± 0.024
ω_c	0.1198 ± 0.0026	0.1201 ± 0.0026	0.1187 ± 0.0017	0.1190 ± 0.0017
n_s	0.9585 ± 0.0070	0.9575 ± 0.0071	0.9608 ± 0.0054	0.9598 ± 0.0055
$ln(10^{10}A_s)$	3.090 ± 0.025	3.087 ± 0.025	3.091 ± 0.025	3.088 ± 0.025
$z_r e$	11.2 ± 1.1	11.0 ± 1.1	11.2 ± 1.1	11.2 ± 1.1

and SPT) and the result obtained with the addition of BAO measurements are shown. The agreement is excellent.
Given the Gaussian appearance of the posterior distribution, this results is reassuring.
We will discuss now the neutrino case. Here the presence of a physical boundary on the masses can induce differences in the two approaches.

3 Massive Neutrinos

3.1 Effects on CMB

The presence of relic neutrinos has a little but detectable impact on the $\mathcal{C}_\ell$.
CMB is sensitive to the sum of neutrino mass $M_\nu = \sum_i m_\nu$ (which are considered degenerated).
At low-ℓ there is an effect on the amplitude of the first peak via the *Early Integrated Sachs Wolfe effect (ISW).*
The best pre-Planck limits on neutrinos has been set by WMAP using this effect and they obtained $\sum m_\nu < 1.3eV$ $(95\%CL)$.
Massive neutrinos cause also a modification of the $\mathcal{C}_\ell$ at high ℓ since they suppress clustering on scales smaller than the horizon size at the non-relativistic transition[1].

3.2 External observable: CMB Lensing

Weak-lensing affects the CMB temperature power spectrum smoothing the acoustic peaks and troughs. Planck has obtained, from the non-Gaussian trispectrum, a measurements of the CMB lensing potential[2] and an estimate of its associated power spectrum $\mathcal{C}_\ell^{\phi\phi}$.
Since it helps in breaking degeneracies among the cosmological parameters that affect the late-time growth of structures, there is in this measurement a new information and the possibility of improving the limits on M_ν.

However, despite the consistency of the lensing measurement with the ΛCDM expectations[2] (see in Fig.2 the consistency of the parameter $A_L^{\phi\phi}$ with unity), there are some tensions which leads to smaller than forecast improvements on the constraint on the sum neutrino masses.
To address this we consider the parameter A_L which takes $\mathcal{C}_\ell^{\phi\phi} \rightarrow A_L \mathcal{C}_\ell^{\phi\phi}$ modulating the lensing effect in the temperature power spectrum.
From Fig.2 is clear that there is a preference for $A_L > 1$ (up to $\sim 2\sigma$). Having more lensing than expected in the $\mathcal{C}_\ell$ can indeed alter the constraint on M_ν.

3.3 Planck results on M_ν

The Bayesian posteriors (Fig.3) gives us the following values: $M_\nu < 0.66$eV (95%; $Planck + WP + High\ell$) and $M_\nu < 0.85$eV adding lensing. Following a naive frequentist interpretation we

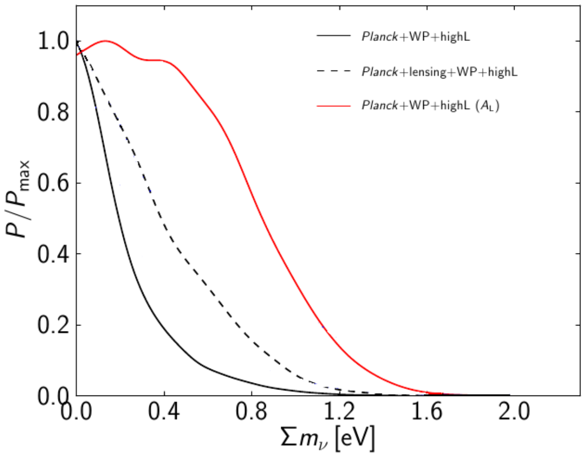

Figure 3 – Posterior distribution for M_ν

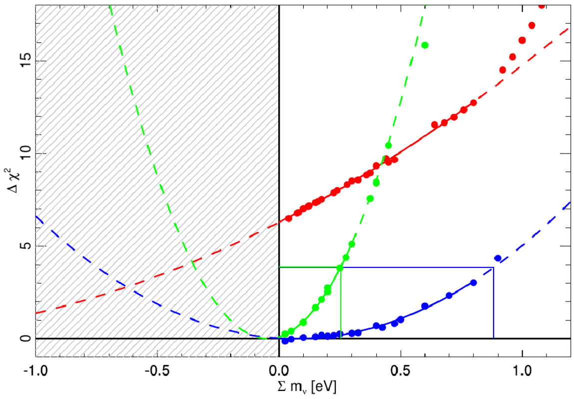

Figure 4 – Profile-likelihood for M_ν: $Planck + WP + High\ell$ (red), $+Lensing$ (blue), $+BAO$ (green)

don't expect a limit to get worse when some information is added, especially since lensing is the observable that should help the most for the constraint.

Without lensing information (marginalizing on A_L) we go back to a limit compatible with WMAP, confirming that there is some information to be gained with lensing.

Profile likelihoods show that the problem is delicate. Planck alone result (in red in Fig.4) seems to be artificially pulled to small values. Frequentist analysis tells us not to use this measurement confirming the concern that what drives A_L high may drive M_ν low.

Adding lensing (blue curve) regularizes the situation and, using the Feldman-Cousins prescription[5], we end up with $M_\nu < 0.85$eV (95%) in agreement with Bayesian limit. With BAO we obtain the best constraint of $M_\nu < 0.26$eV and there is again a perfect agreement with Bayesian approach.

4 Conclusions

Since Planck 2013 constrained cosmological parameters with unprecedented precision it is worth to cross check results with a different methodology beside the standard one. Reliable best-fit values from MINUIT allow, for example, to search for indications of parameter-volume and prior range effects on posterior samples. The excellent agreement with the Bayesian method on ΛCDM shows that results are robust to statistical methodology.

The neutrinos case is the more subtle one since we are in presence of a physical boundary ($M_\nu > 0$). In this case the frequentist approach helps in understanding results on M_ν.

Full Mission and Polarization data, that will be released in October 2014, will help to set better limits.

References

1. Planck 2013 results. XVI. Cosmological parameters.
2. Planck 2013 results. XVII. CMB-Lensing
3. Planck intermediate results. XVI. Profile likelihoods for cosmological parameters.
4. James, F. and Roos, M. 1975, Comput. Phys. Commun., 10, 343
5. Feldman, G. J. and Cousins, R. D. 1998, Phys. Rev. D, 57, 3873, arXiv:physics/9711021
6. The Cosmic Linear Anisotropy Solving System (CLASS) II: Approximation schemes,by D. Blas, J. Lesgourgues, T. Tram, arXiv:1104.2933

NEUTRINO MASS FROM THE LYMAN-ALPHA FOREST

GRAZIANO ROSSI
Department of Astronomy and Space Science, Sejong University, Seoul, 143-747, Korea

The quest for the neutrino mass is a central goal in contemporary cosmology, subject to intense scrutiny, and among different large-scale structure tracers the Lyman-α forest is re-emerging as a unique tool to probe the neutrino mass at high-redshift – through characteristic imprints on the transmitted Lyman-α flux. However, a detailed modeling of the low-density regions of the intergalactic medium in presence of massive neutrinos on scale ranging from a few to hundreds of megaparsecs is still missing, but is required if one wants to interpret state-of-the-art data from the observations of quasar spectra. To this end, we provide a suite of hydrodynamical simulations made with Gagdet-3, spanning different volumes and having a range of resolutions and neutrino masses (from $M_\nu = 0.1$ to 0.8 eV in 3 degenerate species), specifically designed to meet the requirements of the Baryon Acoustic Spectroscopic Survey (BOSS). We adopt a particle-type implementation of massive neutrinos, and choose cosmological parameters compatible with the latest Planck (2013) results. While the resolution requirements have been targeted to match the quality of the SDSS-III/BOSS data, our numerical simulations will also establish a useful theoretical ground for upcoming surveys such as SDSS-IV/eBOSS and DESI. In the very near future, data from leading spectroscopic surveys will allow one to measure the absolute mass scale of neutrinos, and to determine the exact nature of the neutrino mass hierarchy; hence, we expect that this modeling will become useful quite soon.

1 Massive Neutrinos and Structure Formation

At the interface between particle physics and cosmology, neutrino science has received renewed interest recently, after the breakthrough discovery over the last decade that neutrinos are massive. Hence, massive neutrinos should be included in the concordance ΛCDM model dominated by a dark energy (DE) component, which in general only assumes a minimal neutrino mass of 0.06 eV. While neutrino oscillation experiments are sensitive only to differences in the squares of neutrino masses, cosmology offers a unique 'laboratory' with the best sensitivity to the neutrino mass: primordial neutrinos leave their imprint into several large-scale structure (LSS) observables, and because of their free-streaming they significantly alter structure formation. Therefore, cosmology can place competitive limits both on the neutrino mass scale and hierarchy.

Neutrinos should be considered as extra radiation while ultrarelativistic, but once non-relativistic they behave as an additional cold dark matter (CDM) component and participate in structure formation on scales greater than their free-streaming scale: the overall result is a suppression of power on small scales, and a delay in matter domination (Lesgourgues & Pastor 2006). Neutrinos in the mass range 0.05 eV $\leq m_\nu \leq$ 1.5 eV become non-relativistic in the redshift interval $3000 \geq z \geq 100$, approximately around $z_{\rm nr} \simeq 2000(m_\nu/1eV)$. While the effect of cosmological neutrinos on the evolution of density perturbations in the linear regime is well-understood, less is known in the nonlinear regime: this fact motivates the present study.

Massive neutrinos can be studied through their impact on the CMB, particularly in the polarization maps, and by using several baryonic tracers of the LSS clustering of matter such as the 3D power spectrum from galaxy surveys, the Sunyaev-Zel'dovich effect in galaxy clusters,

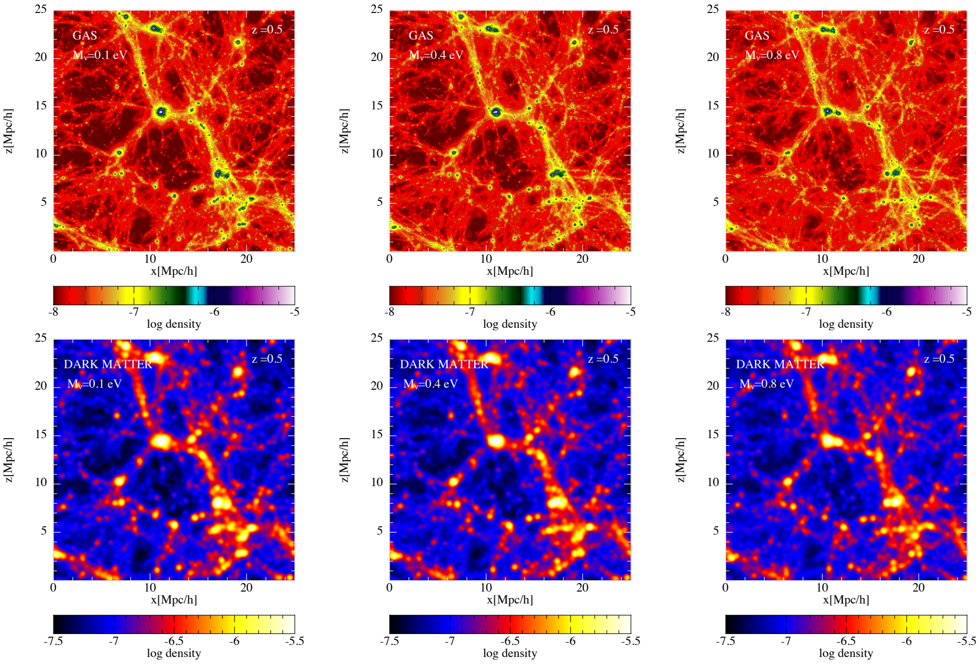

Figure 1 – Examples of snapshots of the gas (top panels) and dark matter (bottom panels) components at $z = 0.5$, from simulations with 25 h^{-1}Mpc box size and resolution $N_\mathrm{p} = 192^3$ particles/type. The panels are full projections of the density field in the x and z directions across y and smoothed with a cubic spline kernel, obtained from simulations having a total neutrino mass $M_\nu = 0.1$ eV (left), $M_\nu = 0.4$ eV (middle), and $M_\nu = 0.8$ eV (right).

cosmic shear through weak lensing, or the Lyman-α (Lyα) forest. The latter observable has generally received less attention in the literature, but is now emerging as a promising window into the high-redshift Universe, being at a redshift range inaccessible to other LSS probes and spanning a wide interval in redshift. In particular, the suppression of growth of cosmological structures on scales smaller than the neutrino free-streaming distance makes the Lyα forest a good tracer of the neutrino mass, and measurements of the mean Lyα transmission flux and its evolution also allow one to constrain the basic cosmological parameters with improved sensitivity.

Currently, the best Lyα forest data and the most precise measurement of the Lyα flux power spectrum come from the Baryon Acoustic Spectroscopic Survey (BOSS; Dawson et al. 2013, Palanque-Delabrouille et al. 2013). In order to interpret the information contained in this remarkable dataset and control the systematics involved, numerical simulations at equivalent or superior precision of this survey are required, particularly at lower redshifts and smaller scales (1- 40 h^{-1}Mpc) where for massive neutrinos the nonlinear evolution of density fluctuations becomes significant. Despite their intrinsic limitations and uncertainties, simulations allow one to self-consistently model the interplay between gravity and gas pressure on the structure of the photo-ionised intergalactic medium (IGM), so that most of the observed properties of the Lyα forest are reproduced, and to gain a better understanding of the role and effects of massive neutrinos in the complex process of structure formation – as we show next.

2 A Suite of Hydrodynamical Simulations with Massive Neutrinos

We have produced a suite of 48 cosmological hydrodynamical simulations with cold dark matter (CDM), baryons, and either a varying neutrino mass and fixed cosmological and astrophysical parameters, or with a fixed neutrino mass and slight variations in the basic cosmological and astrophysical parameters around what we termed the 'best guess' – i.e. the reference simulation set with Planck (2013) cosmological parameters and a massless neutrino component. Box sizes and resolutions range from 25 h^{-1}Mpc to 100h^{-1}Mpc, and from $N_\mathrm{p} = 192^3$ to $N_\mathrm{p} = 768^3$,

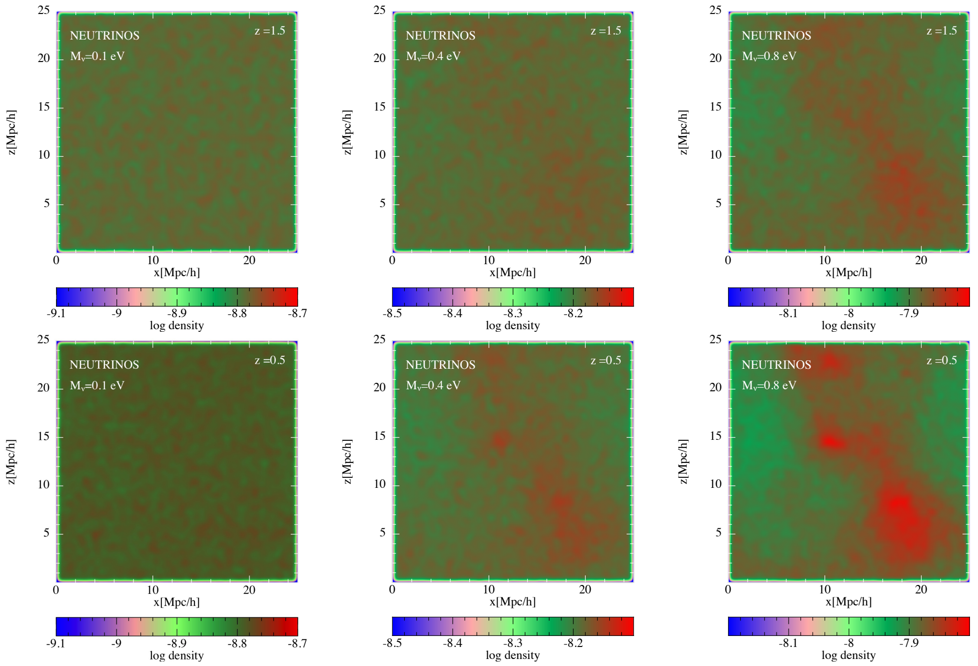

Figure 2 – Density evolution of the neutrino component at $z = 1.5$ (top panels) and $z = 0.5$ (bottom panels), from simulations with $25h^{-1}$Mpc box size and resolution $N_\mathrm{p} = 192^3$/type. The total neutrino mass increases from left to right, being $M_\nu = 0.1$ eV (left), $M_\nu = 0.4$ eV (central) and $M_\nu = 0.8$ eV (right). The distribution of the neutrino density has been smoothed with a cubic spline kernel to eliminate spurious Poisson noise at small scales.

respectively. Visual examples of the density distribution of the gas and dark matter components at $z = 0.5$ in cosmologies with varying neutrino mass are shown in Figure 1. Extensive details on the numerical aspects of these simulations can be found in Rossi et al. (2014). In particular, along the lines of Viel et al. (2010), we have modeled the neutrinos as an additional type of particle in the N-body setup, and carried out a full hydrodynamical treatment well-inside the nonlinear regime, without making any approximations for the evolution of the neutrino component. We have considered 3 degenerate species of massive neutrinos implemented as a single particle-type, where $M_\nu = 0.1, 0.2, 0.3, 0.4, 0.8$ eV. Figure 2 is a visual example of the density evolution of the neutrino component for different mass ranges, at $z = 1.5$ (top panels) and $z = 0.5$ (bottom panels). Simulations have been made with Gadget-3 (Springel 2005), CAMB (Lewis, Challinor & Lasenby 2000) and 2LPT (Crocce et al. 2006) initial conditions starting at redshift $z = 30$, and contain improvements at all levels with respect to previous work. We store snapshots at redshifts between $z = 4.6$ till $z = 2.2$ in intervals of $\Delta z = 0.2$, and for each simulations we extract 100,000 random pencil beam lines of sight (LOS).

3 Results, Applications, and Future Prospects

The free-streaming of neutrinos results in a suppression of the power spectrum of the total matter distribution at scales probed by the Lyα forest data, which is larger than the linear theory prediction by about $\sim 5\%$ at scales $k \sim 1h$/Mpc when $M_\nu = 0.4$ eV, and strongly redshift dependent. This effect propagates into the 1D flux power spectrum, and affects the statistical properties of the transmitted flux fraction. Figure 3 shows an example of the 1D flux power spectrum across several redshift slices, and for a varying neutrino mass – with $M_\nu = 0.1$ eV (left), $M_\nu = 0.4$ eV (center), $M_\nu = 0.8$ eV (right). Results are averaged over 100,000 LOS at different z, as indicated in the panels, and are obtained with the splicing technique introduced by McDonald (2003) and extensively tested in Borde et al. (2014). This allows us to achieve an equivalent resolution of $3 \times 3072^3 \simeq 87$ billion particles in a $(100h^{-1}\mathrm{Mpc})^3$ box size with a

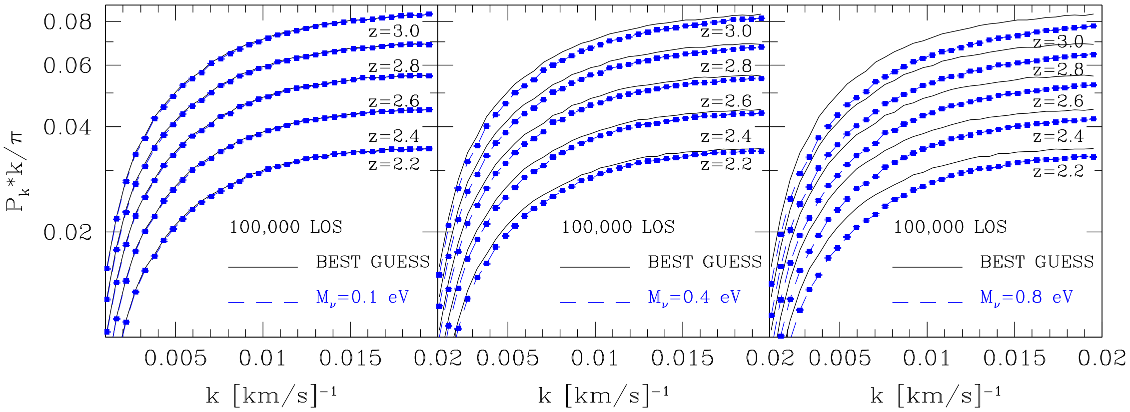

Figure 3 – Normalized 1D flux power spectra computed from the suite of simulations described in the main text, for different values of the neutrino mass (dashed lines and points) as specified in the panels, and averaged over 100,000 LOS and at different z-intervals. Black lines are the corresponding measurements obtained from the 'best guess', which contains only a massless neutrino component. Results are after application of the splicing technique.

global error at the 2% level across the full k-range of interest – which is at the same level of the current uncertainties in available observational data – without the need of running a single but computationally prohibited numerical simulation. The flux power spectrum is sensitive to a wide range of cosmological and astrophysical parameters and instrumental effects, and can be used as a probe of the primordial matter power spectrum on scales of 0.5 – 40 Mpc/h at $2 \leq z \leq 4$ and to determine cosmological parameters, the nature of dark matter through its shape and redshift dependence, and the neutrino mass.

We are currently combining results of these simulations with Lyα forest data from BOSS, in order to constrain cosmological parameters and the neutrino mass with improved sensitivity, and fully exploit the orthogonality of the Lyα forest with other LSS probes. Similar techniques can also be useful for upcoming surveys such as SDSS-IV/eBOSS (Comparat et al. 2013) and DESI (Schlegel et al. 2001), and will eventually lead to the determination of the absolute mass scale of neutrinos in the very near future.

Acknowledgments

This work and the participation to the 'Rencontres de Moriond' (March 2014) in La Thuile, Aosta Valley, Italy, were supported by the faculty research fund of Sejong University in 2014. It is a pleasure to thank Jacques Dumarchez for the superb organization, along with the scientific and organizing committees and the secretariat. It has been an enjoyable and stimulating meeting.

Selected References

1. Rossi, G., Palanque-Delabrouille, N., Borde, A., et al. 2014, arXiv:1401.6464
2. Borde, A., Palanque-Delabrouille, N., Rossi, G., et al. 2014, arXiv:1401.6472
3. Palanque-Delabrouille, N., Yèche, C., Borde, A., et al. 2013, A&A, 559, A85
4. Dawson, K. S., Schlegel, D. J., Ahn, C. P., et al. 2013, AJ, 145, 10
5. Viel, M., Haehnelt, M. G., & Springel, V. 2010, JCAP, 6, 15
6. McDonald, P., Seljak, U., Burles, S., et al. 2006, ApJS, 163, 80
7. Seljak, U., Makarov, A., McDonald, P., et al. 2005, Phys. Rev. D, 71, 103515

HALO ABUNDANCES AND CLUSTERING IN NEUTRINO COSMOLOGIES

EMANUELE CASTORINA
SISSA- International School for Advanced Studies, Via Bonomea 265, I-34136 Trieste – Italy
INFN - sezione di Trieste, via Valerio 2, I-34127 Trieste – Italy

We use a large suite of N-body simulations to study halo abundances and clustering in cosmologies with massive neutrinos. We show that measurements of the halo mass function are in agreement with analytic expressions found in the literature only if the variance of the cold dark matter rather than the total mass field, i.e., $\sigma^2_{cdm}(M,z)$ rather than $\sigma^2_m(M,z)$, is used to describe the halo abundances. This choice yields more universal results in terms of both cosmology and redshift. Similar conclusions can be drawn for halo bias: when large-scale halo bias is defined with respect to the cold dark matter power spectrum, the result is both more universal, and less scale- or k-dependent.

1 Introduction

Massive neutrino leave a very characteristic imprint in the Large Scale Structure of the Universe [4], making cosmology a perfect tool to constraint neutrino masses. In particular it has been suggested that the tension between the Planck CMB temperature anisotropies measurements and low redshift measurements could be explained by a sum of neutrino masses $\sum m_\nu$ in the range $0.2 - 0.3$ eV [5,6]. Motivated by this, in a recent series of paper we reinvestigated the effect of massive neutrinos on the halo mass function and the halo power spectrum, focusing on universality of the former and scale dependence of the latter [1,2,3].

1.1 The Neutrino Background

After the non-relativistic transition, massive neutrinos contribute to the amount of dark matter in the Universe, both at the background and the perturbations level. However neutrinos decoupled as hot dark matter in the very early universe, and therefore neutrino fluctuactions are suppressed below their free streaming length, which is inversely proportional to neutrino masses. As a result the total matter Power Spectrum can be written as

$$P_{mm}(k) = \begin{cases} P_{cc}(k) & \text{if } k < k_{nr} \\ (1-f_\nu)^2\, P_{cc}(k) & \text{if } k \gg k_{nr}\,. \end{cases} \tag{1}$$

where P_{cc} is the CDM Power Spectrum and k_{nr} is the free streaming wave-number at the time of the non-relativistic transition [4].

1.2 Halo Mass Function and Halo bias

At any redshift z the comoving number density of halos of mass M can be written as

$$n(M) = \frac{\rho}{M}\, f(\sigma, z)\frac{d\ln\sigma^{-1}}{dM} \tag{2}$$

where

$$\sigma^2(M,z) = \int d^3k\, P(k,z)\, W_R^2(k) \tag{3}$$

is the variance of linear fluctuactions, ρ is the background density and $W(k,R)$ is the Fourier Tranform of a Top-Hat window function of radius R. In this contest, universality of the halo mass function means that the shape of $f(\sigma,z)$ is independent of redshift and cosmology. Universality is more often described by introducing the scaling variable $\nu = \delta_{cr}/\sigma(M,z)$, where δ_{cr} is the critical density required for collapse.

Ragarding the relation between spatial clustering of halos of given mass M and the underlying matter distribution, we consider for simplicity only linear bias models

$$\delta_h(x;M) \simeq b(M)\delta_m(x) \tag{4}$$

Linear bias is expected to be scale-independent on large scale, and from eq.(2) it can be estimated to be

$$b(\nu) = 1 - \frac{1}{\delta_{cr}}\frac{d\ln f(\nu)}{d\ln\nu}\,. \tag{5}$$

Linear bias coefficients are universal as long as $f(\nu)$ is universal.

2 Results

We employ a large set of N-body simulations to study massive neutrino effects on the Large Scale Structure of the Universe. We used three different value for the sum of neutrino masses, $\sum m_\nu = 0,\, 0.3,\, 0.6$ eV, keeping fixed Ω_m in order to highlight massive neutrino effects. We refer to Villaescusa et al. [1] for a more detailed description of the simulations setup.

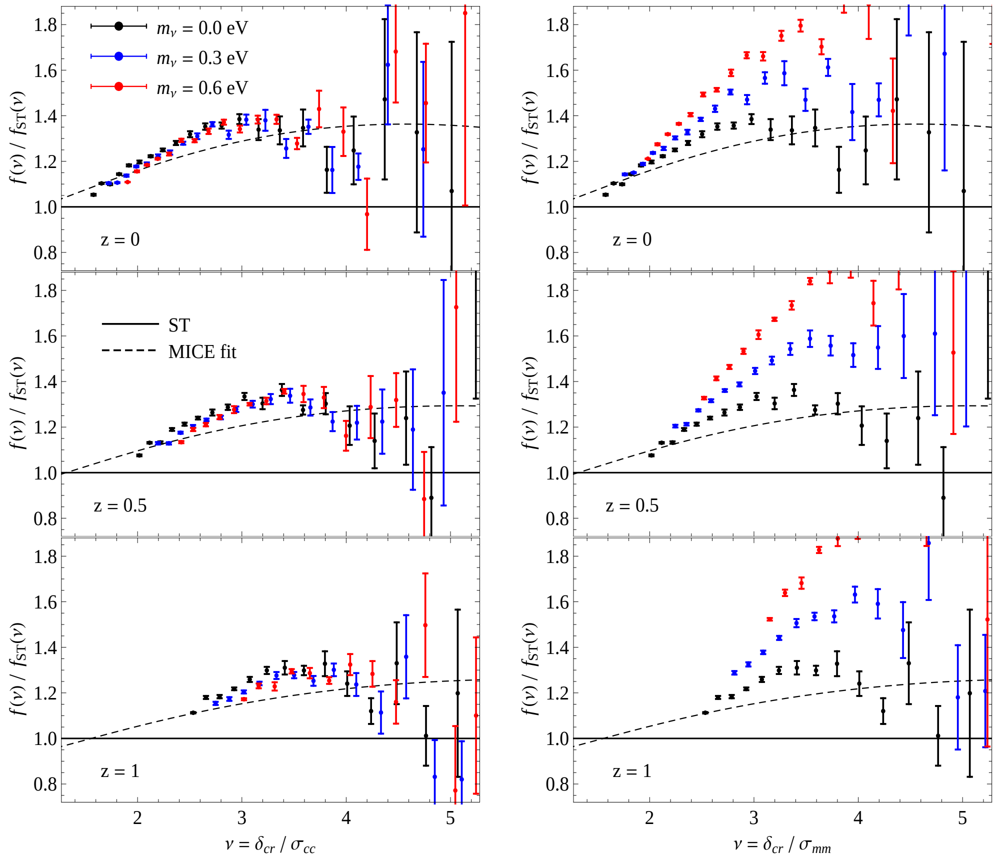

Figure 1 – Univerality of the halo mass function for cosmologies with different values of neutrino masses.

2.1 The halo mass function

In a massive neutrino cosmology it is not obvious what to use in eq. (2) for ρ and σ. In Castorina et al.[2] we argue that the right quantities to use are ρ_c and σ_{cc}, because the scales associated with halo formation are typically $\gg k_{nr}$, and therefore it is reasonable to consider only the CDM clustering. In Figure 1 we show measurements in simulations for the three different value of neutrino masses in terms of the scaling varialbe ν. It is clear that the same level of agreement we get with the Sheth-Tormen[7] fit in the ΛCDM cosmology is obtained only if the mass variance is computed from the CDM fluctuactions only. The non-universality of a mass function defined through σ_{mm} could have important consequences for cosmology from galaxy clusters counts. Indeed all previous analysis used analytic prediction for the halo mass function computed from σ_{mm} assuming universality with respect to cosmological parameters, and therefore they could suffer of a systematic effect in the case of non-zero neutrino masses.

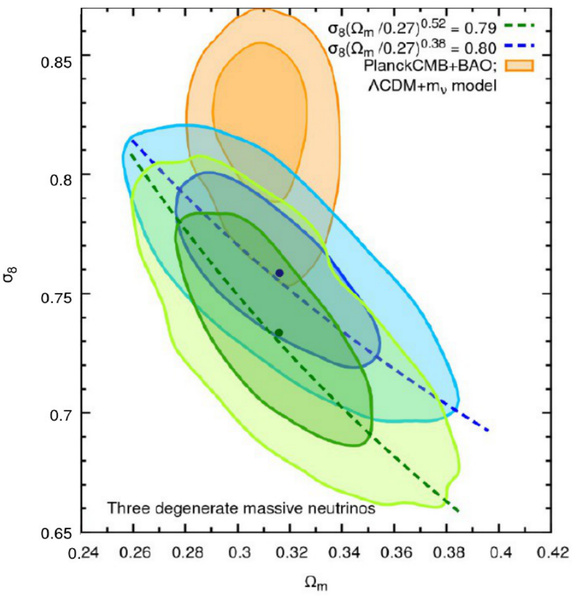

Figure 2 – Confidence level in the $\Omega_m - \sigma_8$ plane for the Planck SZ-clusters sample. For comparison the contour from Planck-TT + BAO is also shown.

In Costanzi et al.[3] we investigated this possibility, focusing on the constraint coming from a Planck SZ-clsuters sample[5]. In Figure 2 we compare the 2-dimensional contours in the plane $\Omega_m - \sigma_8$ when neutrinos are allowed to have non-zero mass, for the two different prescription of the mass variance. When the correct variable σ_{cc} is used, the tension between the Planck-TT best fit value of σ_8 and the Planck SZ-clusters one become even larger, reflecting the fact that $\sigma_{cc} \geq \sigma_{mm}$.

2.2 Halo bias

In a massive neutrino simulations we can define linear bias either with respect to the total matter Power Spectrum or to the CDM only Power Spectrum. Clearly only one of them will meet the condition of being scale-independent(on large scales) and universal, in analogy with a standard ΛCDM model. As expected from the discussion in Section 2.1 scale independent bias coefficients are obtained only if defined with respect to the CDM Power Spectrum. Figure 3 shows measurements of linear bias from the halo-halo Power Spectrum, and we see that, while on very large scales the two definitions agree with each other, reflecting the fact that $P_m = P_{cc}$, on smaller scales the bias defined with respect to P_m exhibits scale-dependence. This result could have implications for the constraints on neutrino masses coming the galaxy Power Spectrum[6].

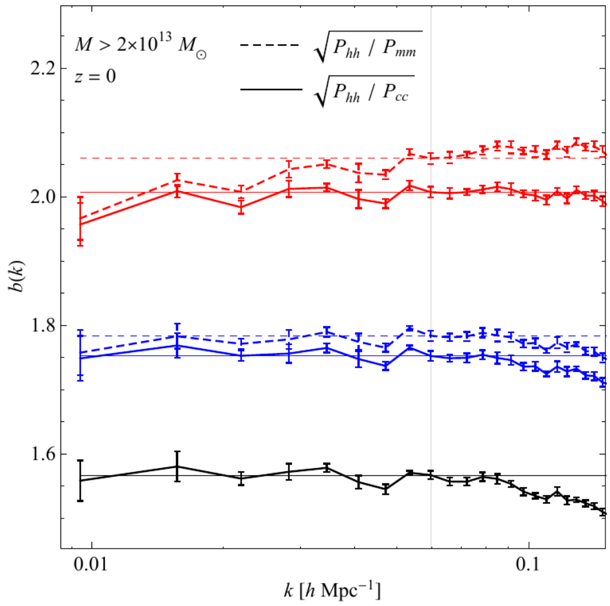

Figure 3 – Linear halo bias for the same cosmologies of Figure 1.

3 Conclusions

We have shown how in a massive neutrino cosmologies the halo mass function and linear halo bias measured in simulations can be understood using the fluctuatcions in the CDM component only. We discussed possible implications of our findings for cosmological parameter estimations with Large Scale Structure Probes.

Acknowledgments

The author would like to thank all the people participating to this project: F. Villaescusa Navarro, M. Costanzi, E. Sefusatti, R. K. Sheth, M. Viel, S. Borgani, F. Marulli, E. Branchini, J. Xia and S.Saito. He also aknowledge INFN for support.

References

1. F. Villaescusa-Navarro et al., *Cosmology with massive neutrinos I: towards a realistic modeling of the relation between matter, haloes and galaxies*, *JCAP* **1403** (2014) 011, [`arXiv:/1311.0866`]
2. E. Castorina et al., *Cosmology with massive neutrinos II: on the universality of the halo mass function and bias clusters*, *JCAP* **1402** (2014) 049 [`arXiv:1311.1514`].
3. M. Costanzi-Alunno-Cerbolini et al., *Cosmology with massive neutrinos III: the halo mass function and an application to galaxy clusters*, *JCAP* **1312** (2013) 012 [`arXiv:1311.1514`].
4. J. Lesgourgues and S. Pastor, *Massive neutrinos and cosmology*, *Phys. Rep.* **429** 307–379, [`astro-ph/0603494`].
5. Planck Collaboration, P. A. R. Ade et al., *Planck 2013 results. XX. Cosmology from Sunyaev-Zeldovich cluster counts*, *ArXiv e-prints* [`arXiv:1303.5080`].
6. F. Beutler et al., *The clustering of galaxies in the SDSS-III Baryon Oscillation Spectroscopic Survey: Signs of neutrino mass in current cosmological datasets*, *ArXiv e-prints* [`arXiv:1403.4599`].
7. R. K. Sheth and G. Tormen, *Large-scale bias and the peak background split*, *MNRAS* **308** 119–126, [`astro-ph/9901122`].

NON-LINEAR DESCRIPTION OF MASSIVE NEUTRINOS IN THE FRAMEWORK OF LARGE-SCALE STRUCTURE FORMATION

H. DUPUY[1,2]
[1] *Institut de Physique Théorique, CEA, IPhT, URA 2306 du CNRS, F-91191 Gif-sur-Yvette, France*
[2] *Institut d'Astrophysique de Paris, UMR 7095 du CNRS, Université Pierre et Marie Curie, 98 bis bd Arago, 75014 Paris, France*

There is now no doubt that neutrinos are massive particles fully involved in the non-linear growth of the large-scale structure of the universe. A problem is that they are particularly difficult to include in cosmological models because the equations describing their behavior in the non-linear regime are cumbersome and difficult to handle. In this manuscript I present a new method allowing to deal with massive neutrinos in a very simple way, based on basic conservation laws. This method is still valid in the non-linear regime. The key idea is to describe neutrinos as a collection of single-flow fluids instead of seeing them as a single hot multi-flow fluid. In this framework, the time evolution of neutrinos is encoded in fluid equations describing macroscopic fields, just as what is done for cold dark matter. Although valid up to shell-crossing only, this approach is a further step towards a fully non-linear treatment of the dynamical evolution of neutrinos in the framework of large-scale structure formation.

1 Introduction

Observational cosmology has been particularly fruitful recently, as evidenced by the great success of the Planck mission [1,2]. From the theoretical point of view, such an achievement naturally opens perspectives. Any component of the universe involved in large-scale structure formation has to be examined minutely. In particular, the discovery of the massiveness of neutrinos has triggered a considerable effort in theoretical and numerical cosmology to infer the impact of this mass on the evolution of cosmological perturbations.

The first study in which massive neutrinos are properly treated in the linear theory of gravitational perturbations dates back from Ma & Bertschinger (1994) [3] (see also its companion paper Ma & Bertschinger (1995) [4]). Besides, the connection between neutrino masses and cosmology is investigated in full detail in Lesgourgues & Pastor (2006) [5]. To a large extent, current and future cosmology projects aim at exploiting this connection to put constraints on the neutrino masses. Such surveys are sensitive to the non–linear growth of structure, whence the importance of studying the non-linear regime in cosmological perturbation theory. In this manuscript, I summarize the results of Dupuy & Bernardeau (2014) [6], in which the authors design analytical tools to explore the impact of massive neutrinos on large-scale structure growth within the non-linear regime.

2 The standard linear description of neutrinos

The strategy usually adopted to describe neutrinos, massive or not, is calqued from that used to describe the radiation fluid: neutrinos are considered as a single hot multi-stream fluid whose evolution is dictated by the behavior of its distribution function in phase-space f. The key equation is the Boltzmann equation. For neutrinos, contrary to radiation, it is taken in the collisionless limit since neutrinos do not interact with ordinary matter (neither at the time of recombination nor after). It leads to the Vlasov equation, $\frac{\mathrm{d}f}{\mathrm{d}\eta} = 0$, where η is a time coordinate.

The standard linear description of neutrinos is based i) on a decomposition of the phase-space distribution function $f(\mathbf{x}, \mathbf{q})$ into a homogeneous part and a first-order inhomogeneous contribution,

$$f(\mathbf{x}, \mathbf{q}) = f_0(q)\,[1 + \Psi(\mathbf{x}, \mathbf{q})] \tag{1}$$

and ii) on a decomposition of the latter into harmonic functions. Using the notations of Dupuy & Bernardeau (2014) [6] and working in the conformal Newtonian gauge, the Vlasov equation leads to the following equation for Ψ (in momentum space),

$$\partial_\eta \tilde{\Psi} + \mathrm{i}\alpha k \frac{q}{a\epsilon} \tilde{\Psi} + \left(\partial_\eta \phi - \mathrm{i}\alpha k \frac{a\epsilon}{q} \psi \right) = 0, \tag{2}$$

where the local momentum is defined through its norm q and its direction $\hat{n}$, $\mathbf{k}$ is the wave vector introduced when moving to Fourier space, $\alpha \equiv \hat{k}.\hat{n}$ and $\tilde{\Psi} \equiv \left(\frac{\mathrm{d}\log f_0(q)}{\mathrm{d}\log q} \right)^{-1} \Psi$. The following step is to expand $\tilde{\Psi}$ using Legendre polynomials thus one introduces the moments $\tilde{\Psi}_\ell$,

$$\tilde{\Psi} = \sum_\ell (-\mathrm{i})^\ell \tilde{\Psi}_\ell \, P_\ell(\alpha), \tag{3}$$

where $P_\ell(\alpha)$ is the Legendre polynomial of order ℓ. By plugging this expansion into the Boltzmann equation (2), one obtains the standard hierarchy,

$$\begin{aligned}
\partial_\eta \tilde{\Psi}_0(\eta, q) &= -\frac{qk}{3a\epsilon} \tilde{\Psi}_1(\eta, q) - \partial_\eta \phi(\eta) && (4)\\
\partial_\eta \tilde{\Psi}_1(\eta, q) &= \frac{qk}{a\epsilon} \left(\tilde{\Psi}_0(\eta, q) - \frac{2}{5} \tilde{\Psi}_2(\eta, q) \right) - \frac{a\epsilon k}{q} \psi(\eta), && (5)\\
\partial_\eta \tilde{\Psi}_\ell(\eta, q) &= \frac{qk}{a\epsilon} \left[\frac{\ell}{2\ell - 1} \tilde{\Psi}_{\ell-1}(\eta, q) - \frac{\ell + 1}{2\ell + 3} \tilde{\Psi}_{\ell+1}(\eta, q) \right] \quad (\ell \geq 2). && (6)
\end{aligned}$$

Finally, relevant physical quantities can be built out of the coefficients $\tilde{\Psi}_\ell(\eta, q)$. This approach is powerful and largely used in the litterature. But, unfortunately, it is valid in the linear regime only.

To get a non-linear description, which is essential to do precision cosmology, one can e.g compute the fully non-linear moments of the Vlasov equation. The corresponding non-linear hierarchy is given in the PhD thesis of N. Van de Rijt (2012) [7],

$$\begin{aligned}
&\partial_\eta A^{i_1 \dots i_n} + (\mathcal{H} - \partial_\eta \phi) \left[(n+3) A^{i_1 \dots i_n} - (n-1) A^{i_1 \dots i_n jj} \right] \\
&+ \sum_{m=1}^{n} (\partial_{i_m} \psi) A^{i_1 \dots i_{m-1} i_{m+1} \dots i_n} + \sum_{m=1}^{n} (\partial_{i_m} \phi) A^{i_1 \dots i_{m-1} i_{m+1} \dots i_n jj} \\
&+ (1 + \phi + \psi) \partial_j A^{i_1 \dots i_n j} + [(2-n)\partial_j \psi - (2+n)\partial_j \phi]\, A^{i_1 \dots i_n j} = 0,
\end{aligned} \tag{7}$$

where

$$A^{ij\dots k} \equiv \int \mathrm{d}^3\mathbf{q} \left[\frac{q^i}{a\epsilon} \frac{q^j}{a\epsilon} \dots \frac{q^k}{a\epsilon} \right] \frac{\epsilon f}{a^3}, \tag{8}$$

ϵ being the energy measured by an observer at rest in the metric. Although interesting because fully non-linear, this hierarchy is obviously very difficult to handle. As a matter of fact, the non-linear equations one can find in the litterature to describe neutrinos are generally not exploitable because of their complexity. An analytical description of neutrinos in the non-linear regime is therefore still missing.

3 The non-linear description of cold dark matter, a model to follow

In this section, I present a non-linear description of cold dark matter (for notations and more details, see Bernardeau (2013)[8]). In this framework, cold dark matter is described as a collection of identical point particles, non-relativistic and sensitive to gravitational interaction only. Using the Newtonian approximation, its time evolution is encoded in the Vlasov-Poisson system, which leads to the continuity and Euler equations

$$\frac{\partial \delta(\mathbf{x},t)}{\partial t} + \frac{1}{a}[(1+\delta(\mathbf{x},t))u_i(\mathbf{x},t)]_{,i} = 0, \tag{9}$$

$$\frac{\partial u_i(\mathbf{x},t)}{\partial t} + \frac{\dot{a}}{a}u_i(\mathbf{x},t) + \frac{1}{a}u_j(\mathbf{x},t)u_i(\mathbf{x},t)_{,j} = -\frac{1}{a}\Phi(\mathbf{x},t)_{,i} - \frac{(\rho(\mathbf{x},t)\sigma_{ij}(\mathbf{x},t))_{,j}}{a\rho(\mathbf{x},t)}. \tag{10}$$

A major simplification comes from *the single-flow approximation*. This approximation consists in neglecting the velocity dispersion term σ_{ij} because, in a cold fluid, it is extremely small compared to the velocity gradients induced by density fluctuations. This assumption breaks down as soon as shell-crossing starts. Very little analytical results are known in presence of shell-crossing so description is then purely numerical.

Besides, the Euler equation shows that, in the single-flow approximation, the velocity field is a gradient. Equations can thus be much simplified when introducing the velocity divergence θ.

Finally, those two specificities of cold dark matter allow to write the motion equations on a compact form (see Bernardeau (2013)[8] for notations)

$$\frac{\partial \Psi_a(\mathbf{k},\eta)}{\partial \eta} + \Omega_a{}^b(\eta)\Psi_b(\mathbf{k},\eta) = \gamma_a{}^{bc}(\mathbf{k}_1,\mathbf{k}_2)\Psi_b(\mathbf{k}_1,\eta)\Psi_c(\mathbf{k}_2,\eta), \tag{11}$$

where $\Psi_a(\mathbf{k},\eta) \equiv (\delta(\mathbf{k},\eta), -\theta(\mathbf{k},\eta))$. This compact expression makes the writing of a formal solution possible

$$\Psi_a(\mathbf{k},\eta) = g_a{}^b(\eta)\Psi_b(\mathbf{k},\eta_0) + \int_{\eta_0}^{\eta} \mathrm{d}\eta' g_a{}^b(\eta,\eta')\gamma_b{}^{cd}(\mathbf{k}_1,\mathbf{k}_2)\Psi_c(\mathbf{k}_1,\eta')\Psi_d(\mathbf{k}_2,\eta'). \tag{12}$$

This is a very good starting point for the development of theories allowing to establish a connection with some interesting observables. The formalism that has to be developed to do this is explained in detail in Bernardeau (2013)[8]. It is now well-established and it can be considered as a model to follow when it comes to study the impact of neutrinos on large-scale structure formation in the non-linear regime.

4 A non-linear alternative to the standard description of neutrinos

The leading idea of Dupuy & Bernardeau (2014)[6] is to describe neutrinos as a collection of single-flow fluids instead of considering them as a single multi-flow fluid in order to take advantage of the single-flow approximation. This approximation can not be applied directly to the overall neutrino fluid because, unlike cold dark matter, there is no reason why velocity dispersion should be small for neutrinos. To circumvent the problem, the overall neutrino fluid is splitted into several flows in this study. Each flow, or each neutrino fluid, is defined as the collection of all the particles that have a given initial velocity. Such fluids are thus actually single-flow fluids and remain single flow-fluids until shell-crossing starts. In practice, it starts when neutrino velocities become low enough for gravity to make neutrinos turn around. So, at that time, neutrinos are not relativistic anymore and behave as cold dark matter. Describing this phenomenon is beyond the scope of this study. So far, it is also beyond the scope of the study of cold dark matter. Actually, the aim is not to do better than the cold dark matter description but to approach this level of description for neutrinos.

The first equation of motion is simply the conservation of the number of particles in each neutrino fluid, which gives in a perturbed Friedmann-Lemaître metric (written in the conformal Newtonian gauge)

$$\partial_\eta n - (1 + 2\phi + 2\psi)\partial_i \left(\frac{P_i}{P_0} n\right) = 3n(\partial_\eta \phi - \mathcal{H}) + n(2\partial_i \psi - \partial_i \phi)\frac{P_i}{P_0}, \tag{13}$$

where n is the proper number density and P_i is the comoving momentum field. To obtain this, only linear terms in the metric perturbations ψ and ϕ have been taken into account. Indeed, observations demonstrate that what matters in the non-linear regime is not metric-metric coupling but the non-linear growth of the fields.

Moreover, for a single-flow fluid, the conservation of the energy-momentum tensor combined with the conservation of the number of particles gives an equation for P_i only,

$$\partial_\eta P_i - (1 + 2\phi + 2\psi)\frac{P_j}{P_0}\partial_j P_i = P_0 \partial_i \psi + \frac{P_j P_j}{P_0}\partial_i \phi. \tag{14}$$

This equation shows in particular that the linear part of P_i is a gradient. This property is interesting since the fact that the velocity field is a gradient is one of the key ingredients of the cold dark matter description. The set of equations (13, 14) is a relativistic generalization of the motion equations of cold dark matter. It is fully equivalent to the non-linear moments of the Boltzmann equation (7). The advantage is that it is much more manageable in the non-linear regime than an infinite non-linear hierarchy.

Some numerical tests have been realized in order to compare this approach to the standard one. The goal was to compute the overall (i.e. integrated over all the neutrino fluids) multipole energy distribution and to check that it gives the same values as integration of the linear Boltzmann hierarchy. Calculations are thus perfomed in the linear regime only. As illustrated on Fig.1, the agreement between both approaches is extremely good.

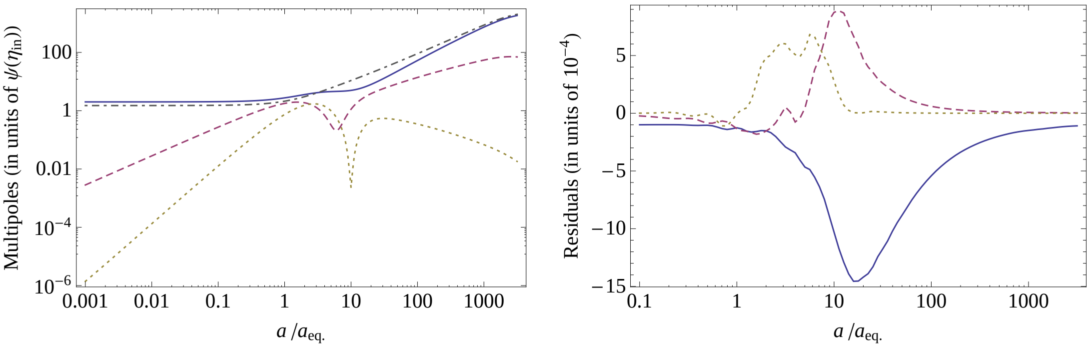

Figure 1 – Time evolution of the energy density contrast (solid line), velocity divergence (dashed line) and shear stress (dotted line) of the neutrinos. The dot-dashed line is presented for comparison and corresponds to the density contrast of the dark matter component. Left panel: the quantities are computed with the multi–fluid approach. Right panel: residuals (defined as the relative differences) when the two methods are compared. Numerical integration has been done with 40 neutrino fluids, k is set to $k_{\rm eq} \approx 0.01h$/Mpc and the neutrino mass m is set to 0.3 eV. The resulting relative differences are of the order of 10^{-3}.

By its specificity, the multi-fluid approach allows also to show the convergence of the number density contrast and of the velocity divergence of each flow to the ones of the cold dark matter component. As an illustration of this phenomenon, the time evolution of the velocity divergences of several neutrino fluids is presented on Fig. 2.

5 Conclusion

This manuscript presents a new method to study analytically the non-linear time evolution of neutrinos. As for cold dark matter, it is valid up to shell-crossing only. Nevertheless, this

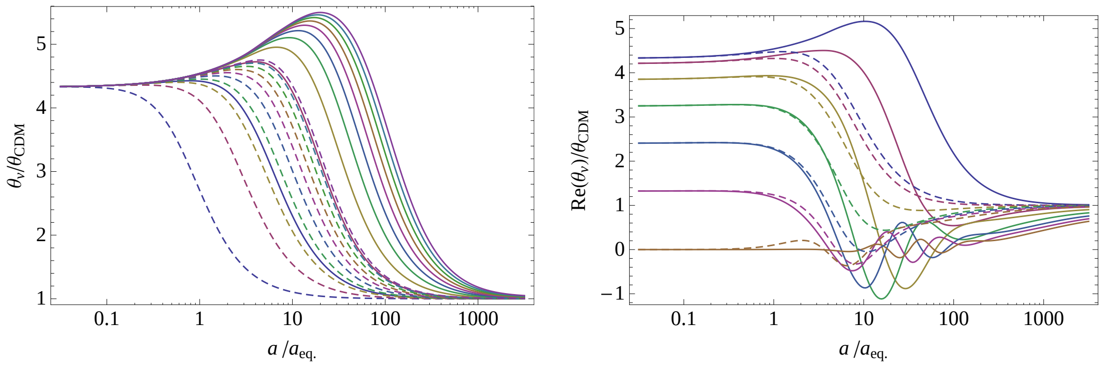

Figure 2 – Time evolution of the velocity divergence. Left panel: values of the initial velocity moduli, denoted τ, range from $0.45\,k_BT_0$ (bottom lines) to $9\,k_BT_0$ (top lines) with $\mu = 0$ (μ being the cosine of the angle between the initial velocity vector and the wave vector). Right panel is for $\tau = 3.6\,k_BT_0$ and μ ranging from $\mu = 0$ (top lines) to $\mu = 1$ (bottom lines). The time evolution of the velocity divergence of each flow is plotted in units of the dark matter velocity divergence. The wave number is set to $k_{\rm eq}$, the solid lines correspond to a 0.05 eV neutrino mass and the dashed lines to a 0.3 eV neutrino mass.

approach is a further step towards a fully non-linear treatment of neutrinos in the framework of large-scale structure formation.

Acknowledgments

H.D thanks the organizing committee of the 49th *Rencontres de Moriond* for offering her the opportunity to attend the cosmology session and to give a talk there. She is also grateful to her advisor F. Bernardeau, with whom she has worked on the study presented in this manuscript. Finally, she thanks Cyril Pitrou, Jean-Philippe Uzan and Pierre Fleury for insightful discussions and encouragements. The work presented here is partially supported by the grant ANR-12-BS05-0002 of the French Agence Nationale de la Recherche.

References

1. Planck Collaboration, P. A. R. Ade, N. Aghanim, C. Armitage-Caplan, M. Arnaud, M. Ashdown, F. Atrio-Barandela, J. Aumont, C. Baccigalupi, A. J. Banday, and et al. Planck 2013 results. I. Overview of products and scientific results. *ArXiv e-prints*, March 2013.
2. Planck Collaboration, P. A. R. Ade, N. Aghanim, C. Armitage-Caplan, M. Arnaud, M. Ashdown, F. Atrio-Barandela, J. Aumont, C. Baccigalupi, A. J. Banday, and et al. Planck 2013 results. XVI. Cosmological parameters. *ArXiv e-prints*, March 2013.
3. C.-P. Ma and E. Bertschinger. A calculation of the full neutrino phase space in cold + hot dark matter models. Astrophys. J. , 429:22–28, July 1994.
4. Chung-Pei Ma and Edmund Bertschinger. Cosmological perturbation theory in the synchronous and conformal Newtonian gauges. *Astrophys. J.*, 455:7–25, 1995.
5. Julien Lesgourgues and Sergio Pastor. Massive neutrinos and cosmology. *Phys. Rept.*, 429:307–379, 2006.
6. H. Dupuy and F. Bernardeau. Describing massive neutrinos in cosmology as a collection of independent flows. *J. of Cosmology and Astr. Phys.* , 1:30, January 2014.
7. N. Van de Rijt. *Signatures of the primordial universe in large-scale structure surveys.* PhD thesis, Ecole Polytechnique & Institut de Physique Théorique, CEA Saclay, 2012.
8. F. Bernardeau. The evolution of the large-scale structure of the universe: beyond the linear regime. *ArXiv e-prints*, November 2013.

Leptonic asymmetry and neutrino hierarchy after PLANCK

L.A. Popa, A. Caramete, D. Tonoiu
Institute of Space Science,
Bucharest-Magurele, Ro-077125 Romania

Recently, the PLANCK satellite found a larger and most precise value of the matter energy density, that impacts on the present values of other cosmological parameters such as the Hubble constant, the present cluster abundances, and the age of the Universe. The existing tension between PLANCK determination of these parameters in the frame of the base ΛCDM model and their determination from other measurements generated lively discussions, one possible interpretation being that some sources of systematic errors in cosmological measurements are not completely understood. An alternative interpretation is related to the fact that the CMB observations, that probe the high redshift Universe are interpreted in terms of cosmological parameters at present time by extrapolation within the base ΛCDM model that can be inadequate or incomplete. In this paper we quantify this tension by exploring several extensions of the base ΛCDM model that include the leptonic asymmetry and neutrino hierarchy.

1 Introduction

The lower value of Hubble parameter, H_0, found by PLANCK [1] in the frame of the base ΛCDM model is consistent (within 1σ) with the value of H_0 obtained by the WMAP experiment [2] but in tension (at about 2.5σ) with H_0 local measures [3,4]. Also, PLANCK found an increased value of the local cluster abundance which is in significant tension (at about 3σ) with similar values reported by other analysis [5,6,7], including the analysis of PLANCK cluster counts [1].
Since clusters provide estimates of the cluster mass normalization condition, this uncertainty is dominated by the impact of Ω_m on the growth function, but also depends on other parameters such as neutrino mass. A recent work [8] illustrate how a more accurate cluster mass-observable relation in determining the cluster mass normalization impacts on the neutrino mass determination, contributing to alleviate this tension significantly.

In this paper we quantify the existing tension between the PLANCK data and other astrophysical measurements by exploring several extensions of the base ΛCDM model that include the leptonic asymmetry. The existence of a large leptonic asymmetry is restricted to be in the form of neutrinos from the requirement of universal electric neutrality. The leptonic asymmetry is most conveniently measured by the neutrino degeneracy parameter defined as $\xi_\nu = \mu_\nu / T_{\nu,0}$, where μ_ν is the neutrino chemical potential and $T_{\nu,0}$ is the present temperature of the neutrino background $[T_{\nu,0}/T_{CMB} = (4/11)^{1/3}]$. The most important impact of the leptonic asymmetry is the increase of the radiation energy density that, for three neutrino species with degenerated chemical potential ξ_ν, can be parametrized by:

$$\Delta N_{eff}(\xi_\nu) = 3\left[\frac{30}{7}\left(\frac{\xi_\nu}{\pi}\right)^2 + \frac{15}{7}\left(\frac{\xi_\nu}{\pi}\right)^4\right] . \tag{1}$$

The radiation extra energy density can then be splitted in two uncorrelated contributions:

$$\Delta N_{eff} = \Delta N_{eff}(\xi) + \Delta N_{eff}^{oth}\,, \tag{2}$$

first due to the net leptonic asymmetry of the neutrino background and second due to the extra contributions from other unknown processes. The radiation extra energy density delays the time of matter-radiation equality, boosting the acoustic Doppler peaks of the CMB power spectrum. For the same reasons the acoustic peaks are shifted to higher multipoles. The leptonic asymmetry also shifts the beta equilibrium between protons and neutrons at the BBN epoch, leading to indirect effects on the CMB anisotropy through the primordial helium abundance, Y_P, that decreases monotonically with increasing ξ_e.

2 Model, methods and datasets

For our cosmological analysis we use a modified version of the latest publicly available package CosmoMC[9] to sample from the space of possible cosmological parameters and generate estimates of the posterior mean of each parameter of interest and the confidence interval. We use the following datasets: first public release of Planck Collaboration temperature data, combined with WMAP-9 year polarization information at low ℓ; High-l data from ground-based telescopes Atacama Cosmology Telescope(ACT)[10,11] and the South Pole Telescope (SPT)[6,12]; geometrical constraints from baryon acoustic oscillation (BAO) extracted from the Sloan Digital Sky Survey (SDSS) Data Releases DR7 and DR9[13] and the 6dF Galaxy Survey (6dFGS)[14,15] measurements; BBN prediction of the helium abundance, Y_P, for different values of $\Omega_b h^2$, ΔN_{eff} and ξ_ν used in the analysis, as given by the BBN PArthENoPE code[16].
For H_0 we use two most recent local determination[3,4] $H_0 = 74.08 \pm 2.25$ kms^{-1}Mpc^{-1} . We also employ the cluster mass-observable relation that gives the dependence of cluster abundances, S_8, on cluster mass calibration in the form[17]:

$$S_8 = S_{8,V09} + 0.024\frac{\Delta \ln M}{0.09}\,, \qquad S_{8,V09} = \sigma_8(\Omega_m/0.25)^{0.47} = 0.813\,, \tag{3}$$

where $\Delta\ln M$ is the cluster mass calibration offset relative to $S_{8,V09}$. We consider two mass calibration offset values, P11 $= -0.12 \pm 0.02$ adopted by Planck team[18] and R12 $= 0.11 \pm 0.04$ corresponding to the cluster mass scale employed in Ref. [19].
For the case of non-degenerate massive neutrinos we consider the mass eigenvalues m_1, m_2 and m_3 ordered in normal hierarchy (NH: $m_1 < m_2 < m_3$) and in inverted one (IH: $m_3 < m_1 < m_2$). The neutrino total mass for each hierarchy is given by:

$$\begin{aligned} \mathrm{NH}: \Sigma m_\nu &= m_{min} + \sqrt{\Delta m_{21}^2 + m_{min}^2} + \sqrt{\Delta m_{31}^2 + m_{min}^2}\,, \;\; m_{min} = m_1\,, \\ \mathrm{IH}: \Sigma m_\nu &= \sqrt{m_{min}^2 - \Delta m_{32}^2 - \Delta m_{21}^2} + \sqrt{m_{min}^2 - \Delta m_{32}^2} + m_{min}\,, \;\; m_{min} = m_3\,, \end{aligned} \tag{4}$$

where Δm_{21}, Δm_{31}, Δm_{32} are the neutrino mass squared differences obtained from the global fit of neutrino mixing parameters[20].

3 Results

Figure 1 presents the marginalized posterior probability distributions for S_8 obtained from the fits of different extentions of the base ΛCDM model to the Planck+WP+highL+BAO+lensing dataset vs. S_8 values obtained by using the cluster mass-observation relation for two mass calibration offset values P11[18] and R12[19] and S_8 - H_0 joint confidence regions obtained for the different extensions of the base ΛCDM model. The extensions by allowing the presence of the extra relativistic species and one thermal sterile neutrino alters the physical scales associated to CMB and BAO, broadening the allowed ranges for H_0 and S_8 posterior distributions to include a

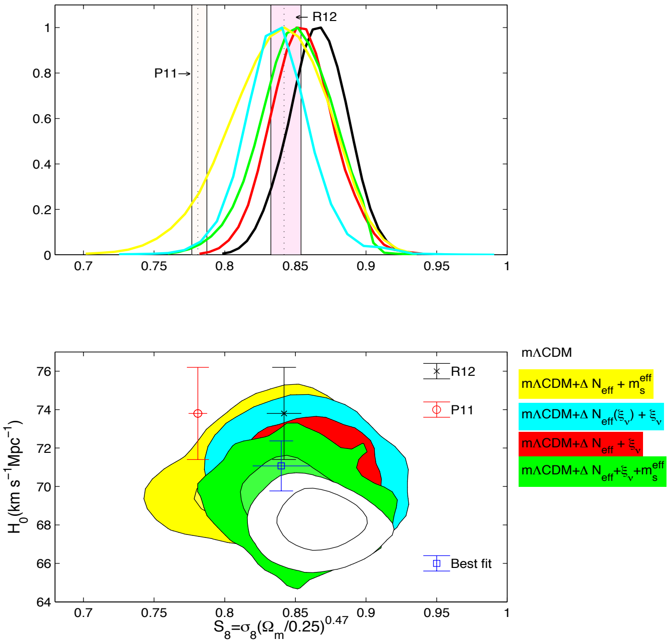

Figure 1 – Top: The marginalized posterior probability distributions for S_8 obtained from the fits of different extentions of the base ΛCDM model to the Planck+WP+highL+BAO+lensing dataset vs. S_8 values obtained by using the cluster mass-observation relation for two mass calibration offset values P11[18] and R12[19] (indicated by bands). Bottom: S_8 - H_0 joint confidence regions (at 68% and 95% CL) obtained from the same analysis.

larger overlap with the corresponding values from other measurements. We find for this models that the discrepancies with the local measure of H_0 and the determination of S_8 are alleviated at 1.35σ and 0.14σ respectively.

Figure 2 presents the neutrino mass eigenstates ordered in normal hierarchy (NH: $m_1 < m_2 < m_3$) and in the inverted one (IH: $m_3 < m_1 < m_2$) as obtained from the fit of different extentions of the base ΛCDM model to the Planck+WP+highL+BAO+lensing dataset.

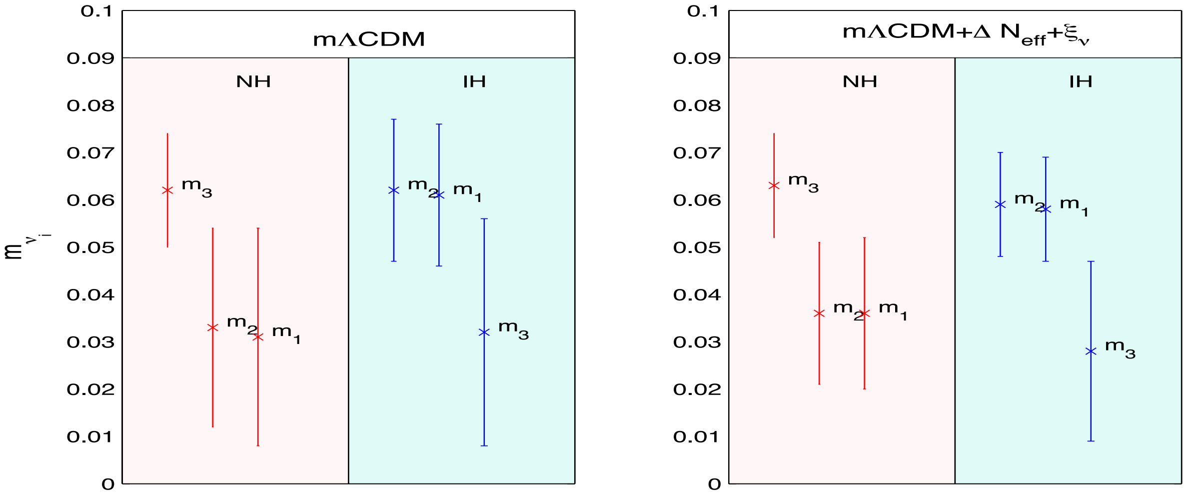

Figure 2 – Neutrino mass eigenstates ordered in the normal hierarchy (NH: $m_1 < m_2 < m_3$) and in the inverted one (IH: $m_3 < m_1 < m_2$) obtained from the fit of different extentions of the base ΛCDM model to the Planck+WP+highL+BAO+lensing dataset (1σ error bars).

The results presented demonstrate the preference of cosmological data for the case of cosmological model involving neutrino chemical potential ($\xi_\nu \neq 0$) and three massive neutrino species (m_s^{eff}=0) with direct mass hierarchy, that favors a total neutrino mass $\Sigma m_\nu \sim 0.132$ eV ($\sim 2\sigma$ statistical evidence). For the case of non-degenerated neutrino masses we find that the best fit values for H_0 and S_8 are in agreement with their local measures within 1.1σ and 0.5σ respectively.

We conclude that the current cosmological data favor the leptonic asymmetric extension of $m\Lambda$CDM cosmological model and normal neutrino mass hierarchy over the models with additional sterile neutrino species and/or inverted neutrino mass hierarchy.

Acknowledgments
This work was supported by CNCSIS Contract 82/2013 and by ESA/PECS Contract C98051. We also acknowledge the use of the GRID computing system facility at the Institute of Space Science Bucharest and would like to thank the staff working there.

References

1. Planck Collaboration, P. A. R. Ade et al., arXiv:1303.5080 (2013).
2. WMAP Collaboration, G. Hinshaw et al., *Astrophys. J. Suppl* **208**, 25 (2013).
3. A. G. Riess, et al., *Astrophys J.* **730**, 119 (2011).
4. W. L. Freedmann et al., *Astrophys J.* **758**, 10 (2012).
5. B. A. Benson, T. de Haan, J. P. Dunkley et al., *Astropys J.* **763**, 21 (2013).
6. C. L. Reichardt et al., *Astropys J.* **755**, 70 (2012).
7. M. Hasselfield, M. Hilton et al., *JCAP* **07**, 008 (2013).
8. E. Rozo et al., arXiv:1302.5086 (2013).
9. A. Lewis and S. Bridle, *Phys. Rev.* **D 66**, 103511 (2002).
10. S. Das et al., arXiv: 1301.1037 (2013).
11. J. Dunkley et al., *JCAP* **07**, 025 (2013).
12. R. Keisler et al., *The Astrophys. J.* **743**, 17 (2011).
13. W. J. Percival et al., *Mon. Not. Roy. Astron. Soc.*, **401**, 2148 (2010).
14. D. H. Jones et al., *Mon. Not. Roy. Astron. Soc.* **399**, 683 (2009).
15. F. Beutler et al., *Mon. Not. Roy. Astron. Soc.* **416**, 3017 (2011) 3017.
16. O. Pisanti et al., *Computer Physics Communications* **178**, 956 (2008) 956.
17. A. Vikhlinin et al., *The Astrophysical Journal* **692**, 1033 (2009) [arXiv:0805.2207].
18. Planck Collaboration, P. A. R. Ade et al., *Astronomy & Astrophysics* **536**, A11 (2011).
19. E. Rozo et al., arXiv:1204.6305 (2012).
20. M. C. Gonzalez-Garcia, M. Maltoni, J. Salvado, T. Schwetz *JHEP* **1212**, 123 (2012).

7.
Theory

DARK ENERGY, NEWTON'S LAW & THE LHC
Vacuum Energy: the Dog that Didn't Bark

C.P. Burgess
Dept. of Physics & Astronomy, McMaster University, Hamilton, ON, Canada, L8S 4M1
Perimeter Institute for Theoretical Physics, Waterloo, ON, Canada N2L 2Y5
Division PH-TH, CERN, CH-1211, Genève 23, Suisse.

This note briefly summarizes two things. First, it states why I believe progress understanding Dark Energy hinges crucially on finding a solution to the 'old' Cosmological Constant Problem, and more generally reviews why technical naturalness provides such an important clue to solving problems in cosmology. A set of criteria are formulated for judging success when discussing prospective solutions to the problem with their proponents, with a goal to helping properly hold everyone's feet to the fire. Second, I summarize what I see as the most promising approach (so far), which is possibly the only known technically natural solution yet proposed. Its consistency tests and observational predictions are summarized, as well as a list of outstanding problems.

1 Naturalness and the Cosmological Constant Problems

Nature is a tease. On one hand fundamental puzzles are all around us: the universe is literally full of stuff — Dark Matter and Dark Energy — whose basic nature we do not understand. Cosmological observations reveal primordial fluctuations that expose properties of the Universe as it was when temperatures and densities were mind-bogglingly high. On the other hand all of the usual experimental approaches to reaching a better understanding of these issues — such as experiments at accelerators, most recently the Large Hadron Collider, or Dark Matter detectors — continue to support the vanilla Standard Model and General Relativity (SM+GR); a 40-year-old theory we know does not describe Dark Energy and Dark Matter.

The relative absence of experimental guidance leaves considerable scope for explaining Dark Matter: it could consist of new kinds of weakly interacting particles or axion-like coherent fields which can come in any number of varieties. The variety of possible theories has spawned a large number of ingenious ways for searching for Dark Matter, either by direct detection on Earth or through indirect detection through astrophysical observations. Although it is frustrating not to have found yet new physics, absence of evidence is not yet evidence for absence because many sensible models predict too small a signal to have been seen. In the meantime let a thousand detectors bloom.

The situation is completely different for Dark Energy. In one sense Dark Energy is boring: as revealed by cosmological observations its properties are completely consistent with it being the gravitational effects of a vacuum energy. It has long been known that such an energy is possible, and (so far) all cosmological observations completely support this interpretation. If true it predicts a relatively boring world in which the Dark energy density is constant in time, and its gravitational effects eventually comes to dominate the Universe completely.

But boredom is not the real problem with Dark Energy; the real problem is that we think we can compute the vacuum's energy and calculations of known contributions from our best theory (SM+GR) are factors of 10^{54} (or more) too big for a successful description of observations. The problem is the vacuum should have a lot of quantum zero-point energy, with each weakly interacting field contributing of order $m^4/(4\pi)^2$, so even the electron, with $m \simeq 5 \times 10^5$ eV, contributes more than 10^{30} times more than the observed value $\rho_{\rm vac} \simeq (3 \times 10^{-3}$ eV$)^4$. Furthermore, the problem gets worse the heavier the particle involved becomes.

The difficulty finding a theory where quantum contributions to the vacuum energy are not enormously larger than the measured Dark Energy density is called the 'old' cosmological constant problem[1,2,3]. (The 'new' problems essentially ask why the measured Dark Energy density is small, given the assumption that some mechanism can be found to make the vacuum energy contribution precisely vanish.)

There is a great opportunity here: because heavier particles contribute the largest amounts, the vacuum energy is an unusually sensitive observable to the properties of physics at the highest energies. It is likely to be very informative to exclude all theories of these scales whose vacuum energy cannot reproduce the observed Dark Energy density.

But there is also disappointment: this criterion is too informative inasmuch as no candidate theories pass this test, at least according to the most prevalent assessments. That is, there is no consensus that any theories satisfy all of the following three criteria:

- Make sense in a quantum context (so zero-point energy can be computed), and give a small Dark Energy density once quantum corrections are included;
- Make sense at energies larger than the cosmological constant (well above 1 eV, say, where particles can be massive enough to be a problem);
- Not ruin anything else we know about Nature, be it particle physics, tests of gravity or cosmology.

It is this lack of any viable candidate at all that is unusual, and has in many quarters led to an abandonment of the cosmological constant problem (and naturalness arguments more generally) as a useful criterion for sifting theories.

This may in the end be right, but I think things are not yet so bad because I think there is an approach to the problem which is promising, and (so far) seems to work.

2 Supersymmetric Large Extra Dimensions: our best shot

Recall what is the essence of the problem: on one hand we believe quantum effects generate large vacuum energies, and the vacuum's Lorentz invariance automatically makes the resulting stress-energy look like a cosmological constant: $T_{\mu\nu} = -\rho_{\rm vac} g_{\mu\nu}$. On the other hand cosmologists measure very small curvatures when they detect the acceleration of the universe's expansion. The problem is that these are directly equated in Einstein's equations,

$$G^{\mu\nu} = \kappa^2 T^{\mu\nu} = \kappa^2 \rho_{\rm vac}\, g^{\mu\nu}\,, \tag{1}$$

which makes the size and simplicity of the vacuum stress energy an obstruction to having a small curvature. It is the inevitability of this obstruction that makes solving the problem so difficult. (The discussion here closely follows that of the review[2].)

The extra-dimensional loophole

It is important to emphasize that it is both the simplicity *and* the size of the vacuum stress-energy that are at the heart of the problem, even though it is only the size that is normally emphasized. To see the role that simplicity plays it is useful to reformulate the problem in a setting where the vacuum's Lorentz invariance is less constraining.

This is most easily done using extra dimensions, because in an extra-dimensional world we only really know that the vacuum must be Lorentz invariant in the four dimensions that we can see. We also only really know that the curvatures are observed to be small in these same dimensions (which are the ones we can access in cosmology). And although it remains true that the vacuum stress energy must curve something, in extra-dimensional models nothing says it must curve the dimensions we see. This is the loophole through which one can try to seek a solution.

The simplest example of how extra dimensions can break the direct link between vacuum energy and curvature is furnished by the gravitational field of a cosmic string in four dimensions. Imagine that a relativistic cosmic string sweeps out a world-sheet along the $z-t$ plane, transverse to the $x-y$ directions. The stress energy of such a string is Lorentz invariant in the $z-t$ directions, $T_{ab} = -\mathcal{T} g_{ab}\, \delta^2(x)$, where $\mathcal{T}$ is the string's tension (*i.e.* mass per unit length), and a, b denotes the $z-t$ directions along the string world-sheet. The gravitational field produced by this stress energy is known[4] and the geometry of the two transverse directions turns out to be a cone, whose apex is located at the position of the string. The tension on the string gives rise to a curvature singularity there, $R \propto \kappa^2 \mathcal{T}\, \delta^2(x)$, appropriate to a cone, but what is important is that the geometry along the two Lorentz-invariant $z-t$ directions remains perfectly flat, regardless of the precise value of $\mathcal{T}$.

This suggests exploring a brane-world framework where we are localized on a 4D version of a cosmic string within six dimensions. In the simplest examples the two extra dimensions might have the geometry of a sphere, and there is a brane located at both the sphere's north and south poles (at which points the transverse curvature also has conical singularities, like for a cosmic string). All standard model particles are imagined to be confined to one of these branes, whose tension (*i.e.* vacuum energy per unit volume) is not particularly small — of order $(1 \text{ TeV})^4$. The hope is that the on-brane geometry seen by an observer can remain flat regardless of the size of the brane vacuum energy density.

Doubling Down: Supersymmetric large extra dimensions

Six-dimensional theories with these properties do indeed exist, however that is not in itself enough to solve the cosmological constant problem. It is not because other solutions also exist for which the on-brane directions are curved too strongly to be consistent with cosmological observations. One must ask what physical choices for the branes suffice to make them flat,[5] and once these are identified the cosmological constant problem in this new context asks whether these choices get ruined by quantum fluctuations.

These questions can be (and have been) asked and answered in simple six-dimensional models, that show that quantum perturbations actually do unacceptably curve the on-brane directions. One way to see why this is plausible is that it is generically possible to have a cosmological constant in the extra dimensions, and even though this is not what is given by the vacuum energy of purely brane-localized particles, its presence in the gravitational field equations amplifies the effects of a brane localized vacuum energy to give an unacceptably large on-brane curvature[6].

There is a better chance if the extra-dimensional physics is supersymmetric,[7,8] however, because in six (and higher) dimensions supersymmetry forbids a cosmological constant (much as would more than one supersymmetry in four dimensions). It turns out that this absence helps suppress the on-brane curvature that is sourced by changes to the vacuum energy on one of the branes, with the result that the curvature is naturally as large as would be expected if the Dark-Energy density were of order the Casimir energy in the extra dimensions: [9,10]

$$\rho_{\rm vac} \simeq \frac{1}{(4\pi L^2)^2}\,, \tag{2}$$

where L is the linear size of the two dimensions transverse to the branes.

Indeed, in certain circumstances the result can even be smaller than this because the branes sometimes fail to break supersymmetry at one loop [8]. In this case the leading quantum contribution to the observed 4D cosmological constant turns out to involve one brane and one bulk loop, and so would be of order

$$\delta\rho_{\rm vac}(1\text{ bulk} + 1\text{ brane loop}) \simeq \frac{k'}{(4\pi)^4}\, M^4\, e^{2\phi} \simeq \frac{k'}{(4\pi L)^4}\,, \tag{3}$$

where $k \simeq k'/(4\pi)^2$ for a new dimensionless constant, k'.

Interestingly, in a six-dimensional brane-world observations allow $1/L \simeq 0.1$ eV, and so L can be large enough that eq. (2) need not be a problem. The best constraints come from by tests of Newton's inverse-square law [11] and from limits on the amount of energy-loss into the extra dimensions from stars and supernovae that is possible [12,13]. Furthermore, because 4D and 6D Planck masses are related by $M_p \simeq M_6^2 L$, having L this large is also what is required to reconcile a 6D scale, $M_6 \simeq \mathcal{O}(10\text{ TeV})$, with the observed 4D Planck mass.

Through the suppression of these loops by bulk supersymmetry, the cosmological constant is asking us to double down; to postulate extra dimensions that are both very large *and* very supersymmetric (*i.e.* Supersymmetric Large Extra Dimensions, or SLED for short [14,2,15]).

Notice that supersymmetry in the bulk does *not* also require the physics on the brane to be supersymmetric, and for most purposes we may simply choose only the Standard Model to live on the brane [16]. Such a brane can nonetheless be coupled consistently to supergravity using the 'Stückelberg trick'; that is, regarding the non-supersymmetric brane to be supersymmetric, but nonlinearly realized, by coupling a Goldstone fermion — the Goldstino — in the appropriate way.

This leads to a novel kind of picture[16,17]: a very supersymmetric gravity (or extra-dimensional, bulk) sector (whose supersymmetry breaking scale is of order $1/L \simeq 10^{-2}$ eV) coupled to a particle (brane) sector that is not supersymmetric at all. In particular, the nonlinear realization of supersymmetry on the brane implies that a supersymmetry transformation of a brane particle like the electron gives the electron plus a Goldstino (or, equivalently, a gravitino) rather than a selectron. One does not expect to find a spectrum of MSSM superpartners for the Standard Model, despite the very supersymmetric gravity sector. This particular prediction was made [16] well before the LHC results showed it to be a huge success.

In the end, what is the mechanism that suppresses loops?

Why does extra-dimensional supersymmetry help so much, even though the on-brane 'particle-physics' sector need not be supersymmetric at all? It is worth distilling the underlying mechanism, since this provides a robust understanding of whether and why it can be a property of any UV completion (such as for string theory).

In essence the six-dimensional models appear to be successful to the extent that they incorporate the following two features, both of which seem obtainable from plausible UV completions:

- *Distributed SUSY breaking:* The explicit 6D models have the property that some supersymmetry is preserved locally within any local patch within the extra dimensions, but is broken globally once these patches are all stitched together. Because of this, the very short-wavelength modes that are the usual problem for the vacuum energy do not 'know' that supersymmetry is broken and so that a nonzero vacuum energy is allowed. It is only once modes with wavelengths of order L are integrated out that the implications of SUSY breaking become felt, generically leading to a Casimir energy size, as in eq. (2).

This type of SUSY breaking is not in itself so unusual, since it arises also in Scherk-Schwarz symmetry breaking by boundary conditions. If it were the entire story, all it would tell us is that the supersymmetry-breaking scale is the Kaluza-Klein (KK) scale, and then the absence of super-partners at the LHC would tell us that the KK scale cannot be lower than the TeV scale, and so SUSY would give no additional vacuum energy suppression below this. What is novel in the 6D theory is that Distributed SUSY breaking coincides with:

- *Accidental brane SUSY:* The most general low-energy effective action for a space-filling 4D brane in 6D, once any brane-localized particles are integrated out, is

  $$\mathcal{L}_b = \sqrt{-g}\; c T_b + {\mathcal{A}_b}^* F + \cdots \,, \tag{4}$$

  where $\mathcal{T}_b$ is the brane tension, and $\mathcal{A}_b$ represents the amount of bulk flux, F_{MN}, that is localized on the brane. This lagrangian automatically preserves some of the bulk supersymmetry, provided $\mathcal{T}_b$ and $\mathcal{A}_b$ are related by a 'BPS-like' condition of the form $\mathcal{T}_b = c_1 \mathcal{A}_b \, e^{\phi_b}$, for some constant c_1, where ϕ_b is the value taken at the brane of the particular bulk field, ϕ, whose value sets the gauge couplings for the bulk field, F_{MN}. What is important is that the value of ϕ is not set by any of the field equations, because ϕ is the dilaton for a classical scale symmetry of the supergravity equations. Its value is ultimately fixed by flux quantization, and so until one samples a the extra dimensions globally, once doesn't know that its value is inconsistent with supersymmetry on the near-brane patch.

This is what ensures that supersymmetry is locally preserved on a patch, even if it contains one of the branes, and even though the physics on each brane is not supersymmetric at all. When combined with distributed supersymmetry, this is what allows non-supersymmetric particle physics to coincide with a Casimir-sized effective vacuum energy density of order $1/L^4$.

Opportunities and worries

Most of the main issues have been checked in these models, but many other issues continue to be explored. These include opportunities for testing this proposal by comparison with observations, and continued consistency checks to ensure there are no hidden pitfalls to the extra-dimensional approach.

Opportunities

There are a variety of tests of this picture, as there must be for any proposal which deals with the 'old' cosmological constant problem. If Nature uses SLED to keep the cosmological constant technically natural, then expect to see:

- *Tests of Newton's inverse square law:* The gravitational inverse-square law must cross over to an inverse 4th-power law [20] at distances tied to the observed dark-energy density (of order a micron). Furthermore, there is a single Brans-Dicke scalar mode that is lighter than the KK scale, and so which leads to an exponential modification, $\exp(-m_{KK}r)$, at slightly larger distances. It would be hard to miss such a combination of modifications!

- *Signals in the LHC:* If the extra-dimensional Planck scale is of order 10 TeV then the Large Hadron Collider must be operating close to a regime where quantum gravity is important. Potential signals must include energy loss into the extra dimensions [21,16,17], although these would not yet have been expected to have been seen for $M_6 = \kappa_6^{-1/2} > 10$ TeV [22,23]. More detailed predictions depend on what the theory of quantum gravity at these scales really is. String theory provides the most precise framework in which to ask the question,[a] and suggests [25] that all Standard Model particles are likely to be accompanied by a tower of

---

[a] Unfortunately it is not yet known how to get the 6D chiral gauged supergravity from string theory, though attempts have been made [24].

string excitations, split by the string scale, M_s. The observable signals for this are likely to be similar to those for excited Kaluza Klein modes, for which searches are on-going [22,23].

- *Neutrino physics* need not, but could, contain observable effects coming from the mixing of brane-localized neutrinos with KK modes of bulk fermions, many of whom are required to be very light because they are tied by supersymmetry to the massless graviton [26,27]. If such mixing is present neutrino physics should contain potentially interesting evidence for a family of sterile neutrinos.

How does the SLED proposal do when compared with the three benchmark criteria given above for putative solutions to the CC problem?

It does very well on criteria 1 and 2: it is among the extremely few theories for which quantum corrections can be incorporated, and it does so for an energy range that includes the weak-scale particles whose masses are at the root of the problem. Work continues on criterion 3, which so far seems to be passed successfully, but for which a definitive statement requires a more robust determination of the effective 4D theory that controls macroscopic gravitational interactions.

Part of this story is the verification that one keeps the successes of standard cosmology. In particular one requires a theory of dark matter, which is still missing within SLED models. One might also worry that the BICEP2 discovery of gravitational waves kills all models with low-scale gravity, however inflationary solutions to 6D supergravity are also known [28], and all predict that the extra dimensions grow during inflation, proportional to $t^{1/2}$. Consequently, a prediction (made well before the BICEP2 results) is that the scales seen during inflation can be much higher than the TeV scales associated with gravity at present.

Another issue of concern asks: Why should the extra dimensions be so large in the first place? Understanding this requires understanding the physics that stabilizes the modulus ϕ_0 of the extra dimensions. Some ways for doing so have been explored and as we have seen flux quantization is one of the options [6]. This is how extra dimensions are stabilized in SLED, although at present the extra dimensions are made large by inserting a very small number directly into the lagrangian (through the value of $\mathcal{A}_b$). It would be preferable to only put a number of order 50 into the lagrangian and find that the extra dimensions acquire a radius that is the exponential of this.

In some ways the extra-dimensional framework does just what is required: it modifies only the gravitational sector of the theory, and does so at very low energies without doing damage to non-gravitational tests. It can do so because only gravity 'sees' the extra dimensions because all Standard Model particles are confined to a brane. Furthermore, it does so specifically for slow rather than fast process, as was argued earlier to be necessary. The slow/fast response arises because it is the way the extra dimensions back-react to the presence of the brane that underlies the small 4D curvature; after all, in the simplest models it is the conical curvature of the extra dimensions that cancels the brane tensions in the effective 4D cosmological constant [31]. But the extra dimensions do not have time to respond to changes on the brane that happen faster than the extra-dimensional light-crossing time: $\tau \simeq L/c \simeq 3 \times 10^{-15}$ sec. (Indeed, the development of tools to handle brane back-reaction [32] was a prerequisite for the systematic exploration of the extra-dimensional mechanism for suppressing the cosmological constant problem.)

So the greatest worry at present is that the same cancellations that make the vacuum energy gravitate less than expected also do the same for static mass distributions. That is, does extra-dimensional back-reaction unacceptably modify how macroscopic and slowly moving objects gravitate? This involves exploring solutions on the brane that are not maximally symmetric; an analysis of which is in progress.

3 Summary

So what is the bottom line? We argue that it is too early to despair about solving the CC problem, and that two supersymmetric large extra dimensions provide a promising direction to explore. It is a promising direction because extra dimensions break the direct link between a 4D Lorentz-invariant vacuum energy and a large 4D curvature. Furthermore, supersymmetry in the extra dimensions combines scale invariance and supersymmetry in a way that partially exploits the advantages of both for suppressing the cosmological constant.

If this is the way the world works we will soon know: besides the absence of superpartners at the LHC we must see deviations from Newton's inverse-square law at micron sizes and likely also see new physics at the LHC (and possibly for neutrinos). Conversely, it is easily falsifiable, such as if no deviations from Newton‘s inverse square law is found over sum-micron distances. One would also be uncomfortable if no evidence for quantum gravity (string excited states, missing energy) were to be found at the full-energy LHC.

Acknowledgments

I thank the organizers of this meeting for a stimulating meeting in a great setting, and for including me in their plans on fairly short notice. My ideas over the years on the cosmological constant and constraints on its solution have benefited from discussions with many people — Niayesh Afshordi, Yashar Aghababaie, Hugo Beauchemin, Jim Cline, Ross Diener, Rich Holman, Doug Hoover, Leo van Nierop, Susha Parameswaran, Maxim Pospelov, Fernando Quevedo, Alberto Salvio, Raman Sundrum, Gianmassimo Tasinato, Matt Williams, Itay Yavin and Ivonne Zavala. My research has been supported in part by the Natural Sciences and Engineering Research Council of Canada. Research at the Perimeter Institute is supported in part by the Government of Canada through Industry Canada, and by the Province of Ontario through the Ministry of Research and Information.

References

1. S. Weinberg, "The Cosmological Constant Problem," Rev. Mod. Phys. **61** (1989) 1-23.
2. For an expanded version of the point of view presented here, see C. P. Burgess, arXiv:1309.4133 [hep-th].
3. For other points of view on the cosmological constant problem see: S. M. Carroll, Living Rev. Rel. **4** (2001) 1 [astro-ph/0004075];
   P. Binetruy, Int. J. Theor. Phys. **39** (2000) 1859 [hep-ph/0005037];
   T. Padmanabhan, Phys. Rept. **380** (2003) 235 [hep-th/0212290];
   J. Frieman, M. Turner and D. Huterer, Ann. Rev. Astron. Astrophys. **46** (2008) 385 [arXiv:0803.0982 [astro-ph]].
4. A. Vilenkin, Phys. Rev. D **23** (1981) 852;
   R. Gregory, Phys. Rev. Lett. **59** (1987) 740;
   A. G. Cohen and D. B. Kaplan, *Phys. Lett.* **B215**, 67 (1988);
   A. Vilenkin and P. Shellard, *Cosmic Strings and other Topological Defects*, Cambridge University Press (1994);
   R. Gregory and C. Santos, Phys. Rev. D **56** (1997) 1194 [gr-qc/9701014].
5. C. P. Burgess, F. Quevedo, G. Tasinato and I. Zavala, JHEP **0411** (2004) 069 [hep-th/0408109];
   Y. Aghababaie, C. P. Burgess, J. M. Cline, H. Firouzjahi, S. L. Parameswaran, F. Quevedo, G. Tasinato and I. Zavala, JHEP **0309** (2003) 037 [hep-th/0308064];
   C. P. Burgess, C. de Rham, D. Hoover, D. Mason and A. J. Tolley, JCAP **0702** (2007) 009 [hep-th/0610078].
6. C. P. Burgess and L. van Nierop, JHEP **1104** (2011) 078 [arXiv:1101.0152 [hep-th]];

C. P. Burgess and L. van Nierop, JHEP **1102** (2011) 094 [arXiv:1012.2638 [hep-th]].

7. D. Hoover and C. P. Burgess, JHEP **0601** (2006) 058 [hep-th/0507293];
   C. P. Burgess and D. Hoover, Nucl. Phys. B **772** (2007) 175 [hep-th/0504004];
   C. P. Burgess, D. Hoover and G. Tasinato, JHEP **0906** (2009) 014 [arXiv:0903.0402 [hep-th]];
   M. Williams, C. P. Burgess, L. van Nierop and A. Salvio, JHEP **1301** (2013) 102 [arXiv:1210.3753 [hep-th]].
8. C. P. Burgess, L. van Nierop, S. Parameswaran, A. Salvio and M. Williams, JHEP **1302** (2013) 120 [arXiv:1210.5405 [hep-th]];
   C. P. Burgess, L. van Nierop and M. Williams, arXiv:1311.3911 [hep-th];
   C. P. Burgess, R. C. Myers and F. Quevedo, Phys. Lett. B **495** (2000) 384 [hep-th/9911164].
9. D. M. Ghilencea, D. Hoover, C. P. Burgess and F. Quevedo, JHEP **0509** (2005) 050 [hep-th/0506164];
   E. Ponton and E. Poppitz, JHEP **0106** (2001) 019 [hep-ph/0105021].
10. The idea that the vacuum energy might be a Casimir energy within a large-dimensional model was also noted in
    P. Chen and J. -A. Gu, astro-ph/0409238.
11. E. G. Adelberger, B. R. Heckel and A. E. Nelson, "Tests of the gravitational inverse-square law," Ann. Rev. Nucl. Part. Sci. **53**, 77 (2003) [arXiv:hep-ph/0307284];
    C. D. Hoyle, D. J. Kapner, B. R. Heckel, E. G. Adelberger, J. H. Gundlach, U. Schmidt and H. E. Swanson, "Sub-millimeter tests of the gravitational inverse-square law," Phys. Rev. D **70** (2004) 042004 [arXiv:hep-ph/0405262]. '
12. S. Cullen and M. Perelstein, "SN1987A constraints on large compact dimensions," Phys. Rev. Lett. **83** (1999) 268 [arXiv:hep-ph/9903422];
    V. D. Barger, T. Han, C. Kao and R. J. Zhang, "Astrophysical constraints on large extra dimensions," Phys. Lett. B **461** (1999) 34 [arXiv:hep-ph/9905474];
    C. Hanhart, D. R. Phillips, S. Reddy and M. J. Savage, "Extra dimensions, SN1987a, and nucleon-nucleon scattering data," Nucl. Phys. B **595** (2001) 335 [arXiv:nucl-th/0007016];
    S. Hannestad and G. G. Raffelt, "Stringent neutron star limits on large extra dimensions," Phys. Rev. Lett. **88** (2002) 071301 [arXiv:hep-ph/0110067]; "New supernova limit on large extra dimensions," Phys. Rev. Lett. **87** (2001) 051301 [arXiv:hep-ph/0103201].
13. D. Atwood, C. P. Burgess, E. Filotas, F. Leblond, D. London and I. Maksymyk, "Supersymmetric large extra dimensions are small and/or numerous," Phys. Rev. D **63** (2001) 025007 [arXiv:hep-ph/0007178];
14. Y. Aghababaie, C. P. Burgess, S. L. Parameswaran and F. Quevedo, Nucl. Phys. B **680** (2004) 389 [hep-th/0304256];
    C. P. Burgess and L. van Nierop, Phys. Dark Univ. **2** (2013) 1 [arXiv:1108.0345 [hep-th]].
15. For some (relatively old) reviews see
    C. P. Burgess, Annals Phys. **313** (2004) 283 [hep-th/0402200];
    C. P. Burgess, AIP Conf. Proc. **743** (2005) 417 [hep-th/0411140].
16. C. P. Burgess, J. Matias and F. Quevedo, Nucl. Phys. B **706** (2005) 71 [hep-ph/0404135].
17. P. H. Beauchemin, G. Azuelos and C. P. Burgess, J. Phys. G **30** (2004) N17 [hep-ph/0407196];
    G. Azuelos, P. H. Beauchemin and C. P. Burgess, J. Phys. G **31** (2005) 1 [hep-ph/0401125];
    J. Matias and C. P. Burgess, JHEP **0509** (2005) 052 [hep-ph/0508156];
18. M. Williams, C. P. Burgess, A. Maharana and F. Quevedo, JHEP **1108** (2011) 106 [arXiv:1103.4556 [hep-ph]];
19. R. Diener and C. P. Burgess, JHEP **1305** (2013) 078 [arXiv:1302.6486 [hep-ph]].
20. P. Callin and C. P. Burgess, Nucl. Phys. B **752** (2006) 60 [arXiv:hep-ph/0511216];
    C. P. Burgess, L. van Nierop and M. Williams, JHEP **1404** (2014) 032 [arXiv:1401.0511

[hep-th]].

21. G. F. Giudice, R. Rattazzi, J. D. Wells, "Quantum gravity and extra dimensions at high-energy colliders," Nucl. Phys. **B544** (1999) 3 [arXiv:hep-ph/9811291];
    T. Han, J. D. Lykken, R. -J. Zhang, "On Kaluza-Klein states from large extra dimensions," Phys. Rev. **D59** (1999) 105006 [arXiv:hep-ph/9811350];
    J. L. Hewett, "Indirect collider signals for extra dimensions," Phys. Rev. Lett. **82** (1999) 4765 [arXiv:hep-ph/9811356];
    G. F. Giudice and A. Strumia, "Constraints on extra dimensional theories from virtual graviton exchange," Nucl. Phys. B **663** (2003) 377 [arXiv:hep-ph/0301232].
22. J. Beringer et al. (Particle Data Group), Phys. Rev. D86, 010001 (2012).
23. For recent summaries see:
    M. Marionneau [on behalf of the ATLAS and CMS Collaboration], "Search for extra-dimensions, top-antitop resonances, 4th generation and leptoquark signatures at the LHC," Proceedings of the Moriond EWK 2013 conference, La Thuile, Italy (arXiv:1305.3169 [hep-ex]);
    F. Santanastasio [ATLAS and CMS Collaborations], "Exotic Phenomena Searches at Hadron Colliders," Proceedings of the PIC 2012, Strbske Pleso, Slovakia, (arXiv:1301.2521 [hep-ex]).
    R. Franceschini, P. P. Giardino, G. F. Giudice, P. Lodone and A. Strumia, "LHC bounds on large extra dimensions," JHEP **1105** (2011) 092 [arXiv:1101.4919 [hep-ph]].
24. M. Cvetic, G. W. Gibbons, C. N. Pope, "A String and M theory origin for the Salam-Sezgin model," Nucl. Phys. **B677** (2004) 164-180. [hep-th/0308026];
    T. G. Pugh, E. Sezgin, K. S. Stelle, "D=7 / D=6 Heterotic Supergravity with Gauged R-Symmetry," JHEP **1102** (2011) 115. [arXiv:1008.0726 [hep-th]];
    M. Cicoli, C. P. Burgess, F. Quevedo, "Anisotropic Modulus Stabilisation: Strings at LHC Scales with Micron-sized Extra Dimensions," [arXiv:1105.2107 [hep-th]].
25. For preliminary studies of string implications with 6 large dimensions see
    I. Antoniadis and K. Benakli, "Large dimensions and string physics in future colliders," Int. J. Mod. Phys. A **15** (2000) 4237 [arXiv:hep-ph/0007226].
    I. Antoniadis, E. Kiritsis, J. Rizos and T. N. Tomaras, "D-branes and the standard model," Nucl. Phys. B **660** (2003) 81.
    D. Lust, S. Stieberger and T. R. Taylor, "The LHC String Hunter's Companion," Nucl. Phys. B **808** (2009) 1 [arXiv:0807.3333 [hep-th]];
    D. Lust, O. Schlotterer, S. Stieberger and T. R. Taylor, "The LHC String Hunter's Companion (II): Five-Particle Amplitudes and Universal Properties," Nucl. Phys. B **828** (2010) 139 [arXiv:0908.0409 [hep-th]];
26. G. R. Dvali and A. Y. Smirnov, "Probing large extra dimensions with neutrinos," Nucl. Phys. B **563**, 63 (1999);
    N. Arkani-Hamed, S. Dimopoulos, G. R. Dvali and J. March-Russell, "Neutrino masses from large extra dimensions," Phys. Rev. D **65**, 024032 (2002).
    A. K. Das and O. C. W. Kong, "On neutrino masses and mixings from extra dimensions," Phys. Lett. B **470**, 149 (1999);
    R. N. Mohapatra, S. Nandi and A. Perez-Lorenzana, "Neutrino masses and oscillations in models with large extra dimensions," Phys. Lett. B **466**, 115 (1999);
    A. Lukas, P. Ramond, A. Romanino and G. G. Ross, "Solar neutrino oscillation from large extra dimensions," Phys. Lett. B **495**, 136 (2000);
    K. R. Dienes, "Extra dimensions and their implications for neutrino physics," Int. J. Mod. Phys. A **16S1C**, 925 (2001);
    R. N. Mohapatra and A. Perez-Lorenzana, "Three flavour neutrino oscillations in models with large extra dimensions," Nucl. Phys. B **593**, 451 (2001);
    C. S. Lam, "Large mixing induced by the strong coupling with a single bulk neutrino,"

Phys. Rev. D **65** (2002) 053009;

C. S. Lam and J. N. Ng, "Neutrino oscillations via the bulk," Phys. Rev. D **64** (2001) 113006;

A. De Gouvea, G. F. Giudice, A. Strumia and K. Tobe, "Phenomenological implications of neutrinos in extra dimensions," Nucl. Phys. B **623**, 395 (2002);

K. R. S. Balaji, A. S. Dighe and R. N. Mohapatra, "Neutrino magnetic moment, large extra dimensions and high energy cosmic neutrino spectra," [hep-ph/0202267];

J. Maalampi, V. Sipilainen and I. Vilja, "A scheme with two large extra dimensions confronted with neutrino physics," Phys. Rev. D **67**, 113005 (2003);

Q. H. Cao, S. Gopalakrishna and C. P. Yuan, "Collider signature of bulk neutrinos in large extra dimensions," Phys. Rev. D **70**, 075020 (2004).

27. J. Matias and C. P. Burgess, "MSLED, neutrino oscillations and the cosmological constant," JHEP **0509** (2005) 052 [arXiv:hep-ph/0508156];
28. L. van Nierop and C. P. Burgess, JCAP **1204** (2012) 037 [arXiv:1108.2553 [hep-th]];

    C. P. Burgess, A. Maharana, L. van Nierop, A. A. Nizami and F. Quevedo, JHEP **1204** (2012) 018 [arXiv:1109.0532 [hep-th]];
29. A. J. Tolley, C. P. Burgess, D. Hoover and Y. Aghababaie, JHEP **0603** (2006) 091 [hep-th/0512218];

    A. J. Tolley, C. P. Burgess, C. de Rham and D. Hoover, New J. Phys. **8** (2006) 324 [hep-th/0608083].
30. For similar ideas beyond the 6D context see

    B. R. Greene and J. Levin, JHEP **0711** (2007) 096 [arXiv:0707.1062 [hep-th]];

    J. P. Conlon, R. Kallosh, A. D. Linde and F. Quevedo, JCAP **0809** (2008) 011 [arXiv:0806.0809 [hep-th]].
31. J. W. Chen, M. A. Luty and E. Ponton, JHEP **0009** (2000) 012 [arXiv:hep-th/0003067];

    F. Leblond, R. C. Myers and D. J. Winters, JHEP **0107** (2001) 031 [arXiv:hep-th/0106140];

    S. M. Carroll and M. M. Guica, [arXiv:hep-th/0302067];

    I. Navarro, JCAP **0309** (2003) 004 [arXiv:hep-th/0302129];

    E. Papantonopoulos and A. Papazoglou, JCAP **0507** (2005) 004 [arXiv:hep-th/0501112].
32. C. P. Burgess, D. Hoover, C. de Rham and G. Tasinato, JHEP **0903** (2009) 124 [arXiv:0812.3820 [hep-th]];

    C. P. Burgess, D. Hoover and G. Tasinato, JHEP **0709** (2007) 124 [arXiv:0705.3212 [hep-th]];

    Y. Aghababaie, C. P. Burgess, S. L. Parameswaran and F. Quevedo, JHEP **0303** (2003) 032 [hep-th/0212091];

    A. Bayntun, C. P. Burgess and L. van Nierop, New J. Phys. **12** (2010) 075015 [arXiv:0912.3039 [hep-th]].

Super versus Sub-Planckian Inflation

A. Mazumdar
Consortium for fundamental Physics, Department of Physics, Lancaster University,
LA1 4YB, England

We will describe how sub-Planckian excursion of an inflaton field can generate tensor to scalar ratio of order $r \simeq 0.1 - 0.2$, and discuss the challenges of super-Planckian excursions

1 Introduction

The non-zero detection of primordial gravitational waves [1] has firmly confirmed one of the key predictions of primordial inflation, for a review, see [2]. During inflation both matter and gravitational fluctuations are dynamically stretched outside the Hubble patch. Both WMAP [3] and Planck [4] have detected the temperature anisotropy in the cosmic microwave background (CMB) fluctuations, and placed bounds on the tensor modes, but the firm detection by BICEP has definitely made a remarkable change in the way we would view primordial inflation nowadays. Ofcourse there are possibilities of mimicking the BICEP data with primordial magnetic field, which would mix both E and B mode poslarizations, see details [5], or a long phase of loitering universe [6], or in bouncing universe [7]. This is also the first direct evidence of quantum nature of gravity. The observed large amplitude of gravitational waves can not be excited without quantum initial conditions. In fact, there is no known classical mechanism to excite such a large amplitude gravitational waves, see [8].

It is standard to compare the amplitude of the primordial gravitational waves with respect to the amplitude of the scalar perturbations, usually denoted by the tensor to scalar ratio, r: $0.15 \leq r(k_*) \equiv \mathcal{P}_T(k_*)/\mathcal{P}_\zeta(k_*) \leq 0.27$, where the amplitudes of the matter power spectrum is denoted by: $\mathcal{P}_\zeta \sim 2.1 \times 10^{-9}$, which signifies the amplitude of the CMB temperature anisotropy. The power spectrum for the tensor fluctuations are denoted by: $\mathcal{P}_T$, at the pivot scale, $k_* = 0.002~\mathrm{Mpc}^{-1}$ [1]. Since the amplitude of the linearized gravitational waves for a slow roll inflation is given by: $\mathcal{P}_T = 16H_{inf}^2/\pi M_p^2 \approx 16V_{inf}/3\pi M_p^4 \sim 5.6 \times 10^{-10}$, where $H_{inf}^2 \approx (V_{inf}/3M_p^2)$ is the Hubble expansion rate during inflation, V_{inf} is the inflationary potential and $M_p \sim 2.44 \times 10^{18}$ GeV. We can extract the total potential, or the scale of inflation close to the Grand Unified Theory scale, ie. $V_{inf}^{1/4} \sim 2 \times 10^{16}$ GeV. This is *indeed* the first evidence of physical scale beyond the Standard Model and the scale of gravity at M_p.

The prime question arises what kind of inflationary potential would give rise to such a large r. In this respect we can discuss two classes of models, one where inflation occurs super-Planckian, such as in the case of chaotic inflation[9], and the other where inflation occurs sub-Planckian, for details, see [10,11,12,13], via inflection point inflation.

2 Super-Planckian inflation and the problem with an effective field theory(EFT)

Indeed, the prime motivation for arguing against super-planckian inflation is due to break down of an EFT. In order to have a valid effective field theory, one would require both, the energy density and the momentum to be below the cut-off, For scales much below the cut-off, the lowest order expansions do make sense, but when the energy/momentum scale reaches that of the cut-off, one would have to take all the terms into account and the validity of an EFT may not hold good in such regimes. The fact that the temperature anisotropy in the CMB is so small, i.e. $\Delta T/T \sim 10^{-5}$, suggests that $\rho_\phi \ll M_p^4$. However, if the VEV of the inflaton exceeds that of the Planck scale, i.e. $\langle\phi\rangle \geq M_p$, then the problem with an EFT comes into the game. Why shall we go for a super-Planckian inflation? because a simple model like *chaotic inflation*, with a potential of type: $V_{inf} \sim m_\phi^2\phi^2$ can yield large $r \sim 0.16$, and match the temperature anisotropy, provided $m_\phi \sim 10^{13}$ GeV. During inflation, $H_{inf} \sim m_\phi\phi/\sqrt{6}M_p$, for a slow roll inflation, the scale factor grows exponentially, i..e $a(t) \sim e^{H_{inf}t} \sim e^{\mathcal{N}}$, where $\mathcal{N}$ is the number of e-foldings of inflation. However, inflation in his case can occur only when $\phi \geq M_p$, roughly when $\phi \sim 10M_p$. This is an issue where the effective field theory breaks down. This happens not just because of the inflation, but the inflaton couplings to matter degrees of freedom.

The inflaton coupling to the Standard Model and hidden degrees of freedom and hidden degrees of freedom are inevitable. For instance, a coupling of type: $g\langle\phi\rangle\bar{\psi}\psi$ would yield a super-Planckian mass to ψ field for $g \sim 10^{-1}$. In which case, a super heavy fermion would collapse to form a primordial blackhole with a Planckian mass and with a Planckian Schwarzschild's radius. In fact if inflaton couples to n_* degrees of freedom, then there will be n_* such blackholes, in principle, one can imagine an inflaton to couple to a sea of blackholes. Then the total energy density stored in this sea of blackholes would be roughly of the order of $\sim (n_* m_\psi)^4 \sim (10ngM_p)^4$, for $m_\psi \sim g\langle\phi\rangle$ and $\langle\phi\rangle \sim 10M_p$. In fact, this energy density should be less than the inflaon energy density, which requires, $(10n_*gM_p)^4 \leq (m_\phi^2\phi^2) \sim 10^{64}$ (GeV)^4, or $n_*g \leq 10^{-3}$.

In fact, this counting is similar to the quantum corrections one would induce from $g\phi\bar{\psi}\psi$ interactions, which would yield: $\lambda\phi^4$ term, for $\lambda \leq 10^{-12}$, we would require: $g \leq 10^{-3}$. Unfortunately, there is no known fundamental theory which would constrain either n_* or g at this moment. Furthermore, there are radiative quantum corrections which would introduce terms like: $\sum_n \lambda_n\phi^n/M_p^{n-4}$, where λ_n could be computed based on the inflaton interaction. Similar corrections could be induced by graviton-loops for $n > 4$ and $\lambda_n \sim \mathcal{O}(1)$, unless the inflaton itself is gauged and protected by quantum gravity corrections.

Besides the potential, there are less-known corrections arise from the kinetic term of the inflaton itself, higher derivative terms. Such higher derivative terms arise in string theory in the context of α' corrections, protect shift symmetry, and they are inevitable once we embed inflation within string theory. Such corrections also arise purely from the gravitational sector, which are ignored typically in the inflationary literature due to *sheer ignorance*[14].

3 Sub-Planckian inflation

Reproducing large $r \sim 0.2$ is also not an easy task for sub-Planckian models of inflation. Sub-Planckian models of inflation will also suffer similar criticism if there were another scale below M_p, such as string scale, M_s or the compactification scale, M_c. However, if we simply assume that there is *only* one scale in nature, i.e. M_p, and if we wish to restrict ourselves only below that scale, i.e. the VEV of the inflaton and the energy density while matching the current data.

The answer is thumping, yes!. A simple example was given in the context of *Assisted Inflation*, where many fields dynamically assist inflation[15]. Suppose we take N-copies of inflaton with: $V \sim \sum_i^N m_i^2 \phi_i^2$. In which case, it is indeed possible to obtain exactly the same predictions as the chaotic inflation, with $r \sim 0.16$, and all $m_i \approx m$ and $\phi_i \sim 0.1 M_p$, but $N \sim 10^3 - 10^4$. Such a realisation was first proposed in Refs. [16].

Here, we will provide a single field realisation which would give rise to large $r \sim 0.27$, while keeping the inflaton VEV below M_p. This happens mainly due to the shape of the potential, it is such that the field evolves from large VEVs, but below M_p and above the *point of inflection*, passes through the *point of inflection* and then monotonically decreases to the minimum of the potential, see[17]. For a *slow roll* inflation this gives rise to a non-monotonic evolution of the two slow roll parameter: ϵ and η. Here, we illustrate the steps, for details, see [18].

<u>**Step 1**</u>: Following Refs. [11,10], let us consider a generic potential, which is expanded in a Taylor series around the sub-Planckian VEV, $\phi_0 < M_P$ as:

$$V(\phi) = V(\phi_0) + V^{'}(\phi_0)(\phi-\phi_0) + \frac{V^{''}(\phi_0)}{2}(\phi-\phi_0)^2 + \frac{V^{'''}(\phi_0)}{6}(\phi-\phi_0)^3 + \frac{V^{''''}(\phi_0)}{24}(\phi-\phi_0)^4 + \cdots \quad (1)$$

where we have truncated the Taylor expansion as: $V(\phi_0) > V^{'}(\phi_0) > V^{''}(\phi_0) > V^{''''}(\phi_0)$ (in the Planckian unit) , which is also the necessary condition for the convergence of the Taylor series. Note that ϕ_0 denotes the VEV where inflation occurs in its vicinity.

<u>**Step 2**</u>: We can derive a simple expression for the tensor-to-scalar ratio, r, as, see [18,12,11,10]:

$$r = \frac{8}{M_p^2} \frac{(1-\epsilon_V)^2 \left[1 - (\mathcal{C}_E + 1)\epsilon_V\right]^2}{\left[1 - (3\mathcal{C}_E + 1)\epsilon_V + \mathcal{C}_E \eta_V\right]^2} \left(\frac{d\phi}{d\ln k}\right)^2 + \cdots , \quad (2)$$

where $\mathcal{C}_E = 4(\ln 2 + \gamma_E) - 5$ with $\gamma_E = 0.5772$ is the *Euler-Mascheroni constant*, ϵ_V, η_V are slow roll parameters, there are higher order terms in slow roll parameters, of order $\mathcal{O}(\epsilon_V^2)$, $\mathcal{O}(\eta_V^2) \cdots$, which will give negligible contributions and would not alter the results of our discussion. We can now derive a bound on $r(k)$ in terms of the momentum scale: $\left|\int_{k_e}^{k_\star} \frac{dk}{k} \sqrt{r(k)/8}\right| \approx (|\Delta\phi|/M_p)(1 + \cdots) \approx |\Delta\phi|/M_p$. where $\Delta\phi = \phi_\star - \phi_e$ and we have neglected the contributions from the $\cdots$ terms as they are small compared to the leading order term due to the convergence of the series mentioned in Eq (1). Here ϕ_e denotes the inflaton VEV at the end of inflation, and $\phi_\star$ denote the field VEV when the corresponding mode $k_\star$ is leaving the Hubble patch during inflation.

<u>**Step 3**</u>: We can perform the momentum integration in the left hand side of $r(k)$ analytically by parameterising it as:

$$r(k) = r(k_\star)\left(\frac{k}{k_\star}\right)^{a + \frac{b}{2}\ln\left(\frac{k}{k_\star}\right) + \frac{c}{6}\ln^2\left(\frac{k}{k_\star}\right)} , \quad a = n_T - n_S + 1, \; b = (\alpha_T - \alpha_S)\,, \; c = (\kappa_T - \kappa_S)\,. \quad (3)$$

which are defined at the scale $k_\star$, and determined by the spectral indices, n_S, n_T, running of the spectral indices, α_S, α_T, and running of the running of the spectral indices, κ_S, κ_T. Here the subscripts, $(S,\ T)$, represent the scalar and tensor modes. After some algebra, we obtain:

$$\int_{k_e}^{k_\star} \frac{dk}{k}\sqrt{\frac{r(k)}{8}} = \sqrt{\frac{r(k_\star)}{8}} \int_{k_e}^{k_\star} \frac{dk}{k} \sqrt{\left(\frac{k}{k_\star}\right)^{a + \frac{b}{2}\ln\left(\frac{k}{k_\star}\right) + \frac{c}{6}\ln^2\left(\frac{k}{k_\star}\right)}} = \sqrt{\frac{r(k_\star)}{8}} \int_{k_e}^{k_\star} \frac{dk}{k_\star} \left(\frac{k}{k_\star}\right)^{A + B\ln\left(\frac{k}{k_\star}\right) + C\ln^2\left(\frac{k}{k_\star}\right)} , \quad (4)$$

where $A = (a/2 - 1)$, $B = b/4$, $C = c/12$. To evaluate the integral analytically, we apply the following technique: $(\ln y)^\alpha$, where $\alpha << 1$, where the exponent α is defined as: $\alpha = A + B\ln(\ln y) + C\ln^2(\ln y)$, where $k/k_* = \ln y$. Note that $|B|$, $|C| \ll 1$, and $|A| < 1$ for certain values of n_T, we know $n_s = 0.96$, but there are no observational constraints on n_T, which we can use it in our favour. Within the momentum interval, $k_e < k < k_\star$: $\Delta N = N_e - N_\star = \ln(k_\star/k_e) \approx \ln(a_\star/a_e)$, $\longrightarrow k_e/k_\star \approx a_e/a_\star = \exp(-\Delta N)$, within this interval sub-Plankian field excursion $|\Delta\phi| < M_p$ implies that, $\left|\frac{\Delta N V'(\phi_0) M_p}{V(\phi_0)}\right| < 1$, where $\Delta N \approx 17$. Further simplifying, we obtain:

$$\begin{aligned}\int_{k_e}^{k_\star} \frac{dk}{k}\sqrt{\frac{r(k)}{8}} = \sqrt{\frac{r(k_\star)}{8}}\Big[\Big(2-\tfrac{a}{2}+\tfrac{b}{2}-\tfrac{c}{2}\Big)\Big[1-e^{-\Delta N}\Big]+\Big(\tfrac{a}{2}-\tfrac{b}{2}+\tfrac{c}{2}-1\Big)\Delta N\ e^{-\Delta N} \\ -\Big(\tfrac{b}{4}-\tfrac{c}{4}\Big)(\Delta N)^2\ e^{-\Delta N}+\tfrac{c}{12}(\Delta N)^3\ e^{-\Delta N}\Big]. \end{aligned} \tag{5}$$

Using these facts, we can recast $a,\ b,\ c$ in terms of the slow-roll parameters , and the final expression becomes:

$$\begin{aligned} 2\times\sqrt{\frac{r(k_\star)}{8}}\,\Bigg|\Bigg\{\frac{r(k_\star)}{16}-\frac{\eta_V(k_\star)}{2}-1-\Big(6\mathcal{C}_E+\tfrac{23}{3}\Big)\epsilon_V^2(k_\star)-\frac{\eta_V^2(k_\star)}{6}+(\mathcal{C}_E-1)\,\frac{\xi_V^2(k_\star)}{2} \\ -\Big(2\mathcal{C}_E-\tfrac{8}{3}\Big)\eta_V(k_\star)\epsilon_V(k_\star)-\frac{\sigma_V^3(k_\star)}{2}+\cdots\Bigg\}\approx\frac{|\Delta\phi|}{M_p}\ll 1 \end{aligned} \tag{6}$$

where the denominators of $r(k_\star)$ can be normalized according to upper bound of BICEP2 and Planck. The above expression is in the form of a simple algebraic (cubic) equation. In order to find the roots of tensor-to-scalar ratio r in terms of the field excursion $|\Delta\phi|/M_p$, one has to solve a cubic equation: $x^3+cx-d=0$, where $c,\ d>0$, one can find one physical solution and 2 imaginary roots. Within the range of field excursion, $\Delta\phi \sim (10^{-1}M_p) < M_p$, it is possible to generate large tensor modes, with $r \geq 0.1$. For an example, in the case of a high scale MSSM inflation, with $\eta_V(k_\star) \sim \mathcal{O}(10^{-2})$, and $\Delta\phi \sim \mathcal{O}(10^{-1}M_p) < M_p$, it is possible to obtain: $r \sim \mathcal{O}(0.12-0.27)$. (See the analogous expressions in Refs. [11] and [12], where the prefactors and the denominators of $r(k_\star)$ were adjusted according to the upper bound of BICEP2 and Planck data.).

References

1. P. A. R. Ade *et al.* [BICEP2 Collaboration], arXiv:1403.3985 [astro-ph.CO].
2. A. Mazumdar and J. Rocher, Phys. Rept. **497**, 85 (2011)
3. G. Hinshaw *et al.* [WMAP Collaboration], Astrophys. J. Suppl. **208**, 19 (2013)
4. P. A. R. Ade *et al.* [Planck Collaboration], arXiv:1303.5076 [astro-ph.CO].
5. C. Bonvin, R. Durrer and R. Maartens, arXiv:1403.6768 [astro-ph.CO].
6. R. H. Brandenberger, A. Nayeri, S. P. Patil and C. Vafa, Phys. Rev. Lett. 98, 231302 (2007). T. Biswas, R. Brandenberger, A. Mazumdar and W. Siegel, JCAP **0712**, 011 (2007) R. H. Brandenberger, A. Nayeri and S. P. Patil, arXiv:1403.4927 [astro-ph.CO].
7. R. Brustein, M. Gasperini, M. Giovannini, and G. Veneziano: Phys. Lett. B **361**, 45 (1995) T. Biswas, T. Koivisto and A. Mazumdar, arXiv:1403.7163 [hep-th].
8. A. Ashoorioon, P. S. B. Dev and A. Mazumdar, arXiv:1211.4678 [hep-th].
9. A. D. Linde, Phys. Lett. **129B**, 177 (1983).
10. S. Choudhury and A. Mazumdar, arXiv:1403.5549 [hep-th].
11. S. Choudhury and A. Mazumdar, Nucl. Phys. B **882**, 386 (2014)
12. S. Choudhury, A. Mazumdar and S. Pal, JCAP **1307**, 041 (2013)
13. S. Hotchkiss, A. Mazumdar and S. Nadathur, JCAP **1202**, 008 (2012)
14. D. Chialva and A. Mazumdar, arXiv:1405.0513 [hep-th].
15. A. R. Liddle, A. Mazumdar and F. E. Schunck, Phys. Rev. D **58**, 061301 (1998) E. J. Copeland, A. Mazumdar and N. J. Nunes, Phys. Rev. D **60**, 083506 (1999) A. Jokinen and A. Mazumdar, Phys. Lett. B **597**, 222 (2004)
16. P. Kanti and K. A. Olive, Phys. Lett. B **464**, 192 (1999) P. Kanti and K. A. Olive, Phys. Rev. D **60**, 043502 (1999)
17. K. Enqvist, A. Mazumdar and P. Stephens, JCAP **1006**, 020 (2010)
18. S. Choudhury and A. Mazumdar, arXiv:1404.3398 [hep-th].

Bubble Observers in Bubbland

Federico R. Urban^1, with David F. Mota^2 and Mikjel Thorsrud^2
^{1} *Service de Physique Théorique, Université Libre de Bruxelles,*
CP225, Boulevard du Triomphe, B-1050 Brussels, Belgium
^{2} *Institute of Theoretical Astrophysics, University of Oslo, P.O. Box 1029 Blindern, N-0315 Oslo, Norway*

Inflation typically produces exponentially too many bubbles. Having access to only one Hubble horizon, we (may) experience a bias in cosmological observations, because modes whose wavelengths are beyond our causal horizon today can have a distinct, quantitative as well as structural, effect on observables. Nonetheless, despite our local patch being only a limited sample of Bubbland, we are still able to infer definite statistical predictions from within our Hubble Bubble.

Introduction

In the standard model of cosmology the Universe kicks off with inflation [1], an accelerating expanding epoch whose final result is Bubbland, a smooth macrobubble typically exponentially larger than our causally accessible Hubble bubble. In this case the link between our observables and the parameters of the high energy theory of inflation may be biassed, because the background of superhorizon infrared modes which eschew our sight — modes that at a given time are larger than the observer's horizon, but within the full inflated patch — represent a space-time dependent framework upon which smaller wavelenghts develop [2]. Observations made in a given bubble might differ from those performed at another location, since the particular realisation we observe needs not coincide with the average across Bubbland. Thus, predictions for observables become a statistical problem, with a mean and average dictated by the parameters of the fundamental theory (the inflaton Lagrangian), and those describing the observer (the size of the patch we have access to).

We explicitly show here how this comes about in a canonical scalar inflation model with a (collection of) subdominant massless gauge field(s) thrown in. We work with the ghost-free interaction Lagrangian I^2F^2, with $I(\phi)$ an inflaton-dependent coupling for the (multitude of) gauge field(s) $A_\mu^{(i)}$, for which $F_{\mu\nu}^{(i)}$ is the strength. The case where $I(\tau) \sim a^{-2}$, with $a(\tau)$ the scale factor of the Friedmann-Lemaître-Robertson-Walker metric (τ is conformal time), is the most interesting one as it is an attractor solution for this type of couplings [3].

The Infrared Background

The gauge kinetic coupling produces a nearly scale-invariant spectrum of frozen electric-type modes $\delta\mathbf{E}(\mathbf{k}) = -I(\phi)\partial_\tau\delta\mathbf{A}(\mathbf{k})/a^2$, while the magnetic-type components decay rapidly. Quantum modes become classical (commuting) as their wavelengths are stretched to superhorizon size. The integral over these $k < \mathcal{H}(\tau)$ modes ($\mathcal{H} \equiv aH \equiv \partial_\tau a/a$ is the comoving Hubble parameter) adds up to a (collection of) classical infrared vector(s) $\mathbf{E}_{IR}^{(i)}(\tau)$. Such vectors appear homogeneous for a local Hubble-limited observer: it will be pointing in a certain direction and will have a constant magnitude over the accessible causal patch. This results in a quadrupolar — courtesy of the shape of the Lagrangian — correction to the total power spectrum $\mathcal{P}(\mathbf{k})$ for the curvature operator $\zeta_\mathbf{k}$ (see below).

Statistics and Physics of the Quadrupole

And it is not the end of the story. The infrared vectors indeed experience a *precession* phenomenon. This can be understood as follows. At each time-step during inflation some new gauge modes go superhorizon; these modes need not (in fact, will not) have the same orientation. The background infrared vector field is the ever-changing sum of these modes, and thus performs a random walk in the space of all possible directions. At different locations the generated quadrupole would be *different*, since there is no reason for the direction of the infrared vectors to be the same in locations separated by more than our Hubble length.

The first consequence of this effect is that the quadrupole will in general not be axisymmetric, as it would be the case if there were no dynamics (one static vector). Five parameters then are needed to fully describe the quadrupolar correction (in a spherical harmonic $Y(\theta, \phi)$ decomposition, these would be the conventional a_{2m}); however, under the assumption that these parameters depend on momentum all in the same way, three of them can be parametrised away thanks to the (approximate) rotational invariance of the background: one is left with two parameters, which we identify in the amplitude g_0 and the shape χ [4].

In practice, the correction to $\mathcal{P}(\mathbf{k})$ is calculated via the in-in formalism

$$\delta \langle \zeta_{\mathbf{k}} \zeta_{\mathbf{p}}(\tau) \rangle = - \int \mathrm{d}\tau_1 \mathrm{d}\tau_2 \left\langle \left[\left[\zeta^{(0)}_{\mathbf{k}} \, \zeta^{(0)}_{\mathbf{p}}, H_{\text{int}}(\tau_1) \right], H_{\text{int}}(\tau_2) \right] \right\rangle \equiv 2\pi^2 \frac{\delta^3(\mathbf{k}+\mathbf{p})}{k^3} \delta\mathcal{P}(\mathbf{k}) \tag{1}$$

where the nested time integrals have to be taken from the beginning of inflation to a given conformal time τ; here $\zeta^{(0)}$ is the unperturbed curvature perturbation, and the effective, dominant interaction Hamiltonian is

$$H_{\text{int}}(\tau) = -\frac{4}{H^4 \tau^4} \int \mathrm{d}^3 k \; \left(\mathbf{E}^{IR}(\tau) \cdot \delta\mathbf{E}(\mathbf{k}, \tau) \right) \zeta^{(0)}_{-\mathbf{k}} \tag{2}$$

One Field

What is the observational relevance of these two parameters? For a single vector the axial symmetry is almost fully unbroken. How? Recall that the only reason for $\mathbf{E}^{IR}(\tau)$ to rotate *after* a given curvature perturbation with wavelength $1/k$ has crossed the horizon, is that new vector fluctuations $\delta\mathbf{E}$ with wavelengths *smaller* than $1/k$ become infrared and are added to $\mathbf{E}^{IR}$. Now, if we are probing a mode smaller than our causal patch, its infrared background includes modes which, despite them being superhorizon during inflation, they can not be viewed as background from the point of view of our observations today (they are smaller than our patch). As first approximation we subtract from $\mathbf{E}^{IR}$ any mode with wavelengths smaller than $1/\mathcal{H}_0$. This means that we evaluate $\mathbf{E}^{IR}(\tau)$ at the time our current Hubble patch has left the horizon during inflation τ_0, some 60 e-folds or so — backward counting from the end. The resulting spectrum only knows about one final gauge vector background configuration [4]:

$$\frac{\delta\mathcal{P}(\mathbf{k})}{\mathcal{P}_0} \simeq \frac{24}{\epsilon} \frac{|\mathbf{E}^{IR}(\tau_0)|^2}{3H^2} (N_{\text{tot}} - N_k)^2 \sin^2 \psi \tag{3}$$

where $\mathcal{P}_0 = H^2/8\pi^2\epsilon$ is the unperturbed spectrum ($\epsilon\mathcal{H}^2 \equiv \mathcal{H}^2 - \mathcal{H}'$) and $\cos\psi \equiv \hat{k} \cdot \mathbf{E}^{IR}(\tau_0)$. The spectrum is not exactly flat due to the logarithmic dependence on the number N_k of e-folds at which a given mode quits the causal patch.

This approximation neglects the effects of the CMB accessible gauge modes which lie in the range 1 Gpc $\lesssim 1/k \lesssim$ 1 Mpc; these modes do have a small imprint which can be roughly quantified, to prove the validity of our approximation above. During inflation all modes with $k > \mathcal{H}_{in}$, the Hubble parameter at the beginning of inflation, experience rotation, up to the one but highest momentum processed by inflation at reheating. Let us look at the 1 Mpc mode. During inflation, up until this mode leaves the horizon, the background $\mathbf{E}^{IR}$ has been changing ever since the beginning; as soon as it becomes superhorizon the background vector stops precessing from the point of view of this mode. Since our present observable universe is much larger than this mode, which has fallen back into the horizon in the past, what we observe is a collection of several bubbles for each of which the rotation experienced by the $k = 1/\mathrm{Mpc}$ mode is random — we could dub it BubbleBubbland, a nested version of Bubbland). Thence, the rotation will be suppressed due to the averaging over the large multitude of bubbles within the Hubble volume (in this Mpc case a $(\mathcal{H}_0\ \mathrm{Mpc})^{3/2} \approx 10^{11/2}$ suppression): the axial symmetry is nearly unbroken.

Many Fields

And if there are many gauge fields? The different uncorrelated vectors then will follow different rotation patterns, and they will all land in different — random — directions. A generic quadrupole-type correction arises, and the curvature perturbation bears the signs of this effect [5]:

$$\frac{\delta\mathcal{P}(\mathbf{k})}{\mathcal{P}_0} = \sum_n \frac{24}{\epsilon}\frac{|\mathbf{E}^{(n)IR}(\tau_0)|^2}{3H^2} N_k^2 \sin^2\psi_{(n)} \equiv g_0\left[\cos\chi\,\hat{Y}_0^2 + \sin\chi\,\hat{Y}_1^2\right] \tag{4}$$

where $4\sqrt{\pi}\,\hat{Y}_m^l \equiv 3\sqrt{5}\,Y_m^l$. Two parameters, g_0 and χ, are needed to characterise the two quadrupole components — the effect is *structural.*

Results

We have studied this effect statistically by performing several Monte Carlo realisation of the model in order to obtain probability distribution functions (PDFs) for the parameters describing the quadrupole, g_0 and χ. We follow the background random walk in direction space (the precession); the mean and spread of g_0 and χ are related to the total number of e-folds N_{tot} inflation has lasted for, and the number of identical gauge fields n.

In the single field case the probability for $g_0 > 0$ is zero. For negative g_0 the PDF depends on the free parameter $N_{ex} = N_{\mathrm{tot}} - N_{\mathcal{H}_0}$. In figure 1, upper left panel, we have plotted the PDFs for three examples with $N_{\mathrm{ex}} = \{4, 8, 16\}$ together with the Planck distribution/constraint [6].

The PDF for the amplitude $g_0 \equiv g(\mathcal{H}_0)$ and the shape χ, for 10^6 Monte Carlo realisations of $\hat{\mathbf{E}}_{IR}^{(i)}(\tau_0)$, and for the three examples $n = 3$, $n = 10$, and $n = 100$ are shown in the top and bottom right panels, respectively. With the normalisation $\tilde{g}_0 \equiv g_0/(N_{ex}/3)$ the PDF of $\tilde{g}_0$ only depends on the number of gauge fields; the corresponding physical parameter g_0 is obtained by picking a value for N_{ex}.

Introducing more of the same gauge vectors effectively results in a widening of the distribution for g_0, which is expected, but also in the possibility of observing *both* negative and positive amplitudes. Thus, the statistical nature of the g_0 parameter prevents us, single Hubble bubble-limited observers, from drawing a definite conclusion on its sign (and amplitude), even with the theory at high energy fully specified. With a very large number of fields the probabilities of positive and negative amplitudes slowly converge.

The shape parameter χ peaks at about $\pi/4$ for $n = 3$, which means that both components a_{20} and a_{21} are of the same order. As the number of fields grows, the distribution tends to peak towards larger values of the angle. The presence of the multitude of fields thus breaks explicitly the axial symmetry, the more so the more fields are thrown into the mix.

We end the presentation of our results by showing the observationally allowed regions of the parameter space $\{n, N_{ex}\}$ for which the generated quadrupole amplitude is at the 2% and 10% levels, relative to the monopole (bottom left panel). The lowest (green) area, below the $|g_0| < 0.02$ (95%CL) dashed line, is the region for which there is 95% chance probability of generating $|g_0| < 0.02$ (and a 5% chance of having a higher value). The following $|g_0| < 0.02$ (68%CL) solid line delimits the looser constraint (light green) for which there is a 68% chance probability of generating a weaker than $|g_0| = 0.02$ quadrupole (and a 32% chance of having a stronger one). If we allow a 10% quadrupole instead the parameter space widens encompassing the two middle (purple and light purple) regions. In the uppermost (white) region the chance of finding a quadrupole below 0.10 shrinks to less than 68%.

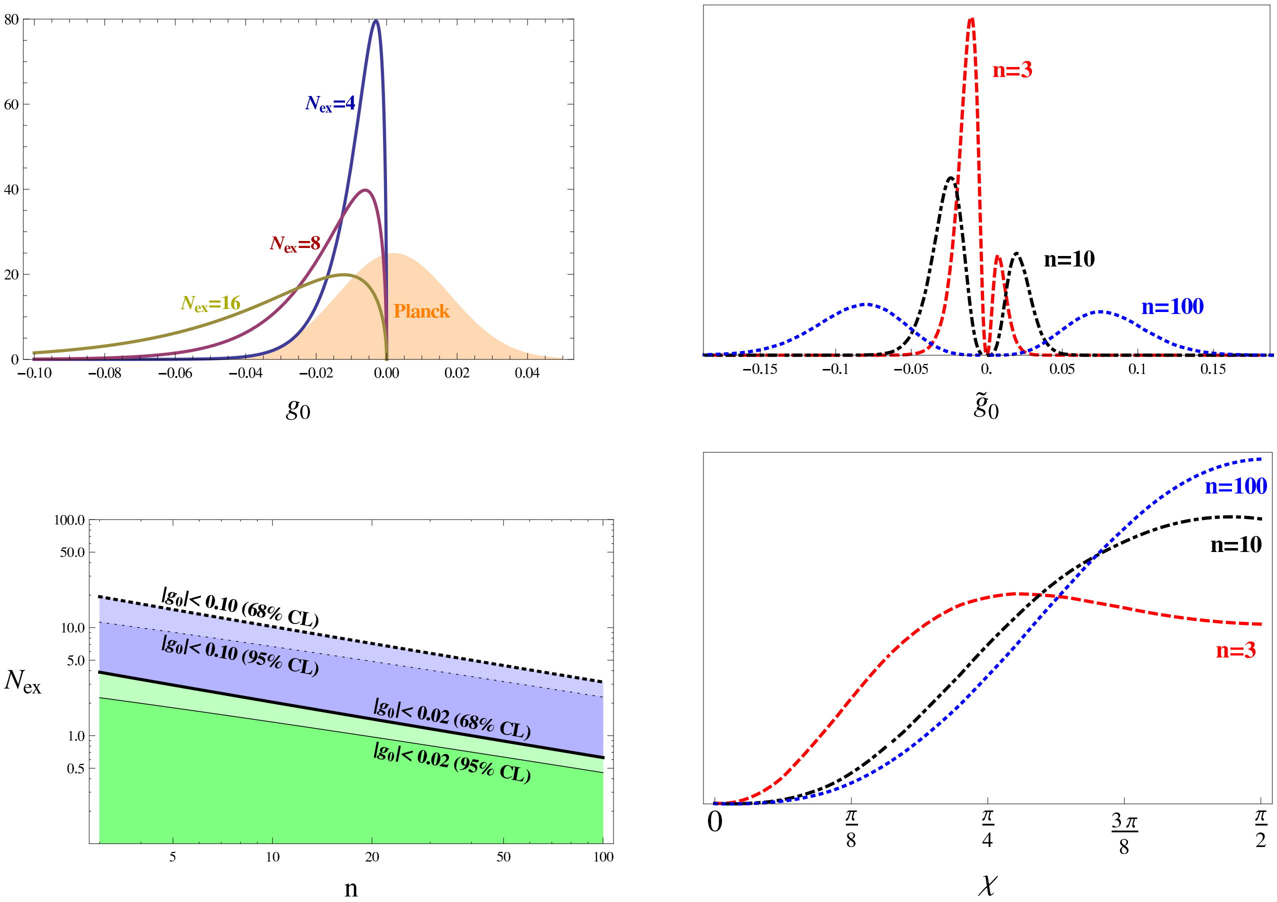

Figure 1 – See the text for all the details.

Closing words

What we see may not coincide with what the gods have decided for us. We have shown how there may be a statistical bias in our observations, which not only impacts the values of our cosmological parameters, but can also pull out new ones from the hat. Nonetheless, albeit only statistically, we are still able to tell truth and nonsense apart when it comes to our theoretical lucubrations — that is, a model that lands in a small probability "compatibility region" may not be the kind of model you would bet your money on.

Acknowledgements

FU is supported by IISN project No. 4.4502.13 and Belgian Science Policy under IAP VII/37. And finally, thanks to the organisers and all participants for the most enjoyable of all workshops!

References

1. D. H. Lyth and A. Riotto, Phys. Rept. **314** (1999) 1 [hep-ph/9807278].
2. N. Bartolo, S. Matarrese, M. Peloso and A. Ricciardone, Phys. Rev. D **87** (2013) 023504 [arXiv:1210.3257 [astro-ph.CO]].
3. J. M. Wagstaff and K. Dimopoulos, Phys. Rev. D **83** (2011) 023523 [arXiv:1011.2517 [hep-ph]].
4. M. Thorsrud, F. R. Urban and D. F. Mota, JCAP **1404** (2014) 010 [arXiv:1312.7491 [astro-ph.CO]].
5. M. Thorsrud, D. F. Mota and F. R. Urban, arXiv:1311.3302 [astro-ph.CO].
6. J. Kim and E. Komatsu, Phys. Rev. D **88** (2013) 101301 [arXiv:1310.1605 [astro-ph.CO]].

DOES PLANCK REALLY RULE OUT MONOMIAL INFALTION?

K. Enqvist and M. Karčiauskas
Physics Department and Helsinki Institute of Physics
PO Box 64, FIN-00014 University of Helsinki

Abstract

We consider the modifications of monomial chaotic inflation models due to radiative corrections induced by inflaton couplings to bosons and/or fermions necessary for reheating. To the lowest order, ignoring gravitational corrections and treating the inflaton as a classical background field, they are of the Coleman-Weinberg type and parametrized by the renormalization scale μ. In cosmology, there are not enough measurements to fix μ so that we end up with a family of models, each having a slightly different slope of the potential. We demonstrate this by explicit calculation within the family of chaotic ϕ^2 models.

1 Introduction

Large-field single-field inflation models with a monomial potential $V \sim \phi^n$ can be considered as effective particle physics theories with heavy degrees of freedom and/or interactions with other fields integrated out. From such a point of view one may justify e.g. neglecting the running of λ in $\lambda\phi^4$ model and treat it as an effective constant. However, we would like to point out that inflaton decay is an essential part of any inflationary scenario that cannot be integrated out. Thus, any model must be augmented by a mechanism that brings inflation to an end and reheats the universe. As is well known, this means adding interaction terms to a model so that to lowest order the potential in monomial inflation would read like

$$V(\phi, \chi, \psi) = \frac{1}{2}\lambda m_{\mathrm{Pl}}^4 \left(\frac{\phi}{m_{\mathrm{Pl}}}\right)^n - \frac{1}{2} g_{\mathrm{b}}^2 \phi^2 \chi^2 - h_{\mathrm{b}} \phi \bar{\psi} \psi + \ldots \tag{1}$$

where χ is a bosonic and ψ a fermionic field, and 'b' denotes bare coupling constant values. Dots represent other terms, which we consider to be negligible. These interactions will then generate through loop corrections operators that modify the effective inflaton potential. Here we focus on the minimal modifications only. We take χ and ψ to be quantum fields while the inflaton ϕ is treated as a classical background field. In particular, this means neglecting the inflaton loops. Moreover, we do not consider quantum corrections due to curved space-time background.

To lowest order the modifications are then of the conventional Coleman-Weinberg type:

$$V_{\mathrm{eff}}(\phi) = \frac{1}{2}\lambda m_{\mathrm{Pl}}^4 \left(\frac{\phi}{m_{\mathrm{Pl}}}\right)^n + \frac{g^4 - 4h^4}{64\pi^2} \phi^4 \ln \frac{\phi^2}{\mu^2}, \tag{2}$$

where g and h are renormalized coupling constants. Renormalizability requires $n \leq 4$ and we have assumed $g\phi \gg m_\chi$ and $h\phi \gg m_\psi$, where m_χ and m_ψ are masses of χ and ψ fields respectively. For self-consistency of the model, radiative corrections to the potential must be taken into account when estimating the number of e-folds and values of the slow-roll parameters.

The importance of radiative corrections for chaotic inflation was already pointed out by Senoguz and Shafi[1]. They considered only fermionic contributions, but more importantly, they chose the renormalization scale as $\mu = hM_P$. The renormalization scale is of course arbitrary; there is no "natural" scale μ except in the technical sense of minimizing higher order corrections. In particle physics, one trades μ with a measured value of some physical amplitude; this is the act of "normalization". For inflationary models, the situation is trickier. For instance, the physical inflaton mass could be defined as the pole mass $m_{\rm phys} = m(p^2 = m^2_{\rm phys})$, where m is the bare mass, which is a parameter in the potential. Unfortunately, there are no prospects for measuring the physical inflaton mass independently of cosmological observations. Thus the question is, what exactly is the meaning of the potential parameters that can be constrained by CMB observations - and which models are truly ruled out?

As far as the observational constraints are concerned, we shall point out that different renormalization points correspond to physically different models of inflation in that they lead to different predictions for the observables n_s and r. The models are different in the sense that the shape of the potential at some fixed ϕ is different for different renormalization points. Alternatively, by fixing, say, the value of the spectral index, one would obtain a family of models with the same n_s but with different physical model parameters m (or λ) and g or h. We should emphasize that we consider only cases where the radiative corrections are always small.

2 The Effect of Radiative Corrections

2.1 Chaotic Inflation with Radiative Corrections

To simplify the expressions let us rewrite the inflaton potential in Eq. (2) as

$$V_{\rm eff}\left(\phi\right) = \frac{1}{2}\lambda m_{\rm Pl}^4\left(\varphi^n + \kappa\varphi^4\ln\frac{\varphi}{\mu}\right), \tag{3}$$

where $\varphi \equiv \phi/m_{\rm Pl}$ and $\kappa \equiv \left(g^4 - 4h^4\right)/16\pi^2\lambda$ and μ is given in units of the Planck mass.

It is clear that radiative corrections change both the slope and the curvature of the potential. Indeed, one can compute the radiatively corrected slow-roll parameters as

$$\begin{aligned}
\epsilon &= \frac{K^2\left(\varphi\right)}{2\varphi^2}\left[n + \kappa\varphi^{4-n}\left(1 + 4\ln\frac{\varphi}{\mu}\right)\right]^2, && (4)\\
\eta &= \frac{K\left(\varphi\right)}{\varphi^2}\left[n\left(n-1\right) + \kappa\varphi^{4-n}\left(7 + 12\ln\frac{\varphi}{\mu}\right)\right], && (5)\\
\xi &= \frac{K^2\left(\varphi\right)}{\varphi^4}\left[n + \kappa\varphi^{4-n}\left(1 + 4\ln\frac{\varphi}{\mu}\right)\right]\left[n\left(n-1\right)\left(n-2\right) + \kappa\varphi^{4-n}\left(14 + 46\ln\frac{\varphi}{\mu}\right)\right] && (6)
\end{aligned}$$

where K is defined as $K^{-1}(\varphi) \equiv 1 + \kappa\varphi^{4-n}\ln\left(\varphi/\mu\right)$ and slow-roll parameters are defined by

$$\epsilon \equiv \frac{m_{\rm Pl}^2}{2}\left(\frac{V'}{V}\right)^2, \eta \equiv m_{\rm Pl}^2\frac{V''}{V}, \xi \equiv m_{\rm Pl}^4\frac{V'V'''}{V^2}. \tag{7}$$

Knowing their values a couple of e-folds after the pivot scale k_* exits the horizon, it is easy to compute the tensor to scalar ratio r, spectral index $n_{\rm s}$ and the running of spectral index n' using

$$\begin{aligned}
r\left(n,\kappa,\mu\right) &= 16\epsilon, && (8)\\
n_{\rm s}\left(n,\kappa,\mu\right) - 1 &= -6\epsilon + 2\eta, && (9)\\
n'\left(n,\kappa,\mu\right) \equiv {\rm d}n_{\rm s}/{\rm d}\ln k &= -24\epsilon^2 + 16\epsilon\eta - 2\xi. && (10)
\end{aligned}$$

However, in contrast to the tree level potential, the values of these parameters are determined not only by the power n but also by the strength of the couplings of the inflaton to other fields κ, as well as by the renormalization scale μ.

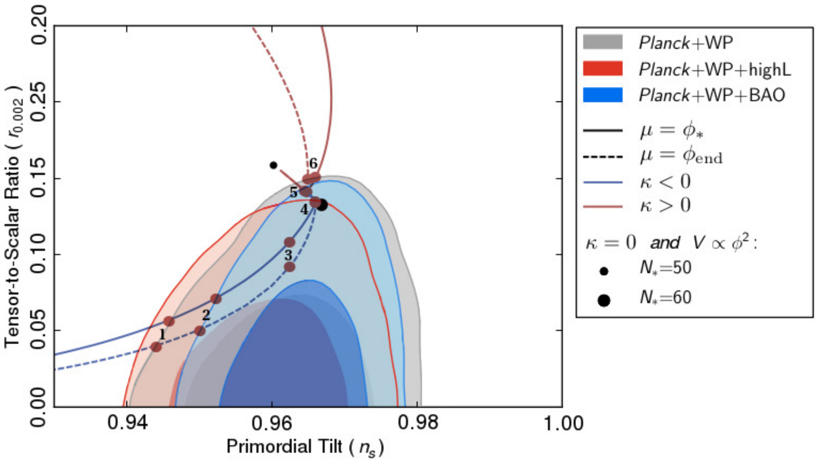

Figure 1 – Planck constraints on $n_{\rm s}$ and r (assuming vanishing n') [2]. Solid and dashed curves correspond to $\mu = \phi_*$ and $\mu = \phi_{\rm end}$ respectively. Blue (red) curve show the effect of radiative corrections when the $\phi \to \bar{\psi}\psi$ ($\phi \to \chi\chi$) decay channel dominates. Numbers denote parameter values given in Table 1.

To find numerical values of slow-roll parameters in Eqs. (4) - (6) we need to solve the system of three coupled equations. The first equation is given by the end of inflation condition

$$\epsilon\left(\varphi_{\rm end}, n, \kappa, \mu\right) \;=\; 1, \tag{11}$$

where $\varphi_{\rm end}$ is the inflaton value at the end of inflation.

The number of e-folds of inflation from the time when a mode k_* leaves the horizon to the end of slow-roll inflation is given by $N_* = m_{\rm Pl}^{-2} \int_{\varphi_{\rm end}}^{\varphi_*} V/V' {\rm d}\varphi$. Hence, using Eq. (7) we can write

$$\int_{\varphi_*}^{\varphi_{\rm end}} \frac{{\rm d}\varphi}{\sqrt{2\epsilon\left(\varphi, n, \kappa, \mu\right)}} = -N_*. \tag{12}$$

One also has to make sure that the solution gives the curvature perturbation amplitude $\mathcal{P}_\zeta\left(k\right) = \left(24\pi^2 m_{\rm Pl}^4\right)^{-1}\left[V\left(\phi\right)/\epsilon\right]_k$ consistent with the observed value $\mathcal{P}_\zeta\left(k_*\right) = 2.20 \times 10^{-9}$ at the the pivot scale $k_* = 0.05\,{\rm Mpc}^{-1}$. This provides a third equation to compute the (renormalised) inflaton self-coupling constant λ

$$\lambda = 24\pi^2 \mathcal{P}_* \frac{\left[n + \kappa\varphi_*^{4-n}\left(1 + 4\ln\frac{\varphi_*}{\mu}\right)\right]^2}{\varphi_*^{2+n}\left[1 + \kappa\varphi_*^{4-n}\ln\frac{\varphi_*}{\mu}\right]^3}. \tag{13}$$

The value of N_* in Eq. (12) depends on the temperature of reheating $T_{\rm reh} \propto \rho_{\rm reh}^{1/4}$ as [3]

$$N_* = 68.5 + \frac{1}{2}\ln\frac{V_*}{m_{\rm Pl}^4} - \frac{1}{3}\ln\frac{V_{\rm end}}{m_{\rm Pl}^4} + \frac{1}{12}\ln\frac{\rho_{\rm reh}}{m_{\rm Pl}^4}, \tag{14}$$

where $V_* \equiv V_{\rm eff}\left(\phi_*\right)$, $V_{\rm end} \equiv V_{\rm eff}\left(\phi_{\rm end}\right)$ and we also used the value of the present day Hubble constant $H_0 = 67.04$ km/s/Mpc. It is assumed in this work that the inflaton decays via a process of perturbative decay with a rate Γ, which gives $\rho_{\rm reh} \simeq 3m_{\rm Pl}^2\Gamma^2$.

Scalar spectral index n_s, spectral running n' and tensor-to-scalar ratio r can be calculated by solving Eqs. (11) - (13) for φ_* and plugging the result into Eqs. (9), (10) and (8). Unfortunately it is impossible to solve them analytically. Therefore, one has to resort to numerical methods.

2.2 The Case of $n = 2$

	$\mu = \phi_*$					$\mu = \phi_{\text{end}}$			
	1	4	5	6		1	4	5	6
$\kappa \times 10^5$	-370.0	-2.0	3.0	40.0	0	-75.0	-0.2	0.8	7.0
n_{s}	0.9459	0.9661	0.9645	0.9661	0.9670	0.9441	0.9660	0.9647	0.9650
r	0.0570	0.1349	0.1417	0.1513	0.132	0.0403	0.1356	0.1425	0.1503
$n' \times 10^4$	-6.345	-5.774	-6.140	-5.166	-5.464	3.627	-5.757	-6.308	-6.630
$h,\, g \times 10^3$	1.268	0.414	0.662	1.280	0	0.889	0.233	0.476	0.818
$m\big(10^{13}\text{ GeV}\big)$	1.009	1.464	1.530	1.566	1.01	1.101	1.471	1.533	1.528
ϕ_*/m_{Pl}	14.49	15.37	15.08	15.22	15.56	13.36	15.34	15.06	15.25
N_*	58.67	58.56	56.23	56.74	60	58.35	58.37	56.06	56.45

Table 1: Numerical values of some parameters for two choices of renormalization scale μ and different values of inflaton interaction strength κ. Top row numbers correspond to points in Figure 1. The 'h, g' row displays the values of the coupling constant h for $\kappa < 0$ and g for $\kappa > 0$.

As an example, consider the quadratic monomial potential with $n = 2$. In this case $\lambda = m^2/m_{\text{Pl}}^2$, where m^2 is the *renormalised* mass of the inflaton. The inflaton decay rate $\Gamma = \Gamma_\chi + \Gamma_\psi$ to bosons $\phi \to \chi\chi$ and to fermions $\phi \to \psi\bar{\psi}$ is given by $\Gamma_\chi = g^4 m/8\pi$ and $\Gamma_\psi = h^2 m/8\pi$. Here we consider only the cases when either Γ_χ or Γ_ψ dominates.

We solve Eqs. (11) - (13) for two choices of renormalization scale μ. In the first case μ is such that radiative corrections vanish when the pivot scale exits the horizon, i.e. $\mu = \phi_*$. In effect, this then corresponds to a "pure" $m^2\phi^2$ model valid at the pivot scale only. The other extreme is the case with $\mu = \phi_{\text{end}}$, where the "pure" $m^2\phi^2$ model is valid at the end of inflation only.

As Eqs. (11) - (13) cannot be solved analytically, we list out for illustrative purposes some numerical results in Table 1. We also plot the results in Figure 1 together with Planck constraints on n_{s} and r.

As one can see in Figure 1, different renormalization scales result in different predictions for the CMB observables if inflaton interactions are of the order of g, $h \sim 10^{-3}$. The gap between the blue solid and dashed curves in Figure 1 is of the order $\Delta r \sim 10^{-2}$, which is well within the sensitivity of future missions to measure CMB B-mode polarization.

3 Conclusions

In this work we showed that predictions of the simplest monomial models of inflation are modified if one considers the effects of inflaton interaction with other fields and not only the tree-level potential. Such interactions are necessary in any realistic model of inflation for the inflaton to reheat the universe into radiation dominated phase. They, however, modify the potential of the inflaton by introducing loop corrections. In effect, the Planck constraints apply only to toy models, and the obvious question is, what are the constraints on (semi)realistic models?

Acknowledgemets

KE is supported by the Academy of Finland grant 1218322; MK is supported by the Academy of Finland grant 1263714.

References

1. Vedat Nefer Senoguz and Qaisar Shafi, *Phys. Lett.* B **668**, 6 (2008).
2. P.A.R. Ade et al., Planck 2013 results. XXII, **arXiv:1303.5082** [astro-ph.CO]
3. Andrew R Liddle and Samuel M Leach, *Phys. Rev.* D **68**, 103503 (2003).

Theories of Modified Gravity

Andrew J. Tolley
CERCA & Physics Department, Case Western Reserve University, OH, USA

We review a class of theoretical models of modified gravity that incorporate the Vainshtein mechanism. These include in particular models based on massive gravity and its generalizations. We review how massive gravity models may be obtained from extra dimensions through the deconstruction framework and discuss the decoupling of bi-gravity and the associated Galileon duality it uncovers.

1 Introduction & Motivations

In what follows we will briefly review a class of models of modified gravity that have the universal feature that they incorporate the Vainshtein mechanism [?]. These models include, Galileons, massive gravity [?], bi-gravity [?], multi-gravity [?], Quasi-Dilaton [?]. Many of these models are related by an interesting web of decoupling limits or dualities. For instance Galileon theories are seen as the decoupling limits of massive gravity models. Galileon models themselves have a self-duality which will be discussed below.

1.1 Why modify gravity?

The principal motivation for current research on modified gravity is to address the questions of dark energy and the cosmological constant problems. These are

- 1. Old Cosmological Constant Problem: Why is the universe not accelerating at a gigantic rate determined by the vacuum energy?
- 2. New cosmological constant problem: Assuming I is solved, what gives rise to the remaining vacuum energy or dark energy which leads to the acceleration we observe?

The old cosmological problem has proven notoriously difficult to solve. One perspective is that we should resort to the anthropic principle, supplemented with a physical framework such as the string theory landscape to give rise to many possible solutions for the cosmological constant. Another possibility is to change how the vacuum energy gravitates by an appropriate modification of gravity from four dimensional general relativity. For instance this is the goal of large extra dimensional models such as SLED which rely on the physics of codimension two sources to alleviate the problem. This is also the idea of more significant modified theories of gravity that change physics at large distances, IR modifications of gravity, such as those that incorporate the degravitation mechanism. What is common among this latter set of ideas is the Vainshtein mechanism, and it is these models that shall be largely our focus in the later sections.

The new cosmological constant problem has prompted the development of a host of 'vanilla' dark energy models such as quintessence which preserve the form of Einstein's equations, but add a new dark energy fluid with potentially variable equation of state. However the majority of these models are poorly motivated, introduce new fine-tuning problems, and lead to little interesting new physics. The current scale of cosmic acceleration is associated with an energy scale $H(\text{today}) \sim 10^{-33}\text{eV}$. A more radical proposal is that this number sets the scale of a modification of gravity that leads to a self-acceleration, i.e. gravity sourcing its own acceleration. In certain theories, such as massive gravity, this scale is associated with a mass scale (the mass of the graviton) which can be kept small in a technically natural way due to the enhanced symmetry that arises in the $m = 0$ limit.

2 From Kaluza-Klein to Deconstruction

One of the earliest modified theories of gravity was Kaluza-Klein theory. In its simplest and original form, this is 5 Dimensional Einstein Gravity compactified on a circle of radius L. The 5 physical propagating models of a massive graviton are separated into 4D massless graviton + 4D massless photon + 4D massless scalar + N 4D massive gravitons. This is a consistent UV modification at KK scale $m = 2\pi/L$. The 5 dimensional metric can be denoted

$$\mathrm{d}s^2 = -\,\mathrm{d}y^2 + [\eta_{\mu\nu} + h_{\mu\nu}(x,y)]\,\mathrm{d}x^\mu\,\mathrm{d}x^\nu \quad y \in [0, L]\,. \tag{1}$$

The metric perturbation can be expanding into a Kaluza-Klein (KK) tower of massive graviton states with wavefunctions $h_{\mu\nu,n}(x)$ according to

$$h_{\mu\nu}(x,y) = \sum_{n=-\infty}^{\infty} e^{2\pi i n y/L} h_{\mu\nu,n}(x)\,. \tag{2}$$

Although the number of KK modes is infinite, there are effectively only a finite number N of weakly coupled graviton states $N \sim M_{\text{Planck}}L$.

The deconstruction framework of Arkani-Hamed et al [?,?,?], can be viewed as a discrete Fourier transform of this approach. We first state with the continuous fifth dimension, and then discretize the extra dimension by replacing it with a one-dimensional lattice of points at

$$y_k = k\frac{L}{N}\,, \quad k = 0 \ldots N\,. \tag{3}$$

The y-derivatives of the metric are replaced by

$$\partial_y h_{\mu\nu}(x, y_k) = \frac{N}{L}\left(h_{\mu\nu}(x, y_{k+1}) - h_{\mu\nu}(x, y_k)\right). \tag{4}$$

This gives rise to a theory of N massive and one massless gravitons. However as it stands the masses are approximately equally spaced along the Kaluza-Klein tower. To compensate this we can replace the regular lattice by a disordered lattice with a random distribution of nearest neighbour interactions. This again gives a theory of N massive and one massless gravitons except they are no longer equally spaced. By making one of the lowest non-zero mass state as low as desired we can obtain a true IR modification of gravity.

All of this may be performed at the non-linear level[?]. This is easiest in the Einstein-Cartan (vielbein formalism) of gravity for which the 5D Einstein-Hilbert action takes the form

$$S = M_5^3 \int \mathrm{d}y \int E \wedge E \wedge E \wedge R_5 \,, \tag{5}$$

and we have suppressed the vielbein indices which should be contracted with the Levi-Civita tensor. Performing the deconstruction directly in the vielbein variables we obtain an action of the schematic form

$$S = M_4^2 \sum_i \int e_i \wedge e_i \wedge R_{4,i} + M_4^2 \sum_i m_i^2 e_i \wedge e_i \wedge (e_{i+1} - e_i) \wedge (e_{i+1} - e_i) \,. \tag{6}$$

This is the multi-gravity extension of the dRGT massive gravity model written in vierbein form [?]. By weighting the discretization we may generate all allowed ghost free mass terms[?].

3 Ghost-free Massive Gravity

3.1 The Model

We have seen that the deconstruction framework naturally leads us to a model of massive gravity (see[?] for a recent review on Massive Gravity). The Lagrangian for massive gravity written in terms of the metric takes the form[?]

$$\mathcal{L} = \frac{M_{\mathrm{Pl}}^2}{2} \sqrt{-g} \left(R + 2m^2 \mathcal{U}(g,f) \right) + \mathcal{L}_M \,, \tag{7}$$

where all quantities are four-dimensional, $f_{\mu\nu}$ is the reference metric that be Minkowski or other [?]. The potential term has only a finite number of possible interactions in any dimensions. In four dimensions, it may be written as

$$\mathcal{U}(g,f) = \mathcal{U}_2 + \alpha_3 \mathcal{U}_3 + \alpha_4 \mathcal{U}_4 \,, \tag{8}$$

with[?]

$$\begin{aligned} \mathcal{U}_2[\mathcal{K}] &= \left([\mathcal{K}]^2 - [\mathcal{K}^2] \right) && (9) \\ \mathcal{U}_3[\mathcal{K}] &= \left([\mathcal{K}]^3 - 3[\mathcal{K}][\mathcal{K}^2] + 2[\mathcal{K}^3] \right) && (10) \\ \mathcal{U}_4[\mathcal{K}] &= \left([\mathcal{K}]^2 - 6[\mathcal{K}]^2[\mathcal{K}^2] + 8[\mathcal{K}^3][\mathcal{K}] + 3[\mathcal{K}^2]^2 - 6[\mathcal{K}^4] \right) \,, && (11) \end{aligned}$$

and

$$\mathcal{K}^\mu_{\ \nu}(g,f) = \delta^\mu_{\ \nu} - \sqrt{g^{\mu\alpha} f_{\alpha\nu}} \,. \tag{12}$$

This model is sometimes referred to as dRGT and we keep the same terminology to avoid confusion. The mass term can equivalently be written as characteristic polynomials[?]

$$\mathcal{L} = \frac{1}{2} \sqrt{-g} \left(M_{\mathrm{Pl}}^2 R - m^2 \sum_{n=0}^{4} \beta_n \mathcal{U}_n[X] \right) + \mathcal{L}_M \,, \tag{13}$$

with

$$X^\mu_{\ \nu} = \sqrt{g^{\mu\alpha} f_{\alpha\nu}} \,. \tag{14}$$

These interactions appear as very non-trivial, yet it can be shown that they are protected by a non-renormalization theorem[?].

3.2 Vainshtein Mechanism

The Vainshtein mechanism is one of a handful of screening mechanisms that have been considered in the context of dark energy and modified gravity models (for a review see [?]). The need for such screening mechanisms is to evade the constraints from fifth forces tests and to recover the predictions of General Relativity in the solar system. The Vainshtein mechanism works by renormalizing the kinetic term of the fluctuations of the Galileon or massive graviton helicity-zero mode that arises in the theories being discussed. In high density regions, the kinetic term normalization becomes large, and the effect coupling to matter becomes small. In low density regions, the fifth force propagates at a comparable level to Newtonian gravity.

More precisely, in the context of massive gravity with graviton mass m, when the spacetime curvature $R \gg m^2$ then we expect to recover GR. When $R \ll m^2$ the fifth force propagates. The transition between these two regions $R \sim m^2$ occurs at a characteristic scale which for a point source of mass M is known as the Vainshtein radius and is given by $R_V = (R_s m^{-2})^{1/3}$ where R_s is the Schwarzschild radius. The screened region is then where $r \ll r_V$.

In the context of massive gravity and bi-gravity models, most of what is understood about the phenomenology of the Vainshtein mechanism comes from looking at the decoupling limit action, discussed below.

4 Decoupling Limits and Dualities

4.1 Decoupling limit of Bi-gravity

We now consider the theory of bi-gravity [?],

$$\mathcal{L} = \frac{1}{2}\sqrt{-g}\left[M_{\rm Pl}^2 R[g] - m^2 \sum_{n=0}^{4} \beta_n \mathcal{U}_n(\mathcal{K})\right] + \frac{1}{2}\sqrt{-f} M_f^2 R[f] + \mathcal{L}_m\,. \tag{15}$$

This is a straightforward extension of dRGT massive gravity in which the reference metric is taken to be dynamical with its own Einstein-Hilbert term.

In massive gravity (without introducing the Stückelberg fields), the mass term breaks a single copy of the local diffeomorphism group down to a global Lorentz group

$$\text{Diff}(M) \quad \longrightarrow \quad \text{Global Lorentz}\,. \tag{16}$$

In Bi-gravity (without introducing the Stückelberg fields), the mass term (or interaction term between the two metrics) breaks two copies of local diffeomorphism group down to a single copy local diffeomorphism group

$$\text{Diff}(M) \times \text{Diff}(M) \quad \longrightarrow \quad \text{Diff}(M)_{\text{diagonal}}\,. \tag{17}$$

As a result bi-gravity is also best understood with the Stückelberg fields for the broken diffs which in turn lead to a Galileon field in its decoupling limit - dominating the interactions of the bi-gravity model[a].

In bi-gravity we can work with the following metrics:

$$\left\{\begin{array}{ll} \text{Dynamical Metric I}: & g_{\mu\nu}(x) \\ \text{Dynamical Metric II}: & F_{\mu\nu} = f_{AB}(\phi)\partial_\mu \phi^A \partial_\nu \phi^B\,, \end{array}\right. \tag{18}$$

where to start with we can express the Stückelberg fields in terms of the helicity-0 mode (and omitting for now the helicity-1 mode)

$$\phi^A = x^a + \frac{1}{m^2 M_{\rm Pl}} \partial^a \pi(x)\,. \tag{19}$$

---

[a] The Stückelberg fields are as necessary or unnecessary in bi-gravity than they are in massive gravity. The physics is easier to follow when the Stückelberg fields are introduced but even with the Stückelberg fields, both theories are still strongly coupled at the scale $\Lambda_3 = (M_{\rm Pl} m^2)^{1/3}$ or the equivalent in terms of M_f.

Denoting by $h_{\mu\nu}$ the fluctuations of the metric $g_{\mu\nu}$ and by $v_{\mu\nu}$ the fluctuations of the metric $f_{\mu\nu}$, then the decoupling limit of bi-gravity is [?] (omitting the helicity-1 modes)

$$\begin{aligned} S_{\mathrm{helicity}-2/0} &= \int \mathrm{d}^4x \bigg[-\frac{1}{4} h^{\mu\nu} \hat{\mathcal{E}}^{\alpha\beta}_{\mu\nu} h_{\alpha\beta} - \frac{1}{4} v^{\mu\nu} \hat{\mathcal{E}}^{\alpha\beta}_{\mu\nu} v_{\alpha\beta} \qquad (20) \\ &\quad + \frac{\Lambda_3^3}{2} h_{\mu\nu}(x) X^{\mu\nu} + \frac{\Lambda_3^3}{2} \frac{M_{\mathrm{Pl}}}{M_f} h_{\mu\nu}(x) X^{\mu\nu} v_{\mu A}[x^a + \Lambda_3^{-3} \partial^a \pi] \left(\eta^a_\nu + \hat{\Pi}^A_\nu \right) Y^{\mu\nu} \bigg] , \end{aligned}$$

with $\hat{\Pi}_{\mu\nu} = \partial_\mu \partial_\nu \pi / \Lambda_3^3$ and

$$X^{\mu\nu} = -\frac{1}{2} \sum_{n=0}^{4} \frac{\hat{\beta}_n}{(3-n)!n!} \epsilon^{\mu\cdots} \epsilon^{\nu\cdots} \left(\eta + \hat{\Pi} \right)^n \eta^{3-n} \qquad (21)$$

$$Y^{\mu\nu} = -\frac{1}{2} \sum_{n=0}^{4} \frac{\hat{\beta}_n}{(4-n)!(n-1)!} \epsilon^{\mu\cdots} \epsilon^{\nu\cdots} \left(\eta + \hat{\Pi} \right)^{n-1} \eta^{4-n} . \qquad (22)$$

As a result, the two massless spin-two fields coupled to a Galileon in a highly non-minimal way. Now including the helicity-1 modes, the decoupling limit of bi-gravity and massive gravity gives the following helicity-1/helicity-0 interactions [?]

$$S_{\mathrm{helicity}-1/0} = -\frac{1}{8} \delta^{\mu\nu\rho\sigma}_{abcd} \left(2G^a_\mu (\delta + \hat{\Pi})^b_\nu \omega^c_\rho \delta^d_\sigma + (\delta + \hat{\Pi})^a_\mu (\delta + \hat{\Pi})^b_\nu [\omega^c_\rho \omega^d_\sigma + \delta^d_\sigma \omega^c_\alpha \omega^\alpha_\rho] \right) ,$$

with

$$\omega_{ab} = \int_0^\infty \mathrm{d}u \epsilon^{-2u} e^{-u\hat{\Pi}^{a'}_a} G_{a'b'} e^{-u\hat{\Pi}^{b'}_b} \qquad (23)$$

$$G_{ab} = \partial_a B_b - \partial_b B_a = \omega_{ac} \left(\delta + \hat{\Pi} \right)^c_b + (\delta + \hat{\Pi})^c_a \omega_{cb} , \qquad (24)$$

where B_a is the helicity-1 mode. Since partially massless gravity (resp. bi-gravity) should only have 4 (resp. 7) propagating degrees of freedom - since the helicity-0 must be pure gauge - and since from the above action we see that the helicity-0 mode always interact with the helicity-1 modes in bi-gravity and in massive gravity, we can conclude that there is no partially massless theory of gravity or bi-gravity [?,?].

Once the decoupling limit action is diagonalized, the helicity-0 mode is seen have the action for a Galileon. However, in addition, due to the diagonalization matter will obtain non-trivial 'disformal couplings' to the Galileon field

$$S_{\mathrm{mattercoupling}} = \int \mathrm{d}^4x \frac{1}{M_{\mathrm{Planck}}} (\pi T + \partial_\mu \pi \partial_\nu \pi T^{\mu\nu} + \dots). \qquad (25)$$

These disformal couplings can lead to interesting phenomelogical features in their own right.

4.2 Galileon Duality

There are actually two (completely equivalent) ways to introduce the Stückelberg fields. Rather than the procedure (**??**)

$$\left\{ \begin{array}{ll} \text{Dynamical Metric I :} & g_{\mu\nu}(x) \\ \text{Dynamical Metric II :} & F_{\mu\nu} = f_{AB}(\phi) \partial_\mu \phi^A \partial_\nu \phi^B \\ \text{Relations between Coordinates :} & \tilde{x}^A = \phi^A(x) = x^A + \partial^A \pi(x) \end{array} \right. \qquad (26)$$

we can of course use instead

$$\left\{ \begin{array}{ll} \text{Dynamical Metric I :} & \tilde{G}_{AB}(\tilde{x}) = g_{\mu\nu}(Z) \partial_A Z^\mu \partial_B Z^\nu \\ \text{Dynamical Metric II :} & f_{AB}(\tilde{x}) \\ \text{Relations between Coordinates :} & x^\mu = Z^\mu(\tilde{x}) = \tilde{x}^\mu + \partial^\mu \rho(\tilde{x}) \end{array} \right. \qquad (27)$$

This leads to a remarkable property. For every Galileon field $\pi(x)$ one can define a dual Galileon field via the implicit field-dependent coordinate transformation [?]

$$\begin{aligned} \tilde{x}^A &= \phi^A(x) = x^A + \partial^A \pi(x) \qquad (28)\\ x^\mu &= Z^\mu(\tilde{x}) = \tilde{x}^\mu + \partial^\mu \rho(\tilde{x})\,. \qquad (29) \end{aligned}$$

Consider a Galileon operator in D dimensions

$$\mathcal{L}_n(\pi) = \pi\epsilon\epsilon(\hat{\Pi})^{n-1}\eta^{D-n+1}\,, \qquad (30)$$

then every Galileon field Lagrangian in D dimensions

$$\mathcal{L}(\pi) = \sum_{n=2}^{D+1} c_n \mathcal{L}_n(\pi) \qquad (31)$$

admits a dual formulation as a Galileon

$$\mathcal{L}(\rho) = \sum_{n=2}^{D+1} p_n \mathcal{L}_n(\rho) \qquad (32)$$

with distinct coefficients [?]

$$p_n = \frac{1}{n}\sum_{k=2}^{D+1}(-1)^k c_k \frac{k(d-k+1)!}{(n-k)!(d-n+1)!}\,. \qquad (33)$$

The coupling to other matter fields transforms in a local way under this duality, [?]. This could have interesting consequences for understanding the features associated with the strong coupling and the Vainshtein mechanism in this types of theories.

5 Cosmology of massive gravity

5.1 A No-go & Ways Out

The simplest model (dRGT massive gravity in Minkowski) does not support spatially flat (or closed) cosmological solutions which are FRW meaning homogeneous and isotropic. The argument is simple: as in GR we have a Friedman equation and a Raychaudhuri equation. In GR, the second follows from the first by diff invariance. In massive gravity diff invariance is broken and so the would-be Raychaudhuri equation no longer follows from the first equation. The consistency of both equations imposes a condition on the scale factor [?]. Indeed, assuming an FRW metric,

$$\mathrm{d}s^2 = -N^2(t)\,\mathrm{d}t^2 + a(t)^2\,\mathrm{d}\mathbf{x}^2\,, \qquad (34)$$

the lagrangian for massive gravity becomes

$$\mathcal{L} = 3M_{\rm Pl}^2\left(-\frac{a\dot{a}^2}{N} - m^2(a^3-a^2) + m^2 N(2Na^3 - 3a^2 + a)\right)\,. \qquad (35)$$

The constraint imposed on the scale factor by consistency of the would be Friedman and Raychaudhuri equation is then [?]

$$m^2\partial_t\left(a^3 - a^2\right) = 0\,, \qquad (36)$$

which is clearly uninteresting.

To bypass this no-go several options can and have been considered:

- **Resolution I: Accept Inhomogeneities**
  The most natural and certainly the most physical resolution to the previous no-go (although also probably the hardest to implement from a purely technical aspect) is to accept the existence of inhomogeneities[?]. While inhomogeneities may be important at large distances (beyond our observable Universe - which is the picture modern cosmology has in mind), the Vainshtein mechanism would guarantee that the inhomogeneities are unobservable at short distance scales (within the observable Universe) and before late times. The inhomogeneities would only appear on a scale set by the graviton mass (which is usually assumed to be close to the current Hubble parameter). Since observational constraints on inhomogeneities at the current Hubble scale are actually very weak, the presence of these inhomogeneities would thus have little observational effects and yet would resolve the previous no-go.

  Moreover, inhomogeneities and anisotropies can be hidden inside the Stückelberg fields which do not directly couple to matter but only indirectly though the Planck scale. Inhomogeneities in the Stückelberg fields are thus observationally very weak.

  To summarize, the metric could even remain perfectly homogeneous and isotropic at the price of introducing some inhomogeneities in the Stückelberg fields that would show up at the level of cosmological perturbations but could easily be small[?,?,?,?,?,?,?,?,?,?,?,?].

- **Resolution II: Modify the Assumptions**
  The previous no-go had several underlying assumptions which can be bypassed to allow for FRW solutions:

  - Considering an open Universe rather than a flat or closed one allow for FRW solutions [?] which are however unstable[?].
  - Consider a de Sitter or FRW reference metric, however this also leads to instabilities [?] as we shall see later. (See also[?] for the decoupling limit of massive gravity on de Sitter).
  - Make the reference metric dynamical, leading to bi-gravity[?]. As we shall see later, this could prevent the instabilities[?,?,?,?,?,?].

- **Resolution III: Extension or modification of the theory**
  Other more significant modifications of the theory allow for FRW solutions:

  - Quasi-Dilaton massive gravity which admits self-accelerating solutions but which appear to be unstable[?,?,?]
  - Generalized Quasi-Dilaton massive gravity which admits stable self-accelerating solutions[?,?,?]
  - Lorentz-violating massive gravity[?]
  - Varying mass gravity[?,?,?]
  - Multi-vierbeins gravity[?]
  - Extended Massive gravity[?,?]
  - Non-local Massive gravity[?,?]

5.2 *Quasi-dilaton massive gravity*

We now present another extension of massive gravity known as quasi-dilaton. The same arguments found previously can be applied to generic cosmological solutions on quasi-dilaton massive gravity[?]

$$S_E = \int \mathrm{d}^4x\sqrt{-g}\left\{\frac{M_{\rm Pl}^2}{2}\left[R - \frac{\omega}{M_{\rm Pl}^2}g^{\mu\nu}\partial_\mu\sigma\partial_\nu\sigma - \frac{m^2}{4}\mathcal{U}[\tilde{K}]\right] + \mathcal{L}_M(g_{\mu\nu},\psi)\right\}, \tag{37}$$

with

$$\tilde{\mathcal{K}}^\mu_{\ \nu} = \delta^\mu_{\ \nu} - e^{\sigma/M_{\rm Pl}}\sqrt{g^{\mu\alpha}\partial_\alpha\phi^a\partial_\nu\phi^b\eta_{ab}}\,. \tag{38}$$

This model avoids the no-FRW argument formulated previously thanks to the quasi-dilaton field σ. Generically one finds a non-zero kinetic term for the helicity-0 mode, showing that the general cosmological solutions are healthy.

A generalized version of the quasi-dilaton was shown to provide stable self-accelerating solutions[?,?]. For the generalized quasi-dilaton, the action takes the same form as in (**??**) with the expression (**??**) for with the generalized expression for the tensor $\tilde{\mathcal{K}}^\mu_{\ \nu}$,

$$\tilde{\mathcal{K}}^\mu_{\ \nu} = \delta^\mu_{\ \nu} - e^{\sigma/M_{\rm Pl}}\sqrt{g^{\mu\alpha}\partial_\alpha\phi^a\partial_\nu\phi^b\tilde{\eta}_{ab}}\,, \tag{39}$$

and

$$\tilde{\eta}_{\mu\nu} = \eta_{\mu\nu} - \frac{\alpha_\sigma}{\Lambda_3^3}e^{-2\sigma/M_{\rm Pl}}\partial_\mu\sigma\partial_\nu\sigma\,. \tag{40}$$

Of course this theory can be generalized to arbitrary reference metrics $\eta_{\mu\nu} \to f_{\mu\nu}$, but it makes more physical sense to keep Minkowski as the reference metric. Effectively this corresponds to a theory of massive gravity with a dynamical mass and couplings and a dynamical reference metric governed by the quasi-dilaton scalar field. The self-accelerating solutions in that generalized theory were shown to be free of instabilities, making them particularly appealing[?,?].

6 Summary

There are a rich family of theoretical modified gravity models that are consistent with GR in high curvature/ high density regions but differ in low curvature/density regions. This is the essence of the Vainshtein mechanism. These infrared modified theories are very testable on a whole range of scales - cosmological, astrophysical, solar system. There is still work to be done to identify consistent stable cosmological solutions and which of the theories are best fit with data but plenty of reason for optimism. These models can be viewed as limits of higher dimensional models through the deconstruction framework, and exhibit a interesting Dualities whose full implications have yet to be determined.

7 Acknowledgements

AJT is supported by Department of Energy Early Career Award DE-SC0010600. AJT wishes to thank the organizers of the Recontres de Moriond for an excellent meeting.

8 References

1. A. I. Vainshtein, Phys. Lett. B **39** (1972) 393.
2. A. Nicolis, R. Rattazzi and E. Trincherini, Phys. Rev. D **79**, 064036 (2009) [arXiv:0811.2197 [hep-th]].
3. S. F. Hassan and R. A. Rosen, JHEP **1202** (2012) 126 [arXiv:1109.3515 [hep-th]].
4. K. Hinterbichler and R. A. Rosen, JHEP **1207** (2012) 047 [arXiv:1203.5783 [hep-th]].
5. G. D'Amico, G. Gabadadze, L. Hui and D. Pirtskhalava, Phys. Rev. D **87**, no. 6, 064037 (2013) [arXiv:1206.4253 [hep-th]].

6. N. Arkani-Hamed, A. G. Cohen and H. Georgi, Phys. Rev. Lett. **86**, 4757 (2001) [hep-th/0104005].
7. N. Arkani-Hamed and M. D. Schwartz, Phys. Rev. D **69**, 104001 (2004) [hep-th/0302110].
8. M. D. Schwartz, Phys. Rev. D **68**, 024029 (2003) [hep-th/0303114].
9. C. de Rham, A. Matas and A. J. Tolley, Class. Quant. Grav. **31**, 025004 (2014) [arXiv:1308.4136 [hep-th]].
10. C. de Rham, arXiv:1401.4173 [hep-th].
11. C. de Rham, G. Gabadadze and A. J. Tolley, Phys. Rev. Lett. **106**, 231101 (2011) [arXiv:1011.1232 [hep-th]].
12. S. F. Hassan, R. A. Rosen and A. Schmidt-May, JHEP **1202**, 026 (2012) [arXiv:1109.3230 [hep-th]].
13. S. F. Hassan and R. A. Rosen, JHEP **1107**, 009 (2011) [arXiv:1103.6055 [hep-th]].
14. C. de Rham, G. Gabadadze, L. Heisenberg and D. Pirtskhalava, Phys. Rev. D **87**, no. 8, 085017 (2013) [arXiv:1212.4128].
15. E. Babichev and Cd. Deffayet, Class. Quant. Grav. **30**, 184001 (2013) [arXiv:1304.7240 [gr-qc]].
16. M. Fasiello and A. J. Tolley, JCAP **1312**, 002 (2013) [arXiv:1308.1647 [hep-th]].
17. N. A. Ondo and A. J. Tolley, JHEP **1311** (2013) 059 [arXiv:1307.4769 [hep-th]].
18. C. de Rham, K. Hinterbichler, R. A. Rosen and A. J. Tolley, Phys. Rev. D **88**, no. 2, 024003 (2013) [arXiv:1302.0025 [hep-th]].
19. C. de Rham, M. Fasiello and A. J. Tolley Phys. Lett. B **733**, no 2, 46 (2014) [arXiv:1308.2702 [hep-th]].
20. C. de Rham, L. Keltner and A. J. Tolley, arXiv:1403.3690 [hep-th].
21. G. D'Amico, C. de Rham, S. Dubovsky, G. Gabadadze, D. Pirtskhalava and A. J. Tolley, Phys. Rev. D **84**, 124046 (2011) [arXiv:1108.5231 [hep-th]].
22. M. S. Volkov, Phys. Rev. D **86**, 061502 (2012) [arXiv:1205.5713 [hep-th]].
23. M. S. Volkov, Phys. Rev. D **86**, 104022 (2012) [arXiv:1207.3723 [hep-th]].
24. N. Khosravi, G. Niz, K. Koyama and G. Tasinato, JCAP **1308**, 044 (2013) [arXiv:1305.4950 [hep-th]].
25. A. E. Gumrukcuoglu, C. Lin and S. Mukohyama, JCAP **1203**, 006 (2012) [arXiv:1111.4107 [hep-th]].
26. A. E. Gumrukcuoglu, C. Lin and S. Mukohyama, Phys. Lett. B **717**, 295 (2012) [arXiv:1206.2723 [hep-th]].
27. P. Gratia, W. Hu and M. Wyman, Phys. Rev. D **86**, 061504 (2012) [arXiv:1205.4241 [hep-th]].
28. M. Wyman, W. Hu and P. Gratia, Phys. Rev. D **87**, no. 8, 084046 (2013) [arXiv:1211.4576 [hep-th]].
29. T. Kobayashi, M. Siino, M. Yamaguchi and D. Yoshida, Phys. Rev. D **86**, 061505 (2012) [arXiv:1205.4938 [hep-th]].
30. A. De Felice, A. E. Gmrkolu, C. Lin and S. Mukohyama, JCAP **1305**, 035 (2013) [arXiv:1303.4154 [hep-th]].
31. A. De Felice, A. E. Gumrukcuoglu and S. Mukohyama, Phys. Rev. Lett. **109**, 171101 (2012) [arXiv:1206.2080 [hep-th]].
32. A. De Felice, A. E. Gmrkolu, C. Lin and S. Mukohyama, Class. Quant. Grav. **30**, 184004 (2013) [arXiv:1304.0484 [hep-th]].
33. G. Tasinato, K. Koyama and G. Niz, Class. Quant. Grav. **30**, 184002 (2013) [arXiv:1304.0601 [hep-th]].
34. A. E. Gumrukcuoglu, C. Lin and S. Mukohyama, JCAP **1111**, 030 (2011) [arXiv:1109.3845 [hep-th]].
35. B. Vakili and N. Khosravi, Phys. Rev. D **85**, 083529 (2012) [arXiv:1204.1456 [gr-qc]].
36. M. Fasiello and A. J. Tolley, JCAP **1211**, 035 (2012) [arXiv:1206.3852 [hep-th]].

37. C. de Rham and S. Renaux-Petel, JCAP **1301**, 035 (2013) [arXiv:1206.3482 [hep-th]].
38. M. von Strauss, A. Schmidt-May, J. Enander, E. Mortsell and S. F. Hassan, JCAP **1203**, 042 (2012) [arXiv:1111.1655 [gr-qc]].
39. D. Comelli, M. Crisostomi, F. Nesti and L. Pilo, JHEP **1203**, 067 (2012) [Erratum-ibid. **1206**, 020 (2012)] [arXiv:1111.1983 [hep-th]].
40. M. S. Volkov, JHEP **1201**, 035 (2012) [arXiv:1110.6153 [hep-th]].
41. Y. Akrami, T. S. Koivisto and M. Sandstad, JHEP **1303**, 099 (2013) [arXiv:1209.0457 [astro-ph.CO]].
42. N. Khosravi, H. R. Sepangi and S. Shahidi, Phys. Rev. D **86**, 043517 (2012) [arXiv:1202.2767 [gr-qc]].
43. M. Berg, I. Buchberger, J. Enander, E. Mortsell and S. Sjors, JCAP **1212**, 021 (2012) [arXiv:1206.3496 [gr-qc]].
44. G. DAmico, G. Gabadadze, L. Hui and D. Pirtskhalava, Class. Quant. Grav. **30**, 184005 (2013) [arXiv:1304.0723 [hep-th]].
45. A. De Felice, A. E. Gmrko?lu, C. Lin and S. Mukohyama, Class. Quant. Grav. **30**, 184004 (2013) [arXiv:1304.0484 [hep-th]].
46. S. Mukohyama, arXiv:1309.2146 [hep-th].
47. A. De Felice, A. E. Gumrukcuoglu and S. Mukohyama, Phys. Rev. D **88**, 124006 (2013) [arXiv:1309.3162 [hep-th]].
48. A. De Felice and S. Mukohyama, Phys. Lett. B **728**, 622 (2014) [arXiv:1306.5502 [hep-th]].
49. D. Comelli, F. Nesti and L. Pilo, arXiv:1307.8329 [hep-th]. D. Comelli, F. Nesti and L. Pilo, arXiv:1305.0236 [hep-th].
50. G. Leon, J. Saavedra and E. N. Saridakis, Class. Quant. Grav. **30**, 135001 (2013) [arXiv:1301.7419 [astro-ph.CO]].
51. D. -J. Wu, Y. -S. Piao and Y. -F. Cai, Phys. Lett. B **721**, 7 (2013) [arXiv:1301.4326 [hep-th]].
52. N. Tamanini, E. N. Saridakis and T. S. Koivisto, JCAP **1402**, 015 (2014) [arXiv:1307.5984 [hep-th]].
53. K. Hinterbichler, J. Stokes and M. Trodden, Phys. Lett. B **725**, , 1 (2013) [arXiv:1301.4993 [astro-ph.CO]].
54. M. Andrews, K. Hinterbichler, J. Stokes and M. Trodden, Class. Quant. Grav. **30**, 184006 (2013) [arXiv:1306.5743 [hep-th]].
55. M. Jaccard, M. Maggiore and E. Mitsou, Phys. Rev. D **88**, no. 4, 044033 (2013) [arXiv:1305.3034 [hep-th]].
56. L. Modesto and S. Tsujikawa, Phys. Lett. B **727**, 48 (2013) [arXiv:1307.6968 [hep-th]].
57. G. D'Amico, G. Gabadadze, L. Hui and D. Pirtskhalava, Phys. Rev. D **87**, no. 6, 064037 (2013) [arXiv:1206.4253 [hep-th]].
58. A. De Felice and S. Mukohyama, Phys. Lett. B **728**, 622 (2014) [arXiv:1306.5502 [hep-th]].
59. A. De Felice, A. E. Gumrukcuoglu and S. Mukohyama, Phys. Rev. D **88**, 124006 (2013) [arXiv:1309.3162 [hep-th]].
60. N. Khosravi, H. R. Sepangi and S. Shahidi, Phys. Rev. D **86**, 043517 (2012) [arXiv:1202.2767 [gr-qc]].

NEWTONIAN AND POST NEWTONIAN COSMOLOGY: C$\rightarrow \infty$ AND BEYOND

D.B. THOMAS
ICG, University of Portsmouth, Dennis Sciama Building,
Burnaby Road, Portsmouth, PO1 3FX, United Kingdom

Newtonian simulations are an important part of a cosmologist's toolkit in the 21st century. However, these simulations do not capture all of the phenomena that are present in General Relativity (GR). Here, I introduce the post-Friedmann formalism, a formalism for deriving not just the non-linear equations in the Newtonian limit, but also the corrections to those equations. These corrections include the GR quantities that have no counterpart in Newtonian theory. I use this formalism to examine weak lensing, in particular noting the extra terms in the deflection angle that exist on non-linear scales, but are not included when ray-tracing through N-body simulations. I then calculate the magnitude of the lowest order correction to ray tracing, the vector potential, showing that its contribution to lensing is negligible. This justifies the use of ray-tracing in a ΛCDM cosmology.

1 Introduction

Cosmologists predominantly perform gravitational calculations using two methods. On the largest scales, cosmological perturbation theory or one of its extensions is used. These schemes have the advantage of fully capturing general relativistic phenomenology, but can only be used on scales where the matter perturbations are small. Conversely, on smaller scales, Newtonian N-body simulations are used. These simulations are valid for arbitrary matter perturbations, but do not include all of the effects of GR (such as gravitational waves, the vector potential and the difference between the scalar potentials). Thus, Newtonian theory is incomplete, even if it is accurately computing the evolution of the cosmological density field and gravitational potential.

In this proceedings I will use the post-Friedmann formalism,[1] a recently developed approach for examining the Newtonian regime in cosmology and the corrections to it, including the beyond-Newtonian quantities. I will use this formalism to examine weak-lensing on fully non-linear scales in the universe and point out the corrections to the standard ray-tracing approach to weak-lensing on non-linear scales. I will then show a calculation of the first correction, the vector potential, and show that it is negligible for weak-lensing studies. I will comment on how this justifies the use of ray-tracing for a ΛCDM cosmology.

2 The post-Friedmann formalism

The post-Friedmann formalism is based on a post-Newtonian-style expansion in inverse powers of the speed of light c.[1] This expansion essentially takes the weak-field, quasi-static, low velocity, sub-horizon and negligible pressure limit of the fully non-linear Einstein equations. However, it does so in a way that doesn't just yield the leading order equations, but also the higher order corrections to them. The perturbed metric is written in Poisson gauge as follows

$$\begin{aligned} g_{00} &= -\left[1 - \frac{2U_N}{c^2} + \frac{1}{c^4}\left(2U_N^2 - 4U_P\right)\right] \\ g_{0i} &= -\frac{aB_i^N}{c^3} - \frac{aB_i^P}{c^5} \\ g_{ij} &= a^2\left[\left(1 + \frac{2V_N}{c^2} + \frac{1}{c^4}\left(2V_N^2 + 4V_P\right)\right)\delta_{ij} + \frac{h_{ij}}{c^4}\right]. \end{aligned} \tag{1}$$

The g_{00} and g_{ij} scalar potentials have been split into the Newtonian (U_N, V_N) and post-Friedmann (U_P, V_P) components. Similarly, the vector potential has been split up into B_i^N and B_i^P. Since this metric is in the Poisson gauge, the three-vectors B_i^N and B_i^P are divergenceless, $B_{i,i}^N = 0$ and $B_{i,i}^P = 0$. In addition, h_{ij} is transverse and tracefree, $h_i^i = h_{ij}^{,i} = 0$. The energy momentum tensor for pressureless dust is also expanded in powers of c, allowing the Einstein equations to be derived, both at leading order and beyond. At leading order, the standard Newtonian continuity and Euler equations are found, along with the following gravitational equations

$$\begin{aligned} &\frac{1}{c^2a^2}\nabla^2 V_N = -\frac{4\pi G}{c^2}\rho_b\delta \\ &\frac{2}{c^2a^2}\nabla^2\left(V_N - U_N\right) = 0 \\ &\frac{1}{c^3}\left[\frac{2\dot{a}}{a^2}U_{N,i} + \frac{2}{a}\dot{V}_{N,i} - \frac{1}{2a^2}\nabla^2 B_i^N\right] = \frac{8\pi G\rho_b}{c^3}\left(1+\delta\right)v_i. \end{aligned} \tag{2}$$

As expected, we have the standard Newtonian Poisson equation and an equation enforcing the equality of the two scalar potentials. In addition, we have an equation for the vector potential: At leading order this is generated by the Newtonian momentum field and setting it to zero would enforce an extra constraint on the Newtonian dynamics. The equations at the next order are given by [1]

$$\begin{aligned} &\frac{1}{c^4}\nabla^2\nabla^2 V_P = \frac{1}{c^4}\left\{\frac{1}{2}\nabla^2\nabla^2\left(V_N^2\right) - \frac{5}{4}\nabla^2\left(V_{N,i}V_N^{,i}\right) - 2\pi G a^2\bar{\rho}\left[\nabla^2\left(v^2\left(1+\delta\right)\right) - 3\dot{a}\left(v_i\left(1+\delta\right)\right)^{,i}\right]\right\} \\ &\frac{1}{c^4}\frac{4}{3}\nabla^2\nabla^2\left(U_P - V_P\right) = \frac{1}{c^4}\left(\mathcal{A}_{i,j}^{j,i} + 8\pi G a^2\bar{\rho}\mathcal{S}_{i,j}^{j,i}\right) \\ &\frac{1}{c^4}\nabla^2\nabla^2\nabla^2 h_i^j = \frac{1}{c^4}\Big[-\mathcal{A}_{k,li}^{l,kj} - \nabla^2\mathcal{A}_{k,l}^{l,k}\delta_i^j + 2\nabla^2\mathcal{A}_{i,k}^{k,j} + 2\nabla^2\mathcal{A}_{l,ki}^{k}\delta^{lj} - 2\nabla^2\nabla^2\mathcal{A}_i^j \\ &\qquad\qquad + 8\pi G a^2\bar{\rho}\left(-\mathcal{S}_{k,li}^{l,kj} - \nabla^2\mathcal{S}_{k,l}^{l,k}\delta_i^j + 2\nabla^2\mathcal{S}_{l,ki}^{k}\delta^{lj} + 2\nabla^2\mathcal{S}_{i,k}^{k,j} - 2\nabla^2\nabla^2\mathcal{S}_i^j\right)\Big] \\ &\mathcal{A}_i^j = 2V_{N,i}V_N^{,j} - \frac{2}{3}\delta_i^j V_{N,k}V_N^{,k} \\ &\mathcal{S}_i^j = \left(1+\delta\right)\left(v_i v^j - \frac{1}{3}\delta_i^j v^2\right). \end{aligned} \tag{3}$$

3 Weak lensing in the post-Friedmann approach

Here I will present the weak-lensing deflection angle obtained in the post-Friedmann approach. Crucially, the equations above from the post-Friedmann approach allow us to relate the metric potentials in the deflection angle to the matter distribution regardless of the size of the matter perturbations, so this deflection angle is valid for fully non-linear scales. We will not present the details of the derivation of the deflection angle here, see Thomas *et al.*[2]

The post-Friedmann deflection angle is given by

$$\alpha^i = \int_0^{\chi_s} d\chi\left(\frac{\chi - \chi_s}{\chi_s}\right)\left[\begin{array}{c} \frac{1}{c^2}(U_N + V_N)^{,i} - \frac{1}{c^3}B_\chi^{,i} \\ + \frac{1}{c^4}(U_N + V_N)^{,i}_{,j}\int_0^\chi d\chi'(\chi - \chi')(U_N + V_N)^{,j} \\ + \frac{2}{c^4}(U_P + V_P)^{,i} - \frac{a}{c^4}\dot{B}^i + \frac{1}{2c^4}h_{\chi\chi}^{,i} \end{array}\right], \tag{4}$$

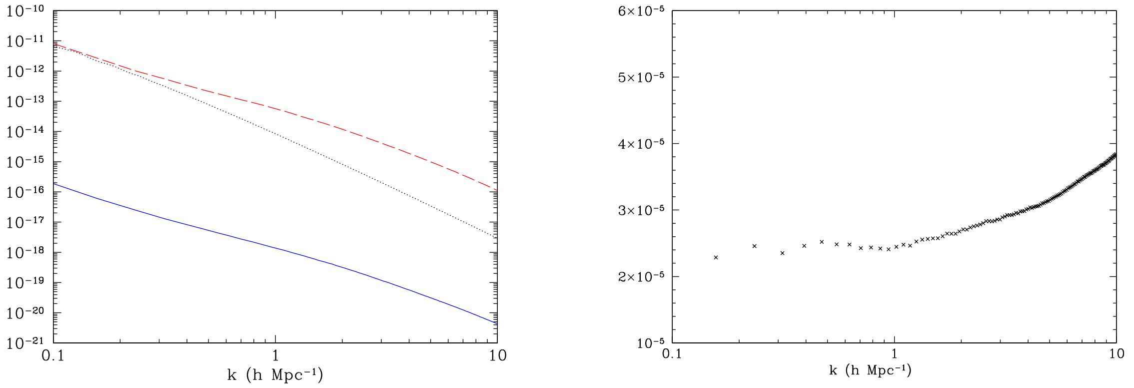

Figure 1 – The left plot shows the scalar potential (dashed red) and vector potential (solid blue) power spectra as extracted from N-body simulations. The linear theory scalar potential is show for reference (black dotted). The plot on the right shows the ratio of the vector potential power spectrum to the scalar potential power spectrum.

where χ is the comoving distance and χ_s is the comoving distance to the source. In this equation, we can see the standard leading order term $(U_N+V_N)^{,i}$ as well as contributions from the tensors, vectors, post-Newtonian scalar potentials, and the higher order contributions from combinations of the leading order potentials. I have highlighted in blue all of the terms that are included in a standard ray-tracing analysis for calculating weak-lensing observables on non-linear scales. The leading order correction to the ray-tracing terms is the contribution from the vector potential $B_\chi^{,i}$, in the next section I will calculate the magnitude of this quantity from N-body simulations. It must be negligible for the standard ray-tracing approach to be valid.

4 Vector potential

The physical effect embodied by the vector potential is frame-dragging, a ubiquitous relativistic effect that has been measured in the Solar System by Gravity Probe B.[3] The vector potential B_i is sourced by the vector part of the momentum field, $(1+\delta)\vec{v}$. Equivalently, it can be computed using

$$\nabla \times \nabla^2 \vec{B} = -\left(16\pi G\rho_b a^2\right) \nabla \times \left[(1+\delta)\vec{v}\right]. \tag{5}$$

In this leading order regime, the density and velocity fields sourcing the vector potential obey the Newtonian equations. Thus, using equation (5), we can extract the curl of the momentum field from N-body simulations and therefore calculate the vector potential. This was done [4,5] using the Delauney Tesselation Field Estimator (DTFE) code [6] to extract the velocity field and its derivatives. We refer the interested reader to those works for the technical details of the extraction and the tests performed to establish the robustness of the extraction. In figure 1, the power spectra of the scalar and vector gravitational potential are plotted, as extracted from N-body simulations.[4] The power spectra plotted here are the dimensionless power spectra. In the right hand plot, I show the ratio of the power spectra of the vector and scalar potentials, showing that the power spectrum of the vector potential is of order 10^5 times smaller than that of the scalar potential. Our simulations [5] show that this ratio holds over this range of scales from $z = 0$ up to $z = 2$. The leading order contributions to the E-mode power spectrum of cosmic shear for the scalar and vector are

$$\begin{aligned} P_E^{\Phi}(l) &= l^4 \int_0^{\chi_\infty} d\chi \frac{g^2(\chi)}{\chi^6} P_\Phi(l/\chi) \\ P_E^{B^N}(l) &= \frac{l^4}{4} \int_0^{\chi_\infty} d\chi \frac{g^2(\chi)}{\chi^6} P_{B^N}(l/\chi), \end{aligned} \tag{6}$$

where $g(\chi)$ is the weak-lensing weight function and source distribution. From these equations, and the result above for the vector potential power spectrum, we can see that the contribution to the E-mode from the vector potential is negligible. However, there is one more effect of the vector potential that needs to be considered, which is that the time derivative of it can generate a B-mode of cosmic shear, an effect that is not generated at leading order by the scalar potential. It is difficult to extract the time derivative from N-body simulations, so we have estimated the magnitude of the B-mode that would be generated by the time derivative of the vector potential,[2] showing it to be negligible for future surveys. We have thus shown that the lowest order corrections to the E- and B-mode power spectra obtained from ray-tracing are negligible. In order for the use of Newtonian N-body simulations to be valid in cosmology, the higher order U_P, V_P and h_{ij} terms would be expected to be no larger than B_i. Thus, the standard ray-tracing approach is valid for a ΛCDM cosmology.

5 Conclusion

Newtonian theory doesn't fully encompass all of the GR phenomena that exist in our universe. In this proceedings I have shown that the post-Friedmann formalism can be used for going beyond Newtonian theory, even on scales where the density fluctuations are not small. I have computed the post-Friedmann weak-lensing deflection angle, which can be related to the matter content regardless of the size of the matter perturbations. This deflection angle is thus valid on fully non-linear scales. I have noted that this deflection angle includes extra terms that are not taken into account when ray-tracing is used to calculate weak-lensing observables on non-linear scales.

The lowest order correction is the contribution of the vector potential, B_i. I have shown that, at leading order, this vector potential is sourced by the vector part of the Newtonian momentum field, $(1+\delta)\vec{v}$. I have shown that this quantity can be calculated from N-body simulations, and presented its power spectrum at redshift zero. By showing that the power spectrum of the vector potential is of order 10^5 times smaller than the power spectrum of the scalar potential, I have shown that the contribution of the vector potential to the E-mode of cosmic shear is negligible. Combined with our estimate of the B-mode generated by the time derivative of the vector potential,[2] I argue that the standard ray tracing approach is justified on fully non-linear scales for a ΛCDM cosmology.

I close by noting that although the deflection angle applies to any metric theory of gravity, the equations relating the matter fluctations to the metric potentials will be different in an alternative theory. Furthermore, the modified evolution of the matter fluctuations may mean that the vector potential and other beyond-Newtonian quantities are no longer negligible. Work is currently underway to apply the post-Friedmann formalism to f(R) gravity and examine the magnitude of the vector potential on fully non-linear scales in an f(R) cosmology.

Acknowledgments

I acknowledge use of SCIAMA at Portsmouth university and COSMOS at Cambridge University.

References

1. I. Milillo, D. Bertacca, M. Bruni and A. Maselli, In prep.
2. D. B. Thomas, M. Bruni and D. Wands, arXiv:1403.4947 [astro-ph.CO].
3. C. W. F. Everitt *et al.*, Phys. Rev. Lett. **106** (2011) 221101
4. M. Bruni, D. B. Thomas and D. Wands, Phys. Rev. D **89** (2014) 044010
5. D. B. Thomas, M. Bruni, and D. Wands, In prep.
6. M. C. Cautun and R. van de Weygaert, arXiv:1105.0370 [astro-ph.IM].

COSMOLOGICAL PROBES OF SCREENING MECHANISMS IN MODIFIED GRAVITY

C. LLINARES
Institute of theoretical astrophysics, University of Oslo,
Oslo, Norway

Several extensions of the standard cosmological model include scalar fields as new degrees of freedom in the underlying gravitational theory. A particular class of these scalar field theories include screening mechanisms intended to hide the scalar field below observational limits in the Solar System, but not on galactic scales, where data still gives the freedom to find possible signatures of their presence. Here I present two different results related to scalar-tensor theories for gravity. In the first place, I propose a particular observable that is sensitive to the underlying gravitational theory and thus can be used to test it. Secondly, I report results that were obtained in the context of N-body simulations and are related to the validity of the quasi-static approximation that is often employed when running such simulations.

1 Introduction

One of the most relevant open problems in present cosmology consists in the determination of the nature and origin of the dark energy responsible for the accelerated expansion of the Universe. Among the different possible solutions to this problem exist the idea of modifying the gravitational theory. Several alternative gravitational theories exist at this moment, all of them including extra degrees of freedom in the form of scalar, vector or even tensor fields.

Since Solar System tests show general relativity (GR) as a valid theory, any alternative theory has to behave as GR when scales, densities or accelerations are as in the Solar System. This gives rise to the concept of screening mechanism, which is mandatory for any universally coupled theory. The key feature of these screening mechanisms is to switch off the extra degrees of freedom inside matter overdensites (small scales), and to switch them on in the cosmological background (large scales). When the scalar fields are *on* a fifth force emerges between the matter particles. When it is *off* (the field is screened) the fifth force disappears and GR is recovered. The determination of observable quantities that are sensitive to this fifth force and therefore can be used as a test for its presence is a fundamental area of research in the context of modified gravity.

Here I present a new test for scalar-tensor theories for gravity which is based in the shape of the dark matter halos. We employed this technique to obtain constraints in the parameters of two different models: symmetron and chameleon. The models are representative of two different screening mechanisms. In the first case, the scalar field is screened by restoring a particular symmetry. On the other hand, the chameleon scalar field is screened by making it very massive and close to zero.

In the second part of this report, I show the consequence of relaxing the widely used quasi-static approximation in N-body simulations with modified gravity. This will be done by comparing results from static and non-static simulations that we run with our novel implementation of scalar fields in the code Ramses.

2 Shapes of clusters as a proof of screening mechanisms

Clusters of galaxies are not spherical, but have shapes that can be approximated with triaxial ellipsoids. The axial ratios of this ellipsoids can be determined observationally by employing three different techniques: optical observations (which gives information about the distribution of galaxies), gravitational lensing (which describes the distribution of the total dynamical mass) and X-ray emission of the intra-cluster medium. Here we are interested in this last observational technique since, under the assumption of hydro-static equilibrium, it gives direct information about the distribution of the total gravitational potential.

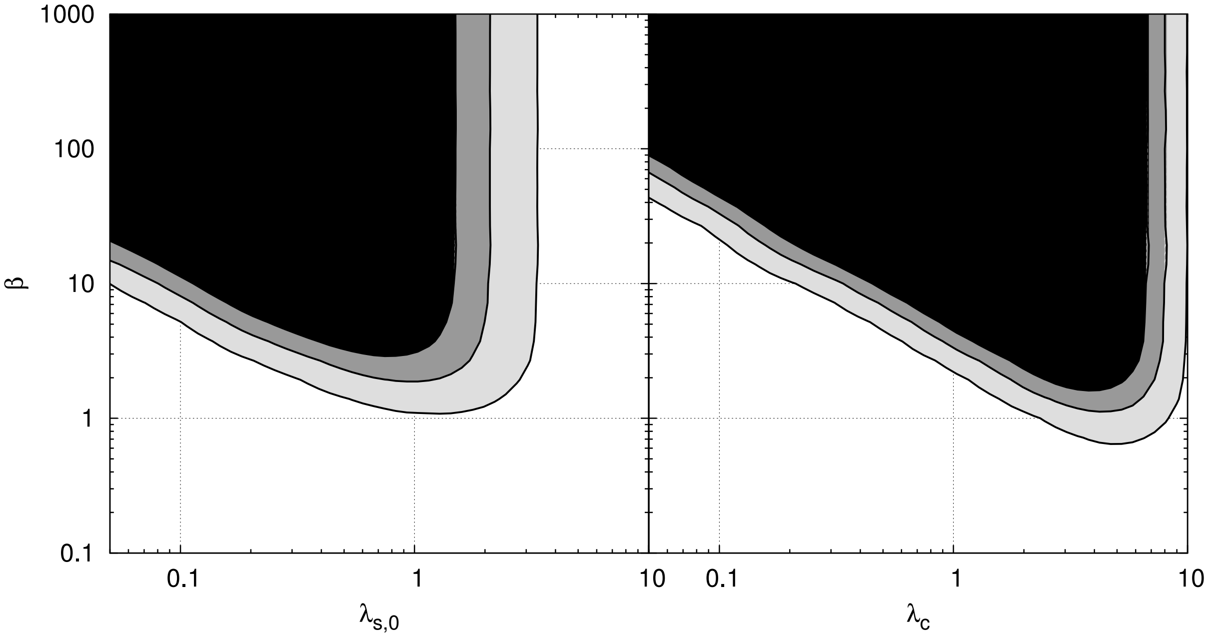

Figure 1 – Contours of relative difference $\Delta\epsilon/\epsilon_N$ between ellipticities that correspond to the modified models with respect to Newtonian gravity. Given the observed value for $\epsilon = 0.18 \pm 0.05$, we find that the set of parameters laying in the black regions are excluded by more than 3σ, while the white regions have ellipticities that lie within 1σ of the observed value (i.e. correspond to accepted values). The left and right panels correspond to symmetron and chameleon models respectively.

In standard gravity it is well known that the surfaces of constant gravitational potential are more spherical than the iso-density contours. In observational terms, this means that the ellipticity of the iso-contours of the X-ray maps are smaller than that of the lensing maps. In the scalar-tensor theories studied here, we found that this is not the case anymore. A simple way to see this, for instance in the chameleon model, consists in taking into account that in the regions where the scalar field is screened, the field is forced to stay close to the minimum of its effective potential. This minimum is uniquely determined by the local matter density thanks to the coupling between the scalar field and the density in the equation of motion. This implies that in the strong coupled limit, the iso-contours of the scalar field will be completely aligned with the contours of the matter density, no matter how the density is distributed. When taking into account this effect in the total gravitational force, we find that the ellipticity of the total iso-potentials is increased with respect to the standard gravity case.

We confirmed this hand waving arguments, by calculating numerically the shape of the iso-surfaces of the total gravitational potential (i.e. including the scalar field contribution) for fixed triaxial dark matter halos. This result can be used to obtain constraints in the model parameters since there will be a subset of the total parameter space for which the ellipticity will go beyond the observed value. In order to perform this test, we employed the value and error reported by Lau and collaborators [1]: $\epsilon = 0.18 \pm 0.05$. The figure 1 shows the constraints that we derived for the coupling constant β and the range of the field λ for the symmetron (left) and chameleon (right) models. Details of this constraints can be found in reference [2].

It is important to note that this calculation was made using a fixed dark matter density profile and that time evolution was not taken into account. As the shape of the dark matter halos are dominated by non-linear effects, N-body simulations are mandatory to make a complete treatment of the problem. We presented results obtained from N-body simulations in ref. [3]. By analyzing the shape of the dark matter halos in the simulations we found that the symmetron model gives results that are consistent with the static analysis (i.e. the ellipticity of the halos increases in the modified gravity case). On the other hand, the chameleon simulations show that the ellipticity can either increase or decrease depending of the model parameters and mass of the dark matter halos with respect to ΛCDM.

3 Cosmological simulations out of the static limit

In several scalar-tensor theories for gravity, the equation of motion for the extra degree of freedom ϕ takes the following form:

$$\ddot{\phi} + 3H\dot{\phi} - \frac{\nabla^2\phi}{a^2} = f(\rho, \phi). \tag{1}$$

When running N-body simulations with this class of theories there is a universally adopted hypothesis which consist in neglecting the time derivatives in this equation. The approximation converts the Klein-Gordon equation in an elliptic equation which can be solved in every time step of an N-body simulation by means of well know multigrid techniques. Here I present results from the first non-static simulations that were run with the symmetron model.

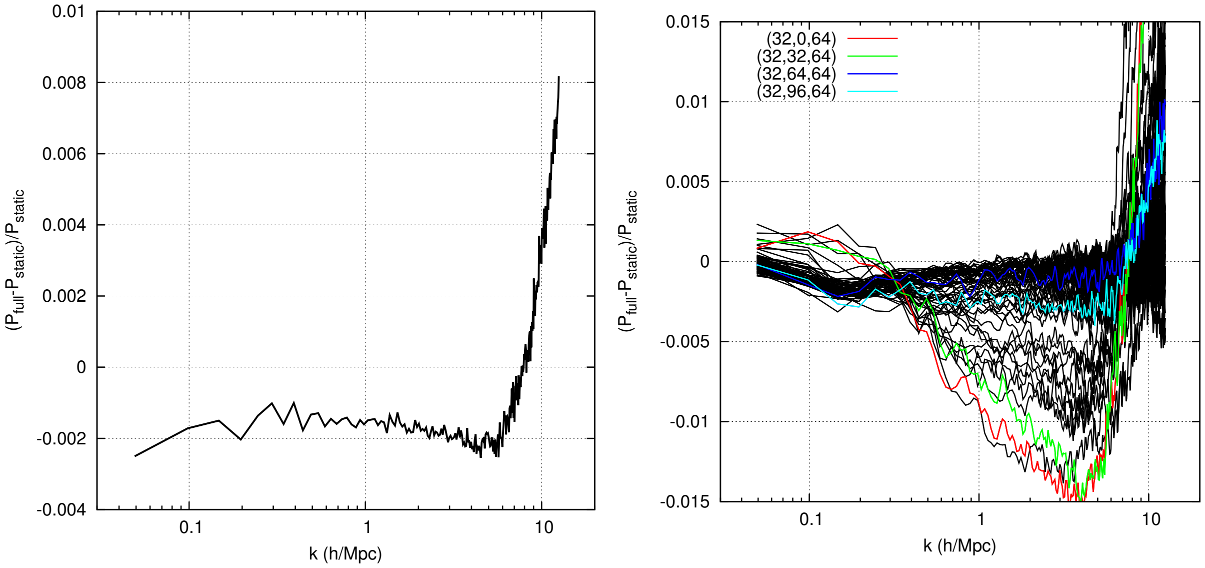

Figure 2 – Left: relative difference between the power spectra obtained from static and non-static cosmological simulations. Right: same as before, but for local power spectra which were obtained by passing the density distribution trough Gaussian filters centered at 64 different positions in the box. The four color lines correspond to four representative locations which are inside (red and green) and outside (light and dark blue) a domain wall.

The N-body code used for this simulations is a modified version of the code Ramses, to which we included static and non-static symmetron solvers for the Klein-Gordon equation. The modification for the non-static case consists in including a leap-frog scheme (similar to the one used to track the position and velocities of the particles) to follow the evolution of the scalar field and its time derivative. As the non-static scalar field solver has to track the very rapid oscillations of the scalar field (which can not be modeled with static codes), we also included a new time step in the code, much smaller than the usual time step used to follow the positions of the particles. Details on the simulations, as well as an extensive description of the code and the tests that were performed to it, can be found in reference [4].

In order to test the consequences of including non-static terms in the Klein-Gordon equation, we run different simulations using both static and non-static solvers. I present here the effects that non-static terms have in the power spectrum of density perturbations. The left panel of figure 2 shows the relative difference between the power spectrum of the static and non-static simulations. Non-static effects are below 1% in this particular quantity. However, it is possible to see that there is an offset of around 0.2% almost in the whole domain of studied frequencies. By running several simulations with different set ups, we found that the offset that appears in the low frequency region is a numerical artifact that can be reduced by using smaller time steps during the simulation. On the other hand, the high frequency offset is physical and related to the domain walls that characterize this particular model. These domain walls are produced by the fact that in the symmetron model the effective potential has two different minima. This produces a domain decomposition in a way that in some regions in space, the scalar field oscillates around positive values while in different regions it oscillates around a negative minimum. These domain walls (interface between different domains) have their own dynamics, which is independent of the evolution of the matter component. As a consequence, the position and shape of the domain walls can not be tracked by using static simulations. By comparing simulations in which the domain walls are present to those in which they are absent, we could confirm that the small scale offset in the power spectrum is produced by the perturbation in the matter distribution produced by the presence of the domain walls. In any case, the offset that appears in the power spectrum when the non-static equation is used is far beyond observational detection and thus, can be neglected (at least for the calculation of the power spectrum of density perturbations).

In order to better understand the effects that domain walls have in the matter distribution, we calculated the power spectrum locally by passing the over-density obtained from the distribution of particles through a Gaussian filter before calculating its Fourier transform. The filter was centered in 64 different positions given by a uniform grid of 4 nodes per dimension. The result can be found in the right panel of figure 2. In the regions that are far from the domain walls, the power spectrum appears unperturbed when non-static terms are included during the simulation. On the other hand, we found that the difference between static and non-static simulations can be up to 1.5% in the regions where the domain walls exist.

Acknowledgments

CLL thanks the Research Council of Norway FRINAT grant 197251/V30.

References

1. E. T. Lau and et al. Constraining Cluster Physics with the Shape of X-ray Clusters: Comparison of Local X-ray Clusters versus LCDM Clusters. *ArXiv e-prints*, January 2012.
2. C. Llinares and D. F. Mota. Shape of Clusters of Galaxies as a Probe of Screening Mechanisms in Modified Gravity. *Physical Review Letters*, 110(15):151104, April 2013.
3. C. Llinares, D. F. Mota, and H. A. Winther. ISIS: a new N-body cosmological code with scalar fields based on RAMSES. Code presentation and application to the shapes of clusters. *A&A*, 562:A78, February 2014.
4. C. Llinares and D. F. Mota. Cosmological simulations of screened modified gravity out of the static approximation: Effects on matter distribution. *Phys. Rev. D*, 89(8):084023, April 2014.

NON-LOCAL INFRARED MODIFICATIONS OF GRAVITY AND DARK ENERGY

YVES DIRIAN[1], STEFANO FOFFA[1], NIMA KHOSRAVI[2], MARTIN KUNZ[1,3], MICHELE MAGGIORE[1], MICHELE MANCARELLA[4] and ERMIS MITSOU[1]
[1]*Département de Physique Théorique and Center for Astroparticle Physics,*
Université de Genève, 24 quai Ansermet, CH–1211 Genève 4, Switzerland
[2]*School of Astronomy, Institute for Research in Fundamental Sciences (IPM),*
P. O. Box 19395-5531, Tehran, Iran
[3]*African Institute for Mathematical Sciences, 6 Melrose Road, Muizenberg, 7945, South Africa*
[4]*Dipartimento di Fisica"Enrico Fermi", Università di Pisa, Largo Bruno Pontecorvo, 3, 56127 Pisa, Italy.*

We discuss a model obtained adding a non-local term $m^2(\Box^{-1}R)^2$ to the Einstein-Hilbert action. This model recovers all successes of GR at solar system and lab scales, and generates a dynamical dark energy on cosmological scales. The resulting equation of state for dark energy turns out to be on the phantom side. We discuss the corresponding cosmological perturbations. The nonlocal model provides a good fit to supernova data and predicts deviations from General Relativity in structure formation and in weak lensing at the level of 3-4%, therefore consistent with existing data but readily detectable by future surveys.

1 Introduction

The experimental observation of the accelerated expansion of the Universe [1,2] has stimulated an intense search for modifications of General Relativity (GR) at cosmological scales. The construction of a consistent infrared deformation of GR turns out however to be extremely challenging. A natural way to proceed is to introduce a mass scale m of the order of the present value of the Hubble parameter H_0. In a recent series of papers [3,4,5,6,7,8,9] our group has developed an approach in which a mass parameter enters the theory as the coefficient of a suitable nonlocal term.

Probably the simplest example that suggests that non-local operators can provide an interesting way of modifying a theory in the infrared is provided by the theory of a massive photon. This is described usually by the Proca Lagrangian,

$$\mathcal{L} = -\frac{1}{4}F_{\mu\nu}F^{\mu\nu} - \frac{1}{2}m_\gamma^2 A_\mu A^\mu \,. \tag{1}$$

As shown in [10,11], this theory is actually equivalent to a theory with Lagrangian

$$\mathcal{L}' = -\frac{1}{4}F_{\mu\nu}\left(1 - \frac{m_\gamma^2}{\Box}\right)F^{\mu\nu} \,. \tag{2}$$

The formulation (1) is explicitly local, but not gauge-invariant. In contrast, the Lagrangian (2) is explicitly gauge-invariant, even in the massive case, at the price of loss of manifest locality. The equivalence can be proved using the "Stückelberg trick", i.e. replacing in the Lagrangian (1)

$A_\mu \to A_\mu + m_\gamma^{-1}\partial_\mu\varphi$, obtaining a Lagrangian $\mathcal{L}(A_\mu, \varphi)$. By construction, the resulting theory is trivially invariant under the local transformation $A_\mu \to A_\mu - \partial_\mu\theta$, $\varphi \to \varphi + m_\gamma\theta$. The equations of motion obtained by taking the variation with respect to φ is $\Box\varphi + m_\gamma\partial_\mu A^\mu = 0$. Solving it formally as $\varphi(x) = -m_\gamma\Box^{-1}(\partial_\mu A^\mu)$ and plugging this back into the Lagrangian $\mathcal{L}(A_\mu, \varphi)$, one gets eq. (2).

The non-local operator $(1 - m^2/\Box)$ also appears in the degravitation proposal [12]. Partly inspired by these examples, we have begun to investigate various possible non-local models, and their cosmological consequences. In the Proca example, the non-local term can eliminated from the equations of motion derived from (2) by a suitable gauge fixing, so in this case the non-locality is of no consequences. In the more general cases that we will study this is not possible, and the non-locality is genuine. In that case, such models should be understood as effective classical equations, derived from some more fundamental and local theory. For example, nonlocal classical equations appear in the effective field theory of cosmological perturbations, which is an effective classical theory for the long-wavelength modes obtained by integrating out the short-wavelength modes [13]. Nonlocal effective classical equations can also appear by performing a quantum averaging. In particular nonlocal field equations govern the effective dynamics of the vacuum expectation values of quantum fields.[14,15]. Thus, nonlocality often appears in physics, but is always derived from some averaging process in a fundamental local theory. Issues of quantum consistency, such as the possible existence of ghosts in the spectrum of the quantum theory, cannot be addressed in the effective nonlocal classical theory, but can only be studied in the underlying fundamental quantum theory.

Of course, there are many possible nonlocal models that one could in principle study (much as, already in local QFT, there is always a wide range of possibility of model building). We present our investigation as an explorative study, in which we try to understand the typical cosmological consequences of nonlocal terms that can be associated to a mass parameter m. Still, some general conclusions can be drawn. For instance, models in which the $\Box^{-1}$ operator is applied to a tensor such as $G_{\mu\nu}$ suffer from cosmological instabilities, and are therefore not viable.[4,6,16,17] We therefore focus our attention on models involving $\Box^{-1}R$. The simplest action involving a mass scale m as a coefficient of a non-local term constructed with $\Box^{-1}R$ is

$$S_{\rm NL} = \frac{1}{16\pi G}\int d^4x\sqrt{-g}\,\left[R - \frac{1}{6}m^2 R\frac{1}{\Box^2}R\right]\,. \tag{3}$$

Observe that, upon integration by parts, we can equivalently write $R\,\Box^{-2}R = (\Box^{-1}R)^2$. In this talk we will focus, for definiteness, on this model. Other options have been studied in [8,18].

2 Background evolution

The corresponding evolution equations for a FRW background can be put into a local form introducing two auxiliary fields $U = -\Box^{-1}R$ and $S = -\Box^{-1}U$. Then, one obtains a coupled system of three differential equations for the Hubble parameter $H(t)$ and the fields $U(t)$ and $S(t)$ (see [8,9] for full details). In particular, the Friedmann equation takes the form $H^2(t) = (8\pi G/3)[\rho_{\rm M}(t) + \rho_{\rm R}(t) + \rho_{\rm DE}(U, S)]$, where $\rho_{\rm DE}$ depends on the auxiliary fields. The model therefore generates an effective dark energy term. Upon integration of the coupled system of differential equations, and using $x = \ln a(t)$ to parametrize the time evolution (where $a(t)$ is the FRW scale factor) one finds for $\rho_{\rm DE}(x)$ the result shown in the left panel of Fig. 1. We see that the effective DE density vanishes deep into the RD phase (the RD-MD transition is at $x_{\rm eq} \simeq -8.1$), and then grows as we enter in the MD phase. It is possible to choose our only free parameter $\gamma \equiv m^2/(9H_0^2)$ so to reproduce the observed value today, which is already a non-trivial result. In particular, tuning γ to the value $\gamma \simeq 0.0089247$ (corresponding to $m \simeq 0.283 H_0$) we get $\Omega_{\rm DE} \simeq 0.6825$ and therefore $\Omega_M \simeq 0.3175$, which is the value suggested by the *Planck* data[19] (assuming ΛCDM; of course, in the end, after computing the cosmological perturbation, in each

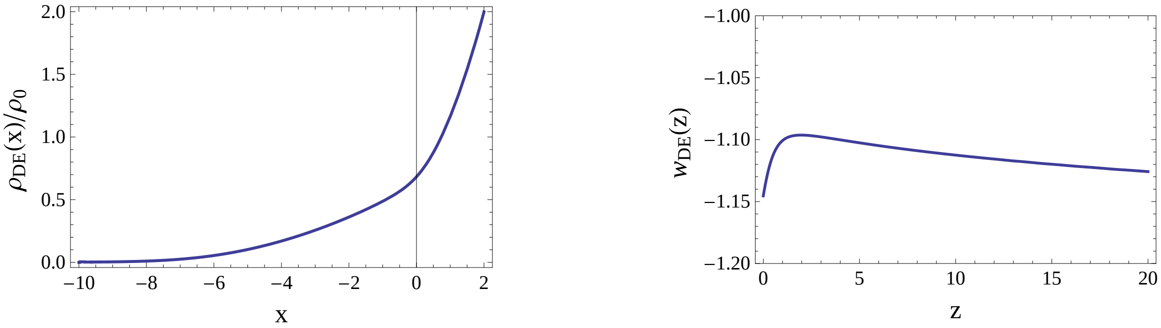

Figure 1 – Left: $\rho_{\rm DE}(x)/\rho_0$. Right: $w_{\rm DE}$ as a function of red-shift.

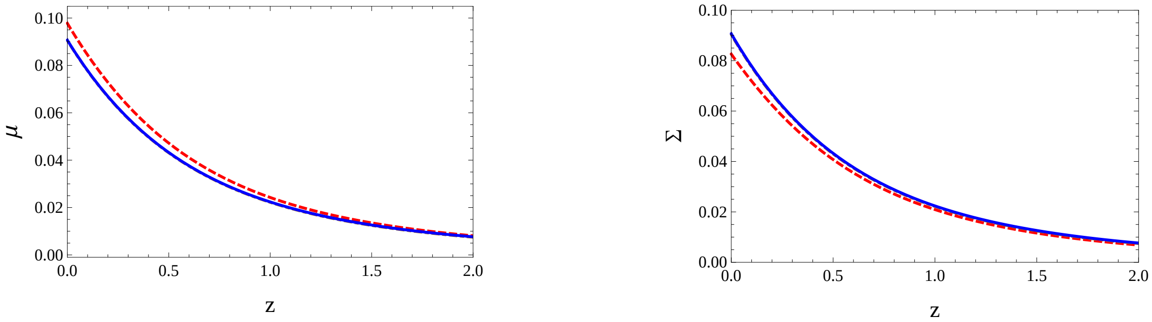

Figure 2 – Left panel: $\mu(z;k)$, as a function of the redshift z, for different values of the wave-number $\kappa = 0.1$ (red dashed) $\kappa = 1$ (brown dot-dashed) and $\kappa = 5$ (blue solid line), where $\kappa \equiv k/k_{\rm eq}$. The curves for $\kappa = 1$ and $\kappa = 5$ are almost indistinguishable on this scale. Right panel: the same for $\Sigma(z;k)$

nonlocal model the corresponding value of the cosmological parameters will be fixed by a global fit to the data). Having fixed γ in this way we have no more free parameters, and we get a pure prediction for the equation of state (EOS) parameter of dark energy $w_{\rm DE}$, defined from

$$\rho'_{\rm DE} + 3(1 + w_{\rm DE})\rho_{\rm DE} = 0\,. \tag{4}$$

The result is shown on the right panel of Fig. 1, where $w_{\rm DE}$ is now shown as a function of the redshift z. Observe that $w_{\rm DE}(z)$ is predicted to be on the phantom side, $w_{\rm DE}(z) < -1$. Supernova data are mostly sensitive to the background evolution of the cosmological model, so these results already allow us to compare our model to SNIa data. Using the data of the recent joint analysis ("JLA") of the SDSS-II and SNLS supernova samples [20] we find that the nonlocal model fits the SNe Ia data as well as ΛCDM, with a difference in χ^2 which is not significant [9].

2.1 Cosmological perturbation

We have performed a detailed analysis of the cosmological perturbations of this model. The perturbations turn out to be well-behaved and quite close to ΛCDM (see [9] for full details). The deviations can be compactly summarized in terms of two functions of redshift and wave-number, $\mu(z;k)$ and $\Sigma(z;k)$, defined by

$$\begin{aligned} \Psi &= [1 + \mu(z;k)]\Psi_{\rm GR}\,, & (5)\\ \Psi - \Phi &= [1 + \Sigma(z;k)](\Psi - \Phi)_{\rm GR}\,, & (6) \end{aligned}$$

where the subscript denotes the same quantities computed in GR, assuming a ΛCDM model with the same value of Ω_M as the modified gravity model. The advantage of this parametrization is that it neatly separates the modifications to the motion of non-relativistic particles, which is described by μ, from the modification to light propagation, which is encoded in Σ.

The results are shown in Fig. 2. We see that, for the sub-horizon modes relevant to observations, and in the range of redshifts relevant for comparison with the data, the deviation from ΛCDM are of about 2 to 4%, both in structure formation (which is determined by $\mu(z;k)$) and in weak lensing. Such deviations are consistent with existing data, but potentially detectable in the near future. In particular, we find that, in the recent epoch, $\mu(a)$ is well reproduced by the parametrization used in ref. [21], $\mu(a) = \mu_s a^s$ with the values $\mu_s = 0.094$ and $s = 2$. By comparison, the forecast for EUCLID on the error $\sigma(\mu_s)$, for fixed cosmological parameters, is $\sigma(\mu_s) = 0.0046$ for $s = 1$ and $\sigma(\mu_s) = 0.014$ for $s = 3$. For our model we therefore expect an accuracy of order 1% or better on μ_s, which would be largely sufficient to test our prediction $\mu_s \simeq 0.09$.

1. A. G. Riess et al. Observational evidence from supernovae for an accelerating universe and a cosmological constant. *Astron.J.*, 116:1009–1038, 1998.
2. S. Perlmutter et al. Measurements of Omega and Lambda from 42 high redshift supernovae. *Astrophys.J.*, 517:565–586, 1999.
3. M. Jaccard, M. Maggiore, and E. Mitsou. A non-local theory of massive gravity. *Phys.Rev.*, D88:044033, 2013.
4. M. Maggiore. Phantom dark energy from nonlocal infrared modifications of general relativity. *Phys.Rev.*, D89:043008, 2014.
5. S. Foffa, M. Maggiore, and E. Mitsou. Apparent ghosts and spurious degrees of freedom in non-local theories. *Phys.Lett.*, B733:76–83, 2014.
6. S. Foffa, M. Maggiore, and E. Mitsou. Cosmological dynamics and dark energy from non-local infrared modifications of gravity. 1311.3435.
7. A. Kehagias and M. Maggiore. Spherically symmetric static solutions in a non-local infrared modification of General Relativity. 1401.8289.
8. M. Maggiore and M. Mancarella. Non-local gravity and dark energy. 1402.0448.
9. Y. Dirian, S. Foffa, N. Khosravi, M. Kunz, and M. Maggiore. Cosmological perturbations and structure formation in nonlocal infrared modifications of general relativity. 1403.6068.
10. G. Dvali. Predictive Power of Strong Coupling in Theories with Large Distance Modified Gravity. *New J.Phys.*, 8:326, 2006.
11. G. Dvali, S. Hofmann, and J. Khoury. Degravitation of the cosmological constant and graviton width. *Phys.Rev.*, D76:084006, 2007.
12. N. Arkani-Hamed, S. Dimopoulos, G. Dvali, and G. Gabadadze. Nonlocal modification of gravity and the cosmological constant problem. hep-th/0209227.
13. D. Baumann, A. Nicolis, L. Senatore, and M. Zaldarriaga. Cosmological Non-Linearities as an Effective Fluid. *JCAP*, 1207:051, 2012.
14. R.D. Jordan. Effective Field Equations for Expectation Values. *Phys.Rev.*, D33:444–454, 1986.
15. E. Calzetta and B.L. Hu. Closed Time Path Functional Formalism in Curved Space-Time: Application to Cosmological Back Reaction Problems. *Phys.Rev.*, D35:495, 1987.
16. L. Modesto and S. Tsujikawa. Non-local massive gravity. *Phys.Lett.*, B727:48–56, 2013.
17. P. G. Ferreira and Antonio L. Maroto. A few cosmological implications of tensor nonlocalities. *Phys.Rev.*, D88:123502, 2013.
18. S. Nesseris and S. Tsujikawa. Cosmological perturbations and observational constraints on non-local massive gravity. 1402.4613.
19. P.A.R. Ade et al. Planck 2013 results. XVI. Cosmological parameters. 1303.5076.
20. M. Betoule, R. Kessler, J. Guy, J. Mosher, D. Hardin, et al. Improved cosmological constraints from a joint analysis of the SDSS-II and SNLS supernova samples. 1401.4064.
21. Y. Song et al. Complementarity of Weak Lensing and Peculiar Velocity Measurements in Testing General Relativity. *Phys.Rev.*, D84:083523, 2011.

LARGE-SCALE STRUCTURE IN MODIFIED GRAVITY MODELS

TSZ YAN LAM
Max Planck Institute for Astrophysics, Karl-Schwarzschild-Str 1,
Garching 85748, Germany

Modified gravity models provide alternative explanations of the cosmic acceleration to the cosmological constant or a dark energy component. These models employ screening mechanisms to evade local gravity tests and many of them would mimic the cosmic expansion history of the LCDM cosmology. In this talk I presented two large-scale structure probes that would be used to constrain these modified gravity models.

1 Introduction

The cosmic acceleration of the Universe is one of the mysterious topics of the modern-day cosmology. The current best fit cosmological model, the LCDM cosmology, includes a cosmological constant (or in general a dark energy component) to explain that within the framework that gravity is described by general relativity (GR). However such treatment is neither theoretically well motivated and the observed value of the cosmological constant is far from the theoretical prediction.

An alternative explanation of the cosmic acceleration is modifying the gravity sector. A number of modified gravity models has been proposed, see for example Jain & Khoury [2] for reference. These modified gravity models require some screening mechanisms so that GR is restored in local environment to satisfy stringent gravity tests. To illustrate this idea we consider the chameleon modified gravity models, in which the screening mechanism is implemented by the chameleon mechanism. One way of implementing the modification is including a scalar field that couples to the matter content. The Lagrangian is given by

$$\mathcal{L} = \frac{1}{2}\left[\frac{\mathcal{R}}{8\pi G} - \nabla^a\nabla_a\phi\right] + V(\phi) - A(\phi)\mathcal{L}_{\rm DM} + \mathcal{L}_{\rm S}, \tag{1}$$

where ϕ is corresponding scalar field with a potential $V(\phi)$ and a coupling term $A(\phi)$. Carefully choosing $V(\phi)$ and $A(\phi)$ would arrive at an effective potential that satisfies the screening requirement (see figure 1 in Jain & Khoury [2]). The effective potential of the scalar field is the sum of the potential and the product of the coupling and its environment density. In regions with high environmental density the effective potential has a deep minimum and hence the fifth force mediated by the scalar field cannot propagate far – GR is restored in high density regions. In particular in section 2.1 we use the following parameterization:

$$V(\phi) = \frac{\Lambda}{\left[1 - \exp(-\sqrt{8\pi G}\phi)\right]} \quad \text{and} \quad A(\phi) = \exp(\gamma\sqrt{8\pi G}\phi). \tag{2}$$

Another popular model, the $f(R)$ model, includes a generalization of the Ricci scalar in the Einstein-Hilbert action and will be the focus in section 2.2.

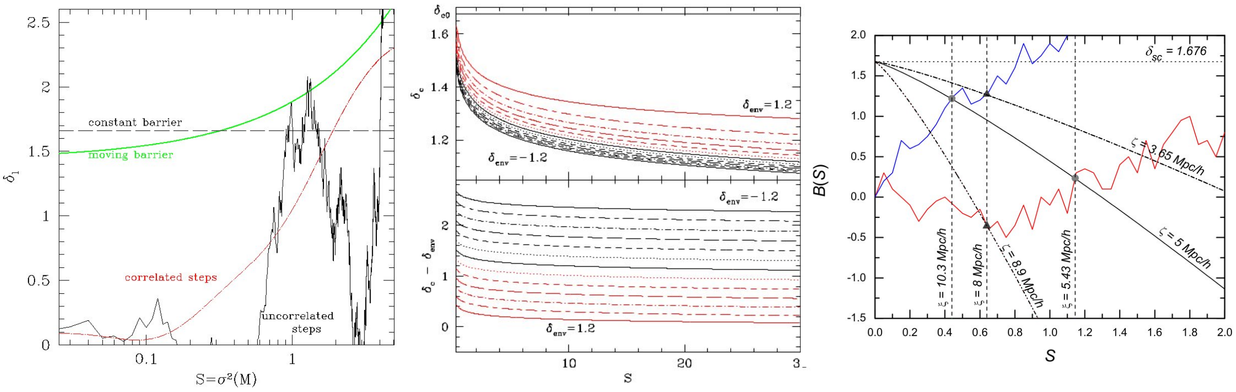

Figure 1 – Illustration of the excursion set approach: (Left) barriers correspond to the halo formation critical density contrast and The first up-crossing across the barriers are then computed to get the halo mass function. (Middle, adapted from Lam & Li [4]) Halo formation barriers depend on environmental density in chameleon modified gravity models. (Right, adapted from Li & Lam [8]) First crossing of the Eulerian environment barriers (barriers decreasing with S) gives the Eulerian environment density. Combining with the barriers in the middle panel results in halo mass function in chameleon modified gravity models.

A useful approximation, the thin-shell approximation, was described in Khoury & Weltman (2004) [3]. For a top-hat region this thin-shell approximation allows one to estimate the strength of the fifth force that would propagate to outside. The thinner the shell, the more effective the screening and hence no modifications would be observed.

In the next section I describe two large-scale structure probes that would constrain these modified gravity models.

2 Large-scale structure in Modified Gravity models

2.1 Abundance of rare objects

The abundance of rare objects, in particular massive clusters and voids, are sensitive probes of cosmology. One needs either numerical simulations or theoretical models to describe how the abundance of these objects depend on cosmological parameters in order to use them as cosmological probes. One of the popular theoretical models in computing halo abundance is the excursion set approach described in Bond et.al. [1]: this involves identifying the critical density (linearly extrapolated to the present time) for halo formation and compute the *first* up-crossing probability across this barrier. The conservation of mass then relates this probability $f(S)$ to the halo mass function:

$$f(S)\mathrm{d}S = \frac{M}{\bar{\rho}}n(M)\mathrm{d}M \quad \text{where } S = \sigma^2(M) = \int \frac{dk}{k}\frac{1}{2\pi^2}k^3P(k)W^2(kR_M) \tag{3}$$

and $W(kR_M)$ is the Fourier space window function. The left panel of figure 1 demonstrates the idea:

1. Critical density contrast for halo formation (constant barrier or scale-dependent barrier);
2. First up-crossing probabiliy across the barrier is computed (analytical expression or Monte-Carlo simulations).

Modified gravity models modify the halo formation criteria, the details of the calculation is described in Li & Efstathiou [7]. In short the gravitational constant is modified to incorporate the enhancement in the growth of structure. This effective gravitational constant include the thin-shell approximation to enforce the screening mechanism. The middle panel in figure 1 shows the critical density for halo formation is lowered from δ_{c0} to a set of mass and environmental density dependent barriers: the lower the environmental density, the bigger is the modification.

In order to compute the halo mass function in modified gravity models, one has to choose an environment. As discussed in Li & Lam [8] an Eulerian environment (one that encompasses the halo in late time) of around 5 Mpc/h is a good choice. The density of a particular random walk within this Eulerian environment would be obtained by looking at the first crossing of the corresponding Eulerian environment (see the right panel in figure 1). As a result a random walk will give the environmental density, which would in turn be used to determine the halo formation barrier, and subsequently the mass of the halo to be formed.

Figure 2 shows the change in the multiplicity function (or equivalently the halo mass function) for two different choices of environment: the red curves show the results for the Eulerian environment while the green symbols are the results of using the Lagrangian environment. At high mass end there is no change in the mass function due to screening mechanism; while in the intermediate mass range an enhancement is seen. At the low mass end, due to the conservation of mass, there is a detriment in the number density.

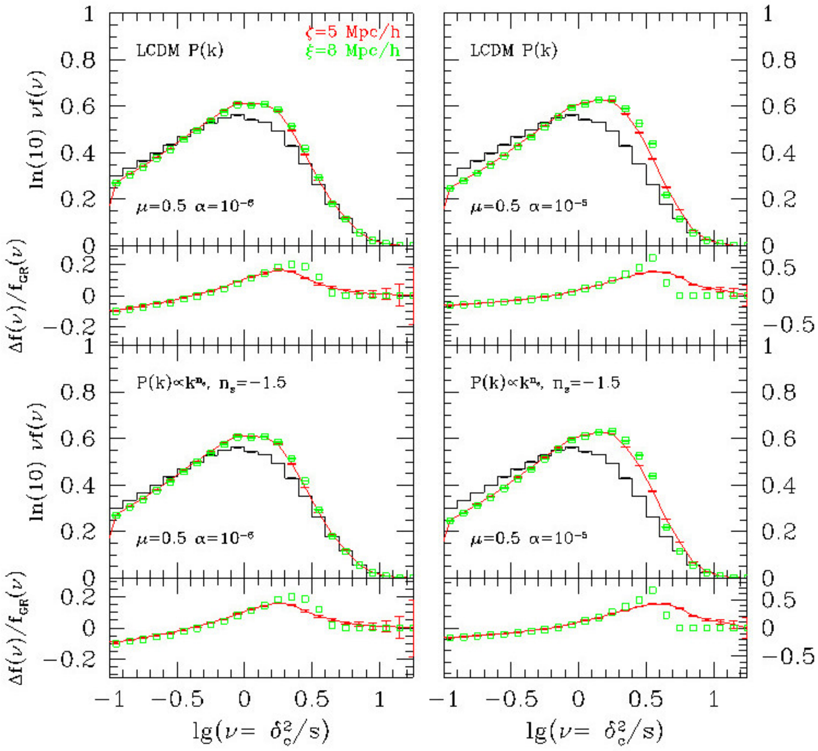

Figure 2 – The change in the halo mass function in Chameleon modified gravity models for two difference choices of environment as well as different parameters and the linear matter power spectra.

2.2 *Gravitational lensing vs dynamical mass estimates*

The second large-scale probe I will present utilise the fact that gravitational lensing masses of clusters are in general not equivalent to their dynamical masses. GR is a special case in which the two are equal and hence this comparison is a unique signature of modified gravity models. In Lam et. al. (2012) and Lam et. al. (2013) I described a method to combine stacked lensing measurement and stacked line-of-sight velocity dispersion measurement to constrain modified gravity models. This requires overlapping imaging and spectroscopic surveys that cover a large area of the sky. The measurement is made in the plane of the projected separation and the relative line-of-sight velocity of galaxies surrounding the massive clusters. By stacking many clusters asymetries within individual clusters are removed. The left panel of figure 3 shows one such example by stacking dark matter particles around 2000 massive clusters from numerical simulations. One trivial statistics is the line-of-sight velocity dispersion as a function of projected separation. The ratios of the velocity dispersion between $f(R)$ modified gravity models, which also utilies the chameleon screening mechanism, and those of GR are shown in the middle panel of figure 3. Statistics analysis expects this method would improve the current constraint on $f(R)$ model by an order of magnitude in the next generation of survey (see the error bars in the upper panel).

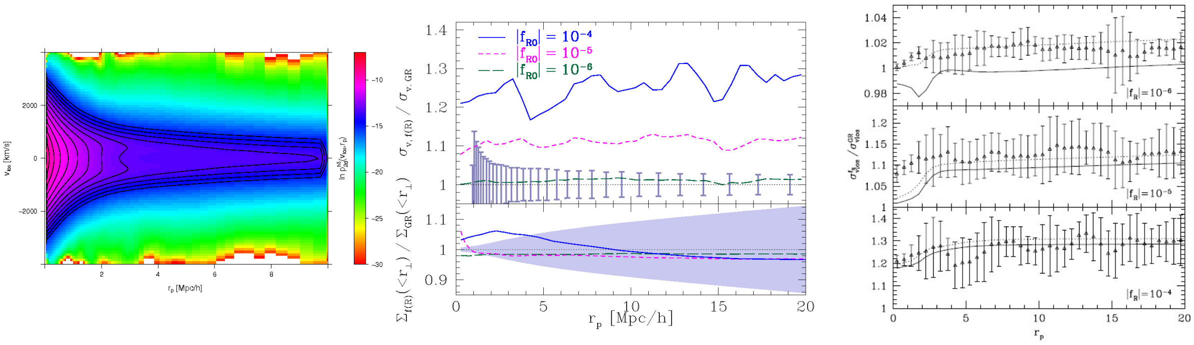

Figure 3 – (Left, adapted from Lam et. al. 2013 [6]) Stacked phase-space distribution of 2000 massive clusters. (Middle, adapted from Lam et. al. 2012 [5]) Ratios of the line-of-sight velocity dispersion between $f(R)$ modified gravity models and GR. (Right, adapted from Lam et. al. 2013 [6]) Halo-model based analytical models match the numerical measurement well.

The change in the line-of-sight velocity dispersion in modified gravity models is well described by an analytical model based on the halo model described in Lam et. al. 2013. The right panel of figure 3 shows the comparison with numerical measurements of the $f(R)$ modified gravity model. The model is general and also matches the measurements of the DGP modified gravity model.

One caveat in this measurement is the contamination of the Hubble flow difference. This Hubble flow contribution would be included in the analytical model and the result matches the numerical measurement very well (see Lam et. al. 2013). Unfortunately the Hubble flow contamination dilutes the change due to modified gravity models. We are now working on developing a technique to extract the modified gravity signal.

3 Summary

In this presentation I describe two large-scale structure probes that would improve the constraints on modified gravity models in the future. Utilising the enhancement of the growth of structure due to the presence of the fifth force and the screening mechanism, large-scale structure provides a very good testing ground for these modified gravity models.

References

1. J.R. Bond *et al*, ApJ **379**, 440 (1991)
2. B. Jain and J. Khoury, Annals of Physics **325**, 1479 (2010)
3. J. Khoury and A. Weltman, *Phys. Rev. Lett.* **93**, 171104 (2004)
4. T.Y. Lam and B. Li, MNRAS **426**, 3260 (2012)
5. T.Y. Lam *et al*, *Phys. Rev. Lett.* **109**, 051301 (2012)
6. T.Y. Lam *et al*, *Phys. Rev.* D **88**, 023012 (2013)
7. B. Li and G. Efstathiou , MNRAS **421**, 1431 (2012).
8. B. Li and T.Y. Lam, MNRAS **425**, 730 (2012)

CONSISTENT BIMETRIC THEORY AND ITS APPLICATION TO COSMOLOGY

ANGNIS SCHMIDT-MAY
Department of Physics & The Oskar Klein Centre,
Stockholm University, AlbaNova University Centre, SE-106 91 Stockholm, Sweden

Recently, the construction of ghost-free nonlinear massive spin-2 interactions solved a long outstanding problem in classical field theory. The consistent formulation requires a second rank-two tensor (or metric) and therefore has the form of a bimetric theory. Besides providing the solution to an old problem in field theory, ghost-free bimetric theory also has an interesting phenomenology: Its homogeneous and isotropic background solutions can reproduce the expansion history of the universe without any input of vacuum energy.

1 Introduction

Our standard picture for cosmology, the ΛCDM model, relies on General Relativity (GR) as the theory for gravity and successfully describes the expansion history of the universe. However, in this model, about 95% of the energy content in our universe is made of unknown constituents, commonly referred to as *dark matter* and *dark energy.* On top of that, we lack an explanation for the absence of a huge amount of vacuum energy (i.e. a large cosmological constant) as expected from quantum field theory.

A lot of effort has been made to extend the Standard Model of Particle Physics and/or GR in order to solve the dark matter, dark energy and cosmological constant problems. Our approach here will not be to construct a new phenomenological model with the aim to account for the unexplained observational data. Instead, we address a fundamental question by constructing a model that is theoretically consistent. Once the consistent formulation is known, we investigate its phenomenology and whether it can explain any of the observations. We will begin by stating a problem in classical field theory. Massless and massive fields with spin 1 and lower play a fundamental role in the formulation of the Standard Model. Their consistent Lagrangians are known and it is possible to quantize them without introducing inconsistencies. For higher spins, however, the situation becomes more difficult.

The unique *classical* theory for a nonlinearly self-interacting massless spin-2 field is known to be GR formulated in terms of the metric tensor $g_{\mu\nu}$, while its fundamental quantum version remains to be found. The obvious next step in constructing classical field theories is to search for a Lagrangian describing massive spin-2 interactions. From our experience of fields with lower spin, we expect the massive theory to have the same kinetic structure as the massless one and we are therefore looking for a consistent deformation of the Einstein-Hilbert action of GR by a mass term for the metric $g_{\mu\nu}$. This mass term should not contain any derivatives and, moreover, Lorentz invariance requires that it must not have any loose indices. But now we already face a problem because the only way to build a scalar out of $g_{\mu\nu}$ alone and without using derivatives is to contract its indices with the inverse metric $g^{\mu\nu}$. But since $g^{\mu\nu}g_{\mu\nu} = \mathrm{Tr}\,(g_{\mu\nu}) = 4$, this cannot give a nontrivial self-interaction term. In order to write down a mass term for a spin-2 field we therefore need to introduce a second rank-two tensor $f_{\mu\nu}$ that can be used to contract the indices on the metric. The interactions of the two fields will then be given in terms of traces of powers of the matrix $g^{\mu\nu}f_{\nu\rho}$.

Clearly, the question arises whether the second metric $f_{\mu\nu}$ should be regarded as a fixed background or receive its own dynamics. From a field theory point of view, the latter choice seems more natural and we therefore also include an Einstein-Hilbert kinetic term for $f_{\mu\nu}$ into the action. The result is a so-called bimetric theory of the form,

$$S[g,f] = m_g^2 \int \mathrm{d}^4x\,\sqrt{g}\,R(g) + m_f^2 \int \mathrm{d}^4x\,\sqrt{f}\,R(f) - m^4 \int \mathrm{d}^4x\,\sqrt{g}\;V(g^{-1}f)\,. \tag{1}$$

Here, the first two terms are standard Einstein-Hilbert kinetic terms for the two metrics with m_f and m_g setting their interaction strengths. The mass scale m is related to the mass of the spin-2 field and V is a generic interaction potential. Since the above action is invariant under diagonal diffeomorphisms, under which both $g_{\mu\nu}$ and $f_{\mu\nu}$ transform simultaneously, we expect the theory to contain a massless spin-2 excitation besides the massive mode.

The problem with this kind of theory is that, for a general form of the interaction potential V, it contains an additional scalar degree of freedom whose kinetic term has the wrong sign and therefore gives rise to a ghost instability.[1] In the presence of this ghost, the Hamiltonian is unbounded from below which renders the theory unstable and hence inconsistent. In order to give a consistent description of massive spin-2 fields, it is therefore of uttermost importance to find a form of the interaction potential that eliminates the ghost mode.

2 Ghost-free Bimetric Theory

Although the linear theory for massive spin-2 in flat backgrounds had been known since 1939,[2] its nonlinear version was constructed [3] [4] and proven to be consistent [5] [6] [7] only very recently. The unique interaction potential that avoids the ghost mode is of the form,[a]

$$V(g^{-1}f) = \sum_{n=0}^{4} \beta_n e_n(S)\,. \tag{2}$$

Here, β_n are arbitrary dimensionless parameters and $S \equiv \sqrt{g^{-1}f}$ is a matrix square root defined through $S^2 = g^{-1}f$. Furthermore, $e_n(S)$ are the elementary symmetric polynomials of the matrix S which can be expressed through a recursion formula,

$$e_n(S) = \frac{1}{n}\sum_{k=0}^{n-1}(-1)^{n+k+1}\,\mathrm{Tr}(S^{n-k})\,e_k(S)\,, \qquad e_0(S) = 1\,. \tag{3}$$

The appearance of the square root and the structure of the elementary symmetric polynomials are crucial for the absence of the dangerous ghost mode. The above potential with its five free parameters exhausts all possible ghost-free interaction terms for the two metrics. Note that, since $e_0(S) = 1$ and $e_4(S) = \det S = (\sqrt{g})^{-1}\sqrt{f}$, the parameters β_0 and β_4 simply correspond to cosmological constant terms for $g_{\mu\nu}$ and $f_{\mu\nu}$, respectively.

---

[a] The corresponding massive gravity theory with nondynamical $f_{\mu\nu}$ is believed to give rise to superluminal propagation and acausality,[8] but so far these pathologies have not been found in bimetric theory.

Coupling the metrics to matter in the standard way (i.e. as in General Relativity) does not reintroduce the ghost. In the simplest case, only one of the metrics couples to matter and thereby fixes the geometry and causal structure of the matter sector, while the other metric interacts with matter only indirectly.[b] Hence, with ϕ collectively denoting all the matter fields, the bimetric action that we will consider in the following is of the form,

$$S[g,f,\phi] = m_g^2 \int \mathrm{d}^4x\,\sqrt{g}\,R(g) \quad + \quad m_f^2 \int \mathrm{d}^4x\,\sqrt{f}\,R(f) \\ \qquad - \quad m^4 \int \mathrm{d}^4x\,\sqrt{g}\,\sum_{n=0}^{4} \beta_n e_n(S) + \int \mathrm{d}^4x\,\sqrt{g}\,\mathcal{L}_{\mathrm{m}}(g,\phi)\,. \qquad (4)$$

The equations of motion obtained from the bimetric action (4) with interaction potential (2) by varying with respect to $g_{\mu\nu}$ and $f_{\mu\nu}$ read as,

$$\mathcal{G}_{\mu\nu}(g) + \frac{m^4}{m_g^2}\mathcal{V}_{\mu\nu}(g,f) = \frac{1}{m_g^2}T_{\mu\nu}\,, \qquad \tilde{\mathcal{G}}_{\mu\nu}(f) + \frac{m^4}{m_f^2}\tilde{\mathcal{V}}_{\mu\nu}(g,f) = 0\,, \qquad (5)$$

where $\mathcal{G}_{\mu\nu}(g)$ and $\tilde{\mathcal{G}}_{\mu\nu}(f)$ are the Einstein tensors for $g_{\mu\nu}$ and $f_{\mu\nu}$, respectively, $\mathcal{V}_{\mu\nu}(g,f)$ and $\tilde{\mathcal{V}}_{\mu\nu}(g,f)$ are the contributions from the interaction potential and $T_{\mu\nu}$ is the stress-energy tensor of the matter Lagrangian $\mathcal{L}_{\mathrm{m}}(g,\phi)$.

3 Bimetric Cosmology

In order to derive cosmological solutions in the theory specified by (4), we make a homogeneous and isotropic ansatz for both of the metrics, such that $g_{\mu\nu}\mathrm{d}x^\mu \mathrm{d}x^\nu = -\mathrm{d}t^2 + a^2\mathrm{d}x^2$ has the same form as in GR.[c] Furthermore, we assume the stress-energy tensor of the matter source to resemble a perfect fluid and be covariantly conserved, i.e. $\nabla^\mu T_{\mu\nu} = 0$, where ∇^μ is the covariant derivative compatible with $g_{\mu\nu}$. After a subset of the equations of motion (5) has been solved to determine the time-dependent functions in the ansatz for $f_{\mu\nu}$, the remaining equations are modified Friedmann equations for the scale factor $a(t)$ in the physical metric $g_{\mu\nu}$,[10 11 12]

$$\left(\frac{\dot{a}}{a}\right)^2 = F_1[\rho]\,, \qquad \frac{\ddot{a}}{a} = F_2[\rho,p]\,, \qquad (6)$$

where $F_{1,2}$ are functions (typically involving square, cubic or even quartic roots) of the energy density ρ and the pressure p of the matter source. Their precise form depends on the choice of interaction parameters. Generically, the evolution equations (6) are very different from GR for which the functions $F_{1,2}$ are linear in ρ and p. Hence, bimetric theory can give rise to very different dynamics and evolution of the universe.

A particularly interesting question is whether it is possible to obtain an accelerating solution ($\ddot{a} > 0$) with a matter source that contains relativistic and non-relativistic matter, but no vacuum energy. In GR this is impossible because, for sources with equation of state $w = p/\rho > -1/3$, acceleration cannot occur. In order to set the vacuum energy contribution in bimetric theory to zero, one assumes a source with only relativistic ($w = 1/3$) and non-relativistic ($w = 0$) matter components. Furthermore, one sets the cosmological constant term in the bimetric interaction potential to zero by fixing $\beta_0 = 0$.

A detailed study of this setup by Akrami *et.al.*[13] revealed that bimetric theory can indeed give rise to cosmological acceleration without the input of vacuum energy. Furthermore, in a statistical analysis the authors found that certain bimetric models can fit observational data and account for the expansion history of the universe just as well as standard ΛCDM. In these cases, the present Hubble scale is set by the mass parameter m in the bimetric interaction potential.

---

[b] The analysis of cosmological solutions has also been carried out with both metrics coupled to matter.[9]

[c] For simplicity, we assume vanishing curvature, $k = 0$. The generalization to $k \neq 0$ is straightforward.

It is expected that, even in cases where the background behaves very similarly to ΛCDM, bimetric theory will differ from GR at the level of perturbations around the homogeneous and isotropic backgrounds.[14] Progress in deriving predictions for CMB and structure formation has only been made very recently, indicating that, while compatible with observational data, bimetric theory will be distinguishable from GR in the near future.[15] [16] On the other hand, although the cosmological solutions are well-behaved for a large spin-2 mass,[17] a mass on the order of the present Hubble scale (as required for self-acceleration) could give rise to an instability.[18] [19]

4 Summary & Discussion

The construction of the consistent description for nonlinear spin-2 interactions in classical field theory resulted in a novel theory of modified gravity which contains two metrics interacting with each other. The cosmological background solutions in ghost-free bimetric theory are still compatible with observational data after all vacuum energy contributions have been removed. Hence, there is no need for a cosmological constant if GR is replaced by bimetric theory.

These results are promising due to the following reason: If a (yet unknown) mechanism or symmetry was able to set the vacuum energy contribution to zero at the quantum level, then the expansion of the universe could still accelerate due to the spin-2 interactions. In this case, the Hubble scale is set by the spin-2 mass which, unlike a cosmological constant, is protected against large quantum corrections due to the restoration of the full diffeomorphism invariance (under which both metrics transform independently) in the limit $m \to 0$.

In order to be able to tell whether bimetric theory is really compatible with all cosmological observations, we still need a better understanding of its perturbation theory. In addition to this, it is necessary to compare the local solutions of the theory to observations in the solar system and verify that the same parameters can fit the data on all distance scales.

References

1. D. G. Boulware and S. Deser, Phys. Rev. D **6** (1972) 3368.
2. M. Fierz and W. Pauli, Proc. Roy. Soc. Lond. A **173** (1939) 211.
3. C. de Rham and G. Gabadadze, Phys. Rev. D **82** (2010) 044020
4. C. de Rham, G. Gabadadze and A. J. Tolley, Phys. Rev. Lett. **106** (2011) 231101
5. S. F. Hassan and R. A. Rosen, Phys. Rev. Lett. **108** (2012) 041101
6. S. F. Hassan, R. A. Rosen and A. Schmidt-May, JHEP **1202** (2012) 026
7. S. F. Hassan and R. A. Rosen, JHEP **1202** (2012) 126
8. S. Deser, K. Izumi, Y. C. Ong and A. Waldron, Phys. Lett. B **726** (2013) 544 arXiv:1306.5457 [hep-th].
9. Y. Akrami, T. S. Koivisto, D. F. Mota and M. Sandstad, JCAP **1310** (2013) 046
10. M. S. Volkov, JHEP **1201** (2012) 035
11. M. von Strauss, A. Schmidt-May, J. Enander, E. Mortsell and S. F. Hassan, JCAP **1203** (2012) 042
12. D. Comelli, M. Crisostomi, F. Nesti and L. Pilo, JHEP **1203** (2012) 067
13. Y. Akrami, T. S. Koivisto and M. Sandstad, JHEP **1303** (2013) 099
14. M. Berg, I. Buchberger, J. Enander, E. Mortsell and S. Sjors, JCAP **1212** (2012) 021
15. F. Könnig and L. Amendola, arXiv: 1402.1988
16. A. R. Solomon, Y. Akrami and T. S. Koivisto, arXiv:1404.4061 [astro-ph.CO].
17. A. De Felice, A. E. Gumrukcuoglu, S. Mukohyama, N. Tanahashi and T. Tanaka, arXiv:1404.0008 [hep-th].
18. D. Comelli, M. Crisostomi and L. Pilo, JHEP **1206** (2012) 085 arXiv:1202.1986 [hep-th].
19. D. Comelli, M. Crisostomi and L. Pilo, arXiv:1403.5679 [hep-th].

Experimental constraints on the uncoupled Galileon model from cosmological observations

Jérémy Neveu, Vanina Ruhlmann-Kleider, Marc Besançon
CEA, Centre de Saclay, Irfu/SPP,
Gif-sur-Yvette, France

The Galileon model is a modified gravity theory that may provide an explanation for the accelerated expansion of the Universe. This model does not suffer from instabilities or ghost problems (normally associated with higher-order derivative theories), restores local General Relativity thanks to the Vainshtein screening effect and predicts late time acceleration of the expansion. In this talk, we derive a new definition of the Galileon parameters that allows us to avoid choosing initial conditions for the Galileon field, and then test this model against precise measurements of the cosmological distances and the rate of growth of cosmic structures, with and without an explicit direct disformal coupling to matter. We find that the Galileon model remains consistent with current observations and is still competitive with the ΛCDM model, and that a non-zero disformal coupling to matter is favoured at the 2.5σ level.

1 The Galileon cosmology

1.1 Introduction to the Galileon model

The Galileon is a new scalar field, hereafter called π, introduced by Nicolis *et al.*[1] to explain the late-time accelerated expansion of the Universe. Its Lagrangian is constructed so that the equation of motion of π is invariant under a Galilean symmetry $\pi \mapsto \pi + a + b_\mu x^\mu$. The consequence is that only five Lagrangian terms L_i are then possible, and thus the theory needs only five free parameters c_i to be described. Imposing a Galilean symmetry is justified by extra-dimension considerations.

The original Galileon Lagrangians were made covariant by Deffayet *et al.*[2], and an interesting parametrisation of the action proposed by Appleby and Linder[3]:

$$S = \int d^4x\sqrt{-g}\left(\frac{M_P^2 R}{2} - L_m - \frac{1}{2}\sum_{i=1}^{5} c_i L_i - L_G\right). \tag{1}$$

The first term corresponds to the General Relativity theory, the second one is the Standard Matter Lagrangian L_m and then we have the five Lagrangian terms from Deffayet *et al.*[2]:

$$L_1 = M^3\pi, \quad L_2 = (\nabla_\mu\pi)(\nabla^\mu\pi), \quad L_3 = (\Box\pi)(\nabla_\mu\pi)(\nabla^\mu\pi)/M^3, \tag{2}$$

$$L_4 = (\nabla_\mu\pi)(\nabla^\mu\pi)\left[2(\Box\pi)^2 - 2\pi_{;\mu\nu}\pi^{;\mu\nu} - R(\nabla_\mu\pi)(\nabla^\mu\pi)/2\right]/M^6, \tag{3}$$

$$L_5 = (\nabla_\mu\pi)(\nabla^\mu\pi)\left[(\Box\pi)^3 - 3(\Box\pi)\pi_{;\mu\nu}\pi^{;\mu\nu} + 2\pi_{;\mu}^{;\nu}\pi_{;\nu}^{;\rho}\pi_{;\rho}^{;\mu} - 6\pi_{;\mu}\pi^{;\mu\nu}\pi^{;\rho}G_{\nu\rho}\right]/M^9, \tag{4}$$

where $M^3 = M_P H_0^2$ (M_P stands for the Planck mass and H_0 for the Hubble constant). The c_i's are dimensionless in this parametrisation, and semi-colons stand for covariant derivatives. L_G is the disformal coupling to matter:

$$L_G = \frac{c_G}{M_P M^3}\partial_\mu\pi\partial_\nu\pi T^{\mu\nu} \tag{5}$$

where c_G is a dimensionless free parameter and $T^{\mu\nu}$ is the matter energy-momentum tensor.

The Galileon model is based on a very restrictive symmetry, which leads to only five free parameters c_i's to constrain (beside the optional couplings to matter). Moreover for theoretical reasons it is usually assumed that $c_1 = 0$.

In the Galileon theory, a screening mechanism called the Vainshtein effect [4] arises near massive objects due to non-linear self-couplings of the π field. These ensure that the Galileon fifth force is screened near massive objects, which preserves General Relativity on local scales where it has been experimentally tested to high precision. Finally, the model does not suffer from instabilities or ghosts problems usually associated with high-order derivatives theories [1 2].

1.2 The Galileon equations

To confront the Galileon model to the recent cosmological data, as in standard cosmology, we have to derive the two Einstein equations to make predictions on the expansion of a "Galilean" Universe. For example, one can derive the first Einstein equation $\partial S/\partial g_{00}$ from action (1) using a Friedmann-Lemaître-Robertson-Walker (FLRW) metric $g_{\mu\nu}$:

$$\bar{H}^2 = \frac{\Omega_m^0}{a^3} + \frac{\Omega_r^0}{a^4} + \frac{c_2}{6}\bar{H}^2 x^2 - 2c_3\bar{H}^4 x^3 + \frac{15}{2}c_4\bar{H}^6 x^4 - 7c_5\bar{H}^8 x^5 - 3c_G\bar{H}^4 x^2, \tag{6}$$

where $\bar{H} = H/H_0$ is the Hubble parameter normalized to its present value, a the FLRW scale parameter and $x = \frac{1}{M_P}\frac{d\pi}{d\ln a}$.

With the two Einstein equations and the π equation of motion, we have a system of three coupled differential equations to solve, with two unknown functions x and H. We faced two problems: the initial condition for x is unknown, and there is a degeneracy to break between the c_i's and x. To solve both issues, we proposed an original reparametrisation of the model with x_0 the present value of x: $\bar{c}_i = c_i x_0^i, \bar{c}_G = c_G x_0^2$ and $\bar{x} = x/x_0$.

Then we can use two of the equations to compute the x and H evolutions, and the third one as a constraint equation to fix $\bar{c}_5$ given the other parameters. At last, $\Omega_m^0, \Omega_r^0, \bar{c}_2, \bar{c}_3, \bar{c}_4$ and possibly $\bar{c}_G$ are the only parameters to constrain.

These equations can also be studied at the perturbation level, to compute the growth of structures in a Galileon Universe. From these perturbation equations, an effective gravitational coupling G_{eff}, evolving with x, can be computed. Moreover, some of these equations are used as theoretical constraints to reduce the Galileon space parameter to be explored.

2 Experimental constraints

2.1 Fitting data

To constrain the Galileon model parameters with the recent cosmological data, we computed cosmological observables related to different data sets, for hundred of millions of sets of parameter values. We then obtained χ^2 maps from which we extracted best fit values with correct uncertainties for the Galileon model parameters.

Type Ia supernovae

We used the 730 well measured supernovae as published by the SuperNova Legacy Survey (SNLS) with all their systematics (Betoule *et al.* [5]). Prediction of the B band magnitude peak for each SN Ia can be easily performed once we know the H evolution with the redshift z for a given set of Galileon parameters:

$$m_B^{mod} = 5\log_{10}\left[(1+z_{hel})\int_0^{z_{CMB}} \frac{dz}{\bar{H}(z,\text{cosmo})}\right] - \alpha(s-1) + \beta.\mathcal{C} + \mathcal{M}_{\mathcal{B}} \tag{7}$$

α, β and $\mathcal{M}_{\mathcal{B}}$ are nuisance parameters which are properly considered in our study.

Cosmological microwave background (CMB) and baryonic acoustic oscillations (BAO)

With our equations we cannot compute a prediction for the full power spectrum of the CMB. We used instead a set of simplified observables from the WMAP9 experiment l_a, R and z_*, related to the first acoustic peak. These observables only require the $H(z)$ function to be determined, and are computed following the prescriptions of Hinshaw *et al.*[6].

The Galileon model fit to the CMB observables is performed jointly to the fit to the BAO observables from 6dFGRS, SDSS-II and BOSS surveys, as they share the same requirements.

Growth of structures

As the Galileon model is a modified gravity model, growth data can distinguish this model from the standard cosmological model ΛCDM. We used rate and Alcock-Paczynski parameter measurements from 6dFGRS, 2dFGRS, WiggleZ, SDSS, and BOSS surveys. These measurements are independent from any fiducial cosmology or General Relativity requirement. The matter perturbation δ_m equation

$$\ddot{\delta}_m + 2H\dot{\delta}_m - 4\pi G_{\text{eff}}(t)\rho_m\delta_m = 0 \tag{8}$$

is solved in the frame of a Galileon gravity (through the G_{eff} parameter) in order to compute these observables.

2.2 Combination and best fit analysis

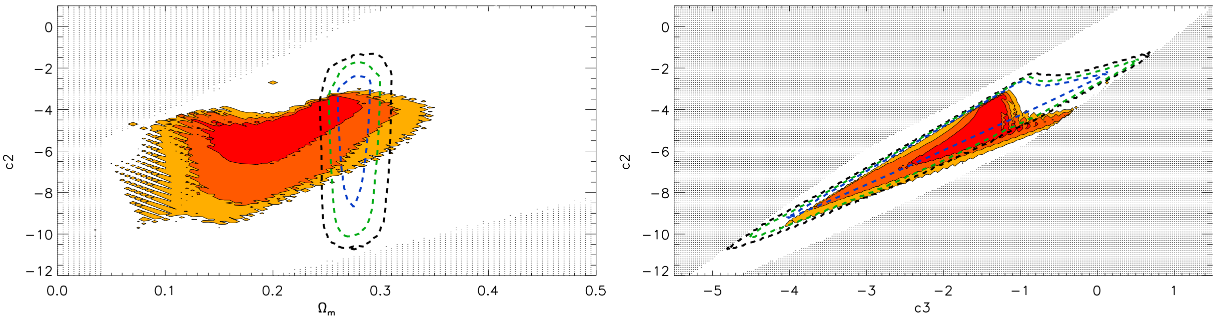

Figure 1 – Experimental constraints on the uncoupled Galileon model from growth data (red) and from SNLS3+WMAP7+BAO+H0 combined constraints (dashed). The filled dark, medium, and light-coloured contours enclose 68.3, 95.4, and 99.7% of the probability, respectively. Dark dotted regions correspond to scenarios rejected by theoretical constraints.

Table 1: Cosmological constraints on the uncoupled Galileon model ($\bar{c}_G = 0$).

Probe	Ω_m^0	$\bar{c}_2$	$\bar{c}_3$	$\bar{c}_4$	χ^2
Growth	$0.205^{+0.046}_{-0.046}$	$-5.337^{+0.883}_{-1.293}$	$-1.721^{+0.299}_{-0.732}$	$-0.628^{+0.221}_{-0.189}$	20.1
SNe Ia+BAO+CMB	$0.275^{+0.014}_{-0.009}$	$-5.269^{+1.832}_{-2.726}$	$-1.837^{+0.924}_{-1.408}$	$-0.630^{+0.461}_{-0.304}$	692.5
All	$0.276^{+0.014}_{-0.009}$	$-4.278^{+0.484}_{-1.097}$	$-1.580^{+0.194}_{-0.597}$	$-0.772^{+0.102}_{-0.058}$	720.9

Table 2: Cosmological constraints on the disformally-coupled Galileon model.

Probe	Ω_m^0	$\bar{c}_2$	$\bar{c}_3$	$\bar{c}_4$	$\bar{c}_G$	χ^2
SNe Ia+BAO+CMB	$0.282^{+0.015}_{-0.009}$	$-4.811^{+1.427}_{-1.990}$	$-1.525^{+0.637}_{-1.073}$	$-0.531^{+0.209}_{-0.275}$	$0.183^{+0.188}_{-0.133}$	693.2
All	$0.279^{+0.013}_{-0.008}$	$-3.401^{+0.315}_{-0.565}$	$-1.043^{+0.195}_{-0.252}$	$-0.614^{+0.087}_{-0.076}$	$0.147^{+0.077}_{-0.060}$	714.8

Our results are presented in Tables 1 and 2, and Figure 1. Our best-fit Galileon scenario points to a Universe with ≈ 28% of matter which is consistent with recent tests of the ΛCDM model. The $\bar{c}_i$ parameters appear well constrained by data inside the theoretically allowed region. As a comparison, with the same data sets and program, our best-fit ΛCDM model scenario obtains a χ^2 of 705.5 (693.0) using all data (only SNe Ia+BAO+CMB), which is close to those obtained in the uncoupled and coupled Galileon models. However, in the coupled case, a non-zero disformal coupling is excluded at the 2.5σ level.

The behaviour of our best-fit uncoupled scenario is presented in Figure 2. A similar behaviour is observed in the coupled case. The evolution of the energy densities is similar to that in the ΛCDM model. However the equation of state parameter w evolves significantly with the redshift, but converges in the future towards -1 (value of w for the cosmological constant Λ).

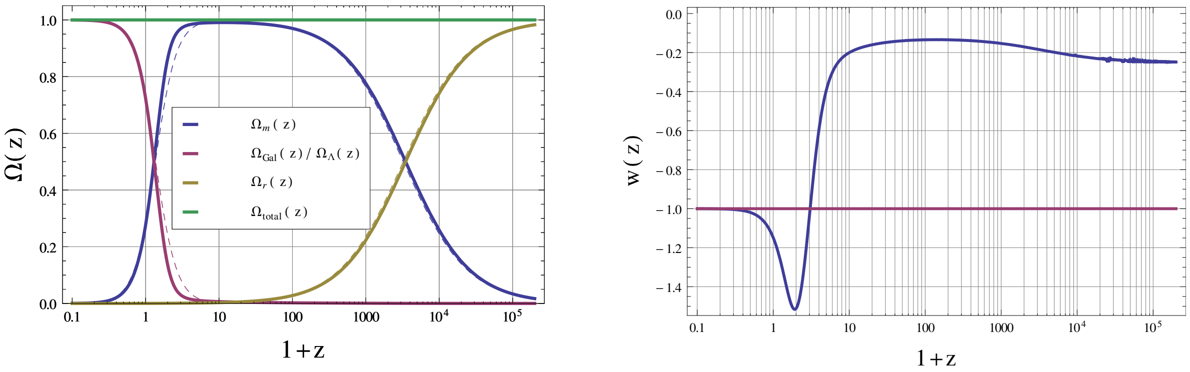

Figure 2 – Evolution of the $\Omega_i(z)$ (left) and of $w(z)$ (right, solid curve) for the best-fit uncoupled Galileon model from all data (last row of Table 1). Our best-fit ΛCDM model is also presented through the dashed curves on the left plot and the constant -1 horizontal purple line on the right plot.

3 Conclusion

The Galileon model is a very good candidate for dark energy, as it offers good theoretical properties, does not modify local gravity and produces an accelerated expansion of the Universe. We showed that this model is in agreement with current cosmological data, and that our best-fit scenario χ^2 is equivalent to the one obtained in the ΛCDM model. The Galileon model is therefore competitive with the current standard cosmological model. We noted also that the disformally-coupled Galileon model is favoured at the 2.5σ level over the uncoupled case.

Our results were then confirmed by a work of Barreira *et al.*[7], including a full CMB power spectrum prediction. In the future, N-body simulations with a better modelling of the Galileon gravity will bring significant improvements to continue testing this model through growth data.

More details, figures and tables are available in Neveu *et al.*[8 9].

References

1. Nicolis A., Rattazzi R., Trincherini E., 2009, Phys.Rev.D, 79, 064036.
2. Deffayet C., Esposito-Farese G., Vikman A., 2009, Phys.Rev.D, 79, 084003.
3. Appleby S.A. & Linder E., 2012, JCAP, 1203, 44.
4. Vainshtein A.I., 1972, Phys.Lett.B, 39, 396.
5. Betoule M., Kessler R., Guy J. et al., 2014, arXiv:1404.4064.
6. Hinshaw G., Larson D., Komatsu E. et al., 2012, Astrophys.J.Suppl., 208, 19.
7. Barreira A., Li B., Baugh C.M. et al., 2013, Phys.Rev.D, 87, 103511.
8. Neveu J., Ruhlmann-Kleider V., Conley A., 2013, A&A, 555, A53.
9. Neveu J., Ruhlmann-Kleider V., Astier P., 2014, arXiv:1403.0854.

AMPLIFICATION OF MAGNETIC FIELDS FROM TURBULENCE IN THE EARLY UNIVERSE

J.M. WAGSTAFF[1], R. BANERJEE[1], D. SCHLEICHER[2], G. SIGL[3]
[1]*Hamburger Sternwarte, Gojenbergsweg 112, 21029 Hamburg, Germany.*
[2]*Institut für Astrophysik, Friedrich-Hund-Platz 1, 37077 Göttingen, Germany.*
[3]*II Institut für Theoretische Physik, Luruper Chaussee 149, 22761 Hamburg, Germany.*

We demonstrate that the amplification of weak magnetic seed fields by the turbulent small-scale dynamo can already strongly magnetize the Universe at very early times. Turbulence produced by the primordial density perturbation and by possible first-order phase transitions in the radiation dominated era fulfil all the necessities for the small-scale dynamo to work. Hence, this mechanism guarantees $B_0 \sim 10^{-6}\varepsilon^{1/2}$ nG on scales up to $\lambda_c \sim 0.1$ pc, and $B_0 \sim 10^{-3}\varepsilon^{1/2}$ nG on scales up to $\lambda_c \sim 100$ pc if there are first-order phase transitions, where ε is the saturation efficiency. Such fields, albeit on small scales, can play an important role in structure formation and could provide an explanation to the apparently observed magnetic fields in the voids of the large-scale structure.

1 Introduction

Magnetic fields of μG order have been observed in galaxies at high and low redshifts, in galaxy clusters and in superclusters (see Refs. within Wagstaff *et al.* [1]). There is also evidence that extragalactic magnetic fields are $> 3 \times 10^{-7}$ nG [2]. Theoretically it is very hard to produce such strong fields on such large scales, with mechanisms such as inflation, phase transitions and battery mechanisms failing to generated the strengths required. However, dynamo amplification of weak seed fields is generally regarded as part of the solution. The galactic dynamo, which operates only for spiral galaxies, requires seed fields of order $B_0 \sim 10^{-21}$ nG to obtain μG strengths today [3]. However, this type of dynamo cannot explain strong fields in much younger galaxies, in galaxy clusters and superclusters or indeed in the voids of the large-scale structure. In this paper, we investigate a second class of dynamo, the small-scale dynamo (SSD), which is almost certainly operational in the early Universe at structure formation and could be an effective mechanism to strongly magnetize the radiation dominated (RD) epoch leading to strong intergalactic magnetic fields [1].

2 The Turbulent Small-Scale Dynamo Mechanism

The SSD mechanism is a very efficient mechanism at converting kinetic energy from turbulent motions to magnetic energy [4,5]. The mechanism can operate with isotropic and homogeneous turbulence and is usually most efficient on small scales. Turbulence develops almost inevitably when the kinetic Reynolds numbers are large [6] $R_e(l) \gtrsim 10^3$, where

$$R_e(l,T) = \frac{v_l^{\rm rms} l}{\eta_s(T)}\,, \qquad (1)$$

given for velocity fluctuations $v_l^{\rm rms}$ correlated on some physical scale l [7]. In the RD era the shear viscosity $\eta_s = (g_{\nu,\gamma}/5g_*)l_{\rm mfp}^{\nu,\gamma}$ is determined by the particles of longest mean free path $l_{\rm mfp}^{\nu,\gamma}$, which are either neutrinos or photons depending on the time. Here, g_* and $g_{\nu,\gamma}$ are the total and component number of effective relativistic degrees of freedom.

The continuous injection of kinetic energy sets up a *direct cascade* of energy on the *inertial range* between the *forcing* L and dissipative scales $l_{\rm diss}$ and turbulence becomes fully developed (or *stationary*) on a time scale of order the *eddy-turnover* time scale at the forcing scale τ_L, where $\tau_l \equiv al_c/v_l^{\rm rms}$ and l_c is a comoving length. In an expanding Universe, this time scale must be at most given by the Hubble time i.e. $\tau_L = 1/H$. Thus, the largest possible forcing scale is $L = v_L^{\rm rms}/H$, where $v_L^{\rm rms}$ is the typical velocity fluctuation on the forcing scale L. The velocity spectrum for stationary turbulence is given by $v_l^{\rm rms} = v_L^{\rm rms}\,(l/L)^{\vartheta}$, where $\vartheta = 1/3$ for incompressible Kolmogorov turbulence and $\vartheta = 1/2$ for highly compressible Burgers turbulence. From here on we assume that the turbulence is of Kolmogorov type, which is relevant for the subsonic velocity fluctuations investigated in this work.

The efficiency of the SSD mechanism depends strongly on three important environmental factors (i) the R_e; stronger turbulence is more effective (ii) the turbulent velocity modes; rotational modes are much more efficient than longitudinal modes [8,9] and (iii) the Prandtl number $P_m \equiv R_m/R_e = 4\pi\sigma\eta_s$, where the Prandtl number is a measure of the relative importance of the magnetic and kinetic diffusion. Here, $R_m(l) = 4\pi\sigma a l_c v_l^{\rm rms}$ is the magnetic Reynolds number and σ is the plasma conductivity. There is a critical magnetic Reynolds number for which if $R_m(L) > R_m^{\rm cr}$ the magnetic field line stretching wins over the resistive reconnection and the dynamo takes effect amplifying the magnetic field. For Kolmogorov turbulence $R_m^{\rm cr} \approx 60$ [9,10,11]. When the SSD takes effect, the fluctuating component of the magnetic field grows exponentially $B_{\rm rms} \propto \exp(\Gamma t)$. Analytically, the Kazantsev model can be used to calculate the growth rate Γ and the $R_m^{\rm cr}$ required for SSD action [5,10,12], where for $P_m \gg 1$ relevant to cosmological plasmas, it is shown that [9,13]

$$\Gamma \simeq R_e(L)^{1/2}\tau_L^{-1}\,. \tag{2}$$

Since the R_e are typically large, the magnetic fields can be amplified very rapidly.

The exponential amplification comes to an end at *saturation* given by the approximate equipartition between magnetic and kinetic energy $E_{\rm M}/E_{\rm kin} \approx \varepsilon$, i.e.

$$\langle \boldsymbol{B}^2(\boldsymbol{x})\rangle \approx 4\pi\varepsilon(\rho+p)\langle \boldsymbol{v}^2(\boldsymbol{x})\rangle = \frac{8}{45}\pi^3\varepsilon g_* T^4 \langle \boldsymbol{v}^2(\boldsymbol{x})\rangle\,, \tag{3}$$

where the last equality applies to the RD era and the parameter ε quantifies the saturation efficiency. Numerical studies indicate that the SSD mechanism is more efficient for rotational modes, where $\varepsilon \approx 1$, whereas $\varepsilon \sim 10^{-3} - 10^{-4}$ for compressive modes [8].

2.1 Kinetic Energy Injected from Primordial Density Perturbations

In the RD era, superhorizon primordial density perturbations (PDP) are continuously entering the horizon and generating velocity perturbations. At first-order, the perturbations in the fluid 3-velocity are purely irrotational with Fourier modes given by $v_i(\eta) = i\frac{3\sqrt{3}}{2}\hat{k}_i\,(2j_1(y) - \sin y)\,\Phi_0$, where Φ_0 is the constant superhorizon gravitational potential, $j_1(y)$ is the first spherical Bessel function and $y \equiv k\eta/\sqrt{3}$ for conformal time η [1,14]. The spectrum of the velocity perturbations $\mathcal{P}_v(k)$, whose amplitude is determined by the initial spectrum of the PDP $\Delta^2_{\mathcal{R}}$, oscillates rapidly on subhorizon scales $k\eta \gg 1$. For an almost scale invariant primordial spectrum $n_s \simeq 1$ we find the average $\overline{\mathcal{P}}_v(k) \simeq \frac{243}{200}\Delta^2_{\mathcal{R}}(k_0)$. Hence, the typical value of the velocity perturbation is [1]

$$v_l^{\rm rms} \sim \sqrt{\overline{\mathcal{P}}_v(k)} \simeq \sqrt{\Delta^2_{\mathcal{R}}(k_0)} \simeq 5\times 10^{-5}c\,. \tag{4}$$

This continuous production of velocity perturbations is continuously *forcing* the fluid on the largest scales. Thereby, if $R_e(L) \gtrsim 10^3$ stationary Kolmogorov turbulence will arise [1].

2.2 Kinetic Energy Injected from First-Order Phase Transitions

In the early Universe, first-order phase transitions (PT) may occur in which bubbles of the new phase collide and merge. The electroweak (EW) and QCD PT are potentially first order. These violent phenomena can inject large kinetic energy into the plasma, generating turbulence. The rate of bubble nucleation $\beta \sim 100H$ gives the characteristic time scale for the PT[15]. With the bubble wall expanding with velocity v_b, the largest bubbles reach a size $\beta^{-1}v_b$ by the end of the PT, giving the largest stirring scale $L \simeq \beta^{-1}v_b$ and $\tau_{\rm stir} = \beta^{-1}$ as the stirring time scale[15]. The phase boundary is expected to propagate via the *detonation* mode where the wall velocity is supersonic[16,17]. This case can be modelled analytically where the wall velocity $v_b(\alpha)$ and the fraction of vacuum energy converted to kinetic energy $\kappa(\alpha) \equiv \rho_{\rm kin}/\rho_{\rm vac}$ become simple functions of $\alpha \equiv \rho_{\rm vac}/\rho_{\rm thermal}$ which determines the strength of the PT. For weak detonations $\alpha \lesssim 1$, we find[15,17] $v_L^{\rm rms} \simeq \sqrt{2\alpha\kappa}/3(2\pi)^{4/3}$. Hence, for PT of strengths in the range $\alpha \sim (10^{-5} - 10^{-1})$, we find velocity fluctuations[1]

$$v_L^{\rm rms} \sim (10^{-4} - 10^{-1})\,. \qquad (5)$$

With large R_e, stationary Kolmogorov turbulence will arise for a time τ_L[1,15].

2.3 Epochs and Scales of Dynamo Action

We consider two early epochs, the *neutrino era*; between the EW scale $T \sim 10^2$ GeV and neutrino decoupling $T_{\rm dec} \simeq 2.6$ MeV and the *photon era*; from neutrino decoupling to a time long after $e^{\pm}$ annihilation $T \simeq 100$ eV, where the neutrinos and photons generate the plasma viscosity respectively. Figure 1 shows the Hubble scale $l_H = 1/aH$ and the stirring scale $L_c = v_L^{\rm rms}/aH$ with the values $v_L^{\rm rms}$ from PDP and PT in eqs. (4) and (5) respectively. However, velocity perturbations are exponentially damped due to neutrino/photon diffusion, where the damping scales are $(l_D^{\nu,\gamma})^2 \simeq \int_0^t l_{\rm mfp,c}^{\nu,\gamma}(t')/a(t')dt'$[18]. In the neutrino era, the l_D^{ν} is the only relevant damping scale. In the photon era, perturbations below $l_D^{\nu} \approx 1/aH|_{\rm dec} \simeq 42$ pc are damped[19] (shaded area in Fig. 1).

Let us first consider the turbulence generated by the PDP. From Fig. 1 we can see that for $T \gtrsim 0.2$ GeV the stirring scale $L_{c,\rm PDP} > l_D^{\nu}$. Hence, the velocity perturbations are not damped. Figure 2 shows that $R_e(L_c) \gg 1$ for $0.2 \lesssim T/\text{GeV} \lesssim 100$. The largest stirring scale, over which large Reynolds numbers are found, is $L_{c,\rm PDP} \sim 10^{-5}$pc. Hence, at these times, between l_D^{ν} and $L_{c,\rm PDP}$, we expect a state of fully developed turbulence. However, for $T \lesssim 0.2$ GeV, the scale $L_{c,\rm PDP} < l_D^{\nu,\gamma}$, which means that velocity perturbations are washed out and $R_e \ll 1$. Thus, below this temperature, and throughout the photon era, the plasma is in a viscous regime and there is no turbulence[1].

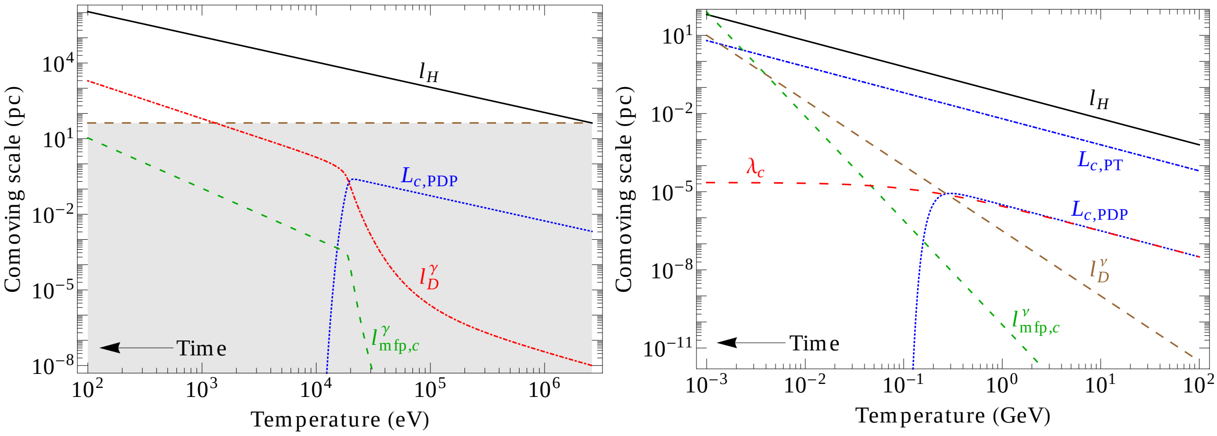

Figure 1 – The evolution of relevant comoving scales in the photon era (left) and neutrino era (right)

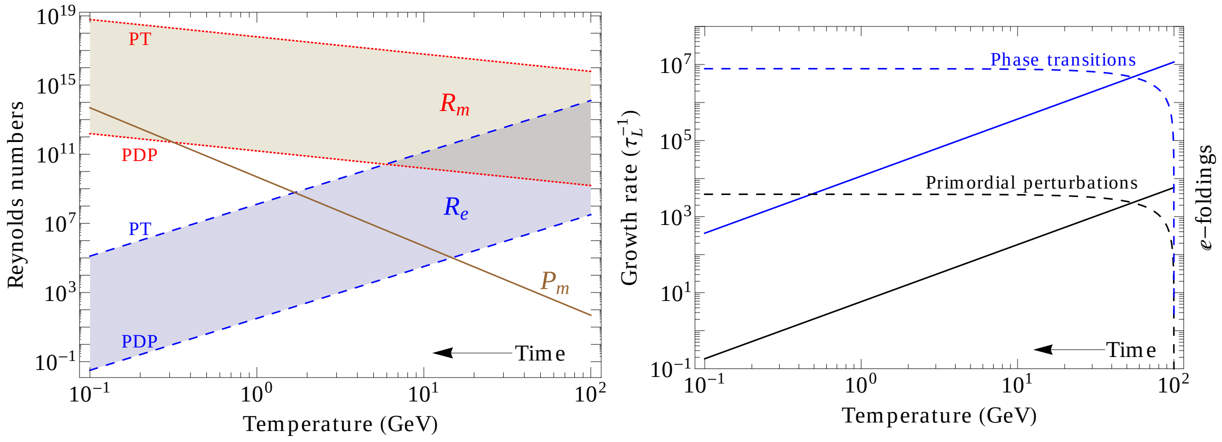

Figure 2 – The Reynolds and Prandtl numbers in the neutrino era (left) and the growth rate and e-foldings (right)

For turbulence generated by PT, the stirring scale can be much larger, since the velocity fluctuations can be much stronger. Hence, if the PT occurs at any time in the epoch between $T \sim (10^2 - 10^{-3})$ GeV, a state of turbulence can be expected. In Fig. 2, the Reynolds numbers are shown to be very large between the EW and QCD scales, indicating a highly turbulent state. The largest stirring scale, over which large Reynolds numbers are found, is roughly given by the horizon size at that time of the PT: $1/aH|_{\mathrm{QCD}} \sim 0.1$ pc and $1/aH|_{\mathrm{EW}} \sim 10^{-4}$ pc.

2.4 *Evolution of Magnetic fields to Present Day*

We now consider the amplification of magnetic seed fields due to SSD action. We use the Kazantsev model to estimate the magnetic field growth rate and number of e-foldings $N \equiv \int \Gamma(t)\mathrm{d}t$, these are shown in Fig. 2. Since the Reynolds numbers are so large in the early epoch, the growth rate is very large and the magnetic field becomes saturated very rapidly. We show that, even for tiny seed fields of strengths $B_0^{\mathrm{seed}} \simeq (10^{-30} - 10^{-20})$ nG, the SSD mechanism can operate for a long enough period of time and be efficient enough to amplify such fields to saturation. The magnetic field strength saturates at $a^2 B_{\mathrm{rms}} \sim 1\varepsilon^{1/2}$ nG on scales at most $\lambda_c \sim 10^{-5}$ pc for turbulence generated by the PDP [1]. Such fields, assumed to be nonhelical, evolve to $B_0^{\mathrm{rms}} \sim 10^{-6}\varepsilon^{1/2}$ nG on scales $\lambda_c \sim 10^{-1}$ pc due to free turbulent decay. For turbulence generated by PT, the SSD mechanism can be even more effective, since the turbulent velocities can be quite large compared to those generated by the PDP. We show that the mechanism can amplify magnetic fields to strengths $a^2 B_{\mathrm{rms}} \sim (10^{-3} - 1)\varepsilon^{1/2}$ μG on scales $\lambda_c \sim (10^{-4} - 10^{-1})$ pc. These initial field configurations evolve to $a^2 B_{\mathrm{rms}} \sim (10^{-6} - 10^{-3})\varepsilon^{1/2}$ nG on scales $\lambda_c \sim (10^{-1} - 10^{2})$ pc due to free turbulent decay [1].

3 Conclusions

We have demonstrated that the conditions are right for the efficient amplification of magnetic fields via the SSD. The mechanism generates large field strengths, albeit on very small scales. Although turbulent velocities are completely erased in viscous and free-streaming regimes, magnetic fields are overdamped and can survive to the present day. Such fields would fill the voids in the large scale structure and provide the seeds for magnetic fields generated by structure formation and galactic dynamo. Unfortunately, the saturated field strengths due to turbulence generated by the primordial density perturbation are too weak on too short scales in the voids of the large scale structure to explain the Fermi observations of TeV Blazars [2]. However, the field strengths obtained due to turbulence generated by first-order phase transitions are strong enough to explain such observations.

Acknowledgments

This work was supported by the Deutsche Forschungsgemeinschaft through the collaborative research centre SFB 676, by the *Helmholtz Alliance for Astroparticle Phyics* (HAP) funded by the Initiative and Networking Fund of the Helmholtz Association. DRGS thanks for funding by the German Science Foundation (DFG) via the SFB 963/1 *Astrophysical Flow Instabilities and Turbulence* (project A12).

References

1. Jacques M. Wagstaff, Robi Banerjee, Dominik Schleicher, and Guenter Sigl. Magnetic field amplification by the small-scale dynamo in the early Universe. *Phys.Rev.*, D89:103001, 2014.
2. A. Neronov and I. Vovk. Evidence for strong extragalactic magnetic fields from Fermi observations of TeV blazars. *Science*, 328:73–75, 2010.
3. Anne-Christine Davis, Matthew Lilley, and Ola Tornkvist. Relaxing the bounds on primordial magnetic seed fields. *Phys.Rev.*, D60:021301, 1999.
4. G. K. Batchelor. On the Spontaneous Magnetic Field in a Conducting Liquid in Turbulent Motion. *Royal Society of London Proceedings Series A*, 201:405–416, April 1950.
5. A.P. Kazantsev. *JHEP*, 53:1806, 1967.
6. Landau and Lifschitz. *Vol. 6. Fluid mechanics.* Pergamon Press, 1987.
7. Robi Banerjee and Karsten Jedamzik. The Evolution of cosmic magnetic fields: From the very early universe, to recombination, to the present. *Phys.Rev.*, D70:123003, 2004.
8. Christoph Federrath, Gilles Chabrier, Jennifer Schober, Robi Banerjee, Ralf S. Klessen, et al. Mach Number Dependence of Turbulent Magnetic Field Amplification: Solenoidal versus Compressive Flows. *Phys.Rev.Lett.*, 107:114504, 2011.
9. J. Schober, D. Schleicher, C. Federrath, R. Klessen, and R. Banerjee. Magnetic field amplification by small-scale dynamo action: Dependence on turbulence models and Reynolds and Prandtl numbers. *Phys.Rev. E*, 85(2):026303, February 2012.
10. Axel Brandenburg and Kandaswamy Subramanian. Astrophysical magnetic fields and nonlinear dynamo theory. *Phys.Rept.*, 417:1–209, 2005.
11. J. Schober, D. Schleicher, S. Bovino, and R. S. Klessen. Small-scale dynamo at low magnetic Prandtl numbers. *Phys. Rev.E*, 86(6):066412, December 2012.
12. K. Subramanian. Dynamics of fluctuating magnetic fields in turbulent dynamos incorporating ambipolar drifts. 1997.
13. S. Bovino, D. R. G. Schleicher, and J. Schober. Turbulent magnetic field amplification from the smallest to the largest magnetic Prandtl numbers. *New Journal of Physics*, 15(1):013055, January 2013.
14. Hideo Kodama and Misao Sasaki. Cosmological Perturbation Theory. *Prog.Theor.Phys.Suppl.*, 78:1–166, 1984.
15. Arthur Kosowsky, Andrew Mack, and Tinatin Kahniashvili. Gravitational radiation from cosmological turbulence. *Phys.Rev.*, D66:024030, 2002.
16. Paul Joseph Steinhardt. Relativistic Detonation Waves and Bubble Growth in False Vacuum Decay. *Phys.Rev.*, D25:2074, 1982.
17. Marc Kamionkowski, Arthur Kosowsky, and Michael S. Turner. Gravitational radiation from first order phase transitions. *Phys.Rev.*, D49:2837–2851, 1994.
18. Scott Dodelson. *Modern cosmology.* Academic Press, 2003.
19. Karsten Jedamzik, Visnja Katalinic, and Angela V. Olinto. Damping of cosmic magnetic fields. *Phys.Rev.*, D57:3264–3284, 1998.


LA THUILE
BAR RISTORANTE
CHAMBRES San Bernardo CAMERE

EXPLORING THE INTERACTION BETWEEN COSMOLOGICAL BLACK HOLES AND SELF-GRAVITATING FIELDS FROM EXACT SOLUTIONS

DANIEL C. GUARIENTO[1,2,a], MICHELE FONTANINI[1]
[1] *Instituto de Física, Universidade de São Paulo, Caixa Postal 66.318, 05315-970, São Paulo, SP, Brazil*
[2] *Perimeter Institute for Theoretical Physics, 31 Caroline St. N., Waterloo, ON, N2L 2Y5, Canada*

Systems which contemplate both local gravitational attraction and the expansion of the Universe constitute an important problem which has been studied since the early days of general relativity. The McVittie black hole is an exact solution to this problem, which provides us with insight on the interaction between compact objects and the cosmological environment. We review some properties of this solution and its matter source, which can be interpreted as a classical fluid but is also an exact solution to a nontrivial scalar field theory.

1 Introduction

The influence the expansion of the Universe exerts on local systems is a problem which can be attacked by many different means, be them numeric studies, perturbative analysis or exact solutions. The last approach is the most challenging, given the non-linear structure of Einstein's equations and dynamics in a curved spacetime. Exact solutions are rare, and few have a clear physical interpretation. Those that remain lack a proper understanding of basic features such as causal structure and nuances of the interaction with the source.

We present here a study of a class of exact solutions of Einstein equations which correspond to a black hole in the presence of self-gravitating matter. In this class, there are two competing mechanisms: the gravitationally bound vicinity of the central object and the expanding universe. The resulting coupling between local effects and cosmological evolution reflects in the causal structure, as interactions are driven by the Einstein equations.

2 The McVittie metric

The oldest exact solution of Einstein's equations to describe a cosmological black hole is the McVittie solution [1]. In isotropic coordinates, the line element reads

$$\mathrm{d}s^2 = -\frac{\left(1 - \frac{m}{2a(t)\hat{r}}\right)^2}{\left(1 + \frac{m}{2a(t)\hat{r}}\right)^2}\mathrm{d}t^2 + a^2(t)\left(1 + \frac{m}{2a(t)\hat{r}}\right)^4 \left(\mathrm{d}\hat{r}^2 + \hat{r}^2\mathrm{d}\Omega^2\right) . \tag{1}$$

with m constant. The limits of the metric parameters suggest an immediate interpretation: for $a(t)$ constant, it reduces to the Schwarzschild metric with central mass m, and for $m = 0$ the line element becomes the flat FLRW metric with scale factor $a(t)$. The metric (1) is also the unique solution that satisfies the following requirements: (i) spherical symmetry; (ii) perfect

---

[a] `carrasco@fma.if.usp.br`

fluid source; (iii) shear-free comoving flow; (iv) asymptotic tendency to a FLRW metric for large radii; and (v) a singularity at the center.

Despite its apparent simplicity, the metric (1) is rich with features without analogue in its limiting Schwarzschild and FLRW cases, such as the presence of a past spacelike singularity at $a = \frac{m}{2\hat{r}}$, as can be seen by examining the Ricci scalar

$$\mathcal{R} = 12H^2 + 6\dot{H}\left(\frac{m+2a\hat{r}}{m-2a\hat{r}}\right), \tag{2}$$

where $H(t) \equiv \dot{a}/a$. The source fluid has homogeneous density

$$\rho(t) = \frac{3}{8\pi}H^2, \tag{3}$$

but an inhomogeneous pressure

$$p(\hat{r},t) = \frac{1}{8\pi}\left[-3H^2 + 2\dot{H}\left(\frac{m+2a\hat{r}}{m-2a\hat{r}}\right)\right], \tag{4}$$

so, even though the source is a perfect fluid, it cannot be described by a barotropic equation of state $p = p(\rho)$.

2.1 Causal structure

The causal structure of McVittie is better visualized in areal radius coordinates [2]. Applying the transformation $r = a(t)\hat{r}\left(1+\frac{m}{2a(t)\hat{r}}\right)^2$ and choosing the positive branch (since the other branch maps into a region of spacetime enclosed between two spacelike singularities), the metric (1) now reads

$$\mathrm{d}s^2 = -R^2\mathrm{d}t^2 + \left[\frac{\mathrm{d}r}{R} - Hr\mathrm{d}t\right]^2 + r^2\mathrm{d}\Omega^2, \tag{5}$$

where $R \equiv \sqrt{1-\frac{2m}{r}}$. In these coordinates, the apparent horizons are defined as the loci of zero expansion of null radial geodesics. These loci are the solutions of null trajectories

$$\left(\frac{\mathrm{d}r}{\mathrm{d}t}\right)_{\pm} = R\left(rH \pm R\right) = 0, \tag{6}$$

where the plus sign corresponds to outgoing geodesics and the minus sign to ingoing ones. It can immediately be seen that only ingoing geodesics can have a real solution to this equation, namely

$$R^2 - H^2(t)\, r_{\pm}^2 = 0. \tag{7}$$

The subscripts on the roots indicate the inner horizon r_- and the outer (cosmological) horizon r_+. Note that, according to equation (7), if $H(t) \to H_0 > 0$ for $t \to \infty$ both apparent horizons become the usual Schwarszchild-de Sitter event horizons. In particular, we denote the inner horizon at this limit as $r_\infty \equiv r_-(t, r \to \infty)$. The behavior of light cones and the position of the apparent horizons for a possible McVittie metric is shown on figure 1.

Since both horizons are solutions of vanishing ingoing radial geodesic expansion, they are anti-trapping surfaces for all finite coordinate times. Moreover, the coordinates in (5) allow us to verify that the singular surface $r_* = 2m$ lies in the past of all events, and is dubbed the McVittie big bang. For an expanding universe ($H > 0$), the temporal and radial coordinates evolve in the same direction as one moves away from the singularity:

$$\frac{\mathrm{d}}{\mathrm{d}t}\left(r - r_*\right) = RrH + \mathcal{O}\left(R^2\right) > 0. \tag{8}$$

Asymptotically into the future, the behavior of the apparent horizons changes dramatically. In particular, if $H_0 > 0$ the inner horizon r_∞ becomes the Schwarzschild-de Sitter event horizon, and is traversable in finite proper time for any null geodesic departing from an event in the McVittie bulk that is causally connected to the horizon. This means that, at future infinity, it is possible to interpret an asymptotically Schwarzschild-de Sitter McVittie metric as describing in fact a black hole. If $H_0 = 0$, the surface r_∞ is sill reachable in finite proper time. However, some curvature scalars become singular at r_∞, which suggests that the interpretation of a Schwarzschild black-hole limit is not as straightforward as in the finite H_0 case.

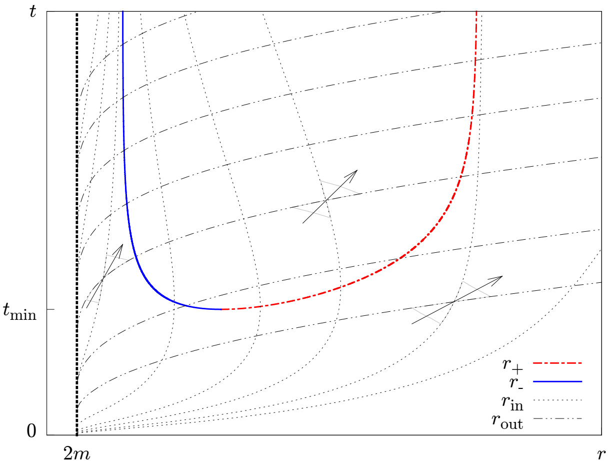

Figure 1: Radial null trajectories, light cones and apparent horizons of the McVittie metric in areal radius coordinates.

It is possible to draw the Penrose diagrams for the McVittie metric through backwards integration of null geodesics[3]. Figures 2(a) and 2(b) show two possible global behaviors of the solution, with the corresponding null-geodesic completions with Schwarzschild-de Sitter patches.

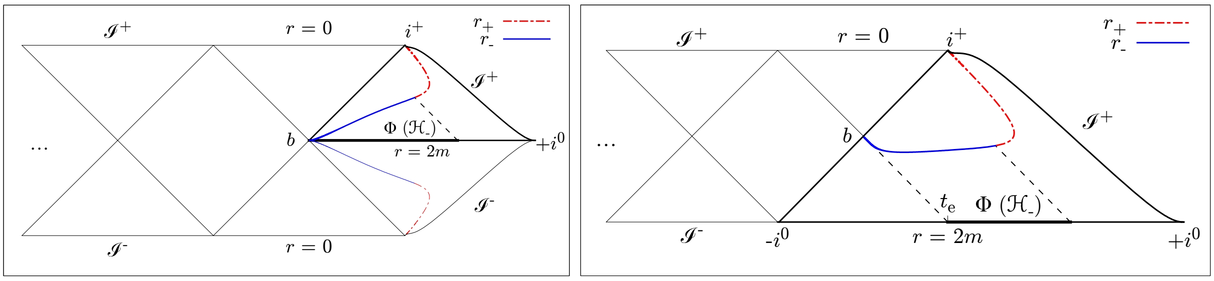

(a) Slowly-converging H.

(b) Rapidly-converging H.

Figure 2: Penrose diagrams for the McVittie solution.

As the figure illustrates, the position of the bifurcating 2-sphere b depends on whether the set $\Phi(\mathcal{H}_-)$ of initial conditions which lead to ingoing geodesics intersecting the inner horizon r_- is compact. It was shown that the compactness of the set can be determined, up to a null measure set, by computing how fast the function $H(t)$ converges to H_0, in comparison to a certain critical rate[4].

2.2 *Scalar field sources*

It was recently shown that the McVittie metric (1) is also a solution of a scalar field with a modified kinetic term minimally coupled to general relativity[5]. The action is given by the *cuscuton* field[6]

$$S = \int \mathrm{d}^4x\sqrt{-g}\left[\frac{1}{2}\mathcal{R} + \mu^2\sqrt{X} - V(\phi)\right] , \tag{9}$$

with $X = -\frac{1}{2}\phi^{;\alpha}\phi_{;\alpha}$. The main characteristic of the cuscuton is that any solution having this field as source has constant mean extrinsic curvature $K^\alpha{}_\alpha$ on the foliation in which the field is homogeneous, a feature that is present in the McVittie metric (1). The Einstein equations and field equation of motion give consistent results, and the solution is

$$\frac{1}{\mu^2}\frac{\mathrm{d}V}{\mathrm{d}\phi} = 3H(t)\,, \tag{10}$$

$$V(\phi) = -6\pi\mu^4\left(\phi + C\right)^2 = \frac{3}{8\pi}H^2\,. \tag{11}$$

The energy-momentum tensor of the homogeneous cuscuton has homogeneous energy density and inhomogeneous pressure, so solutions with uniform expansion and shear-free motion on the comoving frame are *unique* to this type of field.

One may then ask the reverse question: is the cuscuton the unique possible field source for the McVittie metric? To answer that question, we start from a general k-essence action:

$$S = \int \mathrm{d}^4x\sqrt{-g}\left[\frac{1}{2}\mathcal{R} + K(X,\varphi)\right]\,. \tag{12}$$

Using the metric (1) as an ansatz for the solution, the Einstein and field equations require

$$2XK_{,XX} + K_{,X} = 0\,, \tag{13}$$

and the unique solution is in fact the cuscuton action (9).

An interesting implication of this analysis comes from the fact that the cuscuton is also dual to Hořava-Lifshitz gravity with anisotropic Weyl symmetry [7]. The fact that McVittie is an exact solution to this theory implies that McVittie can be thought of as a vacuum solution of a modified gravity theory.

3 Conclusions and future steps

The expansion of the Universe implies an important change in setting for the studies of cosmological black holes. From the point of view of exact solutions, the absence of a stationary or asymptotically flat background means that many concepts taken for granted in those cases (such as the notion of the event horizon or a classical equivalent of energy) either no longer exist or have to be reinterpreted altogether.

Beyond the study of the McVittie metric, there are new directions this analysis may take. A simple generalization leads to a black-hole mass which may evolve with time [8], at the expense of the surrounding source. In this simple approximation, the mechanism involved is interpreted in terms of a heat flow [9]. The causal structure of this new metric has new complexities that require a deep analysis in the lines of the one described here. There are still other shear-free members of the family of solutions of which McVittie is a part: the Kustaanheimo-Qvist class, which contains many physically interesting solutions which are also not fully understood.

These are all questions with various degrees of physical relevance, connecting field theory models and classical general relativity with cosmology into the slow-treading yet insightful realm of exact solutions.

Acknowledgments

D. C. G. is supported by FAPESP Grants No. 2010/08267-8 and No. 2013/01854-3. Research at Perimeter Institute is supported by the Government of Canada through Industry Canada and by the Province of Ontario through the Ministry of Economic Development & Innovation.

References

1. G. C. McVittie. The mass-particle in an expanding universe. *Mon. Not. R. Astron. Soc.*, 93:325–339, 1933.

2. Nemanja Kaloper, Matthew Kleban, and Damien Martin. McVittie's legacy: Black holes in an expanding universe. *Phys. Rev. D*, 81:104044, May 2010.
3. Kayll Lake and Majd Abdelqader. More on McVittie's legacy: A Schwarzschild–de Sitter black and white hole embedded in an asymptotically ΛCDM cosmology. *Phys. Rev. D*, 84:044045, August 2011.
4. Alan M. da Silva, Michele Fontanini, and Daniel C. Guariento. How the expansion of the universe determines the causal structure of McVittie spacetimes. *Phys. Rev. D*, 87:064030, March 2013.
5. Elcio Abdalla, Niayesh Afshordi, Michele Fontanini, Daniel C. Guariento, and Eleftherios Papantonopoulos. Cosmological black holes from self-gravitating fields. *Phys. Rev. D*, 89:104018, May 2014.
6. Niayesh Afshordi, Daniel J. H. Chung, and Ghazal Geshnizjani. Causal field theory with an infinite speed of sound. *Phys. Rev. D*, 75:083513, April 2007.
7. Niayesh Afshordi. Cuscuton and low energy limit of Hořava-Lifshitz gravity. *Phys. Rev. D*, 80:081502, October 2009.
8. Valerio Faraoni and Audrey Jacques. Cosmological expansion and local physics. *Phys. Rev. D*, 76:063510, September 2007.
9. Daniel C. Guariento, Michele Fontanini, Alan M. da Silva, and Elcio Abdalla. Realistic fluids as source for dynamically accreting black holes in a cosmological background. *Phys. Rev. D*, 86:124020, December 2012.

Effective gravitational interactions of dark matter axions

Toshifumi Noumi
Mathematical Physics Laboratory, RIKEN Nishina Center, Saitama 351-0198, Japan

Ken'ichi Saikawa
Department of Physics, Tokyo Institute of Technology, Ookayama, Meguro-ku, Tokyo 152-8551, Japan

Ryosuke Sato
Theory Center, High Energy Accelerator Research Organization (KEK), 1-1 Oho, Tsukuba, Ibaraki 305-0801, Japan

Masahide Yamaguchi [a]
Department of Physics, Tokyo Institute of Technology, Ookayama, Meguro-ku, Tokyo 152-8551, Japan

In this talk, we investigated the structure of gravitational self interactions of coherently oscillating axions in the general relativistic framework. Based on such interactions, we also estimated the interaction rate of dark matter axions in coherent states. This talk is based on Ref. [1].

1 Introduction

Axion is one of the most powerful candidates of dark matter, which gives the solution to the strong CP problem of quantum chromodynamics (QCD). It is produced non-thermally in the early universe and described as a coherently oscillating scalar field. Since this coherent oscillation is interpreted as the highly condensed Bose gas of axions, there is some possibility for dark matter axions of forming Bose-Einstein condensate (BEC) in the universe. This possibility has received considerable interest recently, due to the suggestion by Sikivie and Yang [2] that gravitational interactions can thermalize the system. In this talk, we investigated all possible elementary processes contributing to the gravitational self interactions of axions in the expanding universe, and to reanalyze the gravitational self interaction rate of axions, based on the work [1].

2 Massive scalar field in the cosmological background

In this section we introduce our setup to discuss gravitational interactions of massive scalar fields in the cosmological background.

By the use of the effective field theory approach to cosmological perturbations [3], a generic action of a massive scalar field ϕ (and the metric $g_{\mu\nu}$) under the FRW background in the unitary gauge is given by

$$S = S_\phi + S_{\rm grav} \,, \tag{1}$$

$$S_\phi = \int d^4x\sqrt{-g}\left[-\frac{1}{2}g^{\mu\nu}\partial_\mu\phi\partial_\nu\phi - \frac{1}{2}m^2\phi^2\right] , \tag{2}$$

---

[a] Talk is given by M. Yamaguchi.

$$S_{\rm grav} \;=\; \int d^4x\sqrt{-g}\left[\frac{1}{2}M_{\rm Pl}^2R + M_{\rm Pl}^2\dot{H}g^{00} - M_{\rm Pl}^2(3H^2+\dot{H}) + \frac{M_2(t)^4}{2}\Big(g^{00}+1\Big)^2\right]\,, \tag{3}$$

where m is the mass of the scalar field, the Plank mass $M_{\rm Pl}$ is related to the Newton's constant G as $M_{\rm Pl}^2 = (8\pi G)^{-1}$, and the Hubble parameter $H(t)$ is that of the background FRW spacetime. We then rewrite the above action in terms of the Arnowitt-Deser-Misner (ADM) decomposition:

$$ds^2 = -(N^2 - N_iN^i)dt^2 + 2N_idx^idt + h_{ij}\,dx^idx^j\,, \tag{4}$$

where the following transverse conditions $h_{ij} = a^2e^{2\zeta}(e^\gamma)_{ij}$ with $\gamma_{ii} = \partial_i\gamma_{ij} = 0$ are imposed. By solving the constraints associated with these auxiliary fields N and N^i, we obtain the following Hamiltonian density $\mathcal{H} = \mathcal{H}_{\rm free} + \mathcal{H}_{\rm int}$ in the interaction picture:

$$\begin{aligned}
\mathcal{H}_{\rm free} &= a^3\Big[M_{\rm Pl}^2\tilde{\epsilon}\Big(\dot{\zeta}^2 + c_s^2\frac{(\partial_i\zeta)^2}{a^2}\Big) + \frac{M_{\rm Pl}^2}{8}\Big(\dot{\gamma}_{ij}^2 + \frac{(\partial_k\gamma_{ij})^2}{a^2}\Big) + \frac{1}{2}\Big(\dot{\phi}^2 + \frac{(\partial_i\phi)^2}{a^2} + m^2\phi^2\Big)\Big] &(5)\\
\mathcal{H}_{\rm int} &= \mathcal{H}_{\zeta\phi^2} + \mathcal{H}_{\gamma\phi^2} + \mathcal{H}_{\phi^4}\,, &(6)\\
\mathcal{H}_{\zeta\phi^2} &= a^3\left[-\frac{1}{2}\zeta\Big(3\dot{\phi}^2 - \frac{(\partial_i\phi)^2}{a^2} - 3m^2\phi^2\Big) + \frac{1}{2H}\dot{\zeta}\Big(\dot{\phi}^2 + \frac{(\partial_i\phi)^2}{a^2} + m^2\phi^2\Big)\right.\\
&\qquad\left. -\Big(\tilde{\epsilon}\dot{\zeta} - \frac{1}{H}\frac{\partial^2\zeta}{a^2}\Big)\Big(\partial^{-2}\partial_i(\dot{\phi}\partial_i\phi)\Big)\right]\,, &(7)\\
\mathcal{H}_{\gamma\phi^2} &= -\frac{a^3}{2}\gamma_{ij}\frac{\partial_i\phi\partial_j\phi}{a^2}\,, &(8)\\
\mathcal{H}_{\phi^4} &= a^3\left[-\frac{1}{4M_{\rm Pl}^2}\Big(\partial^{-2}\partial_i(\dot{\phi}\partial_i\phi)\Big)^2 - \frac{1}{M_{\rm Pl}^2}(\dot{\phi}\partial_i\phi)\partial^{-2}(\dot{\phi}\partial_i\phi)\right.\\
&\qquad\left. + \frac{1}{16M_{\rm Pl}^2H^2\tilde{\epsilon}}\Big(\dot{\phi}^2 + \frac{(\partial_i\phi)^2}{a^2} + m^2\phi^2\Big)^2\right]\,, &(9)
\end{aligned}$$

where we have introduced the sound speed c_s of adiabatic perturbations and the parameter $\tilde{\epsilon}$ as

$$c_s^2 = \frac{-M_{\rm Pl}^2\dot{H}}{-M_{\rm Pl}^2\dot{H} + 2M_2^4}\,, \qquad \tilde{\epsilon} = -c_s^{-2}\frac{\dot{H}}{H^2}\,. \tag{10}$$

3 Effective quartic interaction from graviton exchange

In the context of axion cosmology, our interests are in the gravitational interaction in the regime $m \gg k/a, H$, since axions are produced when $m \gtrsim H$ is satisfied. In this regime, the mode function φ_k of the scalar field is given by

$$\varphi_k \simeq \frac{1}{\sqrt{2ma^3}}e^{-imt}\,, \tag{11}$$

where we have dropped sub-leading terms suppressed by the factor $\dfrac{H}{m}$ or $\dfrac{k/a}{m}$. Then, the leading contribution from $\zeta\phi^2$ type interaction is given by

$$H_{{\rm int},\zeta\phi^2} \;\simeq \tfrac{m}{H}\int\tfrac{d^3k_1}{(2\pi)^3}\int\tfrac{d^3k_2}{(2\pi)^3}\int\tfrac{d^3k_3}{(2\pi)^3}(2\pi)^3\delta^{(3)}(\mathbf{k}_1+\mathbf{k}_2+\mathbf{k}_3)\,\dot{\zeta}_{\mathbf{k}_3}a^\dagger_{\mathbf{k}_1}a_{-\mathbf{k}_2}\,, \tag{12}$$

and that from ϕ^4 type interactions is given by

$$H_{{\rm int},\phi^4} \simeq \frac{m^2}{4M_{\rm Pl}^2a^3H^2\tilde{\epsilon}}\int\frac{d^3k_1}{(2\pi)^3}\int\frac{d^3k_2}{(2\pi)^3}\int\frac{d^3k_3}{(2\pi)^3}\int\frac{d^3k_4}{(2\pi)^3}(2\pi)^3\delta^{(3)}(\mathbf{k}_1+\mathbf{k}_2+\mathbf{k}_3+\mathbf{k}_4)a^\dagger_{\mathbf{k}_1}a^\dagger_{\mathbf{k}_2}a_{-\mathbf{k}_3}a_{-\mathbf{k}_4}\,, \tag{13}$$

where the fields ϕ and ζ in the interaction picture are expanded as

$$\begin{aligned} \phi(\mathbf{x},t) &= \int \tfrac{d^3k}{(2\pi)^3} e^{-i\mathbf{k}\cdot\mathbf{x}}\phi_{\mathbf{k}}(t) = \int \tfrac{d^3k}{(2\pi)^3}\left[e^{i\mathbf{k}\cdot\mathbf{x}}\varphi_k(t)a_{\mathbf{k}} + e^{-i\mathbf{k}\cdot\mathbf{x}}\varphi_k^*(t)a_{\mathbf{k}}^\dagger\right], \qquad (14)\\ \zeta(\mathbf{x},t) &= \int \tfrac{d^3k}{(2\pi)^3} e^{-i\mathbf{k}\cdot\mathbf{x}}\zeta_{\mathbf{k}}(t) = \int \tfrac{d^3k}{(2\pi)^3}\left[e^{i\mathbf{k}\cdot\mathbf{x}}\mathcal{Z}_k(t)a_{z\mathbf{k}} + e^{-i\mathbf{k}\cdot\mathbf{x}}\mathcal{Z}_k^*(t)a_{z\mathbf{k}}^\dagger\right]. \qquad (15) \end{aligned}$$

Here $a_{\mathbf{k}}$ and $a_{z\mathbf{k}}$ are the annihilation operators satisfying the standard commutation relations.

These two interactions can be unified as an effective scalar quartic interaction at the tree level as

$$H_{\text{eff}}(t) = \int \tfrac{d^3k_1}{(2\pi)^3}\int \tfrac{d^3k_2}{(2\pi)^3}\int \tfrac{d^3k_3}{(2\pi)^3}\int \tfrac{d^3k_4}{(2\pi)^3}(2\pi)^3\delta^{(3)}(\mathbf{k}_1+\mathbf{k}_2-\mathbf{k}_3-\mathbf{k}_4)F(t;|\mathbf{k}_1-\mathbf{k}_3|)a_{\mathbf{k}_1}^\dagger a_{\mathbf{k}_2}^\dagger a_{\mathbf{k}_3}a_{\mathbf{k}_4}, \qquad (16)$$

where the function $F(t;k)$ is defined as

$$F(t;k) = \tfrac{m^2}{4M_{\text{Pl}}^2a^3H^2\tilde{\epsilon}} + \tfrac{i}{2}\int_{t_0}^t dt'\,\tfrac{m^2}{H(t)H(t')}\Big(\dot{\mathcal{Z}}_k^*(t)\dot{\mathcal{Z}}_k(t') - \dot{\mathcal{Z}}_k(t)\dot{\mathcal{Z}}_k^*(t')\Big). \qquad (17)$$

In the radiation dominated universe $a(t) \propto t^{1/2}$, the mode function $\mathcal{Z}_k$ is given by

$$\mathcal{Z}_k(t) = \frac{c_s}{2\sqrt{2}aM_{\text{Pl}}}\frac{1}{\sqrt{c_sk}}e^{-ic_sk\tau}, \qquad (18)$$

where the conformal time τ satisfies $\tau = 1/(aH) \propto t^{1/2}$. Then, the function $F(t;k)$ is estimated as

$$F(t;k) = -\frac{m^2}{4M_{\text{Pl}}^2a^3}\frac{1}{(k/a)^2}f\Big(\frac{c_sk/a}{H}\Big) = -\frac{2\pi Gm^2}{a^3}\frac{1}{(k/a)^2}f\Big(\frac{c_sk/a}{H}\Big) \qquad (19)$$

with $f(x) = 1 - \cos x - x\sin x$. The function $f(x)$ behaves as

$$f(x) = \begin{cases} 1 + (\text{highlyoscillatingterms}) & \text{for} \quad x \gg 1, \\ -\dfrac{1}{2}x^2 & \text{for} \quad x \ll 1. \end{cases} \qquad (20)$$

Then, the effective quartic interaction reproduces the Newtonian approximation when the momentum transfer is subhorizon scale $c_sk/(aH) \gg 1$:

$$\begin{aligned} H_{\text{eff}} \simeq &\int \frac{d^3k_1}{(2\pi)^3}\int \frac{d^3k_2}{(2\pi)^3}\int \frac{d^3k_3}{(2\pi)^3}\int \frac{d^3k_4}{(2\pi)^3}(2\pi)^3\delta^{(3)}(\mathbf{k}_1+\mathbf{k}_2-\mathbf{k}_3-\mathbf{k}_4) \\ &\times\left[-\frac{2\pi Gm^2}{a^3}\frac{1}{(|\mathbf{k}_1-\mathbf{k}_3|/a)^2}\right]a_{\mathbf{k}_1}^\dagger a_{\mathbf{k}_2}^\dagger a_{\mathbf{k}_3}a_{\mathbf{k}_4}, \qquad (21) \end{aligned}$$

where we have dropped highly oscillating terms.

Assuming that the interactions are absent at sufficiently early times, we can estimate the number of axions occupying the state labeled by a (comoving) momentum $\mathbf{p}$ by using the number operator

$$\mathcal{N}_{\mathbf{p}} = \frac{1}{V}a_{\mathbf{p}}^\dagger a_{\mathbf{p}}, \qquad (22)$$

which diagonalizes the free Hamiltonian. Since we are interested in the self interaction of axions in the coherent states, the time evolution of the expectation value of $\mathcal{N}_{\mathbf{p}}$ can be evaluated as

$$\langle\mathcal{N}_{\mathbf{p}}(t)\rangle \simeq \mathcal{N}_{\mathbf{p}}(t_0) + i\int_{t_0}^t dt_1\langle[H_{\text{eff}}(t_1),\mathcal{N}_{\mathbf{p}}]\rangle, \qquad (23)$$

where $\langle\ldots\rangle$ denotes the expectation value for the coherent states. Then, the interaction rate can be estimated as

$$\Gamma = \frac{1}{\langle\mathcal{N}_{\mathbf{p}}(t)\rangle}\frac{d\langle\mathcal{N}_{\mathbf{p}}(t)\rangle}{dt}. \qquad (24)$$

For quartic gravitational interactions of axions, we can consider the following three classes of interactions:

1. All external lines attached to the quartic coupling are subhorizon sized ($k_1, k_2, k_3, p > k_H$).
2. One or two external lines are superhorizon sized, while the other external lines and the momentum transfer $|\mathbf{k}_1 - \mathbf{p}|$ are subhorizon sized ($k_1, k_2 > k_H$ and $k_3, p < k_H$, etc.).
3. All external lines are superhorizon sized ($k_1, k_2, k_3, p < k_H$).

Among these three cases, we are interested in the case 2, since it represents a transition from (into) modes with higher momentum (subhorizon sized waves) into (from) almost homogeneous modes (superhorizon sized waves), which is relevant to the transition into (from) BEC.

First, we consider the case where PQ symmetry is broken before inflation. In both cases 1 & 2, the interaction rates are estimated as

$$\Gamma \sim \frac{Gm^2 n}{(\delta p)^2}, \tag{25}$$

which reproduces the previous result derived on the basis of the Newtonian approximation.

Finally, we consider the case where PQ symmetry is broken before inflation. For the case 1, we obtain $\Gamma_1 \sim \mathcal{O}(10^{-10}) \times Gm^2 n/(\delta p)^2$. Since there is a severe suppression factor, we expect that the process classified to the case 1 remains irrelevant at least during the radiation dominated era. On the other hand, for the case 2 (with $p > k_H$), we obtain $\Gamma_2 \sim Gm^2 n/(\delta p)^2$.

4 Summary

In this talk, we investigated the structure of gravitational self interactions of coherently oscillating axions in the general relativistic framework. Based on such interactions, we estimated the interaction rate of dark matter axions in coherent states. If PQ symmetry is broken after inflation, $\Gamma \sim Gm^2 n/(\delta p)^2$, while Γ_1 is suppressed by a factor of $\mathcal{O}(10^{-10})$ compared with Γ_2 if PQ symmetry is broken before inflation. What is notable is that in both cases the rate of the process corresponding to the transition between modes inside and outside the horizon (case 2) is estimated by Eq. 25. We interpret this contribution as the process where the modes with short wavelength fall into those with long wavelength by exchanging gravitons with short wavelength. Although the homogeneous mode does not feel the gravitational force, it is possible for the modes with short wavelength to annihilate and produce a homogeneous wave. In this sense, this process can be regarded as a causal one, which is mediated by the modes whose wavelength is shorter than the horizon, and hence there is a possibility for it to have relevance to the gravitational thermalization.

Acknowledgments

T. N. is supported by Special Postdoctoral Researchers Program at RIKEN. K. S. and R. S. are supported by the Japan Society for the Promotion of Science (JSPS) through research fellowships. The work of M. Y. is supported in part by the Grant-in-Aid for Scientific Research No. 25287054 and 26610062.

References

1. T. Noumi, K. 'i. Saikawa, R. Sato and M. Yamaguchi, Phys. Rev. D **89**, 065012 (2014) [arXiv:1310.0167 [hep-ph]]. See also references in this paper.
2. P. Sikivie and Q. Yang, Phys. Rev. Lett. **103**, 111301 (2009) [arXiv:0901.1106 [hep-ph]].
3. C. Cheung, P. Creminelli, A. L. Fitzpatrick, J. Kaplan and L. Senatore, JHEP **0803**, 014 (2008) [arXiv:0709.0293 [hep-th]].

COSMOLOGY WITH THE JUBILEE AND MULTIDARK SIMULATIONS

S. GOTTLÖBER[1], I. ILIEV[2], G. YEPES[3]
[1]*Leibniz Institute for Astrophysics Potsdam, An der Sternwarte 16, 14482 Potsdam, Germany*
[2]*Astronomy Centre, Department of Physics & Astronomy, Pevensey II Building, University of Sussex, Falmer, Brighton BN1 9QH, United Kingdom*
[3] *Grupo de Astrofísica, Universidad Autónoma de Madrid, Madrid E-28049, Spain*

We review a series of Dark Matter only simulations with up to 216 and 57 billion particles, performed within the Jubilee and MultiDark projects, respectively. All the data products from these simulations are made available to the community through interactive public databases.

1 Introduction

It is almost 50 years since the cosmic microwave background (CMB) radiation was first detected. This radiation was imprinted on the sky just a few hundred thousand years after the Big Bang. The measured temperature fluctuations of the CMB radiation tell us that shortly after the Big Bang the Universe was almost homogeneous with tiny density fluctuations of the order of 10^{-5}. Starting from these tiny fluctuations generated during the early inflationary phase all the observed structures in the universe have been formed: huge clusters of galaxies with masses up to a few 10^{15} solar masses in the knots of the cosmic web which comprise galaxies in a wide range of masses from dwarfs (10^9 solar masses) to massive elliptical galaxies (10^{13} solar masses).

Comparing the power spectrum of measured temperature fluctuations with theoretical models, cosmologists conclude that the Universe is spatially flat and consists at present of about 69% of some unknown Dark Energy, 26% of also unknown Dark Matter and 5% of baryons[a]. In the evolved universe one can directly observe the distribution of baryons and indirectly deduce (e.g. by gravitational lensing, velocity measurements, X-ray emission) the distribution of Dark Matter.

The formation of structure on large scales is well understood. The initial small perturbations grow by gravitational instability and form bound objects called halos which decouple from the expansion of the universe. These bound objects grow hierarchically by accretion of matter and merging with smaller halos. The gravitational clustering becomes increasingly non-linear. Dark Matter is more abundant than baryons and hence becomes most important for formation of large scale structures where gravity dominates. The vastness of scales and the non-linearity of gravitational clustering are the reasons why numerical simulations and the intensive use of the largest supercomputers are the only methods suited to study the gravitationally driven growth of structures down to the high over densities in halos and the formation of galaxies therein. Cosmological simulations follow the clustering of matter by numerically solving the gravitational interaction based on an N-body approach. Additionally one would need to model hydrodynamical processes, radiative cooling, star formation and the feedback of stars, in order to simulate in detail the formation of galaxies in their different environments. However, in large volumes and

---

[a] These are the recent Planck values, the WMAP 5-year values differ slightly, see Table 1

for a large number of galaxies it is practically impossible to follow the hydrodynamical processes. Therefore, Dark Matter only simulations are performed with very high resolution so that the evolution of halos and subhalos can be followed numerically. These halos and sub-halos host the galaxies. In a second (postprocessing) step the properties of the galaxies can be determined by semi-analytical or abundance matching algorithms. Semi analytical methods are based on the formation history of the dark matter halos and on recipes which predict the properties of galaxies formed in these halos. Abundance matching algorithms compare observed luminosity functions with halo mass or velocity functions deduced from dark matter only N-body simulations. In case of subhalos one needs also some information about the evolution, namely the properties of the subhalo at infall.

In order to simulate the formation of structure in the universe fulfilling the above requirements, a very high mass and spatial resolutions are necessary which imposes a strong challenge for present day computational algorithms. Moreover, such simulations need a large amount of computational time and require huge amounts of available memory as well as large data storage facilities for further analyses of results. Therefore, they can be performed only at the largest supercomputer centres. In the following two sections we review briefly two projects of Large Scale Structure formation in Gpc size cosmological volumes, the Jubilee and the MultiDark projects.

2 The Jubilee simulation

The Jubilee simulation [7] is a N-body simulation with 6000^3 (216 billion) particles in a volume of $(6\ h^{-1}\mathrm{Gpc})^3$ performed with the CUBEP^{3}M N-body code, a P^{3}M (particle-particle-particle-mesh) code [2]. CUBEP^{3}M calculates the long-range gravity forces on a 2-level mesh and short-range forces exactly, by direct summation over local particles. The code is massively-parallel, using hybrid (combining MPI and OpenMP) parallelization and has been shown to scale well up to tens of thousands of computing cores. The cosmological and simulation parameters used in the Jubilee simulation are listed in § 2.1. The minimum resolved halo mass (with 20 particles) is $1.49 \times 10^{12}\ h^{-1}\mathrm{M}_{\odot}$, corresponding to galaxies slightly more massive than the Milky Way.

Due to the large volume of the simulation, very massive objects exist so that the high end of the mass function can be determined with unprecedented accuracy. For instance, when comparing with the predictions of the widely-used Tinker mass function, we showed that there is an over prediction of these extreme objects [6,8].

During the last decade the precision in the determination of the Hubble parameter has reached the per cent level. Within the Jubilee simulation we studied statistical properties of the local Hubble parameter as measured by local observers and showed that the distribution of the local Hubble parameter depends not only on the scale of inhomogeneities, but also on how one defines the positions of observers in the cosmic web and what reference frame is used [9]. The predictions for the local Hubble parameter from the simulation can be compared with observational constraints based on Type Ia supernova (SNIa) and CMB observations. Due to cosmic variance, for observers located in random haloes the Hubble constant determined from nearby SNIa may differ from that measured from the CMB by ±0.8 per cent at 1σ statistical significance. This scatter is too small to significantly alleviate a recently claimed discrepancy between current measurements assuming a flat ΛCDM model. However, for observers located in the centres of the largest voids permitted by the standard ΛCDM model the local Hubble constant measurements could differ from SNIa as high as 5 per cent.

In future the ISW signal will be used to help to discriminate between cosmological models. At present the ISW effect does not constrain the ΛCDM model to anything like the precision of the standard datasets (CMB and BAOs). However, for a universe containing an amount of warm dark matter or one with a temporally varying dark energy component, the ISW effect will be an aid in constraining the theoretical models and predictions. For alternative cosmological models a variety of expectations of ISW signal arise. The ISW signal from the Jubilee simulation has been cross-correlated with the catalogue of mock Luminous Red Galaxies (LRGs) [8]. The ISW-LRG cross-correlation signal for a full-sky survey and $\ell < 30$ is strongest for lower redshift bins ($z \sim 0.2$ to 0.5), whereas for $\ell > 30$ the signal is best observed with surveys covering $z \sim 0.6 - 1.0$.

2.1 *The Jubilee database*

The Jubilee database `http://www.jubilee-project.org` contains data produced by two simulations, namely the Small Jubilee simulation ($(3.072\ h^{-1}\mathrm{Gpc})^3$ cubic box with 3072^3 particles) and the Big Jubilee simulation ($(6.0\ h^{-1}\mathrm{Gpc})^3$ cubic box with 6000^3 particles). Both simulations were done with the CUBEP^{3}M parallel N-body code in the Juropa Supercomputer at the Juelich Supercomputer Center (Germany). The simulation parameters are $\Omega_m = 0.27$, $\Omega_\Lambda = 0.73$, $h = 0.70$, $\Omega_b = 0.044$, $\sigma_8 = 0.80$, $n_s = 0.96$, gravitational smoothing $50\ h^{-1}$kpc comoving, mass resolution $7.49 \times 10^{10}\ h^{-1}\mathrm{M}_\odot$, starting redshift $z = 100$.

The simulations have been post-processed to extract with spherical overdensity halos (AHF and SO) as well as Friends-of-Friends (FOF) algorithms catalogs of halos. These catalogs are very large, containing up to 400 million halos per snapshot. To avoid huge data transfers the user can choose which specific properties she/he wants to download.

3 The MultiDark simulations

The MultiDark simulations are a series of large Dark Matter only simulations summarized in Table 1. These simulations have been performed with different codes: the ART code [1] (first two lines in Table 1) and the Gadget code [5] (all remaining simulations in Table 1). The first MultiDark database [4] has been built with the two ART simulations.

Accurate predictions of the abundance and clustering of dark matter haloes play a key role in testing the standard cosmological model. However, it poses significant challenges when it comes to testing its predictions for the distribution and properties of galaxies. The simulations provide very detailed predictions on the distribution of dark matter, but connecting the luminous galaxies with their dark matter haloes is a much more difficult task. There are different possibilities to make this galaxy-halo connection. Halo Abundance Matching (HAM) is a simple and yet realistic way to bridge the gap between dark matter haloes and galaxies. One key ingredient of these models are the subhaloes of more massive halos. They must be included in the abundance matching prescription because each lump of dark matter with enough mass and concentration should host a galaxy regardless whether that is the central object or a satellite. However a simple abundance matching model is not applicable because subhalos may loss a substantial fraction of mass due to tidal stripping while the stellar mass hosted by these subhalos is not expected to be reduced by stripping. Therefore, using the properties of the subhalos at infall to the host halo is more appropriate. In the large volume cosmological simulations of the MultiDark project convergence at the 10% accuracy for the abundance of haloes and subhaloes, and the correlation functions can be achieved with ~ 150 particles per halo [3].

3.1 *The MultiDark database*

The CosmoSim database (`www.cosmosim.org`) is the successor of the MultiDark database (`www.multidark.org`). It currently provides access to six cosmological simulations - including a high-resolution resimulation of selected regions with hydrodynamics and star formation - which originate from the MultiDark and CLUES (`www.clues-project.org`) projects.

Outputs of large cosmological simulations are typically stored at supercomputer centres with restricted access and encompass terabytes of data - too much to be downloaded by everyone. By providing the data via a database everybody can easily access the data, filter or combine the results directly on the server and use them for his own research.

Table 1: Numerical and cosmological parameters for the simulations. The columns give the box size, the number of particles, the particle mass, the adopted values for $\Omega_{\rm Matter}$, $\Omega_{\rm Baryon}$, Ω_Λ , the clustering at $8h^{-1}$ Mpc, σ_8, the spectral index n_s and the Hubble parameter h.

box [Mpc/h]	particles	m_p [$h^{-1}\,M_\odot$]	Ω_M	Ω_B	Ω_Λ	σ_8	n_s	h
1000	2048^3	8.6×10^9	0.27	0.047	0.73	0.82	0.95	0.7
250	2048^3	1.4×10^8	0.27	0.047	0.73	0.82	0.95	0.7
2500	3840^3	2.1×10^{10}	0.27	0.047	0.73	0.82	0.95	0.7
2500	3840^3	2.2×10^{10}	0.29	0.047	0.71	0.82	0.95	0.7
2500	3840^3	2.2×10^{10}	0.29	0.047	0.71	0.90	0.95	0.7
2500	3840^3	2.4×10^{10}	0.31	0.047	0.69	0.82	0.95	0.7
2500	3840^3	2.4×10^{10}	0.31	0.047	0.69	0.82	0.96	0.678
1000	3840^3	1.5×10^9	0.31	0.047	0.69	0.82	0.96	0.678
400	3840^3	9.7×10^7	0.31	0.047	0.69	0.82	0.96	0.678

The available data products include catalogues of dark matter halos, their inner properties, merging histories, information about the cosmic web and for selected snapshots even the raw particle distributions allowing for much deeper studies of dark matter halos and their environment. All the simulations and database tables are made available through a web interface including an extensive documentation.

The increase in resolution for cosmological simulations has led to larger data volumes, with individual tables reaching sizes in the terabyte range. By exploring a new database technology, it is now possible to store and analyse snapshots from simulations with nearly 60 billion particles directly in the CosmoSim database. The new database technology, the Spider engine for MariaDB/MySQL, allows to spread the data over many server nodes, and one head node, resulting in a distribution of the computational task over many server nodes.

Acknowledgments

The simulations described here have been performed at the JSC Juelich, the NAS Ames and the LRZ Munich. Publishing the simulations in databases would be impossible without the permanent help of the IT groups in Potsdam and Madrid, special thanks to Kristin Riebe, Harry Anke, Adrian Partl and Fernando Campos.

References

1. S. Gottlöber, A. Klypin, “The ART of Cosmological Simulations “, in: High Performance Computing in Science and Engineering, Springer-Verlag, 2008, p.29
2. J. Harnois-Déraps, U.-L. Pen, I. T. Iliev , H. Merz, J. D. Emberson, V. Desjacques, MNRAS **436**, 540 (2013)
3. A. Klypin, F. Prada, G. Yepes, S. Hess, S. Gottlöber, 2013, arXiv, arXiv:1310.3740
4. K. Riebe, et al. AN **334**, 691 (2013)
5. V. Springel, MNRAS **364**, 1105 (2005)
6. W. A. Watson, I. T. Iliev, A. D’Aloisio, A. Knebe, P. R. Shapiro, G. Yepes, MNRAS **433**, 1230 (2013)
7. W. A. Watson, I. T. Iliev, J. M. Diego, S. Gottlöber, A. Knebe, E. Martínez-González, G. Yepes, MNRAS **437**, 3776 (2014)
8. W. A. Watson, et al. MNRAS **438**, 412 (2014)
9. R. Wojtak, A. Knebe, W. A. Watson, I. T. Iliev, S. Heß, D. Rapetti, G. Yepes, S. Gottlöber, MNRAS **438**, 1805 (2014)

ASTROPHYSICAL TESTS OF THE STABILITY OF FUNDAMENTAL COUPLINGS

C.J.A.P. MARTINS, M.C. FERREIRA, M.D. JULIÃO, A.C.O. LEITE, A.M.R.V.L. MONTEIRO,
P.O.J. PEDROSA, M.F. SILVA, J.P.P. VIEIRA and P.E. VIELZEUF
Centro de Astrofísica da Universidade do Porto, Rua das Estrelas, 4150-762 Porto, Portugal

The recent observational evidence for the acceleration of the universe demonstrates that canonical theories of cosmology and particle physics are incomplete—if not incorrect—and that new physics is out there, waiting to be discovered. The most exciting task for the next generation of astrophysical facilities is therefore to search for, identify and ultimately characterise this new physics.
Here we summarise ongoing work by CAUP's Dark Side Team aiming to develop the cience case and optimize observational stratrgies for forthcoming facilities. The discussion is centred on tests of the stability of fundamental couplings, but synergies with other probes are also briefly considered. A new generation of precision consistency tests of the standard paradigm will soon become possible.

1 Introduction

In the middle of the XIX century Urbain Le Verrier and others mathematically discovered two new planets by insisting that the observed orbits of Uranus and Mercury agreed with the predictions of Newtonian physics. The first of these—which we now call Neptune—was soon observed by Johann Galle and Heinrich d'Arrest. However, the second (dubbed Vulcan) was never found. We now know that the discrepancies in Mercury's orbit were a consequence of the fact that Newtonian physics can't adequately describe Mercury's orbit, and accounting for them was the first success of Einstein's General Relativity.

Over the past several decades, cosmologists have mathematically discovered two new components of the universe—which we have called dark matter and dark energy—but so far these have not been directly detected. Whether they will prove to be Neptunes or Vulcans remains to be seen but even their mathematical discovery highlights the fact that the standard ΛCDM paradigm, despite its phenomenological success, is at least incomplete.

Something similar applies to particle physics, where to some extent it is our confidence in the standard model that leads us to the expectation that there must be new physics beyond it. Neutrino masses, dark matter and the size of the baryon asymmetry of the universe all require new physics, and, significantly, all have obvious astrophysical and cosmological implications. Recent years have indeed made it clear that further progress in fundamental particle physics will increasingly depend on progress in cosmology.

After a quest of several decades, the recent LHC evidence for a Higgs-like particle [1,2] finally provides strong evidence in favour of the notion that fundamental scalar fields are part of Nature's building blocks. A pressing follow-up question is whether the associated field has a cosmological role, or indeed if there is some cosmological counterpart.

It goes without saying that fundamental scalar fields already play a key role in most paradigms of modern cosmology. Among others they are routinely invoked to describe period of exponential expansion of the early universe (inflation), cosmological phase transitions and their relics (cosmic defects), the dynamical dark energy which may be powering the current acceleration phase, and the possible spacetime variation of nature's fundamental couplings.

Even more important than each of these paradigms is the fact that they don't occur alone: whenever a scalar field plays one of the above roles, it will also leave imprints in other contexts that one can look for. For example, in realistic models of inflation, the inflationary phase ends with a phase transition at which cosmic defects will form (and the energy scales of both will therefore be unavoidably related).

More importantly, in realistic models of dark energy, where the dark energy is due to a dynamical scalar field, this field will couple to the rest of the model and lead to potentially observable variations of nature's fundamental couplings; we will return to this point later in this contribution. Although this complementary point is often overlooked, it will be crucial for future consistency tests.

2 Varying fundamental couplings

Nature is characterised by a set of physical laws and fundamental dimensionless couplings, which historically we have assumed to be spacetime-invariant. For the former this is a cornerstone of the scientific method (it's hard to imagine how one could do science at all if it were not the case), but for the latter it is only a simplifying assumption without further justification. These couplings determine the properties of atoms, cells, planets and the universe as a whole, so it's remarkable how little we know about them. We have no 'theory of constants' that describes their role in physical theories or even which of them are really fundamental. If they vary, all the physics we know is incomplete.

Fundamental couplings are indeed expected to vary in many extensions of the current standard model. In particular, this will be the case in theories with additional spacetime dimensions, such as string theory. Interestingly, the first generation of string theorists had the hope that the theory would ultimately predict a unique set of laws and couplings for low-energy physics. However, following the discovery of the evidence for the acceleration of the universe this claim has been pragmatically replaced by an 'anything goes' approach, sometimes combined with anthropic arguments. Regardless of the merit of such approaches, experimental and observational tests of the stability of these couplings may be their best route towards a testable prediction.

It goes without saying that a detection of varying fundamental couplings will be revolutionary: it will immediately prove that the Einstein Equivalence Principle is violated (and therefore that gravity can't be purely geometry) and that there is a fifth force of nature. But even improved null results are important and useful. The simple way to understand this is to realise that the natural scale for cosmological evolution of one of these couplings (driven by a fundamental scalar field) would be Hubble time. We would therefore expect a drift rate of the order of $10^{-10}\mathrm{yr}^{-1}$. However, current local bounds, coming from atomic clock comparison experiments, are 6 orders of magnitude stronger [3].

Recent astrophysical evidence suggests a parts-per-million spatial variation of the fine-structure constant α at low redshifts [4]. Although no known model can explain such a result without some fine-tuning (see Silva *et al.*[5] for an example), it should also be said that there is also no identified systematic effect that can explain it.

One possible cause for concern (with these and other results) is that almost all of the existing data has been taken with other purposes in mind, whereas this kind of measurements needs customised analysis pipelines and wavelength calibration procedures beyond those supplied by standard pipelines. This is one of the reasons for the ongoing ESO UVES Large Programme, whose first results appeared recently[6,7].

A recent joint analyis of all existing measurements [8] indicates some inconsistencies, and highlights the need for future more precise measurements. In the short term the PEPSI spectrograph at the LBT can play a role here, and in the longer term a new generation of high-resolution, ultra-stable spectrographs like ESPRESSO (for the VLT) and ELT-HIRES, which have these tests as a key science driver, will significantly improve the precision of these measurements and should be able to resolve the current controversy. A key technical improvement will be that ultimately one must do the wavelength calibration with laser frequency combs.

In theories where a dynamical scalar field yields varying α, the other gauge and Yukawa couplings are also expected to vary. In particular, in Grand Unified Theories the variation of α is related to that of energy scale of Quantum Chromodynamics, whence the nucleon masses necessarily vary when measured in an energy scale that is independent of QCD (such as the electron mass). It follows that we should expect a varying proton-to-electron mass ratio, $\mu = m_p/m_e$.

Obviously, the specific relation between $\alpha(z)$ and $\mu(z)$ will be highly model-dependent, but this very fact makes this a unique discriminating tool between competing models. It follows from this that it's highly desirable to identify systems where various constants can be simultaneously measured, or systems where a constant can be measured in several independent ways. Systems where combinations of constants can be measured are also interesting, and may lead to consistency tests [9,10].

In passing, let us also briefly comment on other probes of varying constants. The CMB is in principle a very clean one, but in most simple models a parts per million variation of at redshifts a few leads to variations at redshift $z \sim 1089$ that are below the sensitivity of Planck. However, these studies do have a feature of interest, namely that they lead to constraints on the coupling between the putative scalar field and electromagnetism, independently (and on a completely different scale) from what is done in local tests, as illustrated in [11]. Compact objects such as solar-type stars and neutron stars have also been leading to interesting constraints [12,13].

3 Dynamical dark energy and varying couplings

Observations suggest that the universe is dominated by an energy component whose gravitational behaviour is quite similar to that of a cosmological constant. Its value is so small that a dynamical scalar field is arguably a more likely explanation. Such a field must be slow-rolling (which is mandatory for $p < 0$) and be dominating the dynamics around the present day. It follows that if the field couples to the rest of the model (which it will naturally do, unless some symmetry is postulated to suppress the couplings) it will lead to potentially observable long-range forces and time dependencies of the constants of nature.

In models where the degree of freedom responsible for the varying constants also provides the dark energy, the redshift of the couplings is parametrically determined, and any available measurements (be they detections of null results) can be used to set constraints on combinations of the scalar field coupling and the dark energy equation of state. One can show that ELT-HIRES will either find variations or rule out—at more than 10 sigma—the simplest classes of these models (containing a single linearly coupled dynamical scalar field).

However, this is not all. Standard observables such as supernovae are of limited use as dark energy probes, both because they probe relatively low redshifts and because to ultimately obtain the required cosmological parameters one effectively needs to take second derivatives of noisy data. A clear detection of varying $w(z)$ is crucial, given that we know that $w \sim -1$ today. Since the field is slow-rolling when dynamically important (close to the present day), a convincing detection of a varying $w(z)$ will be tough at low redshift, and we must probe the deep matter era regime, where the dynamics of the hypothetical scalar field is fastest.

Varying fundamental couplings are ideal for probing scalar field dynamics beyond the domination regime [14]: such measurements can presently be made up to redshift $z \sim 4$, and future facilities such as the E-ELT may be able to significantly extend this redshift range. Importantly, even null measurements of varying couplings can lead to interesting constraints on dark energy scenarios. ALMA, ESPRESSO and ELT-HIRES can realise the prospect of a detailed characterisation of dark energy properties all the way until $z \sim 4$, and possibly beyond. In the case of ELT-HIRES, a reconstruction using quasar absorption lines is expected to be more accurate than using supernova data (its key advantage being huge redshift lever arm) [15]. Further discussion of this issue can also be found in Ana Catarina Leite's contribution to these proceedings.

Importantly, these measurements have an additional key role: that of breaking degeneracies, when combined with more 'classical' probes, for constraining dynamical dark energy models. A case in point is that of ESA's Euclid mission, as was recently studied in [16].

Dark energy reconstruction using varying fundamental constants does assume that the same dynamical degree of freedom is responsible for both. There are various examples of modes for which this is not the case, from BSBM-like toy models to string-inspired runaway dilaton models (the latter is briefly discussed in Pauline Vielzeuf's contribution to these proceedings). Nevetheless there are in-built consistency checks, so that inconsistent assumptions can be identified and corrected. Explicit examples of incorrect assumptions that lead to observational inconsistencies can be found in [17].

It's important to keep in mind that the E-ELT will also contribute to the above task by further means. First and foremost there is the detection of the redshift drift signal. This is a key driver for ELT-HIRES, and possibly—at a fundamental level—ultimately the most important E-ELT deliverable. Indeed, as shown in [17], having the ability to measure the stability of fundamental couplings and the redshift drift with a single instrument is a crucial strategic advantage. (Other facilities such as PEPSI at the LBT, the SKA and ALMA may also be able do measure the redshift drift.)

Additionally, it should be pointed out that the ELT-IFU (in combination with JWST) should also find Type Ia supernovas up to a redshift $z \sim 5$. An assessment of the impact of these future datasets on fundamental cosmology is currently in progress. Interesting synergies are also expected to exist between these ground-based spectroscopic methods and Euclid, which need to be further explored.

4 Consistency tests

Whichever way one finds direct evidence for new physics, it will only be trusted once it is seen through multiple independent probes. This was manifest in the case of the discovery of the recent acceleration of the universe, where the supernova results were only accepted by the wider community once they were confirmed through CMB, large-scale structure and other data. It is clear that history will repeat itself in the case of varying fundamental couplings and/or dynamical dark energy. It is therefore crucial to develop consistency tests, in other words, astrophysical observables whose behaviour will also be non-standard as a consequence of either or both of the above.

The temperature-redshift relation,

$$T(z) = T_0(1+z) \tag{1}$$

is a robust prediction of standard cosmology; it assumes adiabatic expansion and photon number conservation, but it is violated in many scenarios, including string theory inspired ones. At a phenomenological level one can parametrise deviations to this law by adding an extra parameter, say

$$T(z) = T_0(1+z)^{1-\beta} \tag{2}$$

Our recent work [18] has shown that forthcoming data from Planck, ESPRESSO and ELT-HIRES will lead to much stronger constraints: Planck on its own can be as constraining as the existing (percent-level) bounds, ESPRESSO can improve on the current constraint by a factor of about three, and ELT-HIRES will improve on the current bound by one order or magnitude. We emphasise that estimates of all these gains rely on quite conservative on the number of sources (SZ clusters and absorption systems, respectively) where these measurements can be made. If the number of such sources increases, future constraints can be correspondingly stronger.

The distance duality relation,

$$d_L = (1+z)^2 d_A \tag{3}$$

is an equally robust prediction of standard cosmology; it assumes a metric theory of gravity and photon number conservation, but is violated if there's photon dimming, absorption or conversion. At a similarly phenomenological level one can parametrise deviations to this law by adding an extra parameter, say

$$d_L = (1+z)^{2+\epsilon} d_A \tag{4}$$

with current constraints also being at the percent level, and improvements are similarly expected from Euclid, the E-ELT and JWST.

In fact, in many models where photon number is not conserved the temperature-redshift relation and the distance duality relation are not independent. With the above parametrisations it's easy to show [18] that

$$\beta = -\frac{2}{3}\epsilon \tag{5}$$

but one can in fact further show that a direct relation exists for any such model, provided the dependence is in redshift only (models where there are frequency- dependent effects are more complex). This link allowed us to use distance duality measurements to improve current constraints on β, leading to

$$\beta = 0.004 \pm 0.016 \tag{6}$$

which is a 40% improvement on the previous constraint. With the next generation of space and ground-based experiments, these constraints can be further improved (as discussed above) by more than one order of magnitude.

In models where the degree of freedom responsible for the varying constants does not provide (all of) the dark energy, the link to dark energy discussed in the previous section no longer holds. However, has shown in [17], such wrong assumptions can be identified through (in)consistency tests. For example, it has been shown in [19] that in Bekenstein-type models one has

$$\frac{T(z)}{T_0} = (1+z)\left[\frac{\alpha(z)}{\alpha_0}\right]^{1/4} \sim (1+z)\left(1+\frac{1}{4}\frac{\Delta\alpha}{\alpha}\right) \tag{7}$$

and

$$d_L(z) \sim d_A(z)(1+z)^2\left(1+\frac{3}{3}\frac{\Delta\alpha}{\alpha}\right) \tag{8}$$

Interestingly these also hold for disformal couplings (but not for chameleon-type models, where the powers of α are inverted), These effects are relevant for the analysis of Planck data: a parts-per-million α dipole leads, in this class of models, to a micro-Kelvin level dipole on the CMB temperature, in addition to the usual milli-Kelvin one due to our motion.

Note that even if this degree of freedom does not dominate at low redshifts it can still bias cosmological parameter estimations, For example. in varying-α models the peak luminosity of Type Ia supernovas will depend on redshift. This scenario has been studied in more detail in an Euclid context [16].

Now, if photon number non-conservation changes $T(z)$, the distance duality relation, etc, this may lead to additional biases, for example for Euclid. In [19] we have quantified how these models weaken Euclid constraints on cosmological parameters, specifically those characterising the dark energy equation of state. Our results show that Euclid can, even on its own, constrain dark energy while allowing for photon number non-conservation.

Naturally, stronger constraints can be obtained in combination with other probes. Interestingly, the ideal way to break a degeneracy involving the scalar-photon coupling is to use $T(z)$

measurements, which can be obtained with ALMA, ESPRESSO and ELT-HIRES (which, incidentally, may nicely complement each other in terms of redshift coverage). It may already be possible to obtain some useful constraints from Planck clusters, and these will be significantly improved with a future COrE+ mission.

Last but not least, the role of redshift drift measurements as a consistency test cannot be over-emphasised [17]. Standard dark energy probes are geometric and/or probe localised density perturbations, while the redshift drift provides a unique measurement of the global dynamics [20,21,22]. It does not map out our (present-day) past light-cone, but directly measures evolution by comparing past light cones at different times. Therefore it provides an ideal probe of dark sector in deep matter era, complementing supernovas and constants.

In fact, as recently shown in [23], its importance as a probe of cosmology does not stem purely from its intrinsic sensitivity, but also from the fact that it is sensitive to cosmological parameters that are otherwise hard to probe (in other words, it can break some key degeneracies). One illustrative example [23] is that the CMB is only sensitive to the combination $\Omega_m h^2$, while the redshift drift is sensitive to each of them.

5 Conclusions

We have highlighted the key role that will be played by forthcoming high-resolution ultra-stable spectrographs in fundamental cosmology, by enabling a new generation of precision consistency tests. The most revolutionary among these is clearly the redshift drift, which is a key driver for ELT-HIRES, but may also be within the reach of other facilities, like PEPSI (at the LBT), SKA or even ALMA (although no sufficiently detailed studies exist for these at present).

Together with the opportunity, afforded by astrophysical tests of the stability of fundamental couplings such as the fine-structure constant and the proton-to-electron mass ratio, to map and constrain additional dynamical degrees of freedom not only through the acceleration phase of the universe but also deep in the matter era (out to redshift $z \sim 4$, and possibly beyond) these will bring forth an exciting new area of research.

Finally, let us point out that the ELT will enable further relevant tests, including tests of strong gravity around the galactic black hole (through ELT-CAM), and astrophysical tests of the Equivalence Principle, which were not discussed in this contribution. Interesting synergies with other facilities, particularly ALMA and Euclid, remain to be fully explored.

Acknowledgments

We acknowledge the financial support of grant PTDC/FIS/111725/2009 from FCT (Portugal). CJM is also supported by an FCT Research Professorship, contract reference IF/00064/2012.

References

1. G. Aad *et al.* (ATLAS Collaboration), *Phys. Lett.* B **716**, 1 (2012).
2. S. Chatrchyan *et al.* (CMS Collaboration), *Phys. Lett.* B **716**, 30 (2012).
3. T. Rosenband *et al.*, Science **319**, 1808 (2008).
4. J.K. Webb *et al.*, *Phys. Rev. Lett.* **107**, 191101 (2011)
5. M.F. Silva, H.A. Winther, D.F. Mota and C.J.A.P. Martins, *Phys. Rev.* D **89**, 024025 (2014).
6. P. Molaro, M. Centurion, J.B. Whitmore, T.M. Evans, M.T. Murphy, I.I. Agafonova, P. Bonifacio, S. D'Odorico, S. A. Levshakov, S. Lopez, C.J.A.P. Martins, P. Petitjean, H. Rahmani, D. Reimers, R. Srianand, G. Vladilo & M. Wendt, A. & A. **555**, A68 (2013) [arXiv:1305.1884].

7. H. Rahmani, M. Wendt, R. Srianand, P. Noterdaeme, P. Petitjean, P. Molaro, J.B. Whitmore, M.T. Murphy, M. Centurion, H. Fathivavsari, S. DOdorico, T.M. Evans, S.A. Levshakov, S. Lopez, C.J.A.P. Martins, D. Reimers & G. Vladilo, MNRAS **435**, 861 (2013) [arXiv:1307.5864].
8. M.C. Ferreira, O. Frigola, C.J.A.P. Martins, A.M.R.V.L. Monteiro & J. Solà, *Phys. Rev.* D **89**, 083011 (2014).
9. M.C. Ferreira, M.D. Julião, C.J.A.P. Martins & A.M.R.V.L. Monteiro, *Phys. Rev.* D **86**, 125025 (2012).
10. M.C. Ferreira, M.D. Julião, C.J.A.P. Martins & A.M.R.V.L. Monteiro, *Phys. Lett.* B **724**, 1 (2013).
11. E. Calabrese, E. Menegoni, C.J.A.P. Martins, A. Melchiorri & G. Rocha, *Phys. Rev.* D **84**, 023518 (2011).
12. J.P.P. Vieira, C.J.A.P. Martins & M.J.P.F.G. Monteiro, *Phys. Rev.* D **86**, 043003 (2012).
13. M.A. Pérez-García & C.J.A.P. Martins, *Phys. Lett.* B **718**, 241 (2012).
14. L. Amendola, A.C.O. Leite, C.J.A.P. Martins, N.J. Nunes, P.O.J. Pedrosa & A. Seganti, *Phys. Rev.* D **86**, 063515 (2012).
15. P.O.J. Pedrosa, A.C.O. Leite & C.J.A.P. Martins, Mem. S. A. It. **85**, 149 (2014).
16. E. Calabrese, M. Martinelli, S. Pandolfi, V.F. Cardone, C.J.A.P. Martins, S. Spiro & P.E. Vielzeuf, *Phys. Rev.* D **89**, 083509 (2014).
17. P.E. Vielzeuf & C.J.A.P. Martins *Phys. Rev.* D **85**, 087301 (2012).
18. A. Avgoustidis, G. Luzzi, C.J.A.P. Martins & A.M.R.V.L. Monteiro, JCAP **1202**, 013 (2012).
19. A. Avgoustidis, C.J.A.P. Martins, A.M.R.V.L. Monteiro, P.E. Vielzeuf & G. Luzzi, arXiv:1305.7031 (2013).
20. A. Sandage, Astrophys. J. **281**, L77 (1962).
21. A. Loeb, Astrophys. J. **499**, 111 (1998).
22. J. Liske *et al.*, MNRAS **386**, 1192 (2008).
23. M. Martinelli, S. Pandolfi, C.J.A.P. Martins & P.E. Vielzeuf, *Phys. Rev.* D **86**, 123001 (2012).

8.
Future Programs in Cosmology

Science with CMB spectral distortions

J. Chluba
Department of Physics and Astronomy, Johns Hopkins University, Bloomberg Center 435,
3400 N. Charles St., Baltimore, MD 21218, USA

The measurements of COBE/FIRAS have shown that the CMB spectrum is extremely close to a perfect blackbody. There are, however, a number of processes in the early Universe that should create spectral distortions at a level which is within reach of present day technology. In this talk, I will give a brief overview of recent theoretical and experimental developments, explaining why future measurements of the CMB spectrum will open up an unexplored window to early-universe and particle physics with possible non-standard surprises but also several guaranteed signals awaiting us.

1 Introduction

Cosmology is now a precise scientific discipline, with detailed theoretical models that fit a wealth of very accurate measurements. Of the many cosmological data sets, the cosmic microwave background (CMB) temperature and polarization *anisotropies* provide the most stringent and robust constraints to theoretical models, allowing us to determine the key parameters of our Universe and address fundamental questions about inflation and early-universe physics [5, 64, 75].

But the CMB holds another, complementary and independent piece of invaluable information: its *frequency spectrum*. Departures of the CMB frequency spectrum from a blackbody – commonly referred to as *spectral distortions* – encode information about the thermal history of the early Universe (from when it was a few month old until today). Since the measurements with COBE/FIRAS, the average CMB spectrum is known to be extremely close to a perfect blackbody, with possible distortions being limited to $\Delta I_\nu / I_\nu \lesssim 10^{-5} - 10^{-4}$ [36, 55]. This impressive measurement was awarded the Nobelprize in Physics 2006, and already rules out cosmologies with extended periods of significant energy release, disturbing the thermal equilibrium between matter and radiation in the early Universe.

Given that no average CMB distortion was found, *why is it still interesting to think about CMB spectral distortions*? First of all, there is a long list of processes that could lead to spectral distortions. These include: *reionization* and *structure formation* [13, 40, 57, 59, 68, 80, 88]; *decaying* or *annihilating particles* [17, 21, 42, 56]; *dissipation of primordial density fluctuations* [e.g., 4, 19, 20, 22, 28, 37, 39, 61, 78]; *cosmic strings* [60, 81, 82]; *primordial black holes* [12, 62]; *small-scale magnetic fields* [46, 53]; the *adiabatic cooling of matter* [15, 26]; *cosmological recombination* [for overview see 76]; and some new

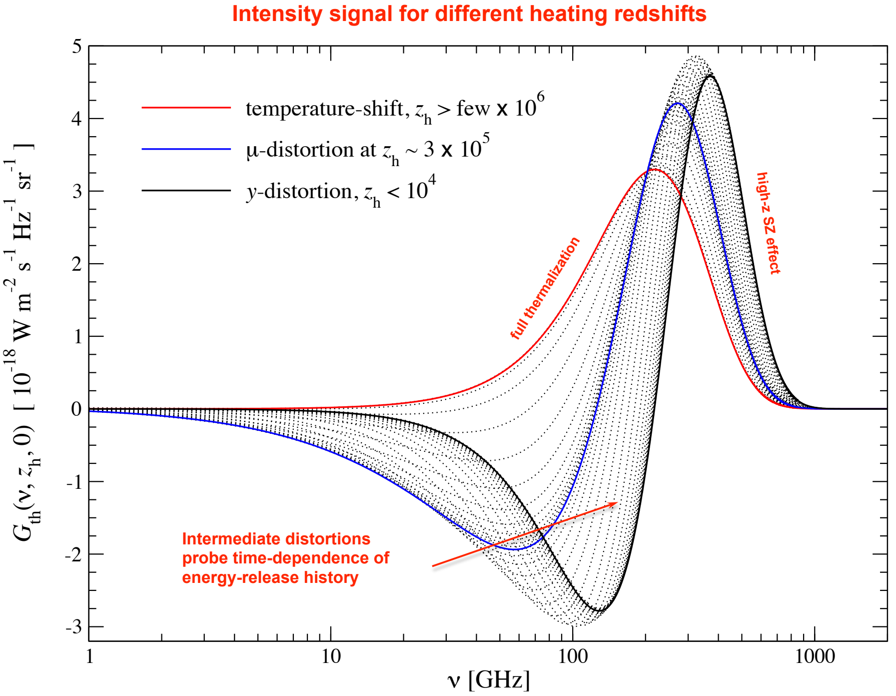

Figure 1 – Change in the CMB spectrum after a single energy release at different heating redshifts, z_h. At $z \gtrsim$ few $\times 10^6$, a temperature shift is created. Around $z \simeq 3 \times 10^5$ a pure μ-distortion appears, while at $z \lesssim 10^4$ a pure y-distortion is formed. At all intermediate stages, the signal is given by a superposition of these extreme cases with a small residual (non-μ/non-y) distortion that contains information about the time-dependence of the energy-release process (Figure adapted from [18]).

physics examples [7, 9, 11, 54, 58, 83]. Most importantly, many of these processes (e.g., reionization and cosmological recombination) are part of our standard cosmology and therefore should lead to guaranteed signals to search for.

The second reason for spectral distortion being interesting is due to technological advances. Although measurements of the CMB temperature and polarization anisotropies have improved significantly in terms of angular resolution and sensitivity since COBE/DMR, our knowledge of the CMB spectrum is still in a similar state as more than 20 years ago. This could change dramatically in the future with experimental concepts like PIXIE [51] and PRISM [2] (or its smaller M4 class version, COrE+) being presently discussed by the cosmology community. These types of experiments could possibly improve the limits of COBE/FIRAS by more than three orders of magnitude, providing a unique way to learn about processes that are otherwise hidden from us. At this stage, CMB spectral distortion measurements are furthermore only possible from space, so that in contrast to B-mode polarization science competition from the ground is largely excluded, making CMB spectral distortions a unique target for future CMB space missions [73]. This immense potential of spectral distortions was also recently recognized in the NASA 30-year Roadmap study, where improved characterization of the CMB spectrum was declared as one of the future targets [52].

2 Thermalization physics and different types of primordial distortions

It is well-known that energy release in the early Universe causes CMB spectral distortions [10, 29, 41, 44, 45, 79, 86]. At redshifts $z \gtrsim$ few $\times 10^6$, the thermalization process, mediated by the combined action of double Compton emission, Bremsstrahlung and Compton scattering, is extremely rapid and erases any distortion to unobservable levels until the present, only leading to an increase of the average CMB temperature. The associated entropy production can be constrained using precise measurements of the light element abundances and the photon to baryon ratio [47, 74]. At lower redshift, however, the CMB spectrum becomes vulnerable and a distortion remains. Traditionally this signal is described as a chemical potential μ- and Compton y-distortion. A μ-type distortion is created at very early epochs

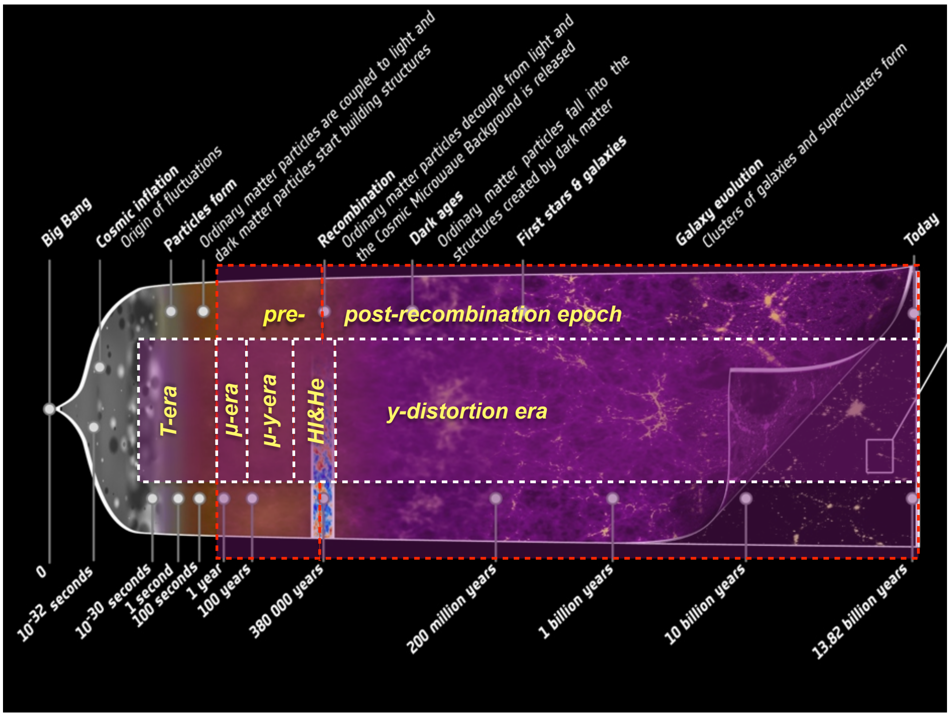

Figure 2 – CMB spectral distortions probe the thermal history of the Universe at many stages during the pre- and post-recombination era. Energy release at $z \gtrsim$ few $\times\, 10^6$ only causes a change of the CMB temperature. A μ-type distortion arises from energy release at $3 \times 10^5 \lesssim z \lesssim$ few $\times\, 10^6$, while a y-type distortions is created at $z \lesssim 10^4$. The signal caused during the μ/y-transition era ($10^4 \lesssim z \lesssim 3 \times 10^5$) is described by a superposition of μ- and y-distortion with some small *residual* distortion that allows probing the time-dependence of the energy-release mechanism. In the recombination era ($10^3 \lesssim z \lesssim 10^4$), additional spectral features appear due to atomic transitions of hydrogen and helium. These could allow us to distinguish pre- from post-recombination y-distortions (Figure adapted from [2]).

($z \gtrsim 5 \times 10^4$) when redistribution of photons over frequency by Compton scattering with free electron is still very rapid, so that full kinetic equilibrium between electrons and photons can be achieved, producing a constant, non-vanishing chemical potential at high frequencies. A y-type distortion is produced in the other extreme, when energy exchange through Compton scattering is already inefficient and photons are only partially up-scattered, creating the high redshift ($z \lesssim 5 \times 10^4$) analogue of the thermal Sunyaev-Zeldovich (SZ) effect known from clusters of galaxies [86].

It was, however, shown that the distortion signature from different energy-release scenarios is generally *not just* given by a superposition of pure μ- and y-distortion [18, 26, 49]. The small residual beyond μ- and y-distortion contains information about the *exact* time-dependence of the energy-release history (see Fig. 1), which in principle can be used to directly constrain, for instance, the shape of the small-scale power spectrum, measure the lifetime of decaying relic particles, or simply to discern between different energy-release mechanisms. In particular, [17, 21] demonstrated that CMB spectrum measurement with a *PIXIE*-type experiment provide a sensitive probe for long-lived particles with lifetimes $t_X \simeq 10^9\,\text{sec} - 10^{10}\,\text{sec}$. Similarly, the shape of the small-scale power spectrum can be directly probed with *PIXIE*'s sensitivity if the amplitude of primordial curvature perturbations exceeds $A_\zeta \simeq$ few $\times\, 10^{-8}$ at wavenumber $k \simeq 45\,\text{Mpc}^{-1}$ [17, 21]. CMB distortion measurements thus provide an unique way for studying early-universe models and particle physics at very different stages of the Universe (see Fig. 2).

These aspects are now rather well understood, and efficient methods for computing the CMB spectral distortions from any energy-release scenario exist [18, 26]. Information from the *residual* (non-μ/non-y) distortion can be used to probe the time-dependence of processes occurring at $10^4 \lesssim z \lesssim 3 \times 10^5$, going well beyond the less informative statement that energy was in fact liberated at some point [21]. However, the thermalization problem is even richer when including the effect of pre-recombination ($z \gtrsim 10^3$) atomic transitions [25]. This might allow us to reach even deeper into the μ- and y-eras by using spectral features of the cosmological recombination radiation [76].

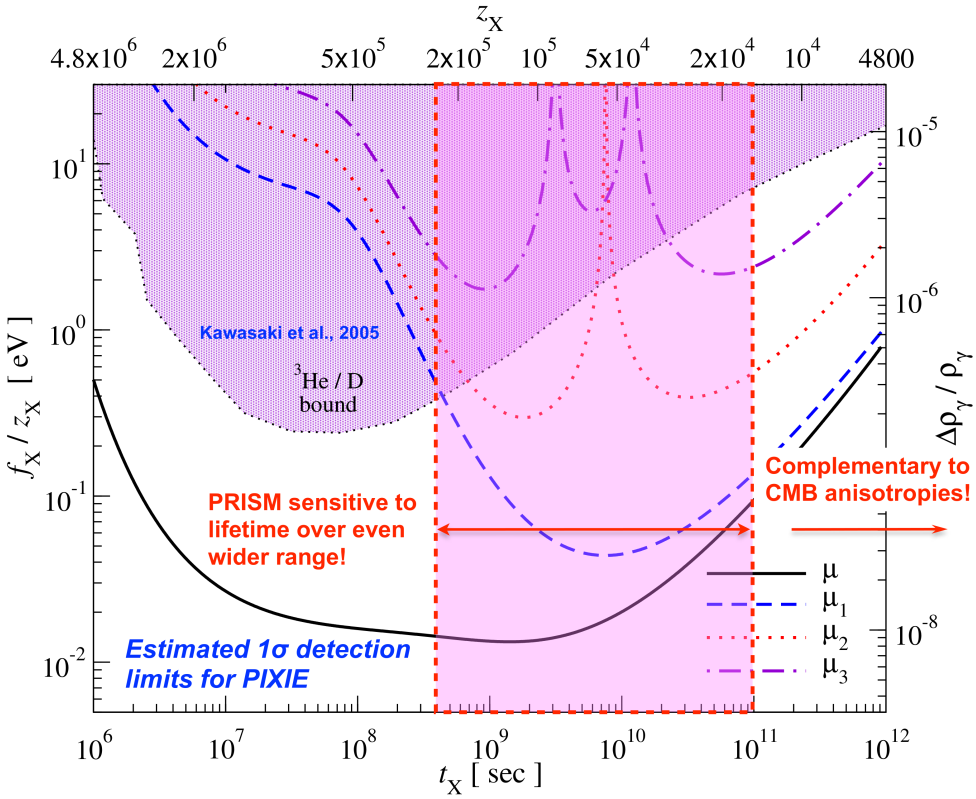

Figure 3 – Decaying particle detection limits (1σ) for a PIXIE-like experiment. The eigenamplitudes μ_i characterize the non-μ/non-y distortion signal [21], which provides time-dependent information of the energy release history. CMB distortion limits could be $\simeq$ 50 times tighter than those derived from light element abundances [48]. A separate determination of lifetime and particle abundance could be possible for lifetimes $t_X \simeq 10^8$ sec – 10^{11} sec, being complementary to constraints derived using the CMB anisotropies [e.g., 14, 87]. The figure is adapted from [21].

3 CMB spectral distortion constraints for various scenarios

In this part we briefly highlight some interesting scenarios that can be constrained using future CMB spectroscopy. We selected a few examples to illustrate the potential of CMB spectral distortions. For more in depth reading and overview we refer to [26], [77], [17] and [21].

3.1 *Reionization and structure formation*

Radiation from the first stars and galaxies [3, 40], feedback by supernovae [59] and structure formation shocks [13, 57, 80] heat the IGM at redshifts $z \lesssim 10 - 20$, producing hot electrons (with temperatures $T_e \simeq 10^4\,\mathrm{K} - 10^5\,\mathrm{K}$) that up-scatter CMB photons, giving rise to a Compton y-distortion with typical amplitude $\Delta I_\nu / I_\nu \simeq 10^{-7} - 10^{-6}$. This signal will be detected at more than a $100\,\sigma$ with a PIXIE-type experiment, providing a sensitive probe of reionization physics and delivering a census of the missing baryons in the local Universe. A PRISM-like experiment may furthermore have the potential to separate the spatially varying signature caused by the WHIM and proto-clusters [68, 88].

3.2 *Decaying and annihilating particle scenarios*

The CMB spectrum allows us to place stringent limits on decaying and annihilating particles in the pre-recombination epoch [16, 26, 42, 56]. This is especially interesting for decaying particles with lifetimes $t_X \simeq 10^8$ sec – 10^{11} sec [17, 21], as the exact shape of the distortion encodes when the decay occurred. Decays or annihilations associated with significant low-energy photon production furthermore create a unique spectral signature that can be distinguished from simple energy release [41]. This would provide an unprecedented probe of early-universe particle physics (e.g., dark matter in excited states

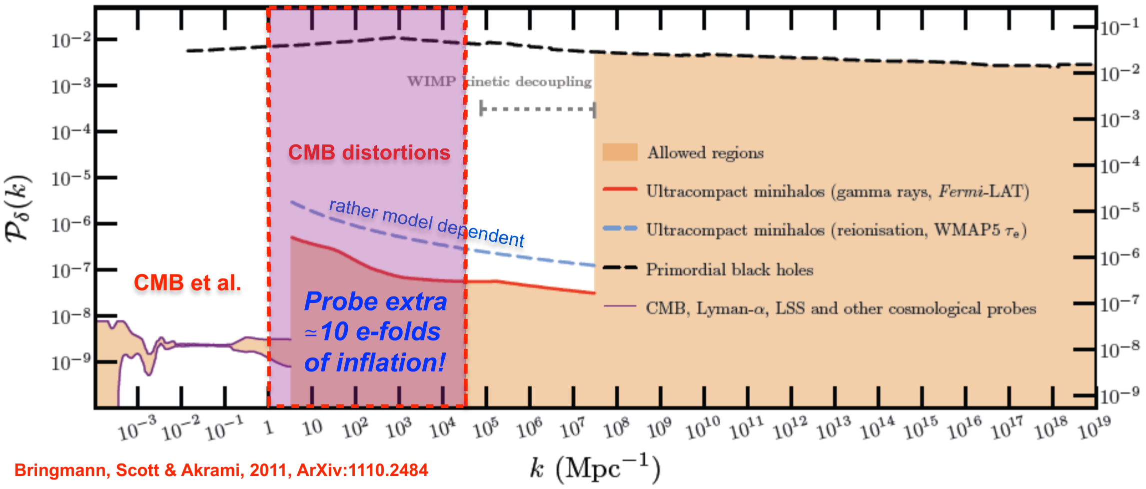

Bringmann, Scott & Akrami, 2011, ArXiv:1110.2484

Figure 4 – Current constraints on the small-scale power spectrum. At large scales ($k \lesssim 3\,\mathrm{Mpc}^{-1}$), CMB anisotropies and large scale structure measurements provide very stringent limits on the amplitude and shape of the primordial power spectrum. At smaller scales, the situation is more uncertain and at $3\,\mathrm{Mpc}^{-1} \lesssim k \lesssim 10^4\,\mathrm{Mpc}^{-1}$ which can be targeted with CMB spectral distortion measurements wiggle room of at least two orders of magnitude is present. CMB distortion measurements could improve these limits to a level similar to the large-scale constraints. The figure is adapted from [8].

[35, 66] or Sommerfeld-enhanced annihilations close to resonance [38]), with many natural particle candidates found in supersymmetric models [33, 34]. For decaying particle scenarios, the 1σ detection limits expected for a PIXIE-like experiment are illustrated in Fig. 3.

3.3 Dissipation of small-scale perturbations

Silk-damping of small-scale perturbations in the photon fluid gives rise to CMB distortions [4, 28, 39, 78] which directly depend on the shape and amplitude of the primordial power spectrum at scales $0.6\,\mathrm{kpc} \lesssim \lambda \lesssim 1\,\mathrm{Mpc}$ (or multipoles $10^5 \lesssim \ell \lesssim 10^8$) [22]. The physics of the mechanism is very simple and only related to the mixing of blackbodies with different temperatures by Thomson scattering, which initially creates a y-distortion [23, 84] that subsequently thermalizes. This process allows constraining the trajectory of the inflaton at stages unexplored by ongoing or planned experiments [19, 21, 50, 67], extending our reach from 7 e-folds of inflation probed with the CMB anisotropies to a total of 17 e-folds. This is particularly interesting, because the experimental constraints on the small-scale power spectrum allow at least two orders of magnitude of wiggle room with respect to the constraints derived at large scales (wavenumber $k \lesssim 3\,\mathrm{Mpc}^{-1}$) from CMB and large scale structure measurements (see Fig. 4).

The distortion signal is also sensitive to the difference between adiabatic and isocurvature perturbations [4, 20, 30, 43], as well as primordial non-Gaussianity in the ultra squeezed-limit, leading to a spatially varying spectral signal that correlates with CMB temperature anisotropies as large angular scales [37, 61]. This effect therefore provides a unique way to study the scale-dependence of f_{NL} [6]. CMB spectral distortions hence deliver a complementary and independent probe of early-Universe physics, which allows capitalizing on the synergies with large-scale B-mode polarization measurements. The expected 1σ detection limits for a PIXIE-like experiment are illustrated in Fig. 5.

3.4 Cosmological recombination radiation

The cosmological recombination of hydrogen and helium introduces distortions [31, 63, 85] at redshifts $z \simeq 10^3 - 10^4$, corresponding to $\simeq 260\,\mathrm{kyr}$ (H I), $\simeq 130\,\mathrm{kyr}$ (He I), and $\simeq 18\,\mathrm{kyr}$ (He II) after the big bang [24, 70, 71]. The overall signal is pretty small ($\Delta I_\nu / I_\nu \simeq 10^{-9}$) but its unique spectral features (see Fig. 6) promise an independent path to determination of cosmological parameters (like the baryon density and *pre-stellar* helium abundance) and direct measurements of the recombination dynamics, probing the Universe at stages before the last scattering surface [76]. Furthermore, if something unexpected

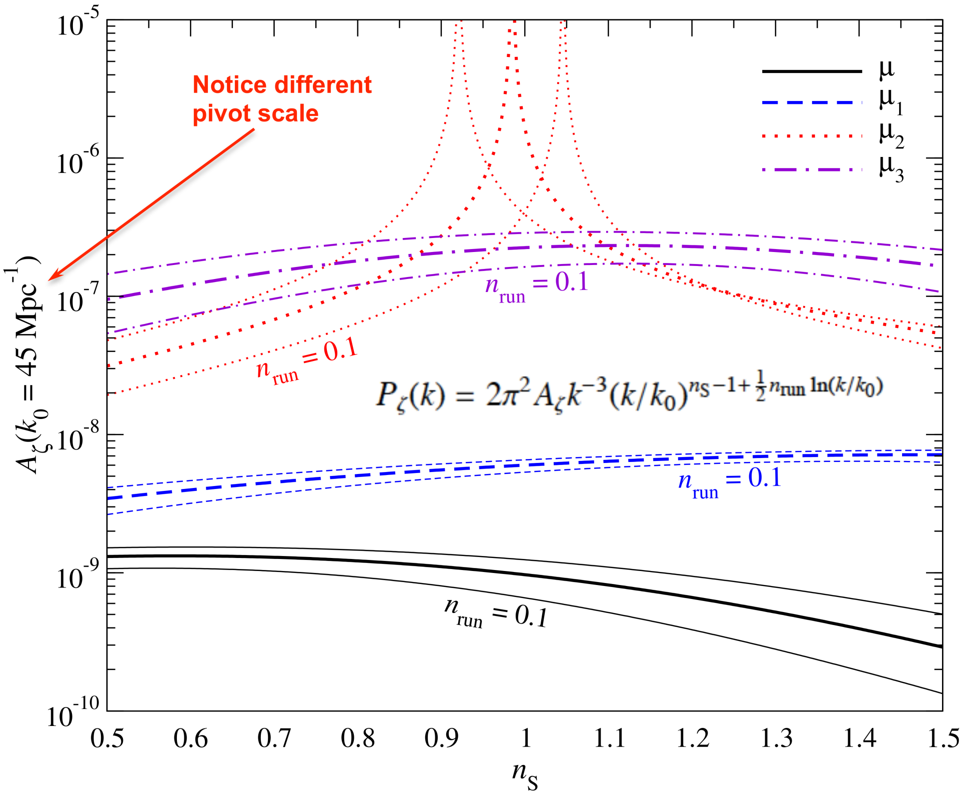

Notice different pivot scale

Figure 5 – Detection limits (1σ) for a PIXIE-like experiment. CMB spectral distortion measurements could rule out early-universe models which create excess power at small scales above the level of $P_\zeta \simeq 10^{-9}$. A PRISM-like experiment may allow gaining an additional order of magnitude on this value. The figure is adapted from [21].

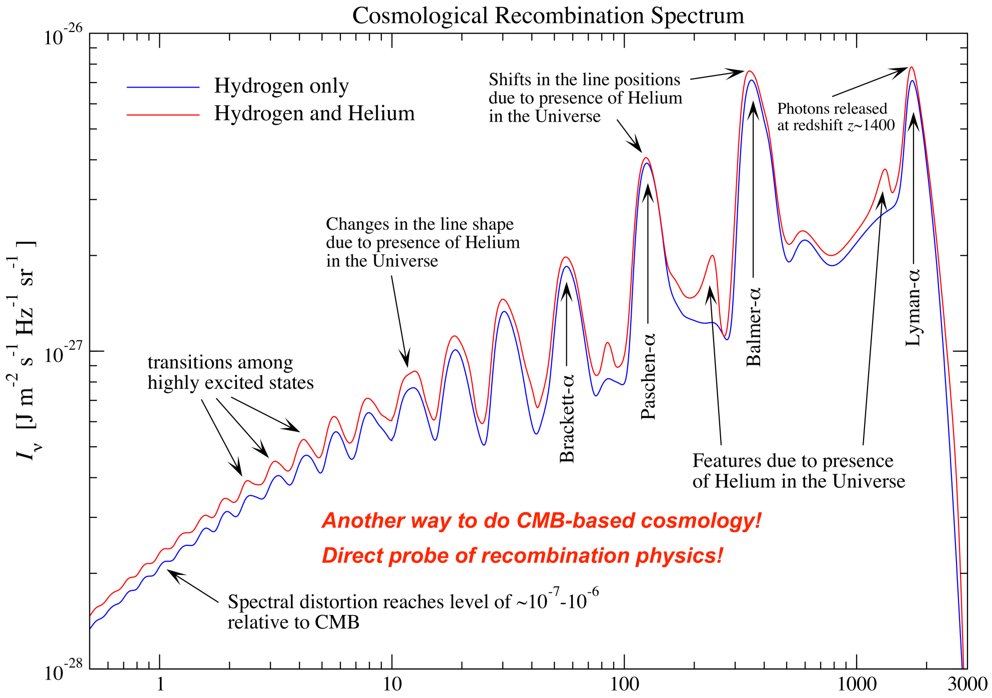

Shifts in the line positions due to presence of Helium in the Universe

Photons released at redshift z~1400

Changes in the line shape due to presence of Helium in the Universe

transitions among highly excited states

Features due to presence of Helium in the Universe

Another way to do CMB-based cosmology!

Direct probe of recombination physics!

Spectral distortion reaches level of ~10^{-7}-10^{-6} relative to CMB

Rubino-Martin et al, 2006 & 2008; JC & Sunyaev, 2006 & 2009

Figure 6 – The cosmological recombination radiation created in the redshift range $z \simeq 10^3 - 10^4$. The presence of helium in the Universe gives rise to unique features in the recombination spectrum. This *fingerprint* of the recombination era in principle allows us to test our understanding of the recombination history which is one on the fundamental ingredients for the computations of the CMB anisotropies.

happened during different stages of the recombination epoch, atomic species will react to this [25] and produce additional distortion features that can exceed those of the normal recombination process. This will provide a unique way to distinguish pre- from post-recombination energy release [16, 25].

To appreciate the importance of the cosmological recombination process at $z \simeq 10^3$, consider that today measurements of the CMB anisotropies are sensitive to uncertainties of the ionization history at a level of $\simeq 0.1\% - 1\%$ [69, 72]. For a precise interpretation of CMB data, uncertainties present in the original recombination calculations had to be reduced by including several previously omitted atomic physics and radiative transfer effects [see 32, 69, for overview]. This led to the development of the new recombination modules CosmoRec [27] and HyRec [1] which are used in the analysis of Planck data [64]. Without these improve treatments of the recombination calculation the value for n_S would be biased by $\Delta n_\mathrm{S} \simeq -0.01$ to $n_\mathrm{S} \simeq 0.95$ instead of $\simeq 0.96$ [72]. We would be discussing different inflation models [65] without these corrections taken into account! Conversely, this emphasizes how important it is to experimentally confirm the recombination process and CMB spectral distortions provide a way to do so.

4 Conclusions

CMB spectral distortion measurements provide a unique way for studying processes in the pre- and post-recombination era. In the future, this could open up a new unexplored window to early-universe and particle physics, delivering independent and complementary pieces of information about the Universe we live in. We highlighted several processes that should lead to distortions at a level within reach of present-day technology. Different distortion signals can be computed precisely for various energy release scenarios. Time-dependent information, beyond the standard μ- and y-type parametrization, may allow us to independently constrain decaying particles and the shape and amplitude of the small-scale power spectrum of primordial perturbations. The cosmological recombination radiation will allow us to check our understanding of the recombination processes at redshifts of $z \simeq 10^3$. It furthermore should allow us to distinguish pre- from post-recombination y-distortions. This emphasizes the immense potential of CMB spectroscopy, both in terms of *discovery* and *characterization* science, and we should make use of this invaluable source of information with the next CMB space mission.

References

[1] Ali-Haïmoud Y., Hirata C. M., 2011, Phys.Rev.D, 83, 043513
[2] André P. et al., 2014, JCAP, 2, 6
[3] Barkana R., Loeb A., 2001, Physics Reports, 349, 125
[4] Barrow J. D., Coles P., 1991, MNRAS, 248, 52
[5] Bennett C. L. et al., 2003, ApJS, 148, 1
[6] Biagetti M., Perrier H., Riotto A., Desjacques V., 2013, Phys.Rev.D, 87, 063521
[7] Brax P., Burrage C., Davis A.-C., Gubitosi G., 2013, JCAP, 11, 1
[8] Bringmann T., Scott P., Akrami Y., 2012, Phys.Rev.D, 85, 125027
[9] Bull P., Kamionkowski M., 2013, Phys.Rev.D, 87, 081301
[10] Burigana C., Danese L., de Zotti G., 1991, A&A, 246, 49
[11] Caldwell R. R., Maksimova N. A., 2013, Phys.Rev.D, 88, 103502
[12] Carr B. J., Kohri K., Sendouda Y., Yokoyama J., 2010, Phys.Rev.D, 81, 104019
[13] Cen R., Ostriker J. P., 1999, ApJ, 514, 1
[14] Chen X., Kamionkowski M., 2004, Phys.Rev.D, 70, 043502
[15] Chluba J., 2005, PhD thesis, LMU München
[16] Chluba J., 2010, MNRAS, 402, 1195
[17] Chluba J., 2013, MNRAS, 436, 2232
[18] Chluba J., 2013, MNRAS, 434, 352
[19] Chluba J., Erickcek A. L., Ben-Dayan I., 2012, ApJ, 758, 76
[20] Chluba J., Grin D., 2013, MNRAS, 434, 1619
[21] Chluba J., Jeong D., 2014, MNRAS, 438, 2065
[22] Chluba J., Khatri R., Sunyaev R. A., 2012, MNRAS, 425, 1129
[23] Chluba J., Sunyaev R. A., 2004, A&A, 424, 389
[24] Chluba J., Sunyaev R. A., 2006, A&A, 458, L29
[25] Chluba J., Sunyaev R. A., 2009, A&A, 501, 29
[26] Chluba J., Sunyaev R. A., 2012, MNRAS, 419, 1294
[27] Chluba J., Thomas R. M., 2011, MNRAS, 412, 748
[28] Daly R. A., 1991, ApJ, 371, 14
[29] Danese L., de Zotti G., 1977, Nuovo Cimento Rivista Serie, 7, 277
[30] Dent J. B., Easson D. A., Tashiro H., 2012, Phys.Rev.D, 86, 023514

[31] Dubrovich V. K., 1975, Soviet Astronomy Letters, 1, 196
[32] Fendt W. A., Chluba J., Rubiño-Martín J. A., Wandelt B. D., 2009, ApJS, 181, 627
[33] Feng J. L., 2010, ARA&A, 48, 495
[34] Feng J. L., Rajaraman A., Takayama F., 2003, Phys.Rev.D, 68, 063504
[35] Finkbeiner D. P., Weiner N., 2007, Phys.Rev.D, 76, 083519
[36] Fixsen D. J., Cheng E. S., Gales J. M., Mather J. C., Shafer R. A., Wright E. L., 1996, ApJ, 473, 576
[37] Ganc J., Komatsu E., 2012, Phys.Rev.D, 86, 023518
[38] Hannestad S., Tram T., 2011, JCAP, 1, 16
[39] Hu W., Scott D., Silk J., 1994, ApJL, 430, L5
[40] Hu W., Scott D., Silk J., 1994, Phys.Rev.D, 49, 648
[41] Hu W., Silk J., 1993, Phys.Rev.D, 48, 485
[42] Hu W., Silk J., 1993, Physical Review Letters, 70, 2661
[43] Hu W., Sugiyama N., 1994, ApJ, 436, 456
[44] Illarionov A. F., Sunyaev R. A., 1975, Soviet Astronomy, 18, 413
[45] Illarionov A. F., Sunyaev R. A., 1975, Soviet Astronomy, 18, 691
[46] Jedamzik K., Katalinić V., Olinto A. V., 2000, Physical Review Letters, 85, 700
[47] Jeong D., Pradler J., Chluba J., Kamionkowski M., 2014, ArXiv:1403.3697
[48] Kawasaki M., Kohri K., Moroi T., 2005, Phys.Rev.D, 71, 083502
[49] Khatri R., Sunyaev R. A., 2012, JCAP, 9, 16
[50] Khatri R., Sunyaev R. A., 2013, JCAP, 6, 26
[51] Kogut A. et al., 2011, JCAP, 7, 25
[52] Kouveliotou C. et al., 2014, ArXiv:1401.3741
[53] Kunze K. E., Komatsu E., 2014, JCAP, 1, 9
[54] Lochan K., Das S., Bassi A., 2012, Phys.Rev.D, 86, 065016
[55] Mather J. C. et al., 1994, ApJ, 420, 439
[56] McDonald P., Scherrer R. J., Walker T. P., 2001, Phys.Rev.D, 63, 023001
[57] Miniati F., Ryu D., Kang H., Jones T. W., Cen R., Ostriker J. P., 2000, ApJ, 542, 608
[58] Moss A., Zibin J. P., Scott D., 2011, Phys.Rev.D, 83, 103515
[59] Oh S. P., Cooray A., Kamionkowski M., 2003, MNRAS, 342, L20
[60] Ostriker J. P., Thompson C., 1987, ApJL, 323, L97
[61] Pajer E., Zaldarriaga M., 2012, Physical Review Letters, 109, 021302
[62] Pani P., Loeb A., 2013, Phys.Rev.D, 88, 041301
[63] Peebles P. J. E., 1968, ApJ, 153, 1
[64] Planck Collaboration et al., 2013, ArXiv:1303.5076
[65] Planck Collaboration et al., 2013, ArXiv:1303.5082
[66] Pospelov M., Ritz A., 2007, Physics Letters B, 651, 208
[67] Powell B. A., 2012, ArXiv:1209.2024
[68] Refregier A., Komatsu E., Spergel D. N., Pen U.-L., 2000, Phys.Rev.D, 61, 123001
[69] Rubiño-Martín J. A., Chluba J., Fendt W. A., Wandelt B. D., 2010, MNRAS, 403, 439
[70] Rubiño-Martín J. A., Chluba J., Sunyaev R. A., 2006, MNRAS, 371, 1939
[71] Rubiño-Martín J. A., Chluba J., Sunyaev R. A., 2008, A&A, 485, 377
[72] Shaw J. R., Chluba J., 2011, MNRAS, 415, 1343
[73] Silk J., Chluba J., 2014, Science, 344, 586
[74] Simha V., Steigman G., 2008, JCAP, 6, 16
[75] Smoot G. F. et al., 1992, ApJL, 396, L1
[76] Sunyaev R. A., Chluba J., 2009, Astronomische Nachrichten, 330, 657
[77] Sunyaev R. A., Khatri R., 2013, International Journal of Modern Physics D, 22, 30014
[78] Sunyaev R. A., Zeldovich Y. B., 1970, Astrophysics and Space Science, 9, 368
[79] Sunyaev R. A., Zeldovich Y. B., 1970, Astrophysics and Space Science, 7, 20
[80] Sunyaev R. A., Zeldovich Y. B., 1972, A&A, 20, 189
[81] Tashiro H., Sabancilar E., Vachaspati T., 2012, Phys.Rev.D, 85, 103522
[82] Tashiro H., Sabancilar E., Vachaspati T., 2013, JCAP, 8, 35
[83] van de Bruck C., Morrice J., Vu S., 2013, Physical Review Letters, 111, 161302
[84] Zeldovich Y. B., Illarionov A. F., Syunyaev R. A., 1972, JETP, 35, 643
[85] Zeldovich Y. B., Kurt V. G., Syunyaev R. A., 1968, ZETF, 55, 278
[86] Zeldovich Y. B., Sunyaev R. A., 1969, Astrophysics and Space Science, 4, 301
[87] Zhang L., Chen X., Kamionkowski M., Si Z., Zheng Z., 2007, Phys.Rev.D, 76, 061301
[88] Zhang P., Pen U.-L., Trac H., 2004, MNRAS, 355, 451

Biased Review of the LSST Project

G. Blanc, for the LSST collaboration
APC, Paris Diderot University, LAL

The Large Synoptic Survey Telescope (LSST) is a US-french projet of 8m class ground-based telescope dedicated to a deep (up to $r = 27.5$) and wide (half-sky that is 20 000 deg^2) survey. Telescope construction is about to start on Cerro Pachón in Chile, and the survey will operate from 2020 to 2030. The quest for dark energy equation of state is part of its main challenges.

1 Introduction

Mapping the sky in the visible light in a wider and deeper way than previously done (such as SDSS survey) needs a new generation of dedicated instruments. The *Large Synoptic Survey Telescope* is such one, with its 8.4m primary mirror and its wide field camera (9.6 square degrees), in order to perform an unprecedently wide and deep survey of half of the visible sky (20000 square degrees) up to 27th magnitude. The idea is to provide a "synoptic[a]" view of the sky within the visible light window.

The paper is organized as: Sec. 2 is reviewing the projet and the following sections will present some highlights of current activities done within the collaboration in a cosmological context. Then Sec. 3 will present some aspects of the simulation of the photometric calibration, especially the atmospheric part of it; Sec. 4 will show some simulations on photometric redshifts reconstruction in order to get a 3D galaxy catalog the less blurred as possible on the distance axis; and Sec. 5 will present a forgotten probe of dark energy, the cosmic magnification.

2 LSST project overview

The telescope will be based on a very compact 3-mirrors modified Paul Baker optical scheme with f/1.234. The secondary mirror is being polished at the center of the primary, that one will actually be in a ring shape of 8.4 m of external diameter (and equivalent to a 6.5m plain mirror as light collecting surface). The mechanical structure will have to be very strong to support more than 300 tons, very stiff to be able to change of field every 40 seconds (with a minimum

---

[a] From the greek words meaning "together" and "view": affording a general view of a whole.

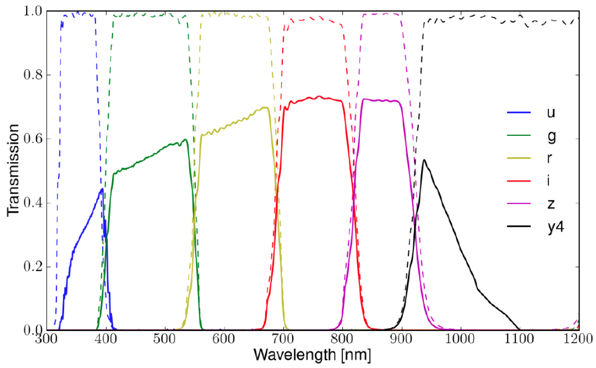

Figure 1 – LSST filters.

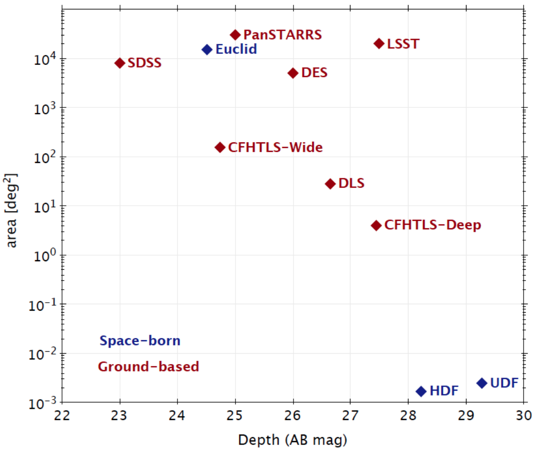

Figure 2 – Comparison of LSST survey depth and sky area with other surveys.

vibrational impact on the images), and very reliable to last for at least the 10 years of the survey duration.

The camera will be very wide, 9.6 square degrees. It will be composed of 189 CCDs of 4k × 4k pixels, that is about 3 billions of pixels. The CCD will have a pixel size of 10 μm, and a resolution on the sky of 0.2 arcseconds. They will be deep depleted to be be more transparent in the near IR. It will survey the sky in six different spectral bands, from the UV (320 μm) to the near IR (1070 μm), that is *ugrizy* (see Fig. 1). To reach its objectives in a reasonnable amount of time, everything is time optimized: then the readout time of the whole camera will be only 2 seconds. If the focal plane will have a diameter of 63.4 cm, the whole camera will be a huge cylinder of 1.65 m long and 3.7 m of diameter, for a weight of 3 tons. It will be placed at the tertiary focus of the telescope.

The site harbouring the LSST has already been chosen. It will be build at the top of Cerro Pachón in Chile, at 2715 m above sea level, situated about 10 km southeast of CTIO and nearby to Gemini South.

The survey is scheduled to last about ten years and to map half of the sky (that is about 20 000 square degrees). Each image will be a sum of two 15 seconds exposures. The sequence of observed fields is optimized to take into account, beyond other parameters, the survey priorities, the weather, the fields visibility. It is planned to visit each field up to 230 times in r and i, 200 times in z and y, 100 times in g and 70 times in u. The single visit depth is expected to be 25 in g and 22.1 in y. The co-added limiting magnitudes will range from 24.9 in y to 27.5 in r.

All these characteristics make it the project with the greatest étendue[b] with 318 $\mathrm{m}^2 \cdot \mathrm{deg}^2$, that is about one order of magnitude above existing instruments or current other projects. Fig. 2 shows how LSST is placed among other surveys.

At a rate of one image every 40 seconds, an average of 30 TB of raw data per night will have to be computed. Over the whole survey, 60 PB of raw data willbe harvested (5.5 millions of images). A real challenge of data processing and storage! The final catalog will contain about 20 billions of objects, roughly half stars and half galaxies.

The total cost of the project is 850 M$ which divides into 40% for the running cost, 40% for the construction (camera, telescope and site) and 20% for the data management. After a R&D phase finishing this year, the construction is about to begin and will last abour three years. The first light is scheduled for 2019 with a running survey from 2020 to 2030.

A large part of visible astronomy and astrophysics is expected to be impacted by LSST, from the very close universe (solar system), the Galaxy (stellar populations, local volume structures...)

---

[b] The étendue is the product of the primary mirror collecting surface with the field of view; it measures a kind of rate at which an instrument is able to observe sources at a given depth.

and the galaxies up to the deep universe (supernovae, strong lenses, large-scale structures, weak lensing...) [6].

Cosmology and the quest for dark energy equation of state is one of the main drivers of LSST, through, among other probes, type Ia supernovae (SNe Ia), baryon acoustic oscillations (BAO) or weak-lensing. About 10 millions supernovae will be gathered over the ten years. Half will be of type Ia (current state of the art is about 700 SNe Ia from SNLS and SDSS [1]). One tenth of this sample will be able to set some constraints better than 5% on the equation of state parameter. BAO will be measured only angularly in redshifts tomographic shell (errors in photometric redshifts suppress the radial BAO information) up to $z \sim 3.0$, while SDSS up-to-date measurement uses Luminous Red Galaxies (LRG) [c] spanning between $0.15 < z < 0.45$ [7]. Cosmic shear measurements will be limited in deepness by the shape measurement of the galaxy sample; an estimate about the effective surface density of galaxies usefull for shear is about 40 arcmin^{-2}, while the galaxy "gold" sample will reach 55 arcmin^{-2} (see below, Sec. 4). Cosmic magnification (see Sec. 5) will be able to exploit to whole galaxy sample.

3 The simulation of the photometric calibration

The photometric calibration will be a key point of the imaging survey. For instance, the measurement of redshifts through the photometric bands (photometric redshifts), the separation of stellar populations, the detection of low amplitude variable objects (such as eclipsing planetary systems), or the search for systematic effects in type Ia supernova light curves are driven specific strigent requirements on the accuracy of the photometry. These requirements are:

- the repeatability should achieve 5 mmag precision at the bright end;
- a zeropoint stability across the sky of 10 mmag;
- some band-to-band calibration errors not larger than 5 mmag.

Moreover, to improve the efficiency, observations will be performed also during non-photometric nights. This means that a non-uniform gray absorption will have to be taken into account within the calibration scheme.

Since the required precision is unprecedented on such a wide survey, it is necessary to simulate in advance the whole processus to check its feasability and to build the software for the calibration. This step has been undertaken.

The whole scheme is the following: from a LSST given pointing, stars are picked up within a Galaxy model, to obtain a star catalog with out of atmosphere magnitudes. Their light fluxes are then simulated crossing the absorbing atmosphere and instrument; the image processing is taken into account, to finally obtain computed observed star magnitudes. An auxiliary telescope of 1.2m will help the main telescope to get an instanneous spectrum of the atmosphere in order to correct for it. A self-calibration is then performed, minimazing the differences between the computed observed magnitudes and a magnitude model.

A detail analysis of main main atmospheric components which attenuate light has been done using data from satellites and ground-based instruments. Its conclusion are [3]:

- *tropospheric gases (oxygen, nitrogen, etc)*: they scale as the barometric pressure, so their absorption is straightforward to modelize.
- *ozone*: a stratospheric gas which is sufficiently slowly varying in time and in space, so that the daily satellite data monitoring the ozone layer are enought to modelize this absorption component. Note that it must be taken into account, since it can induced a change of $\sim$ 4 milli-magnitudes for reddest stars in the bluest bands.

---

[c] But SDSS-III Baryon Oscillation Spectroscopic Survey used the Lyman-α forest in quasars spectra to measure the BAO scale at much larger redshifts [4].

- *water vapor* is mainly located in the troposphere; however, it's a highly variable component at small temporal and spatial scales (a few millimeters of precipitable water vapour per hour, which means a change of a few milli-magnitudes in z and y bands). However a dedicated micro-wave radiometer co-pointed with the telescope can measured this component accurately enough to correct for it.

- *aerosols*: there is a wide variety of micron-size particules or droplets in the atmosphere which scatter the light. They can induced an absorption of a few tens of milli-magnitudes in the u band, and a few milli-magnitudes in the g band. They are highly variable in time and space, with a non predictable spectral response (due to the variety of grain size) Current monitoring is done on day-time, which non usable for LSST. The adopted solution is an auxiliary 1.2m telescope to monitor the atmosphere and especially the aerosols if the LSST field. This telescope is being simulated in order to define the right strategy: either a spectrograph or an imager with appropriate thin spectral bands.

An analysis of about 10 years of data for ozone, water vapor and aerosol led to a realistic simulator of these components above the LSST site[3].

4 Photometric redshifts

Among the expected 10 billion galaxies catalog, a sub-"gold" sample of high signal-to-noise ratio[d] of about $4 \cdot 10^9$ galaxies (or a surface density of 55 arcmin^{-1} [e]) will be defined for cosmological purposes.

It will be impossible (actually using current technology) to get systematic spectra, and then spectroscopic redshifts, for such an amount of galaxies, it would be too time-consuming on class 10m telescopes. Then computing photometric redshifts will be a necessary evil. Because they actually are a true limitation for cosmology (BAO, SNe, weak lensing...). To be as good as possible, they need a very accurate photometry. The requirements on photometric redshifts are actually driven the requirements on the photometric calibration; they are the following:

- Root mean square (RMS) scatter: $\sigma_z/(1+z) < 0.05$ (goal 0.02);
- Fraction η of outliers at more than 3σ at all redshifts should be less than 10%;
- the average of the error, or bias, $e_z = \langle (z_p - z)/(1+z) \rangle$, should be less than 0.3%.

An algorithm of reconstruction has been set up together with a simulation of galaxies in large scale structures for LSST[5]. It is based on a classical template fitting method, but defining a sub-sample of well reconstructed redshifts galaxies based on cuts on a ad-hoc parameter, the likelihood ratio. This parameter of "goodness reconstruction" is defined as:

$$L_R(\text{parameters}) = \frac{P(\text{parameters}|\text{Galaxies OK})}{P(\text{parameters}|\text{Galaxies OK}) + P(\text{parameters}|\text{Outliers})}$$

where P is the probability density function, "Galaxie OK" stands for well reconstructed galaxies ($|z_p - z|/(1+z) < 0.15$, with z the spectroscopic redshift and z_s the photometric redshift), "Outliers" stands for not well-reconstructed galaxies ($|z_p - z|/(1+z) > 0.15$) and the "parameters" are a set of 17 variables including most important caracteristics (peak numbers, relative height, width...) of marginalized probability density functions and some color terms.

---

[d] Defined as $i < 25.3$ which corresponds to a signal-to-noise ratio better than 20 for point sources under median observing conditions.

[e] Note that this is the "ground asymptote": beyond, the atmosphere is cutting the red part of the spectrum, limiting the high redshift galaxy number.

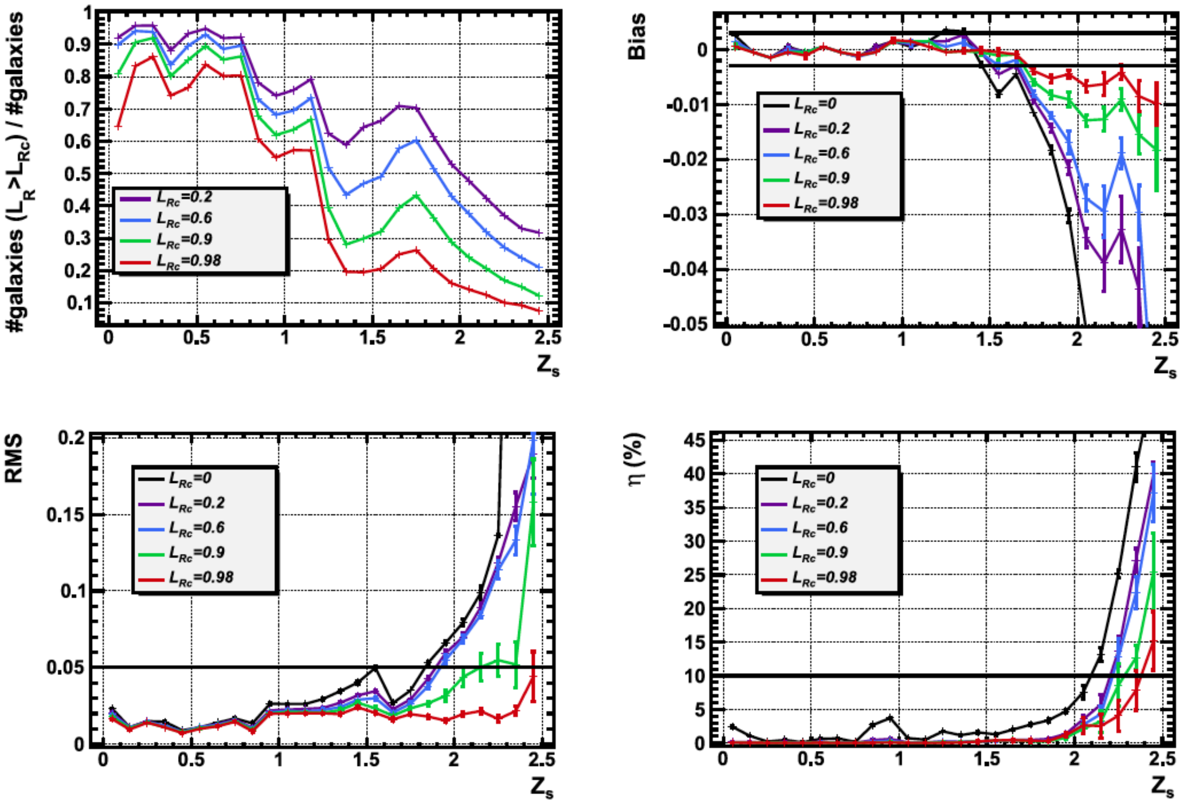

Figure 3 – Results for differents cuts on LR: *top left*, evolution of fraction of detected galaxies as a function of photometric redshift, *top right*, evolution of biais, *bottom*, evolution of the RMS and the fraction of outliers. LSST requirements are shown as horizontal lines [5].

A cut on this likelyhood ratio (LR) parameter turned out to be very powerful to reject outliers. It has been trained on CFHTLS data and on LSST simulations with similar results. Fig. 3 shows the results of reconstruction for different values of the cut on LR: for galaxies with LR > 0.9, the LSST goals are reached up to $z_s = 2.5$. However this is obtained with a large galaxy loss. A new promising method is being developped, based on a boosted decision tree.

5 Cosmic magnification

The propagation of distant sources' light is distorded by foregrounds masses due to the gravitationnal lens effect. At a reasonable distance of the line-of-sight, in the weak regime, the effect can be measure in a statistical way, considering many sources and lenses. Two distinct effects can actually be measured separatly: either the systematic distorsion of background sources shapes by foreground masses, also known as the cosmic shear, or the systematic magnification of these sources, which is the cosmic magnification.

The later is the resulting overlap of an increase of the distant sources flux, while the solid angle is being stretched. Then if the apparent limiting magnitude gets deeper, the source density surface on the images is diluted. The induced cross-correlation between physically separated foreground and background populations provides a positive or negative result depending on how the loss of sources due to dilution is balanced by the gain of sources due to flux magnification.

Contrary to the shear, which needs accurate shape measurements and is then limited in distance to get spatially resolved objects, the cosmic magnification depends only on flux measurements (and redhifts). LSST appears well suited for that (deep limiting magnitude, but ground based) [2].

Simulations show that for such a survey, the shot noise is not anymore the dominant error, it will be actually the intrinsic clustering. The covariance matrix of the cosmic magnification measurement depends on the power spectra of the auto-correlation of both populations (foreground and background), as well as of the cross-correlation power spectrum, as seen on Fig. 4. A Fischer matrix analysis allows to forecast the constraints that cosmic magnification will be able to set on dark energy equation of state parameters. They are presented on Fig. 5 together with the shear constraints.

It appears that the cosmic magnification competes well with the cosmic shear, in a independant and complementary way. It is lighlty less efficient to constrain the dark energy, however it is easier to measure, and is subject to different systematic errors.

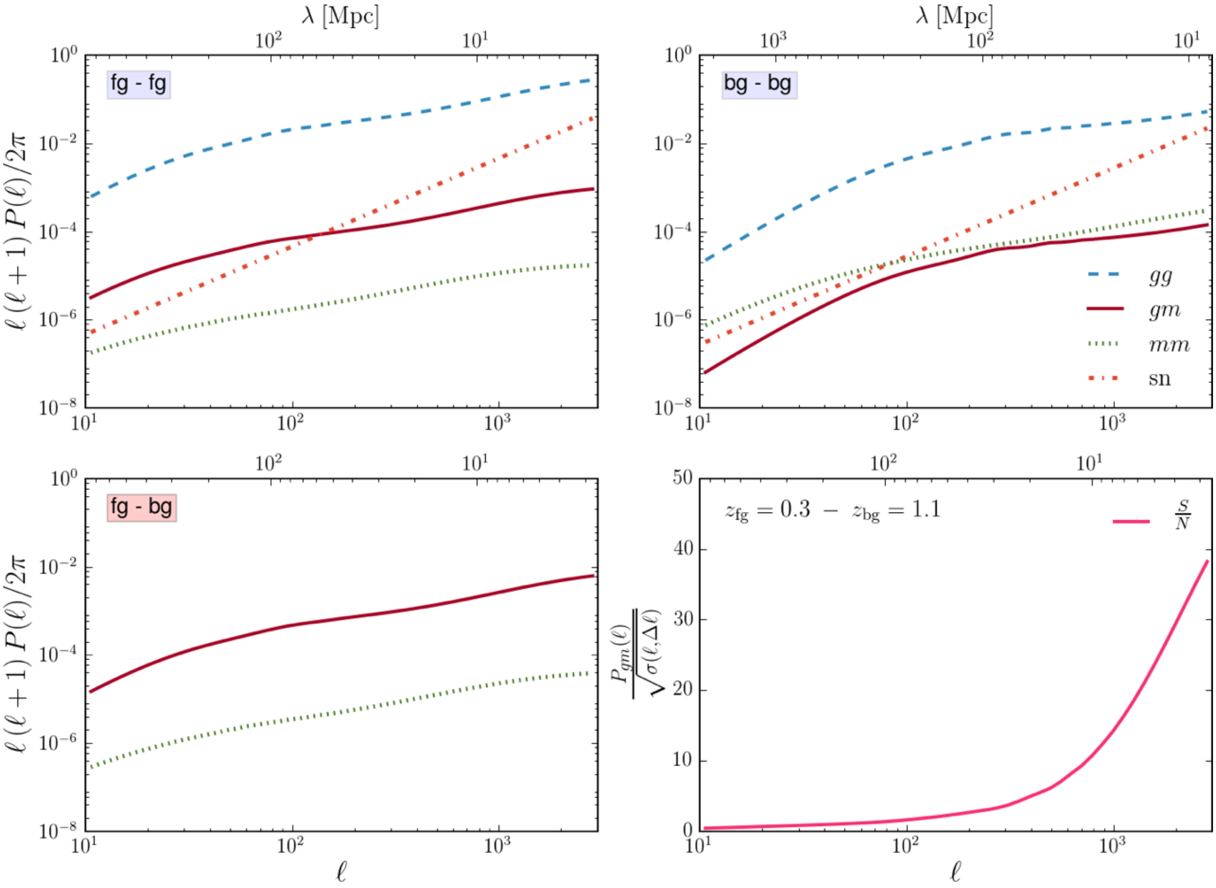

Figure 4 – Power spectra contributing to the covariance matrix for two redshift bins at $z = 0.3$ (foreground - fg) and $z = 1.1$ (background - bg) from the LSST redshift distribution, as a function of wavemode ($\ell = 2\pi/\theta$, θ being the angular size on the sky); on top is the auto-correlation of both populations, bottom left is the cross-correlation, and bottom right is the signal-to-noise[3].

6 Conclusion

The LSST survey will be powerfull in the cosmology field; it will be particularly well suited to measure the cosmic magnification, which will bring some independant contrains on dark energy. However measuring such a cross-correlation requires to control accurately the photometric calibration and the measurement of redshifts through the wide band photometry. Current simulations are showing promising results.

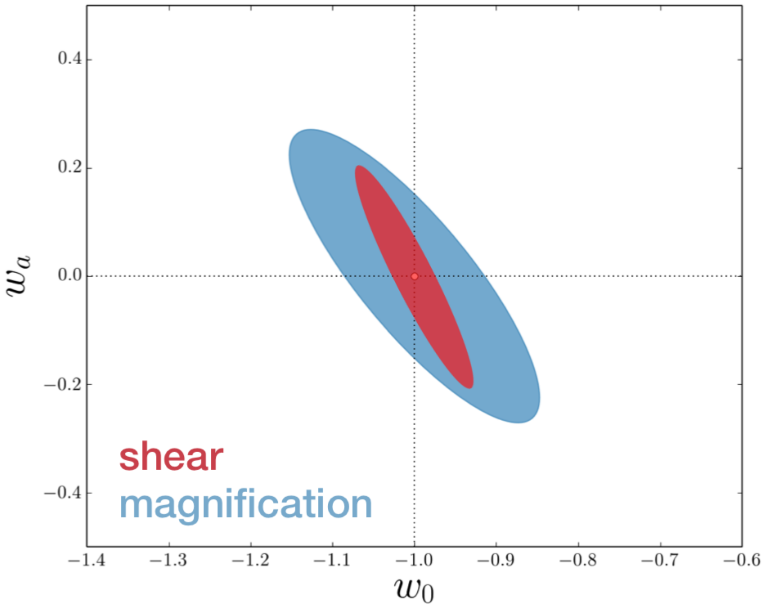

Figure 5 – Confidence contours on the dark energy equation of state parameters from cosmic magnification cross correlation alone at 95% confidence level with no systematics error [3]. The shear forecasts have been extracted from the LSST Science Book[6].

References

1. M. Betoule et al., 2014, arXiv:1401.4064
2. A. Boucaud, J.G. Bartlett and G. Blanc, Proceeding of Rencontres de Moriond Cosmology, 2012, p. 165
3. A. Boucaud, PhD thesis, 2013, Paris Diderot University, http://tel.archives-ouvertes.fr/tel-00983440
4. T. Delubac, 2014, this issue and arXiv:1404.1801
5. A. Gorecki, A. Abate, R. Ansari, A. Barrau, S. Baumont, M. Moniez and J.-S. Ricol, Astronomy & Astrophysics **561**, A128 (2014).
6. LSST Science Collaborations and LSST Project 2009, LSST Science Book, Version 2.0, arXiv:0912.0201, http://www.lsst.org/lsst/scibook
7. N. Padmanabhan, X. Xu, D. J. Eisenstein, R. Scalzo, A. J. Cuesta, K. T. Mehta, E. Kazin, Monthly Notices of the Royal Astronomical Society **427**, 2132 (2012)

The SZ effect: space-borne and ground-based future opportunities

S. COLAFRANCESCO
School of Physics, University of the Witswatersrand,
Privtae Bag 3, WITS-2050, Johannesburg, South Africa

The Sunyaev-Zel'dovich effect (SZE) is a deep probe of the atmospheres of cosmic structures. A multi-frequency approach to study the SZE in cosmic structures turns out to be crucial in the use of this probe for astrophysics and cosmology. Future directions for the study of the SZE and its polarization from ground-based and space-borne experiments are briefly outlined.

1 The physics of the SZ effect

The SZE, as produced by the inverse Compton scattering (ICS) of CMB photons off the electrons confined in the atmospheres of cosmic structures, has various manifestations: i) spectral distortions of the CMB due to up-scattering of CMB photons induced by high-E electrons (thermal, non-thermal, relativistic SZE); ii) spectral distortion of the CMB due to a bulk motion of the electron plasma w.r.t. the Hubble flow (kinematic SZE); iii) polarization of the CMB due to dynamical and plasma effects (SZE polarization).

The SZE. The SZE observable in the direction of a galaxy cluster writes [24,1,2] as

$$\Delta I(x) = 2\frac{(kT_{CMB})^3}{(hc)^2} y \; g(x) \; , \tag{1}$$

where $\Delta I(x) = I(x) - I_0(x)$, $I(x)$ is the up-scattered CMB spectrum in the direction of the cluster and $I_0(x)$ is the unscattered CMB spectrum in the direction of a sky area contiguous to the cluster. Here $x \equiv h\nu/kT_{CMB}$, h is the Planck constant, k is the Boltzmann constant, $T_{CMB} = 2.726$ K is the CMB temperature today and ν is the observing frequency. The Comptonization parameter $y = \frac{\sigma_T}{m_e c^2} \int P_e d\ell$ depends on the total pressure P_e contributed by the electronic population (here σ_T is the Thomson cross section, m_e the electron mass, and c the speed of light). The spectral function $g(x)$ of the SZE

$$g(x) = \frac{m_e c^2}{\langle \varepsilon_e \rangle} \left\{ \frac{1}{\tau_e} \left[\int_{-\infty}^{+\infty} i_0(xe^{-s}) P(s) ds - i_0(x) \right] \right\} \tag{2}$$

depends on the photon redistribution function $P(s)$ and on $i_0(x) = I_0(x)/[2(kT_{CMB})^3/(hc)^2] = x^3/(e^x - 1)$, where the quantity $\langle \varepsilon_e \rangle \equiv \frac{\sigma_T}{\tau_e} \int P_e d\ell = \int_0^\infty dp f_e(p) \frac{1}{3} p v(p) m_e c$ is the average energy

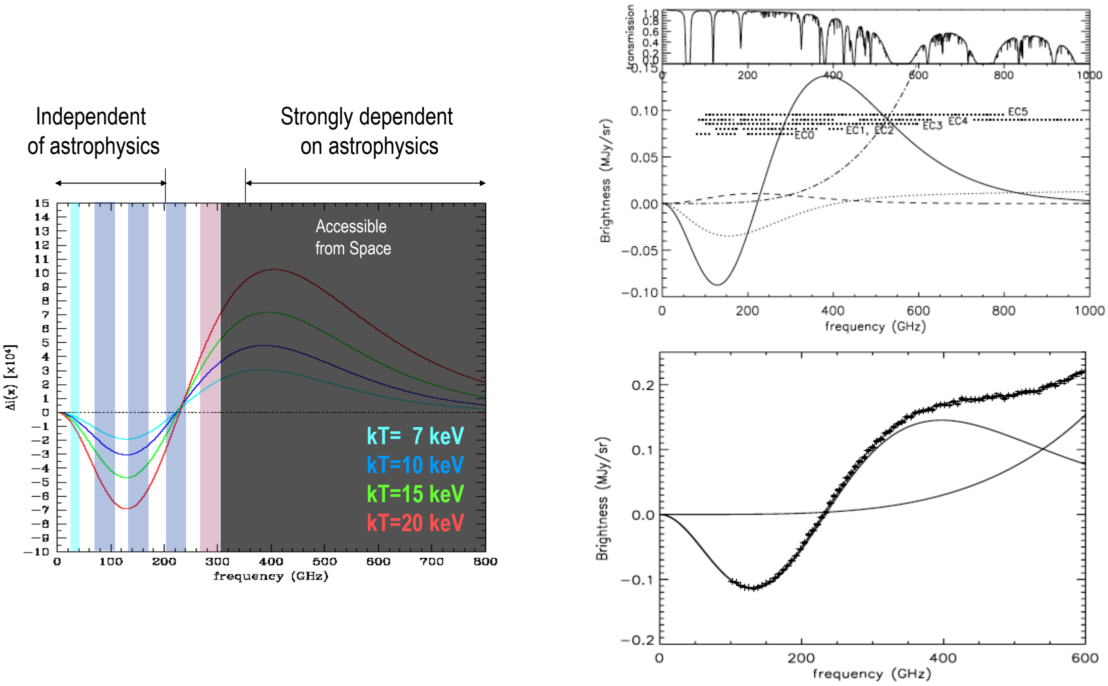

Figure 1 – **Left**:thermal SZE for various plasma temperatures and the same value of the optical depth. The low-ν part ($\nu \lesssim 220$ GHz) of the spectrum depends mostly on the Compton parameter y with no strong spectral dependence on the temperature. The high-ν part of the spectrum ($\nu \gtrsim 300$ GHz) shows a strong spectral dependence from the plasma temperature. Typical frequency bands where the SZE is observed from the ground are shown as blue-cyan bands, while the region accessible from space observations is shown by the gray shaded area. **Right top**: thermal SZE spectrum (solid line in bottom panel), compared to the atmospheric transmission of a dry, cold, atmosphere (PWV= 0.5 mm), and to the spectra of non-thermal SZE (dotted line), CMB anisotropy and kinematic SZE (dashed line), and dust anisotropy (dot-dashed line). The parameters of the different spectra are $\tau_{th} = 5 \times 10^{-3}$, $T_e = 8.5$ keV, $\Delta T_{CMB} = 22\mu$K, $\tau_{non-th} = 10^{-4}$, $\alpha = -2.7$, $p_1 = 1.4$ MeV/c, $\Delta I_d(150GHz) = 600$ Jy. The frequency coverage of different experiments is shown as dotted horizontal lines, labelled with the experimental configuration (EC) number. **Right bottom**: simulated data sets for the spectroscopic configurations EC5 (differential cold FTS on a L2-orbit satellite, with cold telescope).

of the electron plasma[2]. The optical depth along the line of sight ℓ of the electron population with number density n_e is $\tau_{\rm e} = \sigma_T \int d\ell n_{\rm e}$. The photon redistribution function $P(s)$, with $s = \ln(\nu'/\nu)$ in terms of the CMB photon frequency increase factor ν'/ν, can be calculated by repeated convolution of the single-scattering redistribution function, $P_1(s) = \int dp f_{\rm e}(p) P_{\rm s}(s;p)$, where $P_s(s;p)$ depends on the physics of inverse Compton scattering. The previous description is relativistically covariant and general enough to be applied to both thermal and nonthermal plasma, as well as to a combination of the two[2,8,17].

Kinematic SZ effect. The velocity (or kinematic) SZE (hereafter kSZE) arises if the plasma causing the thermal, or non-thermal, SZE is moving relative to the Hubble flow. In the reference frame of the scattering particle the CMB radiation appears anisotropic, and the effect of the ICS is to re-isotropize the radiation slightly. Back in the rest frame of the observer the radiation field is no longer isotropic, but shows a structure towards the scattering atmosphere with amplitude $\propto \tau_e V_t/c$, where V_t is the component of the peculiar velocity of the scattering atmosphere along the line of sight. The brightness change of the CMB due to the kSZE is given by $\frac{\Delta I}{I} = -\tau_e \beta_t \frac{xe^x}{e^x - 1}$ with $\beta_t \equiv \frac{V_t}{c}$ A general description of the kSZE has been given in the framework of the general Boltzmann equation[15] and in the relativistic covariant formalism[17].

SZ effect polarization. ICS yields naturally a polarized upscattered radiation field. The polarization Π of the SZE arises from various dynamical and plasma effects [22,12]: galaxy clusters transverse motion ($\Pi_k \propto \beta_t^2 \tau$ in the Rayleigh-Jeans, RJ, regime), transverse motions of plasma within the cluster ($\Pi_v \propto \beta_t \tau^2$ in the RJ regime) and multiple scattering between electrons and CMB photons within the cluster ($\Pi_{th} \propto \tau^2 \cdot (kT_e/m_e c^2)$ in the RJ regime for the thermal SZE). A general, covariant, relativistic derivation of the SZE polarization for thermal, non-thermal and relativistic plasma can be derived [12] and generalizes the non-relativistic derivation [22] in a way similar to the general derivation of the SZE described above [2].

1.1 The road to astrophysics

The SZE has been searched in galaxy clusters since it was originally proposed [23,24] using various techniques [6]. Ground-based SZE experiments (e.g., SPT, ACT, APEX, AMI, GBT, among others) provided excellent results in terms of imaging and blind search surveys with their low-ν, multiple-band observations, but they have neither true spectroscopic capabilities nor a wide frequency band, and they are not sensitive to the high-ν range ($\gtrsim 400$ GHz) of the SZE signals, which is crucial to exploit the astrophysical information contained in the SZE [6] (see Fig. 1). Even though ground-based instruments improved SZE source statistics (crucial to obtain cosmological information) and the angular resolution of SZE images (crucial to disentangle the extended SZE signal from point-source contamination), they can add little to the physical specification of the SZE sources, and therefore they need multi-ν (e.g., X-ray and optical) follow-up to fully characterize the physical parameters derived from SZE observations.

The Planck satellite allowed for the first time to access a wide frequency range ($\sim 30 - 850$ GHz) in the study of the SZE. Planck SZE catalog contains 1227 SZE sources (S/N ¿ 4.5), with 683 known clusters, 178 confirmed clusters and 366 candidates [18], providing the largest sample so far of SZE detected clusters. These results show that the SZE selection is a powerful method for the detection of new distant and massive clusters. Planck also unveiled a population of dynamically perturbed clusters at $z \gtrsim 0.3$, possibly under-represented in X-ray surveys. The inability to determine independently cluster parameters with SZE observations only, requires that Planck detected SZE clusters are followed-up with a multi-ν observation program in the X-rays and optical bands to obtain confirmation, redshift estimation and estimates of the global physical parameters. The information collected so far strengthens our overall view of the thermal ICM properties and mass content in galaxy clusters, and extends sensibly our statistical and astrophysical understanding of non-thermal phenomena occurring in the cluster atmospheres [13]. We stress that the SZE has also been observed in a few clusters with the HERSCHEL Spire instrument operating in the range $\nu \sim 600 - 1200$ GHz. Spectroscopic measurements in these high-ν bands opens the way to the deep astrophysical exploitation of the SZE. As an example, the additional data points on the SZE spectrum of the Bullet cluster observed with Herschel-Spire allowed to establish various properties for the thermal and non-thermal plasma superposition in the atmosphere of this strong merging cluster [9,19,20]. In addition, these measurements allowed to probe that the temperature distribution in the Bullet cluster is strongly inhomogeneous along the line of sight and provides a new method for studying galaxy clusters in depth. In fact, the Bullet cluster temperature distribution was fund to have a high value of of the temperature standard deviation $\sigma_T = 10.6 \pm 3.8$ keV [21]. These results have been obtained mostly because of the access to the very high-ν part of the SZE spectrum that contains detailed information on the relativistic effect on the single thermal plasma and on the presence of additional plasmas of either thermal or non-thermal nature [9,11].

Planck and Herschel observations of the SZE opened, thus, a rich field of investigation that will fully blossom in the next years with the full exploitation of spatially-resolved spectroscopic SZE observations. In the following we discuss some of the astrophysical and cosmological studies that will be possible with a full spectro-polarimetric study of the SZE.

2 A future outline on the SZE

Studying the complete spectro-polarimetric properties of the SZE provides many insights on the energetics, pressure and dynamical structure of various cosmic atmospheres [7]. In addition, the combination of SZE with other emission mechanisms related to the same particle distribution (i.e., synchrotron, high-E ICS emission, bremsstrahlung emission) provides further information on the radiation, matter and magnetic fields that are co-spatial with the electrons producing the SZE in various cosmic structures [7].

The spectral shape of the SZE, and of its polarization, guide our investigation on its exploitation (see Fig.1): high-ν observations are mostly sensitive to the physics of the electron distribution and hence will improve our astrophysical knowledge of cosmic structures; low-ν observations are mostly insensitive to the spectral details of the electron distributions but are strongly depending on the spectral shape of the CMB, and hence will allow to use spectral distortions of the CMB to probe early cosmology.

Precise observations of the SZE at $\nu \gtrsim 350$ GHz are crucial for unveiling the detailed structure of cluster atmospheres, their temperature distribution [8], and the possible presence of suprathermal and/or nonthermal plasma [2,4] because the high-ν part of the SZE spectrum is more sensitive to the relativistic effects of the electron momentum distribution. This is even more so for galaxy clusters with a complex plasma distribution as found for powerful merging clusters, like the exemplary case offered by the Bullet cluster [9]. Such SZE observations can also add relevant information on the electron distribution function (DF) in the ICM, a subject that - even though relevant to a proper analysis of astrophysical plasmas - has not been addressed in details so far: the relativistic kinetic theory, on which the DF derivation is based, is in fact still a subject of numerous debates [19]. The SZE analysis of the DF is best fulfilled in hot, massive clusters because the SZE intensity change due to using a relativistic correct DF instead of a Maxwell-Boltzman DF are much larger in hot clusters because relativistic SZE corrections scale as $\propto T^{5/2}$. The method used to derive the electron DF using SZE multi-ν observations of massive hot clusters [19] makes use of Fourier analysis representation of the approximate electron DF whose parameters are best fitted using observations in the (optimal) frequency range $\sim 350 - 850$ GHz.

Such high-ν SZE observations will further allow to extract unique information on the physical structure, the particle content and the overall energetics of other cosmic structures like cluster cavities [3], radiogalaxy lobes [5,11] and wind-driven galactic halos [6].

Spectro-polarimetric measurement of the SZE are able to add further information on the transverse plasma motions within the cluster and on the pressure substructure of the plasma. SZE polarization signals in galaxy clusters are quite low (typically below μK level) even for high-T clusters [6] but it is interesting to note that the SZE polarization in cluster has quite different spectra w.r.t. the intensity SZE spectrum, a property that then requires to use spectro-polarimetry to fully disentangle the physical information contained in the SZE. Combining intensity and polarization observations of the SZE can uncover unique details of the velocity structure of the ICM, of its pressure structure and of the influence of a structured magnetic field in the stratification of the ICM, and therefore provides a full tomography of cluster atmospheres. Analogously, the combination of intensity and polarization observations of the kSZE can yield crucial information on the 3d distribution of the cosmological velocity field traced by galaxy clusters. Specifically, the ratio $\Delta I_{th}/\Pi_{th}$ yields direct information on the plasma optical depth τ, and the ratio $\Delta I_{th}/\Pi_{v}$ on the combination $\tau \cdot \beta_t$, thus allowing to use intensity and polarization SZE measurements to fully disentangle the pressure and velocity structure of the cluster atmospheres [12]. SZE polarization measurements are at the limit of next generation experiments, but stacking analysis of even small samples (order of ~ 20) of hot and dense galaxy clusters would allow to determine statistically the polarization signals of the thermal SZE for clusters with $kT > 10$ keV and $\tau > 0.03$ in the optimal frequency range $\approx 90 - 250$ GHz.

The sensitivity and spectro-polarimetry capabilities of an EC5 experimental configuration (e.g., similar to the one expected for the Millimetron mission [6]) will allow to address for the

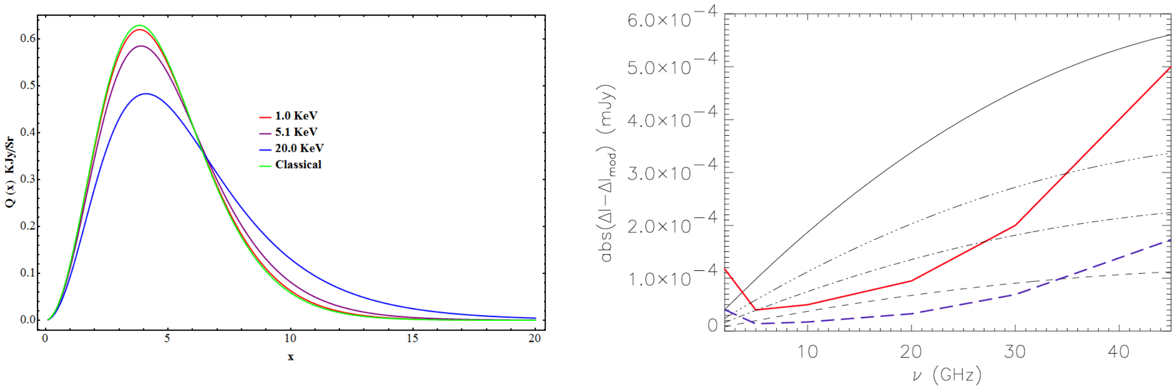

Figure 2 – **Left**: The spectrum of the Stokes parameter Q of the polarized SZE induced by the scattering of the CMB quadrupole (assumed here to be $\alpha_{2,2} = 3 \times 10^{-4}$) is shown for various temperatures of the cluster plasma. **Right**: difference between the standard thermal SZE calculated for A2163 in 2-45 GHz range and integrated in a 1 arcmin^2 area and the one modified for values $E^* = 5 \times 10^{-9}$ eV (solid line), 3×10^{-9} eV (dash - 3 dots), 2×10^{-9} eV (dot-dashed), and 1×10^{-9} eV (dashed). The sensitivity achievable with SKA in ~ 30 hours (red thick solid line) and in ~ 260 hours (blue thick long-dashed line) are shown (Colafrancesco & Marchegiani 2014).

first time fundamental questions in cosmology and fundamental astrophysics with the SZE [6]. As an example, we note that high-sensitivity observations of the (thermal and kinematic) SZE and its polarization can be used to test the homogeneity of our universe through probes of the Copernican Principle (CP) [16,13]. Large variations of the thermal SZE due to CMB temperature arriving at galaxy cluster from points inside our light cone that are significantly different from the blackbody temperature we observe directly could, in fact, indicate a violation of the CP and homogeneity. Analogously, large variations of the CMB dipole measured by the cluster kSZE could also indicate a violation of the CP and homogeneity. The SZE polarization contains more refined information on the CMB temperature and thus it can also provide a powerful probe of CP and homogeneity. Thus, observations of large SZE and of its polarization w.r.t. to the expectations of the SZE produced from a pure blackbody CMB spectrum might provide indications of a non-FLRW universe. In addition, we stress that the measurement of the CMB multipoles via the polarized SZE (see Fig.2) will also add a unique probe of the primordial CMB polarization patterns in various locations of the universe where clusters reside [12].

Furthermore, it has been shown [10] that the combination of an EC5 experiment (see Fig.1) with radio observations of the low-ν part of the SZE spectrum can also be used to probe even more fundamental aspects of astrophysics, like the fundamental properties of the photon. Measurements of the SZE with sensitivity of order of < 0.1 Jy, in the range $\sim 10 - 50$ GHz, can set very stringent constraints on the photon decay time [10]. This frequency band is also the one less affected by other sources of astrophysical contamination, and it will be best explored with the advent of the SKA telescope. At higher frequencies (i.e., $\sim 120 - 180$ and $\sim 200 - 300$ GHz), there are other spectral windows where the SZE method is again competitive if not advantageous in this respect. The necessary sensitivity in the high-ν range can be achieved with the next coming Millimetron space mission [6], whose EC5-like configuration is also advantageous in disentangling other astrophysical sources of contamination (e.g., sources of non-thermal SZE and/or special distortions of the SZE due to multiple-temperature regions) that could contaminate these measurements.

2.1 Concluding remarks

The impact of SZE observation for astrophysical and cosmological application is steadily increasing since the advent of dedicated experiments and large-scale surveys in the mm and sub-mm frequency range. The quality and the spatial resolution of SZE images is reaching arcsec precision and the spectral coverage is systematically extending in the sub-mm region where the highest spatial resolutions can be achieved, and with a wide spectral coverage able to decipher the physical details of the electron distribution in the atmosphere of various cosmic structures. New paths of theoretical investigations are underway and concern both the detailed study of the SZE and the impact of the various plasma structure and fields in cosmic structures. In this context, the possibility to perform precise measurements of the various SZE signals and to extract the relevant astrophysical information depends crucially on the capability to have spatially-resolved spectral (and polarization) observations of SZE sources over a wide ν band, from radio to sub-mm. In particular, the important condition for such study is to have a wide-band continuum spectroscopy (polarimetry) and especially a good spectral coverage and sensitivity in the high-ν band, where most of the astrophysical effects reveals more clearly. Spatially resolved spectroscopic and polarimetric observations of the SZE in the frequency range from ~ 100 GHz to ~ 1 THz, complemented by analogous observations in the radio band $\sim 1 - 30$ GHz, are the key to improve our understanding of the structure of cosmic atmospheres through analysis of the intensity and polarized SZE signal, and will allow to use this technique to probe the fundamental properties of the universe.

Acknowledgments

S.C. acknowledges support by the South African Research Chairs Initiative of the Department of Science and Technology and National Research Foundation and by the Square Kilometre Array.

References

1. Birkinshaw, M., 1999, Physics Reports, 310, 97
2. Colafrancesco, S., Marchegiani, P. & Palladino, E. 2003, A&A, 397, 27
3. Colafrancesco, S. 2005, A&A, 435, L9
4. Colafrancesco, S., 2007, New Astronomy Reviews, 51, 394
5. Colafrancesco, S. 2008, MNRAS, 385, 2041
6. Colafrancesco, S. 2013, AcPol, 53, 560
7. Colafrancesco, S. 2014, AAS, #223 # 34005
8. Colafrancesco, S. & Marchegiani, P., 2010, A&A, 520, 31
9. Colafrancesco, S., Marchegiani, P. & Buonanno, R. 2011, A&A, 527, L1
10. Colafrancesco, S. & Marchegiani, P., 2014, A&A, 562, L2
11. Colafrancesco, S. et al., 2013, A&A, 550, 92
12. Colafrancesco, S., Tullio, M. and Emritte, S. 2014, preprint
13. Colafrancesco, S., et al. 2014, A&A, 566, 42
14. De Bernardis, P., Colafrancesco, S. et al. 2012, A&A, 538, 86
15. Itoh, N., Kohyama, Y. & Nozawa, S. 1998, ApJ, 502, 7
16. Maartes, R. 2011, arXiv:1104.1300
17. Nozawa, S., Kohyama, Y. & Itoh, N. 2010b, PhRvD, 82, 3009
18. Planck Collaboration 2013, arXiv1303.5089P
19. Prokhorov, D., Colafrancesco, S. et al. 2011a, A&A, 529, 39
20. Prokhorov, D., Colafrancesco, S. et al. 2011b, MNRAS, 416, 302
21. Prokhorov, D. and Colafrancesco, S., 2012, MNRAS, 424, L49
22. Sazonov, S. & Sunyaev, R. 1999, MNRAS, 310, 765
23. Sunyaev, R.A. & Zel'dovich, Y.B.: Comments Astrophys. Space Phys. 1972, 4, 173
24. Sunyaev, R. A. & Zeldovich, Ia. B. 1980, ARA&A, 18, 537

QUBIC: a Fizeau interferometer targeting primordial B-modes

A. Tartari, On Behalf of QUBIC Collaboration
Laboratoire APC and Paris Centre for Cosmological Physics
10, rue Alice Domon et Léonie Duquet, 75205 Paris Cedex 13, France

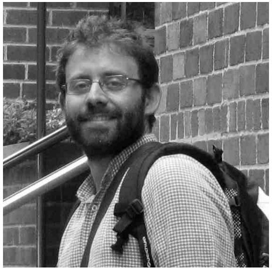

QUBIC (Q and U Bolometric Interferometer for Cosmology) is a Fizeau interferometer sensitive to linear polarisation, to be deployed at the Antarctic Station of Dome C. This experiment in its final configuration will be operated at 97, 150 and 220 GHz, and is intended to target CMB primordial B-modes in a multipole window $20 \leq \ell \leq 150$, to achieve a final sensitivity of r=0.01 (90%CL) after 1 year of operation. Here we review in particular its working principles and we show how QUBIC interferometric configuration can be considered equivalent to a pupil-plane filtered imaging system. In this context, we show how our instrument can be self-calibrated. Finally, we conclude by showing an overall view on the 150 GHz unit, which will play the role of a demonstrator for the subsequent modules, and review the technological choices we did for each subsystem.

1 Introduction

The importance of primordial B-mode detection can hardly be overestimated [1]. We know that from primordial B-mode amplitude measurement, knowing the amplitude of the stronger E-mode signal, we can infer the energy scale at which Inflation occurred. In fact, the ratio of B-mode and E-mode angular power spectra at $\ell = 2$ gives directly the tensor to scalar ratio r, while Inflation energy scale is related to r through the relation $V^{1/4} = 1.06 \times 10^{16}$ GeV $(r/0.01)^{1/4}$. Nowadays, a first claim of B-mode detection by the BICEP2 collaboration [2] is having a large echo within the scientific community and on the media. If BICEP2 $r = 0.2$ detection will be confirmed, this will be the further demonstration that ground-based experiments can still play the role of pathfinders. In passing, we remind that also E-modes have been detected first from the ground by DASI [3] (precisely from the South Pole, exactly where BICEP2 is installed). In general, *suborbital* experiments provide also the way to test and validate experimental techniques and state-of-the-art devices. This is a critical point for current CMB experimental research, since to target extremely faint signals, once our devices are photon noise-limited the only way to increase the sensitivity is to go towards kilo pixel arrays, or hundred pixel arrays provided they are illuminated through a multi-moded optics. Nonetheless, precision is not the only issue. Accuracy is critical as well, and must follow closely precision requirements. Systematics control is therefore a key point to address, and the landscape of running, scheduled and proposed experiments is particularly rich with this respect. If we concentrate on the experiments explicitly designed to target primordial B-modes, we find imagers modulated with warm or cryogenic temperature Half Wave Plates (ABS [4], at room temperature; EBEX [5], at 4K), or with Variable Polarization Modulators (CLASS [6], PIPER [7]) on top of small telescopes. Correlation polarimeters are known to be robust against systematics, and they will fly on the STRIP [8] module of LSPE. The option of large throughput optics will be demonstrated by the SWIPE [9] instrument on LSPE, and is proposed also for MuSE [10]. In this landscape, QUBIC [11] is the only interferometer, endowed with kilo pixel arrays of Transition Edge Sensors.

2 QUBIC: the concept

The most common technique to make mm-wave interferometers is certainly multiplicative (heterodyne) interferometry. In this case, long baselines (up to 10 km, or more) can be achieved, and IF bandwidth $\sim$ some GHz wide allow sensitive operation when observing *continuum* sources. The drawback is that pairwise correlation of antennas is achieved through fast digital correlators, whose complexity and costs make it practically unfeasible for systems with hundreds of antennas. In adding interferometry, on the contrary, correlation is achieved *through* direct bolometric detection, so that in principle hundreds of signals can be correlated at a time. In the particular case of an adding all-to-one interferometer, all the signals are combined on each detector (see Fig.1), so that each detector's output is a linear combination of total intensities collected by each antenna, plus interference terms that are proportional to the visibilities corresponding to the Fourier modes selected by the antenna array. In the case of QUBIC, the linear combination of the antenna signals is achieved by means of an optical beam combiner (which is essentially a very fast telelescope). As shown in [11], 400 closely packed back-to-horns observe the sky and re-emit towards the beam combiner located within the cryostat. In turn, the families of parallel rays re-emitted from the back horns are summed in phase on each detector by the combiner. This is the implementation of a Fizeau interferometer scheme.

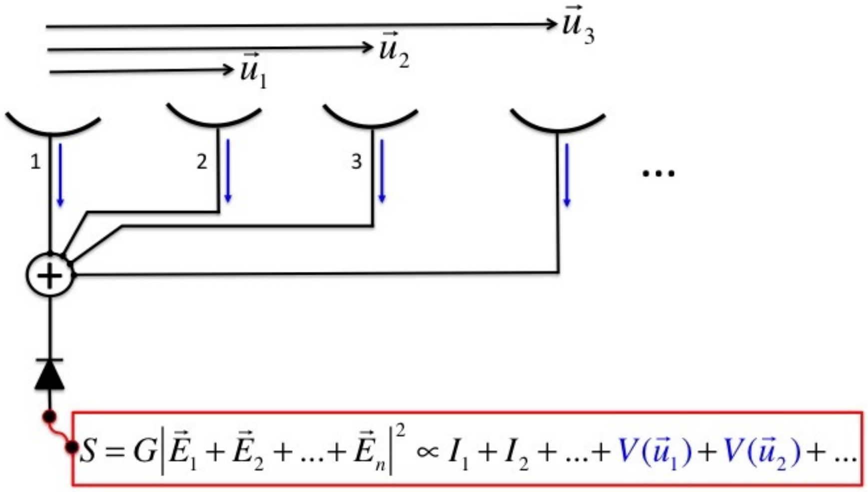

Figure 1 – A generic adding all-to-one interferometer. Antennas collect signals that are sent towards an adding unit. After linear superposition, a detector responding to the intensity of the incoming signals correlates the incoming fields, in such a way that its output is a combination of single antenna intensities, plus visibility terms (in blue in the formula). The Fourier spatial frequency $\vec{u}$ correspond to the multipole $\ell = 2\pi|\vec{u}|$.

Now, if we imagine to remove the back-to-back horn array, we are left with an imager (by construction, our combiner is a telescope). If we put the horns back again, what we obtain is again an imager, but with a pupil plane filtering structure (our horn array). Therefore, our instrument makes images using only a subset of those modes that would be otherwise accepted by the bare telescope. The Fourier mode bandpass is fixed by horn aperture and arrangement. The far-field pattern of the instrument is represented in a qualitative way in Fig.2: (1) for a uniformly illuminated pupil (that mimic our bare combiner), to obtain an Airy diffraction pattern and (2) in the case of an illumination profile formed by a set of gaussian apertures, producing a beam with higher order maxima. The synthetic beam of QUBIC central pixel will be qualitatively close to the case (2), even though we have to stress that each pixel will observe the sky through slightly different synthetic beams. For what we have just said, QUBIC is essentially an imager, and as such it must be used, from the scanning strategy to the map-making procedure [12].This is a very nice fact in itself, but doesn't explain why Fizeau architecture is powerful for our experiment. The key point is that each back-to-back horn of QUBIC is endowed with a shutter that allows us to switch-on, or switch-off, all the baselines we like. This fact, as demonstrated by [13], allows the self-calibration of our interferometer. Especially the Fourier modes corresponding to the short baselines can be realised (one by one!) by hundreds of horn pairs (380 realisations for the shortest baseline, corresponding to $\ell \sim 50$). Especially the shortest baselines, so relevant for Cosmology, will be those that will be better self-calibrated by virtue of their large redundance, with suppression of systematic effects adequate to reach a final sensitivity equivalent to $r \simeq 0.01$ (90%).

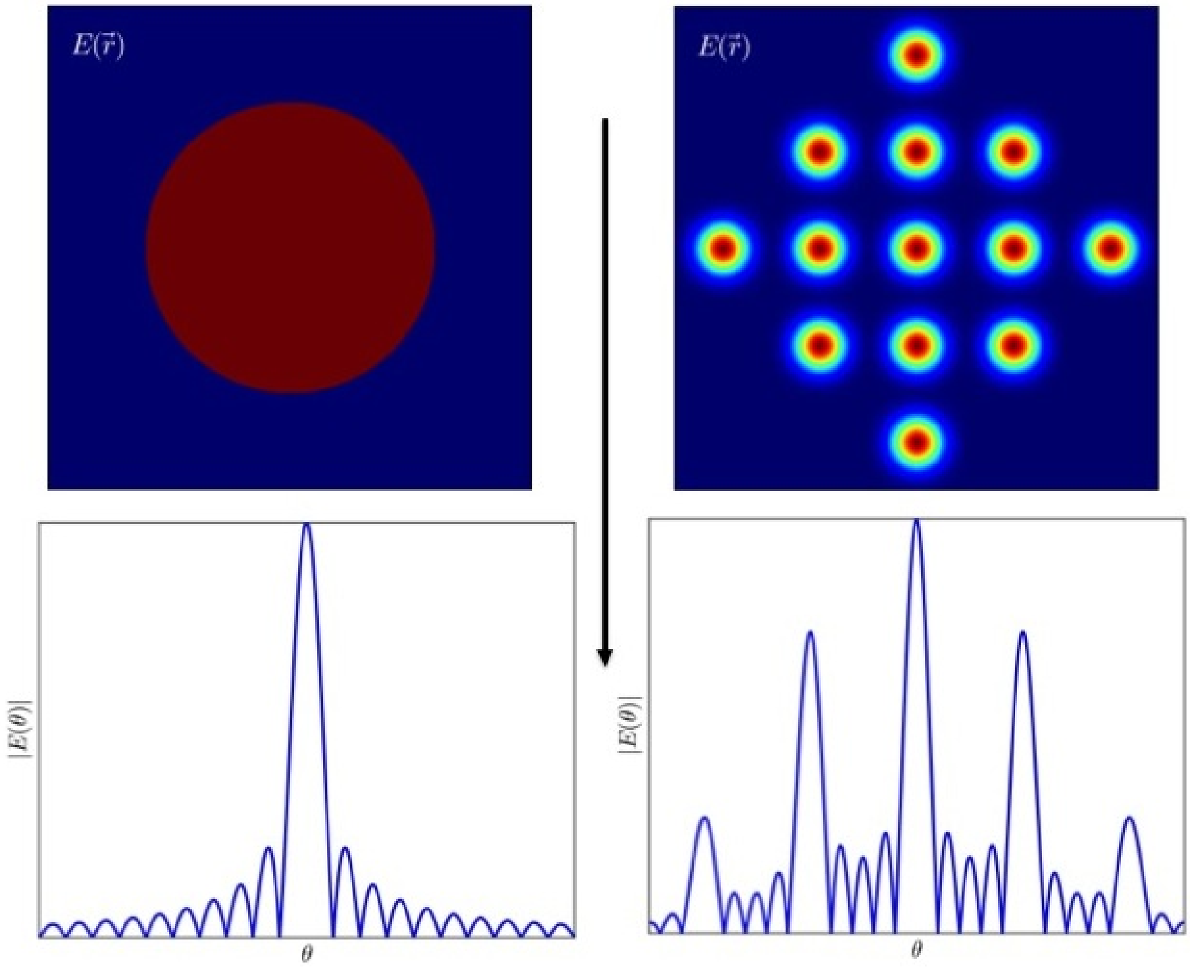

Figure 2 – A qualitative view of far-field patterns discussed in the text. Top Left panel: uniformly illuminated aperture with, in the Bottom Left panel, its far-field pattern. Top Right panel: series of apertures with gaussian illumination, and the corresponding far-field pattern (Bottom Right Panel).

3 First module and perspectives

QUBIC, in its final configuration will be operated at 97, 150 and 220 GHz, with 2 modules per frequency (each one endowed with 2000 TES), and is intended to target CMB primordial B-modes in a multipole window $20 \leq \ell \leq 150$, to achieve a final sensitivity of r=0.01 (90%CL) after 1 year of on-sky operation. The first module to be deployed at the Antarctic station of Dome C is the one at 150 GHz. Dome C has been demonstrated as one of the most transparent and most stable places on Earth for mm-wave astronomy: a relevant fact for an efficient use of observation time. The first 150 GHz module will observe the sky through a field of view of $\sim 14^\circ$, with a resolution of $\sim 0.54^\circ$. It is nowadays completely dimensioned, and the different subsystems are being realised. Subsystem assembly is scheduled in 2015. The primordial B-mode signal peaks slightly below $\ell \sim 100$ ($\sim 2^\circ$), where QUBIC has its maximum sensitivity, and its best systematic rejection capabilities. QUBIC, with its novel way of controlling systematics, together with a deployment of kilo-pixel focal planes, can play an important role to confirm the BICEP2 claim, which is opening a new era in our understanding of Inflation.

Acknowledgments

We acknowledge the financial support from the UnivEarthS Labex program of Sorbonne Paris Cité (ANR-10-LABX-0023 and ANR-11-IDEX-0005-02).

References

1. D. Baumann, et al., arXiv:0811.3919v2, 2009
2. The BICEP2 Collaboration, arXiv:1403.3985, 2014
3. J.M.Kovac, et al., *Nat.* **420**, 772 (2002)
4. T.Essinger-Hileman, *LTD13 - AIP Conference Proceedings* **1185**, 494 (2009)
5. B. Reichborn-Kjennerud, et al., *Proceedings of SPIE* **7741**, 77411C (2010)
6. K.Rostem, et al., *Proceedings of SPIE* **8452**, 84521N (2012)
7. A.Kogut, et al., *Proceedings of SPIE* **8452**, 84521J (2012)
8. M.Bersanelli, et al., *Proceedings of SPIE* **8446**, 84467C (2012)
9. P. de Bernardis, et al., *Proceedings of SPIE* **8452**, 84523F (2012)
10. A. Kusaka, et al., *Proceedings of SPIE* **8452**, 84521L (2012)
11. The QUBIC Collaboration, *Astropart. Phys.* **34**, 705 (2011).
12. P.Chanial, et al., *in preparation*
13. M.-A. Bigot-Sazy, A&A **550**, A59 (2013)

CMB Polarization can constrain cosmology better than CMB temperature

Silvia Galli
CNRS, UMR 7095, Institut dAstrophysique de Paris, F-75014, Paris, France. Sorbonne Universites, UPMC Univ Paris 06, UMR 7095, Institut dAstrophysique de Paris,F-75014, Paris, France

We demonstrate that for a cosmic variance limited experiment, CMB E polarization *alone* places stronger constraints on cosmological parameters than CMB temperature. We expose the physical effects at play behind this remarkable result and study how it depends on the multipole range included in the analysis. In most relevant cases, C_ℓ^{TE} or C_ℓ^{EE} surpass the C_ℓ^{TT} based cosmological constraints. We perform the same analysis for a Planck-like experiment, and conclude that even in this case C_ℓ^{TE} alone should determine the constraint on $\Omega_c h^2$ *better* than $C_\ell^{TT}$by $\sim 15\%$, while determining $\Omega_b h^2$, n_s and θ with comparable accuracy.

1 Introduction and Methodology

In [1], we argue that the CMB E polarization data is much more than a mere improvement over the temperature anisotropies measurement. We demonstrate that either the temperature-polarization cross-correlation C_ℓ^{TE} or the C_ℓ^{EE} polarization power spectra can provide tighter constraints on cosmological parameters than the temperature power spectrum C_ℓ^{TT}, in the case of a Cosmic Variance Limited experiment (hereafter CVL). The constraining power of C_ℓ^{EE} had already been noticed in[3]. Here we show, for the first time, that C_ℓ^{TE} as well is more constraining than the C_ℓ^{TT} power spectrum, and explicit the physical reasons behind this conclusion.

We forecast constraints using the Fisher Information Matrix (FIM) (see e.g. [4]) methodology. We assume that foreground contamination, beam uncertainties and other systematics have been corrected to a level much smaller than the statistical error. We forecast the constraints on the parameters of a ΛCDM cosmology. We focus on the following 6 parameters: the physical baryon and CDM densities, $\omega_b = \Omega_b h^2$ and $\omega_c = \Omega_c h^2$, the angular dimension of the sound horizon at recombination θ, the normalization of the primordial power spectrum, $\ln(10^{10}\mathrm{A_s})$, with pivot scale $k_0 = 0.05\,\mathrm{Mpc}^{-1}$, the scalar spectral index, n_s, and the optical depth to reionization, τ.

We consider two experimental settings: a full sky cosmic variance limited experiment (CVL) and a Planck-like mission. For the CVL experiment, we have no instrumental noise and $f_{\mathrm{sky}} = 1$. Changing the smallest available scale ($\ell_{\max}$) as we do in section 2 allows the reader to evaluate quickly what will be the behaviour of a more realistic experiment.

The Planck-like mission corresponds to 30 months worth of combined observations by the

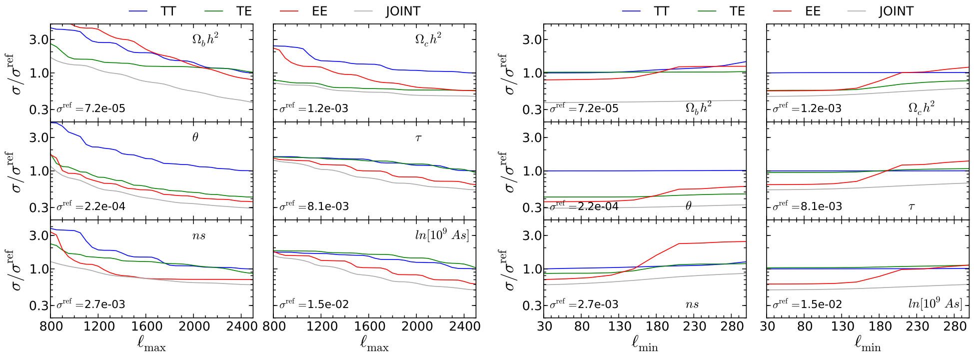

Figure 1 – Left: standard deviations on ΛCDM parameters as function of $\ell_{\rm max}$, normalized to the standard deviation $\sigma^{\rm ref}$ obtained from C_ℓ^{TT} with $\ell_{\rm max} = 2500$. We consider a CVL experiment with $\ell_{\rm min} = 30$ and a prior on τ. We consider here lensed CMB power spectra. Right: standard deviations on ΛCDM parameters as function of $\ell_{\rm min}$, normalized to the standard deviation $\sigma^{\rm ref}$ obtained from C_ℓ^{TT} with $\ell_{\rm min} = 30$. We consider a CVL experiment with $\ell_{\rm max} = 2500$ and a prior on τ. We consider here lensed CMB power spectra.

two best Planck CMB channels at 143 GHz and 217 GHz. We assume that due to galactic dust contamination only half of the sky is available for cosmological use, $f_{\rm sky} = 0.5$. We compute the characteristics of this experiment according to the Planck Blue Book [5]. This setting gives a reasonable estimate of the expected sensitivity of the second Planck data release.

2 Cosmic variance limited experiment

We present in this section forecasts on cosmological parameters in case of a CVL Experiment for C_ℓ^{TT}, C_ℓ^{EE} or C_ℓ^{TE} considered separately or from the combination of all the spectra. Our baseline in this Section has $\ell_{\rm min} = 30$ and $\ell_{\rm max} = 2500$ unless otherwise specified, and always includes a prior on τ, $\sigma(\tau) = 0.013$. In this way, we can compare the information content of the different power spectra assuming nearly the same information about reionization, that can otherwise be more tightly constrained observing its signature at large scales ($\ell \lesssim 30$) in polarization.

We first analyze how the constraints change as a function of maximum multipole ($\ell_{\rm max}$) included. In Fig. 1 we show how the constraints evolve with $\ell_{\rm max}$ for lensed CMB spectra (reference constraints). By observing Fig. 1, we notice that at $\ell_{\rm max} = 2500$, C_ℓ^{EE} is the best at constraining all parameters, as already noticed by [3]. In particular, the C_ℓ^{EE} power spectrum constrains the angular size of the sound horizon θ better than C_ℓ^{TT} by a factor ~ 2.8, $\Omega_c h^2$, $\ln(10^{10}{\rm A_s})$, τ, $n_{\rm s}$ by a factor 1.9, 1.7, 1.6 and 1.4 respectively, while the smallest improvement is on the baryon density $\Omega_b h^2$ by a factor ~ 1.3. The C_ℓ^{TE} power spectrum constrains the dark matter density $\Omega_c h^2$ as strongly as C_ℓ^{EE}, θ and $n_{\rm s}$ slightly worse than C_ℓ^{EE} (only by a factor ~ 1.2), while it constrains the other parameters ($\Omega_b h^2$, $\ln(10^{10}{\rm A_s})$ and τ) at a level comparable to C_ℓ^{TT}. It is interesting to notice however that C_ℓ^{TE} becomes the best at constraining the matter densities $\Omega_b h^2$ and $\Omega_c h^2$ if $\ell_{\rm max} \lesssim 2100$, while the other parameters keep being constrained best by C_ℓ^{EE}. Finally, combining all the spectra leads to a substantial improvement only to the constraint on $\Omega_b h^2$ (by a factor ~ 2.1 compared to C_ℓ^{EE} alone), while the other parameters improve only by a factor ~ 1.2 compared to the constraints from C_ℓ^{EE} alone.

In order to gain some physical insight into why the constraints are stronger when determined from the C_ℓ^{EE} power spectrum, we have forecasted results for two additional cases. In the first, the constraints are obtained as the inverse of the diagonal of the Fisher Matrix, i.e. *without marginalizing* over the degeneracies among all the parameters (we will refer to this as the 'diagonal' case). This is equivalent to calculating constraints for one parameter at the time, assuming the others fixed to their fiducial value. This plot is useful to understand whether the reference constraints in Fig. 1 are limited by degeneracies among parameters or by the intrinsic information encoded in the CMB, limited only by cosmic variance. In the second, we have assessed whether the information coming from the effect of weak lensing at high multipoles impacts the results by calculating constraints using unlensed CMB spectra.

By comparing these cases, we notice the following features:

Constraint on θ. As already mentioned and shown in Fig. 1, the angular size of the sound horizon θ is better determined using the C_ℓ^{EE} or C_ℓ^{TE} power spectra alone than by using C_ℓ^{TT} alone. This is due to the fact that the peaks in C_ℓ^{EE} and C_ℓ^{TE} are *sharper* than in C_ℓ^{TT} [6], because polarization is only produced by the gradient of the velocity field in the photo-baryonic fluid, while temperature is sourced both by the perturbations in the density field and by the ones in the velocity field [6]. The position of the peaks can therefore be better determined from polarization.

Breaking the $\tau - \ln(10^{10}\mathrm{A_s})$ degeneracy with lensing. The C_ℓ^{EE} power spectrum alone is also better at constraining the reionization optical depth and the amplitude of the primordial power spectrum $\ln(10^{10}\mathrm{A_s})$. This is due to degeneracy breaking effect of lensing at small scales, which depends on $\ln(10^{10}\mathrm{A_s})$ but not on τ. The effect is more relevant in polarization as the smoothing of the peaks due to lensing in more effective on sharper peaks.

Fig. 1 shows the evolution of the constraints with ℓ_{min}, varied between $30 < \ell_{\mathrm{min}} < 300$ at a fixed $\ell_{\mathrm{max}} = 2500$. In the CVL case considered here, we naively expect that cutting the noisier low-ℓ part of the spectrum should only marginally affect the results. Indeed, we find that the C_ℓ^{TT} constraints are marginally affected even when the most dramatic cut ($\ell_{\mathrm{min}} = 300$) is applied. Only the constraint on $\Omega_b h^2$ is worsened by $\sim 50\%$ for $\ell_{\mathrm{min}} \gtrsim 200$, due to the fact that with such a cut, the first peak is not observed anymore, reducing the information on the baryon load coming from the difference in height between the first and the second peak [7].

On the other hand, the constraints from the C_ℓ^{EE} polarization are more drastically affected by cutting the low-ℓ part. In particular, there is a strong worsening of the constraints of all parameters when $\ell_{\mathrm{min}} \gtrsim 130$. This is due to the fact that the inclusion of the multipoles $\ell \lesssim 200$ alleviates degeneracies, in particular between the scalar spectral index n_{s} and other parameters. We confirmed this by checking correlation coefficients between couples of parameters (mainly n_{s} versus the others) as a function of ℓ_{min}. For ℓ_{min} larger than $\ell_{\mathrm{min}} \gtrsim 130$, n_{s} becomes almost $\sim \pm 100\%$ correlated with the other parameters for C_ℓ^{EE}. Furthermore, we verified that if we fix n_{s} (thus marginalizing over only 5 parameters), this sharp worsening of the constraints disappears, while if we fix any of the other parameters, the step is still present, although when fixing $\Omega_c h^2$ it appears only in the constraints for $\Omega_b h^2$ and n_{s}. This suggests that cutting at $\ell_{\mathrm{min}} \gtrsim 130$ largely impacts the constraints from C_ℓ^{EE} due to the increasing degeneracies between n_{s} and other parameters, in particular with $\Omega_c h^2$ and $\Omega_b h^2$. The physical reason of why this happens is detailed in [?]

3 Planck

In this section, we repeat the analysis performed in the previous Sections for the case of a Planck-like experiment, assuming full mission data (30 months of data). We combine the 143 and 217 GHz channels following the specifications in [5]. Clearly, the forecasts in this Section are overly simplified. However, we verified that for a Planck-like nominal mission experiment (14 months of data), the error bars obtained from our Fisher Matrix forecast for C_ℓ^{TT} alone are similar to the ones obtained using the published Planck data from the first data-release [2], within a factor $1.3 - 1.5$. We therefore expect the forecasts to be in the right ballpark.

The most interesting result in Figure 2 is that we forecast that C_ℓ^{TE} should provide a constraint on the dark matter density $\Omega_c h^2$ stronger than the one obtained from C_ℓ^{TT} alone, namely $\sigma_{TE}(\Omega_c h^2) = 1.7 \times 10^{-3}$ [1.4%] versus $\sigma_{TT}(\Omega_c h^2) = 2.0 \times 10^{-3}$ [1.7%], while providing constraints comparable to C_ℓ^{TT} for $\Omega_b h^2$, n_s and θ. We underline that this is the first time that the power of C_ℓ^{TE} alone is forecasted in a paper. This opens the interesting possibility of cross-checking the results obtained from C_ℓ^{TT} alone, also considering that C_ℓ^{TE} is expected to have a

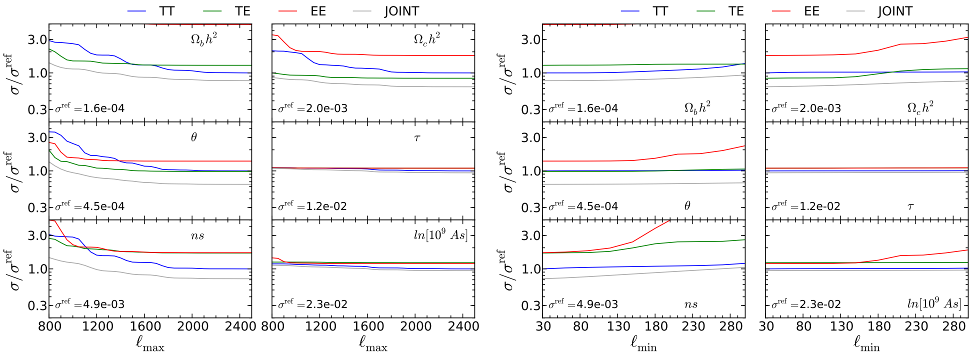

Figure 2 – Left: standard deviations on ΛCDM parameters as function of $\ell_{\rm max}$, normalized to the standard deviation $\sigma^{\rm ref}$ obtained from C_ℓ^{TT} with $\ell_{\rm max} = 2500$. We consider a Planck-like full mission experiment with two channels at 143 GHz and 217 GHz with $\ell_{\rm min} = 30$ and a prior on τ. Right: standard deviations on ΛCDM parameters as function of $\ell_{\rm min}$, normalized to the standard deviation $\sigma^{\rm ref}$ obtained from C_ℓ^{TT} with $\ell_{\rm min} = 30$. We consider a Planck-like full mission experiment $\ell_{\rm max} = 2500$ and a prior on τ.

lower level of foreground contamination at small scales than C_ℓ^{TT}. Furthermore, the constraints from C_ℓ^{TE} do not seem to improve extending $\ell_{\rm max} \gtrsim 1500$, as shown in Fig. 2, or by cutting at $\ell_{\rm min} \lesssim 150$, as shown in Fig. 2. This provides the possibility of obtaining strong constraints even when eliminating the most problematic multipole ranges, where polarized contamination from the galaxy (at large scales) or from extragalactic foregrounds (at small scales) are expected to be most relevant. Furthermore, comparing constraints calculated from lensed spectra with those calculated from unlensed ones, we notice that the degeneracy-breaking effect of lensing on $\ln(10^{10}{\rm A_s}) - \tau$ is effective only for C_ℓ^{TT} alone, as C_ℓ^{TE} and C_ℓ^{EE} apparently do not have a high enough signal-to-noise ratio to sufficiently observe such an effect at small scales. Moreover, the constraints on the other parameters are only marginally affected by the additional information provided by lensing.Figure 2 shows the evolution of the constraints with $\ell_{\rm min}$. As previously noted for the CVL case in Section 2, the constraints from C_ℓ^{EE} rapidly worsen when $\ell_{\rm min} \gtrsim 130$, due to the fact that multipoles between $130 \lesssim \ell \lesssim 200$ help breaking degeneracies between $n_{\rm s}$ and other parameters. We notice in particular that $n_{\rm s}$ worsens by a factor ~ 3 if we cut $\ell_{\rm min} = 200$. This indicates that for C_ℓ^{EE}, the proper handling of the galactic dust contamination at large scales is crucial to have accurate results, as the observation in this $\ell-$range has such large impact on the constraints.

References

1. Galli, S., Benabed, K., Bouchet, F., et al. 2014, arXiv:1403.5271
2. Planck Collaboration, P. A. R. Ade, N. Aghanim, C. Armitage-Caplan, M. Arnaud, M. Ashdown, F. Atrio-Barandela, J. Aumont, C. Baccigalupi, A. J. Banday, et al., ArXiv e-prints (2013), `1303.5076`.
3. G. Rocha, R. Trotta, C. J. A. P. Martins, A. Melchiorri, P. P. Avelino, R. Bean, and P. T. P. Viana, MNRAS **352**, 20 (2004), `astro-ph/0309211`.
4. M. Tegmark, A. N. Taylor, and A. F. Heavens, ApJ **480**, 22 (1997), `astro-ph/9603021`.
5. Planck Collaboration (2005), http://www.rssd.esa.int/ SA/PLANCK/docs/Bluebook-ESA-SCI%282005%291_V2.pdf.
6. M. Zaldarriaga, Measuring and Modeling the Universe p. 309 (2004), `astro-ph/0305272`.
7. W. Hu and N. Sugiyama, ApJ **444**, 489 (1995), `arXiv:astro-ph/9407093`.

FUNDAMENTAL COSMOLOGY WITH ESPRESSO and ELT-HIRES

A. C. O. LEITE, C. J. A. P. MARTINS and P. O. J. PEDROSA
Centro de Astrofsica, Universidade do Porto, Rua das Estrelas, 4150-762 Porto, Portugal

The observational evidence for the acceleration of the universe demonstrates that canonical theories of cosmology and particle physics are incomplete, if not incorrect. Forthcoming high-resolution ultra-stable spectrographs will play a crucial role in the quest for new physics by enabling a new generation of precision consistency tests, including tests of the stability of nature's fundamental couplings. We discuss the improvements that can be expected with ESPRESSO and ELT-HIRES and quantify their impact on cosmology.

1 Introduction and Methods

We will drescribe how astrophysical measurements of natures dimensionless fundamental coupling constants can be used to study the properties of Dark Energy. (Nunes & Lidsey 2004 [2]). Our formalism is described in Amendola *et al.*[1], to which we refer the reader for further details. Here we will simply provide a brief summary of the features that will be relevant for our subsequent comparison with data.

One can divide the relevant redshift range into N bins such that in bin i the equation of state parameter takes the value w_i. The precision on the measurement of w_i can be inferred from the Fisher matrix of the parameters w_i. If the Fisher matrix is diagonalized, it defines a new basis in which the new coefficients α_i are uncorrelated. In this processes one also obtains the eigenvalues λ_i (ordered from largest to smallest) and the variance of the new parameters, $\sigma_i^2 = 1/\lambda_i$.

We consider models for which the variation of the fine-structure constant α is linearly proportional to the displacement of a scalar field, and further assume that this field is a quintessence type field, i.e. responsible for the current acceleration of the Universe. We take the coupling between the scalar field and electromagnetism to be

$$\mathcal{L}_{\phi F} = -\frac{1}{4} B_F(\phi) F_{\mu\nu} F^{\mu\nu}, \tag{1}$$

where the gauge kinetic function $B_F(\phi)$ is linear, $B_F(\phi) = 1 - \zeta\kappa(\phi - \phi_0)$, $\kappa^2 = 8\pi G$ and ζ is a constant to be marginalized over. This can be seen as the first term of a Taylor expansion, and should be a good approximation if the field is slowly varying at low redshift. Then, the evolution of α is given by

$$\frac{\Delta\alpha}{\alpha} \equiv \frac{\alpha - \alpha_0}{\alpha_0} = \zeta\kappa(\phi - \phi_0)\,. \tag{2}$$

For a flat Friedmann-Robertson-Walker Universe with a canonical scalar field, $\dot{\phi}^2 = (1+w(z))\rho_\phi$, hence, for a given dependence of the equation of state parameter $w(z)$ with redshift, the scalar field evolves as

$$\phi(z) - \phi_0 = \frac{\sqrt{3}}{\kappa} \int_0^z \sqrt{1+w(z)} \left(1 + \frac{\rho_m}{\rho_\phi}\right)^{-1/2} \frac{dz}{1+z}. \tag{3}$$

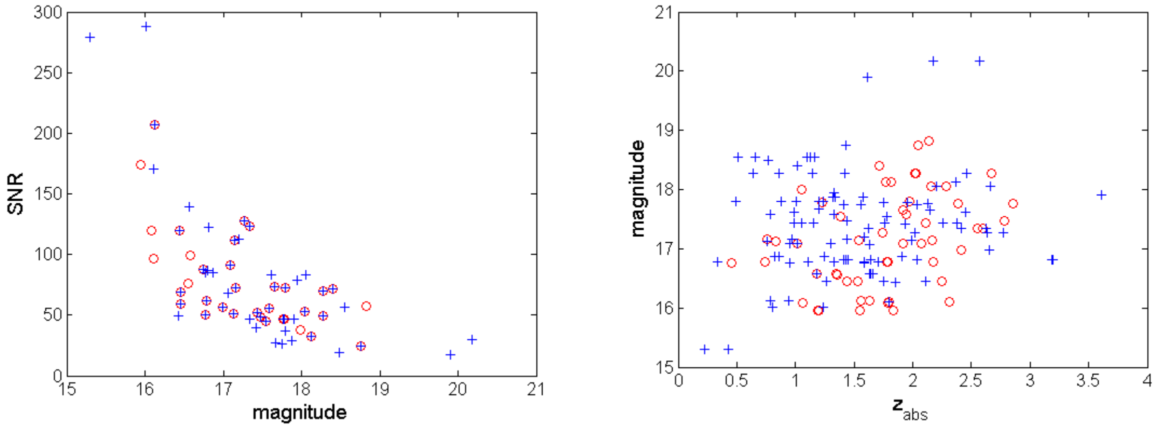

Figure 1 – Left: SNR-Magnitude correlation. Right: Absorption redshift-Magnitude correlation. In both cases the circles represent the best measurements (better then 10ppm accuracy) and crosses the other measurements.

where we have chosen the positive root of the solution.

From this one can calculate the Fisher matrix using standard techniques, as discussed in Amendola *et al.*[1]. As in that work, we will consider three fiducial forms for the equation of state parameter: $w_c(z) = -0.9$, $w_s(z) = -0.5 + 0.5 \tanh(z - 1.5)$, and $w_b(z) = -0.9 + 1.3 \exp\left(-(z-1.5)^2/0.1\right)$. At a phenomenological level, these describe the three qualitatively different scenarios. In what follows we will refer to these three cases as the *constant*, *step* and *bump* fiducial models.

In order to systematically study possible observational strategies, it's of interest to find an analytic expression for the behaviour of the uncertainties of the best determined PCA modes. We explore the range of parameters such as the number of α measurements (N_α) and the uncertainty in each measurement (σ_α). For simplicity we will assume that this uncertainty is the same for each of the measurements in a given sample. We take N_α between 20 and 200, uniformly distributed in redshift up to $z = 4$, and individual measurement uncertainties between 10^{-5} and 10^{-8}, and we find that the following fitting formula for the uncertainty σ_n for the n-th best determined PCA mode

$$\sigma_n = A \frac{\sigma_\alpha}{N_\alpha^{0.5}} \left[1 + B(n-1)\right]. \tag{4}$$

The present expression is accurate for all values up to and including $n = 6$, while for a smaller number of measurements the number of accurately determined modes is less than 6. The coefficients A and B will depend on the choice of fiducial model, and also on the number of PCA bins assumed for the redshift range under consideration. Assuming the constant fiducial model and 20 bins,the coefficients will be: $A = 1.14$ and $B = 0.52$, further results will be presented elsewhere[3].

2 Current VLT Data

The next step is to connect these theoretical tools to observational specifications. We can assume a simple (idealised) observational formula, $\sigma^2_{sample} = C/T$, where C is a constant, T is the time of observation necessary to acquire a sample of N measurements and σ_{sample} is the uncertainty in $\Delta\alpha/\alpha$ for the whole sample. This is expected to hold for a uniform sample (ie, one in which one has N_α identical objects, each of which produces a measurement with the same uncertainty σ_α in a given observation time). Clearly any real-data sample will not be uniform, so there will be corrections to this behaviour.

The uncertainty of the sample will be given by $\sigma^2_{sample} = 1/\sum_{i=1}^{N} \sigma_i^{-2}$, and for the above simulated case with N measurements all with the same α uncertainty we simply have $\sigma^2_{sample} =$

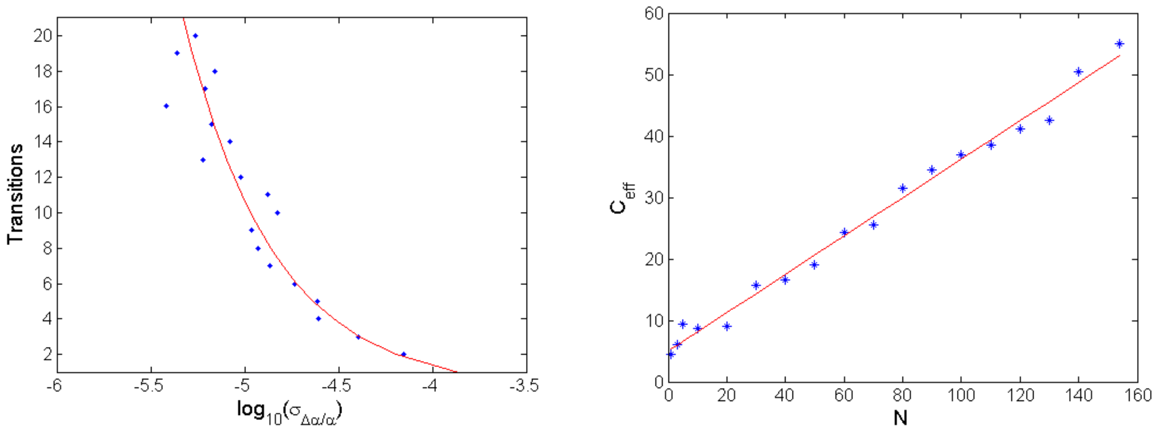

Figure 2 – Left: Correlation between the number of transitions used for a measurement and its uncertainty. Right: Values of the effective parameter C as a function of the number of systems considered. In both cases the red line is the best fit discussed in the text.

σ^2_α/N. Clearly there are also other relevant observational factors that a simple formula like this does not take into account, anyway this formula is adequate for our present purposes, as will be further discussed below.

We have used the UVES data from Julian King's PhD thesis[4], complemented by observation time data kindly provided by Michael Murphy, to build a sample to calibrate the observational formula. As can be seen in Figs. 1 , this sample is far form ideal, as it does not display the types of correlations that one would expect from such a sample.

We do find a strong correlation between the number of transitions used to make one measurement (N_λ) and the uncertainty corresponding to it, as can be observed in Fig. 2 where, for each N_λ, we plot the average uncertainty in the α measurements achieved with that number of transitions. We find the following approximate relation

$$\sigma_{\Delta\alpha/\alpha} = 1{,}39 \times 10^{-4} N_\lambda^{-1{,}11}\,. \tag{5}$$

One consequence of these properties of the sample is that the simple observational relation assumed will not strictly hold. Nevertheless, there is a simple way to correct it, which consists of allowing the former constant C to itself depend on the number of sources. This is easy to understand: in a small sample one typically will have the best available sources; by increasing our sample we'll be adding sources which are not as good as the previous ones, and therefore the overall uncertainty in the α measurement will improve more slowly than in the ideal case. Using standard Monte Carlo techniques we have generated several tens of thousands of sub-samples of the VLT sample, from which we infer the behaviour for the empirical function $C(N)$. The results of this analysis are shown in Fig. 2. We find that a good fit is provided by the linear relation

$$C(N) = 0.31\,N + 5.02\,. \tag{6}$$

here the constant has been normalised such that σ_{sample} is given in parts per million and T is in nights.

3 Future observational strategies

Putting together the observational studies from the previous sections we can combine Eq.4, the simple observational hypothesis and Eq.6, and get a general expression

$$\sigma_n = A[1 + B(n-1)]\left[\frac{aN_\alpha + b}{T}\right]^{0.5}\,. \tag{7}$$

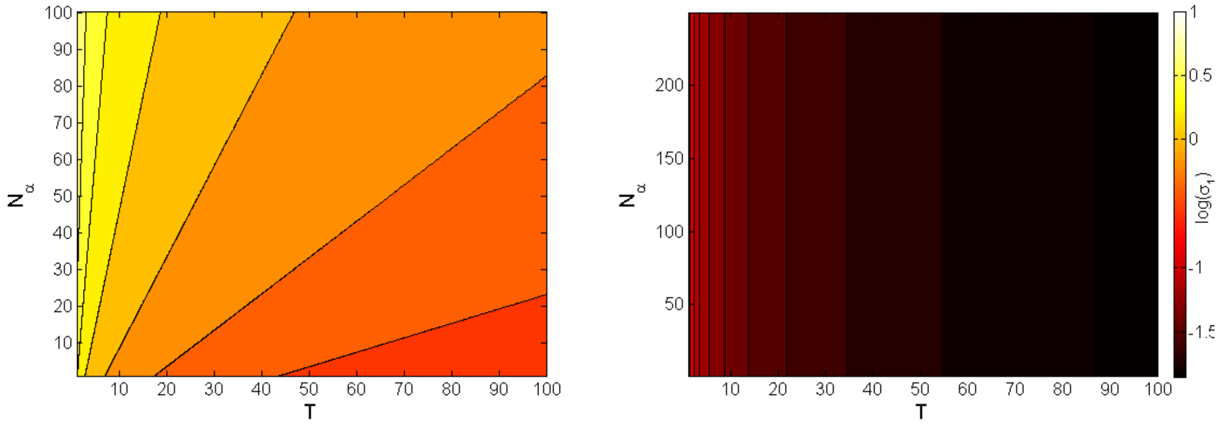

Figure 3 – Uncertainty of first mode in fuction of the observational time and the number of measurements. Left: A baseline scenario for ESPRESSO; Right: For ELT-HIRES.

The way we can extrapolate this formula to ESPRESSO and ELT-HIRES will be explored in detail in future work [3]. In Fig. 3 we show the behaviour of the uncertainty of the first mode with the time of observation and the number of measurements, assuming the constant fiducial model. It can be seen that indeed there is expected a big improvement using HIRES-ELT. Future improvements will come from a better sample selection, optimised acquisition/calibration methods and (in the case of the ELT-HIRES) from collecting power.

Further improvements will come from adding additional datasets. For example, the impact of adding supernova surveys such those of Euclid and ELTs to the PCA analysis can be quantified. The E-ELT case is particularly interesting due to the potentially higher redshift coverage (up to $z = 5$). A detailed study will be reported elsewhere [3].

Acknowledgments

We are grateful to Luca Amendola, Paolo Molaro, Michael Murphy, Nelson Nunes and John Webb for many interesting discussions and suggestions. Special thanks to Michael Murphy for providing us with the observation times for the VLT sources. We acknowledge the financial support of grant PTDC/FIS/111725/2009 from FCT (Portugal). CJM is also supported by an FCT Research Professorship, contract reference IF/00064/2012.

References

1. L. Amendola *et al.*, *Phys. Rev.* D **86**, 063515 (2012).
2. N.J. Nunes and J.E. Lidsey, *Phys. Rev.* D **69**, 123511 (2004).
3. A.C.O. Leite *et al.*, in preparation (2014).
4. J.A. King, PhD Thesis (UNSW, 2011), arXiv:1202.6366.

9.

Posters

Polarbear experiment: Data analysis of the first season

J. PELOTON* for the POLARBEAR collaboration: P.A.R. Ade, Y. Akiba, A.E. Anthony, K. Arnold, M. Atlas, D. Barron, D. Boettger, J. Borrill, S. Chapman, Y. Chinone, M. Dobbs, T. Elleflot, J. Errard, G. Fabbian, C. Feng, D. Flanigan, A. Gilbert, W. Grainger, N.W. Halverson, M. Hasegawa, K. Hattori, M. Hazumi, W.L. Holzapfel, Y. Hori, J. Howard, P. Hyland, Y. Inoue, G.C. Jaehnig, A.H. Jaffe, B. Keating, Z. Kermish, R. Keskitalo, T. Kisner, M. Le Jeune, A.T. Lee, E.M. Leitch, E. Linder, M. Lungu, F. Matsuda, T. Matsumura, X. Meng, N.J. Miller, H. Morii, S. Moyerman, M.J. Myers, M. Navaroli, H. Nishino, H. Paar, D. Poletti, E. Quealy, G. Rebeiz, C.L. Reichardt, P.L. Richards, C. Ross, I. Schanning, D.E. Schenck, B.D. Sherwin, A. Shimizu, C. Shimmin, M. Shimon, P. Siritanasak, G. Smecher, H. Spieler, N. Stebor, B. Steinbach, R. Stompor, A. Suzuki, S. Takakura, T. Tomaru, B. Wilson, A. Yadav, O. Zahn
AstroParticule et Cosmologie, Univ Paris Diderot, CNRS/IN2P3, CEA/Irfu, Obs de Paris, Sorbonne Paris Cité, France

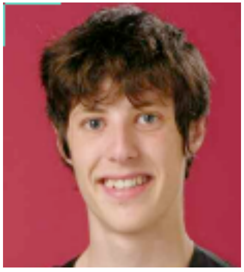

POLARBEAR is a ground-based cosmic microwave background (CMB) polarization experiment located on the Atacama Desert in Chile. The experiment has recently reported its first science results based on the analysis of the first data set collected during 2013 observational campaign. In this proceeding, I focus on the data analysis pipelines, which lead to the production of these results. I describe the data analysis challenge faced by the collaboration, highlighting some steps of the analysis from time-ordered data processing and map mapking to the power spectra estimation.

1 Introduction

In this short proceeding, I describe some parts of the data analysis pipeline used by the POLARBEAR collaboration to analyze the data recorded during the first season of observation [1] [2] [3]. For a detailed description, see also the proceeding by Giulio Fabbian[4].

2 Calibration and Low-level processing

Regular scientific observations of the CMB by POLARBEAR started in May 2012. The first season data set analysis focused on data collected between that date and June 2013. During this period, 3,300 hours of CMB observations and 500 hours of calibration were recorded. The first step of the data analysis is to produce high quality timestreams for each bolometers.

2.1 Instrument models

We model four primary instrument properties to calibrate our timestreams: individual detector pointing, thermal-response calibration, polarization angle, and the instrument effective beam. To be able to constrain these models, we perform several observations per week of astrophysical objects, and ground-based calibrators were also used.

2.2 Data cuts

We reject data which were recorded when the instrument was not functioning properly by using a data selection model. The amount of data removed each time depends on the type of problem detected. We also completely discard data acquired when the scanning velocity of the telescope was not constant. After this procedure, 30,9% of the data by weight is removed. Of the 1274 optical TES bolometers in the POLARBEAR focal plane, 810 bolometers are used in the reported measurement and the resulting median number of bolometers used to make maps after cuts is 602. Then pixel-pair bolometers are summed and differenced to derive temperature and polarization timestreams from each pixel.

2.3 Filtering and noise weights

The noise weights used for the co-addition are estimated by averaging the time domain power spectral density from 1-3 Hz per subscan with a typical scan speed of 0.75°/s, under the assumption that the noise is white. Our investigations show that this hypothesis gives a nearly optimal solution. As far as temperature is concerned, the most important source of excess low frequency noise is the atmosphere, therefore we filter using a cubic polynomial per constant velocity subscan. Being the atmosphere largely unpolarized, the contamination is less important for the differenced timestreams so linear polynomials are subtracted in polarization. A low pass filter is also applied with a knee frequency at 7.5 Hz to avoid the aliasing of high frequencies during the map making step.

Finally, we project out scan-synchronous signals by averaging the timestreams in 0.08° azimuth bins for each bolometer to build a scan-synchronous signal template during a Constant Elevation Scan (CES). The template is then subtracted from the timestreams

3 Map making and power spectrum estimation

Once timestreams are cleaned, sky maps are produced. Our data model connects the time-ordered data d_t to the sky signal s_p via the pointing matrix A_{tp}:

$$d_t = A_{tp} s_p + n_t, \tag{1}$$

where n_t is the noise component. Considering the raw data of POLARBEAR , the number of time samples $\mathcal{N}_t$ is of the order of 10^{13}. The processing of such large data set was a challenge faced by the collaboration [5]. After the filtering of the timestreams to suppress the modes with a low signal-to-noise ratio, we construct per day a set of flat maps per CES, using the cylindrical equal area projection centered at the nominal patch center with a pixel width of $2'$. We co-add the single-CES, all-detector maps into a set of single-day I, Q and U maps, leading to a number of pixels per map $\mathcal{N}_{pixels}$ of the order of 10^5. The three patches observed by POLARBEAR have 148, 139 and 189 daily maps respectively. Finally, pure pseudo-power spectrum approach is used to extract power spectra [6].

References

1. POLARBEAR Collaboration 2013a, *Phys. Rev. Lett.* **112**, 131302 (2014)
2. POLARBEAR Collaboration 2013b, accepted by *Phys. Rev. Lett* (arXiv:1312.6646)
3. POLARBEAR Collaboration 2014, arXiv:1403.2369
4. Fabbian, G. 2014, Proceedings of the 49th Rencontres de Moriond
5. Borrill, Julian, *AIP Conf. Proc.* **476**, 277-282 (1999)
6. Smith, K. M., *Phys. Rev.* D **74**, 083002 (2006)

THE 3D SHAPE OF GALAXY CLUSTERS: THEORETICAL EXPECTATIONS FROM THE MILLENNIUM XXL SIMULATION

MARIO BONAMIGO[1], MARCEAU LIMOUSIN[1], RAUL ANGULO[2], GENEVIÈVE SOUCAIL[3]
[1] *Aix Marseille Université, CNRS, Laboratoire d'Astrophysique de Marseille UMR 7326, 13388 Marseille, France*
[2] *Centro de Estudios de Física del Cosmos de Aragón, Plaza San Juan 1, Planta-2, 44001, Teruel, Spain*
[3] *Observatoire Midi-Pyrénées, Institut de Recherche en Astrophysique et Planétologie, F31400 Toulouse, France*

While clusters of galaxies are considered one of the most important cosmological probes, their standard spherical modeling is only a rough approximation; it is well established that they are much better described as triaxial objects and it has been shown that the spherical assumption has a strong impact on the inferred cluster's properties which constitute the key ingredients of several cosmological tests. We present the first results of a triaxial analysis of the Millennium XXL simulation. Our goal is to derive axis ratio distributions of the dark matter inferred within a triaxial framework and their dependence on mass and dynamical state of clusters.

1 Why going triaxial?

A new framework has been recently developed to simultaneously fit complementary data sets (X-ray, SZ, lensing) within a triaxial context [?]; it has shown that the spherical assumption has a strong impact on the inferred cluster's properties which constitute the key ingredients of several cosmological tests. For example, adopting this triaxial model [?], the long lasting puzzle of Abell 1689 can be solved; in a spherical analysis the cluster has a very high concentration (up to 15) and shows a discrepancy (a factor of 2) between masses obtained from Strong Lensing and X-Ray. This framework has been successfully applied also to MACS 1423, Abell 383 and Abell 1835. These results strongly suggest that in the road map of "precision cosmology" with galaxy clusters, triaxial modeling is the next milestone. However we lack of theoretical expectations from simulations of the shape of large galaxy clusters; the aim of this work is to provide these crucial prediction in a mass range never explored before.

2 Halo catalogue

We have studied haloes from the Millennium XXL [?] a DM only Nbody simulation with $6720^3 \approx 3 \times 10^{11}$ particles of mass $6.174 \times 10^9 h^{-1}\mathrm{M}_\odot$, in a box of side $3h^{-1}$Gpc. The cosmology is the same of the Millennium simulation (WMAP): $\Omega_m = 0.25$, $\Omega_\Lambda = 0.75$, $\Sigma_8 = 0.9$ and $h = 0.73$. We restricted the analysis to only Friend of Friend (FOF) groups with mass $M_{FOF} > 10^{14} h^{-1}\mathrm{M}_\odot$ (781059 haloes) and computed the triaxial shape from the eigenvalues of the mass tensor [?], which we used to get a new set of particles and iterate this procedure until convergence. Finally we discarded all new triaxial haloes with a virial mass lower than $10^{14} h^{-1}\mathrm{M}_\odot$, which represent an incomplete sample, and those which centre of mass is at a distance greater than 5% of their radius from their minimum of potential; this leaves 357515 (45.7%) unperturbed haloes.

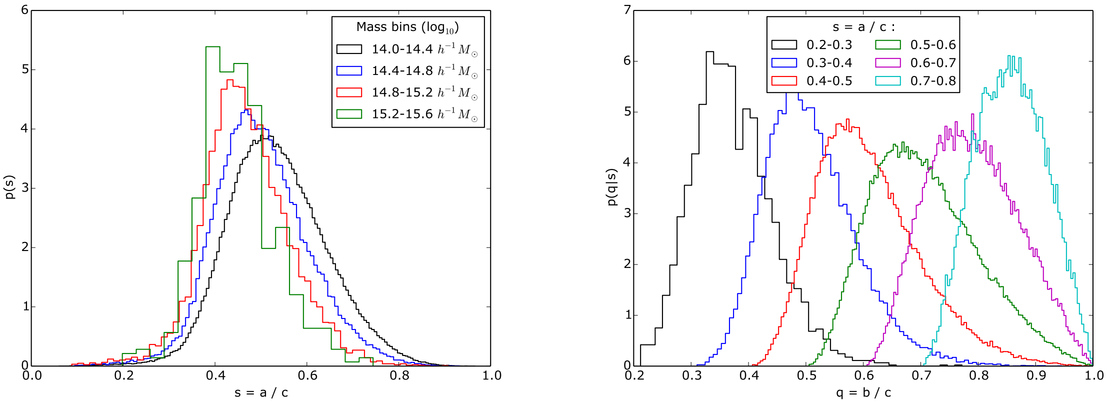

Figure 1 – (right panel): Probability distribution function of $s = a/c$ binned in mass. (left panel): Conditional distributions $p(q|s)$, with $q = b/c$. Different colors represent the distributions for six bins in s

3 Measured shapes

Left panel of Fig. 1 shows the distributions of minor to major axis ratio $s = a/c$ in different mass bins, where $c > b > a$ are the axes of the ellipsoid; it can be seen that more massive haloes have a lower s which means they are more aspherical. The conditional probability distribution function of the intermediate to major axis ratio $q = b/c$, given a value of s, is shown on the right panel; we can see that, although triaxial, haloes tend to be prolate rather than oblate.

We were able also to retrieve the distribution of the projected ellipsoid in the plane of the sky, using two different orientation of the major axis with respect to the line of sight: a random orientation and the orientation distribution of massive strong lensing clusters [?].

4 Conclusions

We have provided the first measurement of the triaxiality in the galaxy clusters mass range from $10^{14}h^{-1}\mathrm{M}_\odot$ to $4 \times 10^{15}h^{-1}\mathrm{M}_\odot$. We have also produced projected ellipsoids with both a random and a biased orientation, which can be directly compared with observational mass distributions. Moreover, we have obtained a functional form of the triaxial shape, which let us produce statistically relevant prediction on the axis ratio of haloes in a range of mass of more than 5 orders of magnitude. These results will be summarized in a paper in preparation.

Acknowledgments

This work has been carried out thanks to the support of the OCEVU Labex (ANR-11-LABX-0060) and the A*MIDEX project (ANR-11-IDEX-0001-02) funded by the "Investissements d'Avenir" French government program managed by the ANR.

References

SZ AND X-RAY TEMPERATURES OF CLASH CLUSTERS WITH AMI

CLARE RUMSEY
Astrophysics Group, Cavendish Laboratory, Cambridge University, Cambridge, UK

Temperatures of CLASH galaxy clusters have been calculated from SZ measurements made with the Arcminute Microkelvin Imager (AMI) [1], a dual array of interferometers observing at 15 GHz, located near Cambridge. The arrangement of ten 3.7 m antennas with baselines of 5–20 m in the Small Array (SA) and eight 12.8 m antennas with baselines of 18–110 m in the Large Array (LA) allows for study of the large-scale SZ effect from clusters and accurate subtraction of confusing source environments. These SZ temperarures are compared with temperatures from *Chandra* X-ray measurements and highlight tensions in measurement methods due to dynamical state.

1 The CLASH sample

The CLASH (Cluster Lensing and Supernova Survey with Hubble) sample consists of 25 massive clusters[2]: 20 selected from *Chandra* X-ray observations to be dynamically relaxed and 5 selected solely for their high lensing strength, consequently including some of the most disturbed clusters known [3]. We have observed all 11 CLASH clusters accessible to AMI and reject one due to a very difficult source environment. This gives good SZ detections of 10 of the CLASH sample, 7 from the X-ray selected members and 3 from the lensing-selected.

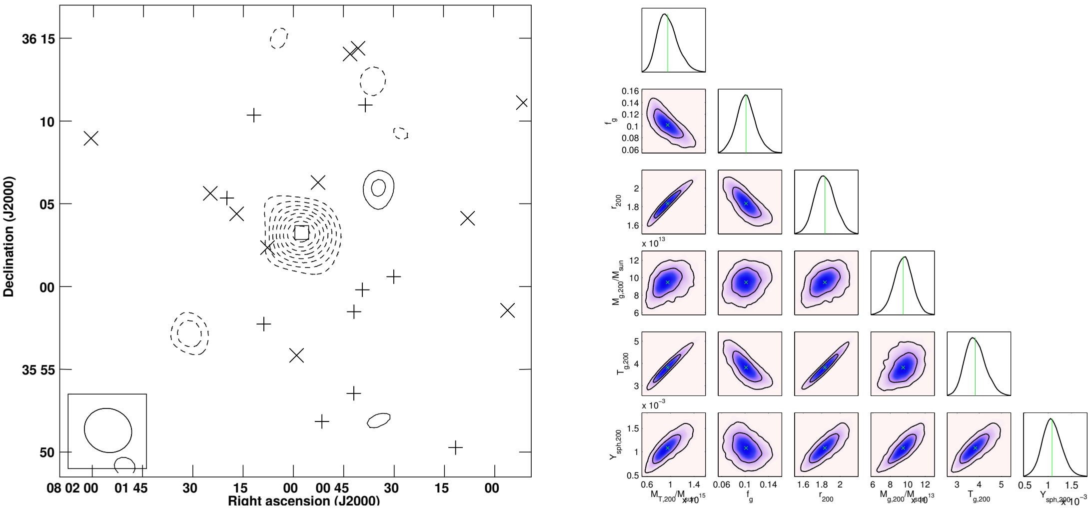

Figure 1 – Left: Source-subtracted SA map for example cluster A611. Solid contours are positive emission, dashed are negative. Right: Probability distributions for some key parameters for A611.

Analysis of this data is carried out in uv-space using our Bayesian analysis package McAdam which uses an NFW model to describe the dark matter distribution in a cluster and a GNFW model to describe the pressure profile of the cluster gas. This determines the probability densities of physical quantities of the clusters (Fig. 1, right). Full details of the model used here can be found in Olamaie, Hobson & Grainge (2012)[4].

Table 1: Some McAdam derived large-scale cluster parameters for the AMI sub-sample. Uncertainties are 1σ

Cluster	$M_{T(r_{200})}(\mathrm{M}_\odot)$	r_{200}(Mpc)	$T_{g(r_{200})}$(keV)	Redshift
A611	9.5×10^{14}	1.8	3.8	0.288
A1423	6.2×10^{14}	1.6	2.8	0.213
A2261	1.6×10^{15}	2.2	5.2	0.224
CLJ1226+3332	5.7×10^{14}	1.3	3.2	0.890
MAJ0647+7015	1.5×10^{15}	1.9	5.9	0.584
MAJ0717+3745	1.6×10^{15}	2.0	6.0	0.548
MAJ0744+3927	1.4×10^{15}	1.8	5.7	0.686
MAJ1149+2223	1.9×10^{15}	2.1	6.7	0.544
MAJ1423+2404	9.8×10^{14}	1.7	4.3	0.545
RXJ1532+3021	8.0×10^{14}	1.7	3.5	0.345

2 Temperature comparison with X-ray

The ACCEPT database[5] provides *Chandra* spectroscopic, annular-averaged temperature profiles for our whole sub-sample. We choose the largest radius reached by the profiles of all 10 of our sub-sample, approximately 700 kpc. McAdam calculates the gas temperature profile from the SZ signal using a tight prior on the value of f_{gas} at r_{200}, and assumptions of hydrostatic equilibrium throughout. Using this, we can compare T_{SZ} with T_{X} at a given radius for each cluster.

A second *Chandra*-based value of T_{X} for A611 is found in Donnarumma et al. (2011)[6] and is included as A611* along with the value from ACCEPT. When interpreting the plot shown in Fig. 2, one should note that: (i) shocking and clumping each push T_{X} high as it is n_{g}^2 weighted, and departure from virialisation will push T_{SZ} high; (ii) MAJ1149+2223 is very disturbed[7] and so non-circular that annular averaging biases T_{X} low; (iii) X-ray imaging suggests that MAJ1423+2404 and A2261 are among the most relaxed in our sample. With these points in mind, it is clear that the dynamical state of a cluster has a significant effect on where it falls on this plot.

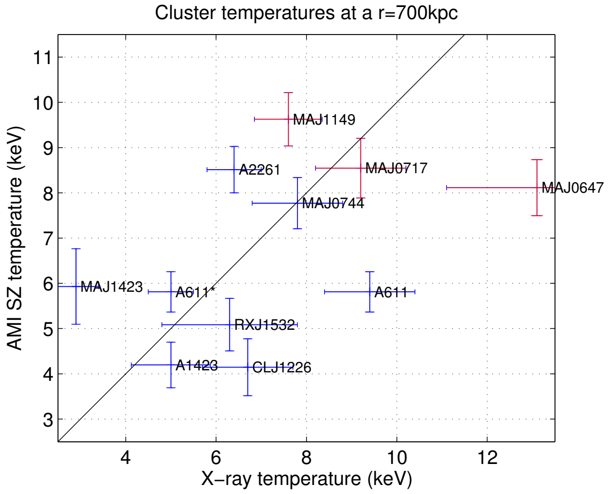

Figure 2 – SZ and X-ray temperatures at r =700 kpc. The 1:1 line is the line of $T_{\mathrm{SZ}} \propto T_{\mathrm{X}}$ and not a fit. Error bars are 1σ. The 3 clusters in red are the lensing-selected CLASH members accessible to AMI.

References

1. AMI Consortium: Zwart J. T. L. et al., 2008, MNRAS, 391, 1545.
2. Postman M. et al., 2012, ApJS, 199, 25.
3. Redlich M. et al., 2012, A&A, 547, A66.
4. Olamaie M., Hobson M. P., Grainge K. J. B., 2012, MNRAS, 423, 1534.
5. Cavagnolo K. W. et al., 2009, ApJS, 182, 12.
6. Donnarumma A. et al., 2011, A&A, 528, 73.
7. Smith G. P. et al., 2009, ApJ, 707, L163.
8. AMI Consortium: Rodríguez-Gonzálvez C. et al., 2012, MNRAS, 425, 162.

High resolution density reconstruction from 3D lensing
Application to galaxy clusters

F. Lanusse, A. Leonard, J.-L. Starck
Laboratoire AIM, UMR CEA-CNRS-Paris 7, Irfu, Service d'Astrophysique, CEA Saclay, France

Using the 3D information provided by photometric or spectroscopic weak lensing surveys, it has become possible in the last few years to address the problem of mapping the matter density in three dimensions from gravitational lensing. We recently proposed a new non linear sparsity based reconstruction method allowing for high resolution reconstruction of the density. This new technique represents a significant improvement over previous linear methods and opens the way to new applications of 3D weak lensing density reconstruction. In particular, we demonstrate that galaxy clusters can now be detected and characterized in mass an redshift from photometric weak lensing data alone.

1 Introduction

While techniques exist to generate high-fidelity two-dimensional projected weak-lensing maps, it was not until recently that several linear methods were developed to reconstruct a full three-dimensional density map from photometric weak lensing measurements[1] [2]. However, even the most successful linear methods for 3D lensing density mapping suffer important limitations. In particular there is a broad smearing of structures along the line of sight, the amplitude of the reconstruction can be severely underestimated and they remain very noisy. To address these issues we recently proposed GLIMPSE [3], a non linear sparsity based method, which drastically improves the quality of reconstructed 3D maps. This method relies on iteratively solving an optimization problem, looking for the sparsest solution in an appropriate wavelet based dictionary. Contrary to the linear methods, structures are no longer smeared along the line of sight and we see no systematic bias in the reconstructed redshifts or in the reconstructed density of these structures.

Thanks to the increased quality of our density maps, it is now possible to measure density contrasts and redshifts of structures directly from the lensing reconstruction. In particular, we demonstrate here that galaxy clusters can be detected and constrained in mass and redshifts in the context of a wide weak lensing survey with photometric information.

2 Reconstruction of simulated galaxy clusters

To statistically assess the performance of GLIMPSE for the reconstruction of galaxy clusters, we generate a large number of simulated weak lensing fields for typical NFW halos. Each field contains the lensing signal for a single cluster of virial mass ranging from $3.10^{13}h^{-1}$ M$_\odot$ to $1.10^{15}h^{-1}$ M$_\odot$ and redshifts between $z = 0.05$ and $z = 0.75$, taking into account photometric redshift errors. Assuming a typical level of noise for space based weak lensing surveys ($n_{gal} = 30$ arcmin^{-2} and galaxy intrinsic ellipticity of $\sigma_\epsilon = 0.25$) we generate for each field 1000 independent noise realisations and perform a 3D reconstruction for each of them. Figure 1(a) shows the fraction of detected clusters over the 1000 noise realisations for each cluster in our sample.

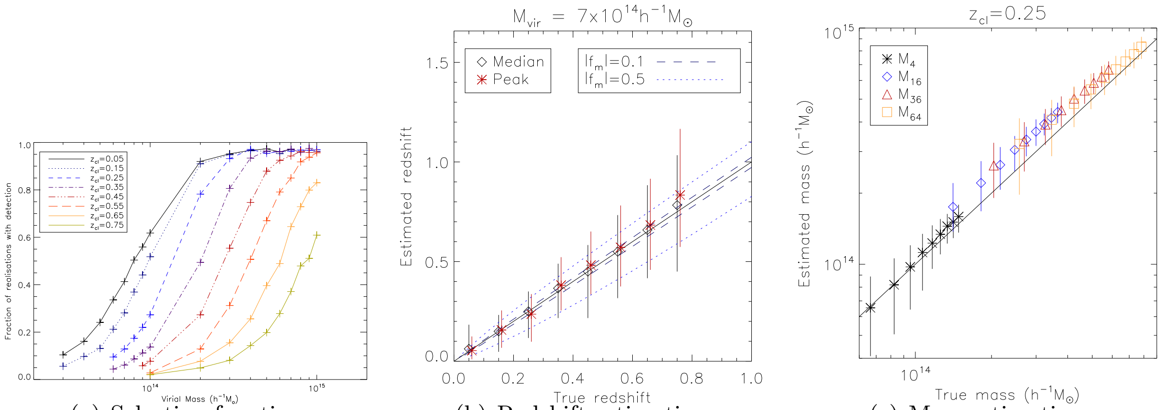

(a) Selection function (b) Redshift estimation (c) Mass estimation

Figure 1 – Left: Fraction of detected cluster over 1000 noise realisations as a function of mass and redshift. Center: Redshift of reconstructed halos as a function of true redshift for a cluster of $7.10^{14}h^{-1}\mathrm{M}_\odot$. Red points indicate the peak of the AKDE distribution while the black points indicate the median of the reconstruction. The dashed and doted lines correspond to the error in redshift that would result in respectively 10 % and 50% error in mass estimate. Right: Estimated mass against true mass for several mass proxies obtained by integrating the density over 4, 16, 32 and 64 pixels for a cluster at $z = 0.25$

Figure 1(b) shows the estimated versus true redshift for clusters in our sample as a function of mass. Shown in the figure are the median estimate and the adaptive kernel density estimate (AKDE) peak redshift, the latter being offset by $\delta z = 0.01$ in both directions for visualisation purposes. Both estimates clearly yield an accurate estimate of the redshift, with the peak estimate seen to have smaller error bars in many cases. No systematic bias is seen in the peak case. Figure 1(c) shows the estimated mass of the reconstructed clusters if the reconstructed redshift is accurate using as a proxy the integrated density within the central 4, 16, 32 and 64 pixels. We see that this very simple proxy gives a good handle on the true mass of the clusters and is certainly competitive with other cluster mass proxies from optical or X-ray surveys.

3 Conclusion

The improvement in three-dimensional map quality allowed by the GLIMPSE algorithm opens the way for new applications of 3D weak lensing map making. In particular, we have characterized the detection limit of dark matter halos as a function of mass and redshift and the accuracy of the redshift and masses estimations of the reconstructions. From these results, we believe that 3D density mapping from weak gravitational lensing has now entered the regime where it can be used as a useful cosmological probe.

Acknowledgments

The authors would like to thank Gabriel Rilling, Jerome Bobin, Florent Sureau, Sandrine Pires, Martin Kilbinger and Paniez Paykari for useful discussions. This work is supported by the European Research Council grant SparseAstro (ERC-228261).

References

1. P. Simon, A. J. Connolly, B. Jain, and M. Jarvis, *MNRAS* **399**, 48-68 (2009).
2. J. T. VanderPlas, A. N. Taylor, and J. Hartlap, *ApJ* **727**, 118 (2011).
3. A. Leonard, F. Lanusse, and J.-L. Starck, *MNRAS* **440**, 1281-1294 (2014).

BAYESIAN INFERENCE OF DARK MATTER VOIDS IN GALAXY SURVEYS

FLORENT LECLERCQ[1,2,3]
[1] *Institut d'Astrophysique de Paris (IAP), UMR 7095, CNRS - UPMC Université Paris 6, 98bis boulevard Arago, F-75014 Paris, France*
[2] *Institut Lagrange de Paris (ILP), Sorbonne Universités, 98bis boulevard Arago, F-75014 Paris, France*
[3] *École polytechnique ParisTech, Route de Saclay, F-91128 Palaiseau, France*

We apply the BORG algorithm to Sloan Digital Sky Survey Data Release 7. The method results in the physical inference of the four-dimensional initial density field at redshift $z = 1000$, evolving gravitationally to the observed density field at redshift $z = 0$, and provides an accurate quantification of corresponding uncertainties. Building upon these results, we generate a set of constrained reconstructions of the present large-scale dark matter distribution. As a physical illustration, we apply a void identification algorithm to them. In this fashion, we access voids defined by the inferred dark matter field, not by galaxies, greatly alleviating the bias problem. In addition, the use of full-scale physical density fields yields a drastic reduction of statistical uncertainty in void catalogs. This new catalog is an enhanced data set for cross-correlation with other cosmological probes.

1 Bayesian physical inference of the initial conditions

We apply [1] the full-scale Bayesian inference code BORG (Bayesian Origin Reconstruction from Galaxies) [2] to the galaxies of the `Sample dr72` of the New York University Value Added Catalogue (NYU-VAGC [a]), based ot the final data release (DR7) of the Sloan Digital Sky Survey (SDSS). The physical model for gravitational dynamics is second-order Lagrangian perturbation theory (2LPT), linking initial density fields ($z = 1000$) to the presently observed large-scale structure, in the linear and mildly non-linear regime. The algorithm explores numerically the posterior distribution by sampling the joint distribution of all parameters involved, via efficient Hamiltonian Markov Chain Monte Carlo (HMC) dynamics.

Each sample (Fig. 1, upper panel) is a "possible version of the truth" in the form of a full physical realization of dark matter particles, tracing both the density and the velocity fields. The variation between samples (Fig. 1, lower panel) quantifies joint and correlated uncertainties (survey geometry, selection effects, galaxy bias, noise) inherent to any cosmological observation.

2 Data-contrained realizations of the Universe

We generate [3] of a set of data-constrained realizations of the present large-scale structure: some samples of inferred primordial conditions are evolved with 2LPT to $z = 69$, then with a fully non-linear cosmological simulation (using GADGET-2 [4]) from $z = 69$ to $z = 0$.

A dynamic, non-linear physical model naturally introduces some correlations between the constrained and unconstrained parts, which yields reliable extrapolations for certain aspects of

---

[a] http://sdss.physics.nyu.edu/vagc/

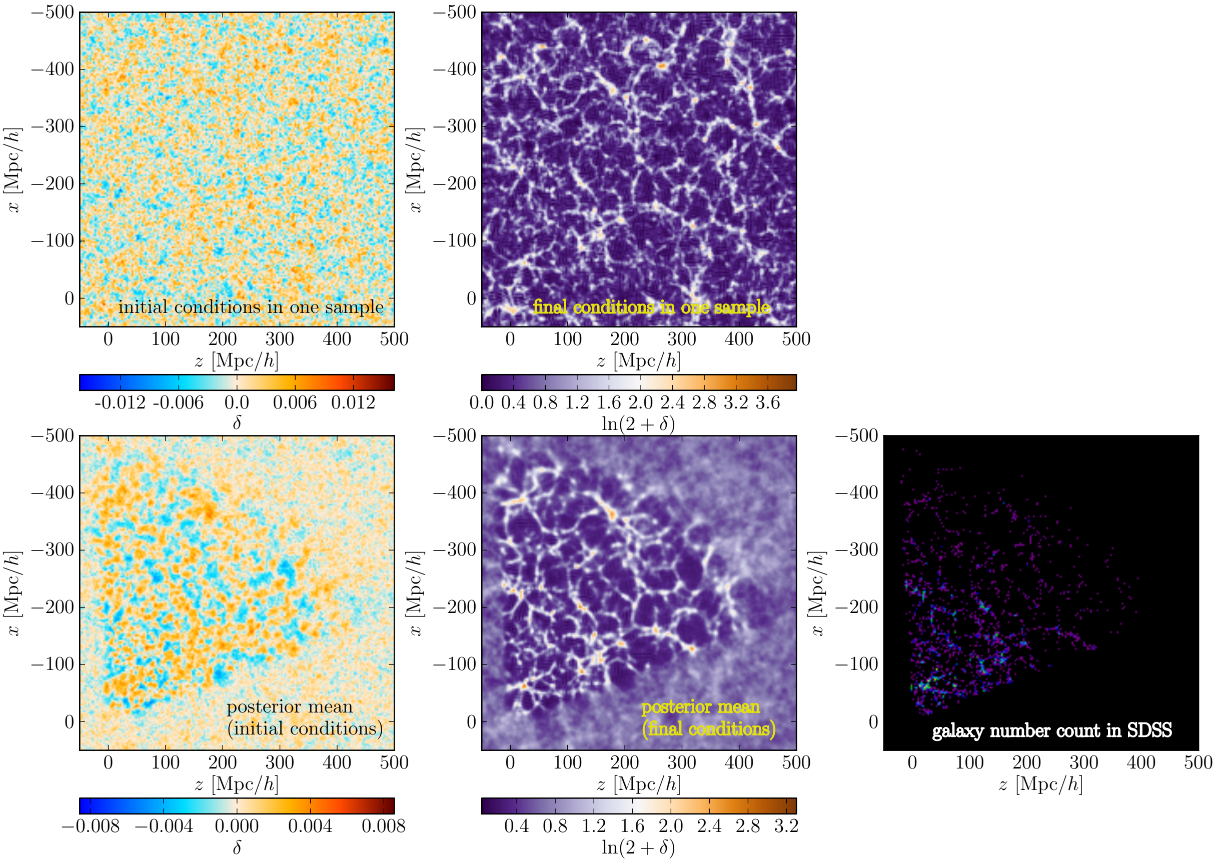

Figure 1 – Bayesian large-scale structure inference with BORG. Upper panel: slices through one sample of the posterior for the initial (left) and final (center) density fields. Lower panel: posterior mean in the initial (left) and final (center) conditions, compared to the input data (right).

the model that have not yet been constrained by the data (e.g. near the survey boundaries or at high redshift).

3 Dark matter voids in the SDSS galaxy survey

We apply[5] VIDE (the Void IDentification and Examination pipeline[b]) to the constrained parts of these realizations. The void finder is a modified version of ZOBOV[6] that uses Voronoi tessellations of the tracer particles to estimate the density field and a watershed algorithm to group Voronoi cells into voids.

We find physical cosmic voids in the field traced by the dark matter particles, probing a level deeper in the mass distribution hierarchy than galaxies, and greatly alleviating the bias problem for cosmological interpretation of final results. Due to the high density of tracers, we find about an order of magnitude more voids at all scales than the voids directly traced by the SDSS galaxies (Fig. 2, left panel), which sample the underlying mass distribution only sparsely[7]. Our inference framework therefore yields a drastic reduction of statistical uncertainty in voids catalogs. For usual voids statistics such as radial density profiles of stacked voids[8], the results we obtain are consistent with N-body simulations prepared with the same setup (Fig. 2, right panel).

---

[b] http://www.cosmicvoids.net/

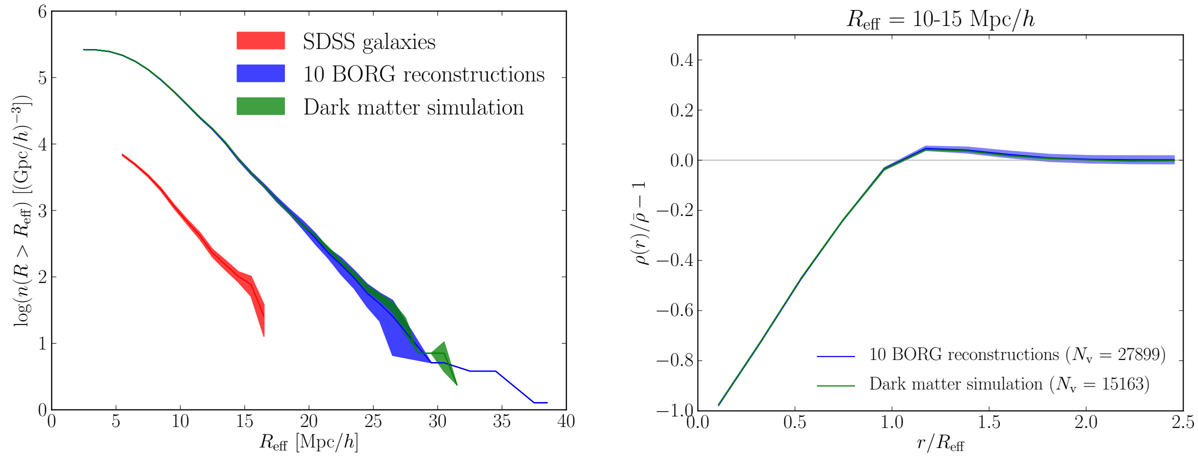

Figure 2 – Left panel: void number count in 10 BORG reconstructions (blue), compared to the voids found in a N-body simulation prepared with the same setup (green) and to the voids directly traced by the SDSS galaxies (red). Right panel: density profile for stacked voids of radius between 10 and 15 Mpc/h in the same void catalogs.

Acknowledgments

I thank Nico Hamaus, Jens Jasche, Paul Sutter and Benjamin Wandelt for fruitful collaborations and useful discussions. I acknowledge funding from an AMX grant (École polytechnique ParisTech) and Benjamin Wandelt's senior Excellence Chair by the Agence Nationale de la Recherche (ANR-10-CEXC-004-01). This work made in the ILP LABEX (ANR-10-LABX-63) was supported by French state funds managed by the ANR within the Investissements d'Avenir programme (ANR-11-IDEX-0004-02).

References

1. J. Jasche, F. Leclercq, B. Wandelt, *in prep.*
2. J. Jasche, B. D. Wandelt, *MNRAS* **432**, 894 (2013).
3. J. Jasche, F. Leclercq, E. Romano-Díaz, B. Wandelt, *in prep.*
4. V. Springel, *MNRAS* **364**, 1105 (2005).
5. F. Leclercq, J. Jasche, P. M. Sutter, N. Hamaus, B. Wandelt, *in prep.*
6. M. C. Neyrinck, *MNRAS* **386**, 2101 (2008).
7. P. M. Sutter, G. Lavaux, B. D. Wandelt, N. Hamaus, D. H. Weinberg, M. S. Warren, arXiv:1309.5087.
8. N. Hamaus, P. M. Sutter, B. D. Wandelt, arXiv:1403.5499.

Improving SNIa detection using Morphological Component Analysis

Anais Möller
CEA Saclay/Irfu/SPP and Université Paris Diderot 7

Detection of supernovae (SNe) and, more generally, of transient events in large surveys can provide numerous fake detections. In the case of a deferred processing of survey images, this leads to reconstruct complete light curves for all detections which requires sizable processing time and resources. Optimizing the detection of transient events is thus an important issue for both present and future surveys. We present here the optimization done in the SuperNova Legacy Survey for the 5-year data differed photometric analysis. In this analysis, detections are derived from stacks of subtracted images with one stack per lunation. The 3-year analysis provided 300,000 detections dominated by signals of bright objects which were not perfectly subtracted. We developed a subtracted image stack treatment to improve detection of SN-like events using morphological component analysis. This technique exploits the morphology of objects to be detected to extract the signal of interest. At the level of our subtraction stacks, SN-like events are rather circular objects while most spurious detections exhibit different shapes. A two-step procedure was necessary to have a proper evaluation of the noise in the subtracted image stacks and thus a reliable signal extraction. When tested on SNLS 3-year data this procedure yielded a reduction of one fourth of the detections with a loss of less than 6% of faint SN-like events.

1 SNLS Photometric Pipeline

SNLS is part of the Deep Synoptic Survey conducted on the Canada-France-Hawaii Telescope (CFHT). It was designed for detecting hundreds of SNe Ia in a redshift range between 0.2 and 1. Using the MegaCam imager [2], an array of 36 CCD with 340 million of pixels, four one square degree fields were targeted throughout 5 or 7 consecutive lunations using four different broadband filters g_M, r_M, i_M and z_M in the wavelength range from 400 to 1000 nm.

The deferred photometric pipeline of SNLS is independent of the real time standard analysis and classifies SNe using only photometric measurements [3]. The feasability of detecting SNIa with this deferred analysis was proven for the 3-year SNLS data [1].

1.1 Detection of transient events

At CFHT images are preprocessed to perform flat-fielding and to remove defects. Images are then matched to sky coordinates applying an astrometric solution. Reference images are constructed taking a set for each field of best quality images which are coadded. Each image of the survey has the reference image subtracted.

Distant SNe in SNLS are detected in the i_M filter since their maximum flux is at this filter wavelenght. Stacks are constructed coadding all subtracted images in a lunation to increase the signal-over-noise ratio. Detection is done by SExtractor using a signal-over-noise ratio.

Detection for the SNLS-3 yielded around 300,000 candidates dominated by spurious objects due to bad subtraction [1]. An optimization is relevant for the detection of SNe in a larger image sample such as the 5-year SNLS photometric analysis.

2 Optimization on the detection of SNe

Spurious detections have particular shapes and sizes which differ from those of a SN in a subtracted image stack, which can be exploited using morphological component analysis [4].

2.1 Morphological component analysis (MCA)

The hypothesis of MCA is that an image can be decomposed in different dictionaries made from signal atoms [4] [5]. An atom is an elementary template which represents a signal, e.g. a sinusoid or a wavelet. A family of atoms at different scales is called a dictionary. An image can be decomposed in a set of given dictionaries. At each scale a threshold can be applied on the decomposition coefficients. The reconstruction of the image is done superimposing selected atoms for a given shape and scale.

2.2 First treatment

Subtracted images contain SNe which are circular-like shaped signals. Spurious detections come mostly from residuals of bright stars, elongated shapes, and other types of residuals as for example imperfect fringe subtraction.

The algorithm by Starck et al. [4] was adapted for the treatment of our subtracted image stacks. Dictionaries chosen for the decomposition were: wavelets(modified starlet and bi-orthogonal wavelet), curvelets and ridgelets. Reconstruction only took into account wavelets at chosen scales and a background of noise residuals. This algorithm supports masks but assumes a stationary and gaussian noise which is not the case in our stacks.

2.3 Second treatment

An utility was developed that handles both non-stationary noise and exploits further morphological decomposition [4]. The utility decomposes the signal in the bi-orthogonal wavelet dictionary and constructs a non stationary noise map using block sizes of 50 pixels. All signals present in the output are considered as transient event candidates.

3 Results

The optimization method was tested on a sample of the 3-year SNLS data within the deferred photometric pipeline. A reduction on the number of detections of almost a factor four is accomplished. The original method yielded 90.971 detections and after the two step treatment only 23.810 remain. Loss of SN-like candidates is less than 6% mostly very faint events not suitable for future cosmological analysis.

The implementation of such optimization for the 5-year analysis gave a similar reduction factor. The original deferred detection resulted in 507.133 detections, while 142.484 detections remained after our optimization .

References

1. G. Bazin, V. Ruhlmann-Kleider, et al., *A&A*, 534, 2011.
2. O. Boulade, X. Charlot et al., *Proc.SPIE*, 4841,2003.
3. J. Guy, M. Sullivan, et al., *A&A*, 523, 2010.
4. J.L. Starck, F. Murtagh, and J. Fadili, Sparse Image and Signal Processing: Wavelets, Curvelets, Morphological Diversity , Cambridge University Press, 2010.
5. M. Elad, J.-L Starck, D. Donoho and P. Querre, *ACHA* , Vol. 19, pp. 340-358, November 2005.

Photometry of Supernovae in an image series

Patrick El-Hage
LPNHE - 4 place Jussieu - CC200
75005 PARIS

The photometry of SNe aims to construct the light curves of these faint objects. Contrary to the photometry of standard stars, this requires us to take into account the light emitted by the SN host galaxy. In order to remain below the uncertainty level of the calibration, we aim to construct a photometry method whose uncertainty does not exceed the per mil level.

1 Photometric Algorithm

1.1 PSF Photometry

SNLS employs direct simultaneous photometry. This consists of fitting a time-independent pixellised galaxy model and a time-variable point source to the image series, forcing the flux to zero in images where the SN is 'off'. Surrounding stars are measured similarly but without fitting a galaxy and without 'off' periods. This approach directly fits the model to the whole data set and is optimal from a statistical point of view (Gauss-Markov theorem). The point sources are fit to a PSF model obtained by fitting a spatially varying Moffat profile and pixellized correction to the stars in the image. The light curve itself can then be modeled as :

$$M_{i,p} = \{[f_i \times \phi_{ref}(\vec{x}_p - \vec{x}_{SN}) + gal_{ref}] \otimes K_i\}_p + s_i \tag{1}$$

Where f_i is the SN flux in image i, gal_{ref} is the galaxy pixel map in the reference image, K_i is the convolution kernel to the reference image, and s_i is the sky level in image i.

1.2 Relative Astrometry of the Image Series

Some field stars are found to move significantly over time. Our astrometric solution aims to take this into account. We therefore fit the proper motions of moving stars. For the star i, its expected position $\vec{P}_{ij}$ in image j is modeled as :

$$\vec{P}_{ij} = T_j(\vec{X}_i + \vec{\mu}_i(t_j - t_0)) \tag{2}$$

where T_j is the coordinate mapping from a reference system to pixels in image j, $\vec{X}_i$ refers to the coordinates of star i in this reference system, $\vec{\mu}_i$ the proper motion of this star, t_j the epoch of image j and t_0 some reference epoch. The parameters of the astrometric fit are T_j (one per image), $\vec{X}_i$ and $\vec{\mu}_i$ (one position and one proper motion per star).

1.3 Photometric Linearity

To test the linearity of our photometry, we employed a Monte Carlo simulation. Field stars are cut and pasted onto nearby galaxies while applying a dimming factor r. We then compare the photometry of the field stars and their corresponding fake star and test our ability to properly estimate r. Note that we expect a bias as a function of the S/N ratio, due to correlations between the flux and position estimators. Our simulation tests for deviations from this already expected bias. We find no significant deviation to well below the per mil level.

2 Calibration

2.1 Calibration Scheme

To calibrate photometric measurements, they need to be compared to stars with a known *Spectral Energy Density* (SED) through observations in similar conditions. This is only possible on photometric nights. To avoid losing observations on non photometric nights, we calibrate field stars which become local standards (or tertiary stars). The SN measurements are then compared to that of the tertiaries. Measurements of the primary standard are made using aperture photometry. The calibrated magnitudes of the tertiaries are therefore also obtained using **aperture** photometry. However, to compare SN fluxes to those of tertiaries, these aperture magnitudes must be converted to **PSF** fluxes.

2.2 Calibration Biases

Converting the **aperture** magnitudes of tertiary stars to **PFS** fluxes leads to significant biases (few per mil) due to systematic differences in the 2 methods. First, aperture photometry does not fit a sky level, this leads to a magnitude dependent bias. To correct for this, residual sky background is fit with the PSF photometry and is used to correct biased aperture photometry. Secondly, the actual shape of point sources depends on their colors, which is not modeled by the PSF, leading to a color dependent bias. The PSF color dependence is well mimicked by the addition of an effective linear filter with an adequately chosen slope. The bias is then interpreted as a difference between the aperture magnitude system and a newly defined PSF magnitude system.

3 Achieving Submillimag Accuracy

Table 1 summarizes the biggest contributions to photometric uncertainty, excluding calibration. It is important that these remain well below the per mil level, as calibration uncertainty can be as precise as 3 per mil in some bands.

Table 1: Dominant photometric uncertainties excluding calibration.

Effect	induced bias	determined using
linearity	2.72×10^{-4}	simulation
PSF color	1.30×10^{-4}	artificial filter
refraction	3.00×10^{-4}	comparison to direct fit

References

1. Astier, P. et al. :*Photometry of supernovae in an image series : methods and application to the Supernova Legacy Survey (SNLS)*, Astronomy & Astrophysics (2013)
2. Betoule, M. et al. : *Improved photometric calibration of the SNLS and the SDSS supernova surveys*, Astronomy & Astrophysics (2014)

The origin of circular subhalo orbits and their connection to Cosmology

Nina Roth
Department of Physics and Astronomy, University College London, London WC1E 6BT, U.K.

Aaron D. Ludlow
Argelander-Institut für Astronomie der Universität Bonn, Auf dem Hügel 71, D-53121 Bonn, Germany

The Monoceros stream (MO) is an extended ($\sim 180°$ in Galactic longitude) stellar overdensity located at a distance of $\sim$ 18 kpc from the Galactic center, whose constituent stars follow nearly circular orbits that closely align with the plane of the Milky Way disk[1,2]. This is a puzzling structure because, according to numerical simulations, Galactic substructures – the likely progenitors of the MO – typically occupy highly eccentric orbits and it remains unclear what dynamical process may be responsible for the circularization of the MOs stars. We use high-resolution cosmological simulations of Milky Way-like halos to study the orbits of dark matter subhalos to investigate possible progenitors of circular stellar streams like Monoceros.

We use 6 individual dark matter halos from the *Aquarius* project[3] which have been selected to resemble the Milky Way in terms of its mass and late-time merger history. Within each simulation we track the orbital history of all subhalos that, at some point in the past, entered within the virial radius, $r_{\rm vir}$, of their host halo. We classify subhalos according to the eccentricity of their orbits and define two subsamples: those on circular orbits and those that are ejected from within the virial volume of their host. We define the orbital eccentricity as $\epsilon = \frac{r_{\rm apo}-r_{\rm peri}}{r_{\rm apo}+r_{\rm peri}}$, where $r_{\rm apo}$ and $r_{\rm peri}$ are, respectively, the apocenter and pericenter of the subhalo's orbit.

Circular orbits are those that satisfy both $\epsilon < 0.2$ and $r(z=0) < r_{\rm vir,host}$. **Ejected orbits** are defined by $r_{\rm apo} > r_{\rm turn}$ and $r(z=0) > r_{\rm vir,host}$, where $r_{\rm turn}$ is the turn-around radius, defined by $r_{\rm turn} = \max(r)|_{z>z_{\rm infall}}$. Several examples of subhalo orbits are shown in Figure 1. For circular orbits, there are two characteristic accretion times: early (these subhalos are "born" on circular orbits) or late (highly eccentric at infall, then quickly circularising).

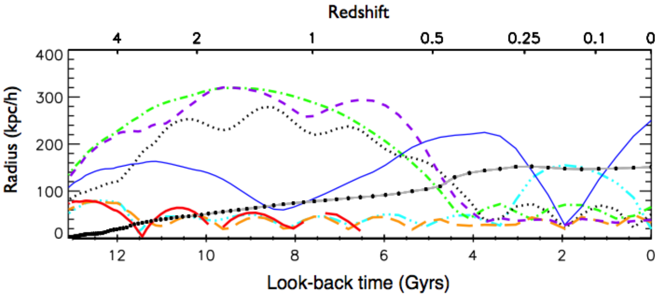

Figure 1 – Examples of subhalo orbits as a function of time (coloured lines). The gray line with black dots shows the virial radius of the host halo.

These two modes of satellite accretion (*early*: responsible for $> 80\%$ of circular subhalos and *late*: through major mergers) are illustrated again in Figure 2, which shows the mass (black points) and subhalo (histograms) accretion history for 2 of the 6 Aquarius halos (dubbed Aq-E and Aq-F). While Aq-E shows a typical accretion history for a quiescent Milky Way-like halo, a late-time major merger in Aq-F (at $z \approx 0.5$) generates a significant number of both circular (red histograms) and

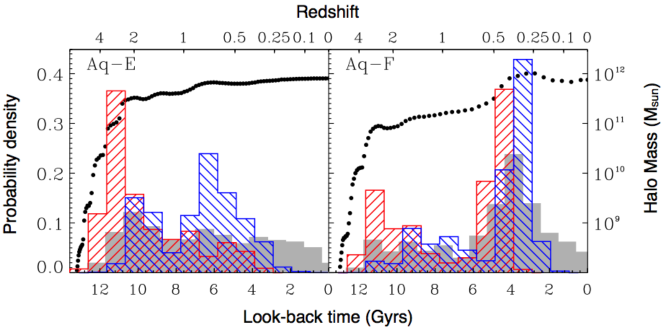

Figure 2 – Accretion history of mass (black points) and subhalos (histograms) for 2 of the 6 Aquarius halos (Aq-E and Aq-F). Accretion times for all subhalos are shown using grey shading; red and blue hatched regions show the accretion times for circular and ejected subhalos, respectively.

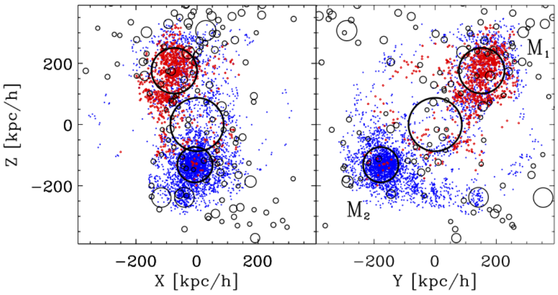

Figure 3 – Projections of halo positions in a cube of sidelength 800 h^{-1}kpc for Aq-F shortly before a major merger. All halos are centred on the host halo (central thick black circle). Thin black circles show isolated FoF halos ($r \propto M^{1/3}$); coloured points show merging subhalos whose orbits are circularized (red) or ejected (blue) at $z = 0$.

ejected (blue histograms) subhalos.

The origin of this anomalous accretion is illustrated in Figure 3, which plots the spatial distribution of subhalos just prior to the merger event (the three merging partners are indicated with thick black circles; M_1 and M_2 label the infalling groups). The subhalos on circular (red) and ejected (blue) orbits are clearly associated with two distinct mergers that occur back-to-back. The merger between M_1 and the host halo occurs slightly before its merger with (the less massive) M_2. The latter merger deepens the host's gravitational potential thereby "trapping" a fraction of M_1's subhalos, confining them to tightly bound and circular orbits.

In order to anticipate which of these subhalos could have potentially hosted a dwarf galaxy (and therefore produce a stellar stream during the interaction), we apply a star formation criterion based on their maximum circular velocity at a plausible reionisation redshift[4]: $v_{\mathrm{max}} \geq 10$ km/s at z=9. Roughly ∼3,700 (out of ∼75,000) of accreted subhalos across all 6 Aquarius simulation pass our star formation criterion, of which only 150 occupy circular orbits, as defined above. Finally, the required proximity to the halo center (18 kpc scaled to $r_{\mathrm{vir,host}}$) reduces the number of possible Monoceros progenitors to 9 across all 6 simulations.

We conclude that substructures on circular orbits are extremely rare in simulated cold dark matter halos. Nevertheless, major mergers may provide the physical conditions needed to rapidly circularize orbits of infalling systems and thereby give rise to stellar streams such as the Monoceros overdensity. Whether these findings apply generally to major mergers, or are the result of idiosyncrasies within the Aquarius halo sample, will require further investigation.

Referencecs

1. H. J. Newberg *et al*, ApJ **569**, 245 (2002).
2. B. Yanny *et al*, ApJ **588**, 824 (2003).
3. V. Springel *et al*, MNRAS **391**, 1685 (2008).
4. T. Okamoto and C. S. Frenk, MNRAS **399**, L174 (2009).

An influence of the matter distribution on the positional accuracy of reference sources

T.I. Larchenkova (1), A.A.Lutovinov (2), N.S.Lyskova (3,2)
(1) ASC of P.N.Lebedev Physical Institute, Leninskiy prospect 53, Moscow, Russia
(2) Space Research Institute, Profsoyuznaya 84/32, Moscow, Russia
(3) MPA, Karl-Schwarzschild-Str. 1, 85748 Garching, Germany

We consider an influence of a non-stationary gravitational field of the Galaxy on the visible positions of extragalactic sources. A contribution of the baryonic component of the galactic matter as well as of the hidden matter (including a population of brown dwarfs) were took into account. The observed variations of the deflection angle of light rays in a gravitational field of randomly moving point-like masses can be considered as a stochastic process. Using such an approach we constructed an autocorrelation function of studied stochastic process and found that its relative changes are about 15% for one year and about 35% for ten years.

In the nearest future technologies will allow one to carry out extremely accurate radio interferometrical observations with an angular resolution of $1\,\mu$as and optical observations with the accuracy of $10\,\mu$as per year. Such an accuracy requires to take into account effects of the general relativity, arising during the propagation of electromagnetic waves in non-stationary gravitational fields. In this respect it is very important to estimate an amplitude of changes of observed positions (coordinates) of extragalactic sources due to the propagation of their emission in the non-stationary gravitational field both visible stars in the galactic disk/bulge and invisible massive objects in the halo.

Measured source coordinates are the random functions of time, therefore variations of the light-ray deflection angle from the direction between the source and observer can be considered as a stochastic process. This process can be described by several statistical values – the mathematical expectation, dispersion and correlation (or autocorrelation) function of the process under consideration.

The electromagnetic signal from a distant extragalactic source is propagated in the gravitational field of N arbitrary moving point-like bodies with different masses. To simplify our calculations we assume that velocities of deflecting bodies do not change in time and the smallest distance between the photon and a deflecting body is much smaller compared to any other distances in the system. Then the deflection angle of the light by the a-th body from the straight line equals [1]:

$$\alpha^i_a(t) = \frac{4Gm_a}{c^2}\frac{1-\vec{k}\vec{v_a}}{\sqrt{1-\vec{v_a}^{\,2}}}\frac{P^i_j r^j_a}{|P^i_j r^j_a|^2}, \tag{1}$$

where $\vec{k}$ is the unit vector, directed from the source to the observer, $\vec{x}_a, m_a, \vec{v}_a$ – coordinates, mass, velocity of the a-th deflecting body, respectively, $\vec{r}_a$ – the distance between the point $\vec{x}(t)$ at the photon trajectory and the a-th deflecting body, c – the speed of light in vacuum, G – the gravitational constant, $P_{ij} = \delta_{ij} - k_i k_j$ – the operator of the vector projection on the plane, which is perpendicular to $\vec{k}$.

A deflection of electromagnetic signals in the non-stationary gravitational field of the Galaxy is a random process $\varepsilon(t)$:

$$\varepsilon(t) = \alpha(t) - \langle \alpha(t) \rangle, \tag{2}$$

where $\langle \alpha(t) \rangle = 0$. For a stationary noise process, the autocorrelation function depends not on the individual times t_i and t_j, but only on their difference τ and can be written as

$$\Re(t,\tau) = \int dm_a d\vec{x}_a d\vec{v}_a f(m_a,\vec{x}_a,\vec{v}_a)\varepsilon(t,m_a,\vec{x}_a,\vec{v}_a)\varepsilon(t+\tau,m_a,\vec{x}_a,\vec{v}_a), \tag{3}$$

where we assume that the statistical ensemble of deflection bodies is defined by uncorrelated parameters, so the distribution function can be approximated by the product of three statistically independent distribution functions [2]

$$f(m_a,\vec{x}_a,\vec{v}_a) \propto f(m_a)f(\vec{x}_a)f(\vec{v}_a). \tag{4}$$

We use an exponential function of the Kroupa model [3] as the mass distribution function of deflection bodies. Let us consider two model density distributions: a multi-component model of the Galaxy [4] which include population of brown dwarfs [5] and a four-component model of the Galaxy [6,7]. The velocity distribution is a truncated Maxwellian profile.

The calculated autocorrelation function is shown in Fig.1, its changes are about 15% for one year and about 35% for ten years.

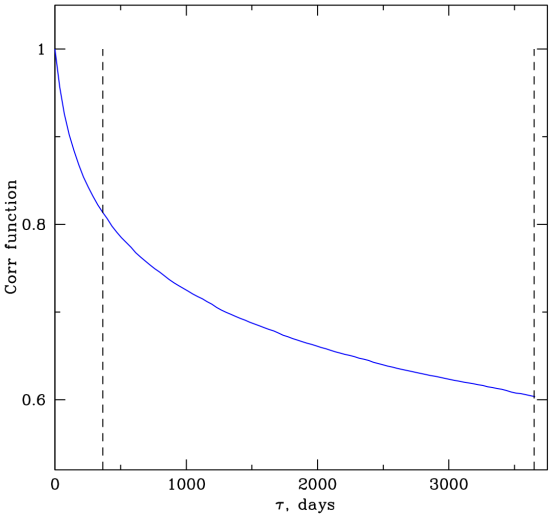

Figure 1 – The autocorrelation function. Dashed lines mark one and ten years periods.

Acknowledgments

TL acknowledge the support by the grant NSh-4235.2014.2, AL acknowledge the support by the grant RFBR 13-02-12094.

References

1. S. M. Kopeikin and G. Schafer, *Phys. Rev.* D **60**, 124002 (1999)
2. T. I. Larchenkova and S. M. Kopeikin, *Astron. Lett.* **32**, 18 (2006)
3. P.Kroupa, *Science* **295**, 82 (2002)
4. W. Dehnen and J. Binney, *Mon. Not. R. Astron. Soc.* **294**, 429 (1998)
5. G. Chabrier, *Publ. Astron. Soc. Pac.* **115**, 763 (2003)
6. J. N. Bahcall and R. M. Soneira, *Astrophys. J., Suppl. Ser.* **44**, 73 (1980)
7. J. N. Bahcall, *Ann. Rev. Astron. Astrophys.* **24**, 577 (1986)

NEUTRINO ANISOTROPIES AFTER PLANCK

M. GERBINO, E. DI VALENTINO and N. SAID
Dipartimento di Fisica, Università di Roma "Sapienza" - Roma, Italy
INFN, Sezione di Roma - Roma, Italy

We present new constraints on the neutrino clustering parameters $c^2_{\rm eff}$ and $c^2_{\rm vis}$ from the recent measurements of the Cosmic Microwave Background anisotropies provided by the Planck satellite. While broadly consistent with the standard expected values $c^2_{\rm eff} = c^2_{\rm vis} = 1/3$, the Planck dataset hints for a higher value of the viscosity parameter and a lower value of the sound speed. We also find a correlation between the anisotropy parameters and the lensing amplitude of the temperature power spectrum $A_{\rm L}$. When the latter parameter is allowed to vary, we mild the tension with the standard model. This result may indicate that the anomalous large value of $A_{\rm L}$ from the Planck measurements can be connected to non-standard neutrino physics.

1 Introduction and method

In this work we test some properties of the Cosmic Neutrino Background (CNB, hereafter) in combination with the lensing amplitude of the temperature power spectrum by means of the measurements from the Planck satellite [1] [2]. Following [3], the CNB can be modelled as a Generalized Dark Matter (GDM) component with a set of equations describing the evolution of perturbations [4] [5] [6], introducing two anisotropy parameters: the sound speed in the CNB rest frame $c^2_{\rm eff}$, describing pressure fluctuations respect to density perturbations, and the "viscosity" parameter $c^2_{\rm vis}$ which parameterizes the anisotropic stress. For standard neutrinos, we have $c^2_{\rm eff} = c^2_{\rm vis} = 1/3$. We also consider variation in the lensing amplitude of the temperature power spectrum, parameterized via $A_{\rm L}$, as defined in [7]: $C_\ell^{\phi\phi} \to A_{\rm L} C_\ell^{\phi\phi}$, where $C_\ell^{\phi\phi}$ is the power spectrum of the lensing field. Interestingly, the Planck data suggest an anomalous value for the lensing amplitude of $A_{\rm L} = 1.22^{+0.11}_{-0.13}$ at 68% c.l., i.e. higher respect to the expected value of $A_{\rm L} = 1$ at about two standard deviations.

We perform a MCMC analysis sampling the standard six-dimensional set of cosmological parameters $\Omega_b h^2$, $\Omega_c h^2$, θ, τ, n_S, $\ln[10^{10} A_s]$. We assume the Planck collaboration [2] baseline model for neutrinos: $N_{\rm eff} = 3.046$, with a single massive eigenstate $m_\nu = 0.06\,$eV. When exploring extended cosmological scenarios, we vary the effective sound speed $c^2_{\rm eff}$, the viscosity parameter $c^2_{\rm vis}$ and the lensing amplitude parameter $A_{\rm L}$. Firstly, we combine them in pair ($c^2_{\rm eff} - c^2_{\rm vis}$, $c^2_{\rm eff} - A_{\rm L}$, $c^2_{\rm vis} - A_{\rm L}$), fixing the third parameter at its standard value ($A_{\rm L} = 1$, $c^2_{\rm vis} = 1/3$, $c^2_{\rm eff} = 1/3$). Finally, we combine the three parameters all together. We adopt the following flat priors: $0 \le c^2_{\rm vis}, c^2_{\rm eff} \le 1$ and $0 \le A_{\rm L} \le 4$. Concerning the datasets, we use the combination refered as *Planck* + *WP* in [1]. Our analysis method is based on the publicly available Monte Carlo Markov Chain package `cosmomc` [8] (March 2013 version) using the Gelman and Rubin statistic as convergence diagnostic.

2 Results

As we can see from Tab.1 and Fig.1, allowing both $c^2_{\rm eff}$ and $c^2_{\rm vis}$ to vary produces posterior values in disagreement with the standard model. In particular, the constraints on $c^2_{\rm vis}$ point towards a value larger than 1/3, being $c^2_{\rm vis} = 0.60 \pm 0.18$ at 68% c.l., in tension with the standard value at about 1.5 standard deviations. On the other hand, $c^2_{\rm eff}$ assumes in our analysis a value lower than the expected one: $c^2_{\rm eff} = 0.304 \pm 0.013$ at 68% c.l., ruling out the standard value at more than 95% c.l.. The situation is significantly different when the lensing amplitude parameter is allowed to vary. In the $c^2_{\rm vis} + A_{\rm L}$ case, the standard value of the viscosity parameter is recovered ($c^2_{\rm vis} = 0.35 \pm 0.12$); similarly, in the $c^2_{\rm eff} + A_{\rm L}$

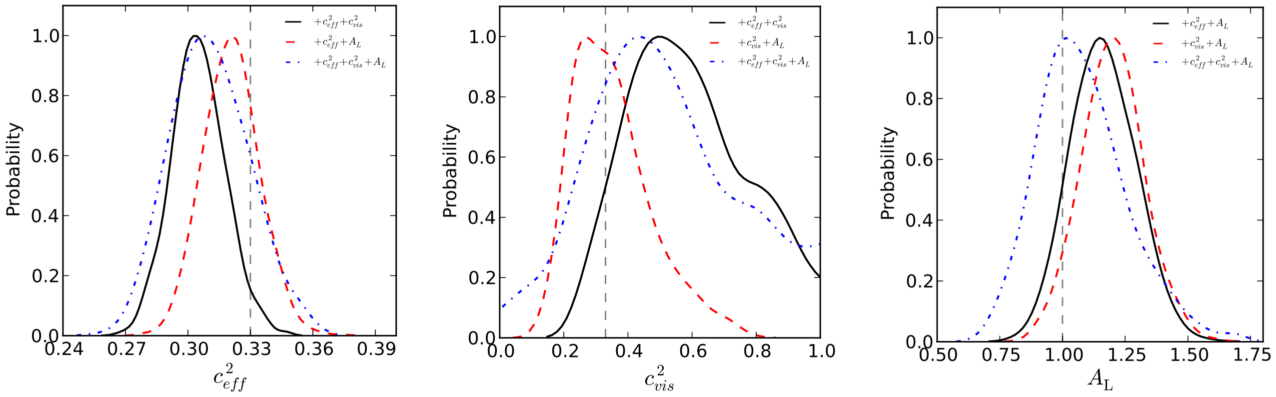

Figure 1 – One-dimensional posterior probabilities of the parameter $c^2_{\rm eff}$ (left), $c^2_{\rm vis}$ (center) and $A_{\rm L}$ (right) for the indicated models for *PlanckWP*. The vertical dashed line indicates the expected value in the standard model.

case, $c^2_{\rm eff}$ is in agreement with the expected value ($c^2_{\rm eff} = 0.321 \pm 0.014$). However, though the $A_{\rm L} = 1$ case is now in better agreement with the data, it is still in disagreement with the standard value at more than 1σ level (respectively, $A_{\rm L} = 1.20 \pm 0.12$ and $A_{\rm L} = 1.16 \pm 0.13$), showing a degeneracy between $A_{\rm L}$ and the clustering parameters $c^2_{\rm vis}$ and $c^2_{\rm eff}$. Finally, when all the three parameters are allowed to vary, their posteriors are in good agreement (within 1σ c.l.) with the standard model: we find $c^2_{\rm eff} = 0.311 \pm 0.019$, $c^2_{\rm vis} = 0.51 \pm 0.22$ and $A_{\rm L} = 1.08 \pm 0.18$.

To conclude, we have found that the Planck dataset hints for anomalous values for the CNB clustering parameters with $c^2_{\rm vis} = 0.60 \pm 0.18$ and $c^2_{\rm eff} = 0.304 \pm 0.013$ at 68% c.l.. We have found a correlation between the neutrino parameters and the lensing amplitude of the temperature power spectrum $A_{\rm L}$. When the latter is allowed to vary we found a better consistency with the standard model with $c^2_{\rm vis} = 0.51 \pm 0.22$, $c^2_{\rm eff} = 0.311 \pm 0.019$, and $A_{\rm L} = 1.08 \pm 0.18$ at 68% c.l.. This result indicates that the anomalous large value of $A_{\rm L}$ measured by Planck could be connected to non-standard neutrino properties.

Table 1: Comparison between extended cosmological models for the *PlanckWP* dataset. Listed are posterior means for the cosmological parameters (errors refer to 68% credible intervals).

Parameter	$c^2_{\rm vis} + c^2_{\rm eff}$	$c^2_{\rm eff} + A_{\rm L}$	$c^2_{\rm vis} + A_{\rm L}$	$c^2_{\rm eff} + c^2_{\rm vis} + A_{\rm L}$
$100\,\Omega_b h^2$	2.118 ± 0.047	2.219 ± 0.045	2.236 ± 0.053	2.162 ± 0.095
$\Omega_c h^2$	0.1157 ± 0.0038	0.1177 ± 0.0032	0.1170 ± 0.0034	0.1159 ± 0.0036
$100\,\theta$	1.0412 ± 0.0014	1.0428 ± 0.0012	1.0421 ± 0.0019	1.0420 ± 0.0020
$\log[10^{10} A_S]$	3.173 ± 0.052	3.086 ± 0.028	3.08 ± 0.05	3.141 ± 0.078
τ	0.089 ± 0.013	0.088 ± 0.013	0.087 ± 0.013	0.089 ± 0.014
n_S	0.998 ± 0.018	0.9732 ± 0.0099	0.970 ± 0.014	0.989 ± 0.023
$A_{\rm L}$	$\equiv 1$	1.16 ± 0.13	1.20 ± 0.12	1.08 ± 0.18
$c^2_{\rm vis}$	0.60 ± 0.18	$\equiv 0.33$	0.35 ± 0.12	0.51 ± 0.22
$c^2_{\rm eff}$	0.304 ± 0.013	0.321 ± 0.014	$\equiv 0.33$	0.311 ± 0.019

References

1. P. A. R. Ade *et al.* [Planck Collaboration], arXiv:1303.5075 [astro-ph.CO].
2. P. A. R. Ade *et al.* [Planck Collaboration], arXiv:1303.5076 [astro-ph.CO].
3. W. Hu, D. J. Eisenstein, M. Tegmark and M. J. White, *Phys.Rev.*D **59**, 023512 (1999).
4. M. Archidiacono, E. Calabrese and A. Melchiorri, *Phys.Rev.*D **84**, 123008 (2011).
5. W. Hu, *Astrophys. J.* **506**, 485 (1998).
6. R. Trotta and A. Melchiorri, *Phys. Rev. Lett.* **95**, 2005 (011305).
7. E.Calabrese,A.Slosar,A.Melchiorri,G.F.Smoot and O.Zahn, *Phys.Rev.*D **77**, 123531 (2008).
8. A. Lewis, *Phys.Rev.*D **87**, 103529 (2013).

PRIMORDIAL TENSOR CORRELATIONS
FROM EFFECTIVE FIELD THEORY APPROACH

Toshifumi Noumi
Theoretical Research Division, RIKEN Nishina Center, Saitama 351-0198, JAPAN

We investigate the relation between the non-Gaussianities of primordial perturbations and the sound speed of tensor perturbations, that is, the propagation speed of gravitational waves. We find that the sound speed of tensor perturbations is directly related not to the auto-bispectrum of tensor perturbations but to the cross-bispectrum of primordial perturbations, especially, the scalar-tensor-tensor bispectrum. This result is in sharp contrast with the case of the scalar (curvature) perturbations, where their reduced sound speed enhances their auto-bispectrum. Our findings indicate that the scalar-tensor-tensor bispectrum and its relevant cosmic microwave background (CMB) bispectra can be a powerful probe for the tensor sound speed.

1 Introduction

Primordial tensor perturbations are one of important probes for inflationary dynamics. Their amplitude directly determines the energy scale of inflation, whereas the bispectra tell us the underlying gravitational structures[2,3]. In this poster presentation,[a] we discussed the relation between the sound speed of tensor perturbations and the bispectrum of primordial perturbations, based on the effective field theory (EFT) approach for inflation[4].

2 Tensor sound speed in the EFT approach

In the unitary gauge, where the inflaton field does not fluctuate, dynamical degrees of freedom in single-clock inflation are the metric field $g_{\mu\nu}$ only and the action should respect the (time-dependent) spatial diffeomorphism invariance. The action at the lowest order in perturbations can be uniquely determined by the background equations of motion and the residual symmetry as

$$S_0 = M_{\rm Pl}^2 \int d^4x\sqrt{-g}\left[\frac{1}{2}R + \dot{H}g^{00} - (3H^2+\dot{H})\right]\,, \tag{1}$$

where $H(t) = \dot{a}/a$ is the background Hubble parameter. The general action for single-clock inflation can then be expanded in perturbations and derivatives as [4]

$$S = S_0 + \int d^4x\sqrt{-g}\left[\frac{M_2^4}{2}(\delta g^{00})^2 - \frac{\bar{M}_1^3}{2}\delta g^{00}\delta K^\mu_\mu - \frac{\bar{M}_2^2}{2}(\delta K^\mu_\mu)^2 - \frac{\bar{M}_3^2}{2}\delta K^\nu_\mu \delta K^\mu_\nu + \dots\right]\,, \tag{2}$$

where M_2 and $\bar{M}_i$'s are free functions of time. The ingredients δg^{00} and $\delta K_{\mu\nu}$ are defined by $\delta g^{00} = g^{00}+1$ and $\delta K_{\mu\nu} = K_{\mu\nu} - Hh_{\mu\nu}$, where $h_{\mu\nu}$ and $K_{\mu\nu}$ are the induced metric and the extrinsic curvature on the constant-t slices, respectively. Let us introduce the scalar perturbation

---

[a] This presentation is mainly based on the reference [1] in collaboration with Masahide Yamaguchi.

ζ and the tensor perturbation γ as $h_{ij} = a^2\, e^{2\zeta}\left(e^{\gamma}\right)_{ij}$ with $\gamma_{ii} = \partial_i\gamma_{ij} = 0$. Then, among the four correction terms in (2), only $\delta K^{\nu}_{\mu}\delta K^{\mu}_{\nu}$ induces the second order tensor perturbations:

$$\delta K^{\nu}_{\mu}\delta K^{\mu}_{\nu} \ni -\frac{1}{4}(\partial_t e^{-\gamma}\partial_t e^{\gamma})_{ii} = \frac{1}{4}(\dot{\gamma}_{ij})^2 + \mathcal{O}(\gamma^4)\,, \tag{3}$$

which deforms the kinetic term for γ with the modified tensor sound speed c_γ as

$$\int d^4x\, a^3 \frac{M_{\rm Pl}^2}{8} c_\gamma^{-2}\left[(\dot{\gamma}_{ij})^2 - c_\gamma^2\frac{(\partial_k\gamma_{ij})^2}{a^2}\right] \quad \text{with} \quad c_\gamma^2 = \frac{M_{\rm Pl}^2}{M_{\rm Pl}^2 - \bar{M}_3^2}\,. \tag{4}$$

Essentially because no cubic interactions of γ arise from the $\delta K^{\nu}_{\mu}\delta K^{\mu}_{\nu}$ operator as in (3), we find that there are no direct relations between tensor auto-bispectra and the tensor sound speed c_γ.[1,3]

3 Importance of cross correlations

Then, which type of bispectra can be a probe of the tensor sound speed? In Table 1, we summarized what types of interactions arise in the decoupling limit from the operators in (2). For technical simplicity, we used the basis of the Goldstone boson π, where the scalar perturbation ζ is given by $\zeta = -H\pi$ at the linear order. We find that the $\gamma^2\pi$-type interaction arises only from the operator $\delta K^{\nu}_{\mu}\delta K^{\mu}_{\nu}$, while $\gamma\pi^2$- and π^3-type interactions arise also from other operators. In this sense, we could say that the scalar-tensor-tensor bispectrum is sensitive to the tensor sound speed c_γ.[b] Indeed, our detailed analysis in [1] shows that when the sound speed of tensor perturbations is modified, the scalar-tensor-tensor bispectrum is significantly enhanced by a factor of $(c_\gamma^{-2} - 1)/\epsilon$ compared to the case of $c_\gamma = 1$, where $\epsilon = -\dot{H}/H^2$ is the slow-roll parameter. Such an enhancement makes it easy to detect the CMB bispectra of two B-modes and one temperature (or one E-mode) anisotropies especially. Thus, we conclude that the scalar-tensor-tensor bispectrum and its relevant CMB bispectra can be powerful probes for the tensor sound speed and the underlying gravitational structure behind inflation.

Table 1: Operators relevant to dispersion relations of primordial perturbations and the induced cubic interactions in the decoupling limit.

operator	$\dot{\pi}^2$	$\frac{(\partial_i\pi)^2}{a^2}$	$\frac{(\partial_i^2\pi)^2}{a^4}$	$(\dot{\gamma}_{ij})^2$	$\frac{(\partial_k\gamma_{ij})^2}{a^2}$	γ^3	$\gamma^2\pi$	$\gamma\pi^2$	π^3
S_0	✓	✓		✓	✓	✓		✓	
$(\delta g^{00})^2$	✓								✓
$\delta g^{00}\delta K$		✓						✓	✓
$(\delta K)^2$			✓					✓	✓
$\delta K^{\nu}_{\mu}\delta K^{\mu}_{\nu}$			✓	✓			✓	✓	✓

Acknowledgments

The work of T.N. is supported by the Special Postdoctoral Researcher Program at RIKEN.

References

1. T. Noumi and M. Yamaguchi, arXiv:1403.6065 [hep-th].
2. J. M. Maldacena and G. L. Pimentel, JHEP **1109**, 045 (2011).
3. X. Gao *et al*, *Phys. Rev. Lett.* **107**, 211301 (2011).
4. C. Cheung *et al*, JHEP **0803**, 014 (2008).

---

[b] Note that this situation is in sharp contrast with the case of scalar curvature perturbations, where their auto-bispectra are significantly enhanced by the reduced sound speed.

MONOPOLE, VECTOR DARK MATTER AND DARK RADIATION FROM A GAUGED HIDDEN SECTOR

WAN-IL PARK
School of Physics, KIAS,
Seoul 130-722, Korea

We show that the 't Hooft-Polyakov monopole model in the hidden sector with Higgs portal interaction makes a viable dark matter model, where monopole and massive vector dark matter (VDM) are stable due to topological conservation and the unbroken subgroup $U(1)_X$. A right amount of VDM thermal relic can be obtained via s-channel resonant annihilation. In addition, the dark photon associated with unbroken $U(1)_X$ contributes to the radiation energy density at present, giving $\Delta N_{\rm eff}^{\nu} \sim 0.1$ as the extra relativistic neutrino species.

1 The model

The stability of DM and the fact that SM is guided by local gauge principle may imply that the dark sector in which the dark matter responsible for the present relic density resides may respect local gauge symmetry, too.

We consider $SU(2)_X$-triplet real scalar field $\vec{\Phi}$ with the following Lagrangian[1]:

$$\mathcal{L} = \mathcal{L}_{\rm SM} - \frac{1}{4} V^a_{\mu\nu} V^{a\mu\nu} + \frac{1}{2} D_\mu \vec{\Phi} \cdot D^\mu \vec{\Phi} - \frac{\lambda_\Phi}{4} \left(\vec{\Phi} \cdot \vec{\Phi} - v_\phi^2 \right)^2 - \frac{\lambda_{\Phi H}}{2} \left(\vec{\Phi} \cdot \vec{\Phi} - v_\phi^2 \right) \left(H^\dagger H - \frac{v_H^2}{2} \right) \quad (1)$$

where $\mathcal{L}_{\rm SM}$ is the standard model Lagrangian and $V^a_{\mu\nu}$ is the field strength tensor of dark gauge field V^a_μ. The Higgs portal interaction is described by the $\lambda_{\Phi H}$ term. The hidden sector Lagrangian describes the 't Hooft-Polyakov monopole[2,3]. After the spontaneous symmetry breaking of $SU(2)_X \approx SO(3)_X$ into $U(1)_X \approx SO(2)_X$ by nonzero vacuum expectation value (VEV) of $\vec{\Phi}$ (i.e., $\langle \vec{\Phi}(x) \rangle = (0, 0, v_\Phi)$), hidden sector particles are composed of massive dark vector bosons $V^\pm_\mu \equiv \left(V^1_\mu \mp i V^2_\mu \right) / \sqrt{2}$ with masses $m_V = g_X v_\Phi$, massless dark photon $\gamma_{h,\mu} \equiv V^3_\mu$, massive real scalar ϕ (dark Higgs boson) and topologically stable heavy (anti-)monopole with mass $m_M = m_V / \alpha_X$.

2 Phenomenology

The mixing between SM- and dark-Higgs bosons after the spontaneous breaking of electroweak symmetry improves the vacuum stability of SM Higgs potential[4], but is constrained by collider experiments in order not to have too large branching fraction of SM-like Higgs decay to non-SM channels[5]. As a result, the mixing angle (α) is constrained to be smaller than $\mathcal{O}(0.1)$.

2.1 Dark matter phenomenology

The massless dark photon (γ_h) can cause a large non-perturbative enhancement of perturbative pair annihilation or self-interactions of dark matter ($V^\pm_\mu$ and (anti)monopoles). When $v \ll$

α_X, the enhancement is proportional to $1/v$, and CMB and small scale dark matter subhalos constrain the dark gauge coupling to be much smaller than the required value for a right amount of thermal relic [6,7]. However, VDM can have a right amount of relic density via the s-channel resonant annihilation, thanks to the Higgs portal interaction. Contrary to VDM, the abundance of monopoles turns out to be negligibly small in the relevant parameter space.

The direct detection cross section of VDM-nucleon scattering occurs through the t-channel exchange of H_1 and H_2. It turned out that XENON1T may probe $m_\phi \lesssim 50\,\text{GeV}$ with m_ϕ being the mass of non-SM Higgs. In case of monopoles, the scattering cross section to nucleon is far below sensitivities of present or near-future direct search experiments.

2.2 Dark Radiation

The massless dark photon associated with the unbroken dark $U(1)_X$ symmetry contributes to the extra relativistic degrees of freedom in the present universe. It is decoupled from VDM at $T_\gamma \sim 10\,\text{MeV}$. However, VDM is decoupled from SM thermal bath at much higher temperature since the thermal equilibrium of VDM is maintained only by Higgs mediation. As a result, the kinetic decoupling temperature is $T_{\rm QCD} < T_{\rm kd} \lesssim \mathcal{O}(1)\,\text{GeV}$, and the contribution of dark photon to the present radiation energy density as the extra neutrino species can be $\Delta N^\nu_{\rm eff} \simeq 0.08 - 0.11$. It is consistent with the recent result of Planck satellite mission, and can be probed at a Stage-IV CMB experiment at 2σ-level [8].

3 Conclusions

In this talk, we considered a 't Hooft-Polyakov monopole model in the dark sector equipped with a Higgs portal interaction, as a logically natural extension of SM to a dark sector in regard of local gauge principle and the stability of dark matter. The dark sector consists of monopoles and massive vector bosons, both of which are stable due to topology and unbroken $U(1)_X$ respectively, and massless dark photons. We showed that, although the constraint from CMB data on the dark matter annihilation cross section is quite stringent, a right amount of thermal relic density can be obtained by resonant thermal freeze-out of massive VDM, thanks to the Higgs portal which was newly introduced in this work. XENON1T experiment for example may probe VDM mass less than about 25 GeV. The massless dark photon associated with the $U(1)_X$ contributes to the present radiation energy density, resulting in $\Delta N^\nu_{\rm eff} \sim 0.1$ as the extra relativistic neutrino species.

Acknowledgments

This work was supported in part by NRF Research Grant 2012R1A2A1A01006053.

References

1. S. Baek, P. Ko and W. -I. Park, arXiv:1311.1035 [hep-ph].
2. G. 't Hooft, Nucl. Phys. B **79**, 276 (1974).
3. A. M. Polyakov, JETP Lett. **20**, 194 (1974) [Pisma Zh. Eksp. Teor. Fiz. **20**, 430 (1974)].
4. S. Baek, P. Ko, W. -I. Park and E. Senaha, JHEP **1211**, 116 (2012)
5. S. Choi, S. Jung and P. Ko, JHEP **1310**, 225 (2013) [arXiv:1307.3948].
6. M. S. Madhavacheril, N. Sehgal and T. R. Slatyer, arXiv:1310.3815 [astro-ph.CO].
7. A. Loeb and N. Weiner, Phys. Rev. Lett. **106**, 171302 (2011) [arXiv:1011.6374 [astro-ph.CO]].
8. K. N. Abazajian, K. Arnold, J. Austermann, B. A. Benson, C. Bischoff, J. Bock, J. R. Bond and J. Borrill *et al.*, arXiv:1309.5383 [astro-ph.CO].

COSMIC INITIAL SINGULARITIES IN A SINGLE REPEATING UNIVERSE AS OPPOSED TO THEIR BEHAVIOR IN A MULTIVERSE

A.W. BECKWITH
Chongqing University department of physics
Chongqing, P.R. China, 400014

When the initial radius of the universe is in four dimensions and there is only one repeating universe then $R_{\text{initial}} \rightarrow 0$ or gets very close to zero if Stoica actually derived the Einstein equations in a formalism that removes in four dimensions the big-bang singularity pathology. So, then the reason for the Planck length no longer holds. The repeating single universe result of $R_{\text{initial}} \sim \frac{1}{\#} 1_{Ng} < l_{\text{Planck}}$ is different from the multiverse value we calculate using Kauffman's final conclusion that R is greater than a nonzero value more than a Plank length.

1 Introduction

We first examine what is to be expected in the four-dimensional case: a single repeating universe. In such a situation, one can employ the following argument as to a singularity with the aforementioned behavior as given below. Before doing this, we investigate via simple scaling arguments for the Friedman equations what to expect if the cosmological "constant" is a constant or has a temperature dependence (T^{β}), according to Park et.al. as cited in [1]. In doing so, a case can be made using the Weinberg argument that if there is a high initial background "viscosity" (for graviton propagation), there is a high initial temperature. This high temperature would be consistent with the modus operandi of a single repeating universe. To make the point of this, we also can refer to the Penrose CCC hypothesis (as cited in [1]) as yet another way to delineate this same repeating universe, with black holes in four dimensions. That is, in the case of the single repeating universe, one may use the Stoica convention (as cited in [1]) as to nonpathological singularities, or a near singularity at the beginning of space-time.

2 In a Single Repeating Universe, What Happens to Entropy and Singularities?

This first part of the article is to investigate what happens physically if there is a nonpathological singularity in terms of Einstein's equations at the start of space-time if there is a single repeating universe. This eliminates the need to have put in the Planck length since, then, there would be no reason to have a minimum nonzero length. The reasons for such a proposal comes from material we cite in [1] given by Stoica who may have removed the reason for the development of Planck's length as a minimum safety net to remove what appears to be unavoidable pathologies at the start of applying the Einstein equations at a space-time singularity, and are commented upon in this article. $\rho \sim H^2/G \Leftrightarrow H \approx a^{-1}$ in particular is remarked upon. This is a counterpart to Fjortoft theorem as given in [1]. The idea is that entanglement entropy will help generate bits, due to the presence of a vacuum energy—as derived at the end of the article—and the presence of a nonzero vacuum energy value is necessary for cosmological evolution. Before we get to that creation of what is a necessary creation of vacuum energy conditions we refer to constructions leading to extremely pathological problems which could lead to minus the presence of initial nonzero vacuum energy. Note a change in entropy formula given by Lee as cited in [1] about the inter relationship between energy, entropy and temperature as given by

$$m \cdot c^2 = \Delta E = T_U \cdot \Delta S = \frac{h \cdot a}{2\pi \cdot c \cdot k_B} \cdot \Delta S. \tag{1}$$

Lee's formula is crucial for what we will bring up in the latter part of this document. Namely, that changes in the initial energy could effectively vanish if the single repeating universe main result we cite from [1] is right, that of Stoica removing the nonpathological nature of a big bang singularity. That is, unless entanglement entropy is used. If the mass m (e.g., for gravitons) is set by acceleration (of the net universe) and a change in entropy between the electroweak regime and the final entropy $\Delta S \sim 10^{38}$ beteween the electroweak regime and the final entropy value of, if $a \cong \frac{c^2}{\Delta x}$ for acceleration is used, so then we obtain $S_{\text{Today}} \sim 10^{88}$.

Then we are really forced to look at Eq. (1) as a paring between gravitons (today) and gravitinos (electro weak) in the sense of preservation of information. Having said this, note by extension $\rho \sim H^2/G \Leftrightarrow H \approx a^{-1}$. As ρ changes due to and , t hen is also altered i.e. goes to zero. We then due to $\rho \sim H^2/G$ and $R_{\text{initial}} \sim \frac{1}{\#} 1_{Ng} < l_{\text{Planck}}$, then a is also altered, going to zero. We then, due to lack of space, go to the conclusion of [1], which gives a counterpart to a vanishing initial singularity in the case of a multiverse.

3 Conclusion: Reexamining the Question of a "Near Singularity" in a Multiverse

Steven Kenneth Kauffmann [2] sets an upper bound to concentrations of energy, in terms of how he formulated the following equation put in below as Eq. (2). Eq. (2) specifies an interrelationship between an initial radius for an expanding universe, and a "gravitationally based energy" expression we will call $T_G(r)$, which leads to a lower bound to the radius of the universe at the start of its initial expansion, with manipulations. The term $T_G(r)$ is defined via Eq. (3) afterwards. We start off with Kauffmann's expression from material given by [2] $R \cdot \left(\frac{c^4}{G}\right) \geq \int_{|r''| \leq R} T_G(r + r'') \mathrm{d}^3 r''$. Kauffmann calls $\left(\frac{c^4}{G}\right)$ a "Planck force" which is relevant due to the fact we will employ Eq. (2) at the initial instant of the universe in the Planckian regime of space-time. Also, we make full use of setting, for small r, the following:

$$T_G(r + r'') \approx T_{G=0}(r) \cdot const \sim V(r) \sim m_{\text{Graviton}} \cdot n_{\text{Initial-entropy}} \cdot c^2 \tag{2}$$

$$n_{\text{Initial-entropy}} \sim S_{\text{Graviton-count-entropy}}. \tag{3}$$

Then Eq. (2) will lead to

$$\begin{aligned} R \cdot \left(\frac{c^4}{G}\right) &\geq \int_{|r''| \leq R} T_G(r + r'') \mathrm{d}^3 r'' \approx const \cdot m_{\text{Graviton}} \cdot \left[n_{\text{Initial-entropy}} \sim S_{\text{graviton-count-entropy}}\right] \\ &\Rightarrow R \cdot \left(\frac{c^4}{G}\right) \geq const \cdot m_{\text{Graviton}} \cdot \left[n_{\text{Initial-entropy}} \sim S_{\text{Graviton-count-entropy}}\right] \\ &\Rightarrow R \cdot \left(\frac{c^4}{G}\right)^{-1} \cdot \left[const \cdot m_{\text{Graviton}} \cdot \left[n_{\text{Initial-entropy}} \sim S_{\text{Graviton-count-entropy}}\right]\right]. \end{aligned} \tag{4}$$

This Eq. (4), due to a multiverse, is very different from what happens in a single cyclical universe. Eq. (4) and $R_{\text{initial}} \sim \frac{1}{\#} 1_{Ng} < l_{\text{Planck}}$, which is the single repeating universe result, are fundamentally different due to details in [1].

References

1. A.W. Beckwith, http://vixra.org/abs/1312.0021.
2. S.K. Kauffman, http://arxiv.org/abs/1212.0426.

DISFORMAL INVARIANCE OF SECOND ORDER SCALAR-TENSOR THEORIES

D. BETTONI
Faculty of Physics, Technion,
Haifa, Israel

The Horndeski action is the most general one involving a metric and a scalar field that leads to second-order field equations in four dimensions. Being the natural extension of the well-known scalar-tensor theories, its structure and properties are worth analysing along the experience accumulated in the latter context. Here, we argue that disformal transformations play, for the Horndeski theory, a similar role to that of conformal transformations for scalar-tensor theories a là Brans–Dicke.

1 Introduction

The quest for the understanding of the present day accelerated phase of the universe has produced an outburst of attention towards modified gravity models. Among them a particular role is played by the Horndeski [1] or Covariant Galileon action [2]. Thought to be the most general action constructed with a metric and a scalar field able to give second order field equations, it represents a generalization of scalar-tensor theories *a là* Brans–Dicke. Apart from phenomenological implications, more formal questions about this action have proven to be fundamental to a better understanding of its properties: Are there redundancies in its formulation that can be eliminated with a suitable redefinition of the metric? Can we envisage a generalization in the metric that couples to matter? A first attempt to answer these questions is presented below.

2 The Horndeski action and disformal transformations

The Horndeski action, rephrased in modern language, is given by

$$S = \int d^4x\sqrt{-g}\sum_i \mathcal{L}_i + S_{(\mathrm{m})}[\bar{g},\psi]\,, \tag{1}$$

$$\begin{aligned}
\mathcal{L}_2 &= G_2(\phi,X)\,, \qquad \mathcal{L}_3 = G_3(\phi,X)\Box\phi\,,\\
\mathcal{L}_4 &= G_4(\phi,X)R - G_{4,X}(\phi,X)\left[(\Box\phi)^2 - (\nabla_\mu\nabla_\nu\phi)^2\right]\,,\\
\mathcal{L}_5 &= G_5(\phi,X)G_{\mu\nu}\nabla^\mu\nabla^\nu\phi + \frac{G_{5,X}}{6}\left[(\Box\phi)^3 - 3(\Box\phi)(\nabla_\nu\nabla_\mu\phi)^2 + 2(\nabla_\mu\nabla_\nu\phi)^3\right]\,,
\end{aligned} \tag{2}$$

where $X = \nabla_\mu\phi\nabla^\mu\phi/2$, while matter is coupled to the so called disformal metric [3] $\bar{g}_{\mu\nu} = A(\phi,X)g_{\mu\nu} + B(\phi,X)\phi_{,\mu}\phi_{,\nu}$. This action represents a great generalization not only in its scalar field part but also in the metric matter is coupled to. However, one can still wonder whether suitable metric transformations can be introduced also in this case, leaving the action invariant and linking alternative frame. Indeed, the answer is provided by the particular form of the metric appearing in the matter action.

The general disformal transformation: a dead end or a new starting point?

The application of the disformal transformation $\bar{g}_{\mu\nu} = A(\phi, X)g_{\mu\nu} + B(\phi, X)\phi_{,\mu}\phi_{,\nu}$ to the Horndeski action introduces extra terms that cannot be reabsorbed into the Horndeski coefficient functions. [4,5] One would then expect the second order nature of the equations of motion to be spoiled thus leaving us with the conclusion that such metric transformation is not viable. However, higher-than-second derivatives can be traded for second order derivatives thanks to hidden constraints coming from the field equations. [5] This fact leaves us with the question if a more general action than Horndeski's that still gives second order field equations may be constructed.

The reduced disformal transformation: framing the Horndeski action

Given the above results we have investigated the effects on the Horndeski action of the less general disformal transformation $\bar{g}_{\mu\nu} = A(\phi)g_{\mu\nu} + B(\phi)\phi_{,\mu}\phi_{,\nu}$. [4] Contrarily to the previous case now the Horndeski action is invariant with the effects of the transformation absorbed into redefinitions of the Horndeski coefficients (2) analogously to what happens in scalar-tensor theories. Schematically, we have that the action is mapped as $S[g, \phi; G_i] \to S[\bar{g}, \bar{\phi}, \bar{G}_i]$ with $\bar{G}_i(\phi, \bar{X}) = f(\phi, \bar{X}; A, B)G_i(\phi, \bar{X}) + g(\phi, \bar{X}; G_{j>i}, \partial A, \partial B, \partial\partial A, \partial\partial B)$ where the $i = 2, 3, 4, 5$. This allowed us to prove that an Einstein frame ($G_4 = 1\,, G_5 = 0$) can be defined only from an initial Jordan frame action that has $G_5 = 0$ and $G_4 = A(\phi)^2\sqrt{1 - 2B(\phi)X}$ and that the two frames are equivalent. Moreover, two more intermediate frames, dubbed Galileon and Disformal, can be defined depending if matter is conformally or disformally coupled to the scalar field. This results, being more than just a theoretical exercise, may help in classifying apparently different theories and simplify the investigation of those in different regimes.

3 Conclusions

A major tool in physics is represented by symmetries. This is a clean and precise way to order models, find their simplest formulations, and identify the minimal set of degrees of freedom required to fully define a theory. Here, we have presented the effects of disformal transformations on the Horndeski action finding a new class of scalar-tensor theories of gravity that admits disformally equivalent frames, thus generalizing the previous results obtained in the context of standard scalar- tensor theories. This may have important consequences in cosmological context as it may allow us to identify a large class of models in different representations of the same theory, and possibly provide an insight on models beyond Horndeski action. [5,6]

Acknowledgements

The work presented here has been accomplished during my PhD at SISSA under the supervision of prof. S. Liberati.

References

1. G. W. Horndeski, Int. J. Theor. Phys. **10** (1974) 363.
2. C. Deffayet, G. Esposito-Farese and A. Vikman, Phys. Rev. D **79** (2009) 084003 [arXiv:0901.1314 [hep-th]].
3. J. D. Bekenstein, Phys. Rev. D **48** (1993) 3641 [gr-qc/9211017].
4. D. Bettoni and S. Liberati, Phys. Rev. D **88** (2013) 084020 [arXiv:1306.6724 [gr-qc]].
5. M. Zumalacárregui and J. García-Bellido, Phys. Rev. D **89** (2014) 064046 [arXiv:1308.4685 [gr-qc]].
6. Jérôm. Gleyzes, D. Langlois, F. Piazza and F. Vernizzi, arXiv:1404.6495 [hep-th].

Probing non-linear clustering in large-scale structure with the three-point phase correlation

RICHARD WOLSTENHULME
Kavli Institute for Cosmology Cambridge and Institute of Astronomy, Madingley Road, Cambridge CB3 OHA, United Kingdom

In a non-Gaussian cosmic field the phase of the density field in Fourier space contains information about the morphology of large-scale structure which is manifestly excluded from the lowest order correlation function, the power spectrum. In this paper we analytically calculate the statistically averaged three-point phase correlation in Fourier space and then the real-space corollary for three points on a line: the line correlation. We do this for an assumed infinite volume using linear Eulerian perturbation theory (PT) and then use numerical fitting to describe mode-coupling in the non-linear regime and compare the calculated line correlation to results from N-body simulations. We find that the analytical calculation is in full agreement in the linear regime and with a modification of the mode-coupling kernel, entirely consistent with simulations at smaller scales, subject to volume-limited cosmic variance.

If the universe is statistically homogenous and isotropic and if the density field is Gaussian, the power spectrum measures all the cosmological information contained in the three-dimensional galaxy maps. Consequently at sufficiently large scales, in the regime where the density field remains linear up to today, the power spectrum is sufficient to completely characterise matter fluctuations in our universe, assuming that primordial perturbations are Gaussian. At small scales however, the situation is more complicated: the non-linear gravitational evolution of the density perturbations generates non-Gaussianities in the galaxy distribution and the power spectrum does not measure all the available information. Additional statistical measures are necessary to completely characterise the density field.

In this work we briefly summarise an upcoming paper in which we study a new observable, the line correlation function $\ell(r)$, which probes phase correlations in the non-linear regime. This observable has been shown to be particularly well adapted to studying non-linearities in large-scale structure, in particular aspherical structure and dark matter clustering properties [1]. We begin by defining a correlation function in real space analogous to the three-point correlation function which describes correlations in the phase only:

$$\begin{aligned}\zeta_3^*(\mathbf{r},-\mathbf{r}) =& \big\langle \epsilon(\mathbf{s})\epsilon(\mathbf{s}+\mathbf{r})\epsilon(\mathbf{s}-\mathbf{r})\big\rangle && (1)\\ =& \iiint\limits_{|\mathbf{k}_1|,|\mathbf{k}_2|,|\mathbf{k}_3|\leq 2\pi/r} d^3\mathbf{k}_1\, d^3\mathbf{k}_2\, d^3\mathbf{k}_3 e^{i\left[\mathbf{k}_1\cdot\mathbf{s}+\mathbf{k}_2\cdot(\mathbf{s}+\mathbf{r})+\mathbf{k}_3\cdot(\mathbf{s}-\mathbf{r})\right]}\big\langle \epsilon(\mathbf{k}_1)\epsilon(\mathbf{k}_2)\epsilon(\mathbf{k}_3)\big\rangle && (2)\end{aligned}$$

Here $\epsilon(\mathbf{r})$ is the inverse Fourier transform of the phase $\epsilon(\mathbf{k}) = \delta(\mathbf{k})/|\delta(\mathbf{k})|$, which is in our convention $\epsilon(\mathbf{r}) = \int \frac{d^3\mathbf{k}}{(2\pi)^3}\, e^{i\mathbf{k}\cdot\mathbf{r}}\epsilon(\mathbf{k})$. This ensemble average is related to the probability distribution function of the phases $\mathcal{P}[\theta]$ by (here $\mathcal{P}$ is a functional of the field $\theta(\mathbf{k})$ defined through $\epsilon(\mathbf{k}) = e^{i\theta(\mathbf{k})}$):

$$\langle \epsilon(\mathbf{k}_1)\epsilon(\mathbf{k}_2)\epsilon(\mathbf{k}_3)\rangle = \int [d\theta]\mathcal{P}[\theta]\epsilon(\mathbf{k}_1)\epsilon(\mathbf{k}_2)\epsilon(\mathbf{k}_3)\,. \tag{3}$$

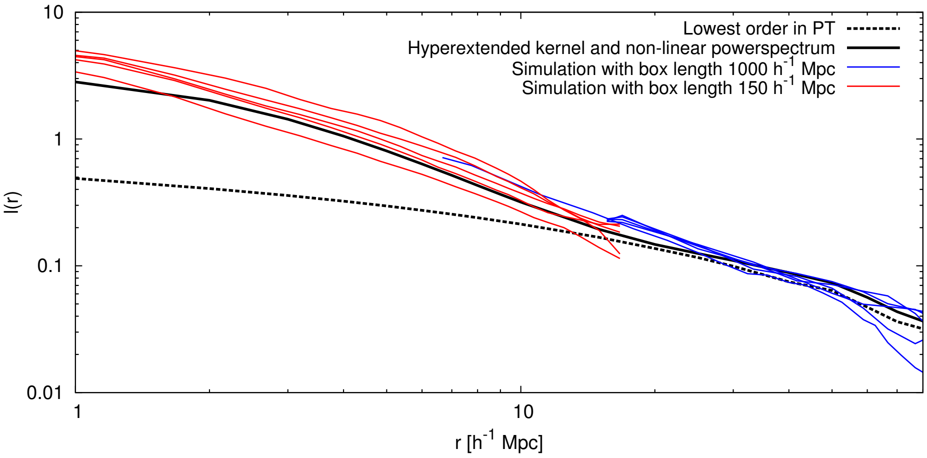

Figure 1 – The comparison between the line correlation as given in eq. 4 (dashed line), the analytical calculation using hyperextended perturbation theory (solid black line), five numerical simulations with a box length of $150\,h^{-1}$ Mpc (red) and five with a box length of $1000\,h^{-1}$ Mpc.

The probability distribution $\mathcal{P}[\theta]$ can be calculated using an Edgeworth expansion for mildly non-Gaussian fields[2]. Using this approximation, we then calculate the expectation of the three-point phase correlation to lowest order in perturbation theory and construct a volume independent, dimensionless observable $\ell(r) \propto \zeta_3^*(\mathbf{r}, -\mathbf{r})$

$$\ell(r) = \frac{(2\pi)^8 r^{9/2}}{4\sqrt{2}} \int_0^{\frac{2\pi}{r}} dk_1\, k_1^2 \int_0^{\frac{2\pi}{r}} dk_2\, k_2^2 \int_{-1}^{\mu_{\rm cut}} d\mu \\ \times F_2(k_1, k_2, \mu) \sqrt{\frac{P_L(k_1,\eta) P_L(k_2,\eta)}{P_L(|\mathbf{k}_1 + \mathbf{k}_2|, \eta)}} \Big[j_0(|\mathbf{k}_2 - \mathbf{k}_1| r) + 2 j_0(|\mathbf{k}_1 + 2\mathbf{k}_2| r) \Big] \qquad (4)$$

with j_0 the spherical Bessel function of order zero, P_L is the linear power spectrum and the value of $\mu_{\rm cut}$ is chosen to enforce the condtion $|\mathbf{k}_1 + \mathbf{k}_2| \leq 2\pi/r$. The kernel $F_2(\mathbf{k}_1, \mathbf{k}_2)$ describes the coupling between modes and is given by $F_2(\mathbf{k}_1, \mathbf{k}_2) = \frac{1}{2}(1+\epsilon) + \frac{\hat{\mathbf{k}}_1 \cdot \hat{\mathbf{k}}_2}{2}\left(\frac{k_1}{k_2} + \frac{k_2}{k_1}\right) + \frac{1}{2}(1-\epsilon)(\hat{\mathbf{k}}_1 \cdot \hat{\mathbf{k}}_2)^2$, with $\epsilon = \frac{3}{7}\left(\frac{\rho_m(\eta)}{\rho_{tot}(\eta)}\right)^{-\frac{1}{143}}$.

In figure 1 we plot the comparison between the result in eq. 4 and the results from different realisations of simulations with box lengths of $150\,h^{-1}$ Mpc and $1000\,h^{-1}$ Mpc. At large scales, $r > 10\,h^{-1}$ Mpc, perturbation theory reproduces very well the numerical result. At small scales however, the gravitational evolution has become highly non-linear and perturbation theory is no longer an adequate description. We instead use a modified coupling kernel which interpolates between the perturbative form and the results of N-body simulations[3,4] and replace the power spectrum by the non-linear power spectrum. We find that the agreement with the perturbative calculation is good, subject to cosmic variance in the volume-limited simulations, on large scales whilst the modified kernel gives us good agreement on smaller scales. Our analytical expression for $\ell(r)$ will allow us to study the dependence of phase correlations on cosmological parameters and how they compliment the two and three-point density correlation functions.

References

1. D. Obreschkow *et al*, ApJ **762**, 115 (2013).
2. T. Matsubara, ApJ **591**, 79 (2003).
3. R. Scoccimarro and H.M.P. Couchman, MNRAS **325**, 1312 (2001).
4. H. Gil-Marín *et al*, JCAP **2**, 47 (2012).

Kinetic Initial Conditions for Inflation

W.J. HANDLEY, S.D. BRECHET, A.N. LASENBY, M.P. HOBSON
Astrophysics Group, Cavendish Laboratory, J. J. Thomson Avenue, Cambridge, CB3 0HE, UK
wh260@mrao.cam.ac.uk, sylvain.brechet@epfl.ch, a.n.lasenby@mrao.cam.ac.uk, mph@mrao.cam.ac.uk,

We consider the classical evolution of the inflaton field $\phi(t)$ and the Hubble parameter $H(t)$ in homogeneous and isotropic single-field inflation models. Under an extremely broad assumption, the universe generically emerges from an initial singularity in a non-inflating state where the kinetic energy of the inflaton dominates its potential energy, $\dot\phi^2 \gg V(\phi)$. In this kinetically-dominated regime, the dynamical equations admit simple analytic solutions for $\phi(t)$ and $H(t)$, which are independent of the form of $V(\phi)$. These solutions may be used as a foundation for further theoretical investigation into the pre-inflationary universe.

The classical equations of motion for an inflating Friedmann Robertson Walker Universe driven by a single homogeneous inflaton field ϕ are:

$$\ddot\phi + 3H\phi + V'(\phi) = 0, \qquad \dot H + H^2 = -\frac{1}{3m_\mathrm{p}^2}\left(\dot\phi^2 - V(\phi)\right), \tag{1}$$

where $H = \dot a/a$ is the Hubble parameter, a is the scale factor of the universe, $V(\phi)$ is the potential energy of the inflaton and dots denote derivatives with respect to cosmic time. Inflation ($\ddot a \propto \dot H + H^2 > 0$) occurs whenever $V(\phi) > \dot\phi^2$. For many choices of potential $V(\phi)$, the *slow roll* solution is an attractor, characterised by $V(\phi) \gg \dot\phi^2$. This approximation enables theorists to make generic predictions about the inflationary phase that have minimal dependence on the exact shape of the unknown potential $V(\phi)$.

Observations of the Cosmic Microwave Background indicate that there must be at least $50-60$ e-folds of inflation, but at the moment there is little data to suggest an upper bound [2]. If there were such an upper bound, then there would be a *pre-inflationary* phase with $\dot\phi^2 > V(\phi)$. It would be helpful to have an approximation of a similar nature to slow roll to characterise this extreme primordial universe. In fact, the correct approximation for the pre-inflationary universe is the opposite of slow roll:

$$\dot\phi^2 \gg V(\phi). \tag{2}$$

As has been previously observed, in this approximation the solutions of (1) take the form:

$$H(t) = \frac{1}{3t}, \qquad \phi(t) = \phi_\mathrm{i} + \sqrt{\frac{2}{3}}m_\mathrm{p}\log\frac{t}{t_\mathrm{i}}, \qquad a(t) = a_\mathrm{i}\left(\frac{t}{t_\mathrm{i}}\right)^{1/3}, \tag{3}$$

where $a_\mathrm{i}, \phi_\mathrm{i}$ are integration constants evaluated at some initial time t_i. Integrating the classical equations of motion (1) backwards in time, this solution is an attractor for any potential $V(\phi)$. More precisely:

$$\begin{gathered}\text{If as } a \to 0, \quad \exists\varepsilon \quad \text{s.t.} \quad |\dot\phi| > \varepsilon > 0,\\ \text{then for any potential } V(\phi), \text{ as } a \to 0,\\ \dot\phi^2 \gg V(\phi) \text{ (except for perhaps a single solution).}\end{gathered}$$

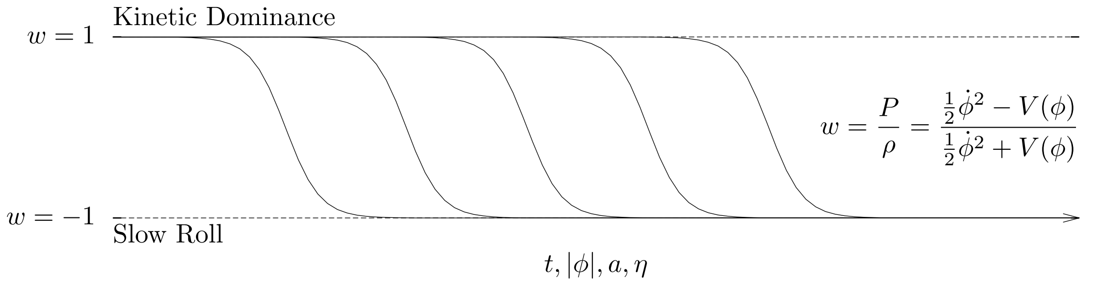

Figure 1 – Schematic of the equation of state parameter w against cosmic evolution. The generic scenario entails beginning in a kinetically dominated phase with $\dot{\phi}^2 \gg V(\phi)$ before moving to the typical slow roll attractor solution with $\dot{\phi}^2 \ll V(\phi)$. We term the intermediate stage "Fast roll".

This statement has been rigorously proved in[1], and the early time classical solutions are therefore divided into three classes:

1. Solutions which violate $|\dot{\phi}| > \varepsilon > 0$. These are either oscillating solutions, or ones where the inflaton "begins" its evolution from a stationary state. Hilltop inflation is an example of the latter.
2. A single special solution, specific to the potential. An example of this is power law inflation for exponential potentials.
3. Kinetically dominated solutions, as in equation (3).

In the kinetically dominated universe, the classical solutions begin in the form (3). As time goes on, $|\dot{\phi}|$, $|\phi|$ and H decrease until $\dot{\phi}^2 \sim V(\phi)$. This marks the onset of a brief period of fast roll inflation prior to a protracted slow roll phase.

This is an identical situation to that described in "Just enough inflation" [3], in which it is suggested that there is a physical mechanism which cuts of the potential at some maximum value. Our work shows that in fact any potential is effectively cut-off by the dominance of $\dot{\phi}^2$. The fast roll phase has been examined in[4], where it has been shown that this could be observable in the CMB as a cut-off of power in the primordial power spectrum $\mathcal{P}_{\mathcal{R}}(k)$ at low-k.

Kinetic Dominance therefore provides a general situation for examining the very early universe. It is a foundation for theoretical investigation, and may have observable consequences. For more detail, consult the full paper[1].

Acknowledgments

S D B thanks the Isaac Newton Trust and the Sunburst Fund for their support. W H thanks STFC for their support.

References

1. W. J. Handley *et al*, *Phys. Rev.* D **89**, 063505 (2014)
2. W.H. Kinney, *arXiv*:1404.4614v1 [astro-ph.CO] (2014)
3. E. Ramirez, *Phys. Rev.* D **85**, 103517 (2012)
4. D. Boyanovsky *et al*, *Phys. Rev.* D **74**, 123007 (2012)

LUNAR SECULAR ACCELERATION SUPPORTS A MODIFIED THEORY FOR GRAVITY

Göran Henriksson
Department of Physics and Astronomy
Uppsala University, Box 516, SE-751 20 Uppsala

In 2011, I performed a new calibration of the sidereal lunar secular acceleration, -30.13 arc seconds/century^2 ($''/\mathrm{cy}^2$), based on 33 total solar eclipses back to 3653 BC. The lunar secular acceleration $-25.85''/\mathrm{cy}^2$, from the Lunar Laser Range (LLR) measurements, must be corrected for the precession of the geodesic in the Earth-Moon-system, $-3.84''/\mathrm{cy}^2$, to get the sidereal lunar secular acceleration, $-29.6''/\mathrm{cy}^2$. The difference between the corrected LLR-result and my new calibration, $-0.44''/\mathrm{cy}^2$, is in good agreement with the so-called cosmological precession of the Moon, as predicted by Gia Dvali et al. in a modified theory of gravity.

A new calibration of the sidereal lunar secular acceleration

A correct identification of ancient solar eclipses is not only important for historical reasons, but also gives the possibility of determining the secular acceleration of the longitude of the moon and testing different theories for gravity, as detailed in Henriksson[1,2]. Carl Schoch[3] calibrated his sidereal lunar secular acceleration, -29.68 arc seconds/century^2 ($''/\mathrm{cy}^2$), from a conjunction between the star Spica and the moon in 283 BC, and from an analysis of total solar eclipses dating back to 600 BC.

The lunar secular acceleration $-5.85''/\mathrm{cy}^2$, determined from the Lunar Laser Range (LLR) measurements, Williams *et al.*[4], must be corrected by $-3.84''/\mathrm{cy}^2$, Nordtvedt[5], for the precession of the geodesic, according to Einstein6), before it can be compared with results from the observations of ancient solar eclipses. After correcting for General Relativity, the sidereal lunar secular acceleration from the LLR measurements is $-29.69''/\mathrm{cy}^2$ which is very close to Schoch?s value, $-29.68''/\mathrm{cy}^2$.

However, Schoch had a third-order term in the formula for the lunar longitude, introduced by Simon Newcomb. I decided to eliminate this term and to optimize the physical value for the sidereal lunar secular acceleration. This value must give the same result as in the earlier successful calculations according to Schoch?s original formulas. A search started for the value of the lunar sidereal secular acceleration that gave the maximum sum of the magnitudes for 33 total, or almost total, solar eclipses between 878 AD and 3653 BC.

The new value for the sidereal lunar secular acceleration, $-30.13''/\mathrm{cy}^2$, gives an even better agreement with the ancient observations than the original formulas by Schoch. It is valid at least during the last 5650 years with a timing error of less than two minutes. The difference, $-0.44''/\mathrm{cy}^2$, between the new calibration and the corrected LLR-measurement is significant and can be interpreted as an additional gravitational effect beyond General Relativity.

Anomalous lunar perigeum precession predicted by modified gravity

Dvali et al. [7] write: "Cosmologically motivated theories that explain small acceleration rates of the Universe via modification of gravity at very large, horizon or super horizon, distances can be tested by precision gravitational measurements at much shorter scales, such as the Earth-Moon distance. [...] The key reason for such corrections is the van Dam-Veltman-Zakharov [8] discontinuity present in linearized versions of all such theories, and its subsequent absence at nonlinear level in the manner of Vainshtein [9]." The aim of this paper is to show that in a large class of theories that modify gravity beyond some horizon distance rc, there are corrections that have effects on much shorter scales $r* << rc$, and could be detectable in precision measurement in the Earth-Moon system.

Before calculating the magnitude of the testable parameters in the solar system, they summarize the properties of the massive graviton behind the observable effects: "In the interval $r* << r << rc$, the linearized approximation is valid. So gravity is still $1/r$, but is of scalar-tensor type. Note that the term 'scalar-tensor' only refers to the similarity in the tensor structure, rather than to the existence of an independent spin-0 state in the theory. Instead the scalar' admixture comes from the extra polarization of the spin-2 graviton."

Dvali et al. continue: "We will restrict ourselves to an order-of-magnitude estimate, but the sign will be very important if the effect is found, ...". Lue and Starkman [10] have pointed out that the cosmological background only affects the sign of the coefficient. It is negative for the standard cosmological branch, and is positive for the self-accelerated one.

The anomalous planetary perihelion precession (the perihelion advance per orbit due to gravity modification is: $\delta\phi = (3\pi/4)\epsilon$. For the actual model $\epsilon = -\sqrt{2}\ rc^{-1}\ rg^{-1/2}\ r^{3/2}$. Numerically, the gravitational radius of the Earth is $rg = 0.886$ cm, the Earth-Moon distance $r=$ 3.84 x 1010 cm and the gravity modification parameter that gives the observed acceleration without dark energy $rc =$ 6 Gpc (1.85 x 1028 cm). If we transform the result to the units used by the observers in the solar system, we get a predicted cosmological precession of -0.52$''$/cy^2. If my excess in sidereal lunar secular acceleration, -0.44$''$/cy^2, see above, is interpreted as the cosmological precession, we get an observed value for $rc = 7$ Gpc and we find ourselves in the standard cosmological branch.

The massive graviton is 5-dimensional and needs a 5D space, but within distances $< rc$, a 4D theory is enough. For distances $> rc$, the gravitons begin to leak to the 5^{th} dimension and the gravitational forces between the galaxies are weakened resulting in the observed acceleration of the universe [11,12]. The latest massive gravity models agree well with the observations, Cardone et al. [13].

Acknowledgments

I am grateful to Drs Andreas Korn and Eric Stempels for their critical reading of my text and to the Department of Physics and Astronomy, Uppsala University for the financial support of my participation in the Rencontres de Moriond 2014.

References

1. G. Henriksson, *Astronomical Society of the Pacific*, Conference Series 409, 166 (2009).
2. G. Henriksson, *Journal of Cosmology* 9, 2259 (2010).
3. C. Schoch, *Astronomische Abhandlungen, Ergnzungs-hefte zu den Astronomischen Nachrichten*, Band 8 B2 (1931).
4. J.G. Williams, D.H. Boggs and W.M. Folkner, DE421 *Lunar orbit, Physical Librations, and Surface Coordinates.* IOM 335-JW,DB,WF-20080314-001, March 14 (2008).
5. K. Nordtvedt, *Physics Today*, May 1996, 49:5, 29 (1996).
6. A. Einstein, Annalen der Physik 49 (1916).
7. G. Dvali, A. Gruzinov, and M. Zaldarriaga, *Phys. Rev.* D, 68, Issue 2, id. 024012 (2003).
8. H. van Dam and M. Veltman, Nucl. Phys. B22, 397 (1970).
9. A.I. Vainshtain, *Phys. Lett.* 39 B, number 3, 393, 1 May 1972 (1972).
10. A. Lue and G. Starkman, *Phys. Rev.* D 67, 064002 (2003).
11. A.G. Riess, et al. (High-z Supernova Team), *Astron.* J. 116, 1009 (1998).
12. S. Perlmutter, et al. (Supernova Cosmology Project),*Astrophys. J.* 517, 565 (1999).
13. V.F. Cardone, N. Radicella, and L. Parisi, *Phys. Rev.* D 85, 124005 (2012).

Evolution of the fine-structure constant in runaway dilaton models

Pauline E. Vielzeuf and C. J. A. P. Martins
Centro de Astrofísica da Universidade do Porto, Portugal

We study the detailed evolution of the fine-structure constant α in the string-inspired runaway dilaton class of models of Damour, Piazza and Veneziano. We provide constraints on this scenario using the most recent spectroscopic measurements and explore possible ways to distinguish it from alternative models for varying α.

Runaway Dilaton Cosmology

String theory predicts the presence of a scalar partner of the spin-2 graviton, the dilaton. Here, we will study the cosmological consequences of a particular class of string-inspired models, the runaway dilaton scenario of Damour et al.[1,2] and assess its testability by future facilities.
The Friedmann and field evolution equation for this class of models can be written as:

$$3H^2 = 8\pi G \sum_i \rho_i + H^2 \Phi'^2 \tag{1}$$

$$\frac{2}{3-\Phi'^2}\Phi'' + \left(1 - \frac{p}{\rho}\right)\Phi' = -\sum_i \alpha_i(\Phi)\frac{\rho_i - 3p_i}{\rho} \tag{2}$$

Here $p = \sum_i p_i$, $\rho = \sum_i \rho_i$, sums over all components except the kinetic part of the scalar field, and $\alpha_i(\Phi)$ are the couplings to the dilaton with each components i, so they characterize the effect of the various components of the universe on the dynamics of the field. Experimental constraints impose a tiny coupling to baryonic matter, $\alpha_{had} \sim 40 b_F c e^{-c\Phi}$, where b_F and c are constant free parameters. From weak equivalence principle tests one will obtain $|\alpha_{had,0}| \leq 10^{-4}$ and using the basic definition of deceleration parameter q one can find that $|\Phi_0'| \leq 0.3$. Using these bounds on initial conditions, one can then numerically solve the field equations.

Variations of fundamental constants

Recent obsevations suggest possible variations of fine-structure constant α, (recent measurements in Ferreira et al.[3] and α measurements from Webb et al. [6]). It's then interesting to study the behaviour of α in this class of models, and as it has been shown in Damour et al. [1], the evolution of α is given by:

$$\frac{1}{H}\frac{\dot{\alpha}}{\alpha} = \frac{b_F c e^{-c\Phi}}{1 - b_F c e^{-c\Phi}}\Phi' \Rightarrow \frac{\Delta\alpha}{\alpha}(z) = \frac{\alpha(z) - \alpha_0}{\alpha_0} = b_F\left(e^{-c\Phi_0} - e^{-c\Phi(z)}\right) \tag{3}$$

The present drift of α is constrained by the Rosenband bound, $\left(\frac{1}{\alpha}\frac{d\alpha}{dt}\right)_0 = (-1.6 \pm 2.3)^{-17} yr^{-1}$ which allows us to get the bound $|\alpha_{\mathrm{had},0}\Phi_0'| \sim |b_F c e^{-c\Phi_0'}| \leq 3 \times 10^{-5}$.

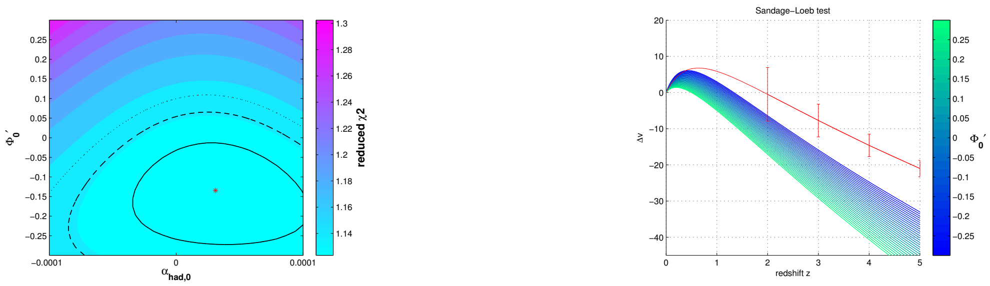

Figure 1 – Minimum reduced-χ^2 and confidence level intervals using alpha and H(z) data from Webb et al.[6], Ferreira et al.[3] and Farooq et al.[5] (left) and Sandage-Loeb signal compare to ΛCDM in red (right)

From here one can then predict the redshift evolution of α taking Φ_0 and Φ_0' as free parameters and make a χ^2 analysis using H(z) data [5] and α data from Webb et al.[6] and Ferreira et al.[3] (fig.1 left panel).

Future tests

The drift in the spectroscopic velocity of an object following the Hubble flow can be obtained from the definition of redshift and expressed as:

$$\Delta v = \frac{c}{(1+z)} \Delta t (H_0(1+z) - H(z)) \tag{4}$$

Here c is the speed of light and Δt the timespan of observation. The precision needed to detect this signal is expected to be reached by future facilities such as the SKA an intensity mapping experiments, but here we focus on ELT-HIRES. The evolution spectrosopic velocity of our model with the corresponding errorbars expected for HIRES is shown in figure(1) (right panel).

Conclusions

The runaway dilaton class of models remains an alternative possibility to the standard model; however, current data already places tight constraints on its free parameters.

Given these constraints, the model predicts distinctive behaviours for α and the redshift drift signal, which will be tested with future facilities such as ELT-HIRES.

Acknowledgments

We acknowledge the financial support of grant PTDC/FIS/111725/2009 from FCT (Portugal). C.J.M. is also supported by an FCT Research Professorship, contract reference IF/00064/2012, funded by FCT/MCTES (Portugal) and POPH/FSE (EC).

References

1. T. Damour, F. Piazza and G. Veneziano. *Phys. Rev. Lett.*, **89**:081601, 2002.
2. T. Damour, F. Piazza and G. Veneziano. *Phys. Rev. D.*, **66**:046007, 2002.
3. M.C. Ferreira, O. Frigola, C.J.A.P. Martins, A.M.R.V.L. Monteiro, and J. Sol *Phys. Rev. D* **89**, 083011 (2014)
4. C. J. A. P. Martins, M. C. Ferreira, M. D. Julião, A. C. O. Leite, A. M. R. V. L. Monteiro, P. O. J. Pedrosa and P. E. Vielzeuf, *Mem. S. A. It.* **85**, 13 (2014)..
5. O. Farooq and B. Ratra.*Astrophys. J.*, **766**(L7), 2013.
6. J. K. Webb, J. A. King, M. T. Murphy, V. V. Flambaum, R. F. Carswell and M. B. Bainbridge, *Phys. Rev. Lett.* **107**, 191101 (2011).

CONSISTENCY TESTS OF THE STABILITY OF FUNDAMENTAL COUPLINGS AND UNIFICATION SCENARIOS

M. C. FERREIRA,[1,2] O. FRIGOLA,[3] C. J. A. P. MARTINS,[1] A. M. R. V. L. MONTEIRO,[1,2] and J. SOLÀ[4]
[1] *Centro de Astrofísica, Universidade do Porto, Rua das Estrelas, 4150-762 Porto, Portugal,*
[2] *Faculdade de Ciências, Universidade do Porto, Rua do Campo Alegre, 4150-007 Porto, Portugal,*
[3] *Institut S'Agulla, Carretera de Malgrat 13, 17300 Blanes, Spain,*
[4] *Institut Manuel Blancafort, Avinguda 11 de Setembre 29, 08530 La Garriga, Spain.*

We summarize an exhaustive analysis [1] of current combined spectroscopic measurements of fundamental couplings, specifically the fine-structure constant α, the proton-to-electron mass ratio μ and the proton gyromagnetic ratio g_p. We also discuss some of the implications of the currently available measurements for fundamental physics, specifically for unification scenarios.

1 Introduction

The stability of nature's fundamental couplings is among the most profound open issues in astrophysics and fundamental physics, and has been identified by ESA and ESO as one of the key drivers for the next generation of ground and space-based facilities. At a phenomenological level, fundamental couplings *run* with energy and in many extensions of the standard model, particularly in theories with additional space-time dimensions, they also *roll* in time and *ramble* in space.

A detection of varying fundamental couplings will be revolutionary: it will prove that the Einstein Equivalence Principle is violated. However, improved null results are also important because they will tighten constraints on fundamental physics and cosmology.

Any Grand-Unified model predicts a relation between the variation of α and those of μ and other couplings, and therefore simultaneous measurements of both provide key consistency tests. The basic formalism for these tests was developed in reference 2 and 3.[2,3].

2 Phenomenological Models

We shall work on the assumption that varying fundamental couplings are due to a dynamical, dilaton-type scalar field (see [4,5,6,7] and references therein). We consider a class of grand unification models where the weak scale is determined by dimensional transmutation and the relative variation of all the Yukawa couplings is the same.

With these assumptions one finds that $\frac{\Delta\mu}{\mu} = [0.8R - 0.3(1+S)]\frac{\Delta\alpha}{\alpha}$ where R and S are phenomenological (model-dependent) parameters.

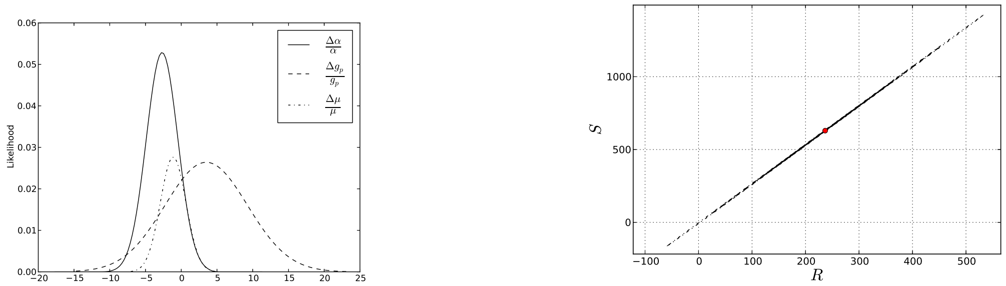

Figure 1 – Left panel: One-dimensional likelihoods for the relative variations of α, μ and g_p from the radio band dataset. Right panel: Constraints on the $R - S$ plane from the radio band dataset.

3 Consistency analyses and Constraints on Unification Scenarios

Different combinations of α, μ and g_p can be measured in the radio band. A joint analysis of this dataset can be done to find the most likely values of each one[1]. The left panel of Figure 1 shows the one-dimensional likelihood contours for each of these parameters. At 68.3% confidence level we find $\frac{\Delta\alpha}{\alpha} = -2.7 \pm 2.2$ ppm, $\frac{\Delta\mu}{\mu} = -1.1 \pm 1.8$ ppm and $\frac{\Delta g_p}{g_p} = 3.5 \pm 5.8$ ppm. In doing this we are neglecting a possible redshift dependence of the variations; more data would allow a more detailed analysis.

By using the phenomenological parametrizations introduced in Section 2, it is possible to translate the available measurements into constraints on the $R-S$ plane. As in previous analyses [4,5] there is a degeneracy direction, *i.e.*, these measurements constrain a particular combination of the parameters R and S. The right panel of Figure 1 shows the constraints in the R-S plane derived from the radio band set of measurements previously referred. At 68.3% confidence level we find $R = 237 \pm 86$ and $S = 630 \pm 230$.

4 Conclusions

We find no significant evidence for varying couplings. We also obtain constraints on the $R - S$ parameter space. Both results stem from radio band measurements of combinations of fundamental couplings.

Acknowledgments

We are grateful to Mariana Julião for useful discussions. This work was done in the context of the project PTDC/FIS/111725/2009 from FCT (Portugal). O.F. and J.S. acknowledge financial support from Programa *Joves i Ciència*, funded by Fundació Catalunya - La Pedrera. C.J.M. is also supported by an FCT Research Professorship, contract reference IF/00064/2012, funded by FCT/MCTES (Portugal) and POPH/FSE (EC).

References

1. M. C. Ferreira *et al*, *Phys. Rev.* D **89**, 083011 (2014).
2. A. Coc *et al*, *Phys. Rev.* D **76**, 023511 (2007).
3. F. Luo *et al*, *Phys. Rev.* D **84**, 096004 (2011).
4. M. C. Ferreira *et al*, *Phys. Rev.* D **86**, 125025 (2012).
5. M. C. Ferreira *et al*, *Phys. Lett.* B **724**, 1 (2013).
6. A. Avgoustidis *et al*, *JCAP* **1202**, 013 (2012).
7. A. Avgoustidis *et al*, arXiv:1305.7031.

Cosmic infrared background measurements from *Planck* and implications for star formation

P. SERRA on behalf of the *Planck* Collaboration
Institut d'Astrophysique Spatiale (IAS),
Bâtiment 121, F- 91405, Orsay (France)

We present new measurements of cosmic infrared background (CIB) anisotropies using *Planck*. Combining HFI data with *IRAS*, the angular auto- and cross-frequency power spectrum is measured from 143 to 3000 GHz, and the auto-bispectrum from 217 to 545 GHz. After careful removal of the contaminants (cosmic microwave background anisotropies, Galactic dust and Sunyaev-Zeldovich emission), and a complete study of systematics, the CIB power spectrum is measured with unprecedented signal to noise ratio from angular multipoles $\ell \sim 150$ to 2500. The interpretation based on the halo model is able to associate star-forming galaxies with dark matter halos and their subhalos, using a parametrized relation between the dust-processed infrared luminosity and (sub-)halo mass and it allows to simultaneously fit all auto- and cross- power spectra very well. In particular, we find that the star formation history is well constrained up to redshifts around 2, and agrees with recent estimates of the obscured star-formation density using *Spitzer* and *Herschel*. However, at higher redshift, the accuracy of the star formation history measurement is strongly degraded by the uncertainty in the spectral energy distribution of CIB galaxies. We also find that the mean halo mass which is most efficient at hosting star formation is $\log(M_{\rm eff}/{\rm M}_\odot) = 12.6$ and that CIB galaxies have warmer temperatures as redshift increases.

1 Introduction and data used

The relic emission from galaxies formed throughout cosmic history appears as a diffuse, cosmic background. The Cosmic Infrared Background (CIB) is the far-infrared part of this emission and it contains about half of its total energy (Dole et al. (2006)). The anisotropies detected in this background light trace the large-scale distribution of star-forming galaxies and, to some extent, the underlying distribution of the dark matter halos in which galaxies reside. The CIB is thus a direct probe of the interplay between baryons and dark matter throughout cosmic time and it allows an accurate determination of the Star Formation History of the Universe, which has long been a fundamental goal in Astronomy. Combining *Planck* HFI data with IRAS, the CIB angular auto- and cross-frequency power spectra are measured from 143 to 3000 GHz and they are interpreted with a Halo Model that associates star-forming galaxies with dark matter halos and their sub-halos, using a parametrized relation between the dust-processed infrared luminosity and (sub-)halo mass. The star formation history is well constrained up to redshifts around z∼2, and agrees with recent estimates of the obscured star formation density using Spitzer and Herschel. However, at higher redshift, the accuracy of the star formation history measurement is strongly degraded by the uncertainty in the spectral energy distribution of CIB galaxies.

We use *Planck* channel maps in Healpix (Gorski et al. 2005) format from the six HFI frequencies: 100, 143, 217, 353, 545, and 857 GHz, together with far-infrared data at 3000 GHz (100 m) from IRAS (IRIS, Miville-Deschenes & Lagache (2005)). Although *Planck* is an all-sky

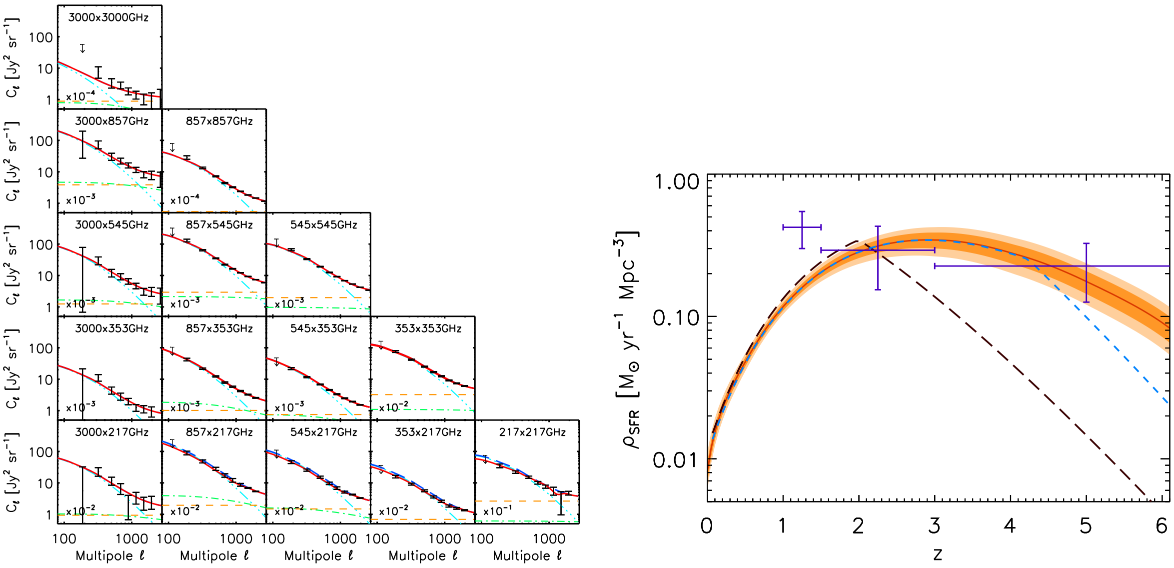

Figure 1 – (Left panel) (Cross-) power spectra of the CIB anisotropies measured by *Planck* and *IRAS*, compared with the best-fit extended halo model. Data points are shown in black. The red line is the sum of the linear, 1-halo and shot-noise components, which is fitted to the data. The orange dashed, green dot-dashed, and cyan three-dots-dashed lines are the best-fit shot-noise level, the 1-halo and the 2-halo terms, respectively. (Right panel) Marginalized constraints on the star formation rate density, as derived from our extended halo model (red continuous line with ±1 and $\pm 2\,\sigma$ orange dashed areas). It is compared with mean values computed imposing different conditions on the redshift evolution of galaxy luminosities (black long-dashed line and blue dashed line). The violet points with error bars are the SFR density determined from the modeling of the CIB-CMB Lensing cross correlation by Planck 2013 Results XVIII.

survey, we restricted our CIB anisotropy measurements to a few fields at high Galactic latitude, where foregrounds can be more easily controlled. The total area used to compute the CIB power spectrum is about 2240 deg^2, 16 times larger than in Planck Collaboration XVIII (2011). Measuring the CIB anisotropies is not easy, and it requires a very accurate component separation. Galactic dust, Cosmic Microwave Background (CMB) anisotropies, emission from galaxy clusters through the thermal Sunyaev-Zeldovich (tSZ) effect, and point sources all have a part to play. To remove the CMB we use a simple subtraction technique, using the HFI lowest frequency channel (100 GHz) as a CMB template and taking into account for its contamination due to CIB and tSZ residuals. For the Galactic dust we use an independent, external tracer of diffuse dust emission, the HI gas. From 100 μm to 1 mm at high Galactic latitude and outside molecular clouds, a tight correlation is observed between far-infrared emission from dust and the 21-cm emission from gas: HI can thus be used as a tracer of cirrus emission and the dust can be removed accordingly.

2 Results: constraints on Star Formation History

With a best-fit χ^2 of 100.7 and 98 degrees of freedom, we obtain a very good fit to the data (see Fig. 1 left panel) using an extended version of the standard halo model. The mean value of the most efficient halo mass for generating the CIB, $\log(M_{\rm eff}/M_\odot) = 12.6 \pm 0.1$, is in good agreement with results obtained from a similar analysis using *Herschel* data. The star formation rate density (SFRD) predicted (see Fig. 1, right panel) is in agreement with other measurements up to redshift z$\sim$2, while at higher redshifts our model predicts higher values for the SFRD respect to other measurements (see e.g. Gruppioni et al. (2013) and also a different analysis of *Planck* data using only linear scales, i.e. multipoles $l < 500$). However, the SFRD predicted is in very good agreement with the estimate obtained from the gravitational lensing-infrared background correlation with *Planck* data (see Planck Collaboration XVIII). Knowing that the

SEDs of the galaxies responsible for the bulk of the CIB is the principal limitation in our modeling framework, the accurate measurement of the SEDs with future surveys will be crucial to properly estimate the obscured star formation rate density at high redshift from the CIB anisotropies and thus determine whether or not the bulk of the star formation is obscured at high redshift, and whether the UV and Lyman-break galaxy populations are a complete tracer of the star formation in the early Universe.

Acknowledgments

The development of Planck has been supported by: ESA; CNES and CNRS/INSU-IN2P3-INP (France); ASI, CNR, and INAF (Italy); NASA and DoE (USA); STFC and UKSA (UK); CSIC, MICINN and JA (Spain); Tekes, AoF and CSC (Finland); DLR and MPG (Germany); CSA (Canada); DTU Space (Denmark); SER/SSO (Switzerland); RCN (Norway); SFI (Ireland); FCT/MCTES (Portugal); and PRACE (EU). A description of the Planck Collaboration and a list of its members with the technical or scientific activities they have been involved into, can be found at `http://www.rssd.esa.int/index.php?project=PLANCK&page=PlanckCollaboration`. The Parkes radio telescope is part of the Australia Telescope National Facility which is funded by the Commonwealth of Australia for operation as a National Facility managed by CSIRO. Some data used in this paper are based on observations with the 100-m telescope of the MPIfR (Max-Planck-Institut fur Radioastronomie) at Effelsberg.

References

1. Dole, H., Lagache, G., Puget, J. L., *et al.* 2006, A&A, **451**, 417
2. Gorski, K. M., Hivon, E., Banday, A. J., *et al.* 2005, ApJ, **622**, 759
3. Miville-Deschenes, M.-A. & Lagache, G. 2005, ApJS, **157**, 302
4. Planck Collaboration XVIII. 2013, submitted to A&A
5. Gruppioni, C., Pozzi, F., Rodighiero, G., *et al.* 2013, ArXiv e-prints


LA VALDOTAINE
GENEPY
RESERVE
DELLA VALLE D'AOSTA
GENEPY NATUREL

Observational appearances of dark matter clumps via gravitational microlensing

E. Fedorova[a], A. Del Popolo, V.I. Zhdanov, A.N. Alexandrov, V. Sliusar
Astronomical Observatory of Taras Shevchenko National University of Kyiv, Kiev 03040, Ukraine

We compare a microlensing of a remote point source on point-like objects (stars or black holes) and on clumps of dark matter of a non-zero size described by circularly symmetric "toy models". The microlensing of the source by one clump is considered in detail. We look for astrometric and photometric features of the microlensing, which depend significantly on the clump compactness and could give us a possibility to test the dark matter models.

1 Introduction. Models of the DM substructure

During the last decade cosmological N-body simulations were performed within different dark matter models (CDM [2,1,5], warm dark matter (WDM) [6], self-interacting dark matter (SIDM) [7,9] etc). These simulations show that the dark matter (DM) distribution is essentially inhomogeneous, and the characteristic scales of these inhomogeneities, as well as their density distributions, depend significantly on the properties of DM particles. The existence of DM clumps with mass in range $10^{-3} - 10M_{\odot}$ typical to microlensing objects was predicted by N-body simulations [3,4,10,13] within CDM and SIDM models, but not within WDM one [6] due to essentially different kinds of structure formation in these cosmologies ("down-top" in CDM and "top-down" in WDM).

The key roles in the DM models belong to the subhalo density profile and the substructure mass fraction, determining the part of the total halo DM mass in substructure formations. Within the CDM model, the substructure mass fraction in a host (i.e. galaxy or cluster halo) depends very strongly on the host halo mass. In CDM cosmology, abundance of the DM clumps with mass the range of 10^{-3} – $10\mathrm{M}_{\odot}$ is near 13% of the total DM mass of a host halo [8]. If we take into account the fact that the larger subhalos (with mass greater than $10M_{\odot}$) also contain smaller substructure, this value can be even larger. However, estimating the probability of the DM subhalo microlensing we should take into account also that up to 90% of the primordial subhaloes in luminous parts of galaxies had to be fully or partially disrupted by tidal forces of stars, thus the percentage of the clumped matter in the areas cannot exceed 10% [11,12]. At the same time in these disruption processes a new kind of object could appear: ultracompact mini halo (UCMH) of DM, surrounding the point-like object (star or black hole) that had disrupted the primordial DM clump and then trapped it by its gravitational field [16]. Main characteristics of these DM models described above are shown in Table 1.

In this view it is interesting to analyze possible observational appearances of the putative DM clumps within CDM and SIDM models and UCMHs via microlensing on Galactic and extragalactic objects. Because of different mass distributions in various clump models one can hope that using the gravitational microlensing we can give preference to some cosmology. However, prior to consideration of sophisticated clump models, it is instructive to study typical qualitative properties of microlensed images that can appear in observations. Such a consideration of a

---

[a] E-mail: efedorova@ukr.net

Table 1: DM models and substructure.

Cosmology/ clump type	0.001-10M$_\odot$ clumps abund.	Surface mass density	Size	Lens equation
CDM/cusped	13-14%	$\sigma(r) = \sigma_0/r^{3/2}$	$R_S = R_{CDM}\left(\frac{M}{M_\odot}\right)^{1/3}$	$\mathbf{y} = \mathbf{r}\left\{1 - \left(\frac{\rho}{r}\right)^{3/2}\right\}$
SIDM/cored	11-12%	$\sigma(r) = \frac{\sigma_0}{(r^2+R_S^2)^2}$	$R_S = R_{SIDM}\left(\frac{M}{M_\odot}\right)^{9/13}$	$\mathbf{y} = \mathbf{r}\left\{1 - \frac{R_E^2}{r^2+R_S^2}\right\}$
CDM/UCMH	?	$\sigma_0 > 1$	-	$\mathbf{y} = \mathbf{r}\left\{1 - \sigma_0 - \frac{R_E^2}{r^2}\right\}$

"screen-like" dark lens model was proposed for the first time by Zakharov [14,15]. Here we consider some other models described in Table 1, which allow a simple analytical treatment. In view of the above discussion, these are special cases of the cusped clump, cored clump and a point mass surrounded by a continuous matter (UCMH).

2 Point lens and cusped clump

The critical curve/caustic pictures of Schwarzschild microlens and cusped clump are very similar: in both cases there is one circular critical curve with Einstein radius R_E in the first case and $\rho = R_S(R_E/R_S)^{4/3}$ in the second one, and no regular caustic curves exist (isolated points only). The analytical solutions for image positions for Schwarzschild lens are widely known. In the case of the cusped DM clump the lens equation also has two solutions that can be written analytically. The first one is: $\mathbf{r} = \frac{\mathbf{y}}{3}\frac{[(\xi+\sqrt{\xi^2+1})^{2/3}-1]^2}{(\xi+\sqrt{\xi^2+1})^{2/3}}$, where $\xi \equiv \frac{3\sqrt{3}}{2}\left(\frac{\rho}{y}\right)^{3/2}$. The second solution can be represented as $\mathbf{r} = \frac{\mathbf{y}}{3}\frac{[(\xi+\sqrt{\xi^2-1})^{2/3}+1]^2}{(\xi+\sqrt{\xi^2-1})^{2/3}}$ for $\xi \geq 1$ and $\mathbf{r} = \frac{4\mathbf{y}}{3}\cos^2[\arccos(\xi)]$ for $\xi < 1$. The lens mapping of a point source by cusped clump is very similar to that of the point microlens. When the microlens moves along the straight line with respect to the source, the total magnification curve in both models has only one maximum when the distance between the source and the microlens is minimal. Therefore, these two situations cannot be distinguished even in the case of accessibility of both the astrometrical and photometrical data about the microlensing event.

3 Circular caustic situations: cored clump and UCMH

Observational appearances of microlensing by cored DM clump depend significantly on the clump compactness. There are two qualitatively different situation: compact clump ($R_s \leq R_E$) and non-compact clump ($R_s > R_E$). If $R_s < R_E$, there are two circular critical $r_c = \sqrt{R_E^2 - R_S^2}$ (mapped onto the origin $\mathbf{y} = 0$) and $r_c^2 = \frac{R_E}{2}\left(\sqrt{R_E^2 + 8R_S^2} - R_E\right) - R_S^2$ (mapped onto circular caustic, the radius is easily recovered by direct substitution into the lens mapping). In opposite case $R_s > R_E$ there is no critical curves and no caustics.

In the case of non-compact clump we have only one solution, as well as for the situation when the source trajectory is outside the caustic of the compact clump. If the source crosses the caustic of the compact clump, the situation becomes more interesting: there are three images of the source, two inside a critical curve and one outside it. The total magnification curves for these situations are shown on the Fig. 1 (left panel). The most notable result here is the appearance of the additional bright maximum on the magnification curve in case of the caustic crossing. In UCMH case ($\sigma_0 > 1$) we have one circular critical curve $r_c = \frac{R_E}{\sqrt{\sigma_0 - 1}}$ and one circular caustic $y_c = 2R_E\sqrt{\sigma_0 - 1}$. In such a system, if source does not cross the caustic, three images exist (one

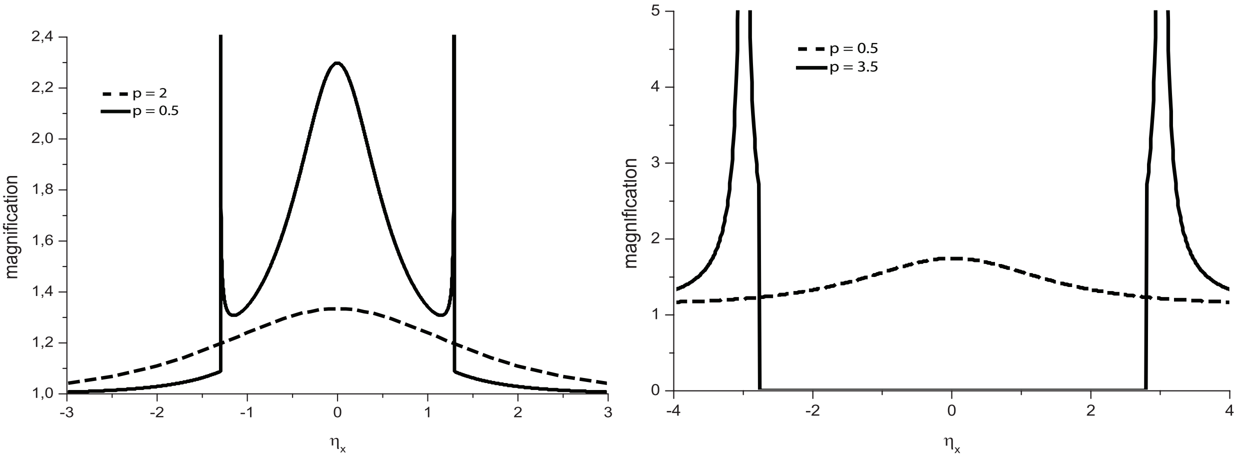

Figure 1 – Total magnification curves: compact cored clump (left) and UCMH (right) for source tracks with different impact parameters p (in units of R_E).

inside the critical curve and one outside it). When source crosses caustic, two images merge and disappear. On the corresponding magnification curve the bright flash followed by an eclipse-like effect can be observed, as it is shown on the right panel of the Fig. 1.

4 Conclusions

The main conclusions can be drawn as follows for DM clumps microlensing in the Galaxy:

(i) the cusped CDM and non-compact SIDM clumps are hardly distinguishable from the point lens;

(ii) compact SIDM clump and UCMH cases can differ significantly from the point lens case, as well as from each other;

(iii) the three-horned lightcurve (instead of usual curve with one maximum) can be considered as an appearance of the SIDM clump;

(iv) two-horned one with significant dilution (eclipse-like effect) between two caustic crossing can be considered as an appearance of an UCMH;

(v) absence of microlensing by DM clumps favors the WDM model.

References

1. E. Contini, G. De Lucia, S. Borgani, *MNRAS* **420**, 2978 (2012).
2. A. El-Zant, I. Shlosman, *Astrophys.Journ.* **560**, 636 (2001).
3. J. Diemand, B. Moore, J. Stadel, *Nature* **433**, 389 (2005).
4. J. Diemand, B. Moore, J. Stadel, *MNRAS* **352**, 535 (2004).
5. J. Hisano,K. Inoue, T. Takahashi, *Phys. Lett.* B **643**, 141 (2006).
6. A. Knebe, B. Arnold, C. Power, B. Gibson, *MNRAS* **386**, 1029 (2008).
7. J. Kormendy, astro-ph0407321.
8. S.K. Lee, A. Ando, M. Kamionkowski, *JCAP* **Is.07**, Id. 007 (2009).
9. M. Rocha et al., astro-ph1208.3025.
10. A. Schneider, L. Krauss L., B. Moore, *Phys. Rev.* D **82**, 063525 (2010).
11. A. Schneider, L. Krauss L., B. Moore, astro-ph1105.4106.
12. L. Shaw, J. Weller, J. Ostriker, P. Bode, *Astrophys.Journ.* **659**, 1082 (2007).
13. M. Vogelsberger et al. *MNRAS* **423**, 3740 (2012).
14. A. Zakharov, *Gen.Rel.Grav.* **42**, 2301 (2010).
15. A. Zakharov, M. Sazhin, *Astron.Astrophys.trans.* **18**, 27 (1999).
16. D. Zhang, *MNRAS* **418**, 1850 (2011).


EPOSITO
SCI
TASI
2010

DARK MATTER PRESSURE AND COSMIC RADIATION COMPRESSIBILITY

M.Ja. Ivanov, V.K. Mamaev, G.B. Zhestkov
Central Institute of Aviation Motors (CIAM)
Moscow, 111116, 2 Aviamotornaya Str., Russia

Fundamental ideas of early XX century theoretical physics (first of all, Planck‘s, Einstein‘s and de Broglie‘s ideas) allows us to indicate a rather motivated solution for Dark Matter problem and for determination of main its parameters. Coming from relation $E = mc^2 = h\nu \approx kT$ and from Cosmic Microwave Background Radiation (CMBR) with temperature $T = 2.725K$ we can define the vacuum particle mass value $m \approx kT/c^2$. The presence of these massive particles in physical vacuum was specified in [1,2], and in [3,4,5,6,7] it was identified with massive particles of Dark Matter (DM). Further, for DM particle concentration n we can determine DM pressure $p = nkT$ and density $\rho = nm$. Consider DM as gaseous medium we define corresponded gas constant $R = k/m$ and for adiabatic coefficient of radiation $\gamma = 4/3$ the specific heat capacities c_ν and c_p [3,4,5] . The DM state equation in this case is $p = \rho RT$ and gets us only positive pressure value. Here we propose thermal equilibrium between CMBR and DM. As typical example we can calculate the critical pressure p^* in the Universe using the critical density of the Universe $\rho^* \approx 10^{(-26)} kg/m^3$ and $T = 2.725K$ from the relation $p^* = \rho^* RTPa \approx 10^{(-9)} Pa$.

Other fundamental idea of the XX century physics is the radiation compressibility (see, for example, [8]). Following [8] we can write the adiabatic relation for radiation $p/\rho^\gamma = const$. The last constant value may be easily defined using the CMBR temperature $T = 2.725K$ and the Stephan-Boltzmann constant $\sigma = 5.67_{+}10^8 W/m^2/\kappa^4$ from the Nernst theorem [3].

The main item of this talk is demonstration of experimental confirmations of DM pressure presence and its registration in the Earth conditions. We can determine additional DM (or radiation) pressure by different temperatures. The special experiment study was provided for registration of this pressure in temperature range from $300K$ up to $1200K$ [9]. We selected metallic sealed container with volume near 1 liter (Fig. 1), where inside measured very accurate pressure p and temperature T simultaneously by very slowly heating. Pressure value was registries with help of sensors ADZ SML 20 at measuring range 0-1.6 *atm* with accuracy 0.25%, temperature value was measured very accurate by 6 thermocouples.

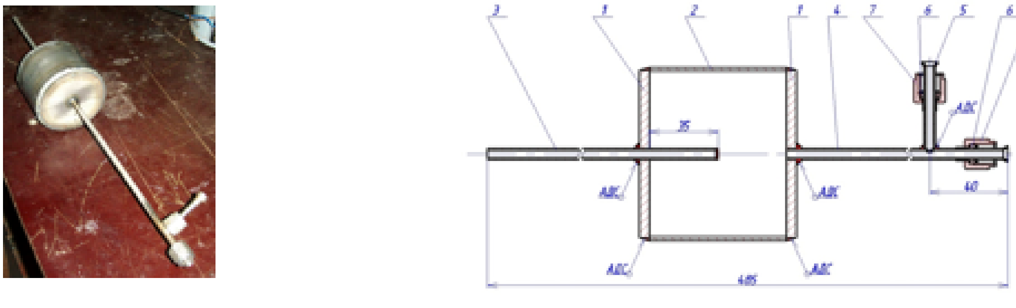

Figure 1 – The metal sealed container (VG-98) with volume near 1 liter: 1 - flat side walls - 5mm; 2 - cylindrical side wall - 2mm; 3,4 pipes; 5,6,7 pressure registration pipe to sensor; 6,7 pipe to pump.

Initial pressures inside the sealed container were selected with help of a pump and changed in the range from 0.05 atm up to 1.5 atm.

Inside container the mixture of air and DM has common pressure $p = p_g + p_r$ and equal temperatures $T_g = T_r$. The value of gas pressure p_g for different temperature we can calculate very accurate theoretically, using well known gas laws. After the DM radiation pressure can be determined as $p_r = p - p_g$. Our experimental data correspond well enough with theoretical value from (5). In particular, we had registries of DM pressure $p = 103Pa$ at $T = 600K$. We studied DM pressure behavior up to temperature $1200K$.

Fig. 2 demonstrates the changing the relative value $R = p/T/\rho$ upon temperature in K. R was divided on R_i. Top lines show heating, bottom lines cooling. Red lines include into account thermal expansion container volume. Differences between top and bottom lines give the relative value of DM pressure. Detail description of these experiments and additional data may be found in [9].

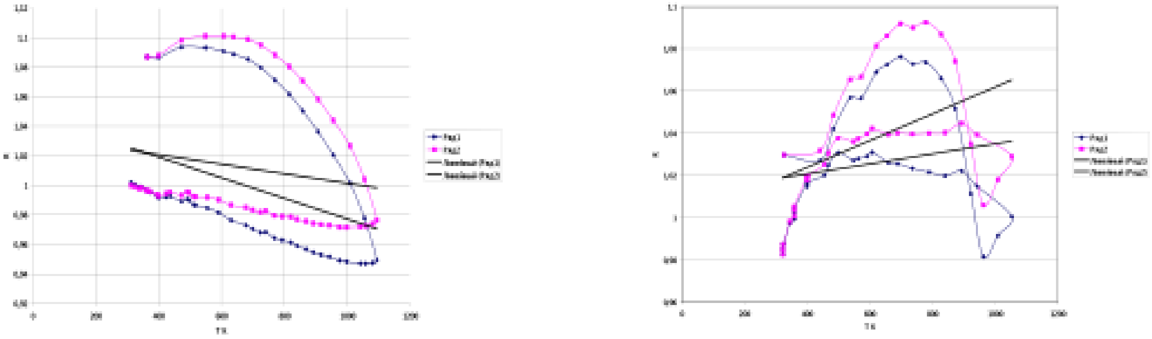

Figure 2 – . Left: Variation of relative value $R/R_{1000} = (p/T)/(p_{1000}/T_{1000})$ with temperature by $p_0 = 0.4$ atm. Right: Variation of relative value $R/R_{1200} = (p/T)/(p_{1200}/T_{1200})$ with temperature by $p_0 = 0.12$ atm.

We show special experimental data for measurement of DM pressure $p \sim 10^3 Pa$ at $T \sim 10^3 K$. This pressure value corresponds adiabatic compression of DM from cosmic conditions with $T = 2.725K$ up to the Earth conditions with $T \sim 10^3 K$ (in special vessel). Also we present implication of DM pressure in design process of high temperature air breathing engines with real practice applications.

1. M.Ja. Ivanov, “Accurate Dark Matter Theory and Exact Solutions” Proc. on IV Int. Symp. on DM&DE, Marina del Rey, CA, USA. Ed by D. B. Cline. Springer, 2001, pp. 281-289.
2. M.Ja. Ivanov, “Newtonian dark matter identification and search” Proc. III Int. Workshop on the Identification of DM. Ed. N.J.C. Spooner, V. Kudryavtsev. World Scientific. 2001. pp. 324-330.
3. M.Ja. Ivanov.“Thermodynamically Compatible Conservation Laws in the Model of Conducting Radiating Gas” J. Comp. Math. & Math. Phys., 2011, Vol. 51, No. 1, pp. 133-142.
4. M.Ja. Ivanov, G.B. Zhestkov.“Dimensional Analysis, Thermodynamics and Conservation Laws in a Problem of Radiation Processes Simulation” J. Mathematics Research, 2012, Vol. 4, No.2, pp. 10-19.
5. M.Ja. Ivanov, V.K. Mamaev. “Hidden Mass Boson” Journal of Modern Physics, 2012, Vol. 3, No. 8, pp.686-693.
6. M.Ja. Ivanov,“Classic Dark Matter Theory with Experimental Confirmations, Exact Solutions and Practical Applications” Cosmology. 47-th Rencontres de Moriond, 10 17 March, 2012, La Thuile, Aosta valley, Italy.
7. M.Ja. Ivanov.“Space Energy” In: Energy Conservation, Ed. A.Z. Ahmed, INTECH, 2012, pp.3-56.
8. R.P.Feynman , R.B.Leighton, M. Sands (1970). The Feynman Lectures on Physics: The Definitive and Extended Edition. 3 volumes (2nd ed.). Addison Wesley (published 2005, originally published as separate volumes in 1964 and 1966).
9. M.Ja.Ivanov, I.V.Tchvetkov, G.B. Zhestkov. Pressure registration inside the metallic hermetic vessel by heating from 300 up to 1200 K with different initial pressure value. In: Technical Report No. 6324 (part 2), CIAM, 2013.

List of Participants

First name	Family name	Institution	Country	Email address
Filipe	Abdalla	University College	UK	fba@star.ucl.ac.uk
Rémi	Adam	LPSC	France	adam@lpsc.in2p3.fr
Yacine	Ali-Haimoud	Institute for Advanced Study	USA	yacine@ias.edu
Marcelo	Alvarez	CITA	Canada	malvarez@cita.utoronto.ca
Mustafa	Amin	University of Cambridge	UK	mustafa.a.amin@gmail.com
Quentin	Arnaud	IPNL	France	q.arnaud@ipnl.in2p3.fr
Pierre	Astier	LPNHE	France	pierre.astier@in2p3.fr
Richard	Battye	Jodrell Bank Centre for Astrophysics	UK	Richard.Battye@manchester.ac.uk
Eric	Baxter	The University of Chicago	USA	ebaxter@uchicago.edu
Andrew	Beckwith	Chongqing University	China	rwill9955b@gmail.com
Ido	Ben-Dayan	DESY	Germany	ido.bendayan@gmail.com
Marc	Betoule	LPNHE	France	marc.betoule@lpnhe.in2p3.fr
Dario	Bettoni	Technion	Israel	dario.bettoni@gmail.com
Florian	Beutler	LBNL	USA	fbeutler@lbl.gov
Fedor	Bezrukov	University of Connecticut	USA	Fedor.Bezrukov@uconn.edu
Guillaume	Blanc	APC	France	blanc@apc.univ-paris7.fr
Alain	Blanchard	IRAP	France	alain.blanchard@irap.omp.eu
Anna	Bonaldi	Jodrell Bank Centre for Astrophysics	UK	anna.bonaldi@manchester.ac.uk
Mario	Bonamigo	LAM Laboratoire d'Astrophysique	France	mario.bonamigo@lam.fr
Cliff	Burgess	McMaster University	Canada	cburgess@pitp.ca
Stefano	Camera	CENTRA - IST	Portugal	stefano.camera@tecnico.ulisboa.pt
Marta Costanza	Campigotto	University of Torino	Italy	marta.campigotto@gmail.com
Emanuele	Castorina	SISSA	Italy	ecastori@sissa.it
David G.	Cerdeno	UAM - IFT	Spain	davidg.cerdeno@uam.es
Jens	Chluba	Johns Hopkins University	USA	jchluba@pha.jhu.edu
Ki-Young	Choi	Korea Astronomy & Space Science Inst.	South Korea	kiyoungchoi@kasi.re.kr
Sergio	Colafrancesco	Wits University	South Africa	sergio.colafrancesco@wits.ac.za
Pierre	Colin	Max Planck Institute	Germany	colin@mppmu.mpg.de
Paolo	Creminelli	ICTP	Italy	creminel@ictp.it
Giuseppe	D'Alessandro	La Sapienza	Italy	giuseppe.dalessandro@roma1.infn.it
David	Daverio	Université de Genève	Switzerland	david.daverio@unige.ch
Jonathan	Davis	Durham University	UK	j.h.davis@durham.ac.uk
Tijmen	de Haan	McGill University	Québec	tijmen@physics.mcgill.ca
Timothée	Delubac	EPFL	Switzerland	timothee.delubac@epfl.ch
Natalia	Di Marco	Lab. Nazionali del Gran Sasso	Italy	natalia.dimarco@lngs.infn.it
Clive	Dickinson	Jodrell Bank Centre for Astrophysics	UK	Clive.Dickinson@manchester.ac.uk
Joy	Didier	Columbia University	USA	didier.joy@gmail.com
Jose M.	Diego	IFCA	Spain	jdiego@ifca.unican.es
Yves	Dirian	Université de Genève	Switzerland	yves.dirian@unige.ch
Jacques	Dumarchez	LPNHE	France	jacques.dumarchez@cern.ch
Hélène	Dupuy	CEA Saclay IPhT	France	helene.dupuy@cea.fr
Patrick	El-Hage	LPNHE	France	patrickelhageuniv@gmail.com
August	Evrard	University of Michigan	USA	evrard@umich.edu
Giulio	Fabbian	SISSA	Italy	gfabbian@sissa.it
Carlos	Faham	LBNL	USA	chfaham@lbl.gov
Yabebal	Fantaye	Tor Vergata Roma 2	Italy	y.t.fantaye@astro.uio.no
Elena	Fedorova	Astronomical Observatory	Ukraine	efedorova@ukr.net
Miguel	Ferreira	CAUP	Portugal	up200802537@fc.up.pt
Raphael	Flauger	Institute for Advanced Study	USA	flauger@ias.edu
Mathilde	Fleury	LPNHE	France	mfleury@lpnhe.in2p3.fr
Silvia	Galli	IAP	France	gallis@iap.fr
Martina	Gerbino	La Sapienza	Italy	martina.gerbino@roma1.infn.it
Tuhin	Ghosh	IAS	France	tghosh@ias.u-psud.fr
Carlo	Giunti	INFN	Italy	giunti@to.infn.it

Elena	Giusarma	La Sapienza	Italy	elena.giusarma@roma1.infn.it
Jinn-Ouk	Gong	Asia Pacific Center for Th. Physics	South Korea	jinn-ouk.gong@apctp.org
Joaquin	Gonzalez-Nuevo	IFCA	Spain	gnuevo@ifca.unican.es
Krzysztof	Gorski	Caltech	USA	krzysztof.m.gorski@jpl.nasa.gov
Stefan	Gottloeber	Leibniz Institute for Astrophysics	Germany	sgottloeber@aip.de
Fabio	Governato	University of Washington	USA	fabio.governato@gmail.com
Daniel	Guariento	Universidade de São Paulo	Brazil	dguariento@pitp.ca
Augustin	Guyonnet	LPNHE	France	guyonnet@lpnhe.in2p3.fr
Luigi	Guzzo	INAF	Italy	luigi.guzzo@brera.inaf.it
Jean-Christophe	Hamilton	APC	France	hamilton@apc.univ-paris7.fr
Will	Handley	Cavendish Lab.	UK	wh260@cam.ac.uk
Matthew	Hasselfield	Princeton University	USA	mhasse@astro.princeton.edu
Phillip	Helbig		Germany	helbig@astro.multivax.de
Göran	Henriksson	University of Uppsala	Sweden	goran.henriksson@astro.uu.se
Hendrik	Hildebrandt	University of Bonn	Germany	hendrikhildebrandt@gmail.com
Jonathan	Horner	Blackett Laboratory Th. Physics	UK	j.horner11@imperial.ac.uk
Mikhail	Ivanov	Central Institute of Aviation Motors	Russia	ivanov@ciam.ru
Mindaugas	Karciauskas	University of Helsinki	Finland	mindaugas.karciauskas@helsinki.fi
Yasuhiro	Kishimoto	Kamioka Observatory ICRR	Japan	kisimoto@suketto.icrr.u-tokyo.ac.jp
Michael	Kopp	LMU	Germany	michael.kopp@physik.lmu.de
Tsz Yan	Lam	Max Planck Institute for Astrophysics	Germany	tszylam@mpa-garching.mpg.de
François	Lanusse	CEA Saclay	France	francois.lanusse@cea.fr
Andrea	Lapi	SISSA	Italy	lapi@sissa.it
Tatiana	Larchenkova	PN Lebedev Physical Institute ASC	Russia	ll7071@rambler.ru
Jean-Marc	Le Goff	CEA Saclay Irfu/SPP	France	jmlegoff@cea.fr
Florent	Leclercq	Institut d'Astrophysique de Paris	France	florent.leclercq@polytechnique.org
Boris	Leistedt	University College	UK	boris.leistedt.11@ucl.ac.uk
Ana	Leite	Centro de Astrofísica CAUP	Portugal	up200901456@fc.up.pt
Antony	Lewis	University of Sussex	UK	antony@cosmologist.info
Jia	Liu	Columbia University	USA	liuxx479@gmail.com
Claudio	Llinares	University of Oslo	Norway	claudio.llinares@astro.uio.no
Alberto	Lusiani	Scuola Normale Superiore	Italy	alberto.lusiani@pi.infn.it
Michele	Maggiore	Université de Genève	Switzerland	Michele.Maggiore@unige.ch
Christophe	Magneville	CEA Saclay DSM/Irfu/SPP	France	christophe.magneville@cea.fr
Marc	Manera	University College	UK	m.miret@ucl.ac.uk
Carlos	Martins	CAUP	Portugal	Carlos.Martins@astro.up.pt
Elena	Massara	SISSA	Italy	emassara@sissa.it
Anupam	Mazumdar	Lancaster University	UK	a.mazumdar@lancaster.ac.uk
Daan	Meerburg	Princeton University	USA	daanmeerburg@gmail.com
Peter	Melchior	The Ohio State University	USA	peter.m.melchior@gmail.com
Marius	Millea	University of California	CA	mmillea@ucdavis.edu
Ayan	Mitra	LPNHE	France	ayan.mitra@lpnhe.in2p3.fr
Anais	Möller	CEA Saclay DSM/Irfu/SPP	France	anais.moller@cea.fr
Adam	Moss	University of Nottingham	UK	adam.moss@nottingham.ac.uk
David F.	Mota	Uni. Oslo - Institute of Th. Astrophysics	Norway	mota@astro.uio.no
Jérémy	Neveu	CEA Saclay Irfu/SPP	France	jeremy.neveu@cea.fr
Toshifumi	Noumi	RIKEN Nishina Center - Math. Ph. Lab.	Japan	toshifumi.noumi@riken.jp
Malak	Olamaie	University of Cambridge	UK	m.olamaie@mrao.cam.ac.uk
Wan-il	Park	KIAS	South Korea	wipark@kias.re.kr
Subodh	Patil	CERN	Switzerland	subodh.patil@cern.ch
Jonathan	Pearson	Durham University	UK	jonathan.pearson@durham.ac.uk
Julien	Peloton	APC	France	julien.peloton@apc.univ-paris7.fr
Laurence	Perotto	LPSC	France	laurence.perotto@lpsc.in2p3.fr
Yvette	Perrott	Cavendish Lab.	UK	ycp21@mrao.cam.ac.uk
Jeffrey	Peterson	Carnegie Mellon University	USA	jbp@cmu.edu

Federico	Piazza	APC / PCCP	France	fedosquare@gmail.com
Davide	Poletti	Université Paris Diderot	France	dpoletti@apc.univ-paris7.fr
Lucia Aurelia	Popa	Institute of Space Science	Romania	lpopa@spacescience.ro
Clem	Pryke	University of Minnesota	USA	pryke@physics.umn.edu
Benjamin	Racine	APC	France	benjamin.racine@apc.univ-paris7.fr
Nicolas	Regnault	LPNHE	France	nicolas.regnault@lpnhe.in2p3.fr
Cécile	Renault	LPSC	France	rcecile@in2p3.fr
Jose M.	Rodriguez-Espinosa	Instituto de Astrofisica de Canarias	Spain	jmr.espinosa@iac.es
Graziano	Rossi	CEA Saclay	France	graziano.rossi@cea.fr
Nina	Roth	University College London	UK	n.roth@ucl.ac.uk
Clare	Rumsey	University of Cambridge	UK	cr461@mrao.cam.ac.uk
Larissa	Santos	Tor Vergata	Italy	lsantos@roma2.infn.it
Angnis	Schmidt-May	Oskar Klein Centre	Sweden	Angnis.Schmidt-May@fysik.su.se
Dominik	Schwarz	Bielefeld University	Germany	dschwarz@physik.uni-bielefeld.de
Paolo	Serra	IAS Paris Sud 11	France	paoloserr@gmail.com
Richard	Shaw	Canadian Institute for Th. Astrophysics	Canada	jrs65@cita.utoronto.ca
Christopher	Sheehy	Kavli Institute for Cosmology	USA	csheehy@uchicago.edu
Jonathan	Sievers	University of KwaZulu- Natal	South Africa	jonathan.sievers@gmail.com
Joe	Silk	IAP	Paris	silk@iap.fr
Marvin	Silva	Universidade do Porto CAUP	Portugal	marvinf.silva@gmail.com
Marta	Spinelli	LAL	France	spinelli@lal.in2p3.fr
Jack	Steinberger	CERN	Switzerland	jack.steinberger@cern.ch
Kyle	Story	University of Chicago	USA	kstory@uchicago.edu
Istvan	Szapudi	University of Hawaii	USA	szapudi@ifa.hawaii.edu
Andrea	Tartari	APC / PCCP	France	tartari@apc.univ-paris7.fr
Daniel	Thomas	Institute of Cosmology and Gravitation	UK	daniel.b.thomas@port.ac.uk
Andrew	Tolley	Case Western Reserve University	USA	andrew.j.tolley@case.edu
Julien	Tréguer	APC	France	jtreguer@apc.univ-paris7.fr
Federico	Urban	ULB	Belgium	furban@ulb.ac.be
Sofia	Vallecorsa	Université de Genève	Switzerland	Sofia.Vallecorsa@cern.ch
Filippo	Vernizzi	CEA Saclay IPhT	France	filippo.vernizzi@cea.fr
Aion	Viana	Max Planck Institute für Kernphysik	Germany	aion.viana@mpi-hd.mpg.de
Pauline	Vielzeuf	Centro de Astrofísica CAUP	Portugal	Pauline.Vielzeuf@astro.up.pt
Alexander	Vikman	LMU Munich ASC	Germany	vikman@cern.ch
Jacques	Wagstaff	Hamburger Sternwarte	Germany	jwagstaff@hs.uni-hamburg.de
Joseph	Walding	University of London	UK	joseph.walding@gmail.com
Quentin	Wallemacq	Université de Liège	Belgium	quentin.wallemacq@ulg.ac.be
Jochen	Weller	Ludwig Maximilians University	Germany	jochen.weller@usm.lmu.de
Richard	Wolstenhulme	Kavli Institute for Cosmology	UK	rw481@cam.ac.uk
Steven	Worm	Rutherford Appleton Lab.	UK	worm@cern.ch
Masahide	Yamaguchi	Tokyo Institute of Technology	Japan	gucci@phys.titech.ac.jp
Gustavo	Yepes	Universidad Autonoma de Madrid	Spain	gustavo.yepes@uam.es
Juande	Zornoza	IFIC CSIV-UV	Spain	zornoza@ific.uv.es